

Fortschritte in der numerischen Modellierung von Photo-Dissoziationsregionen

Markus Röllig

I. Physikalisches Institut der Universität zu Köln

Habilitationsschrift

eingereicht bei der Mathematisch-Naturwissenschaftlichen
Fakultät der Universität zu Köln, November 2012

Aufbau der Habilitationsschrift

Die vorliegende Habilitationsschrift beschreibt die Entwicklung des numerischen PDR Modell Codes KOSMA- τ während der letzten Dekade. In der Astrophysik ist es selten möglich ein Experiment zu präparieren, um damit einzelne Einflussgrößen isoliert zu studieren. Astronomische Beobachtungen messen Vorgänge immer in ihrer *vollen Komplexität*. Astrophysikalische Modelle nehmen daher oft den Platz ein, den Experimente in der klassischen Physik haben. Sie machen es möglich, den Einfluss einzelner Prozesse auf das ganze System zu studieren.

Entwicklung, Tests und Verfeinerungen solcher Modelle gehen immer Hand in Hand mit astronomischen Beobachtungen und Analysen, die ihrerseits von jeweiligen Stand der Beobachtungstechnik abhängen. Wie immer in der Physik führen Beobachtungen mit neuen, modernen Instrumenten oft zu Erkenntnissen, die die Veränderung oder Erweiterung der physikalischen Modelle erfordern und damit unser Verständnis der lokalen astrophysikalischen Prozesse voran treiben.

Beides, Entwicklung **und** Anwendung des Modells zur Interpretation astronomischer Messungen, stehen aber in engem Zusammenhang. Das spiegelt sich in der Zusammenstellung der präsentierten Publikationen wider, bei der ich sowohl die theoretischen Veröffentlichungen, wie auch eine kleine Auswahl der wichtigsten anwendungsbezogenen Publikationen berücksichtigt habe.

Auflistung der als Habilitationsschrift eingereichten Veröffentlichungen

Publikation 1: M. Röllig, V. Ossenkopf, S. Jeyakumar, J. Stutzki und A. Sternberg, 2006, *[C II] 158 μm emission and metallicity in photon dominated regions*, *Astronomy & Astrophysics*, 451, 917-924

Publikation 2: M. Röllig, et al., 2007, *A photon dominated region code comparison study*, *Astronomy & Astrophysics*, 467, 187-206
Highlighted Paper in Astronomy & Astrophysics

Publikation 3: V. Ossenkopf, M. Röllig, R. Simon, et al., 2010, *HIFI observations of warm gas in DR21: Shock versus radiative heating*, *Astronomy & Astrophysics*, 518, L79

Publikation 4: M. Röllig, 2011, *Refit to numerically problematic UMIST reaction rate coefficients*, *Astronomy & Astrophysics*, 530, A9

Publikation 5: M. Röllig, R. Simon, R. Güsten, et al., 2012, *[C II] gas in IC 342*, 2012, *Astronomy & Astrophysics*, 542, L22

Publikation 6: J. L. Pineda, N. Mizuno, M. Röllig, et al., 2012, *Submillimeter line emission from LMC 30 Doradus: The impact of a starburst on a low-metallicity environment*, *Astronomy & Astrophysics*, 544, 84

Publikation 7: M. Röllig, R. Szczerba ,V. Ossenkopf und C. Glück, 2012, *Full SED fitting with the KOSMA- τ PDR code - I. Dust modelling*, *Astronomy & Astrophysics*, im Druck

Publikation 8: M. Röllig und V. Ossenkopf, 2012, *Carbon fractionation in PDRs*, *Astronomy & Astrophysics*, im Druck

Publikation 9: V. Ossenkopf, M. Röllig, et al., 2012, *Herschel/HIFI observations of [C II]/[^{13}C II] in PDRs*, *Astronomy & Astrophysics*, im Druck

Beschreibung des Fremdbeitrages bei Veröffentlichungen mit mehreren Autoren

Publikation 1

V. Ossenkopf, damals *Calibration scientist* am SRON National Institute for Space Research in Groningen, Niederlande, hat an der Beschreibung der untersuchten Heiz- und Kühlprozesse mitgearbeitet und die Näherung für die H₂ Vibrationsheizung erstellt. S. Jeyakumar war von 2001-2003 wissenschaftlicher Mitarbeiter am I. Physikalischen Institut der Universität zu Köln und war in dieser Zeit zuständig für die Wartung und Betreuung des PDR Codes. Von 2003 an habe ich diese Aufgabe übernommen. Die Untersuchung des metallizitätseinflusses, die semi-analytischen Näherungen für die heiz- und Kühlprozesse, sowie die Variation der C⁺ Schichtdicke und ihre Linienemission bei verschiedenen Metallizitäten wurden von mir erstellt. A. Sternberg hat den ursprünglichen numerischen PDR für plan-parallele Konfiguration geschrieben und an der Erweiterung auf sphärische Geometrie mitgearbeitet. J. Stutzki ist ordentlicher Professor am I. Physikalischen Institut der Universität zu Köln und hat die Entwicklung von KOSMA- τ initiiert und begleitet.

Publikation 2

Publikation 2 ist eine große, internationale Vergleichsstudie aller renommierter PDR Modell Codes. Sie fasst die wesentlichen Ergebnisse des ersten internationalen Workshops zur PDR Modellierung im Jahr 2004 zusammen. Ich war bei der Vorbereitung und Durchführung des Workshops wesentlich beteiligt und war federführend bei der Aufarbeitung und Analyse der Ergebnisse sowie der anschließenden Veröffentlichung der Workshopergebnisse.

In der Studie werden wichtige Einflussgrößen auf die Modellergebnisse identifiziert und studiert sowie die Modellergebnisse für eine Reihe von Benchmark-Problemen präsentiert und verglichen. Die Ko-Autoren der Publikation sind die verantwortlichen Entwickler aller beteiligten PDR-Modelle und haben die Modellergebnisse ihre Modells beigetragen.

Die Publikation wurde von *Astronomy & Astrophysics* als "Highlighted Paper" besonders hervorgehoben.

Publikation 3

V. Ossenkopf ist PI des Herschel Guaranteed Time Key Projects WADI: *Warm and Dense ISM*, dessen Daten in Teilen präsentiert und mit Modellergebnissen verglichen werden. Die weiteren Ko-Autoren sind Mitglieder des internationalen WADI-Konsortiums. Herr Ossenkopf hat die Datenreduktion und -analyse

durchgeführt, ich habe die PDR-Modellierung und die anschließende Interpretation der Modellergebnisse beigesteuert.

Publikation 5

R. Simon ist wissenschaftlicher Mitarbeiter am I. Physikalischen Institut der Universität zu Köln. Die weiteren Ko-Autoren sind Mitglieder des internationalen GREAT-Konsortiums unter der Leitung des GREAT PI: R. Güsten, deren vorbereitender Beitrag zu den GREAT Beobachtungen in den GREAT First-Light Veröffentlichungen gewürdigt wird. R. Simon und R. Güsten haben die Beobachtungen durchgeführt und begleitet. R. Simon hat die Datenreduktion und -aufarbeitung durchgeführt. Ich habe die Beobachtungen geplant und die Datenanalyse und PDR-Modellierung durchgeführt sowie die Ergebnisse interpretiert.

Publikation 6

J. Pineda hat mit dem NANTEN2 Teleskop die 460/90 und 810 GHz Beobachtungen der Großen Magellanschen Wolken durchgeführt, zusammen mit N. Mizuno von der Nagoya University in Japan. Von ihm stammen die Datenreduktion und -analyse, die Anregungsanalyse sowie die Interpretation der Ergebnisse. Die PDR-Modellierung der Daten wurde von mir durchgeführt.

Publikation 7

R. Szczerba ist Entwickler des numerischen MCDRT Codes zur Berechnung des thermischen Gleichgewichts und des Kontinuum-Strahlungstransports für Mehrkomponenten-Staub und hat an der Integration der MCDRT Ergebnisse in KOSMA- τ mitgearbeitet. V. Ossenkopf leitet das Teilprojekt C1: *Modelling of irradiated molecular clouds* des Sonderforschungsbereichs 956, in dessen Rahmen die PDR Modellierung mittels des KOSMA- τ Modells seit 2011 angesiedelt ist. Er hat an der Planung und Durchführung der Staub-Erweiterung mitgearbeitet. Die Integration der MCDRT-Ergebnisse in KOSMA- τ , die Erweiterung der H₂-Bildung ist von mir und C. Glück, Doktorand am I. Physikalischen Institut, geleistet worden. Die Untersuchung der Photodissoziationsraten bei unterschiedlichen Staubeigenschaften sowie die Analyse des Einflusses der Codeänderung ist von mir geleistet worden.

Publikationen 8 und 9

V. Ossenkopf leitet das Teilprojekt C1: *Modelling of irradiated molecular clouds* des Sonderforschungsbereichs 956, in dessen Rahmen die PDR Modellierung

mittels des KOSMA- τ Modells seit 2011 angesiedelt ist. Er hat an der Analyse der chemischen Fraktionierungsergebnisse mitgearbeitet. Er ist außerdem Projektleiter (*principal investigator PI*) des Herschel Guaranteed Time Key Projects WADI: *Warm and Dense ISM*. WADI hat die Beobachtungen geliefert, die mit den Modellierungsergebnissen verglichen werden. Ich habe die Routine zur Isotopisierung erstellt und angewendet, sowie das Fraktionierungsverhalten analysiert. V. Ossenkopf hat die [^{13}C II] Beobachtungen reduziert und analysiert. Die restlichen Ko-Autoren sind Mitglieder des WADI Konsortiums und verantwortlich für die Planung und Durchführung der Beobachtungen.

Inhaltsverzeichnis

Inhaltsverzeichnis	3
1 Einleitung	5
1.1 Photodissoziations-Regionen	7
2 Numerische PDR Modellierung	11
2.1 Das gekoppelte chemisch-physikalische Problem	11
2.2 Einflussgrößen von PDR Modellen	13
3 Entwicklung des KOSMA-τ PDR Modells	29
3.1 Metallarme/-reiche PDRs	30
3.2 Benchmark	32
3.3 Klumpige PDR-Struktur	34
3.4 Isotopenchemie	36
3.5 Selbstkonsistente Behandlung der Staubeigenschaften	37
3.6 Modellanwendung	38
4 Ausblick	43
Literatur	45
A Publikationen	55
[C II] 158 μ m emission and metallicity in PDRs	57
A photon dominated region code comparison study	71
HIFI observations of warm gas in DR21: Shock versus radiative heating	99
Refit to numerically problematic UMIST reaction rate coefficients . .	105
[C II] gas in IC 342	117
Submillimeter line emission from LMC 30 Doradus: The impact of a starburst on a low-metallicity environment	121
Full SED fitting with the KOSMA- τ PDR code - I. Dust modelling . .	133
Carbon fractionation in PDRs	155
Herschel/HIFI observations of [C II] / [^{13}C II] in PDRs	181

B Lebenslauf	195
C Publikationsliste	197

1 Einleitung

Das sichtbare Universum ist dominiert von Sternen. Ihre Verteilung, ihre Leuchteigenschaften sowie ihr Lebenszyklus bestimmen die Struktur aller bekannten Galaxien. Nur wenige Prozent der gesamten baryonischen Masse einer Galaxie liegt in Form von Gas und Staub vor, dem sogenannten *interstellaren Medium (ISM)*, das zu großen Teilen in Form von Molekülwolken vorliegt. Trotz seines relativ kleinen Massenanteils steht das ISM in regem Austausch mit den Sternen:

- Bei genügend großer Masse werden Molekülwolken gravitativ instabil (Jeans-Instabilität), kollabieren und bilden die Geburtsstätten neuer Sterne.

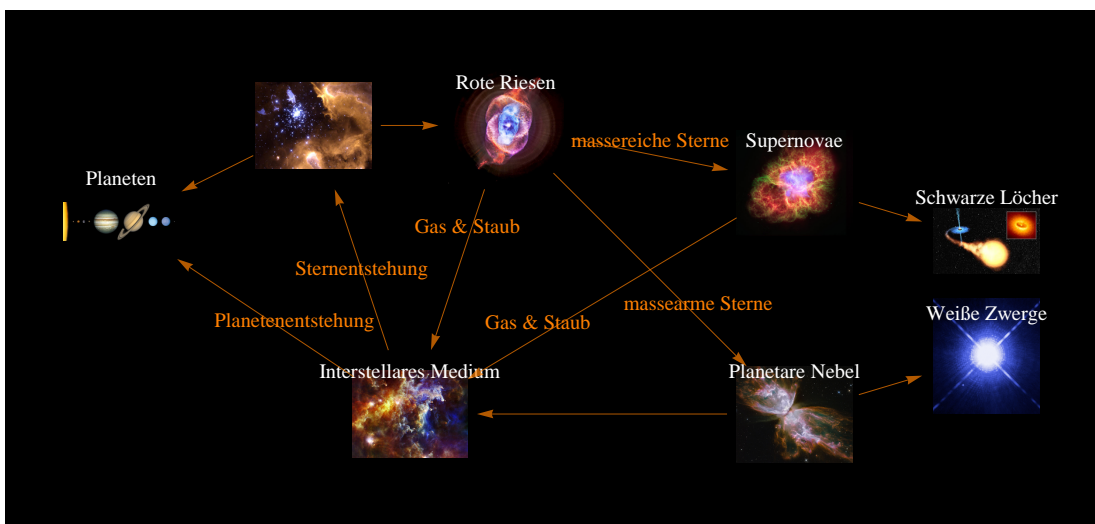


Abbildung 1.1: Kosmischer Materiekreislauf

- Ein großer Teil der Sternmasse wird im Laufe eines Sternlebens in Form von Sternwinden wieder an das umgebende ISM abgegeben, bei sehr massiven Sternen bis über 90%.
- Jeder Stern jenseits einer Masse von ca. 8 Sonnenmassen M_{\odot} endet als Supernova (SN), einer enorm energiereichen Sternenexplosion, die noch-

mals große Mengen von Material explosiv in den umgebenden Raum abgibt.

- Rote Riesensterne und Überriesen auf dem sogenannten *asymptotischen Riesenast, AGB*, gelten als wichtigste Produktionsorte interstellaren Staubes (Gail u. a. 2009). Die hohe Konzentration schwerer Elemente, verbunden mit vergleichsweise niedrigen Temperaturen und UV-Strahlungsintensitäten, erlaubt die Bildung von kohlenstoff- und silikatbasierten Riesenmolekülen und Staubkörnern. Sternwind, Strahlungsdruck und Schockwellen von Supernova-Explosionen verteilen den Staub an das ISM.
- Bei einer massenmäßigen Sternentstehungseffizienz (*star formation efficiency*) von nur wenigen Prozent wird jeweils nur ein geringer Anteil der Geburtswolke in Sterne gewandelt. Der Rest verbleibt als Gas und Staub. Nach der Bildung von sehr massereichen Sternen folgt schon wenige Millionen Jahre nach der Geburt der Sterntod in Form einer SN-Explosion, die große Mengen an kinetischer Energie in das umgebende Medium platziert und starke Schockwellen erzeugt (Elmegreen und Lada 1977). Diese Schocks können die umgebenden Molekülwolken entweder weiter verdichten und weitere Sternentstehung triggern oder aber das ISM zerstreuen und weitere Sternentstehung verhindern (z.B. Sandford, Whitaker und Klein 1982; Whitworth u. a. 1994; Dale, Bonnell und Whitworth 2007; Dirienzo u. a. 2012).
- Sterne bestimmen die chemische und physikalische Struktur von Molekülwolken und haben damit weiteren Einfluss darauf, ob eine Wolke weiter Sterne bilden kann oder nicht. Energieriche Strahlung der Sterne wechselwirkt mit dem ISM, sie heizt Gas und Staub und ionisiert und dissoziert Atome und Moleküle. Massereiche Sterne emittieren UV-Strahlung und erzeugen Blasen heißen ionisierten Gases um sie herum, sogenannte HII Regionen, in denen keine Sternentstehung möglich ist.
- Sterne sorgen für eine chemische Anreicherung des ISM. Das primordiale Gas, d.h. das ISM kurz nach dem Urknall, enthielt nur Wasserstoff, Helium und Spuren schwererer Elemente wie Lithium. Nur durch Kernfusion im Inneren von Sternen kann sich die elementare Zusammensetzung des Gases verändern. Mit jeder Generation von Sternen, die ihr Material an die Umgebung abgeben, wird das ISM weiter mit schwereren Elementen angereichert.

Die theoretischen Aspekte der Sternentstehung sind beispielsweise in McKee und Ostriker (2007) zusammengefasst.

1.1 Photodissoziations-Regionen



Abbildung 1.2: 3-Farben Komposit-Aufnahme des Rosette Molekülwolkenkomplexes, beobachtet mit dem Herschel Weltraumteleskop (PACS 70 μ m (blau), PACS 160 μ m (grün), und SPIRE 250 μ m (rot)). Die Aufnahme wurde während der *Science Demonstration Phase* des HOBYS Key Programms beobachtet.

Photodissoziations-Regionen, oft auch Photonendominierte Regionen genannt, sind Bereiche im ISM, in denen Fern-ultraviolet-Photonen (FUV: 6-13.6 eV) das Energiegleichgewicht und/oder die chemische Zusammensetzung des Gases dominieren (Tielens und D. Hollenbach 1985; D. J. Hollenbach und Tielens 1997; D. J. Hollenbach und Tielens 1999; Tielens 2005). Uns interessieren dabei vor allem die Grenzregionen zwischen dem molekularen und dem ionisierten/atomaren Gas¹. Salopp gesagt, interessiert uns die *Haut* von Mole-

¹Aus diesem Grund bevorzugen wir den Begriff der Photodissoziationsregion (PDR), da er besser von anderen Regionen, in denen Photonen dominieren, wie z. Bsp. HII -Regionen oder Sternatmosphären, unterscheidet.

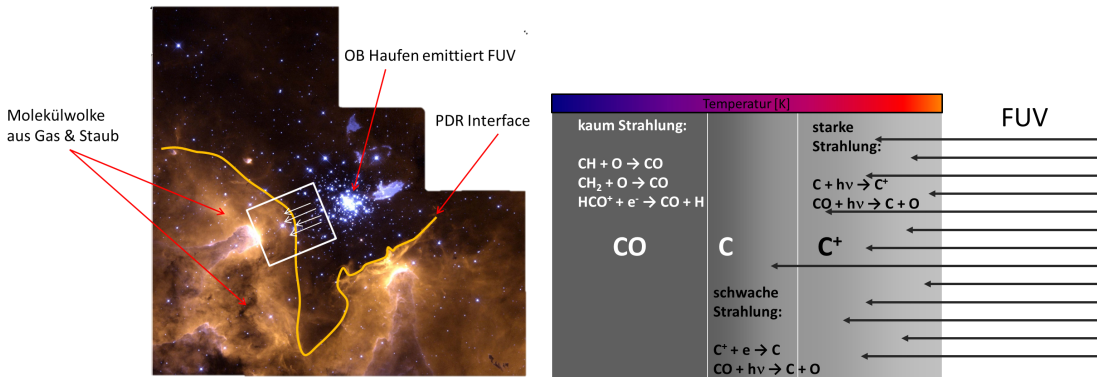


Abbildung 1.3: **Links:** PDR Interfaceregion am Beispiel von NGC 3603 (gelb hervorgehoben). **Rechts:** Beispielhafte chemische Schichtung einer PDR (entspricht einer Ausschnittsvergrößerung der weißen Box im linken Bild).

külwolken (siehe auch Abb. 1.3). PDRs lassen sich umso leichter beobachten, je stärker die auftreffende FUV Strahlung ist, da hoher Energieinput mittels FUV einen hohen Energieoutput in Form von Linien- und Kontinuumsemissionen bewirkt.

Da FUV Photonen im Wesentlichen von massereichen Sternen emittiert werden, deren Strahlungsfluss mit dem Abstandsquadrat abnimmt, beobachtet man PDRs vor allem in der unmittelbaren Nachbarschaft von aktiven Sternentstehungsregionen mit massiver Sternentstehung². Das Studium von PDRs ist damit eng verbunden mit dem Studium der Entstehung massiver Sterne, vor allem wenn man bedenkt, dass Gas und Staub innerhalb der PDR Überreste des Ausgangsmaterials der jungen Sterne sind. Wenn wir wissen, welche chemische Zusammensetzung in der PDR herrscht, kennen wir die Startbedingungen innerhalb der jungen Sterne.

Formal grenzt man eine PDR von der näher zum Stern liegenden HII - Region durch die Abwesenheit von Photonen mit Energien $h\nu > 13.6 \text{ eV}$, der Ionisationsenergie von atomarem Wasserstoff, ab. Auf ihrem Weg in die Molekülwolke schwächt sich die FUV Strahlung weiter ab und erlaubt zuerst die Bildung von molekularem Wasserstoff H₂. Andere Elemente liegen vor allem in ihrer ionisierten oder atomaren Form vor. Bei höheren Extinktionen A_V können diese Ionen dann mit den freien Elektronen rekombinieren und komplexe Moleküle formen.

Von besonderer Bedeutung ist dabei die Kohlenstoffchemie. Kohlenstoff ist nach H, He und O das vierhäufigste Element im Universum und bildet zu-

²Aufgrund der niedrigen Lebensdauer massiver Sterne in der Größenordnung von wenigen Millionen Jahren, haben junge, massive Sterne zu wenig Zeit um ihren Geburtscluster zu verlassen.

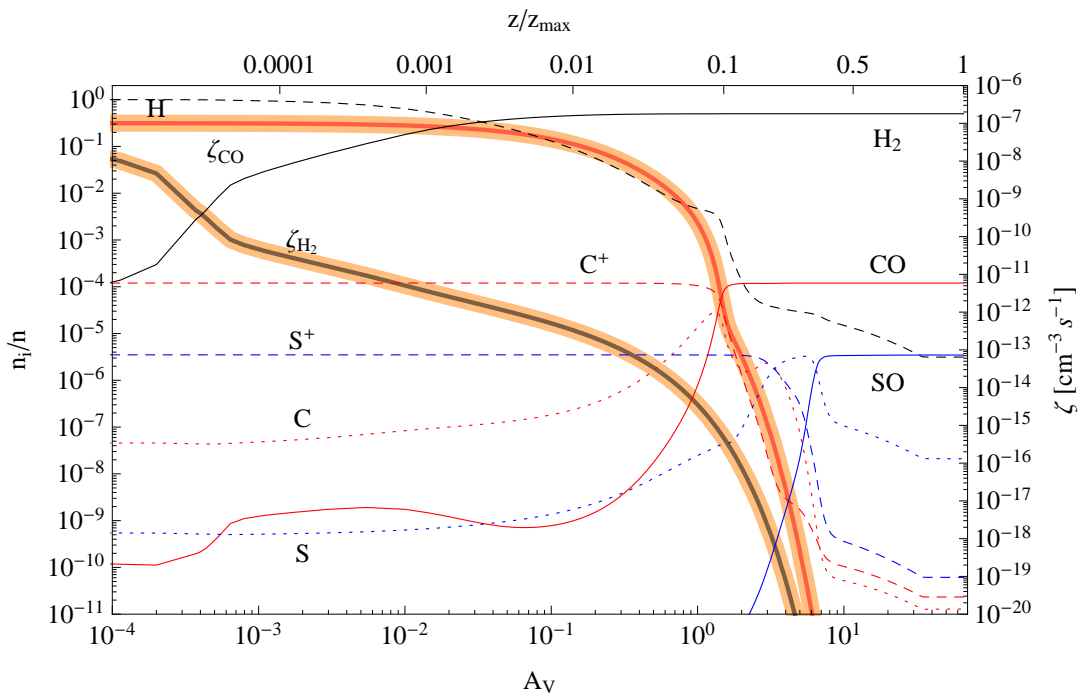


Abbildung 1.4: Dichteprofil einer Modellwolke mit $n = 10^5 \text{ cm}^{-3}$, $M = 10 M_\odot$, und $\chi = 1000$, aufgetragen gegen die optische Extinktion A_V . Orange unterlegt sind die Photodissoziationsraten von CO, ζ_{CO} , und H_2 , ζ_{H_2} , gezeigt. Die obere Abszisse zeigt die zugehörigen relativen Wolkentiefen z/z_{\max} . Die rechte Ordinate zeigt die Photodissoziationsraten.

sammen mit Sauerstoff Kohlenmonoxid CO, dem nach H_2 häufigsten Molekül im ISM. CO wird vor allem durch Photodissoziation wieder zerstört, sodass ein Großteil des verfügbaren Kohlenstoff in Form von CO vorliegt, sobald es ausreichend vor FUV Photonen abgeschirmt ist. Da die Photodissoziation von CO, genau wie die von H_2 , ein Linienabsorptionsprozess ist, können die entsprechenden Absorptionslinien sehr schnell hohe optische Tiefen τ entwickeln (van Dishoeck und Black 1988; Visser, van Dishoeck und Black 2009), was einer effektiven Abschirmung entspricht.

Der Effekt wird in Abb. 1.4 verdeutlicht. Die Abbildung zeigt Modellergebnisse einer sphärischen Modellwolke mit einer Dichte $n \approx 2 \times 10^5 \text{ cm}^{-3}$, einer Wolkenmasse von 10 Sonnenmassen M_\odot , und einer isotropen FUV Einstrahlung von $\chi = 1000$ in Einheiten des Draine Feldes (B. T. Draine 1978). Die relativen Häufigkeiten einiger wichtiger Spezies ist gegen A_V und die zugehörige relative Tiefe (obere Abszisse) gezeigt. In zunehmend tieferen Wolkenschichten rekombiniert erst H_2 , dann CO und SO. Die resultierende Schichtung ist ein typisches, theoretisch vorhergesagtes, Merkmal von PDRs. Ein weiteres prominentes Beispiel für eine ähnliche Schichtstruktur ist in Abb. 1.5 zu se-

hen.

Mit zunehmender Tiefe in die PDR hinein sieht man die Schichtung von PAHs (Polyzyklische Aromatische Kohlenwasserstoffe), molekularem Wasserstoff H₂ und Kohlenmonoxid CO. PAHs zeigen die Bereiche mit sehr heißem Staub. Etwas tiefer leuchtet der H₂ 1–0 S(1) ro-vib Übergang auf ($\Delta E = 1015 \text{ K}$) und noch tiefer in der Wolke sieht man die $J = 1 - 0$ Rotationslinie von CO. Diese Schichtung entspricht genau den Vorhersagen numerischer PDR Modelle (D. J. Hollenbach und Tielens 1999).

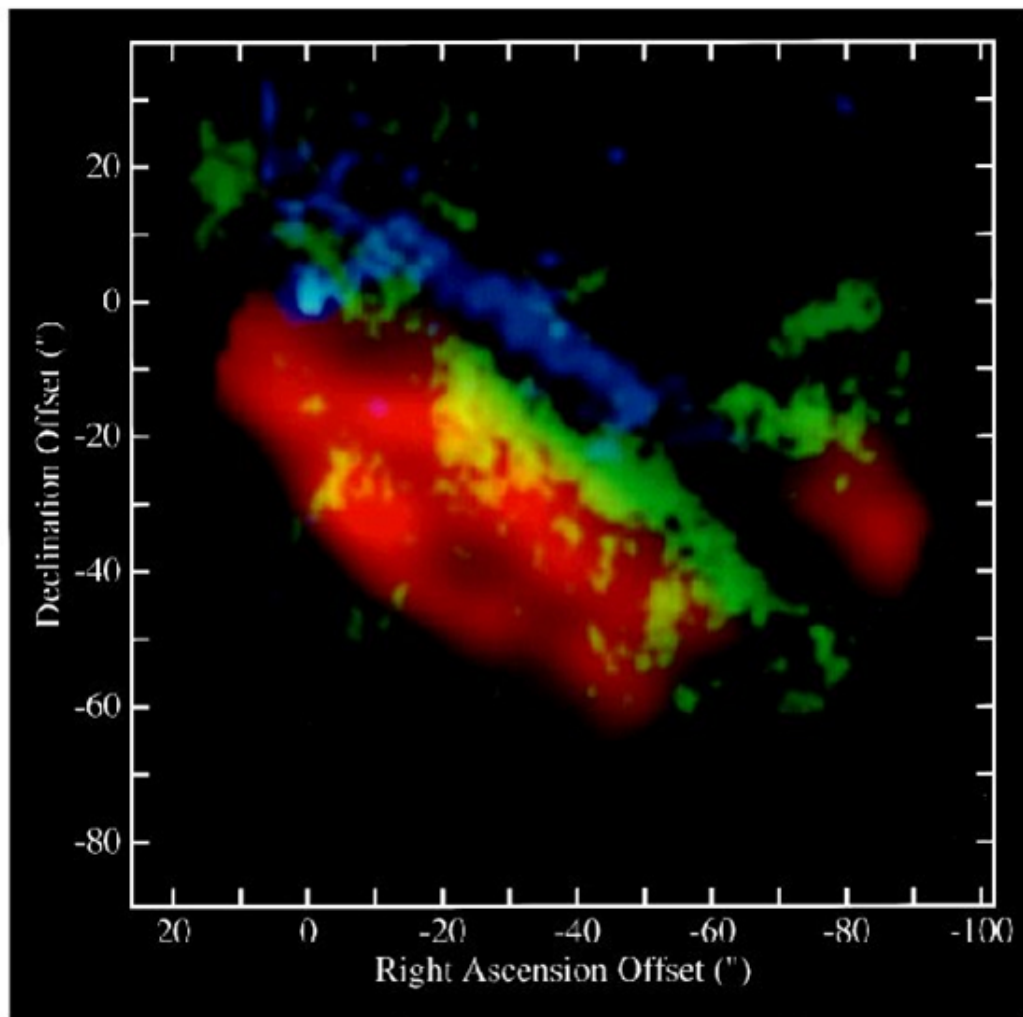


Abbildung 1.5: Kartierung der sogenannten *Orion Bar* Region. In blau sieht man PAH Emission bei 3.3 μm , in gelb, H₂ 1-0 S(1) Emission und in rot CO(1-0) Strahlung. Der anregende Stern $\theta^1 \text{ C Ori}$ liegt oben oben rechts (Abbildungsnnachweis: D. J. Hollenbach und Tielens 1999).

2

Numerische PDR Modellierung

2.1 Das gekoppelte chemisch-physikalische Problem

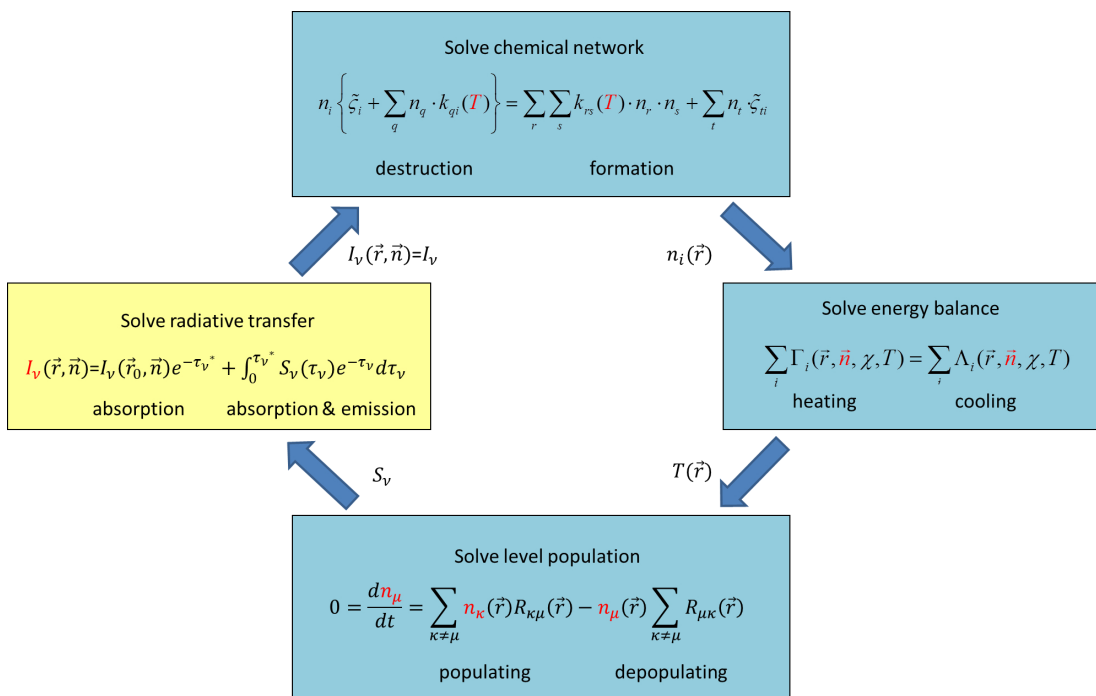


Abbildung 2.1: Schematische Darstellung eines üblichen Iterationsschemas in PDR Modellen. Blau signalisiert ein lokales Problem, gelb ein nicht-lokales Problem.

PDR Modelle werden seit über 30 Jahren verwendet, um die physikalische und chemische Struktur des ISM zu entschlüsseln. Grundsätzlich arbeiten alle PDR Modelle nach dem gleichen Prinzip. Es gilt, 4 prinzipielle Probleme iterativ numerisch zu lösen und zur Konvergenz zu bringen:

- Lösung des Energiegleichgewichts zur Bestimmung der lokalen Temperatur von Gas und Staub. Das beinhaltet die Berücksichtigung der relevanten Heiz- und Kühlprozesse.

- Lösung des chemischen Gleichgewichts, also Lösung des chemischen Ratengleichungssystems¹, zur Bestimmung der lokalen Häufigkeiten aller beteiligten chemischen Spezies.
- Lösung des Populationsproblems, also die Bestimmung der relativen Besetzung aller relevanten Energiezustände, in denen sich eine Spezies befinden kann. Das geschieht durch die Lösung des zugehörigen Ratengleichungssystem, welches alle populierenden und de-populierenden Prozesse für alle Energiezustände aller Spezies erfasst.
- Lösung des Strahlungstransportproblems, also nicht-lineare, nicht-lokale Kopplung der verschiedenen Ortspunkte entlang eines Sehstrahls durch die PDR für alle relevanten Sehstrahlen.

Dabei kann jedes einzelne der genannten Problembereich in eine Vielzahl von Unterproblemen zerlegt werden. So bedeutet Lösung des Energiegleichgewichts beispielsweise die lokale Bilanzierung aller wichtigen Heiz- und Kühlprozesse. Welche Prozesse wichtig bzw. unwichtig sind, hängt im Wesentlichen von dem Anwendungsbereich des Modells und dem jeweiligen Parameterbereich ab. Heizung durch kosmische Strahlung dominiert beispielsweise im strahlungsabgeschirmten Zentrum von Molekülwolken, ist an deren Oberflächen jedoch vernachlässigbar. Ambipolare Diffusion wiederum wird meistens vernachlässigt, kann jedoch bei C Schocks eine wichtige Rolle spielen. Auch die Art und Weise, in der einzelne Prozesse modelliert werden, kann sich von Modell zu Modell wesentlich unterscheiden (Details dazu habe ich in Publikation 2 diskutiert). Die Berechnung, ausgehend von *first principles* bzw. Berücksichtigung aller mikrophysikalischen Vorgänge, ist extrem rechenaufwendig, kann aber starken Einfluss auf die Modellergebnisse haben (Beispiel: Berechnung der photoelektrischen Heizrate mittels genauer Bilanz des Ladungszustandes aller Staubpartikel (van Hoof u. a. 2004; Le Petit, Nehmé u. a. 2006) gegenüber einer parametrisierten Näherungsformel (Bakes und Tielens 1994; J. C. Weingartner und B. T. Draine 2001) oder die Berechnung des chemischen Gleichgewichts mittels Ratengleichungen gegenüber dem Master-Gleichungs-Ansatz (z.Bsp. Le Petit, Barzel u. a. 2009).)

Abbildung 2.1 zeigt einen weiteren wesentlichen Punkt bei der PDR Modellierung, nämlich die Kopplung von lokalen und nicht-lokalen Prozessen. Im Prinzip sind die Bestimmung von Dichte, Temperatur und Anregungszustand des ISM lokale Probleme. Durch ihre Abhängigkeit von der Strahlungsintensität erfolgt jedoch eine nicht-lokale Kopplung dieser Prozesse entlang

¹auch chemisches Netzwerk genannt

aller Sehstrahlen. Über die Strahlungstransportgleichung sind die verschiedenen Bereiche einer PDR miteinander gekoppelt, womit die geometrische Struktur der Wolke sowie die räumlich-physikalischen Eigenschaften (Streueigenschaften, Isotropie des FUV Strahlungsfeldes, usw.) Einfluss nehmen auf die Mikrophysik. Diese nicht-lokale, nicht-lineare Kopplung macht numerische PDR Modellierung zu einem äußerst komplexen Problem.

2.2 Einflussgrößen von PDR Modellen

Wie im vorherigen Abschnitt erläutert, umfasst die numerische PDR Modellierung eine Vielzahl von Konzept- und Implementierungsentscheidungen, die einander in einigen Fällen auch gegenseitig ausschließen. Aus diesem Grund sind PDR Modelle häufig für einen bestimmten Anwendungsbereich maßgeschneidert. Einige Beispiele umfassen: Galaktische Sternentstehungsregionen, Planetare Nebel, Kerne aktiver Galaxien (AGNs), Protoplanetare Akkretions scheiben, Bipolare Ausflüsse von T Tauri Sternen, Bok-Globulen und massearme Sternentstehung, das diffuse ISM in der Galaktischen Ebene, FUV be strahlte Schocks, usw.. Die Modellierung von Röntgen-Dominierten Regionen (XDRs) in AGNs ist eng verwandt mit der von PDRs, impliziert jedoch andere dominante physikalische Effekte. Planetare Nebel legen sphärische Modellgeometrie näher, wohingegen protoplanetare Scheiben einfacher mittels plan-parallelen PDR Modellen genähert werden können. Die vielfältigen Anwendungsbereiche erschweren gleichzeitig die Vergleichbarkeit von Modellergebnissen verschiedener numerischer Modell-Codes. In Publikation 2 habe ich einige der damit verbundenen Schwierigkeiten und Chancen vorgestellt und diskutiert. Bereits solch einfache Konzepte, wie das einer Säulendichte ($N_i = \int n_i(s)ds$) oder der optischen Extinktion A_V , sind nicht ohne weiteres von einer Modellgeometrie auf die andere übertragbar.

Modell-Geometrie

Eine wesentliche Modelleigenschaft ist die Modellgeometrie, also die geometrische Anordnung des ISM sowie die Richtungseigenschaften der FUV Ein strahlung. Die allermeisten PDR Modelle lösen ein eindimensionales Problem und realisieren die Modellgeometrie mittels entsprechender Symmetrieeigen schaften. Die Eindimensionalität legt einmal eine klassische, plan-parallele Struktur (einseitig infinit oder finit, beidseitig beschienen) nahe oder aber eine finite, sphärische Konfiguration, was jedoch gleichzeitig eine isotrope Beleuch

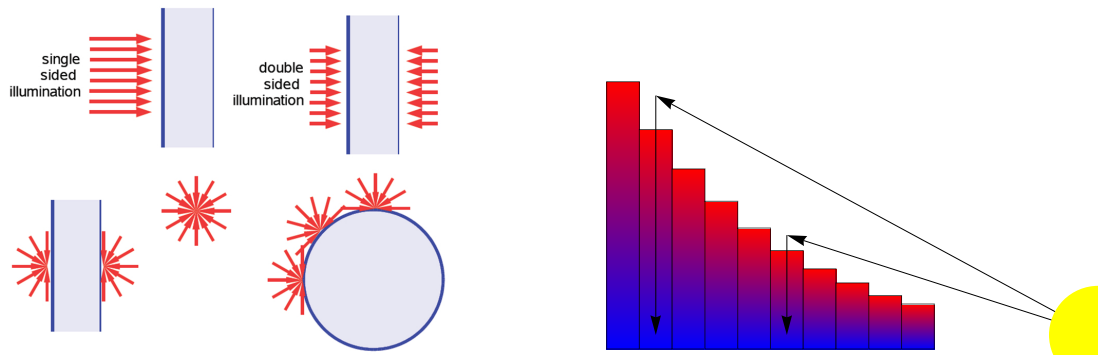


Abbildung 2.2: **Links:** Überblick über übliche Modellgeometrien der Molekülwolke sowie des FUV Strahlungsfeldes. **Rechts:** Beispiel für eine 1D+1D Geometrie bei der Näherung zirkumstellarer Scheiben durch geschichtete planparallele Schichten.

tung impliziert. Abbildung 2.2 skizziert einige mögliche Konfigurationen².

Selbstverständlich sollte eine Modellgeometrie die realen Verhältnisse bestmöglich widerspiegeln. Sie liefert damit zusätzliche, wichtige Einschränkungen der Modellparameter. Auch wenn es oft schwierig ist, aus astronomischen Beobachtungen, auf die geometrische Struktur eines Objekts zu schließen (die De-Projektion der Daten in eine 3-D Vorstellung ist eines der großen, grundlegenden astronomischen Probleme), lassen sich oft eine ganze Reihe von Randbedingungen formulieren, die von Modellen beachtet werden müssen. Beispiele dafür sind die gesamte Säulendichte verschiedener Spezies, die gesamte Masse im Beam, die Entfernung usw..

Unterschiedliche Geometrien implizieren auch unterschiedliche Verhältnisse von Wolkenoberfläche zu Wolkenvolumen. Das ist relevant, da verschiedene Wolkenregionen unterschiedlich zu der Emission der einzelnen Spezies beitragen. Die heiße, vorwiegend ionisierte Oberfläche liefert beispielsweise die gesamte Intensität der C⁺ Feinstruktur-Emissionslinie $^2P_{3/2} - 2P_{1/2}$ bei 158 μ m oder der hoch-angeregten Rotationsübergangslinien (*high-J*) von CO, wohingegen die tieferen, kalten Wolkenschichten hauptsächlich die low-*J* Linien von CO und anderen linearen Rotatoren produzieren. Vergrößert man die Oberfläche der Modell-PDR bei gleich bleibender Masse, verändern sich zwangsläufig die Verhältnisse der Linienintensitäten. Die beobachteten Linienvorhältnisse sind also geprägt von der lokalen Struktur der Quelle, was bei der Modellierung berücksichtigt werden muss.

Eine simple Möglichkeit, die Emission komplexerer Strukturen zu emu-

²Inzwischen gibt es Ansätze von PDR Modellen mit voller Berücksichtigung dreidimensionaler Geometrie. Genannt sei an dieser Stelle exemplarisch 3D-PDR Bisbas u. a. 2012, eine Weiterentwicklung des UCL-PDR Codes. (Bell u. a. 2005)

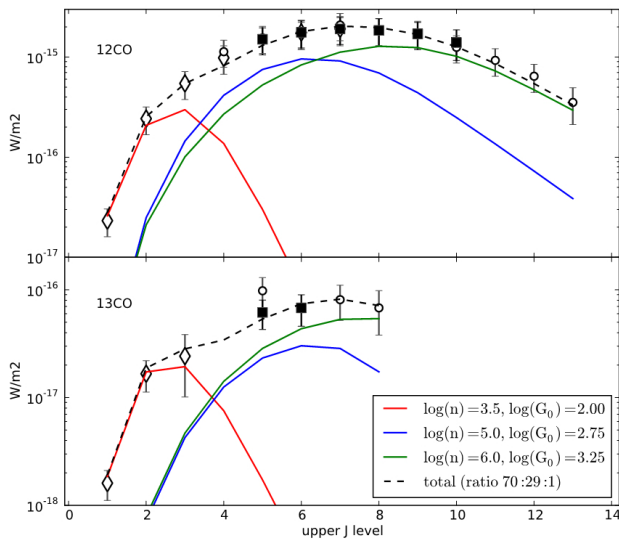


Abbildung 2.3: Vergleich der beobachteten und modellierten SLED von CO und ^{13}CO der zentralen Region von M82. (Abbildung aus Loenen u. a. 2010)

lieren, ist die Überlagerung verschiedener PDR-Komponenten. Besonders intensiv beleuchtete PDRs zeigen die maximale CO Emission bei höheren J -Übergängen als weniger stark beleuchtete. Um die gemessene Form einer Spektrallinien-Energieverteilung (*spectral line energy distribution*, SLED) zu reproduzieren, kann man mehrere Modellkomponenten überlagern. Ein Beispiel zeige ich in Abb. 2.3. Hier werden drei PDR Komponenten benötigt, um Beobachtungen der Zentrumsregion von M82 zu reproduzieren. Der offensichtliche Nachteil dieses Ansatzes ist, dass die relativen Verhältnisse der einzelnen Komponenten Fit-Parameter sind und nicht notwendigerweise auch physikalisch sinnvoll oder motiviert sind. Auch kann bei Bedarf immer noch eine weitere Komponente hinzugefügt werden, so dass sich prinzipiell jede beliebige Form der SLED realisieren lässt, was die Aussagekraft des Fits mindert.

Es ist offensichtlich, dass eine Struktur, wie z.B. in Abb. 1.2 gezeigt, keiner simplen, plan-parallelen oder sphärischen Konfiguration gleicht. Es stellt sich die Frage, wie weit diese simplen Konfigurationen trotzdem genügen und bei welchen Fragestellungen man sie in welcher Form modifizieren muss. Jeder PDR-Modellcode beantwortet diese Fragen unterschiedlich. In Abschnitt 3.3 gehe ich auf Lösungsstrategien im Rahmen des KOSMA- τ PDR Modells ein.

Modell-Physik

Modellseitig ist es natürlich wünschenswert, physikalische Prozesse möglichst komplett zu simulieren und damit für möglichst viele Anwendungsgebiete gewappnet zu sein. Der erforderliche numerische Aufwand und die Komplexität der einzelnen Prozesse macht dies jedoch unmöglich. Turbulenz und Schocks sind beispielsweise keine räumlich eindimensionalen Prozesse, sondern erfor-

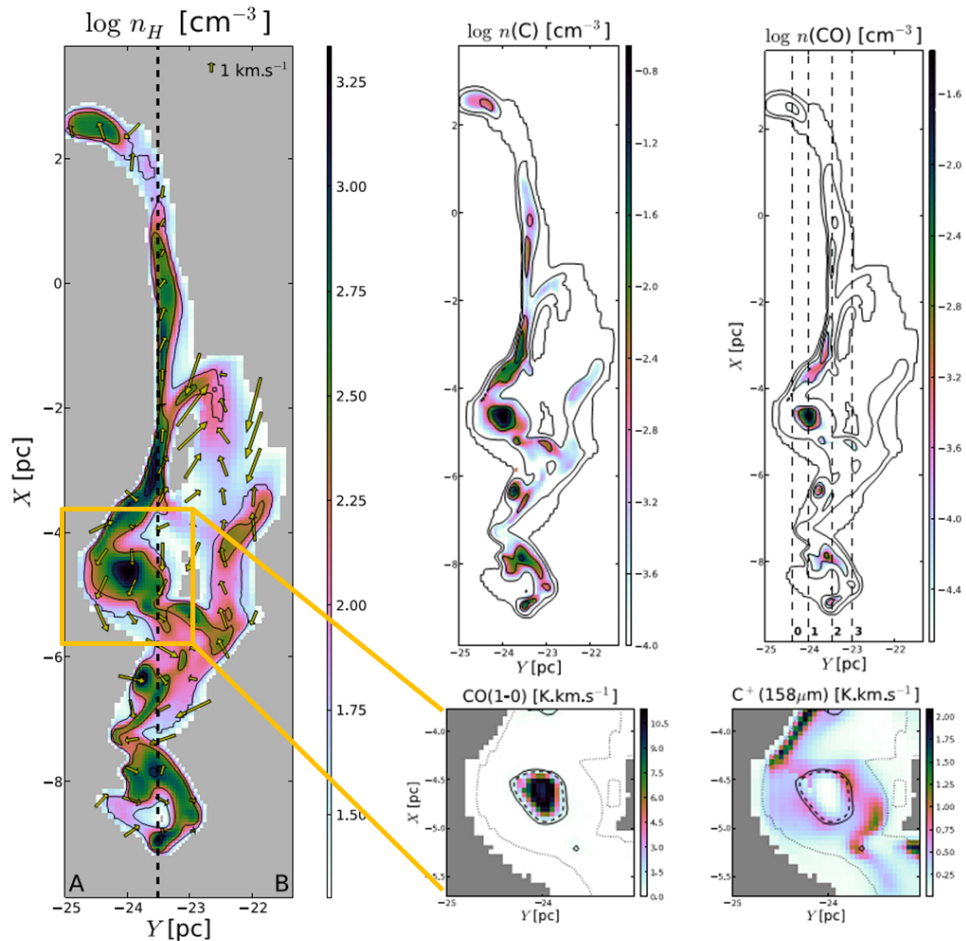


Abbildung 2.4: Anwendung des Meudon PDR Modells auf Ergebnisse aus Magneto-Hydrodynamischen (MHD) Simulationen (Levrier u. a. 2012).

dern eine dreidimensionale Betrachtung. Eine möglichst realitätsnahe Simulation im Rahmen von PDR Modellen ist derzeit nicht möglich. Stattdessen versucht man entweder die einzelnen Simulationsschritte zu entkoppeln oder aber die Beschreibung der Prozesse durch einfachere Näherungen zu ersetzen.

In Abb. 2.4 ist ein Beispiel für diese Entkopplung gezeigt. Zuerst wurde die Dichtestruktur im turbulenten, diffusen ISM ohne Sternentstehungsaktivität mittels einer Magneto-Hydrodynamischen (MHD) Simulation erzeugt (linke Abb.). Die resultierende Dichtestruktur diente dann als Input für eine PDR Modellierung, um die chemische Struktur (oben Mitte und oben rechts) sowie die resultierenden Intensitätskarten (unten Mitte und unten rechts) zu berechnen (Levrier u. a. 2012). Die Brauchbarkeit dieser Methode hängt vom Vergleich der dynamischen Zeitskala mit der chemischen Zeitskala sowie der relevanten mittleren Energiedichten ab. Nur, wenn die FUV Heizung und die damit verbundenen thermodynamischen Energiedichten klein sind gegenüber der turbulent-dynamischen Energiedichte, ist eine Entkopplung physikalisch

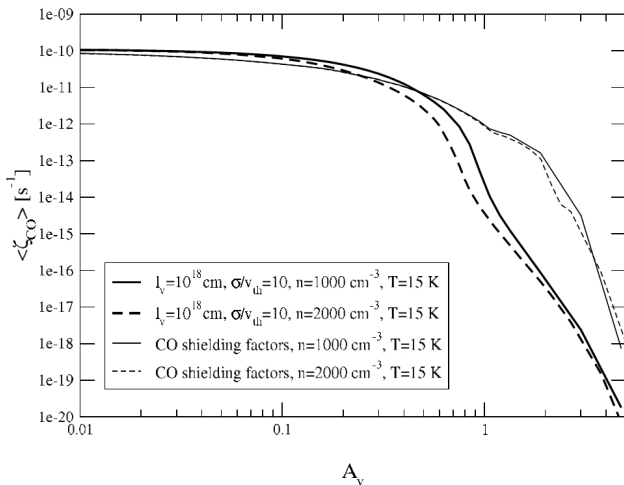


Abbildung 2.5: Vergleich der CO Photodissoziationsraten aus mikroturbulenten genäherten *shielding rates* und aus einer stochastischen Beschreibung des Geschwindigkeitsfeldes.

sinnvoll. Im Folgenden diskutieren wir exemplarisch einige Beispiele für die Umsetzung verschiedener physikalischer Prozesse in PDR Modellen.

Turbulenter Strahlungstransport Abbildung 2.5 zeigt eine alternative Berücksichtigung von Turbulenz innerhalb von PDR Modellen mittels stochastischer Beschreibung des Geschwindigkeitsfeldes (Röllig, Hegmann und Kegel 2002a). Der Plot vergleicht die Photodissoziationsrate von CO, geschätzt mittels klassischer Abschirmungsraten (*shielding rates*, (van Dishoeck und Black 1988; Lee u. a. 1996; Visser, van Dishoeck und Black 2009)), mit den explizit über alle Absorptionslinien integrierten Raten. Man erkennt eine verringerte Eindringtiefe von FUV Photonen im Fall von meso-turbulenten Geschwindigkeitsfeldern³. Das ist ein gutes Beispiel für ein kontra-intuitives physikalisches Verhalten; die naive Vorstellung, dass Turbulenz und die damit verbundene Dopplerverschiebung der Absorptionslinien zu einer flacheren Wachstumskurve und insgesamt zu niedrigeren optischen Tiefen führt, was Photonen ein tieferes Eindringen in die Wolke erlaubt, bestätigt sich im mesoturbulenten Fall nicht. Stattdessen zeigt sich, dass es statistisch gesehen immer genügend Gaselemente entlang des Sehstrahls mit ausreichend optischen Tiefen gibt, die insgesamt eine effektivere Abschirmung erzwingen.

Neben dem Strahlungstransport und der Kinematik der Wolke gibt es noch eine Vielzahl weiterer Bereiche, in denen Details der numerischen Realisierung großen Einfluss auf die Modellergebnisse haben. Besonders die angewandten Staubeigenschaften beeinflussen die physikalische Struktur der Modellwolke. Abel u. a. (2008) haben am Beispiel des Photo-Ionisations/PDR Mo-

³ Die Lösung des angewandten stochastischen Strahlungstransports ist immer noch sehr rechenaufwendig und bisher nur im Fall von semi-infiniten plan-parallelen Modellen mit reiner Absorption angewendet worden. Siehe auch Hegmann und Kegel (2003); Hegmann u. a. (2006).

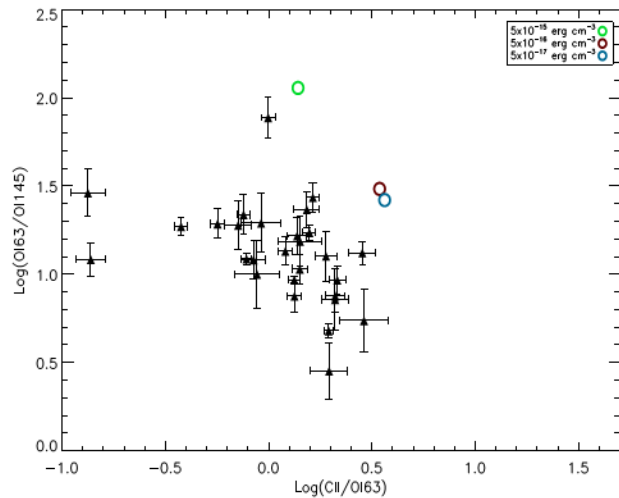


Abbildung 2.6: Einfluss der Stärke der Ionisation durch kosmische Strahlung auf die Linienverhältnisse wichtiger Feinstruktur-Kühllinien des ISM (entnommen aus (Vasta u. a. 2010)).

dellcodes Cloudy gezeigt, wie stark Modellergebnisse von der verwendeten Größenverteilung der interstellaren Staubkörner und dem spektralen Verlauf der FUV Einstrahlung abhängen. Sie haben gezeigt, dass die resultierenden Staubtemperaturen um bis zu eine Größenordnung variieren können, je nach Staubeigenschaften. In Publikation 7 gehe ich ausführlich auf den Einfluss verschiedener Staubzusammensetzungen und -größenverteilungen auf die wichtige optische, thermische und chemische Prozesse ein.

Ionisationsrate der kosmischen Strahlung Ein besonders einflussreicher Parameter in der PDR Modellierung ist die Ionisationsrate von Wasserstoff durch kosmische Strahlung (*cosmic rays*, CR). Da kosmische Strahlung auf ihrem Weg in eine Molekülwolke nur marginal abgeschwächt wird, ist sie für die Heizung des Dunkelwolkenbereichs ($A_V \gg 1$) der Wolke von herausragender Bedeutung. Tief innerhalb der Wolken sind die optischen Tiefen von möglichen Kühllinien sehr hoch. Dadurch kann kosmische Strahlung effektiv Wolkenkerne heizen. Doch nicht nur energetisch, auch chemisch hat kosmische Strahlung einen starken Einfluss. Bereits in Publikation 2 habe ich gezeigt, dass eine um einen Faktor 4 höhere Ionisationsrate ζ_{CR} zu enormen Änderungen in den chemischen Häufigkeiten einiger Spezies führen kann - bis zu einem Faktor 1000 unterschiedlich. Auch Vasta u. a. (2010) konnten zeigen, wie stark die Modellvorhersagen von Linienverhältnissen der starken Feinstruktur-Kühllinien durch ein verändertes ζ_{CR} betroffen sind.

Die beobachtungsmäßige Unsicherheit bezüglich der lokalen Ionisationsraten ζ_{CR} ist groß. In diffusen Wolken versucht man ζ_{CR} zu bestimmen, indem man Säulendichten von Spezies bestimmt, deren Chemie von Ionisation durch kosmische Strahlung dominiert wird. Beispielsweise wird H_3^+ gebildet durch $\text{H}_2 + \text{H}_2^+$, wobei H_2^+ durch CR ionisiert wird. Zerstört wird H_3^+ durch disso-

zitative Rekombination mit Elektronen. Im Gleichgewicht von Zerstörung und Bildung gilt:

$$\zeta_{\text{CR}} = \frac{k_e n(e) n(\text{H}_3^+)}{2.3 n(\text{H}_2)} \quad (2.1)$$

Einsetzen des Ratenkoeffizienten für die Rekombination k_e sowie üblicher Werte für das diffuse Medium ergibt $\zeta_{\text{CR}} = 3 \times 10^{-16}$ (Tielens 2005), wobei die Ergebnisse für unterschiedliche (aber durchaus benachbarte) Sichtlinien stark voneinander abweichen können. Auch andere Spezies, beispielsweise OH und NH, können auf ähnliche Weise benutzt werden, um ζ_{CR} zu bestimmen. Man findet Werte zwischen $10^{-17} \dots 10^{-14} \text{ s}^{-1}$ (O'Donnell und Watson 1974; Hartquist, Doyle und Dalgarno 1978; Webber 1998; McCall u. a. 2003; Indriolo, Geballe u. a. 2007; D. Hollenbach, Kaufman u. a. 2012; Indriolo, Neufeld u. a. 2012). Der starke Einfluss von ζ_{CR} auf einzelne Modellergebnisse sowie die Unsicherheit bezüglich seines numerischen Wertes machen deutlich, wie groß die Fehlerbalken an Modellergebnissen sein können.

Modell-Chemie

Die Lösung des chemischen Problems entspricht der Lösung eines gekoppelten Systems von N_S Differentialgleichungen (DGLs) der Form:

$$\frac{dn_i}{dt} = n_i \left\{ \tilde{\zeta}_i + \sum_q n_q k_{qi} \right\} - \sum_r \sum_s k_{rs} n_r n_s + \sum_t n_t \tilde{\zeta}_{ti}, \quad (2.2)$$

n_i bezeichnet die Anzahldichte der i -ten von insgesamt S Spezies, die Photoionisations-/dissoziationsratenkoeffizienten ζ werden in Einheiten von s^{-1} angegeben, alle anderen Ratenkoeffizienten k in Einheiten von $\text{cm}^3 \text{ s}^{-1}$. Einige PDR Modelle lösen das chemische Ratengleichungssystem zeitabhängig. Das ist verbunden mit enormen numerischen Schwierigkeiten: die Ratenkoeffizienten k sowie die Dichten n_i unterscheiden sich teilweise um mehr als 10 Größenordnungen. Ein solches System von steifen DGLs ist numerisch schwierig zu lösen. Gleichzeitig benötigt eine zeitabhängige Lösung einen wohldefinierten, aber grundsätzlich unbekannten Anfangsdichtevektor \mathbf{n} . Auch das Stopkriterium, also die Zeit, bei der die Berechnung beendet wird, ist a priori schwierig zu bestimmen.

Die zweite Klasse von Modellen untersucht die Chemie im Gleichgewichtsfall $\frac{dn_i}{dt} = 0$ (*steady-state*). Das chemische Ratengleichungssystem ist zwar immer noch ein hoch-nichtlineares Gleichungssystem, kann aber numerisch gelöst werden, wobei der Rechenaufwand stark mit N_S steigt (abhängig von der Lösungsmethode, mindestens aber mit $\mathcal{O}(N_S^2)$)⁴.

⁴Wie für alle nichtlinearen Systeme (z. B. auch das Besetzungsproblem der Energiezustände)

Zusätzlich zu der Unterscheidung zwischen zeitabhängigen und *steady-state* Modellen unterscheidet man auch noch zwischen reiner Gasphasen-Chemie sowie chemischen Prozessen auf der Oberfläche von Staubkörnern und in deren Eismanteln. Besonders in sehr kalten Wolken, in denen Gasmoleküle auf Stauboberflächen ausfrieren, oder in sogenannten *hot cores*, in denen Eismantel nach der Bildung eines Protosterns rapide verdampfen, und die Gasphase chemisch anreichern, spielt die Oberflächenchemie eine wichtige Rolle. Abgesehen von diesen besonderen Umgebungen gibt es aber auch eine Reihe von Spezies, deren Bildung in der Gasphase nur sehr ineffizient, d.h. langsam, passiert, auf Stauboberflächen aber um ein Vielfaches schneller stattfindet. Das wohl prominenteste Beispiel ist molekularer Wasserstoff H_2 , dessen Bildung in der Gasphase vernachlässigbar ist. Aber auch andere wichtige Moleküle wie beispielsweise Wasser (H_2O) und Methanol (CH_3OH) werden vermutlich dominant auf Oberflächen gebildet und gelangen erst per Desorption in das Gas. Auch bezüglich der Modell-Chemie wollen wir einige Bereiche exemplarisch herausgreifen und im Folgenden diskutieren.

H_2 Bildung Es ist offensichtlich, dass das mit Abstand häufigste Molekül korrekt in astrochemischen Modellen abgebildet werden muss. Aus diesem Grund müssen alle PDR Modelle die Bildung von H_2 auf Staubkörnern berücksichtigen, auch wenn es sich um reine Gasphasen-Modelle handelt (siehe z.B. Sternberg und Dalgarno 1995, und Referenzen darin). Bereits Jura (1974) konnte eine mittlere H_2 -Bildungsrate von $5 \times 10^{-17} \text{ s}^{-1}$ ableiten. Besonders wichtig bei der Effizienz der H_2 -Bildung ist die Verweildauer der H-Atome auf der Oberfläche. Je länger Wasserstoffatome auf der Oberfläche sind, desto höher ist ihre Wahrscheinlichkeit, einen Bindungspartner zu finden. Diese Dauer ist abhängig von der Bindungsart und -stärke des Atoms auf dem Festkörper sowie der Staubtemperatur T_d . Je höher T_d , desto höher ist die Desorptionswahrscheinlichkeit; je stärker die Bindung zwischen dem Atom und der Oberfläche ist, desto niedriger ist die Desorptionswahrscheinlichkeit (Cazaux und Tielens 2002; Cazaux und Tielens 2004; Cazaux und Tielens 2010). Unterstellt man, dass H sich nicht nur mittels Van der Waals-Wechselwirkungen (Physisorption) an die Oberfläche bindet (*Langmuir-Hinshelwood Mechanismus*), sondern auch chemische, kovalente Bindungen eingehen kann (Chemisorption, bzw. *Eley-Rideal Mechanismus*), dann erhöht sich die Staubtemperatur, die notwendig ist, um das H-Atom abzudampfen, erheblich (Cazaux und Tielens 2004; Cazaux und Tielens 2010). Berücksichtigt man H_2 -Bildung nur mittels des

de in Strahlungstransportrechnungen) ist jedoch weder die Existenz einer Lösung noch deren Eindeutigkeit beweisbar. Ein großes Problem in diesem Zusammenhang ist das mögliche Vorhandensein von Mehrfachlösungen.

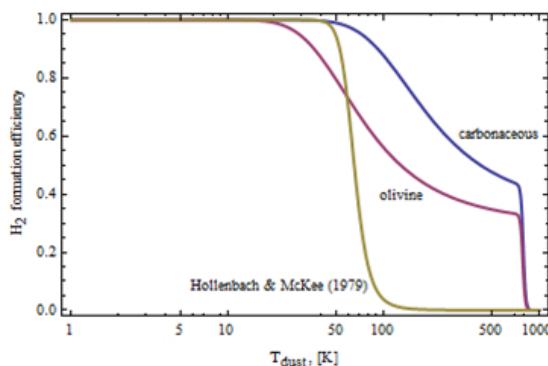


Abbildung 2.7: Vergleich der Effizienz der H₂-Bildung mittels Chemisorption (D. Hollenbach und McKee 1979) und Physisorption (Cazaux und Tielens 2004).

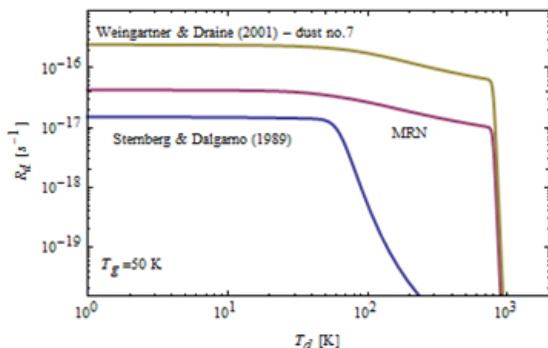


Abbildung 2.8: Kombinierter Einfluss einer höheren Effizienz und einer höheren Stauroberfläche auf die Bildungsrate von H₂.

Langmuir-Hinshelwood Mechanismus, so verringert sich die Bildungseffizienz für $T_d > 60$ K rapide und ist jenseits von 100 K praktisch Null (siehe auch Abb. 2.7). Das ist problematisch, da sich viele Beobachtungen von molekularem Wasserstoff nur erklären lassen, wenn sich auch im heißenen ISM H₂ bilden und angeregt werden kann (z. Bsp. Habart, Abergel u. a. 2011).

In Publikation 7 habe ich im Detail untersucht, welchen Einfluss H₂-Bildung per Eley-Rideal-Mechanismus auf die thermischen und chemischen Eigenschaften von Modellwolken hat und wie sich dieser Einfluss bei unterschiedlichen Staubeigenschaften ändert. Die Bildung von H₂ setzt eine große Menge an Bildungsenergie frei (4.5 eV). Die meisten Modelle nehmen eine Equipartition der Energie zwischen kinetischer Energie, H₂-Anregung und Heizung des Staubkorns an, wobei bereits seit einiger Zeit alternative Szenarien diskutiert werden (Black und van Dishoeck 1987). Darüber hinaus wurde kürzlich in Laborexperimenten gezeigt, dass die Bildung auf kalten Graphit- (Islam u. a. 2010) und Silikatoberflächen (Lemaire u. a. 2010) präferentiell hochvibrationsangeregtes H₂ erzeugt.

Die Art der H-Bindung auf Stauroberflächen ist ein wesentlicher Faktor für die Bildung von H₂. Die Bildungsrate ist zusätzlich abhängig von der zur Verfügung stehenden Stauroberfläche bzw. ihrem geometrischen Querschnitt (Tielens und D. Hollenbach 1985). Unterschiedliche Staubkorn-Größenverteilungen beeinflussen damit die Bildungsrate von H₂ durch Bereitstellung oder

Verknappung von Oberfläche. J. C. Weingartner und B. T. Draine 2001 stellen eine Reihe von Staubmodellen für unterschiedliche astrophysikalische Bedingungen vor. Eine große Population von sehr kleinen Staubkörnern (*very small grains VSG* bzw. *PAHs*) trägt überproportional zur gesamten Oberfläche bei und kann damit die Wasserstoffbildung wesentlich steuern (Habart, Bou-langer u. a. 2003) (siehe Abb. 2.8). Dabei ist noch nicht abschließend geklärt, ob PAH-Oberflächen zur Bildung von H_2 beitragen können. Kürzlich von Men-nella u. a. 2012 durchgeführte Laborexperimente zeigen aber, dass PAHs die Bildung von H_2 katalytisch begünstigen können.

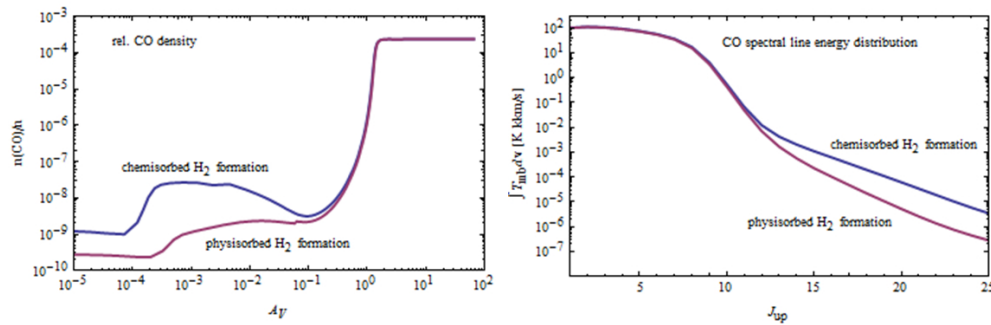


Abbildung 2.9: Einfluss einer höheren H_2 -Bildungseffizienz auf die CO Häufigkeitsverlauf (links) und die resultierende CO-SLED der Modellwolke (rechts).

Eine erhöhte H_2 -Bildungsrate am Rand von PDRs liefert einen zusätzlichen starken Beitrag zur Gasheizung und kann die Gastemperaturen in diesen Bereichen auf einige Tausend Kelvin anheben. Bei gleichbleibender FUV-Intensität hat eine höhere kinetische Temperatur eine beschleunigte Chemie zur Folge. Chemische Spezies, die bevorzugt in den Randregionen gebildet werden, können sich damit um einiges effizienter formen. Besonders leichte Hydride, wie CH , CH^+ , OH und OH^+ zeigen eine deutliche Erhöhung der lokalen Häufigkeiten (siehe Abb. 23 u. 24 in Publikation 7). Aber auch Spezies, die sich eigentlich erst in tieferen Wolkenregionen ausbilden, können betroffen sein. CO bildet sich erst ab einer Extinktion von $A_V \approx 1$ aus. Jedoch existiert bereits bei niedrigeren Extinktionen eine kleine Population von CO-Molekülen, die sich auch bei höheren Temperaturen, aufgrund effizienterer H_2 -Bildung, einstellt. Zum einen wird CO häufiger, vor allem aber sind die lokalen Temperaturen nun ausreichend, um auch sehr hohe Rotationszustände anzuregen. Abbildung 2.9 vergleicht die CO-Häufigkeiten bei unterschiedlich effizienten H_2 -Bildungsraten, sowie die daraus resultierenden CO-SLEDs. Es ist deutlich zu sehen, dass eine verstärkte Wasserstoffbildung die Emission von high- J Linienübergängen deutlich anhebt. Die Beobachtungen von sehr intensiven CO

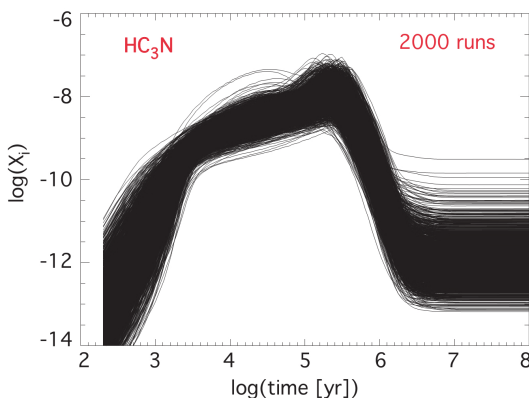


Abbildung 2.10: Vergleich der HC_3N Häufigkeit in einem zeitabhängigen chemischen Modell bei zufälliger Variation der Reaktionsraten innerhalb des tabellierten Unsicherheitsbereichs (Wakelam, Smith u. a. 2010).

high- J Rotationsübergänge wie in Abb. 2.3 kann damit teilweise erklärt werden (Le Bourlot u. a. 2012).

Chemische Reaktionsraten-Koeffizienten Bei der Lösung des chemischen Ratengleichungssystems 2.2 benutzt man üblicherweise Ratenkoeffizienten k , die in einer astrochemischen Datenbank bereitgestellt werden. Derzeit sind einige wenige dieser Datenbanken verfügbar: die *UMIST Database for Astrochemistry* (UDfA) (Woodall u. a. 2007), die Ohio Database (OSU) von Eric Herbst⁵, *NIST Chemical Webbook*⁶, und die *KInetic Database for Astrochemistry* (KIDA Wakelam, Herbst, Loison u. a. (2012)). Einige Modellcodes, wie beispielsweise der Meudon-Code (Le Petit, Nehmé u. a. 2006), unterhalten zusätzlich ihre eigene Zusammenstellung von Ratenkoeffizienten. Dabei variiert die Schnittmenge an Reaktionen und der dazugehörigen Koeffizienten von Datenbank zu Datenbank erheblich. Das liegt zum einen an dem ursprünglichen astrophysikalischen Kontext, in dem die chemischen Netze angewendet wurden. OSU wurde vorwiegend für die Modellierung kalter Dunkelwolken verwendet. Die geringen kinetischen Energien in diesen Regionen machen alle Reaktionen mit hohen Aktivierungsenergien bzw. endotherme Reaktionen sehr langsam, entsprechend fehlen diese Reaktionen in der Datenbank. Andererseits fehlen in UDfA viele Reaktionen mit komplexen Kohlenstoffketten, die im heißen PDR-Medium nur sehr selten auftreten. Aber auch die tabellierten Ratenkoeffizienten variieren teilweise und die Wahl der chemischen Datenbank kann bereits einen signifikanten Einfluss auf die chemischen Modellrechnungen haben (Wakelam, Herbst und Selsis 2006; Wakelam, Herbst, Loison u. a. 2012). In Publikation 8 zeige ich, wie stark einige chemische Häufigkeiten von der verwendeten Datenbank abhängen.

Ein häufig übersehenes Problem ist, dass die meisten Reaktionsraten nur in einem eingeschränkten Temperaturbereich gültig sind. Außerhalb ihres Gültigkeitsbereichs können sie zu falschen Ergebnissen führen. Dies ist insbesondere bei der Modellierung von PDRs von Bedeutung, da die Temperatur in diesen Regionen oft nicht konstant ist. Eine mögliche Lösung ist es, verschiedene Datenbanken zu verwenden, um die Ergebnisse zu vergleichen und zu überprüfen.

⁵<http://www.physics.ohio-state.edu/~eric/research.html>

⁶<http://webbook.nist.gov/chemistry/>

tigkeitsbereichs können die Raten in einigen Fällen stark divergieren. Das liegt vor allem an der Form der verwendeten Parametrisierung: $k = \alpha(T/300K)^\beta \exp(-\gamma/T)$. Einige Messergebnisse lassen sich am besten mit einem $\gamma < 0$ beschreiben, was jedoch für niedrige Gastemperaturen T zu Divergenz führen kann. In Publikation 4 zeige ich am Beispiel von UDfA, wie sich dieses Verhalten durch eine Re-Parametrisierung beheben lässt, ohne gleichzeitig die Fehlerbalken der Raten signifikant zu vergrößern. Für tabellierte Reaktionen, die mehrfach, für unterschiedliche Temperaturbereiche, aufgeführt sind, ist es zusätzlich möglich, einen temperaturübergreifenden Fit zu finden, der das ursprüngliche Verhalten akzeptabel reproduziert. Das ist wichtig, um Diskontinuitäten im Temperaturverhalten der Ratenkoeffizienten zu vermeiden, welche numerisch ansonsten zu großen Problemen führen würden.

Schließlich sind alle Reaktionsraten mit teilweise sehr großen Unsicherheiten behaftet. Fehlerbalken von 100% sind nichts Ungewöhnliches, viele Reaktionsraten sind nur auf einen Faktor 10 genau angegeben. Es ist offensichtlich, dass die Nichtlinearität des chemischen Netzes diese Unsicherheiten enorm verstärken kann. In Abb. 2.10 sieht man, wie stark die Häufigkeit von HC_3N in zeitabhängigen Modellen variieren kann, wenn man die Reaktionsraten innerhalb des Fehlerbalkens zufällig variiert. Wakelam, Smith u. a. (2010) haben gezeigt, dass es einzelne Reaktionen gibt, deren Reaktionsraten die gesamte Chemie enorm beeinflussen können, indem sie sekundäre, tertiäre usw. Folgeprodukte in der chemischen Kette modifizieren. So hat die Reaktion:



starken Einfluss (Korellationskoeffizient > 0.3) auf insgesamt 73 andere Spezies. Das ist zwar ein extremer Fall, aber es kommt relativ häufig vor, dass die chemische Häufigkeit einer Spezies kritisch von nur einer einzigen Reaktionsrate abhängt. Jegliche Unsicherheiten haben somit einen starken Effekt. Andererseits ist auch der Umkehrschluss gültig, nämlich, dass der größte Teil der aufgeführten chemischen Reaktionen individuell nur geringen Einfluss auf das Ergebnis der chemischen Rechnungen hat. Das lässt allerdings nicht automatisch den Schluss zu, dass man diese Reaktionen auch aus dem Netzwerk streichen könnte, ohne das Ergebnis deutlich zu verändern. Wieder ist es der nichtlineare Charakter des Ratengleichungssystems, der es verbietet, die kumulative Wirkung der einzelnen Elemente zu vernachlässigen. Darüber hinaus wird die Komplexität des numerischen Problems durch die Zahl der beteiligten chemischen Spezies und nicht durch die Zahl der involvierten chemischen Reaktionen bestimmt, das Weglassen einzelner Reaktionen hat damit kaum Auswirkungen auf die Rechenzeit (womöglich aber auf das Konvergenzverhalten).

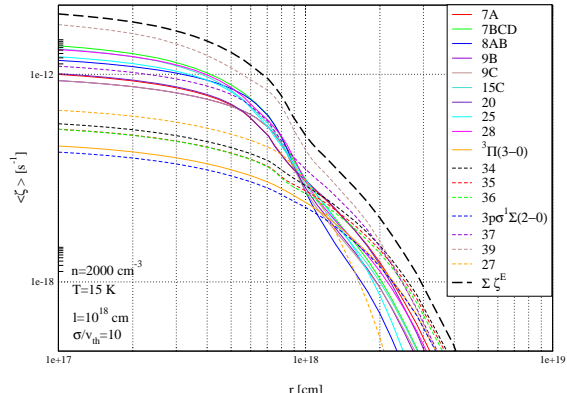
Stöße mit vibrationsangeregtem Wasserstoff H_2^* Aufgrund seiner elementaren Häufigkeit ist molekularer Wasserstoff der häufigste Stoß-/Reaktionspartner in Molekülwolken. In dichten Wolken stellt FUV gepumptes H_2^* einen nicht zu vernachlässigen Anteil an dem gesamten H_2 . In Publikation 1 diskutiere ich den Einfluss der Stoßabregung von vibrationsangeregtem Wasserstoff als Heizprozess in dichten PDRs und gebe eine simple Parametrisierung der Heizrate an, für den Fall, dass man das volle multi-Level Problem nicht lösen möchte oder kann. Diese H_2^* -Population trägt eine enorme Energie; so entspricht die Anregungsenergie des ersten vibrationsangeregten H_2 -Niveaus einer Temperatur von ca. 6000 K. Es ist plausibel anzunehmen, dass Reaktionen mit H_2^* diese innere Energie nutzen können, um Aktivierungsenergien oder endotherme Reaktionsenthalpien aufzubringen (Agúndez u. a. 2010). In Publikation 2 machen wir die Annahme, dass Reaktionen mit H_2^* keine Aktivierungsenergie-Barriere überwinden müssen, und zeigen den starken Effekt am Beispiel der Reaktion $C + H_2 \longrightarrow CH + H$. Wie im Abschnitt zur H_2 -Bildung bereits beschrieben, weisen jüngste Laborexperimente auf eine präferentielle Besetzung hoher Vibrationszustände bei der H_2 -Bildung hin. Es existieren jedoch keine Messungen oder Rechnungen zu *state-to-state* Reaktionsraten, um H_2^* genauer in chemischen Modellen zu berücksichtigen.

Chemisch-physikalische Kopplung

Viele der oben beschriebenen chemischen und physikalischen Prozesse sind nicht nur für sich relevant, sondern koppeln auch an andere chemische und physikalische Eigenschaften (wie schon aus Abb. 2.1 ersichtlich). Ich habe bereits am Beispiel der H_2 -Bildung gezeigt, wie eine höhere chemische Bildungsrate eine höhere Heizrate bedingt und damit die thermischen Eigenschaften der Wolken verändert, was wiederum vielfache, sekundäre chemische und physikalische Effekte hat. Diese Kopplung ist ein besonderes Merkmal von PDR Modellen und soll anhand einiger prominenter Beispiele hervorgehoben werden.

CO Selbst-Abschirmung Die Photodissoziation von CO ist ein prädissoziierter Linienabsorptionsprozess und unterliegt sehr viel stärker optischen Tiefeneffekten als bei Kontinuumsabsorption (van Dishoeck und Black 1988). Am Rand der Wolke tragen die Absorptionsbanden mit starken und engen Linien dominant zur Photodissoziationsrate bei. In größeren Tiefen tragen jedoch die Linienflügel stärker zur Photodissoziationsrate bei als die Linienmitte, da die teilweise sehr engen Linien der UV-Absorptionsbanden in der Linienmitte schneller optisch dick werden als in den Flügeln. D.h. Banden,

Abbildung 2.11:
Tiefenabhängiger Beitrag einzelner prädissoziierter Absorptionsbanden von CO zur gesamten Photodissoziationsrate.



die am Rand der Wolke vernachlässigbare Beiträge zur Photodissoziationsrate leisten, können im Wolkeninneren dominieren (siehe Abb. 2.11). Zusätzlich zur Selbstabschirmung (*self shielding*) überlappen auch viele Absorptionslinien von H₂ mit denen von CO. Aufgrund der viel höheren Säulendichte sind die H₂-Absorptionslinien optisch bereits sehr dick und haben sehr viel größere Linienbreiten, wodurch CO zusätzlich durch molekularen Wasserstoff abgeschirmt wird.

Sobald die wichtigen Absorptionslinien optisch dick werden, lagert sich sehr effizient der Großteil des verfügbaren Kohlenstoffs in CO ab. Die exponentielle Abschwächung der Intensität mit τ_{CO} hat einen scharfen räumlichen C⁺-C-CO Übergang zur Folge; die klassische Kohlenstoffsignatur aller PDR Modelle. In Abb. 1.4 ist gut zu sehen, wie die Häufigkeiten von sowohl H₂ als auch CO schnell ansteigen, sobald die zugehörigen Photodissoziationsraten stark genug abgeschwächt sind. Die detaillierte Berücksichtigung der Abschirmungseigenschaften von CO bzw. H₂ ist sehr rechenaufwendig. Auf der anderen Seite sind inzwischen eine ganze Reihe von H₂-Emissionslinien beobachtet, die als sehr starke Randbedingungen für die Modellierung herangezogen werden können. Wenn man modellseitig den Aufwand des vollen, wellenlängenabhängigen Strahlungstransports nicht machen möchte, bedient man sich sogenannter Abschirmungsfaktoren (*self-shielding factors*), tabellierter Werte, um die Selbst- und Fremdabschirmung von CO in parametrisierter Form zu berücksichtigen (van Dishoeck und Black 1988; Visser, van Dishoeck und Black 2009).

Photodissoziation und -ionisation bei unterschiedlichen Staubzusammensetzungen Verändert man die optischen Eigenschaften des Staubanteils der Modellwolke, sei es durch veränderte Größen-Verteilungsfunktionen oder

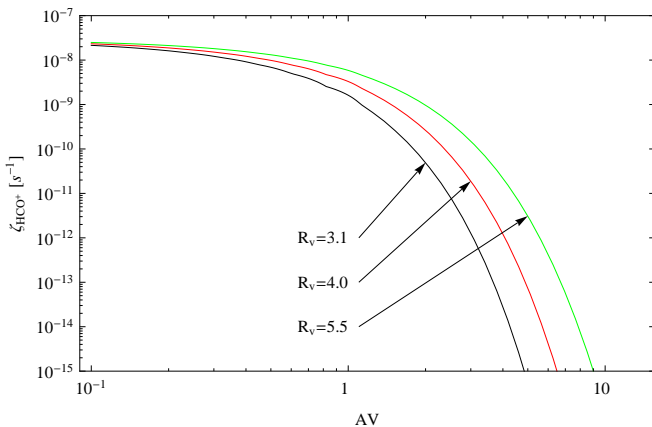


Abbildung 2.12: Variation der HCO^+ -Photodissoziationsrate bei unterschiedlicher Staubzusammensetzung.

durch veränderte Materialeigenschaften, so hat dies tiefgreifende Auswirkungen auf die Modellergebnisse. In Abb. 2.12 zeige ich die Variation der HCO^+ -Photodissoziationsratenkoeffizienten bei unterschiedlicher Staubzusammensetzung

$R_V = A_V/E(B-V)$ von 3.1, 4 und 5.5 (J. C. Weingartner und B. T. Draine 2001). A_V ist die absolute visuelle Extinktion bei $V = 5500 \text{ Å}$ und $E(B-V) = A_B - A_V$. Ein größeres R_V bewirkt eine schwächere Extinktion bei kürzeren Wellenlängen; entsprechend kann FUV Strahlung in diesem Wellenlängenbereich tiefer eindringen und Moleküle photodissoziieren. Die Photodissoziationsratenkoeffizienten ζ in Abb. 2.12 wurden durch die explizite Integration des tiefenabhängigen Strahlungsfeldes über den Absorptionsquerschnitt σ des Moleküls berechnet:

$$\zeta = 4\pi \int J_\lambda(r)\sigma(\lambda)d\lambda. \quad (2.3)$$

Man erkennt die unterschiedlichen Abschirmungseigenschaften in Abhängigkeit von R_V . In Publikation 7 untersuche ich, wie sich verschiedene Staubeigenschaften auf die Photodissoziations- und Photoionisationsraten von Atomen und Molekülen im chemischen Netz auswirken. Ich zeige Möglichkeiten auf, die Ratenkoeffizienten auf eine veränderte Staubzusammensetzung anzupassen, ohne die detaillierten Berechnungen mittels Glg. 2.3 explizit ausführen zu müssen.

3

Entwicklung des KOSMA- τ PDR Modells

Das *sphärische* KOSMA- τ PDR-Modell ist die Weiterentwicklung eines planparallelen PDR-Modells, welches ursprünglich von A. Sternberg von der Universität Tel Aviv, Israel, entwickelt wurde (Sternberg und Dalgarno 1989; Sternberg und Dalgarno 1995). Dadurch erklärt sich auch der Name des Modells: **KOSMA** steht für **Kölner Observatorium für Submillimeter-Astronomie**, **TAU** steht für **Tel Aviv University**. In den 90er Jahren wurde der Modellcode in einer Kollaboration der Universitäten Köln und Tel Aviv auf sphärische Geometrie erweitert (Gierens, Stutzki und Winnewisser 1992; Köster u. a. 1994; Störzer, Stutzki und Sternberg 1996; Zielinsky, Stutzki und Störzer 2000) und wird seitdem, von Köln aus, gepflegt und weiterentwickelt.

Meine Hauptbeiträge bei der Entwicklung des KOSMA- τ PDR-Modells sind die Erweiterung des Modells um die Einflüsse der Metallizität, die Untersuchung der Fraktionierung und der Isotopenchemie, die selbstkonsistente Behandlung der Staubeigenschaften und der Einfluss einer klumpigen Struktur auf die beobachtbaren Strahlungseigenschaften. Die Anwendung des Modells bei der Interpretation von Beobachtungsergebnissen war dabei ebenfalls immer ein wesentlicher Aspekt meiner Arbeit. Der bereits erwähnte PDR-Modellierungs Benchmark (veröffentlicht, mit mir als Erstautor) sei an dieser Stelle noch einmal besonders erwähnt, da seine Ergebnisse eine unverzichtbare Referenz für alle PDR-Modellierungscodes darstellen und seit ihrer Veröffentlichung auch entsprechend oft zitiert wurden. Vor allem aber führte er zu einem wesentlich besseren Verständnis der Stärken und der Schwächen der verschiedenen numerischen PDR-Modelle.

Der Benchmark füllte damit eine große Lücke in der bisherigen Forschung und ist somit sicher eines meiner Schlüsselpunkte der letzten Jahre. In den folgenden Abschnitten fasse ich meine wesentlichen Entwicklungsbeiträge mit Verweis auf die beiliegenden Artikel kurz zusammen.

3.1 Metallarme/-reiche PDRs

Der Anteil schwerer Elemente im ISM ist keine konstante Größe. Jede Stern-generation erhöht die sogenannte Metallizität¹ Z. Das bedeutet, dass extra-galaktische Quellen oft ein sehr viel metallärmeres ISM aufweisen als in der Milchstraße. Aber auch metallreichere Quellen, oft mit sehr hoher Sternent-stehungsaktivität, z.B. *starbursts*, können beobachtet werden.

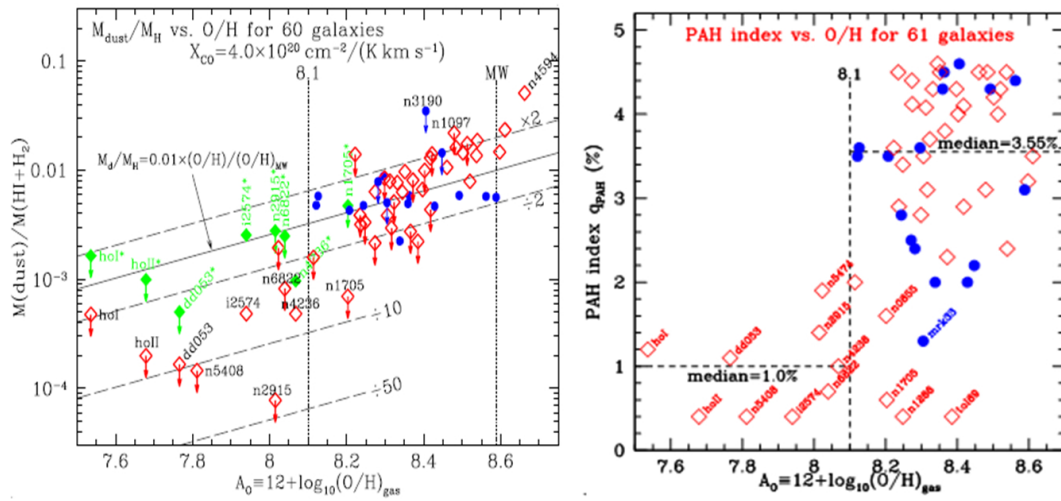


Abbildung 3.1: Einfluss der Metallizität auf den Staubanteil des ISM. **Links:** Das Gas-zu-Staub Verhältnis in Abhängigkeit der Metallizität. **Rechts:** Anteil der PAHs an der gesamten Staubpopulation.

Zum einen bedeutet eine veränderte Metallizität veränderte elementare Häufigkeiten, was unmittelbar die chemischen Rechnungen beeinflusst. Da jedoch meistens alle Elemente (außer H und H₂) betroffen sind, findet oft nur eine relative Verschiebung der Häufigkeiten gegenüber wasserstoffhaltigen Verbindungen statt. Viel stärker ist der Staubinhalt des ISM betroffen, schließlich besteht Staub vorwiegend aus Kohlenstoffen und Silikaten. Der Einfluss einer verringerten Metallizität auf den Staubinhalt ist nicht trivial. In KOSMA- τ unterstellen wir eine lineare Skalierung der relevanten Staubeigen-schaften, wie beispielsweise visuelle Extinktion und Effizienz der photoelek-trischen Heizung. Beobachtungen zeigen jedoch, dass unterschiedlich große Staubkörner unterschiedlich betroffen sind. Abbildung 3.1 zeigt die Variation

¹Astronomisch bezeichnet man alle Elemente außer H und He als Metalle. Ein eindeutiges Maß für die Metallizität ist nur schwer zu finden. Prinzipiell müsste jede Elementhäufigkeit separat bestimmt werden, was oft unmöglich ist. Daher beschränkt man sich meist nur auf O Häufigkeiten, die vorwiegend aus Beobachtungen von HII -Regionen bestimmt werden können und gibt die Metallizität in der Form $12 + \log_{10}(\text{O}/\text{H})$ an, wobei O/H für die relative Sauerstoffhäufigkeit steht.

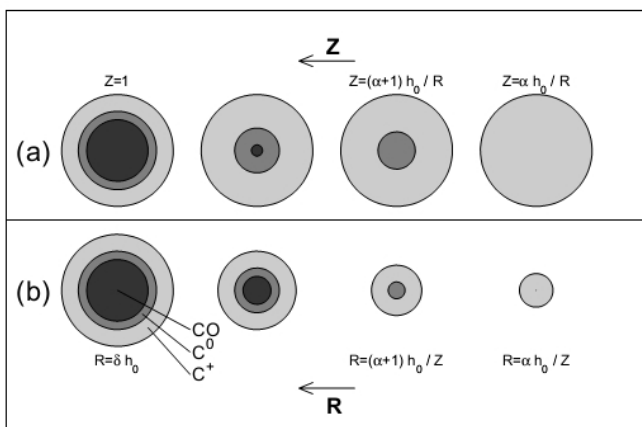


Abbildung 3.2: Einfluss der Metallizität Z auf die C^+ -CO-Schichtung in sphärischen Modellen bei gleichbleibendem (a) und abnehmendem (b) Wolkenradius (entnommen aus Bolatto, Jackson und Ingalls 1999).

des Staub-zu-Gas Verhältnisses (links) sowie den relativen Anteil der sehr kleinen Staubkörner an der gesamten Staubpopulation mit der Metallizität. Man sieht deutlich, dass die Gesamtmenge an Staub mit abnehmender Metallizität abnimmt. Es ist aber auch ein deutlicher Phasenübergang bei den PAHs sichtbar. Unterhalb einer Metallizität von $12 + \log(\text{O/H}) = 8.1$ ist deren Population sprungartig reduziert. Der Grund hierfür ist noch unklar. Diskutiert werden unter anderem verstärkte Zerstörung durch UV Strahlung aufgrund der reduzierten Abschwächung im ISM bzw. reduzierte PAH-Bildungsraten aufgrund einer geringerer Anzahl an kohlenstoffreichen Sternen (*carbon stars*), in deren Atmosphäre PAHs vorwiegend gebildet werden.

In Publikation 1 beschreibe ich unsere Arbeiten zur Berücksichtigung von Z als neuen Modellparameter von KOSMA- τ und untersuche, welche Modellbereiche am stärksten betroffen sind. Abbildung 3.2 unterstreicht, welchen Einfluss niedrige Metallizitäten auf finite Wolken haben. Durch die geringeren Abschirmungseigenschaften des ISM dringt FUV Strahlung tiefer ein und verschiebt den Übergang von C^+ zu C und CO in tiefere Wolkenschichten. Als Resultat ist zum einen die Menge molekularen Materials geringer, aber auch die projizierte Fläche, die CO am Himmel einnimmt, der sogenannte *filling factor*, ist kleiner, was den beobachtbaren Strahlungsfluss zusätzlich reduziert. In Abb. 3.3 sieht man Modellvorhersagen für die $[\text{C II}]/\text{CO}(1-0)$ und $[\text{C I}]/\text{CO}(1-0)$ Linienverhältnisse, sowie entsprechende Beobachtungsdaten.

Zusätzlich zu dem chemischen Einfluss der Metallizität kommt der thermische, d.h. eine Veränderung der Heiz- und Kühlraten. Photoelektrische Heizung, einer der dominanten Heizprozesse in PDRs (Bakes und Tielens 1994; J.C. Weingartner und B. Draine 2001), ist in ihrer Effizienz bei niedrigerem Z reduziert. Gleiches gilt für die H_2 -Bildungs-Heizung. Auf der anderen Seite ist die Kontinuumsabstrahlung auch vermindert sowie die Kühlung durch Linienemission von CO , $[\text{C I}]$ und $[\text{C II}]$. Andere Prozesse, wie die Stoßabregung (und dadurch das Gas heizend) von vibrationsangeregtem H_2 , sind jedoch we-

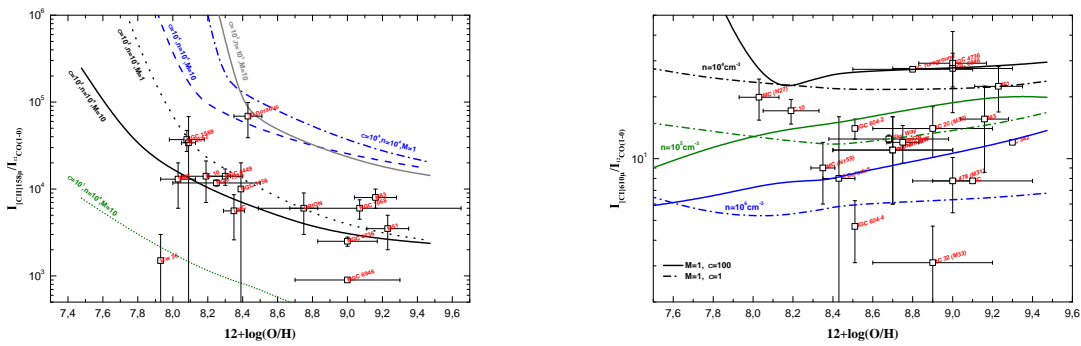


Abbildung 3.3: Einfluss der Metallizität Z auf die Linienemission von PDRs. **Links:** [CII]/CO(1-0) Linienverhältnis **Rechts:** [CI]_{610 μ m}/CO(1-0) Linienverhältnis.

niger stark betroffen. Der Metallizitätseffekt auf das resultierende thermische Gleichgewicht ist damit kaum a priori vorherzusagen und es bedarf immer der detaillierten Modellrechnungen.

3.2 Benchmark

PDR Modelle sind im Laufe der letzten 35 Jahre zu sehr komplexen Programm-codes geworden. Die kontinuierliche Gegenüberstellung von Modell- und Beobachtungsergebnissen führte zu einem wachsenden Verständnis der wichtigen astrophysikalischen und astrochemischen Prozesse und zu einer ständigen Weiterentwicklung der Modelle. Die hohe Nichtlinearität des betrachteten Problems sowie die komplexen numerischen Algorithmen, die bei seiner Lösung zum Einsatz kommen, machen es unbedingt notwendig, einen Vergleichsstandard (*Modell-Benchmark*) zu etablieren, um die Programme besser debuggen und testen, aber vor allem *besser verstehen zu können*.

Aus diesem Grund haben wir in der Zeit von 2004-2007 eine große, internationale Vergleichsstudie aller etablierten PDR-Modellcodes durchgeführt (Publikation 2). An einer Reihe von reduzierten Testproblemen konnte eine Vielzahl von Prozessen und Lösungsansätzen verglichen und evaluiert werden. Damit haben wir die erste und bisher einzige Referenzdatenbank von PDR Test-Modellen erstellen und öffentlich verfügbar machen können.²

In Abbildung 3.4 zeige ich als Beispiel den Vergleich der CH und OH Dichteprofile der beteiligten Modellcodes **vor** und **nach** dem Vergleichs-Benchmark. Vergleiche von PDR-Modellergebnissen unterschiedlicher Modelle sind schwierig. Die sehr unterschiedlichen Modellannahmen und Lösungsansätze erschwe-

²<http://www.astro.uni-koeln.de/pdr-comparison>

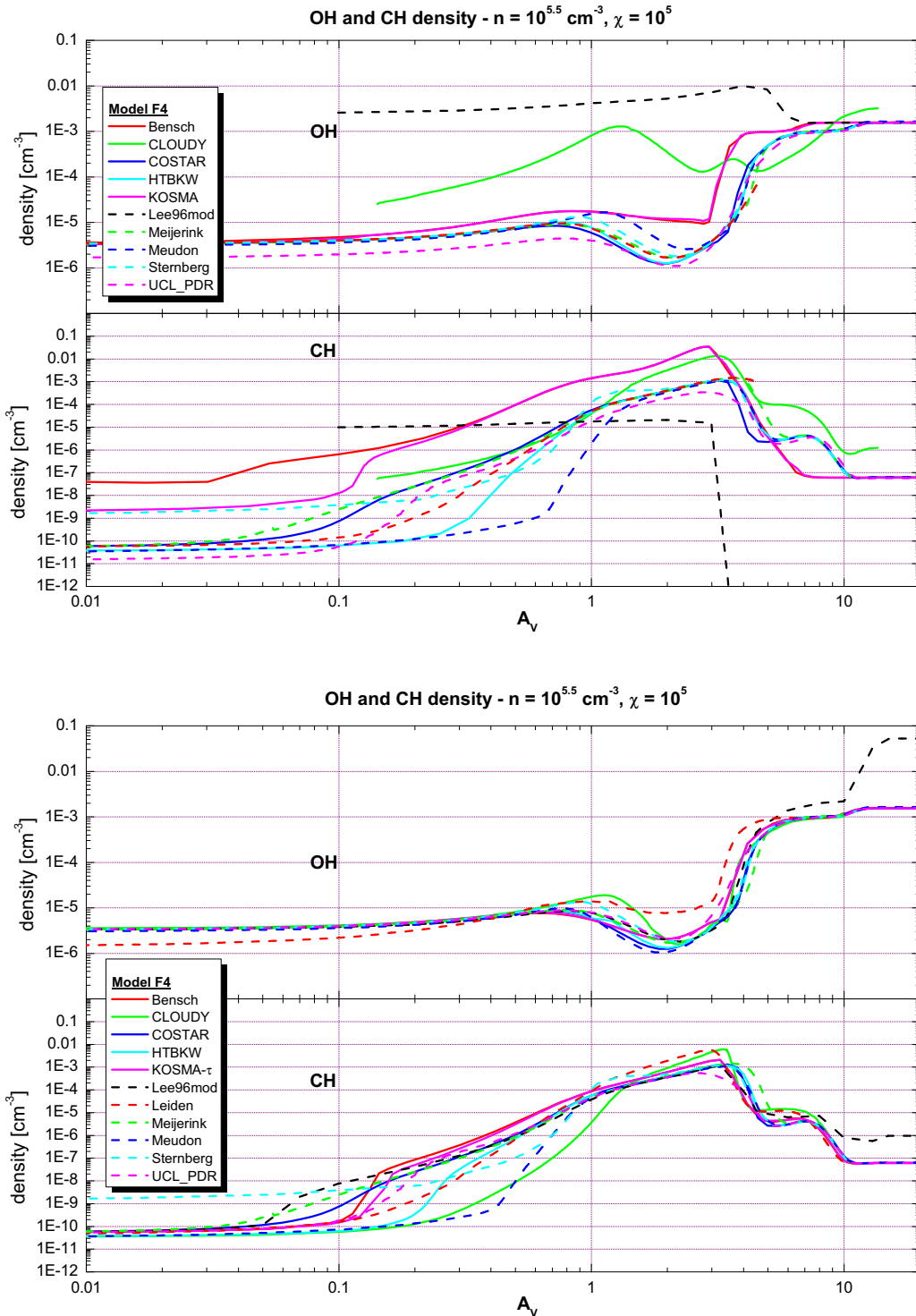


Abbildung 3.4: Vergleich von CH und OH Dichteprofilen des PDR-Benchmark Modells F4 ($n = 10^{5.5} \text{ cm}^{-3}$, $\chi = 10^5$, $T_{\text{gas}} = 50 \text{ K}$, $T_{\text{dust}} = 20 \text{ K}$) vor (oben) und nach (unten) dem Benchmark.

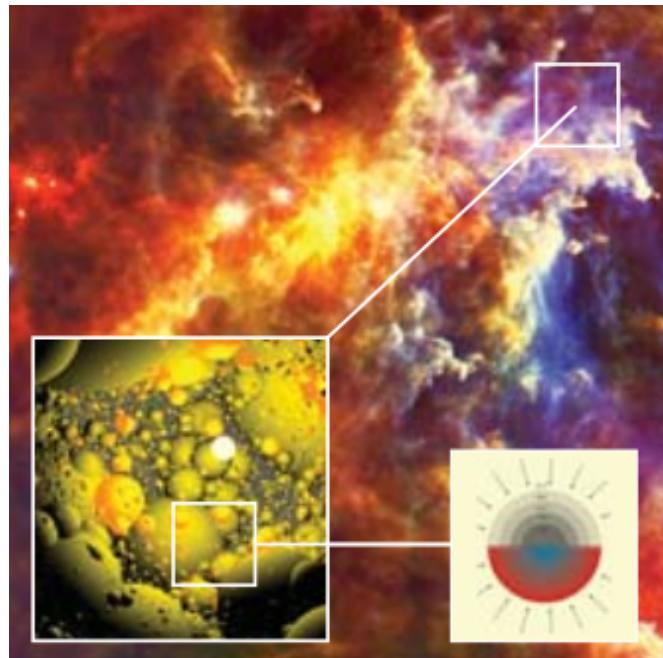


Abbildung 3.5: Künstlerische Darstellung des klumpigen Modellkonzepts.

ren dabei den direkten Vergleich. Die Veränderungen (vorher-nachher in Abb. 3.4) demonstrieren mehrere Punkte:

- Ein verbessertes Verständnis davon, welche Programmteile modifiziert werden müssen, um eine bessere Vergleichbarkeit sicherzustellen.
- Eine erfolgreiche Fehlersuche in allen beteiligten Codes, die erst durch die gestiegene Vergleichbarkeit ermöglicht wurde.
- Ein verbessertes Verständnis über wichtige, nicht zu vernachlässigende Prozesse im ISM.
- Die Erkenntnis, dass dieses Verständnis immer noch sehr lückenhaft ist (sichtbar an dem verbleibenden breiten Lösungsraum der Dichteprofile).

Es zeigte sich, dass solche konzentrierten Bemühungen notwendig sind, um eine hohe Qualität der Modellierung zu gewährleisten und auch für die Zukunft sicher zu stellen.³

3.3 Klumpige PDR-Struktur

Es stellt sich die Frage, wie man beobachtete Strukturen von interstellaren Molekülwolken, wie beispielsweise in Abb. 1.2, modellseitig abbilden kann. Wir wählen einen Ansatz, der sich die sphärische, finite Modellgeometrie zu

³Ähnliche Bemühungen haben auch in anderen Modellierungs-Bereichen erfolgreich stattgefunden (z.B. Ivezić u. a. 1997; van Zadelhoff u. a. 2002; Pinte u. a. 2009).

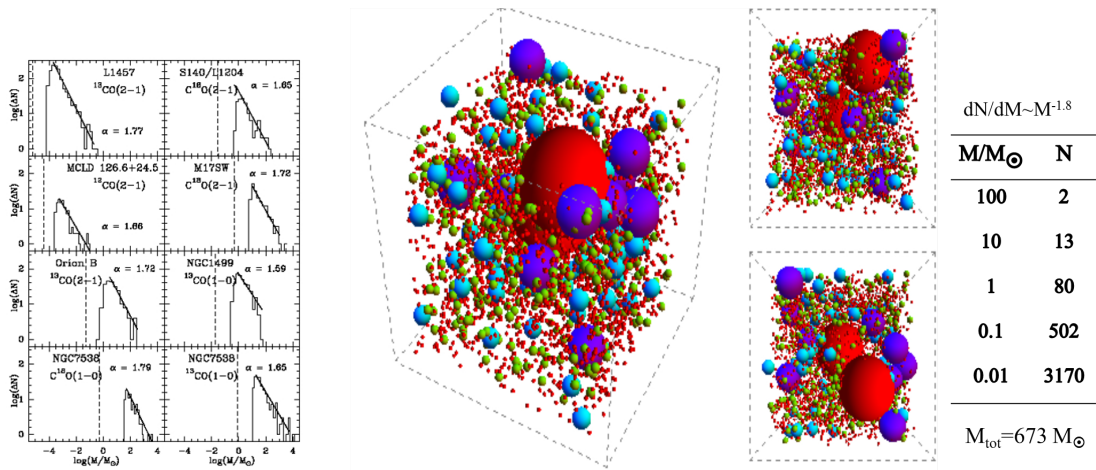


Abbildung 3.6: **Links:** Klumpen-Massenspektrum in verschiedenen GMCs (entnommen aus Kramer, Stutzki u. a. (1998)). **Rechts:** Zufällige Realisation eines Klumpenensembles entsprechend der beobachteten Massenspektren. Die Tabelle listet die Zahl der dargestellten Klumpen mit ihren Massen auf.

Nutzen macht, indem wir eine Vielzahl einzelner Modellklumpen, bzw. deren Emission, superpositionieren (Cubick, Stutzki u. a. 2008; Kramer, Cubick u. a. 2008; Sun, Ossenkopf u. a. 2008; Ossenkopf u. a. 2010a; Dedes u. a. 2010). Abbildung 3.5 veranschaulicht diesen Ansatz graphisch. Beobachtungen haben gezeigt, dass Riesen-Molekülwolken (*giant molecular clouds, GMC*) aus einer Vielzahl kleiner Klumpen zusammengesetzt sind. Dabei folgt die zahlenmäßige Zusammensetzung der Klumpen einer exponentiellen Klumpen-Massenverteilung der Form $dN/dM \propto M^{-\alpha}$ mit einem bemerkenswert universellen Exponenten $\alpha \approx 1.6 - 1.8$ (Kramer, Stutzki u. a. 1998). Die Größe der Klumpen ist mit ihrer Masse entsprechend der Massen-Größen-Relation korreliert: $M \propto R^\gamma$, mit $\gamma = 2.3$ (Heithausen u. a. 1998).

Ein Exponent $\alpha > 1$ bedeutet, dass es sehr viel mehr massearme Klumpen als massereiche gibt. Wenn $\alpha < 2$, dann ist die gesamte Ensemblemasse⁴ von den wenigen massereichen Klumpen dominiert. Betrachtet man jedoch nicht die Masse, sondern die Oberfläche, so dominieren deutlich die massearmen Klumpen. Der Massen-Größen-Relation zufolge sind die kleineren Klumpen gleichzeitig dichter als die massereichen. In Abb. 3.6 zeigen wir die zufällige Realisation eines solchen Ensembles mit einer Gesamtmasse von $673 M_\odot$.

Der Übergang von Einzelklumpen zu einem Klumpenensemble-Szenario hat deutlichen Einfluss auf die gesamte Emission. Die stark vergrößerte Oberfläche in einem Klumpenensemble favorisiert Emissionslinien, die bevorzugt in den äußeren Schichten der PDR erzeugt werden. Entweder, weil die entspre-

⁴Wir bezeichnen die Gesamtheit aller superpositionierten Einzelklumpen als Klumpenensemble.

chenden Spezies vorwiegend dort vorkommen, wie beispielsweise C^+ , CH^+ und CH , oder aufgrund der dort günstigen Anregungsbedingungen⁵. Besonders hochangeregte *high-J* Rotationsübergänge von CO benötigen heißes, dichtes Gas, um angeregt zu werden. Das spiegelt sich in der Gesamtemission des Ensembles wieder, welches eine deutlich erhöhte Intensität der hohen *J*-Linien aufweist.

Ein großer Vorteil der Komposition zu einem Ensemble ist, dass die Zerlegung in mehrere (willkürlich viele), unkorrelierte Gaskomponenten, die unabhängig voneinander an die Daten gefittet werden, entfällt. An ihre Stelle tritt eine, durch Beobachtungen motivierte, Gesetzmäßigkeit, die implizit die strukturelle Physik massereicher Sternentstehung beinhaltet. Der klumpige Modellansatz wird seit seiner programmatischen Umsetzung standardmäßig verwenden. In Abschnitt 3.6 zeige ich einige Anwendungsbeispiele.

3.4 Isotopenchemie

Bereits in Abschnitt 2.2 bin ich auf die Bedeutung des chemischen Netzwerkes eingegangen. Ein Aspekt, der in chemischen Datenbanken üblicherweise vernachlässigt wird, ist die Chemie der Isotopologe.⁶ Die Erweiterung des chemischen Netzwerkes um chemische Reaktionen mit Isotopologen ist ein komplexes Problem, das ich in Publikation 8 ausführlich beschreibe. Zur Umsetzung habe ich eine automatisierte Programmroutine entwickelt, die die Isotopisierung des chemischen Netzes automatisiert. Von besonderer Bedeutung bei der Isotopenchemie sind sogenannte Fraktionierungsreaktionen, also chemische Reaktionen, die das Häufigkeitsverhältnis der einzelnen Isotopologe untereinander verschieben. Ein Beispiel für eine solche Reaktion ist:



Die unterschiedliche Bindungsstärke der $^{13}\text{C}\equiv\text{O}^+$ und $\text{C}^-\equiv\text{O}^+$ Bindungen sorgt für unterschiedliche Reaktionsgeschwindigkeiten der Hin- und Rückreaktion bei Temperaturen $T < 100\text{ K}$. Im kühlen Gas reichert sich folglich ^{13}CO gegenüber ^{12}CO an, gleiches gilt umgekehrt für C^+ und $^{13}\text{C}^+$: CO **und** C^+ fraktionieren.

Die Fraktionierung hängt allerdings nicht nur von der Temperatur, sondern auch von der Verfügbarkeit der Reaktionspartner ab. Um C^+ zu fraktionieren benötigt man ausreichend CO und kühles C^+ Gas. Das Häufigkeitsverhältnis von $\text{C}^+/^{13}\text{C}^+$ kann dann auf einige Tausend steigen; $^{13}\text{C}^+$ ist kaum

⁵Anschaulich gesprochen vergrößert man den Anteil der PDR an der gesamten Masse.

⁶Isotopologe sind Moleküle, die sich nur in ihrer Isotopenzusammensetzung unterscheiden, also z. Bsp. sind ^{13}CCH und C^{13}CH Isotopologe von CCH.

noch vorhanden. Damit ist in diesen kühlen Regionen nicht gleichzeitig die Anreicherung von ^{13}CO möglich, die ausreichende $^{13}\text{C}^+$ Stoßpartner benötigt. Umgekehrt kann sich ^{13}CO gegenüber dem Hauptisotopolog anreichern, falls genügend $^{13}\text{C}^+$ bei nicht zu heißen Temperaturen ($T < 100 \text{ K}$) vorhanden ist. Solche Bedingungen findet man bei $A_V < 1$. Interessant ist, dass für beide Spezies Fraktionierung vorwiegend in Wolkenregionen stattfindet, in denen ihr Effekt auf die gesamte Säulendichten gering ist.

CO Fraktionierung lässt sich im diffusen Medium beobachten, wobei die Beobachtungsdaten Fraktionierung in beide Richtungen, also Ab- und Anreicherung von ^{13}CO zeigen, was in Modellrechnungen bisher nicht reproduziert werden kann. Die Fraktionierung von C^+ (immer zugunsten des Hauptisotops) ist ebenfalls schwer zu beobachten. In Publikation 9 diskutieren wir mögliche Bedingungen, die eine Beobachtung von C^+ Fraktionierung begünstigen, und präsentieren C^+/C^{13} Beobachtungen des Herschel/HIFI Instrumentes.

3.5 Selbstkonsistente Behandlung der Staubeigenschaften

Im vorherigen Kapitel haben wir bereits den starken Einfluss der Staubeigenschaften auf die gesamten Modellergebnisse unterstrichen. Ein wesentlicher Entwicklungspunkt der letzten Jahre war bei KOSMA- τ daher, eine möglichst selbstkonsistente Staubbeschreibung zu realisieren. Ziel war es, die Zusammensetzung des Staubes als neuen Modellparameter zu etablieren, und automatisch bei allen beteiligten Prozessen die entsprechenden Eigenschaften zu berücksichtigen. Zentraler Punkt war dabei die Kopplung von KOSMA- τ mit dem von Ryszard Szczerba entwickelten *Multi Component Dust Radiative Transfer Code MCDRT* (Yorke 1980; Szczerba u. a. 1997). MCDRT löst den frequenzabhängigen Staub-Strahlungstransport und berechnet die Staubtemperaturen aller Staubkomponenten in sphärischer Geometrie. In guter Näherung sind Kontinuums-Strahlungstransport und Staubtemperaturen von den restlichen PDR Prozessen entkoppelt, die MCDRT Ergebnisse können also als Input für KOSMA- τ dienen.

In Publikation 7 beschreibe ich detailliert diese Erweiterung und zeige erste Vorhersagen der spektralen Energieverteilung (SED) der Staubemission. Die wesentlichsten betroffenen Modellbereiche sind:

- Staubzusammensetzung/-verteilung nach J. C. Weingartner und B. T. Draine (2001): Es ist nun möglich, je nach Modellierungsumgebung die Stau-

beigenschaften anzupassen. Vor allem die Eigenschaften der PAHs und sehr kleinen Staubkörner ist nun enthalten.

- FUV Strahlungsfeld innerhalb der Modellwolke: Die mittlere Intensität, sowie die spektrale Signatur des FUV Feldes, ist nun an jedem Punkt innerhalb der Wolke bekannt. Aktuell sind davon die Berechnung der Photodissoziations- und Photoionisationsraten der beteiligten chemischen Spezies betroffen. Zukünftig kann die volle spektral Auflösung benutzt werden, um die Anregung von H₂ explizit zu berechnen.
- Photoelektrische Heizrate: J.C. Weingartner und B. Draine (2001) beschreiben die Photoelektrischen Heizraten der in J. C. Weingartner und B. T. Draine (2001) vorgestellten Staubverteilungen. Ich habe die Parametrisierung der Raten auf unseren Parameterbereich angepasst und in KOSMA- τ realisiert. Für MRN Staubverteilungen (Mathis, Rumpl und Nordsieck 1977) benutzen wir weiterhin die Photoelektrischen Heizraten von Bakes und Tielens (1994).
- Stauboberflächenchemie: Wir kennen nun die verfügbare Gesamtoberfläche aller Staubkomponenten und Korngrößen sowie die zugehörigen Staubtemperaturen. Das ist die wichtigste Voraussetzung, um chemische Prozesse auf Staub zu berücksichtigen. Als wichtigsten Prozess haben wir bereits die Bildung von H₂ auf der Oberfläche nach Cazaux und Tielens 2004; Cazaux und Tielens 2010 realisiert (siehe Abschnitt 2.2). Für die Zukunft ist die Erweiterung auf weitere wichtige Stauboberflächen-Reaktionen geplant.
- Kontinuumsemission: MCDRT berechnet die Staubemission der Modellwolke, die SED, welche nun zusätzlich zu den Linienemissionen mit Beobachtungsdaten verglichen werden kann. Abbildung 3.7 zeigt ein Beispiel für diesen Ansatz. Es ist deutlich zu sehen, dass die detaillierte Reproduktion der kurzweligen PAH-Emission bisher nur teilweise möglich ist. Die Übereinstimmung mit dem langwelligen Staubkontinuum ist jedoch bereits sehr gut.

3.6 Modellanwendung

Die KOSMA- τ -Modellergebnisse sind in der Vergangenheit bereits vielfach erfolgreich auf Beobachtungsdaten angewendet worden (z.B. Timmermann, Koester und Stutzki 1998; Bensch u. a. 2003; Bensch 2006; Mookerjea, Kramer, Röllig u. a. 2006; Pineda und Bensch 2007; Cubick, Stutzki u. a. 2008; Kramer,

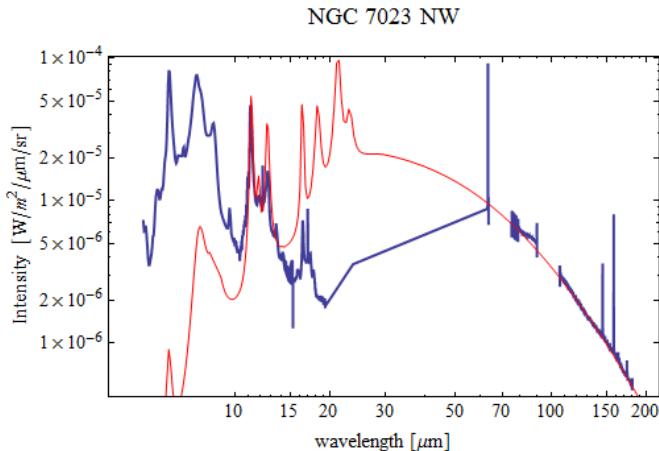


Abbildung 3.7: Spektrale Energieverteilung der Region NGC 7023NW (blau) und einem KOSMA- τ Modellklumpen mit $n = 10^{4.5} \text{ cm}^{-3}$, $M = 0.6 M_{\odot}$, und $\chi = 10^{3.7} \chi_{\text{Draine}}$.

Cubick u. a. 2008)⁷. Mit den modernen Ferninfrarot-Instrumenten, an Bord des Weltraumteleskops Herschel und der Stratosphärenteleskops SOFIA, sind weitere Wellenlängenbereiche erschlossen worden, die viele Beobachtungen kritischer Kühllinien von PDRs in großem Maßstab erst ermöglichen - damit aber auch die Anforderungen an die Modelle weiter erhöhen.

Extragalaktische Quellen mit niedriger Metallizität Wenige PDR Modelle erlauben die Berücksichtigung von veränderter Metallizität. Das prädestiniert KOSMA- τ zur Auswertung extragalaktischer Beobachtungen. Besonders Beobachtungen der Großen Magellansche Wolke (*Large Magellanic Cloud, LMC*), mit einer Metallizität von nur 40% des solaren Wertes, wurden mit Hilfe von KOSMA- τ -Modellen analysiert. Pineda, Mizuno, Stutzki u. a. (2008); Pineda, Mizuno, Röllig u. a. (2012)(Publikation 6) haben in LMC die N159W Region, die hellste Quelle von CO Linienemission in LMC, sowie 30 Doradus, die hellste und aktivste Sternentstehungsregion im lokalen Universum, beobachtet.

Mit Hilfe von KOSMA- τ konnten die physikalischen Parameter der beiden Regionen stark eingegrenzt und bestimmt werden. Die explizite Berücksichtigung des niedrigen Wertes von Z war dabei zentral, vor allem bei der simultanen Anpassung der Rotations- und der Feinstrukturkühllinien. Abbildung 3.8 zeigt die Modellergebnisse. Im linken und zentralen Schaubild repräsentieren die durchgezogenen Linien die Vorhersagen der ^{12}CO und ^{13}CO SLEDs, erstellt aus einer non-LTE Anregungsanalyse mit RADEX, für 30 Dor-10 (Publikation 6) und in N159W (Pineda, Mizuno, Stutzki u. a. 2008). Die grauen, gestrichelten Linien sind Ergebnisse des klumpigen KOSMA- τ PDR Fits. Zum Vergleich mit einer Galaktischen Sternentstehungsregion sind im rechten Schaubild die Ergebnisse für Carina-N und Carina-S gezeigt (Kramer,

⁷Wir stellen zusätzlich einen öffentlichen Zugang zu den Modellergebnissen bereit:<http://hera.ph1.uni-koeln.de/~pdr/>

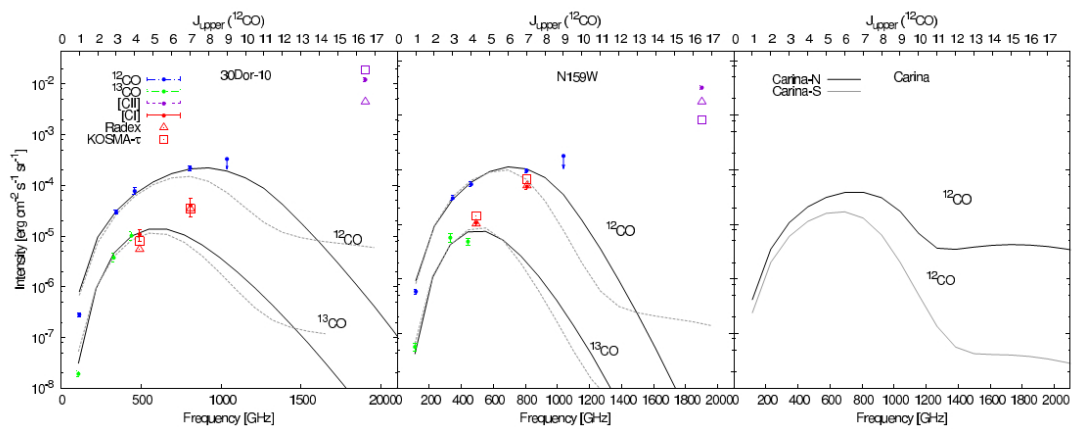


Abbildung 3.8: SLED für eine Reihe von Millimeter und Submillimeter Linien beobachtet in 30 Dor-10 (links), N159W (Mitte), und Carina-N und -S (rechts). Entnommen aus Pineda, Mizuno, Röllig u. a. (2012).

Cubick u. a. 2008). Die von KOSMA- τ hervorgesagten mittleren Gasdichten und FUV Strahlungsfelder stimmen dabei sehr gut mit Ergebnissen aus komplementären Untersuchungen überein.

In Publikation 5 präsentiere ich Geschwindigkeitsaufgelöste [C II] SOFIA/GREAT Beobachtungen der Zentrumsregion von IC 342, einer gasreichen Spiralgalaxie mit aktiver Sternentstehung im Zentrum. Ich vergleiche die spektrale Signatur der [C II] Spektren mit komplementären Daten und analysiere mittels PDR-Modellierung den Beitrag möglicher zentrumsnaher PDRs zur gesamten Emission.

Galaktische Sternentstehungsregionen Aufgrund der höheren räumlichen Auflösung ist die PDR Modellierung Galaktischer Quellen oft aufwendiger. Die geometrische Struktur der Wolke muss stärker bei der Modellierung berücksichtigt werden. In Abb. 3.9 zeigen wir die Modellanpassung an Herschel/HIFI Daten der massereichen Sternenstehungsregion DR 21 (Ossenkopf u. a. 2010a, Publikation 3). Eingebettet in dichtes, klumpiges Gas ist ein massereicher, junger Stern, der das ISM von innen stark beleuchtet und heizt. Die Geometrie der Quelle legt eine Kugelschalenanordnung des klumpigen PDR-Ensembles nahe. In dem konkreten Fall war es sogar notwendig, zwei geschachtelte Kugelschalen anzutragen, eine innere, heiße Komponente und eine kühlere, massereichere äußere Komponente (die eigentliche Struktur der Quelle ist um einiges komplexer und umfasst einen massiven Ausfluss und Schocks). Mit dieser Modell-Konfiguration war es uns möglich, die vielen verschiedenen Emissionslinien der Region simultan gut zu fitten und die lokalen physikalischen Parameter zu bestimmen (Tabelle rechts oben in der Abb.).

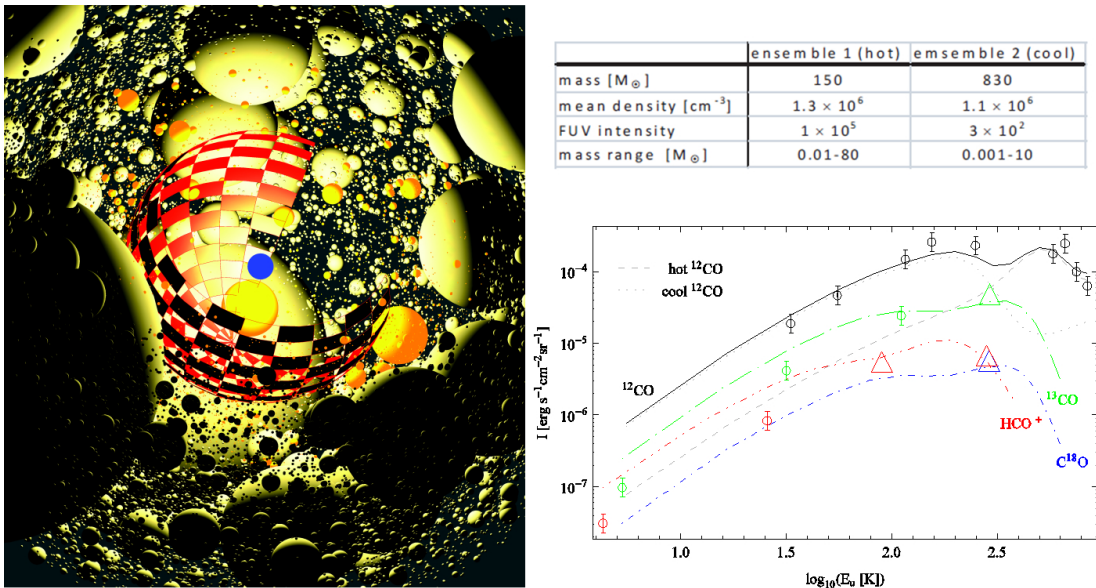


Abbildung 3.9: Visualisierung der klumpigen Modellstruktur von DR21. Ein-gebettet in die zentral H II -Region ist ein massereicher Stern. Die H II -Region umgibt klumpiges Gas, das wir durch 2 klumpige PDR-Ensembles nähern: Eine heiße Komponente (orangene Klumpen) und eine kühle Komponente (gelbe Klumpen).

Der Plot rechts unten in Abb. 3.9 zeigt den quantitativen Vergleich zwischen Modell und Beobachtungen. Die Doppelhöcker-Struktur der CO-SLEDs resultiert aus dem 2-Komponenten Ansatz. Man sieht deutlich, dass die Modell-Intensitäten die Beobachtungen gut repräsentieren. Eine strukturell und konzeptionell ähnliche Modellierung habe ich in Dedes u. a. (2010) für die Quelle S140 durchgeführt und konnte auch dort die Beobachtungsdaten zufriedenstellend reproduzieren.

Eine weitere, im Ansatz verwandte, Anwendung ist in Abbildung 3.10 zu sehen. Die plan-parallele Struktur der Quelle (Skizze rechts oben), des sogenannten Orion-Bars, ist durch zwei hintereinander angeordnete PDR-Ensembles genähert. Das Ensemble, das dem anregenden Stern näher steht, ist heißer, sieht also eine höhere FUV Intensität. Das dahinter liegende Ensemble ist bereits etwas abgeschirmt und entsprechend kühler. Die beiden Plots unten zeigen wieder den Vergleich der Modell- und beobachteten Intensitäten. Man sieht sehr gut, dass die CO SLEDs bis zu einem sehr hohen $J \approx 15$ gut getroffen werden. Erst die noch höheren Rotationsübergänge können nicht mehr korrekt im Modell erzeugt werden - ein Problem, dass alle gegenwärtigen PDR-Modell haben, und das gegenwärtig Gegenstand intensiver Untersuchungen ist.

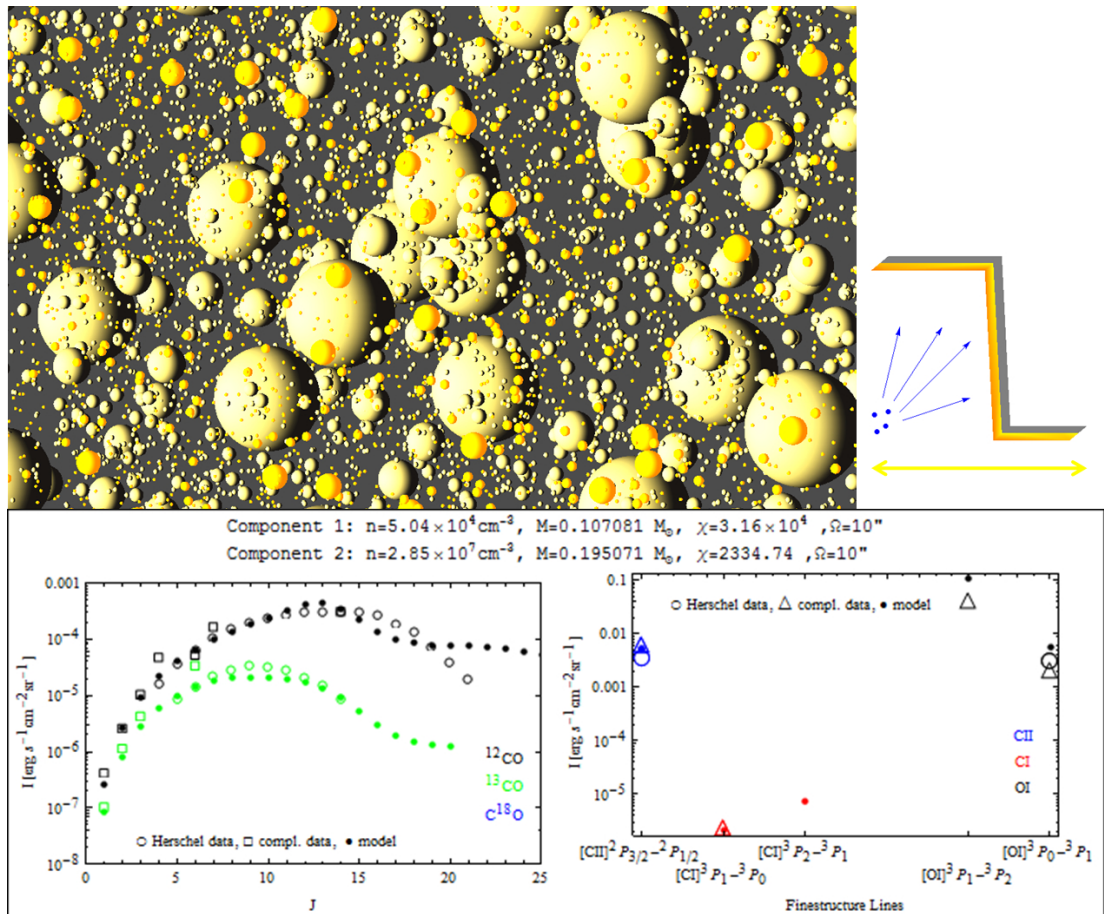


Abbildung 3.10: Visualisierung der klumpigen Modellstruktur des Orion-Bars. Zwei unterschiedlich stark beleuchtete Klumpenensemble sind hintereinander geschichtet. Die beiden Plots zeigen den Vergleich von Modell- und Beobachtungsdaten.

Ausblick

Die Entwicklung eines PDR-Modells ist, genau wie die jedes anderen vergleichbar komplexen Systems, niemals abgeschlossen. Es wird immer Bereiche geben, die verbessert oder hinzugefügt werden können. Die in den vorherigen Kapiteln beschriebenen Entwicklungsschritte von KOSMA- τ sind dabei eingebettet in ein langfristiges Entwicklungskonzept. Einige Punkte dieses Konzepts sind:

- Erweiterung von MCDRT: In Zukunft soll der MCDRT Staub-Code auch nicht-isotrope Streuung berücksichtigen. Aus Beobachtungen wissen wir, dass interstellarer Staub einen mittleren Streuwinkel $g = \langle \cos(\theta) \rangle \approx 0.7$ aufweist, also deutlich von der bisher angenommenen isotropen Streuung abweicht. Ein zweiter Entwicklungspunkt bei MCDRT ist die Berücksichtigung nicht-stationärer, stochastischer Heizprozesse von sehr kleinen Staubkörnern, welche die Temperaturverteilung der PAHs wesentlich beeinflussen wird. Dies wird die Staubemission bei Wellenlängen unter 30 μm stark beeinflussen und die Übereinstimmung mit den Beobachtungsdaten verbessern.
- Oberflächen-Chemie: KOSMA- τ soll in Zukunft zusätzlich zur reinen Gasphasen-Chemie auch Oberflächenreaktionen berücksichtigen. Mit der Integration der MCDRT Ergebnisse in KOSMA- τ haben wir bereits einen wesentlichen Grundstein für diese Entwicklung gelegt. Weitere Entwicklungsschritte in diese Richtung sind für die nahe Zukunft geplant.
- Erweiterte Anregungsmechanismen: Jüngste Beobachtungen zeigen deutliche Defizite bei der Berechnung des Anregungszustandes einzelner Spezies auf. Chemisches Pumpen sowie Kontinuums-Pumpen könnten dabei helfen, die Beobachtungen verbessert wiederzugeben. Ein Schritt in diese Richtung ist dabei der Übergang zur Modellierung des Strahlungstransports mit Hilfe des Strahlungstransportprogramms SimLine (Ossenkopf, Trojan und Stutzki 2001).

- Zeitabhängige Chemie: Längerfristig sollen die chemischen Ratengleichungssysteme auch zeitabhängig gelöst werden (GEAR Algorithmen).

Darüber hinaus ist und bleibt die Anwendung der Modellergebnisse auf Beobachtungsdaten auch zukünftig ein zentraler Punkt. Damit gehen eine ganze Reihe von weniger tiefgreifenden, womöglich aber sehr einflussreichen Modifikationen, einher. Zum Beispiel wird die bessere Anpassung der Modellparameter an die beobachteten Quellen zunehmend wichtiger. Das erfordert z.B. die spektrale Signatur der leuchtstarken Sterne genauer zu berücksichtigen. Auch eine Variation der Staubeigenschaften als Funktion der Wolkentiefe ist eine Möglichkeit für die Zukunft.

Literatur

- Abel, N. P. u. a. (Okt. 2008). „Sensitivity of PDR Calculations to Microphysical Details“. In: *ApJ* 686, S. 1125–1136.
- Agúndez, M. u. a. (Apr. 2010). „The Chemistry of vibrationally Excited H₂ in the Interstellar Medium“. In: *ApJ* 713, S. 662–670.
- Bakes, E. L. O. und A. G. G. M. Tielens (Juni 1994). „The photoelectric heating mechanism for very small graphitic grains and polycyclic aromatic hydrocarbons“. In: *ApJ* 427, S. 822–838.
- Bell, T. A. u. a. (März 2005). „The chemistry of transient microstructure in the diffuse interstellar medium“. In: *MNRAS* 357, S. 961–966.
- Bensch, F. (März 2006). „Neutral carbon and CO emission in the core and the halo of dark cloud Barnard 5“. In: *A&A* 448, S. 1043–1060.
- Bensch, F. u. a. (Juli 2003). „[C I] 492 GHz Mapping Observations of the High-Latitude Translucent Cloud MCLD 123.5+24.9“. In: *ApJ* 591, S. 1013–1024.
- Bernst, I. u. a. (Juli 2011). „MAGIX: A Generic Tool for Fitting Models to Astrophysical Data“. In: *Astronomical Data Analysis Software and Systems XX*. Hrsg. von I. N. Evans u. a. Bd. 442. Astronomical Society of the Pacific Conference Series, S. 505.
- Bisbas, T. G. u. a. (Sep. 2012). „3D-PDR: A new three-dimensional astrochemistry code for treating Photodissociation Regions“. In: *ArXiv e-prints*.
- Black, J. H. und E. F. van Dishoeck (Nov. 1987). „Fluorescent excitation of interstellar H₂“. In: *ApJ* 322, S. 412–449.
- Bolatto, Alberto D, James M Jackson und James G Ingalls (März 1999). „A Semi-analytical Model for the Observational Properties of the Dominant Carbon Species at Different Metallicities“. In: *The Astrophysical Journal* 513.1, S. 275–286. ISSN: 0004-637X.
- Boquien, M. u. a. (Juli 2010). „100 μm and 160 μm emission as resolved star-formation rate estimators in M 33 (HERM33ES)“. In: *A&A* 518, L70, S. L70.
- Braine, J. u. a. (Juli 2010). „Cool gas and dust in M 33: Results from the HERschel M 33 Extended Survey (HERM33ES)“. In: *A&A* 518, L69, S. L69.
- Cazaux, S. und A. G. G. M. Tielens (2002). „Molecular Hydrogen Formation in the Interstellar Medium:“ In: *ApJ* 575, S. L29–L32.

- Cazaux, S. und A. G. G. M. Tielens (2004). „H₂ Formation on Grain Surfaces“. In: *ApJ* 604, S. 222–237.
- (2010). „Erratum: H₂ Formation on Grain Surfaces (2004, ApJ, 604, 222“). In: *ApJ* 715, S. 698–699.
- Combes, F. u. a. (März 2012). „Dust and gas power spectrum in M 33 (HERM33ES)“. In: *A&A* 539, A67, A67.
- Cubick, M., J. Stutzki u. a. (Sep. 2008). „A clumpy-cloud photon-dominated regions model of the global far-infrared line emission of the Milky Way“. In: *A&A* 488, S. 623–634.
- Cubick, M. u. a. (Aug. 2005). „PDR modeling of the COBE far-infrared data of the milky way.“ In: *Astronomische Nachrichten* 326, S. 524–525.
- (Sep. 2007). „PDR Modelling of the Galactic FIR line emission“. In: *Astronomische Nachrichten* 328, S. 643.
- (2008). „Modelling of clumpy photon dominated regions“. In: *EAS Publications Series*. Hrsg. von C. Kramer, S. Aalto und R. Simon. Bd. 31. EAS Publications Series, S. 19–22.
- Dale, J. E., I. A. Bonnell und A. P. Whitworth (März 2007). „Ionization-induced star formation - I. The collect-and-collapse model“. In: *MNRAS* 375, S. 1291–1298.
- Dedes, C. u. a. (Okt. 2010). „The origin of the [C II] emission in the S140 photon-dominated regions. New insights from HIFI“. In: *A&A* 521, L24, S. L24.
- Dirienzo, W. J. u. a. (Okt. 2012). „Triggered Star Formation in Six H II Regions“. In: *ArXiv e-prints*.
- Draine, B. T. (Apr. 1978). „Photoelectric heating of interstellar gas“. In: *ApJS* 36, S. 595–619.
- Elmegreen, B. G. und C. J. Lada (Juni 1977). „Sequential formation of subgroups in OB associations“. In: *ApJ* 214, S. 725–741.
- Falgarone, E. u. a. (Juli 2010). „Strong CH⁺ J = 1-0 emission and absorption in DR21“. In: *A&A* 518, L118, S. L118.
- Fuente, A. u. a. (Okt. 2010). „Herschel observations in the ultracompact HII region Mon R2. Water in dense photon-dominated regions (PDRs)“. In: *A&A* 521, L23, S. L23.
- Gail, H.-P. u. a. (Juni 2009). „Stardust from Asymptotic Giant Branch Stars“. In: *ApJ* 698, S. 1136–1154.
- Gierens, K. M., J. Stutzki und G. Winnewisser (Juni 1992). „UV irradiated clumps in the Orion A molecular cloud - Interpretation of low-J CO observations“. In: *A&A* 259, S. 271–282.

- Goicoechea, J. R. u. a. (Juni 2011). „OH emission from warm and dense gas in the Orion Bar PDR“. In: *A&A* 530, L16, S. L16.
- Gratier, P., J. Braine, N. J. Rodriguez-Fernandez, K. F. Schuster, C. Kramer, E. M. Xilouris, F. S. Tabatabaei, C. Henkel, E. Corbelli, F. Israel, P. P. van der Werf, D. Calzetti, S. Garcia-Burillo, A. Sievers, F. Combes, T. Wiklind, N. Brouillet, F. Herpin, S. Bontemps, S. Aalto, B. Koribalski, F. van der Tak, M. C. Wiedner, M. Rollig u. a. (Okt. 2010). „M33 CO(2-1) and HI integrated intensity maps (Gratier+, 2010)“. In: *VizieR Online Data Catalog* 352, S. 29003.
- Gratier, P., J. Braine, N. J. Rodriguez-Fernandez, K. F. Schuster, C. Kramer, E. M. Xilouris, F. S. Tabatabaei, C. Henkel, E. Corbelli, F. Israel, P. P. van der Werf, D. Calzetti, S. Garcia-Burillo, A. Sievers, F. Combes, T. Wiklind, N. Brouillet, F. Herpin, S. Bontemps, S. Aalto, B. Koribalski, F. van der Tak, M. C. Wiedner, M. Röllig u. a. (Nov. 2010). „Molecular and atomic gas in the Local Group galaxy M 33“. In: *A&A* 522, A3, A3.
- Gratier, P. u. a. (März 2012a). „Giant molecular clouds in M33 (Gratier+, 2012)“. In: *VizieR Online Data Catalog* 354, S. 29108.
- (Juni 2012b). „Giant molecular clouds in the Local Group galaxy M 33★“. In: *A&A* 542, A108, A108.
- Habart, E., A. Abergel u. a. (März 2011). „Excitation of H₂ in photodissociation regions as seen by Spitzer“. In: *A&A* 527, A122, A122.
- Habart, E., F. Boulanger u. a. (Jan. 2003). „H₂ infrared line emission across the bright side of the rho Ophiuchi main cloud“. In: *A&A* 397, S. 623–634.
- Hartquist, T. W., H. T. Doyle und A. Dalgarno (Aug. 1978). „The intercloud cosmic ray ionization rate“. In: *A&A* 68, S. 65–67.
- Hegmann, M. und W. H. Kegel (Juni 2003). „Radiative transfer in clumpy environments: absorption and scattering by dust“. In: *MNRAS* 342, S. 453–462.
- Hegmann, M. u. a. (2000). „Fitting a Turbulent Cloud Model to CO Observations of Starless Bok Globules“. In: *Astronomische Gesellschaft Meeting Abstracts*. Hrsg. von R. E. Schielicke. Bd. 17. Astronomische Gesellschaft Meeting Abstracts, S. 10.
- (Juli 2003). „Physical Parameters of Bok Globules“. In: *Astronomische Nachrichten Supplement* 324, S. 130.
- (Jan. 2006). „The formation of interstellar molecular lines in a turbulent velocity field with finite correlation length. IV. Physical parameters of Bok Globules“. In: *A&A* 445, S. 591–600.

- Heithausen, A. u. a. (März 1998). „The IRAM key project: small-scale structure of pre-star forming regions. Combined mass spectra and scaling laws“. In: *A&A* 331, S. L65–L68.
- Hengel, C. u. a. (2000). „Determination of the physical parameters of Bok-globules by means of a stochastical radiative transfer method“. In: *Young European Radio Astronomers' Conference (YERAC)*.
- Hitschfeld, M. u. a. (Feb. 2008). „ ^{12}CO 4-3 and [CI] 1-0 at the centers of NGC 4945 and Circinus“. In: *A&A* 479, S. 75–82.
- Hollenbach, D. J. und A. G. G. M. Tielens (1997). „Dense Photodissociation Regions (PDRs)“. In: *ARA&A* 35, S. 179–216.
- (Jan. 1999). „Photodissociation regions in the interstellar medium of galaxies“. In: *Reviews of Modern Physics* 71, S. 173–230.
- Hollenbach, D., M. J. Kaufman u. a. (Aug. 2012). „The Chemistry of Interstellar OH^+ , H_2O^+ , and H_3O^+ : Inferring the Cosmic-Ray Ionization Rates from Observations of Molecular Ions“. In: *ApJ* 754, 105, S. 105.
- Hollenbach, D. und C. F. McKee (Nov. 1979). „Molecule formation and infrared emission in fast interstellar shocks. I Physical processes“. In: *ApJS* 41, S. 555–592.
- Indriolo, N., T. R. Geballe u. a. (Dez. 2007). „ H_3^+ in Diffuse Interstellar Clouds: A Tracer for the Cosmic-Ray Ionization Rate“. In: *ApJ* 671, S. 1736–1747.
- Indriolo, N., D. A. Neufeld u. a. (Aug. 2012). „Chemical Analysis of a Diffuse Cloud along a Line of Sight Toward W51: Molecular Fraction and Cosmic-Ray Ionization Rate“. In: *ArXiv e-prints*.
- Islam, F. u. a. (Dez. 2010). „Formation Pumping of Molecular Hydrogen in Dark Clouds“. In: *ApJ* 725, S. 1111–1123.
- Ivezic, Z. u. a. (Okt. 1997). „Benchmark problems for dust radiative transfer“. In: *MNRAS* 291, S. 121–124.
- Joblin, C. u. a. (Okt. 2010). „Gas morphology and energetics at the surface of PDRs: New insights with Herschel observations of NGC 7023“. In: *A&A* 521, L25, S. L25.
- Jura, M. (Juli 1974). „Formation and destruction rates of interstellar H_2 .“ In: *ApJ* 191, S. 375–379.
- Köster, B. u. a. (Apr. 1994). „Carbon monoxide line emission from photon dominated regions“. In: *A&A* 284, S. 545–558.
- Kramer, C., C. Buchbender u. a. (Juli 2010). „PACS and SPIRE photometer maps of M 33: First results of the HERschel M 33 Extended Survey (HERM33ES)“. In: *A&A* 518, L67, S. L67.

- Kramer, C., M. Cubick u. a. (Jan. 2008). „Clumpy photon-dominated regions in Carina. I. [C I] and mid-J CO lines in two 4'×4' fields“. In: *A&A* 477, S. 547–555.
- Kramer, C., J. Stutzki u. a. (Jan. 1998). „Clump mass spectra of molecular clouds“. In: *A&A* 329, S. 249–264.
- Le Bourlot, J. u. a. (Mai 2012). „Surface chemistry in the interstellar medium. I. H₂ formation by Langmuir-Hinshelwood and Eley-Rideal mechanisms“. In: *A&A* 541, A76, A76.
- Le Petit, F., B. Barzel u. a. (Okt. 2009). „Incorporation of stochastic chemistry on dust grains in the Meudon PDR code using moment equations. I. Application to the formation of H{2} and HD“. In: *A&A* 505, S. 1153–1165.
- Le Petit, F., C. Nehmé u. a. (Juni 2006). „A Model for Atomic and Molecular Interstellar Gas: The Meudon PDR Code“. In: *ApJS* 164, S. 506–529.
- Lee, H.-H. u. a. (Juli 1996). „Photodissociation of H₂_ and CO and time dependent chemistry in inhomogeneous interstellar clouds.“ In: *A&A* 311, S. 690–707.
- Lemaire, J. L. u. a. (Dez. 2010). „Competing Mechanisms of Molecular Hydrogen Formation in Conditions Relevant to the Interstellar Medium“. In: *ApJ* 725, S. L156–L160.
- Levrier, F. u. a. (Aug. 2012). „UV-driven chemistry in simulations of the interstellar medium. I. Post-processed chemistry with the Meudon PDR code“. In: *A&A* 544, A22, A22.
- Loenen, A. F. u. a. (Okt. 2010). „Excitation of the molecular gas in the nuclear region of M 82“. In: *A&A* 521, L2, S. L2.
- Mathis, J. S., W. Rumpl und K. H. Nordsieck (Okt. 1977). „The size distribution of interstellar grains“. In: *ApJ* 217, S. 425–433.
- McCall, B. J. u. a. (Apr. 2003). „An enhanced cosmic-ray flux towards ζ Persei inferred from a laboratory study of the H₃⁺-e⁻ recombination rate“. In: *Nature* 422, S. 500–502.
- McKee, C. F. und E. C. Ostriker (Sep. 2007). „Theory of Star Formation“. In: *ARA&A* 45, S. 565–687.
- Mennella, V. u. a. (Jan. 2012). „The Catalytic Role of Coronene for Molecular Hydrogen Formation“. In: *ApJ* 745, L2, S. L2.
- Möller, T. u. a. (Okt. 2012). „Modeling and Analysis Generic Interface for eXternal numerical codes (MAGIX)“. In: *ArXiv e-prints*.
- Mookerjea, B., C. Kramer und M. Roellig (Dez. 2005). „Emission from the Photon Dominated Regions in Cepheus B“. In: *American Astronomical Society Meeting Abstracts*. Bd. 37. Bulletin of the American Astronomical Society, S. 1303.

- Mookerjea, B., C. Kramer, M. Röllig u. a. (Sep. 2006). „Study of photon dominated regions in Cepheus B“. In: *A&A* 456, S. 235–244.
- Mookerjea, B., K. Sun u. a. (Aug. 2005). „CI/CO Mapping of IC 348 and Cepheus B using SMART on KOSMA.“ In: *Astronomische Nachrichten* 326, S. 581–582.
- Mookerjea, B. u. a. (Aug. 2011). „The Herschel M 33 extended survey (HerM33es): PACS spectroscopy of the star-forming region BCLMP 302“. In: *A&A* 532, A152, A152.
- (Jan. 2012). „The Herschel M 33 extended survey (HerM33es): PACS spectroscopy of the star forming region BCLMP 302 (Corrigendum)“. In: *A&A* 537, C3, S. C3.
- O'Donnell, E. J. und W. D. Watson (Juli 1974). „Upper limits to the flux of cosmic rays and X-rays in interstellar clouds.“ In: *ApJ* 191, S. 89–92.
- Okada, Y., O. Berné u. a. (Nov. 2011). „PDR properties and spatial structures probed by Herschel and Spitzer spectroscopy“. In: *EAS Publications Series*. Hrsg. von M. Röllig u. a. Bd. 52. EAS Publications Series, S. 293–294.
- Okada, Y., R. Güsten u. a. (Juni 2012). „Dynamics and photodissociation region properties in IC 1396A“. In: *A&A* 542, L10, S. L10.
- Ossenkopf, V., M. Gerin, R. Güsten u. a. (2008). „Prospectives of Herschel PDR observations“. In: *EAS Publications Series*. Hrsg. von C. Kramer, S. Aalto und R. Simon. Bd. 31. EAS Publications Series, S. 193–194.
- Ossenkopf, V., M. Gerin, G. Rolf u. a. (2010). „The chemistry of the warm and dense ISM seen by Herschel“. In: *38th COSPAR Scientific Assembly*. Bd. 38. COSPAR Meeting, S. 2478.
- Ossenkopf, V., H. S. P. Müller u. a. (Juli 2010). „Detection of interstellar oxidaniumyl: Abundant H_2O^+ towards the star-forming regions DR21, Sgr B2, and NGC6334“. In: *A&A* 518, L111, S. L111.
- Ossenkopf, V., M. Rollig, M. Cubick u. a. (Dez. 2007). „What are molecular clouds? - PDRs everywhere“. In: *Molecules in Space and Laboratory*.
- Ossenkopf, V., M. Rollig, A. Fuente u. a. (Mai 2011). „Carbon fractionation in photon-dominated regions“. In: *IAU Symposium*. Bd. 280. IAU Symposium, 280P.
- Ossenkopf, V., M. Röllig, C. Kramer u. a. (Nov. 2011). „The WADI key project: New insights to photon-dominated regions from Herschel observations“. In: *EAS Publications Series*. Hrsg. von M. Röllig u. a. Bd. 52. EAS Publications Series, S. 181–186.
- Ossenkopf, V., M. Röllig, D. A. Neufeld u. a. (Nov. 2012). „Herschel/HIFI observations of [CII] and [^{13}CII] in PDRs“. In: *ArXiv e-prints, accepted for publication in A&A*.

- Ossenkopf, V., C. Trojan und J. Stutzki (Nov. 2001). „Massive core parameters from spatially unresolved multi-line observations“. In: *A&A* 378, S. 608–626.
- Ossenkopf, V. u. a. (Juli 2010a). „HIFI observations of warm gas in DR21: Shock versus radiative heating“. In: *A&A* 518, L79, S. L79.
- (Juli 2010b). „HIFI observations of warm gas in DR21: Shock versus radiative heating“. In: *A&A* 518, L79, S. L79.
- Pineda, J. L. und F. Bensch (Aug. 2007). „Photon-dominated region modeling of the CO and [C I] line emission in Barnard 68“. In: *A&A* 470, S. 615–623.
- Pineda, J. L., N. Mizuno, M. Röllig u. a. (Aug. 2012). „Submillimeter line emission from LMC 30 Doradus: The impact of a starburst on a low-metallicity environment“. In: *A&A* 544, A84, A84.
- Pineda, J. L., N. Mizuno, J. Stutzki u. a. (Apr. 2008). „Submillimeter line emission from LMC N159W: a dense, clumpy PDR in a low metallicity environment“. In: *A&A* 482, S. 197–208.
- Pinte, C. u. a. (Mai 2009). „Benchmark problems for continuum radiative transfer. High optical depths, anisotropic scattering, and polarisation“. In: *A&A* 498, S. 967–980.
- Plume, R. u. a. (Jan. 2007). „The James Clerk Maxwell Telescope Spectral Legacy Survey“. In: *PASP* 119, S. 102–111.
- Röllig, M. (Aug. 2005). „[CII]/CO(1-0) line ratio at low metallicities.“ In: *Astronomische Nachrichten* 326, S. 529–530.
- (2008). „Metallicity Effects in PDRs“. In: *EAS Publications Series*. Hrsg. von C. Kramer, S. Aalto und R. Simon. Bd. 31. EAS Publications Series, S. 129–135.
- (Juni 2011). „Refit to numerically problematic UMIST reaction rate coefficients“. In: *A&A* 530, A9, A9.
- Röllig, M., N. P. Abel u. a. (Mai 2007). „A photon dominated region code comparison study“. In: *A&A* 467, S. 187–206.
- Röllig, M., C. Dedes u. a. (Nov. 2011). „Before and After Herschel - Modeling Photo-Induced Chemistry and PDR Line Emission in the Warm and Dense ISM (WADI)“. In: *EAS Publications Series*. Hrsg. von M. Röllig u. a. Bd. 52. EAS Publications Series, S. 301–302.
- Röllig, M., M. Hegmann, C. Hengel u. a. (2000). „Formation of CO in turbulent PDR’s“. In: *Young European Radio Astronomers’ Conference (YERAC)*.
- Röllig, M., M. Hegmann und W. H. Kegel (2001). „Photodissociation of CO in Turbulent Media“. In: *Astronomische Gesellschaft Meeting Abstracts*. Hrsg. von E. R. Schielicke. Bd. 18. Astronomische Gesellschaft Meeting Abstracts, S. 82.

- Röllig, M., M. Hegmann und W. H. Kegel (Sep. 2002a). „Photodissociation of CO in turbulent molecular clouds“. In: *A&A* 392, S. 1081–1088.
- (Sep. 2002b). „Photodissociation of CO in turbulent molecular clouds“. In: *A&A* 392, S. 1081–1088.
- Röllig, M., S. Jeyakumar und J. Stutzki (Juli 2003). „The CII-Layer of Low Metallicity PDR's“. In: *Astronomische Nachrichten Supplement* 324, S. 131.
- Röllig, M., W. H. Kegel u. a. (März 1999). „A search for methanol masers at 9.978 GHz and 10.058 GHz“. In: *A&A* 343, S. 939–942.
- Röllig, M., C. Kramer u. a. (Jan. 2011). „Photon dominated regions in NGC 3603. [CI] and mid-J CO line emission“. In: *A&A* 525, A8, A8.
- Röllig, M. und V. Ossenkopf (Nov. 2012). „Carbon fractionation in PDRs“. In: *ArXiv e-prints, accepted for publication in A&A*.
- Röllig, M., V. Ossenkopf, S. Jeyakumar u. a. (Juni 2006). „[CII] 158 μm emission and metallicity in photon dominated regions“. In: *A&A* 451, S. 917–924.
- Röllig, M., V. Ossenkopf und J. Stutzki (Aug. 2004). „The Surface Temperature of PDFs under Varying Metallicity Conditions“. In: *Astronomische Nachrichten Supplement* 325, S. 97.
- Röllig, M., R. Simon, R. Güsten u. a. (Juni 2012). „[CII] gas in IC 342“. In: *A&A* 542, L22, S. L22.
- Röllig, M., R. Simon, V. Ossenkopf u. a., Hrsg. (Nov. 2011). *Conditions and Impact of Star Formation*. Bd. 52. EAS Publications Series.
- Röllig, M., R. Szczerba u. a. (Nov. 2012). „Full SED fitting with the KOSMA- τ PDR code - I. Dust modelling“. In: *ArXiv e-prints, accepted for publication in A&A*.
- Sandford II, M. T., R. W. Whitaker und R. I. Klein (Sep. 1982). „Radiation-driven implosions in molecular clouds“. In: *ApJ* 260, S. 183–201.
- Schneider, N. u. a. (Juni 2012). „Globules and pillars seen in the [CII] 158 μm line with SOFIA“. In: *A&A* 542, L18, S. L18.
- Schulz, A. u. a. (Mai 2007). „The interstellar medium of the Antennae galaxies“. In: *A&A* 466, S. 467–479.
- Simon, R., V. Ossenkopf und M. Röllig (Nov. 2010). „JD14 - Examining the PDR-molecular cloud interface at mm and IR wavelengths“. In: *Highlights of Astronomy* 15, S. 399–400.
- Simon, R., N. Schneider u. a. (2008). „The PDR structure of the Monoceros Ridge in the Rosette Molecular Cloud“. In: *EAS Publications Series*. Hrsg. von C. Kramer, S. Aalto und R. Simon. Bd. 31. EAS Publications Series, S. 205–207.

- Sternberg, A. und A. Dalgarno (März 1989). „The infrared response of molecular hydrogen gas to ultraviolet radiation - High-density regions“. In: *ApJ* 338, S. 197–233.
- (Aug. 1995). „Chemistry in Dense Photon-dominated Regions“. In: *ApJS* 99, S. 565–+.
- Störzer, H., J. Stutzki und A. Sternberg (Juni 1996). „FUV irradiated molecular clumps: spherical geometry and density gradients.“ In: *A&A* 310, S. 592–602.
- Sun, K., C. Kramer, B. Mookerjea u. a. (2007). „Study of photon dominated regions in IC 348“. In: *IAU Symposium*. Hrsg. von B. G. Elmegreen und J. Palous. Bd. 237. IAU Symposium, S. 477–477.
- Sun, K., C. Kramer, H. Ungerechts u. a. (2008). „A Multiline Study of the Cepheus B Cloud“. In: *EAS Publications Series*. Hrsg. von C. Kramer, S. Aalto und R. Simon. Bd. 31. EAS Publications Series, S. 209–210.
- Sun, K., V. Ossenkopf u. a. (Okt. 2008). „The photon dominated region in the IC 348 molecular cloud“. In: *A&A* 489, S. 207–216.
- Szczerba, R. u. a. (Feb. 1997). „IRAS 22272+5435 - a source with 30 and 21 μm features.“ In: *A&A* 317, S. 859–870.
- Tielens, A. G. G. M. (Sep. 2005). *The Physics and Chemistry of the Interstellar Medium*.
- Tielens, A. G. G. M. und D. Hollenbach (Apr. 1985). „Photodissociation regions. I - Basic model. II - A model for the Orion photodissociation region“. In: *ApJ* 291, S. 722–754.
- Timmermann, R., B. Koester und J. Stutzki (Aug. 1998). „[CII] 158 and [OI] 63 μm ISO-Observations of L1457“. In: *A&A* 336, S. L53–L56.
- van der Tak, F. F. S. u. a. (Jan. 2012). „Detection of HF emission from the Orion Bar“. In: *A&A* 537, L10, S. L10.
- van Dishoeck, E. F. und J. H. Black (Nov. 1988). „The photodissociation and chemistry of interstellar CO“. In: *ApJ* 334, S. 771–802.
- van Hoof, P. A. M. u. a. (Juni 2004). „Grain size distributions and photoelectric heating in ionized media“. In: *MNRAS* 350, S. 1330–1341.
- van Zadelhoff, G.-J. u. a. (Nov. 2002). „Numerical methods for non-LTE line radiative transfer: Performance and convergence characteristics“. In: *A&A* 395, S. 373–384.
- Vasta, M. u. a. (Juni 2010). „Testing PDR models against ISO fine structure line data for extragalactic sources“. In: *MNRAS* 404, S. 1910–1921.
- Visser, R., E. F. van Dishoeck und J. H. Black (Aug. 2009). „The photodissociation and chemistry of CO isotopologues: applications to interstellar clouds and circumstellar disks“. In: *A&A* 503, S. 323–343.

- Wakelam, V., E. Herbst, J.-C. Loison u. a. (März 2012). „A KInetic Database for Astrochemistry (KIDA)“. In: *ApJS* 199, 21, S. 21.
- Wakelam, V., E. Herbst und F. Selsis (Mai 2006). „The effect of uncertainties on chemical models of dark clouds“. In: *A&A* 451, S. 551–562.
- Wakelam, V., I. W. M. Smith u. a. (Okt. 2010). „Reaction Networks for Interstellar Chemical Modelling: Improvements and Challenges“. In: *Space Sci. Rev.* 156, S. 13–72.
- Webber, W. R. (Okt. 1998). „A New Estimate of the Local Interstellar Energy Density and Ionization Rate of Galactic Cosmic Cosmic Rays“. In: *ApJ* 506, S. 329–334.
- Weingartner, J. C. und B. T. Draine (Feb. 2001). „Dust Grain-Size Distributions and Extinction in the Milky Way, Large Magellanic Cloud, and Small Magellanic Cloud“. In: *ApJ* 548, S. 296–309.
- Weingartner, J.C. und B. Draine (2001). „Photoelectric Emission from Interstellar Dust: Grain Charging and Gas Heating“. In: *ApJS* 134, S. 263–281.
- Weiβ, A. u. a. (Okt. 2010). „HIFI spectroscopy of low-level water transitions in M 82“. In: *A&A* 521, L1, S. L1.
- Whitworth, A. P. u. a. (Mai 1994). „The Preferential Formation of High-Mass Stars in Shocked Interstellar Gas Layers“. In: *MNRAS* 268, S. 291.
- Woodall, J. u. a. (Mai 2007). „The UMIST database for astrochemistry 2006“. In: *A&A* 466, S. 1197–1204.
- Yorke, H. W. (Juni 1980). „Numerical solution of the equation of radiation transfer in spherical geometry“. In: *A&A* 86, S. 286–294.
- Zielinsky, M., J. Stutzki und H. Störzer (Juni 2000). „On the isotopomeric CO line brightnesses in clumpy photon dominated regions: apparent fractionation of $^{13}\text{CO}/\text{C}^{18}\text{O}$ “. In: *A&A* 358, S. 723–727.

Publikationen

[CII] 158 μm emission and metallicity in photon dominated regions[★]

M. Röllig¹, V. Ossenkopf^{1,2}, S. Jeyakumar, J. Stutzki¹, and A. Sternberg³

¹ I. Physikalisches Institut, Universität zu Köln, Zülpicher Str. 77, 50937 Köln, Germany
e-mail: roellig@ph1.uni-koeln.de

² SRON National Institute for Space Research, PO Box 800, 9700 AV Groningen, The Netherlands

³ School of Physics and Astronomy, Tel Aviv University, Ramat Aviv 69978, Israel

Received 18 July 2005 / Accepted 14 November 2005

ABSTRACT

We study the effects of a metallicity variation on the thermal balance and [CII] fine-structure line strengths in interstellar photon dominated regions (PDRs). We find that a reduction in the dust-to-gas ratio and the abundance of heavy elements in the gas phase changes the heat balance of the gas in PDRs. The surface temperature of PDRs decreases as the metallicity decreases except for high density ($n > 10^6 \text{ cm}^{-3}$) clouds exposed to weak ($\chi < 100$) FUV fields where vibrational H₂-deexcitation heating dominates over photoelectric heating of the gas. We incorporate the metallicity dependence in our KOSMA- τ PDR model to study the metallicity dependence of [CII]/CO line ratios in low metallicity galaxies. We find that the main trend in the variation of the observed CII/CO ratio with metallicity is well reproduced by a single spherical clump, and does not necessarily require an ensemble of clumps as in the semi-analytical model presented by Bolatto et al. (1999).

Key words. ISM: abundances – ISM: structure – ISM: clouds – ISM: general – galaxies: ISM – galaxies: abundances

1. Introduction

The bright line emission from photon-dominated regions (PDRs) is one of the key tracers of the star formation activity throughout the evolution of galaxies in the course of the cosmological evolution. Hence, proper modeling of PDR emission is of central importance for the interpretation of the observations, in order to derive the physical parameters and the chemical state of the ISM in external galaxies. The extensive literature on PDR emission, both observationally and from the modeling side, has largely concentrated on bright Galactic sources and starburst galaxies. The effect of different metallicity for the resulting PDR emission has, up to now, drawn little attention. It is, however, very important in order to cover the full course of galactic evolution, starting with low metallicity material of cosmological origin. Many nearby galaxies, such as dwarf galaxies, irregular galaxies and the Magellanic Clouds have a low metallicity (Lisenfeld & Ferrara 1998; Kunth & Östlin 2000; Pustilnik et al. 2002; Lee et al. 2003). Within the Galaxy, as well as in other spiral galaxies, there is a radial decrease in the metallicity of molecular clouds and associated HII regions (Zaritsky et al. 1994; Arimoto 1996; Giveon et al. 2002; Bresolin et al. 2004). These systems provide the opportunity to study star formation and photon-dominated regions (PDRs) for a variety of metallicities.

In PDRs the molecular gas is heated by the far-ultraviolet (FUV) radiation field, either the strong FUV radiation in the vicinity of hot young stars, or weak average FUV fields in the Galaxy. The gas cools through the spectral line radiation of atomic and molecular species (Hollenbach & Tielens 1999; Sternberg 2004). The gas-phase chemistry together with a depth dependent FUV intensity lead to the formation of atomic and

molecular species at different depths through the cloud. This typical stratification of PDRs is for example reflected by the H/H₂ and C⁺/C/CO transitions (Sternberg & Dalgarno 1995; Boger & Sternberg 2005). At low visual extinctions the gas is cooled by emission of atomic fine-structure lines, mainly [CII] 158 μm and [OI] 63 μm . At larger depths, millimeter, sub-millimeter and far-infrared molecular rotational-line cooling (CO, OH, H₂O) becomes important together with the interaction of dust and gas. Physical conditions such as temperature and density can be derived, by comparing the observed line emissions with model predictions (Le Bourlot et al. 1993; Wolfire et al. 1995; Störzer et al. 1996; Warin et al. 1996; Kaufman et al. 1999; Zielsky et al. 2000; Störzer et al. 2000; Gorti & Hollenbach 2002).

[CII] emission is a widely used diagnostic indicator of star formation (Stacey et al. 1991; Pierini et al. 1999; Malhotra et al. 2000; Boselli et al. 2002b; Pierini et al. 2003; Kramer et al. 2004). Observations suggest that low metallicity systems have higher [CII] to CO rotational line ratios compared to the Galactic value. In particular, the intensity ratio $I_{\text{CII}}/I_{\text{CO}}$ may vary from ~ 1000 in the inner Milky Way, up to $\sim 10^5$ in extremely low metallicity systems (e.g. Madden et al. 1997; Mochizuki et al. 1998; Bolatto et al. 1999; Madden 2000; Hunter et al. 2001). Several studies have suggested that a lower abundance of heavy elements affects the chemical structure of PDRs and the cooling line emission, and that estimates of molecular gas masses from the observed CO($J = 1-0$) line intensities using the standard conversion factor may underestimate the true masses in such objects (Wilson 1995; Israel 1997; Israel et al. 2003; Rubio et al. 2004).

Bolatto et al. (1999) modelled the metallicity variation of the line ratio [CII]/CO(1–0), for an ensemble of spherical “clumps”, assuming an inverse relation between the size of the C⁺ region

[★] Appendices are only available in electronic form at
<http://www.edpsciences.org>

and the metallicity. However the sizes of the C⁺, C and CO regions also depend on the chemistry in PDRs and the chemical network is modified at low metallicities (Lequeux et al. 1994). Additionally it has been suggested that the size of the C⁺, C and CO regions may also significantly depend on the overall cloud morphology, e.g. density variations (Hegmann & Kegel 2003) and velocity fluctuations (Röllig et al. 2002). Moreover the temperature of the molecular gas might depend on the metallicity which affects the observable line intensities (Wolfire et al. 1995).

We study the effects of metallicity changes on the temperature and chemical structure of PDRs. In Sect. 2 we consider the dependence of the PDR gas temperature on the metallicity using a simplified semi-analytic model and compare it with numerical results from full PDR model calculations. Our computations were carried out using an updated version of our spherical KOSMA- τ model (Störzer et al. 1996) which was originally adapted from the plane-parallel model presented by Sternberg & Dalgarno (1995). In Sect. 3 we examine the predicted size of the C⁺ zones as a function of metallicity. We then model the strength of the [CII] emission and investigate the dependence of the [CII]/CO($J = 1-0$) line ratio on the metallicity. Finally we compare the results with observational data in Sect. 4.

2. Metallicity dependence of the surface temperature

The basic cooling and heating processes in PDRs, are affected by the abundances of elements as well as the content and the composition of dust grains (Wolfire et al. 1995; Kaufman et al. 1999). The dust-to-gas ratio (D/G) and the optical properties of the dust may depend on the metallicity, Z . Fits to observations suggest that the ratio depends almost linearly on the metallicity, $D/G \propto Z^{1.146}$ (Boselli et al. 2002a). There are other studies that find deviations from linearity for higher values of D/G (Lisenfeld & Ferrara 1998). Li & Draine (2002) suggested that the mixture of PAHs in the metal-poor SMC differs from the Milky Way. There are a few observations indicating that PAHs could have been destroyed by intense UV fields at low metallicities (Thuan et al. 1999; Bolatto et al. 2000), but the detailed composition of dust in low metallicity environments and the influence on its optical properties is not yet understood. Because of the insufficient knowledge we assume in our model that the composition of the grains does not change with metallicity and that the dust-to-gas ratio and the gas-phase abundance of heavy elements scale linearly with Z .

Changes in Z affect the abundances of major coolants as well as the electron densities in PDRs. Additionally, a reduction in the dust abundance diminishes the UV opacity, the photo electric heating rate, and the H₂ formation rate. These changes affect the temperature and chemistry in the surface layers where C⁺ is most abundant.

The dependence of the surface gas temperature on Z can be estimated considering the balance of cooling and heating. The dominant cooling processes depend predominantly on the total hydrogen gas density n , [OI]63 μm , [CII]158 μm emission, and gas-grain collisions are important cooling processes (Burke & Hollenbach 1983; Störzer et al. 1996). Their relative importance in the different regimes is discussed in Sect. 2.2.1. The dominant heating process depends on the far-ultraviolet (FUV; 6–13.6 eV) field and the density. Grain photo-electric emission (PE) (d'Hendecourt & Léger 1987; Lepp & Dalgarno 1988; Verstrate et al. 1990; Bakes & Tielens 1994), collision deexcitation of FUV pumped molecular hydrogen H₂*

(Sternberg & Dalgarno 1989; Burton et al. 1990) and heating from H₂ formation play important roles. They are discussed in detail in Sect. 2.2.2. By explicitly considering the metallicity dependence of each of these cooling and heating processes and identifying the dominant processes in the different parameter regimes we will show how the energy balance in PDRs depends on Z for a quantitative understanding of the PDR surface temperature.

2.1. The KOSMA- τ PDR model

In our study we use an updated version of the spherical PDR code described in detail by Störzer et al. (1996). Briefly, this model solves the coupled equations of energy balance (heating and cooling), chemical equilibrium, and radiative transfer in spherical geometry. The PDR-clumps are characterized by a) the incident FUV field intensity χ , given in units of the mean interstellar radiation field of Draine (1978); b) the clump mass; and c) the average density of the clump, for a radial power-law density distribution with index γ . We incorporate the effects of varying metallicity by varying the assumed abundance of dust grains and heavy elements. The following parameters are multiplied by the metallicity factor Z : (a) the total effective FUV dust absorption cross section per hydrogen nucleus σ ; (b) the photoelectric heating rate; (c) the H₂ formation rate; (d) the metal abundance. We consider a range of Z from 0.2 to 1. For $Z = 1$ we use $\sigma = 1.9 \times 10^{-21} \text{ cm}^2$, C/H = 1.4×10^{-4} , and O/H = 3×10^{-4} as standard values for the local ISM (Hollenbach & Tielens 1999). These values are slightly lower than recent solar values of $12 + \log(\text{O/H}) \approx 8.7$ by Asplund et al. (2004). For a detailed discussion see Baumgartner & Mushotzky (2005). We do not consider gas depletion on grains.

2.2. Semi-analytic approximations

The results of the full numerical computations can be understood and anticipated using some simplifying semi-analytical approximations. Here, we focus on the surface temperature of the PDR at $A_V = 0$, as we are not interested in the shielding properties of low-metal PDRs but in the thermal behavior of the low-extinction region dominating the CII emission. We study how the thermal properties respond to altered elemental abundance. We assume the molecular cloud is sufficiently thick such that it absorbs all radiation coming from the backside, leading to an emission line escape probability $\beta(\tau = 0) = 1/2$ at the surface.

2.2.1. Cooling

In the simplified model we include the three main cooling processes: [CII] and [OI] line cooling and gas-grain collisional cooling (Burke & Hollenbach 1983; Störzer et al. 1996). Gas cooling is generally dominated by fine structure emission of [CII] and [OI]. Gas-grain cooling starts to contribute significantly for high densities. At $n \gtrsim 10^6 \text{ cm}^{-3}$ the coupling between gas and dust is strong enough so that the efficient cooling of the dust by infrared radiation also provides a major coolant to the gas. The total cooling rate per unit volume by these radiative processes is the sum

$$\Lambda_{\text{tot}} = \Lambda_{\text{CII}} + \Lambda_{\text{OI}} + \Lambda_{\text{g-g}}. \quad (1)$$

With the abundance of carbon, oxygen, and dust scaling with the metallicity, the total cooling rate is also linear in Z .

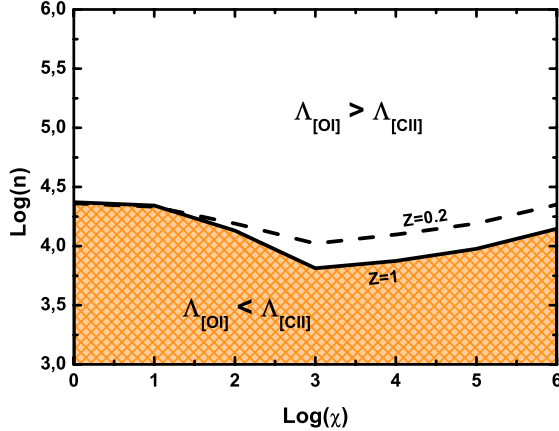


Fig. 1. The solid and dashed line represent the points in $n - \chi$ -parameter space where $\Lambda_{\text{OI}} = \Lambda_{\text{CII}}$ for metallicities of $Z = 1$ and $Z = 0.2$ respectively.

Analytic expressions for the three cooling processes are derived in Appendix A. In Fig. 1 we show the relation between the fine-structure line cooling contributions as a function of n and χ for two different values of Z . The region in parameter space where [CII] cooling dominates over [OI] is shaded in gray. For densities above $10^{4.5} \text{ cm}^{-3}$ [CII] cooling is quenched and [OI] cooling dominates. At all lower densities [CII] cooling dominates. Every point in Fig. 1 corresponds to a different equilibrium temperature and resulting ratio $\Lambda_{\text{CII}}/\Lambda_{\text{OI}}$. The dependence on χ in Fig. 1 results from the implicit temperature dependence of the fine-structure cooling rates. Grain cooling dominates only for densities greater than 10^6 cm^{-3} .

2.2.2. Heating

The dominant heating process depends on the FUV field intensity and density. For high intensities grain photo-electric heating dominates. The rate for this process, given by Bakes & Tielens (1994), is $\Gamma_{\text{PE}} = 10^{-24} \epsilon G_0 n_{\text{H}} Z \text{ erg s}^{-1} \text{ cm}^{-3}$ where ϵ is the photoelectric heating efficiency and G_0 is the UV intensity in units of the Habing field. Following Bakes & Tielens (1994) the photoelectric heating efficiency is given by:

$$\epsilon = \frac{3 \times 10^{-2}}{1 + 2 \times 10^{-4} (G_0 T^{1/2} / n_e)} \quad (2)$$

with n_e being the electron density in cm^{-3} and T the dust temperature in K. We set $G_0 = 1.71 \times 0.5 \chi$ to account for the relative factor of 1.71 between the Habing and Draine fields, and the fact that at the surface of optically thick clouds radiation is incident from a solid angle of 2π rather than 4π steradians. In evaluating the efficiency ϵ we use the analytic expression for the electron density derived in Appendix B:

$$n_e \approx 0.84 \times 10^{-4} n Z \left(1 + \sqrt{1 + 14.4 \frac{T^{0.75}}{n Z^2}} \right) \text{ cm}^{-3}. \quad (3)$$

It is common to express the net PE heating rate as $\Gamma_{\text{PE}}^{\text{net}} = \Gamma_{\text{PE}} - \Lambda_{\text{rec}}$, where Λ_{rec} is the cooling rate due to electron recombination. We adopt the analytical fit from Bakes & Tielens (1994):

$$\Lambda_{\text{rec}} = 3.49 \times 10^{-30} T^{0.944} \left(\frac{G_0 T^{1/2}}{n_e} \right)^{0.735} n_e n Z. \quad (4)$$

In dense PDRs a second important heating source is the collisional deexcitation of vibrationally excited H_2^* . The rate for this process can be expressed as

$$\Gamma_{\text{H}_2^*} = \chi P n_{\text{H}_2} \Delta E f \text{ erg s}^{-1} \text{ cm}^{-3}, \quad (5)$$

with n_{H_2} is the density of molecular hydrogen, $P = 2.9 \times 10^{-10} \text{ s}^{-1}$ is the pumping rate for a unit FUV field, $\Delta E \approx 23500 \text{ K}$ is the characteristic vibrational transition energy, and an efficiency factor f accounting for all processes that may reduce the number of de-exciting collisions (see Appendix B). The balance equation for the formation and destruction of H_2 is

$$n n_{\text{H}} R = \chi D n_{\text{H}_2} \quad (6)$$

where $D = 2.6 \times 10^{-11} \text{ s}^{-1}$ is the total dissociation rate in a $\chi = 1$ FUV field, and $R = R_0 Z$ is the grain surface H_2 formation rate coefficient ($\text{cm}^3 \text{ s}^{-1}$). Here, it is implicitly assumed that dust grains are always covered by enough H atoms, so that the recombination rate is only limited by the number of H-dust collisions. We use the standard recombination rate R_0 by Hollenbach & Salpeter (1971); Hollenbach et al. (1971):

$$R_0 = 3 \times 10^{-18} f_a S T^{1/2} \text{ cm}^3 \text{ s}^{-1}, \quad (7)$$

where the accommodation coefficient, f_a and the sticking probability S are independent of Z (Hollenbach & McKee 1979). Cazaux & Spaans (2004) show that gas-phase formation of H_2 becomes important for $Z < 10^{-3}$, well below the minimum value of Z we consider here.

The density of atomic and molecular hydrogen is determined by Eq. (6) and can be written as

$$n_{\text{H}} = n \frac{1}{1 + 2\alpha} \text{ and } n_{\text{H}_2} = n \frac{\alpha}{1 + 2\alpha} \quad (8)$$

respectively, with $\alpha = n R / (\chi D)$ being the ratio between formation and destruction rate coefficients. For example, for $\chi = 1$ and $n = 10^3 \text{ cm}^{-3}$ more than 99% of the gas at the surface is atomic. For $Z = 1$ and a unit Draine field, $\alpha = 1$ and $n_{\text{H}} = n_{\text{H}_2}$, for densities $n \approx 10^6 \text{ cm}^{-3}$. As only R depends on Z , it follows that $\alpha \propto Z$ and the density n at which the H and H_2 densities are equal at the cloud surface scales as $1/Z$.

From Eqs. (5)–(7) it follows that

$$\Gamma_{\text{H}_2^*} = \left(\frac{P}{D} \right) R_0 Z n n_{\text{H}} \Delta E f \text{ erg s}^{-1} \text{ cm}^{-3}. \quad (9)$$

We see that $\Gamma_{\text{H}_2^*}$ is maximized when $n_{\text{H}} = n$ and all of the hydrogen is atomic. The efficiency factor f in Eq. (5) is largest in the limit of high gas density and low FUV intensity, where radiative processes become negligible in depopulating the excited vibrational levels compared to collisional deexcitation. For a temperature of $T = 100 \text{ K}$, $Z = 1$, $\chi = 1$, and $n = 10^3 \text{ cm}^{-3}$ we obtain $\Gamma_{\text{H}_2^*}^{\text{max}} \approx 1.8 \times 10^{-24} \text{ erg cm}^{-3} \text{ s}^{-1}$ with $f = 2.8 \times 10^{-3}$.

This is in good agreement with the results from the numerical PDR model shown in Fig. C.1 in Appendix C. The assumption of a constant formation rate R_0 is valid for $\chi \lesssim 10^3$. A higher UV field the dust temperature increases leading to a rapid reduction of the accommodation coefficient f_a . Hence in our calculations the maximum H_2 heating rate drops for $\chi \gtrsim 10^3$ as shown in the bottom plot in Fig. C.1 in Appendix C.

H_2 not only contributes to the heating, but cools the gas at higher temperatures (Sternberg & Dalgarno 1989). To account for the cooling we define the net heating rate $\Gamma_{\text{H}_2}^{\text{net}} = \Gamma_{\text{H}_2^*} - \Lambda_{\text{H}_2}$.

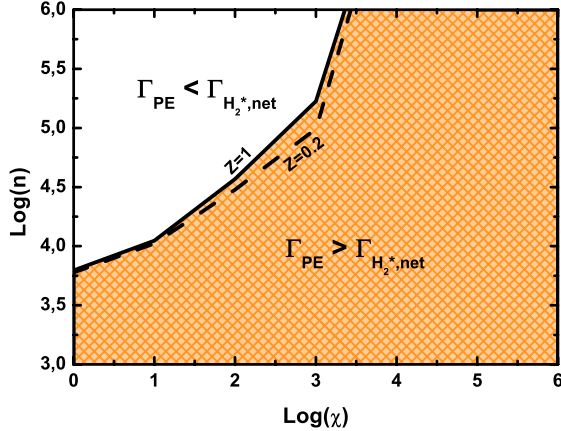


Fig. 2. The solid and dashed line represent the points in $n - \chi$ -parameter space where $\Gamma_{H_2^*,\text{net}} = \Gamma_{\text{PE}}$ for metallicities of $Z = 1$ and $Z = 0.2$ respectively.

Using the analytic approximations to the molecular level structure of H₂ derived in Appendix C we obtain

$$\begin{aligned} \Gamma_{H_2^*} &= n_{H_2} \frac{\chi P}{1 + \left(\frac{A_{\text{eff}} + D_{\text{eff}}}{\gamma n} \right)} \Delta E \\ &= n_{H_2} \frac{9.4 \times 10^{22} \chi}{1 + \left(\frac{1.9 \times 10^{-6} + 4.7 \times 10^{-10} \chi}{\gamma n} \right)} \end{aligned} \quad (10)$$

$$\begin{aligned} \Lambda_{H_2} &= n n_{H_2} \Delta E \gamma \exp(-\Delta E/kT) \\ &\quad \times \frac{A + D}{\gamma n + A + D} \\ &= n n_{H_2} 9.1 \times 10^{-13} \gamma \exp(-6592 \text{ K}/T) \\ &\quad \times \frac{8.6 \times 10^{-7} + 2.6 \times 10^{-11} \chi}{\gamma n + 8.6 \times 10^{-7} + 2.6 \times 10^{-11} \chi} \end{aligned} \quad (11)$$

with a collisional rate coefficient $\gamma = 5.4 \times 10^{-13} \sqrt{T} \text{ s}^{-1} \text{ cm}^{-3}$. As the molecular constants do not depend on the metallicity, only the Z -dependence of n_{H_2} changes the H₂ de-excitation heating.

The relative reduction of the H₂ heating at high radiation fields is demonstrated in Fig. 2 comparing the PE heating and the H₂ de-excitation heating for the different parameter regimes. We see that at any given density $\Gamma_{\text{PE}}^{\text{net}}$ exceeds $\Gamma_{H_2^*}^{\text{net}}$ beyond a certain χ value, but that this limit increases with the gas density.

Although Γ_{PE} and $\Gamma_{H_2^*}$ are the two main heating terms it is necessary to account for a third process in order to achieve a reasonable approximation of the full energy balance. For UV fields $\chi < 10^3$, and densities $n < 10^4 \text{ cm}^{-3}$, H₂ formation heating may contribute significantly. Assuming that each formation process releases 1/3 of its binding energy to heat the gas (Sternberg & Dalgarno 1989), the corresponding heating rate is:

$$\Gamma_{\text{form}} = 2.4 \times 10^{-12} R n n_H \text{ erg cm}^{-3} \text{ s}^{-1}. \quad (12)$$

Summing over all three processes we obtain the total heating rate

$$\Gamma_{\text{tot}} = \Gamma_{\text{PE}}^{\text{net}} + \Gamma_{H_2^*}^{\text{net}} + \Gamma_{\text{form}}. \quad (13)$$

2.2.3. Metallicity dependence

An inspection of the heating and cooling functions described above reveals their metallicity dependence. Table 1 summarizes the scaling relations. The radiative cooling functions are linear in Z . The photoelectric heating depends on the metallicity

Table 1. Metallicity dependence of the individual heating processes.

	Low UV field $\chi < 100$	High UV field $\chi \gg 100$
high density ($n \gtrsim 10^6$)	$\Gamma_{\text{PE}} \sim Z$	$\Gamma_{\text{PE}} \sim Z^2$
	$\Gamma_{H_2^*} \sim \frac{Z}{1+2Z}$	$\Gamma_{H_2^*} \sim Z$
	$\Gamma_{H_2\text{-form}} \sim Z$	$\Gamma_{H_2\text{-form}} \sim Z$
	$\Lambda_{\text{rec}} \sim Z^{1.5}$	$\Lambda_{\text{rec}} \sim Z^{1.5}$
low density ($n \lesssim 10^3$)	$\Lambda_{\text{tot}} \sim Z$	$\Lambda_{\text{tot}} \sim Z$
	$\Gamma_{\text{PE}} \sim Z$	$\Gamma_{\text{PE}} \sim Z \dots Z^{1.5}$
	$\Gamma_{H_2^*} \sim Z$	$\Gamma_{H_2^*} \sim Z$
	$\Gamma_{H_2\text{-form}} \sim Z$	$\Gamma_{H_2\text{-form}} \sim Z$
	$\Lambda_{\text{rec}} \sim Z$	$\Lambda_{\text{rec}} \sim Z \dots Z^{1.5}$
	$\Lambda_{\text{tot}} \sim Z$	$\Lambda_{\text{tot}} \sim Z$

via $\epsilon(Z) \times Z$. The influence of $\epsilon(Z)$ can be neglected as long as $n/\chi \gtrsim 100$. Thus, for low UV fields $\Gamma_{\text{PE}} \sim Z$. For higher values of χ the efficiency accounts for an additional influence due to the electron density which is proportional to Z for high densities, and independent of Z for very low densities. The metallicity dependence for densities between $10^3 \dots 10^5 \text{ cm}^{-3}$ is not trivial. Equation (3) shows that the electron density is linear in Z for very high n . In the intermediate range this dependence roughly shifts from Z^0 to Z^1 . This leads to $\Gamma_{\text{PE}} \sim Z^2$ for high values of n and $\Gamma_{\text{PE}} \sim Z$ for very low densities.

The recombination cooling depends on the metallicity through the electron density, resulting in $\Lambda_{\text{rec}} \sim Z$ and $Z^{1.5}$ for low and high densities respectively. The Z -dependence in the hydrogen heating (Eqs. (10) and (11)) comes from the hydrogen density which depends on the metallicity as $Z/(1 + 2Z)$ for high densities and low values of χ , and as Z otherwise.

As a result we show in Fig. 3 the surface temperature of model clouds for a variety of different UV field strengths and densities computed from the analytic approximation and from the full KOSMA- τ PDR model. We covered a parameter space ranging from $n = 10^3 \dots 10^6 \text{ cm}^{-3}$ and $\chi = 10^0 \dots 10^6$. It is obvious that the metallicity dependence varies strongly over the parameter space. We obtain a good agreement for low and high UV fields. Even in the intermediate UV and density range, where the quantitative accord is weaker, the qualitative dependence of T_{surf} on Z is well reproduced by the semi-analytical model.

The Z -dependence of the temperature can be understood by comparing the dominant net rates of heating Γ/Z and cooling Λ/Z . At high UV fields, where the PE heating dominates, the heating is proportional to Z^2 at high densities. For a density of $n = 10^3$ the PE heating is $\sim Z \sqrt{Z^2 + 1}$. Due to the high UV field $n/\chi < 100$ for all given densities thus the electron density influences the heating also for small values of n . If the density increases the term $14.4 T^{0.75}/n$ vanishes and $\Gamma_{\text{PE}} \sim Z^2$. This is reflected in the slopes of the surface temperature in Fig. 3(top). For intermediate FUV fields we find a similar behavior with the addition that n/χ is < 100 for high densities and ≥ 100 for low densities, thus the metallicity dependence shifts from Z^2 to Z with increasing density. This shift can be seen in the middle plot in Fig. 3.

When H₂ vibrational de-excitation heating dominates (compare Fig. 2), the corresponding rate varies as $Z/(1 + 2Z)$, hence the surface temperature drops as $1/(1 + 2Z)$. This is shown for $n = 10^6 \text{ cm}^{-3}$ in Fig. 3(middle) and for $n \geq 10^4 \text{ cm}^{-3}$ in the bottom panel of Fig. 3 which gives the temperatures for a FUV field strength of $\chi = 1$. For low FUV fields and low densities the temperature is proportional to Z due to the PE heating as seen in Fig. 3(bottom).

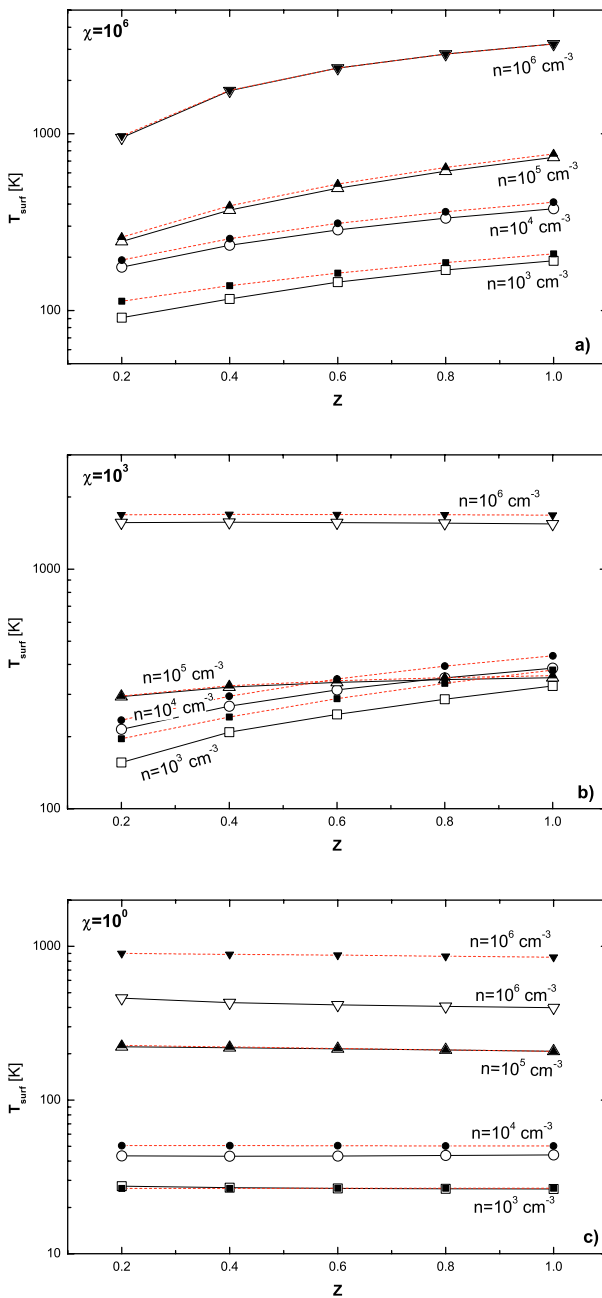


Fig. 3. Comparison of the KOSMA- τ results (open symbols) and the semi-analytic values (filled symbols) for the surface temperature against the metallicity. The top panel a) is for an UV field of $\chi = 10^6$, the bottom plot b) is for $\chi = 10^3$, and the bottom panel c) is for an UV field strength of $\chi = 1$. The different symbols indicate different surface densities.

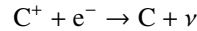
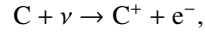
The offset between the semi-analytical approximation and numerical result for $\chi = 10^3$ is due to a small contribution of additional cooling processes in that parameter range. This increases the total cooling efficiency and hence the temperatures in the full numerical calculations are smaller. This also holds for $n = 10^6 \text{ cm}^{-3}$ and $\chi = 1$. In that case the cooling is dominated by CO line cooling which is stronger than [OI] 63 μm and also by H₂O cooling which is comparable to [OI] 63 μm . Here our initial assumptions are clearly underestimating the overall cooling. Even so this does not change the behavior with Z which is well reproduced.

As there is some debate on D/G we tested as an extreme example $D/G \propto Z^2$ instead of linearity. This mainly changes the behavior of the heating rates. The dominant surface cooling processes do not depend on D/G , but only on the elemental abundances, while the heating processes are affected by an altered D/G . This leads to a decreased heating efficiency for $Z < 1$, hence the surface temperature is significantly lower if we assume $D/G \propto Z^2$. In the extreme example of $\chi = 10^6$, $n = 10^6 \text{ cm}^{-3}$, and $Z = 0.2$ we find $T_{\text{surf}} = 240 \text{ K}$, a factor of 4 smaller than for $D/G \propto Z$. The cooling inside the cloud also depends somewhat on D/G , since the escape probability of cooling lines depends on the dust attenuation.

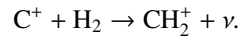
3. Variation of the C⁺ layer size with metallicity

At the surface of the PDR the FUV radiation ionizes almost all of the carbon atoms. At larger depths the FUV intensity decreases and carbon recombines and is eventually incorporated into CO molecules. Thus, a PDR clump can be subdivided into a CO core surrounded by an atomic carbon shell and an outer C⁺ envelope. We examine here, the thickness of the C⁺ envelope as a function of metallicity Z . We define the C⁺ envelope thickness as the distance from the cloud surface to the depth where the abundances of C and C⁺ are equal.

The dominant reaction channels for the formation and destruction of C⁺ are



and



Assuming, that these are the only reactions which influence the C⁺ abundance, the balance equation for the abundance of C⁺ can be written as,

$$\chi I n_C = a_C n_{\text{C}^+} n_e + k_C n_{\text{C}^+} n_{\text{H}_2} \quad (14)$$

where I is the photoionization rate, a_C and k_C are the recombination and radiative association rate coefficients. We assume that the photoionization rate is attenuated exponentially as $\exp(-p A_V)$ where the factor $p = 3.02$ accounts for the difference in the opacity between visual and FUV wavelengths. As A_V is determined by dust extinction it scales linearly with Z . In the KOSMA- τ model we account for an isotropic FUV field, and integrate over 4π ray angles. The ionization rate is then given by,

$$I = 3 \times 10^{-10} \chi \int_1^\infty \frac{\exp(-3.02 A_V \mu)}{\mu^2} d\mu . \quad (15)$$

The integral is the second order exponential integral $E_2(3.02 A_V)$ where $\mu = \cos \Theta$ and Θ is the angle between the ray and the normal direction.

We have defined the radial point r_{C^+} as the location where the abundances of C⁺ and C are equal, $n_{\text{C}^+} = n_C$. If we neglect the contribution of CO at r_{C^+} then $n_{\text{C}^+} = X_C n/2$ there. Results from the PDR model suggest, that the electron density, $n_e(Z) \approx 2 n_{\text{C}^+}(Z)$, thus $n_e(Z) \approx \hat{n}_C(Z=1) Z$. For the sake of simplicity we chose this expression for n_e rather than the one introduced in Eq. (3) which would introduce an additional temperature dependence. With $X_C = 1.4 \times 10^{-4} Z$ and molecular

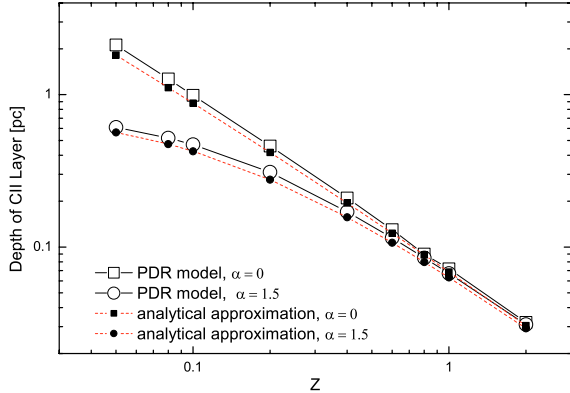


Fig. 4. The width of the C⁺ layer is plotted against the metallicity. The open circles represent spherical clump of mass $M = 10^3 M_{\odot}$, density $n_0 = 10^4 \text{ cm}^{-3}$, FUV field $\chi = 100$, and the power-law index of the density profile, $\gamma = 1.5$, whereas the open squares represent a spherical clump of mass of $10^6 M_{\odot}$ with $\gamma = 0$. The filled circles and squares represent our analytical estimates as explained in Sect. 3.

hydrogen dominating the gas density, $n_{\text{H}_2} = n/2$, we can resolve Eq. (14) for the density at r_{C^+}

$$n(r_{\text{C}^+}) = \frac{3 \times 10^{-10} \chi E_2(3.02 A_V(r_{\text{C}^+}))}{a_C Z 1.4 \times 10^{-4} + 0.5 k_C}. \quad (16)$$

For a given radial density distribution $n(r)$ and FUV field χ , Eq. (16) can be numerically solved to obtain r_{C^+} , or correspondingly the width of the C⁺ layer $D_{\text{C}^+} = R - r_{\text{C}^+}$. In Fig. 4 we compare the results from this equation with detailed PDR model calculations using the KOSMA- τ model for $n_0 = 10^4 \text{ cm}^{-3}$ and $\chi = 100$. Here two types of density structures are used: (a) $n(r) = n_0 (r/R)^{-\gamma}$ for $0.2R \leq r < R$, $n(r) = 0$ for $r > R$, and $n = n_0 0.2^{-\gamma}$ for $r < 0.2R$, with the total cloud radius R ; (b) a constant density, $n(r) = n_0$, or equivalently $\gamma = 0$.

The squares representing the constant density model show that the C⁺ layer width depends approximately as $Z^{-1.1}$ on the metallicity which closely matches with the assumption of an inverse proportionality by Bolatto et al. (1999). The circles in Fig. 4 represent the model by the $\gamma = 1.5$. They can be numerically fitted with function, $D_{\text{C}^+} = (1.195 + 5.758Z)^{-1.47}$ pc. Figure 4 shows that our results using Eq. (16) agrees well with the model calculations. However the estimated widths are slightly higher than the model calculations, which reflects the fact that there are more reactions which quantitatively influence the chemistry of C⁺.

4. [CII] emission as a function of Z

The [CII] emission as well as the [CII]/CO(1–0) line ratio is typically considered to be a good tracer of star formation (Stacey et al. 1991). The intensity ratio $I_{\text{[CII]}158 \mu\text{m}}/I_{\text{CO}(1-0)}$, observed in many nearby low metal galaxies, is higher than for sources with solar and super-solar metallicities (Madden et al. 1997; Mochizuki et al. 1998; Bolatto et al. 1999; Madden 2000; Hunter et al. 2001). Table 2 summarizes available line ratios and metallicities of nearby galaxies. The corresponding numbers for Orion are also given as a Galactic reference.

This dependence has been modelled by Bolatto et al. (1999) assuming that the size of the C⁺ region scales inversely with metallicity, and assuming a constant temperature for the gas.

Table 2. Metallicities and observed [CII]/CO(1–0) line ratios of nearby galaxies and Galactic star forming regions.

Object	$12 + \log(\text{O/H})$	[CII]/CO(1–0)	References
NGC 1068	9.07	6000	14, 2, 12
NGC 1156	8.39	10 000	4
NGC 1313	8.25	11 740	14, 7
NGC 1569	8.08	37 000	13, 4, 6
NGC 4449	8.3	14 000	8, 6
NGC 4736	9	2500	14, 2, 12, 10
NGC 6946	9	900	14, 12
IC 10	8.19	14 000	14, 8, 6
IZw 36	7.93	<3000	8
M83	9.16	8000	14, 2, 5
M51	9.23	3500	14, 9, 5
IC 4622	8.09	34 000	3, 4
Orion	8.75	6000	2, 11
LMC	8.35	5600	1
30 Doradus	8.43	69 000	1
SMC	8.03	13 000	1

References. (1) Bolatto et al. (1999); (2) Crawford et al. (1985); (3) Heydari-Malayeri et al. (1990); (4) Hunter et al. (2001); (5) Kramer et al. (2005); (6) Lord et al. (1995); (7) Luhmann et al. (2003); (8) Mochizuki et al. (1998); (9) Nikola et al. (2001); (10) Petritpas & Wilson (2003); (11) Simon et al. (1997); (12) Stacey et al. (1991); (13) Talent (1980); (14) Zaritsky et al. (1994).

For our spherical PDR model we compute the surface brightness as function of clump mass/radius and metallicity. The surface brightness is the projected average intensity

$$\bar{I} = \frac{2\pi \int_0^R I(p)p dp}{\pi R^2} \quad (17)$$

of the spherical clump, where $I(p)$ is the specific intensity along a ray with impact parameter p (Störzer et al. 1996). The line intensities depend on the thermal and chemical structure of the cloud. Additionally, for spherical clouds an effective area-filling factor of the emissive region has to be considered. Particularly lines, which are formed in central regions of the cloud are influenced by this area-filling factor. A good example is the surface brightness of ¹²CO(1–0). For a density of $n = 10^3 \text{ cm}^{-3}$ and low metallicities almost the whole cloud is devoid of CO due to photodissociation. A higher density or metallicity results in a larger CO core and a higher surface brightness. For species which are mainly emitting at the surface of the cloud this filling effect is negligible.

In the prior sections we derived approximate expressions for the surface temperature of a PDR as well as for the expected depth of the C⁺ envelope. We can use these approximations to estimate the total [CII] surface brightness of the PDR. The local emissivity $\Lambda_{\text{[CII]}}(r)$ from Eq. (A.2) can be used to calculate the line integrated intensity of the PDR in the optically thin case

$$I_{\text{int}} = \int_{r_{\text{C}^+}}^R 4\pi r^2 \frac{\Lambda_{\text{[CII]}}(r)}{4\pi} dr \text{ erg s}^{-1} \text{ sr}^{-1} \quad (18)$$

with the total radius R . From Eq. (18) follows the mean surface brightness of the cloud

$$\bar{I}_{\text{[CII]}} = \frac{I_{\text{int}}}{\pi R^2} \text{ erg s}^{-1} \text{ cm}^{-2} \text{ sr}^{-1}. \quad (19)$$

To calculate $I_{\text{[CII]}}$ we assume an exponential temperature profile $T(r) = T_c + T_{\text{surf}} E_2(\lambda A_V)$ with the second order exponential integral E_2 , and an arbitrary fitting parameter λ . The central temperature T_c and the parameter λ are different for each

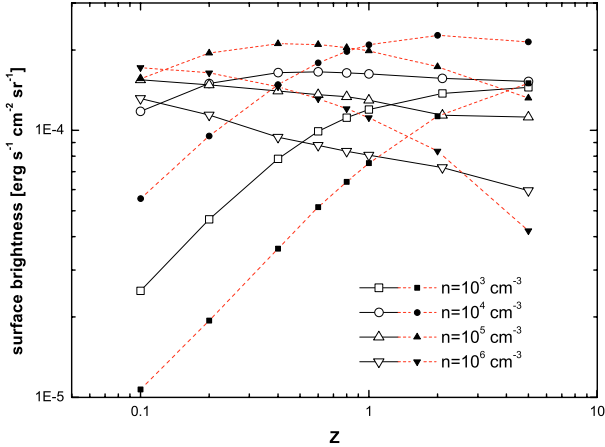


Fig. 5. The surface brightnesses of the [CII] 158 μ m (dashed-dotted) emission lines from the KOSMA- τ results (open symbols) and the approximation from Eq. (19) (filled symbols) plotted against the metallicity for different densities. The cloud mass is $M = 10 M_\odot$, the UV field strength is $\chi = 100$, the assumed central temperature is $T_c = 35$ K, and $\lambda = 4$.

set of PDR parameters. For demonstration purposes we chose $T_c = 35$ K and $\lambda = 4$ to estimate the surface brightnesses for multiple PDRs simultaneously. In Fig. 5 we compare these approximations with the detailed KOSMA- τ results for $I_{\text{[CII]}}$. The metallicity dependent behavior is reproduced very well and the quantitative agreement is within a factor of 2 assuming the same temperature profile for all 4 models! If we drop this assumption and use individual temperature profiles for each model the agreement is 10–30%.

Importantly, the total surface brightness does not scale linearly with the surface density of the clouds. Rather it peaks for intermediate values of n , depending on Z . This is mainly a geometrical effect, which can be understood by some qualitative arguments. If we assume that [CII] is optically thin, we see all C⁺ atoms. In the low density case, where ionized carbon fills the whole cloud, the surface brightness is then proportional to $n(V/A)$, with the volume of the cloud V and the projected area A , hence $\bar{I}_{\text{[CII]}} \propto nR$. But $R \propto n^{-1/3}$, since we kept the cloud mass constant, and thus we find $\bar{I}_{\text{[CII]}} \propto n^{2/3}$. For higher densities the width of the C⁺ layer decreases faster than it is compensated by the growing n . The relative thickness of the C⁺ layer becomes very small for higher densities (i.e. if $D_{\text{C}^+} \ll R$). The surface brightness then is proportional to $n 4 \pi R^2 D_{\text{C}^+}/(\pi R^2)$, hence $\bar{I}_{\text{[CII]}} \propto n D_{\text{C}^+}$. We observe a reduced surface brightness caused by the geometry of the cloud. This is inverse to the common area filling effect for optically thick lines, like e.g. CO (1–0), where the projected area of the CO core decreases with decreasing density as demonstrated in Fig. 5. This was also mentioned by Störzer et al. (1996). This means, that even though the local emissivity $\Lambda_{\text{[CII]}}$ scales linearly with n (see Eq. (A.2)), this is not true for the total surface brightness. As a second order effect we also notice a temperature dependence of the local emissivity. The differences between our analytical model and the detailed temperature structures from the PDR calculations are responsible for most of the deviations shown in Fig. 5.

We use our PDR model calculations to study the metallicity dependence of the [CII]/CO(1–0) line ratio. We adopt a density of 10^4 cm^{-3} , a $\gamma = 1.5$, and a UV field, $\chi = 10^2$ similar to the values assumed by Bolatto et al. (1999). Their prediction is an average over a clump ensemble as a model for the large scale emission from the ISM. In contrast, we start here by

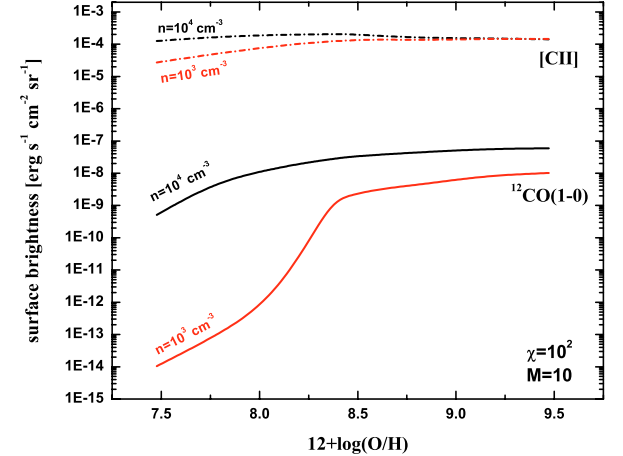


Fig. 6. The surface brightnesses of the [CII] 158 μ m (dashed-dotted) and $^{12}\text{CO}(1-0)$ 2.6 mm (solid) emission lines plotted against the metallicity for two different densities. The cloud mass is $M = 10 M_\odot$ and the UV field strength is $\chi = 100$.

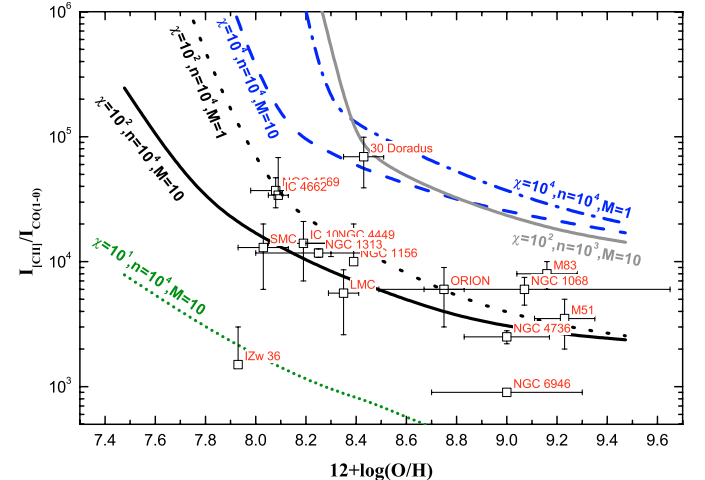


Fig. 7. The intensity ratio $I_{\text{[CII]}}/I_{\text{CO}(1-0)}$ is plotted against the metallicity ($Z = 1$ is equivalent to $12 + \log(\text{O/H}) = 8.48$). The lines denote the KOSMA- τ results for two different clump masses $M = 1$ and $M = 10 M_\odot$. The density at the surface of the clumps and the UV field strength in units of the standard Draine field are given in the plot. The observed ratios of nearby galaxies are plotted as squares.

investigating the metallicity dependence for a single, typical clump. The discussion below shows that this is already sufficient to reproduce the observed trends versus metallicity. The detailed investigation of the effects of averaging over a clump ensemble are left to a subsequent paper. Figure 6 summarizes the results for this typical clump. The dominance of the geometrical effect is reflected in the almost constant [CII] surface brightnesses in Fig. 6. Hence the line ratio [CII]/CO decreases for increasing metallicities and tends to be constant for very high values of Z .

Figure 7 shows that the trend in the observed ratios in normal galaxies can be represented by a single-clump model with $M = 1 \dots 10^4 M_\odot$, shown as solid and dotted lines in Fig. 7. We also plotted model results for different cloud parameters to demonstrate how different observations may be explained by different local physical conditions, e.g. the higher observed ratio for the 30 Doradus region can be explained by a similar model, but exposed to an UV field of $\chi = 10^4$ (or alternatively by a clump of less mass). This is consistent with derived FUV strengths for 30 Doradus (Kaufman et al. 1999). The peculiar source IZw 36,

with a very low [CII]/CO ratio at extremely low metallicity can be approximated by a model with a lower FUV field of $\chi \approx 10$, consistent with estimations by Mochizuki et al. (1998).

Our model results for single clumps reproduce qualitatively the results shown by the semi-analytical clumpy model of (Bolatto et al. 1999) for a clump ensemble in reproducing the trends versus metallicity. Thus we can confirm Bolatto's findings when taking the detailed physical and chemical structure of the clumps into account.

From a practical point of view it is obvious that a clumpy ensemble of different clouds should be closer to the true local conditions than a single spherical clump, but we find that a clumpy approach is not necessary to explain the observed trend with Z . To model the [CII]/CO line ratio of a particular source in detail it may of course be necessary to apply a clumpy approach. But to understand the general behavior for different metallicities it is sufficient to consider a single, typical clump.

5. Summary

We study the effects of metallicity variations on the gas temperature and [CII] emission line properties of spherical PDRs. We find that the surface temperature of PDRs at high UV fields varies linearly with metallicity. For low UV fields and high densities this metallicity behavior of the surface temperature is converse, showing an inverse dependence with metallicity due to the dominant H₂ heating. We introduce a new two level FUV H₂ heating and cooling function that properly accounts for energy losses via vibrational collisional excitations.

We examine the dependence of the C⁺ envelope on metallicity and find that its geometrical depth scales inversely with Z . This produces a higher [CII]/CO($J = 1-0$) line ratio at lower metallicities. We used the numerical results from the KOSMA- τ model to study the dependence of PDR emission lines with metallicity. The observed variation of [CII]/CO($J = 1-0$) with metallicity can be explained well by a single-clump model and it is not necessary to refer to an average over a clump ensemble. We conclude that the [CII]/CO($J = 1-0$) line ratios for sources with differing metallicities do not provide a strong constraint on the clumpy morphology of a molecular clouds.

Acknowledgements. This work is supported by the Deutsche Forschungs Gemeinschaft (DFG) via Grant SFB 494. A.S. thanks the Israel Science Foundation for support. We thank the anonymous referee for her/his helpful comments.

References

- Arimoto, N., Sofue, Y., & Tsujimoto, T. 1996, PASJ, 48, 275
- Asplund, M., Grevesse, N., Sauval, A. J., Allende Prieto, C., & Kiselman, D. 2004, A&A, 417, 751
- Bakes, E. L. O., & Tielens, A. G. G. M. 1994, ApJ, 427, 822
- Baumgartner, W. H., & Mushotzky, R. F. 2005, ApJ, submitted
- Boeger, G. I., & Sternberg, A. 2005, ApJ, 632, 302
- Bouissé, P. 1990, A&A, 228, 483
- Bolatto, A. D., Jackson, J. M., & Ingalls, J. G. 1999, ApJ, 513, 275
- Bolatto, A. D., Jackson, J. M., Wilson, C. D., & Moriarty-Schieven, G. 2000, ApJ, 532, 909
- Boselli, A., Lequeux, J., & Gavazzi, G. 2002a, A&A, 384, 33
- Boselli, A., Gavazzi, G., Lequeux, J., & Pierini, D. 2002b, A&A, 385, 454
- Bresolin, F., Garnett, D. R., & Kennicutt, R. C. 2004, ApJ, 615, 228
- Burke, J. R., & Hollenbach, D. J. 1983, ApJ, 265, 223
- Burton, M. G., Hollenbach, D. J., & Tielens, A. G. G. M. 1990, ApJ, 365, 620
- Cazaux, S., & Tielens, A. G. G. M. 2004, ApJ, 604, 222
- Cazaux, S., & Spaans, M. 2004, ApJ, 611, 40
- Crawford, M. K., Genzel, R., Townes, C. H., & Watson, D. M. 1985, ApJ, 291, 755
- d'Hendecourt, L., & Léger, A. 1987, A&A, 180, L9
- Draine, B. T. 1978, ApJS, 36, 595
- Elmegreen, B. G., & Falgarone, E. 1996, ApJ, 471, 816
- Federman, S. R., Sheffer, Y., Lambert, D. L., & Gilliland, R. L. 1993, ApJ, 413, L51
- Giersz, K. M., Stutzki, J., & Winnewisser, G. 1992, 259, 271
- Giveon, U., Sternberg, A., Lutz, D., Feuchtgruber, H., & Pauldrach, A. W. A. 2002, ApJ, 566, 880
- Gorti, U., & Hollenbach, D. 2002, ApJ, 573, 215
- Hegmann, M., & Kegel, W. H. 2003, MNRAS, 342, 453
- Heydari-Malayeri, M., Melnick, J., & Martin, J.-M. 1990, A&A, 234, 99
- Heithausen, A., Bensch, F., Stutzki, J., Falgarone, E., & Panis, J. F. 1998, A&A, 331, L65
- Hollenbach, D., & Salpeter, E. E. 1971, ApJ, 163, 155
- Hollenbach, D., Werner, M. W., & Salpeter, E. E. 1971, ApJ, 163, 165
- Hollenbach, D. J., & Tielens, A. G. G. M. 1997, ARA&A, 35, 179
- Hollenbach, D. J., & Tielens, A. G. G. M. 1999, Rev. Mod. Phys., 71, 173
- Hollenbach, D., & McKee, C. F. 1979, ApJS, 41, 555
- Hollenbach, D. J., Takahashi, T., & Tielens, A. G. G. M. 1991, ApJ, 377, 192
- Howe, J. E., Jaffe, D. T., Genzel, R., & Stacey, G. J. 1991, ApJ, 373, 158
- Hunter, D. A., Kaufman, M., Hollenbach, D. J., et al. 2001, ApJ, 553, 121
- Israel, F. P. 1997, A&A, 328, 471
- Israel, F. P., Baas, F., Rudy, R. J., Skillman, E. D., & Woodward, C. E. 2003, A&A, 397, 871
- Kaufman, M. J., Wolfire, M. G., Hollenbach, D. J., & Luhman, M. L. 1999, ApJ, 527, 795
- Kobulnicky, H. A., & Skillman, E. D. 1997, ApJ, 489, 636
- Köster, B., Störzer, H., Stutzki, J., & Sternberg, A. 1994, A&A, 284, 545
- Kramer, C., Stutzki, J., Rohrig, R., & Corneliusen, U. 1998, A&A, 329, 249
- Kramer, C., Jakob, H., Mookerjea, B., et al. 2004, A&A, 424, 887
- Kramer, C., Mookerjea, B., Bayet, E., et al. 2005, A&A, submitted
- Kunth, D., & Östlin, G. 2000, A&ARv, 10, 1K
- Le Bourlot, J., Pineau Des Forets, G., Roueff, E., & Flower, D. R. 1993, A&A, 267, 233
- Lee, H., Grebel, E. K., & Hodge, P. W. 2003, A&A, 401, 141
- Lepp, S., & Dalgarno, A. 1988, ApJ, 335, 769
- Lequeux, J., Le Bourlot, J., Des Forets, G. P., et al. 1994, A&A, 292, 371
- Li, A., & Draine, B. T. 2002, ApJ, 576, 762
- Lisenfeld, U., & Ferrara, A. 1998, ApJ, 496, 145
- Lord, S. D., Hollenbach, D. J., Colgan, S. W. J., et al. 1995, ASP Conf. Ser., 73, 151
- Luhman, M. L., Satyapal, S., Fischer, J., et al. 2003, ApJ, 594, 758
- Madden, S. C. 2000, NewAR, 44, 249
- Madden, S. C., Poglitsch, A., Geis, N., Stacey, G. J., & Townes, C. H. 1997, ApJ, 483, 200
- Malhotra, S., Hollenbach, D., Helou, G., et al. 2000, ApJ, 543, 634
- McKee, C. F. 1989, ApJ, 345, 782
- Meixner, M., & Tielens, A. G. G. M. 1993, ApJ, 405, 216
- Millar, T. J., Farquhar, P. R. A., & Willacy, K. 1997, A&AS, 121, 139
- Mochizuki, K., Onaka, T., & Nakagawa, T. 1998, ASP Conf. Ser., 132, 386
- Nikola, T., Geis, N., Herrmann, F., et al. 2001, ApJ, 561, 203
- Pak, S., Jaffe, D. T., van Dishoeck, E. F., Johansson, L. E. B., & Booth, R. S. 1998, ApJ, 498, 735
- Petitpas, G. R., & Wildson, C. D. 2003, ApJ, 587, 649
- Pierini, D., Leech, K. J., Tuffs, R. J., & Völk, H. J. 1999, MNRAS, 303, L29
- Pierini, D., Leech, K. J., & Völk, H. J. 2003, A&A, 397, 871
- Pustilnik, S. S., Kniazev, A. Y., Musegosa, J., et al. 2002, A&A, 389, 779
- Röllig, M., Hegmann, M., & Kegel, W. H. 2002, A&A, 392, 1081
- Rubio, M., Boulanger, F., Rantakyro, F., & Contursi, A. 2004, A&A, 425, L1
- Simon, R., Stutzki, J., Sternberg, A., & Winnewisser, G. 1997, A&A, 327, L9
- Simon, R., Jackson, J. M., Clemens, D. P., Bania, T. M., & Heyer, M. H. 2001, ApJ, 551, 747
- Spaans, M. 1996, A&A, 307, 271
- Spaans, M., & van Dishoeck, E. F. 1997, A&A, 323, 953
- Stacey, G. J., Geis, N., Genzel, R., et al. 1991, ApJ, 373, 423
- Steiman-Cameron, T. Y., Haas, M. R., Tielens, A. G. G. M., & Burton, M. G. 1997, ApJ, 478, 261
- Sternberg, A. 2004, Proceedings, The dense interstellar medium in galaxies, Proc. of the 4th Cologne-Bonn-Zermatt Symposium, Zermatt, Switzerland, 22–26 September 2003, ed. S. Pfalzner, C. Kramer, C. Staubmeier, & A. Heithausen, Springer proceedings in physics, 91 (Berlin, Heidelberg: Springer)
- Sternberg, A., & Dalgarno, A. 1989, ApJ, 338, 197
- Sternberg, A., & Dalgarno, A. 1995, ApJS, 99, 565
- Störzer, H., Stutzki, J., & Sternberg, A. 1996, A&A, 310, 592
- Störzer, H., Zielinsky, M., Stutzki, J., & Sternberg, A. 2000, A&A, 358, 682
- Stutzki, J., Stacey, G. J., Genzel, R., et al. 1988, ApJ, 332, 379
- Talent, D. L. 1980, BAAS, 12, 866
- Thuan, T. X., Sauvage, M., & Madden, S. 1999, ApJ, 516, 783
- Tielens, A. G. G. M., & Hollenbach, D. 1985, ApJ, 291, 722
- van Dishoeck, E. F. 1988, in Rate Coefficients in Astrochemistry, ed. T. J. Millar, & D. A. Williams (Dordrecht: Kluwer Academic Publishers), 49
- Verstrate, L., Léger, A., d'Hendecourt, L., Dutuit, O., & Defourneau, D. 1990, A&A, 237, 436
- Warin, S., Benayoun, J. J., & Viala, Y. P. 1996, A&A, 308, 535
- Wilson, C. D. 1995, ApJ, 448, L97
- Wolfire, M. G., Hollenbach, D., McKee, C. F., Tielens, A. G. G. M., & Bakes, E. L. O. 1995, ApJ, 443, 152
- Zaritsky, D., Kennicutt, R. C., Jr., & Huchra, J. P. 1994, ApJ, 420, 87
- Zielinsky, M., Stutzki, J., & Störzer, H. 2000, A&A, 358

Online Material

Appendix A: Cooling functions

The cooling of the gas is dominated by fine structure line emission of [CII] and [OI]. The line cooling rate can always be written as $\Lambda_{\text{ul}} = n_u A_{\text{ul}} E_{\text{ul}} \beta(\tau_{\text{ul}}) \text{ erg s}^{-1} \text{ cm}^{-3}$ where β is the escape probability, A_{ul} is the transition probability and n_u the number of atoms in the upper state u and E_{ul} is the corresponding transition energy (Hollenbach & McKee 1979). Below the critical density for the [OI] emission $n_{\text{cr}} = 8.5 \times 10^{-5} (100K/T)^{0.69} \text{ cm}^{-3}$, the main cooling is provided by the 158 μ m [CII] line. The general cooling rate of a two-level system S can be expressed as:

$$\Lambda_{\text{ul}} = \frac{n_S A_{\text{ul}} E_{\text{ul}} \beta}{1 + \frac{g_u}{g_{\text{ul}}} \exp(E_{\text{ul}}/kT)(1 + \frac{n_{\text{cr}} \beta}{n})} \text{ erg cm}^{-3} \text{ s}^{-1}. \quad (\text{A.1})$$

The critical density for collisional de-excitation $n_{\text{cr}} = A_{\text{ul}}/\gamma_{\text{ul}}$ for the [CII] 158 μ m transition is $2.6 \times 10^3 \text{ cm}^{-3}$. The densities we are interested in are in the range of $10^3 \dots 10^6 \text{ cm}^{-3}$. Inserting the numerical values for [CII] and assuming a relative carbon abundance of $1.4 \times 10^{-4} \times Z$ we obtain the cooling rate for the [CII] 158 μ m transition:

$$\Lambda_{\text{CII}} = \frac{2.02 \times 10^{-24} n Z}{1 + \frac{1}{2} \exp(92/T) \left(1 + \frac{1300}{n}\right)} \text{ erg cm}^{-3} \text{ s}^{-1}. \quad (\text{A.2})$$

The general cooling rate of the [OI] 63 μ m (${}^3P_1 \rightarrow {}^3P_2$) and [OI] 146 μ m (${}^3P_0 \rightarrow {}^3P_1$) transitions, only accounting for transitions between neighboring levels, are:

$$\Lambda_{12} = A_{12} E_{12} \beta Z \left(\frac{n_{\text{OI}} \exp(E_{01}/T) g_1 n (n + \beta n_{\text{cr},01})}{g_0 n^2 \exp(E_{01}/T) (n + \beta n_{\text{cr},01}) (g_1 n + \exp(E_{12}/T) g_2 (n + \beta n_{\text{cr},12}))} \right) \text{ erg cm}^{-3} \text{ s}^{-1} \quad (\text{A.3})$$

$$\Lambda_{01} = A_{01} E_{01} \beta Z \left(\frac{n_{\text{OI}} g_0 n^2}{g_0 n^2 \exp(E_{01}/T) (n + \beta n_{\text{cr},01}) (g_1 n + \exp(E_{12}/T) g_2 (n + \beta n_{\text{cr},12}))} \right) \text{ erg cm}^{-3} \text{ s}^{-1}. \quad (\text{A.4})$$

Inserting the numerical values for [OI] and a relative oxygen abundance of $3 \times 10^{-4} \times Z$ in the above equation leads to:

$$\begin{aligned} \Lambda_{63 \mu\text{m}} &= 3.15 \times 10^{-14} 8.46 \times 10^{-5} \frac{1}{2} Z \\ &\times \frac{3 \times 10^{-4} n \exp(98 \text{ K}/T) 3 n \left(n + \frac{1}{2} \frac{1.66 \times 10^{-5}}{1.35 \times 10^{-11} T^{0.45}}\right)}{n^2 + \exp(98 \text{ K}/T) \left(n + \frac{1}{2} \frac{1.66 \times 10^{-5}}{1.35 \times 10^{-11} T^{0.45}}\right) \left(3 n + \exp(228 \text{ K}/T) 5 \left(n + \frac{1}{2} \frac{8.46 \times 10^{-5}}{4.37 \times 10^{-12} T^{0.66}}\right)\right)} \text{ erg cm}^{-3} \text{ s}^{-1} \end{aligned} \quad (\text{A.5})$$

$$\begin{aligned} \Lambda_{146 \mu\text{m}} &= 1.35 \times 10^{-14} 1.66 \times 10^{-5} \frac{1}{2} Z \\ &\times \frac{3 \times 10^{-4} n n^2}{n^2 + \exp(98 \text{ K}/T) \left(n + \frac{1}{2} \frac{1.66 \times 10^{-5}}{1.35 \times 10^{-11} T^{0.45}}\right) \left(3 n + \exp(228 \text{ K}/T) 5 \left(n + \frac{1}{2} \frac{8.46 \times 10^{-5}}{4.37 \times 10^{-12} T^{0.66}}\right)\right)} \text{ erg cm}^{-3} \text{ s}^{-1}. \end{aligned} \quad (\text{A.6})$$

This leads to the total [OI] cooling rate $\Lambda_{\text{OI}} = \Lambda_{63 \mu\text{m}} + \Lambda_{146 \mu\text{m}}$. In the high density case gas-grain collisional cooling is also contributing to the total cooling of the cloud:

$$\Lambda_{\text{g-g}} = 3.5 \times 10^{-34} \sqrt{T} (T - T_{\text{grain}}) n^2 Z. \quad (\text{A.7})$$

T_{grain} is the dust temperature as given by Hollenbach et al. (1991). The total cooling rate is the sum of the above individual rates

$$\Lambda_{\text{tot}} = \Lambda_{\text{CII}} + \Lambda_{\text{OI}} + \Lambda_{\text{g-g}}. \quad (\text{A.8})$$

Appendix B: The electron density at PDR surfaces

At the surface of a PDR atomic carbon and sulfur are ionized by the impinging, unshielded FUV radiation and atomic hydrogen is ionized by cosmic rays (FUV ionization of H is prevented by the Lyman limit). Electrons from dust are negligible due to the small number density of dust grains. The relative contribution from these electron donors to the total electron density n_e is shown in Fig. B.1 for the low (left) and high FUV (right) case. The values are computed with the KOSMA- τ PDR model. The histogram shows the increasing importance of atomic carbon as main electron source with increasing density. Nevertheless the additional contributions of atomic hydrogen and sulfur are not negligible. Even at very high UV fields, $\chi \approx 10^6$, a relevant fraction of the electrons is generated in the additional ionization processes. At gas densities $\sim 10^{5.5} \text{ cm}^{-3}$ still 16–20% of the electrons stem from the ionization of atomic hydrogen and sulfur. This fraction increases rapidly with decreasing density, with the result that at a number density of $\sim 1000 \text{ cm}^{-3}$ only <40% of the electrons are due to ionization of atomic carbon. We present an analytic approximation to the electron density at PDR surfaces which fits the actual behavior quite accurately and which allows an easy interpretation of the metallicity dependence. We assume

$$n_e = (X_C + X_S) n Z + n_{\text{H}^+} \quad (\text{B.1})$$

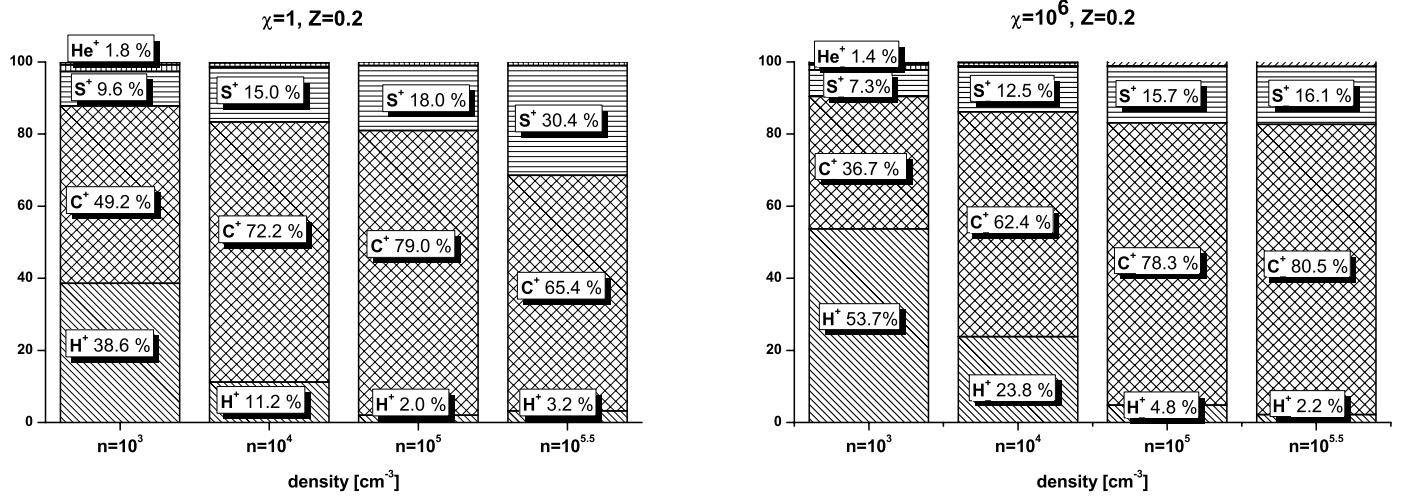


Fig. B.1. The relative contribution of the various electron donors to the total electron density n_e at the cloud surface as computed in the KOSMA- τ model. The percentages are given for different values of surface density n (columns) at FUV fields $\chi = 1$ (left) and $\chi = 10^6$ (right) and a fixed metallicity of $Z = 0.2$.

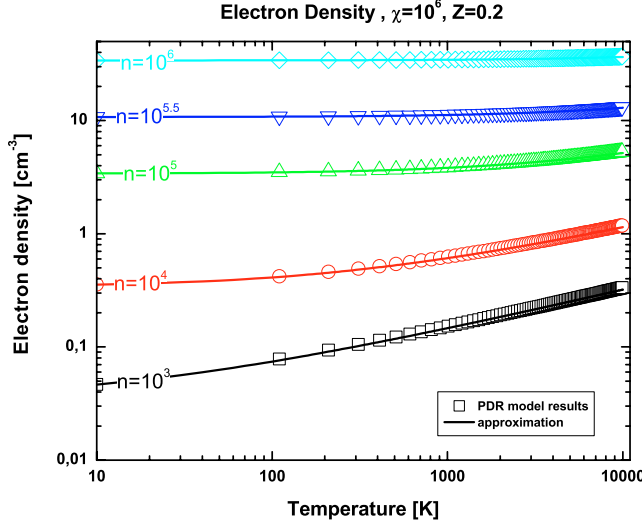


Fig. B.2. A comparison of numerically obtained electron densities (symbols) with the analytical expression (lines) in Eq. (B.4), at $A_V = 0$, $\chi = 10^6$, $Z = 1$ for different surface densities.

X_C and X_S are the relative elemental abundances of carbon and sulfur ($X_C = 1.4 \times 10^{-4}$, $X_S = 2.8 \times 10^{-5}$, Hollenbach & Tielens 1999; Federman et al. 1993). Together with the balance equation for hydrogen:

$$n_H \zeta = a_H n_{H^+} n_e, \quad (B.2)$$

where $\zeta = 2.3 \times 10^{-17} \text{ s}^{-1}$ is the ionization rate due to cosmic rays (Sternberg & Dalgarno 1995), and $a_H = 3.5 \times 10^{-12}(T/300K)^{-0.75} \text{ s}^{-1}$ is the recombination rate, we get the following expression for the electron density:

$$n_e = \frac{X}{2} n Z \left[1 + \sqrt{1 + \frac{T^{0.75}}{n Z^2} \left(\frac{6.05 \times 10^{-4}}{X} \right)} \right] \text{ cm}^{-3} \quad (B.3)$$

with $X = X_C + X_S$. This is in reasonable agreement with the numerical results from the detailed PDR calculations but deviates by 5–10%. The deviations are due to the different net recombination rates when considering all ionized species. To account for this changed rate we have fitted the parameter a in Eq. (B.2) to match the electron density from the full PDR model. Assuming $n_{H^+} \approx C n_H \zeta / n_e a_H$ and fitting the constant C to the numerical values we obtain

$$n_e = \frac{X}{2} n Z \left[1 + \sqrt{1 + \frac{T^{0.75}}{n Z^2} \left(\frac{7.52 \times 10^{-4}}{X} \right)} \right] \text{ cm}^{-3}. \quad (B.4)$$

The agreement with the KOSMA- τ results is shown in Fig. B.2. Please note that in the high radiation case all C and S at the surface are ionized so that the ratio of electrons contributed by them directly reflects their abundance ratio.

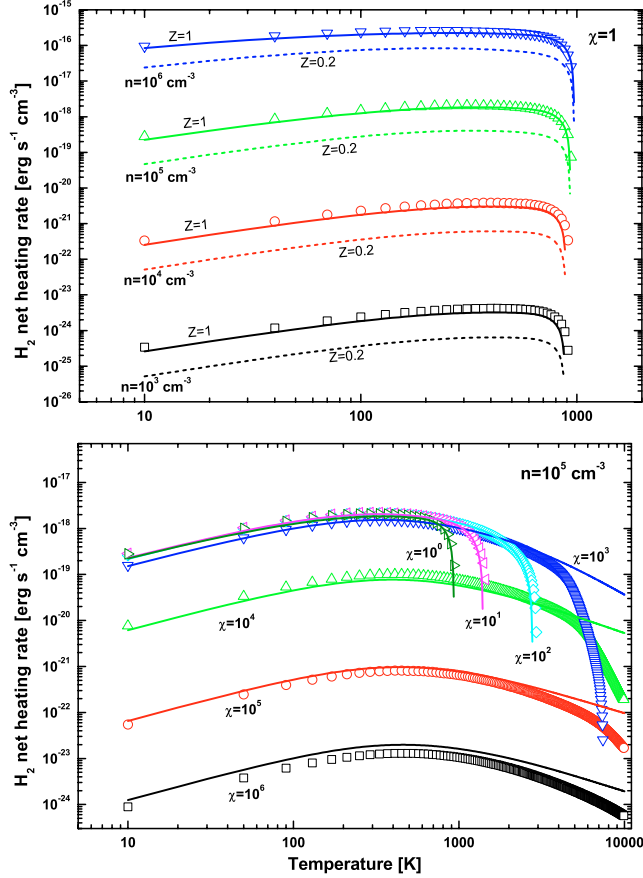


Fig. C.1. The net H_2 heating rate is plotted for different values of surface density n at a $\chi = 1$ FUV field (top) and for different UV field strengths for a fixed density of $n = 10^5 \text{ cm}^{-3}$ (bottom) over the temperature range. The symbols are the numerical results from the 15-level system in the KOSMA- τ model, the curves show the results using our effective two-level approximation. For $\chi = 1$ we also plot a low Z case (solid, $Z = 1$, and dashed, $Z = 0.2$). The deviations at the highest temperatures and radiation fields are due to cooling transitions from higher vibrational levels in this regime which are ignored in our approximation.

Appendix C: H_2 vibrational heating

An important heating processes in dense PDRs is collisional deexcitation of FUV-pumped H_2 molecules (Sternberg & Dalgarno 1995). Here we present a two level approximation for the H_2 vibrational heating and cooling valid in the parameter range where the process plays a major role (see Sect. 2.2.2). The approximation reproduces the net heating rate computed by SD95 assuming transitions among all 15 vibrational levels in the ground electronic state, but neglecting the rotational structure.

Vibrational cooling reduces the net heating at large gas temperatures (see Fig. C.1, bottom). The vibrational cooling is most effective at low χ for which a large H_2 density is maintained. With PDR temperatures of typically less than 2000 K (see Sect. 2) and the energy gap between the two lowest vibrational levels $\Delta E_{0,1} = 5988 \text{ K}$, we can assume that most of the H_2 is always in the ground ($v = 0$) level in this regime. Vibrational cooling is thus basically given by collisional excitation to $v = 1$ followed by either radiative decay or photodissociation. Using the molecular constants for the lowest vibrational transition we obtain the collisional cooling rate

$$\Lambda_{H_2} = -\Delta E_{1,0} \gamma_{1,0} \exp\left(\frac{-\Delta E_{1,0}}{k T}\right) n n_{H_2} \frac{A_{1,0} + \chi D_1}{\gamma_{1,0} n + A_{1,0} + \chi D_1} \quad (\text{C.1})$$

with the spontaneous emission rate coefficient $A_{1,0} = 8.6 \times 10^{-7} \text{ s}^{-1}$, the collisional rate coefficient $\gamma_{1,0} = 5.4 \times 10^{-13} \sqrt{T} \text{ s}^{-1} \text{ cm}^{-3}$, and the standard photodissociation rate for the $v = 1$ level of $D_1 = 2.6 \times 10^{-11} \text{ s}^{-1}$ (Sternberg & Dalgarno 1995). We found that the fit can be improved if $\Delta E_{0,1}$ is increased by 10%.

In contrast vibrational heating is important when the FUV radiation field provides a significant pumping to higher vibrational states. Thus we define a separate equivalent two-level system for the heating. It is characterized by the effective coefficients ΔE_{eff} , A_{eff} , γ_{eff} , and D_{eff} providing the same heating rate as the full 15 level system

$$\Gamma_{H_2^*} = n_{H_2} \sum_j \sum_{i \geq j} \frac{\chi P_i \Delta E_j}{1 + [A_j + \chi D_j]/[\gamma_j n]} \quad (\text{C.2})$$

$$= n_{H_2} \frac{\chi P_{\text{tot}} \Delta E_{\text{eff}}}{1 + [A_{\text{eff}} + \chi D_{\text{eff}}]/[\gamma_{\text{eff}} n]}. \quad (\text{C.3})$$

The quantity P_i denotes the formation rate of vibrationally excited H₂ for the different levels, P_{tot} represents the sum rate over all levels. The effective coefficients can be easily obtained by considering different asymptotic values of the density n and the radiation field χ . This yields $P_{\text{tot}} \cdot \Delta E_{\text{eff}} = 9.4 \times 10^{-22}$ erg s⁻¹, $\gamma_{\text{eff}} = \gamma_{1,0}$, $D_{\text{eff}} = 4.7 \times 10^{-10}$ s⁻¹, and $A_{\text{eff}} = 1.9 \times 10^{-6}$ s⁻¹. A comparison of the heating rates using our effective two-level system with the results using the 15-level molecule in our KOSMA- τ model is shown in Fig. C.1. Here, we scan the parameter ranges where the H₂ vibrational heating and cooling gives a major contribution to the overall energy balance (see Fig. 2). In the upper plot representing low radiation fields and varying densities we find an almost perfect agreement of the two level approximation with the full numeric treatment. At high densities and varying radiation fields shown in the lower plot, we find a good match at temperatures below about 3000 K. The deviation at higher temperatures is due to the neglect of cooling contributions from higher vibrational levels. It has no impact on the overall PDR model, because photoelectric heating clearly supersedes the vibrational contribution at these conditions.

With the simple analytic two-level approximation, we can easily understand the quantitative behavior of the H₂ vibrational energy balance from basic principles thus providing a handy tool for estimates of temperature structures. Burton et al. (1990) also introduced a two-level approximation for the H₂ heating. However, they considered only a single pseudo excited level with an energy corresponding to $v = 6$ and hence did not properly account for cooling via rapid excitation to $v = 1$, or heating via pumping and collisional deexcitation from all 15 levels.

A photon dominated region code comparison study*

M. Röllig^{1,4}, N. P. Abel², T. Bell^{3,17}, F. Bensch¹, J. Black¹⁵, G. J. Ferland², B. Jonkheid⁵, I. Kamp⁶, M. J. Kaufman⁷, J. Le Bourlot⁸, F. Le Petit^{8,15}, R. Meijerink⁵, O. Morata¹⁶, V. Ossenkopf^{4,10}, E. Roueff⁸, G. Shaw², M. Spaans⁹, A. Sternberg¹¹, J. Stutzki⁴, W.-F. Thi¹², E. F. van Dishoeck⁵, P. A. M. van Hoof¹³, S. Viti³, and M. G. Wolfire¹⁴

¹ Argelander-Institut für Astronomie**, Universität Bonn, Auf dem Hügel 71, 53121 Bonn, Germany
e-mail: roellig@ph1.uni-koeln.de

² University of Kentucky, Department of Physics and Astronomy, Lexington, KY 40506, USA

³ Department of Physics & Astronomy, University College London, Gower Street, London WC1E 6BT, UK

⁴ I. Physikalisches Institut, Universität zu Köln, Zülpicher Str. 77, 50937 Köln, Germany

⁵ Leiden Observatory, PO Box 9513, 2300 RA Leiden, The Netherlands

⁶ Space Telescope Science Division of ESA, Space Telescope Science Institute, Baltimore, MD 21218, USA

⁷ Department of Physics, San Jose State University, 1 Washington Square, San Jose, CA 95192, USA

⁸ LUTH UMR 8102, CNRS and Observatoire de Paris, Place J. Janssen, 92195 Meudon Cedex, France

⁹ Kapteyn Astronomical Institute, PO Box 800, 9700 AV Groningen, The Netherlands

¹⁰ SRON National Institute for Space Research, Postbus 800, 9700 AV Groningen, The Netherlands

¹¹ School of Physics and Astronomy, Tel Aviv University, Ramat Aviv 69978, Israel

¹² Institute for Astronomy, The University of Edinburgh, Royal Observatory, Blackford Hill, Edinburgh EH9 3HJ, UK

¹³ Royal Observatory of Belgium, Av. Circulaire, 3 - Ringlaan 3, 1180 Brussel, Belgium

¹⁴ Astronomy Department, University of Maryland, College Park, MD 20742-2421, USA

¹⁵ Onsala Space Observatory, 439 92 Onsala, Sweden

¹⁶ LAEFF, Villafranca del Castillo, Apdo. 50727, 28080 Madrid, Spain

¹⁷ California Institute of Technology, 1200 E. California Blvd, Pasadena CA 91125, USA

Received 27 June 2006 / Accepted 2 February 2007

ABSTRACT

Aims. We present a comparison between independent computer codes, modeling the physics and chemistry of interstellar photon dominated regions (PDRs). Our goal was to understand the mutual differences in the PDR codes and their effects on the physical and chemical structure of the model clouds, and to converge the output of different codes to a common solution.

Methods. A number of benchmark models have been created, covering low and high gas densities $n = 10^3, 10^{5.5} \text{ cm}^{-3}$ and far ultraviolet intensities $\chi = 10, 10^5$ in units of the Draine field (FUV: $6 < h\nu < 13.6 \text{ eV}$). The benchmark models were computed in two ways: one set assuming constant temperatures, thus testing the consistency of the chemical network and photo-processes, and a second set determining the temperature self consistently by solving the thermal balance, thus testing the modeling of the heating and cooling mechanisms accounting for the detailed energy balance throughout the clouds.

Results. We investigated the impact of PDR geometry and agreed on the comparison of results from spherical and plane-parallel PDR models. We identified a number of key processes governing the chemical network which have been treated differently in the various codes such as the effect of PAHs on the electron density or the temperature dependence of the dissociation of CO by cosmic ray induced secondary photons, and defined a proper common treatment. We established a comprehensive set of reference models for ongoing and future PDR model bench-marking and were able to increase the agreement in model predictions for all benchmark models significantly. Nevertheless, the remaining spread in the computed observables such as the atomic fine-structure line intensities serves as a warning that there is still a considerable uncertainty when interpreting astronomical data with our models.

Key words. ISM: abundances – astrochemistry – ISM: clouds – ISM: general – radiative transfer – methods: numerical

1. Introduction

Interstellar photon dominated regions or photodissociation regions (PDRs) play an important role in modern astrophysics as they are responsible for many emission characteristics of the ISM, and dominate the infrared and sub-millimetre spectra of star formation regions and galaxies as a whole. Theoretical models addressing the structure of PDRs have been available for approximately 30 years and have evolved into advanced

computer codes accounting for a growing number of physical effects with increasing accuracy. These codes have been developed with different goals in mind: some are geared to efficiently model a particular type of region, e.g. HII regions, protoplanetary disks, planetary nebulae, diffuse clouds, etc.; others emphasize a strict handling of the micro-physical processes in full detail (e.g. wavelength dependent absorption), but at the cost of increased computing time. Yet others aim at efficient and rapid calculation of large model grids for comparison with observational data, which comes at the cost of pragmatic approximations using effective rates rather than detailed treatment. As a result, the different models have focused on the detailed simulation of particular processes determining the structure in the main

* Appendix A is only available in electronic form at
<http://www.aanda.org>

** Founded by merging of the Sternwarte, Radiastronomisches Institut and Institut für Astrophysik und Extraterrestrische Forschung.

regions of interest while using only rough approximations for other processes. The model setups vary strongly among different model codes. This includes the assumed model geometry, their physical and chemical structure, the choice of free parameters, and other details. Consequently it is not always straightforward to directly compare the results from different PDR codes. Taking into account that there are multiple ways of implementing physical effects in numerical codes, it is obvious that the model output of different PDR codes can differ from each other. As a result, significant variations in the physical and chemical PDR structure predicted by the various PDR codes can occur. This divergence would prevent a unique interpretation of observed data in terms of the parameters of the observed clouds. Several new facilities such as Herschel, SOFIA, APEX, ALMA, and others will become available over the next years and will deliver many high quality observations of line and dust continuum emission in the sub-millimeter and FIR wavelength regime. Many important PDR tracers emit in this range ([CII] (158 μm), [OI] (63 and 146 μm), [CI] (370 and 610 μm), CO (650, 520, ..., 57.8 μm), H₂O, etc.). In order to reliably analyze these data we need a set of high quality tools, including PDR models that are well understood and properly debugged. As an important preparatory step toward these missions an international cooperation between many PDR model groups was initiated. The goals of this PDR-benchmarking were:

- to understand the differences in the different code results;
- to obtain (as much as possible) the same model output with every PDR code when using the same input;
- to agree on the correct handling of important processes;
- to identify the specific limits of applicability of the available codes.

To this end, a PDR-benchmarking workshop was held at the Lorentz Center in Leiden, Netherlands in 2004 to jointly work on these topics¹. In this paper we present the results from this workshop and the results originating from the follow-up activities. A related workshop to test line radiative transfer codes was held in 1999 (see van Zadelhoff et al. 2002).

It is not the purpose of the benchmarking to present a preferred solution or a preferred code. PDRs are found in a large variety of objects and under very different conditions. To this end, it was neither possible nor desirable to develop a *generic* PDR code, able to model every possible PDR. Furthermore, the benchmarking is not meant to model any “real” astronomical object. The main purpose of this study is technical not physical. This is also reflected in the choice of the adopted incomplete chemical reaction network (see Sect. 4).

In Sect. 2 we briefly introduce the physics involved in PDRs, in Sect. 3 we introduce some key features in PDR modeling. Section 4 describes the setup of the benchmark calculations and Sect. 5 presents the results for a selection of benchmark calculations and gives a short review over the participating codes. In Sect. 6 we discuss the results and summarize the lessons learned from the benchmark effort. A tabular overview of the individual code characteristics is given in the Appendix.

2. The physics of PDRs

PDRs are traditionally defined as regions where H₂-non-ionizing far-ultraviolet photons from stellar sources control the gas heating and chemistry. Any ionizing radiation is assumed to be absorbed in the narrow ionization fronts located between adjacent

HII regions and the PDRs². In PDRs the gas is heated by the far-ultraviolet radiation (FUV, $6 < h\nu < 13.6 \text{ eV}$, from the ambient UV field and from hot stars) and cooled via the emission of spectral line radiation of atomic and molecular species and continuum emission by dust (Hollenbach & Tielens 1999; Sternberg 2004). The FUV photons heat the gas by means of photoelectric emission from grain surfaces and polycyclic aromatic hydrocarbons (PAHs) and by collisional de-excitation of vibrationally excited H₂ molecules. Additional contributions to the total gas heating comes from H₂ formation, dissociation of H₂, dust-gas collisions in case of dust temperatures exceeding the gas temperature, cosmic ray heating, turbulence, and from chemical heating. At low visual extinction A_V into the cloud/PDR the gas is cooled by emission of atomic fine-structure lines, mainly [OI] 63 μm and [CII] 158 μm . At larger depths, millimeter, sub-millimeter and far-infrared molecular rotational-line cooling (CO, OH, H₂, H₂O) becomes important, and a correct treatment of the radiative transfer in the line cooling is critical. The balance between heating and cooling determines the local gas temperature. The local FUV intensity also influences the chemical structure, i.e. the abundance of the individual chemical constituents of the gas. The surface of PDRs is mainly dominated by reactions induced by UV photons, especially the ionization and dissociation of atoms and molecules. With diminishing FUV intensity at higher optical depths more complex species may be formed without being radiatively destroyed immediately. Thus the overall structure of a PDR is the result of a complex interplay between radiative transfer, energy balance, and chemical reactions.

3. Modeling of PDRs

The history of PDR modeling dates back to the early 1970’s (Hollenbach et al. 1971; Jura 1974; Glassgold & Langer 1975; Black & Dalgarno 1977) with steady state models for the transitions from H to H₂ and from C⁺ to CO. In the following years a number of models, addressing the chemical and thermal structure of clouds subject to an incident flux of FUV photons have been developed (de Jong et al. 1980; Tielens & Hollenbach 1985; van Dishoeck & Black 1988; Sternberg & Dalgarno 1989; Hollenbach et al. 1991; Le Bourlot et al. 1993; Störzer et al. 1996). Additionally, a number of models, focusing on certain aspects of PDR physics and chemistry were developed, e.g. models accounting for time-dependent chemical networks, models of clumped media, and turbulent PDR models (Hill & Hollenbach 1978; Wagenblast & Hartquist 1988; de Boisanger et al. 1992; Bertoldi & Draine 1996; Lee et al. 1996; Hegmann & Kegel 1996; Spaans 1996; Nejad & Wagenblast 1999; Röllig et al. 2002; Bell et al. 2005). Standard PDR models generally do not account for dynamical properties of gas but there are some studies that consider the advection problem rather than the steady state approach (e.g. Störzer & Hollenbach 1998). For a more detailed review see Hollenbach & Tielens (1999).

In order to numerically model a PDR it is necessary to compute all local properties of a cloud such as the relative abundances of the gas constituents together with their level populations, temperature of gas and dust, gas pressure, composition of dust/PAHs, and many more. This local treatment is complicated by the radiation field which couples remote parts of the cloud. The local mean radiation field, which is responsible for photochemical reactions, gas/dust heating, and excitation of molecules

² This distinction is clearer when referring to PDRs as Photo-Dissociation Regions, since molecules are hardly found in HII regions.

¹ URL: <http://www.lorentzcenter.nl/>

depends on the position in the cloud and the (wavelength dependent) absorption along the lines of sight toward this position. This non-local coupling makes numerical PDR calculations a CPU time consuming task.

PDR modelers and observers approach the PDRs from opposite sides: PDR models start by calculating the local properties of the clouds such as the local CO density and the corresponding gas temperature and use these local properties to infer the expected global properties of the cloud like total emergent emissivities or fluxes and column densities. The observer on the other hand starts by observing global features of a source and tries to infer the local properties from that. The connection between local and global properties is complex and not necessarily unambiguous. Large variations e.g. in the CO density at the surface of the cloud may hardly affect the overall CO column density due to the dominance of the central part of the cloud with a high density. If one is interested in the total column density it does not matter whether different codes produce a different surface CO density. For the interpretation of high- J CO emission lines, however, different CO densities in the outer cloud layers make a huge difference since high temperatures are required to produce high- J CO fluxes. Thus, if different PDR model codes deviate in their predicted cloud structures, this may affect the interpretation of observations and may prevent inference of the “true” structure behind the observed data. To this end it is very important to understand the origin of present differences in PDR model calculations. Otherwise it is impossible to rule out alternative interpretations. The ideal situation, from the modelers point of view, would be a complete knowledge of the true local structure of a real cloud and their global observable properties. This would easily allow us to calibrate PDR models. Since this case is unobtainable, we take one step back and apply a different approach: If all PDR model codes use exactly the same input and the same model assumptions they should produce the same predictions.

Because of the close interaction between chemical and thermal balance and radiative transfer, PDR codes typically iterate through the following computation steps: 1) solve the local chemical balance to determine local densities; 2) solve the local energy balance to estimate the local physical properties like temperatures, pressures, and level populations; 3) solve the radiative transfer; 4) for finite models it is necessary to successively iterate steps 1)–3). Each step requires a variety of assumptions and simplifications. Each of these aspects can be investigated to great detail and complexity (see for example van Zadelhoff et al. (2002) for a discussion of NLTE radiative transfer methods), but the explicit aim of the PDR comparison workshop was to understand the interaction of all computation steps mentioned above. Even so it was necessary to considerably reduce the model complexity in order to disentangle cause and effect.

3.1. Description of sensitivities and pitfalls

Several aspects of PDR modeling have shown the need for detailed discussion, easily resulting in misleading conclusions if not treated properly.

3.1.1. Model geometry

Two common geometrical setups of model PDRs are shown in Fig. 1. Most PDR models feature a plane-parallel geometry, illuminated either from one side or from both sides. This geometry naturally suggests a directed illumination, perpendicular to the cloud surface. This simplifies the radiative transfer problem

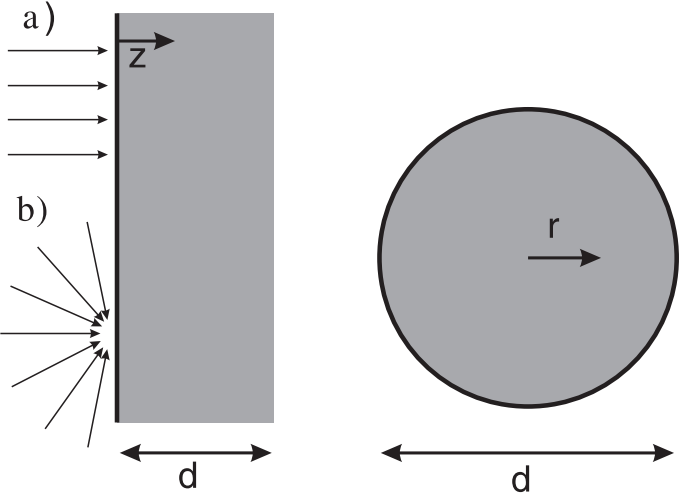


Fig. 1. Common geometrical setups of a model PDR. The surface of any plane-parallel or spherical cloud is illuminated either **a)** uni-directional or **b)** isotropically.

significantly, since it is sufficient to account for just one line of sight, if we ignore scattering out of the line of sight (Flannery et al. 1980). Since most plane-parallel PDR models are infinite perpendicular to the cloud depth z it is also straightforward to account for an isotropic FUV irradiation within the pure 1-D formalism. For a spherical geometry one can exploit the model symmetry only for a FUV field isotropically impinging onto the cloud. In finite plane-parallel and spherical models iterations over the depth/radial structure are mandatory because radiation is coming from multiple directions, passing through cloud elements for which the physical and chemical structure and hence opacities have not been calculated in the same iteration step. To account for this “backside” illumination it is essential to iterate on the radiation field.

The most important quantity describing the radiation field in PDR models is the local mean intensity (or alternatively the energy density) as given by:

$$J_\nu = \frac{1}{4\pi} \int I_\nu d\Omega \quad [\text{erg cm}^{-2} \text{ s}^{-1} \text{ Hz}^{-1} \text{ sr}^{-1}] \quad (1)$$

with the specific intensity I_ν being averaged over the solid angle Ω . Note that when referring to the ambient FUV in units of Draine χ (Draine 1978) or Habing G_0 (Habing 1968) fields, these are always given as averaged over 4π . If we place a model cloud of sufficient optical thickness in such an average FUV field, the resulting local mean intensity at the cloud edge is half the value of that without the cloud.

The choice between directed and isotropic FUV fields directly influences the attenuation due to dust. In the unidirectional case the FUV intensity along the line of sight is attenuated according to $\exp(-\tau_\nu)$, where τ_ν is the optical depth of the dust at frequency ν . For pure absorption the radiative transfer equation becomes:

$$\mu \frac{dI_\nu(\mu, x)}{dx} = -\kappa_\nu I_\nu(\mu, x). \quad (2)$$

with the cosine of the radiation direction $\mu = \cos \Theta$, the cloud depth x , and the absorption coefficient κ_ν , with the simple solution $J_\nu/J_{\nu,0} = \exp(-\tau_\nu \mu)$ for a semi-infinite cloud. For the

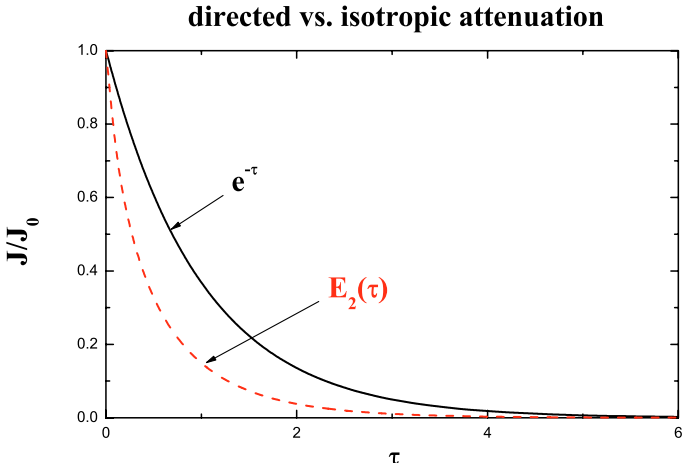


Fig. 2. Comparison of attenuation of the mean intensity for the case of an uni-directional and isotropically illuminated medium. The solid line gives the attenuation due to uni-directional illumination, while the dashed line gives the attenuation for an isotropic FUV radiation where τ means the optical depth perpendicular to the surface of the cloud.

isotropic case, $I_{v,0}(\mu) = J_{v,0} = \text{const.}$, integration of Eq. (2) leads to the second order exponential integral:

$$J_v/J_{v,0} = E_2(\tau_v) = \int_0^1 \frac{\exp(-\tau_v \mu)}{\mu^2} d\mu. \quad (3)$$

As seen in Fig. 2 the attenuation with depth in the isotropic case is significantly different from the uni-directional case. A common way to describe the depth dependence of a particular quantity in PDRs is to plot it against A_V , which is a direct measure of the traversed column of attenuating material. In order to compare the uni-directional and the isotropic case it is necessary to rescale them to the same axis. It is possible to define an effective $A_{V,\text{eff}} = -\ln[E_2(A_V k)]/k$ with $k = \tau_{\text{UV}}/A_V$ in the isotropic case, where A_V is the attenuation perpendicular to the surface and UV is in the range $6 < h\nu < 13.6$. In this paper all results from spherical models are scaled to $A_{V,\text{eff}}$. Figure 3 demonstrates the importance of scaling results to an appropriate A_V scale. It shows the local H_2 photo-dissociation rate for two different FUV illumination geometries. The solid line represents a standard uni-directional illumination perpendicular to the cloud surface as given in many standard plane-parallel PDR codes. The dashed line is the result from an isotropic illumination plotted against the standard “perpendicular” A_V . The offset to the uni-directional case is significant. After rescaling to an appropriate $A_{V,\text{eff}}$ both model results are in good agreement. Please note, that in general it is not possible to achieve perfect agreement as there is a spectrum involved with a spread of k values across the UV.

The attenuation of FUV radiation is additionally complicated if we account for dust scattering. For a full treatment by Legendre polynomials see Flannery et al. (1980). In case of small scattering angles $g = \langle \cos \theta \rangle \approx 1$ the scattering can be approximated by an effective forward attenuation $\tau(1-\omega)$, where ω is the scattering albedo. Thus, more material is needed to obtain the same attenuation as in the case without scattering. Hence a proper scaling of A_V is necessary. In case of clumped gas this becomes even more complex. The presence of stochastic density fluctuations leads to a substantial reduction of the effective optical depth as demonstrated by Hegmann & Kegel (2003). All this has to be considered when calculating the photodissociation and photoionization rates, when the attenuation with depth is represented by simple exponential forms, $\exp(-k_i A_V)$ (e.g.

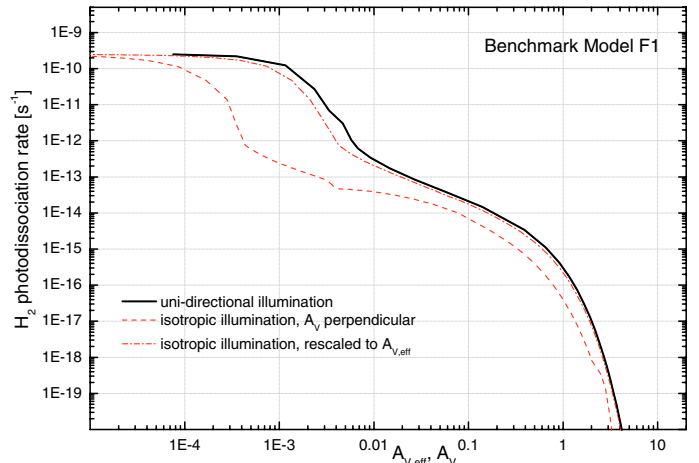


Fig. 3. H_2 photo-dissociation rates resulting from uni-directional FUV illuminated clouds compared to an isotropic illumination. The results from isotropic models are plotted vs. the perpendicular A_V and vs. $A_{V,\text{eff}}$.

van Dishoeck 1988; Robege et al. 1991), where the factor k_i accounts for the wavelength dependence of the photoprocess i^3 .

3.1.2. Chemistry

PDR chemistry has been addressed in detail by many authors (Tielens & Hollenbach 1985; van Dishoeck & Black 1988; Hollenbach et al. 1991; Fuente et al. 1993; Le Bourlot et al. 1993; Jansen et al. 1995; Sternberg & Dalgarno 1995; Lee et al. 1996; Bakes & Tielens 1998; Walmsley et al. 1999; Savage & Ziurys 2004; Teyssier et al. 2004; Fuente et al. 2005; Meijerink & Spaans 2005). These authors discuss numerous aspects of PDR chemistry in great detail and give a comprehensive overview of the field. Here we repeat some crucial points in the chemistry of PDRs in order to motivate the benchmark standardization and to prepare the discussion of the benchmark result.

In PDRs photoprocesses are very important due to the high FUV intensity, as well as reactions with abundant hydrogen atoms. The formation and destruction of H_2 , heavily influenced by the FUV field, is of major importance for the chemistry in PDRs. H_2 forms on grain surfaces, a process which crucially depends on the temperatures of the gas and the grains (Hollenbach & Salpeter 1971; Cazaux & Tielens 2004), which themselves depend on the local cooling and heating, governed by the FUV. The photo-dissociation of H_2 is a line absorption process and, thus is subject to effective shielding (van Dishoeck & Black 1988). This leads to a sharp transition from atomic to molecular hydrogen once the H_2 absorption lines are optically thick. The photo-dissociation of CO is also a line absorption process, additionally complicated by the fact that the broad H_2 absorption lines overlap with CO absorption lines. Similar to H_2 this leads to a transition from atomic carbon to CO. For $A_V < 1$ carbon is predominantly present in ionized form. For an assumed FUV field of $\chi = 1$, CO is formed at about $A_V \approx 2$. This results in the typical PDR stratification of H/H_2 and $C^+/C/CO$. The depth of this transition zone depends on the physical parameters but also on the contents of the chemical network: for example the inclusion of PAHs into the chemical balance calculations shifts the C^+ to C transition to smaller $A_{V,\text{eff}}$ (e.g. Lepp & Dalgarno 1988; Bakes & Tielens 1998).

³ In this context the term photoprocess refers to either photodissociation or photoionization.

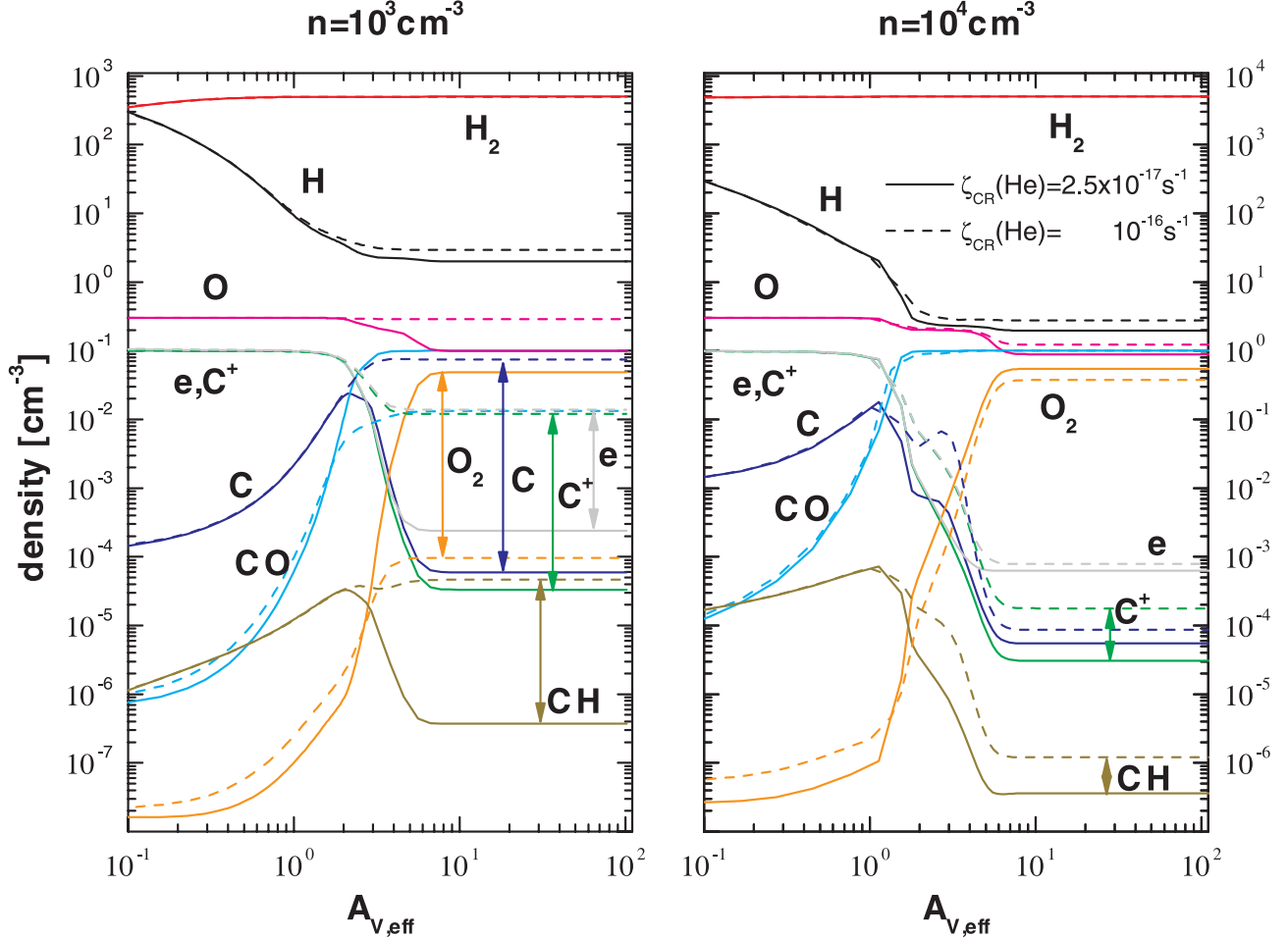


Fig. 4. The influence of the cosmic ray ionization rate on the chemical structure of a model cloud. The left panel shows results for Model F1 ($n = 10^3 \text{ cm}^{-3}$, $\chi = 10$), the right panel gives results for 10 times higher densities ($n = 10^4 \text{ cm}^{-3}$, $\chi = 10$). The solid lines give the results for a cosmic ray ionization rate of Helium, enhanced by a factor 4, the dashed lines are for the lower ionization rate. The different colors denote different chemical species. The most prominent differences are highlighted with colored arrows.

The solution of the chemical network itself covers the destruction and formation reactions of all chemical species considered. For each included species i this results in a balance equation of the form:

$$\frac{dn_i}{dt} = \sum_j \sum_k n_j n_k R_{jki} + \sum_l n_l \zeta_{li} - n_i \left(\sum_l \zeta_{il} + \sum_l \sum_j n_j R_{ijl} \right). \quad (4)$$

Here n_i denotes the density of species i . The first two terms cover all formation processes while the last two terms account for all destruction reactions. R_{jki} is the reaction rate coefficient for the reaction $X_j + X_k \rightarrow X_i + \dots$ (X stands for species X), ζ_{il} is the local photo-destruction rate coefficient for ionization or dissociation of species $X_i + h\nu \rightarrow X_l + \dots$, either by FUV photons or by cosmic ray (CR) induced photons, and ζ_{li} is the local formation rate coefficient for formation of X_i by photo-destruction of species X_l . For a stationary solution one assumes $dn_i/dt = 0$, while non-stationary models solve the differential Eq. (4) in time. The chemical network is a highly non-linear system of equations. Hence it is not self-evident that a unique solution exists at all, multiple solution may be possible as demonstrated e.g. by Le Bourlot et al. (1993) and Boger & Sternberg (2006).

They showed that bistability may occur in gas-phase models (neglecting dust chemistry) of interstellar dark clouds in a narrow parameter range of approximately $10^3 \text{ cm}^{-3} \gtrsim n/\zeta_{-17} \gtrsim 10^2 \text{ cm}^{-3}$ with the cosmic-ray ionization rate of molecular hydrogen $\zeta_{\text{CR}} \equiv 10^{-17} \zeta_{-17} \text{ s}^{-1}$. Within this range the model results may depend very sensitively on variations of input parameters such as ζ_{CR} or the H_3^+ dissociative recombination rate. To demonstrate this we show the influence of varying ionization rates in Fig. 4. The left panel gives abundance profiles for benchmark model F1 ($n = 10^3 \text{ cm}^{-3}$, $\chi = 10$) the right panel shows a similar model but with higher density ($n = 10^4 \text{ cm}^{-3}$). The higher density was chosen to make sure that we are outside the bistability regime. The solid lines in both panels are for a cosmic ray helium ionization rate of $\zeta_{\text{CR}}(\text{He}) = 2.5 \times 10^{-17} \text{ s}^{-1}$, the dashed lines denote an ionization rate increased by a factor four. Different colors denote different chemical species. The most prominent differences are highlighted with colored arrows. The factor four in $\zeta_{\text{CR}}(\text{He})$ results in differences in density up to three orders of magnitude in the lower density case! A detailed analysis shows that the strong abundance transitions occur for $\zeta_{\text{CR}}(\text{He}) > 8 \times 10^{-17} \text{ s}^{-1}$. This highly non-linear behavior disappears if we leave the critical parameter range as demonstrates in the right panel of Fig. 4. Boger & Sternberg (2006) emphasize that this effect is a property of the gas phase chemical network, and is damped if gas-grain processes such as grain

assisted recombination of the atomic ions are introduced (see also Shalabiea & Greenberg 1995). They conclude that the bistability phenomenon probably does not occur in realistic dusty interstellar clouds while Le Bourlot (2006) argues that what matters for bistability is not the number of neutralisation channels but the degree of ionisation and that bistability may occur in interstellar clouds. They suggest this could be one of the possible reasons of the non detection of O₂ by the ODIN satellite (Viti et al. 2001). Yet, another possible explanation for the absence of O₂ is freeze-out onto dust. However it is clear that bistability is a real property of interstellar gas-phase networks and not just a numerical artifact. Furthermore it is important to emphasize that standard PDR models may react very sensitively on the variation of input parameters (e.g. ζ_{CR} , the H₂ formation rate, the PAH content of the model cloud, etc.) and one has to be careful in the interpretation of surprising model signatures.

The numerical stability and the speed of convergence may vary significantly over different chemical networks. Three major questions have to be addressed:

1. which species i are to be included?
2. which reactions are to be considered?
3. which reaction rate coefficients are to be applied?

A general answer to question 1 cannot be given, since this depends on the field of application. In steady state one has to solve a system of M nonlinear equations, where M is the number of included species, thus the complexity of the problem scales with the number of species ($\propto N^2 \dots N^3$) rather than with the number of chemical reactions. Nowadays CPU time is not a major driver for the design of chemical networks. Nevertheless, in some cases a small network can give similar results as a big network. Several studies have shown that very large networks may include a surprisingly large number of “unimportant” reactions, i.e. reactions that may be removed from the network without changing the chemical structure significantly (Markwick-Kemper 2005; Wakelam et al. 2005a). It is more important to identify crucial species not to be omitted, i.e. species that dominate the chemical structure under certain conditions. A well known example is the importance of sulfur for the formation of atomic carbon at intermediate A_V where the charge transfer reaction S + C⁺ → C + S⁺ constitutes an additional production channel for atomic carbon, visible in a second rise in the abundance of C (Sternberg & Dalgarno 1995). In these benchmarking calculations, sulfur was not included in order to minimize model complexity, in spite of its importance for the PDR structure.

Regarding question 2 a secure brute force approach would be the inclusion of all known reactions involving all chosen species, under the questionable assumption that we actually *know* all important reactions and their rate coefficients. This assumption is obviously invalid for grain surface reactions and gas-grain interactions such as freeze-out and desorption. It is important not to create artificial bottlenecks in the reaction scheme by omitting important channels. The choice of reaction rate coefficients depends on factors like availability, accuracy, etc. A number of comprehensive databases of rate coefficients is available today, e.g. NSM/OHIO (Wakelam et al. 2004, 2005b), UMIST (Millar, Farquhar, & Willacy 1997; Le Teuff et al. 2000), and Meudon (Le Bourlot et al. 1993), which collect the results from many different references, both theoretical and experimental.

An example for the importance of explicitly agreeing on the details of the computation of the reaction rate is the reaction:

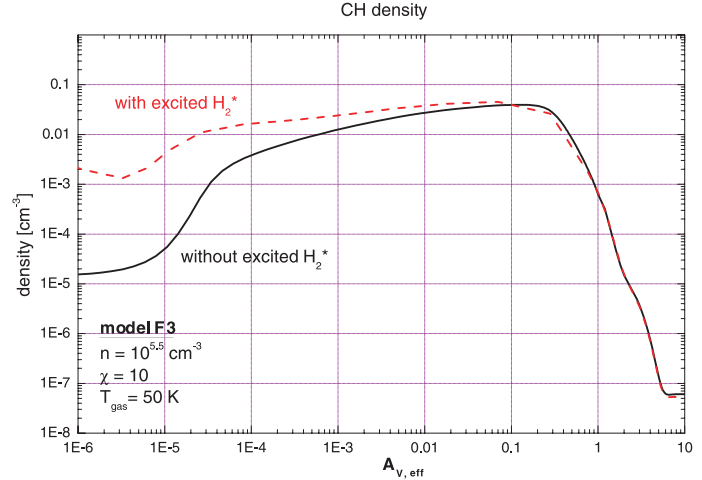


Fig. 5. Comparison between model codes with (dashed line) and without (solid line) excited molecular hydrogen, H₂^{*}. The abundance profile of CH is plotted for both models against $A_{V,\text{eff}}$. Benchmark model F3 has a high density ($n = 10^{5.5} \text{ cm}^{-3}$) and low FUV intensity ($\chi = 10$).

It has an activation energy barrier of 11 700 K (Millar, Farquhar, & Willacy 1997), effectively reducing the production of CH molecules. If we include vibrationally excited H₂^{*} into the chemical network and assume that reaction (5) has no activation energy barrier for reactions with H₂^{*} we obtain a significantly higher production rate of CH as shown in Figure 5. Even this approach is a rather crude assumption, but it demonstrates the importance of explicitly agreeing on how to handle the chemical calculations in model comparisons.

Another example is the formation of C in the dark cloud part of a PDR, i.e. at values of $A_V > 5$. A possible formation channel for atomic carbon is the dissociation of CO by secondary UV photons, induced by cosmic rays (Le Teuff et al. 2000). In the outer parts of the PDR the impinging FUV field dominates the dissociation of CO, but for high A_V the FUV field is effectively shielded and CR induced UV photons become important. For CO, this process depends on the level population of CO, and therefore is temperature dependent (Gredel et al. 1987), however this temperature dependence is often ignored. The reaction rate given by Gredel et al. (1987) has to be corrected by a factor of $(T/300 \text{ K})^{1.17}$ effectively reducing the dissociation rate for temperatures below 300 K (Le Teuff et al. 2000). In Fig. 6 we plot the density profile of atomic carbon for an isothermal benchmark model with temperature $T = 50 \text{ K}$. The solid line represents the model result for an uncorrected photo-rate using the average reaction rate for $T = 300 \text{ K}$, compared to the results using the rate corrected for $T = 50 \text{ K}$ by $(50/300)^{1.17}$, given by the dashed curve.

3.1.3. Heating and cooling

To determine the local temperature in a cloud, the equilibrium between heating and cooling has to be calculated. The heating rates mainly depend on the H₂ formation rate, the electron density, the grain size distribution, grain composition, and H₂ treatment (i.e. two-line approximation vs. full ro-vib model), while the cooling rates are dominantly influenced by the abundance of the main cooling species and the dust opacity in the FIR. Table 1 gives an overview of the most important heating and cooling processes. Most of them can be modelled at different levels of detail. This choice may have a major impact

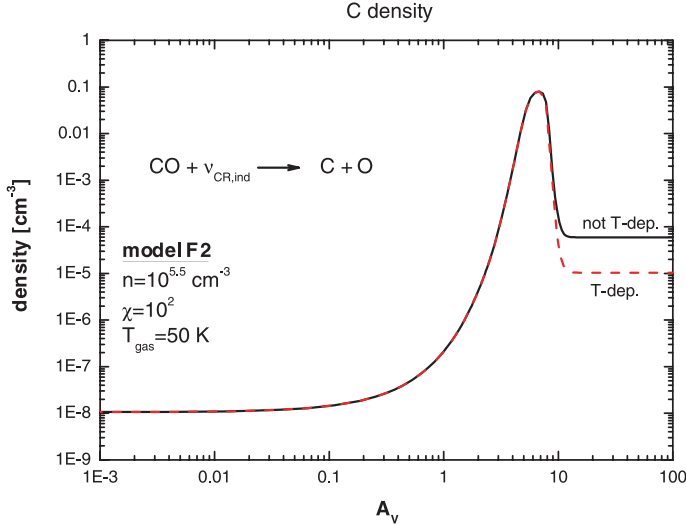


Fig. 6. The density profile of atomic carbon for the benchmark model F2 (low density, high FUV, $T = \text{const.} = 50 \text{ K}$, as discussed in Sect. 4). The solid curve results from a constant dissociation by CR induced secondary photons (implicitly assuming $T = 300 \text{ K}$), the dashed curve shows the influence of a temperature dependent dissociation, i.e. the corresponding dissociation rate was corrected by a factor of $(T/300 \text{ K})^{1.17}$ with $T = 50 \text{ K}$.

Table 1. Overview over the major heating and cooling processes in PDR physics.

Heating	Cooling
photoelectric heating (dust & PAH)	[CII] 158 μm
collisional de-excitation of vib. excited H ₂	[OI] 63, 145 μm
H ₂ dissociation	[CI] 370, 610 μm
H ₂ formation	[SiII] 35 μm
CR ionization	CO, H ₂ O, OH, H ₂
gas-grain collisions	Ly α , [OI], [FeII]
dissipation of turbulence	gas-grain collisions

on the model results. One example is the influence of PAHs on the efficiency of the photoelectric heating, which results in a significantly higher temperature e.g. at the surface of the model cloud if PAHs are taken into account. Bakes & Tielens (1994) give convenient fitting formulas for the photoelectric heating. Another important case is the collisional de-excitation of vibrationally excited H₂. A detailed calculation of the level population shows that for temperatures above 800 K the lower transitions switch from heating to cooling. This imposes a significant influence on the net heating from H₂ vibrational de-excitation. When using an approximation for the heating rate it is important to account for this cooling effect (Röllig et al. 2006). The cooling of the gas by line emission depends on the atomic and molecular constants as well as on the radiative transfer. A common approximation to the radiative transfer problem is by assuming escape probabilities for the cooling lines (de Jong et al. 1980; Stutzki 1984; Störzer et al. 1996). The excitation temperature at any point can be computed by balancing the collisional excitation and the photon escape probability. The local escape probability is obtained by integrating $\exp(-\tau_y)$ over 4π . In the escape probability approximation it is now assumed that the radiative interaction region is small enough so that the optical depth in each direction is produced by molecules with the same excitation temperature. Then the excitation problem becomes a local one. The [OI] 63 μm line may also become very optically thick and can act both as heating

and cooling contribution. Under certain benchmark conditions (low density, constant temperature $T_{\text{gas}} = 50 \text{ K}$) the [OI] 63 μm line even showed weak maser behavior (see data plots at <http://www.ph1.uni-koeln.de/pdr-comparison>). Collisions between the gas particles and the dust grains also contribute to the total heating or cooling.

3.1.4. Grain properties

Many aspects of PDR physics and chemistry are connected to dust properties. We will give only a short overview of the importance of dust grains in the modeling of PDRs. Dust acts on the energy balance of the ISM by means of photoelectric heating; it influences the radiative transfer by absorption and scattering of photons, and it acts on the chemistry of the cloud via grain surface reactions, e.g. the formation of molecular hydrogen and the depletion of other species. One distinguishes three dust components: PAHs, very small grains (VSGs) and big grains (BGs).

The properties of big grains have been reviewed recently by Draine (2003, and references therein). The first indirect evidence for the presence of VSGs in the ISM was presented by Andriesse (1978) in the case of the M17 PDR. The dust grains themselves consist of amorphous silicates and carbonaceous material and may be covered with ice mantles in the denser and colder parts of the ISM. For details of the composition of grains and their extinction due to scattering and absorption see Li & Draine (2002) and references therein.

The influence and proper treatment of electron densities together with grain ionization and recombination is still to be analyzed. Not only the charge of dust and PAHs but also the scattering properties are still in discussion (Weingartner & Draine 2001). This heavily influences the model output, e.g. the inclusion of back-scattering significantly increases the total H₂ photodissociation rate at the surface of the model cloud compared to calculations with pure forward scattering.

3.1.5. Radiative transfer

The radiative transfer (RT) can be split into two distinct wavelength regimes: FUV and IR/FIR. These may also be labeled as “input” and “output”. FUV radiation due to ambient UV field and/or young massive stars in the neighborhood impinges on the PDR. The FUV photons are absorbed on their way deeper into the cloud, giving rise to the well known stratified chemical structure of PDRs. In general, reemission processes can be neglected in the FUV, considerably simplifying the radiative transfer problem. Traveling in only one direction, from the edge to the inside, the local mean FUV intensity can usually be calculated in a few iteration steps. In contrast to the FUV, the local FIR intensity is a function of the temperature and level populations at all positions due to absorption and reemission of FIR photons. Thus a computation needs to iterate over all spatial grid points. A common simplifying approximation is the spatial decoupling via the escape probability approximation. This allows to substitute the intensity dependence by a dependence on the relevant optical depths, ignoring the spatial variation of the source function. The calculation of emission line cooling then becomes primarily a problem of calculating the local excitation state of the particular cooling species. An overview of NLTE radiative transfer methods is given by van Zadelhoff et al. (2002).

Table 2. List of participating codes. See Appendix for short description of the individual models.

Model Name	Authors
Cloudy	G. J. Ferland, P. van Hoof, N. P. Abel, G. Shaw (Ferland et al. 1998; Abel et al. 2005; Shaw et al. 2005)
COSTAR	I. Kamp, F. Bertoldi, G.-J. van Zadelhoff (Kamp & Bertoldi 2000; Kamp & van Zadelhoff 2001)
HTBKW	D. Hollenbach, A. G. G. M. Tielens, M. G. Burton, M. J. Kaufman, M. G. Wolfire (Tielens & Hollenbach 1985; Kaufman et al. 1999; Wolfire et al. 2003)
KOSMA- τ	H. Störzer, J. Stutzki, A. Sternberg (Störzer et al. 1996), B. Köster, M. Zielinsky, U. Leuenhagen Bensch et al. (2003), Röllig et al. (2006)
Lee96mod	H.-H. Lee, E. Herbst, G. Pineau des Forêts, E. Roueff, J. Le Bourlot, O. Morata (Lee et al. 1996)
Leiden	J. Black, E. van Dishoeck, D. Jansen and B. Jonkheid (Black & van Dishoeck 1987; van Dishoeck & Black 1988; Jansen et al. 1995)
Meijerink	R. Meijerink, M. Spaans (Meijerink & Spaans 2005)
Meudon	J. Le Bourlot, E. Roueff, F. Le Petit (Le Petit et al. 2005, 2002; Le Bourlot et al. 1993)
Sternberg	A. Sternberg, A. Dalgarno (Sternberg & Dalgarno 1989, 1995; Boger & Sternberg 2005)
UCL_PDR	S. Viti, W.-F. Thi, T. Bell (Taylor et al. 1993; Papadopoulos et al. 2002; Bell et al. 2005)

4. Description of the benchmark models

4.1. PDR code characteristics

A total number of 11 model codes participated in the PDR model comparison study during and after the workshop in Leiden. Table 2 gives an overview of these codes. The codes are different in many aspects:

- finite and semi-infinite plane-parallel and spherical geometry, disk geometry;
- chemistry: steady state vs. time-dependent, different chemical reaction rates, chemical network;
- IR and FUV radiative transfer (effective or explicitly wavelength dependent), self- and mutual shielding, atomic and molecular rate coefficients;
- treatment of dust and PAHs;
- treatment of gas heating and cooling;
- range of input parameters;
- model output;
- numerical treatment, gridding, etc.

This manifold in physical, chemical and technical differences makes it difficult to directly compare results from the different codes. Thus we tried to standardize the computation of the benchmark model clouds as much as possible. This required all codes to reduce their complexity and sophistication, often beyond what their authors considered to be acceptable, considering the actual knowledge of some of the physical processes. However as the main goal of this study was to understand why and how these codes differ these simplifications are acceptable. Our aim was not to provide a realistic model of real astronomical objects. The individual strengths (and weaknesses) of each PDR code are briefly summarized in the Appendix and on the website: <http://www.ph1.uni-koeln.de/pdr-comparison>.

4.2. Benchmark frame and input values

A total of 8 different model clouds were used for the benchmark comparison. The density and FUV parameter space is covered by accounting for low and high densities and FUV fields under isothermal conditions, giving 4 different model clouds. In one set of models the complexity of the model calculations was reduced by setting the gas and dust temperatures to a given constant value (models F1–F4, “F” denoting a fixed temperature), making the results independent of the solution of the local energy balance.

Table 3. Specification of the model clouds that were computed during the benchmark. The models F1–F4 use constant gas and dust temperatures, while V1–V4 have their temperatures calculated self consistently.

F1 $T = 50 \text{ K}$ $n = 10^3 \text{ cm}^{-3}, \chi = 10$	F2 $T = 50 \text{ K}$ $n = 10^3 \text{ cm}^{-3}, \chi = 10^5$
F3 $T = 50 \text{ K}$ $n = 10^{5.5} \text{ cm}^{-3}, \chi = 10$	F4 $T = 50 \text{ K}$ $n = 10^{5.5} \text{ cm}^{-3}, \chi = 10^5$
V1 $T = \text{variable}$ $n = 10^3 \text{ cm}^{-3}, \chi = 10$	V2 $T = \text{variable}$ $n = 10^3 \text{ cm}^{-3}, \chi = 10^5$
V3 $T = \text{variable}$ $n = 10^{5.5} \text{ cm}^{-3}, \chi = 10$	V4 $T = \text{variable}$ $n = 10^{5.5} \text{ cm}^{-3}, \chi = 10^5$

Table 4. Chemical content of the benchmark calculations.

Chemical species in the models
H, H ⁺ , H ₂ , H ₂ ⁺ , H ₃ ⁺ O, O ⁺ , OH ⁻ , OH, O ₂ , O ₂ ⁺ , H ₂ O, H ₂ O ⁺ , H ₃ O ⁺ C, C ⁺ , CH, CH ⁺ , CH ₂ , CH ₂ ⁺ , CH ₃ , CH ₃ ⁺ , CH ₄ , CH ₄ ⁺ , CH ₅ ⁺ , CO, CO ⁺ , HCO ⁺ He, He ⁺ , e ⁻

In a second benchmark set, the thermal balance has been solved explicitly thus determining the temperature profile of the cloud (models V1–V4, “V” denoting variable temperatures). Table 3 gives an overview of the cloud parameter of all eight benchmark clouds.

4.2.1. Benchmark chemistry

One of the crucial steps in arriving at a useful code comparison was to agree on the use of a standardized set of chemical species and reactions to be accounted for. For the benchmark models we only included the four most abundant elements H, He, O, and C. Additionally only the species given in Table 4 are included in the chemical network calculations:

The chemical reaction rates are taken from the UMIST99 database (Le Teuff et al. 2000) together with some corrections suggested by A. Sternberg. The complete reaction rate

file is available online (<http://www.ph1.uni-koeLn.de/pdr-comparison>). To reduce the overall modeling complexity, PAHs were neglected in the chemical network and were only considered for the photoelectric heating (photoelectric heating efficiency as given by Bakes & Tielens 1994) in models V1–V4. Codes which calculate time-dependent chemistry used a suitably long time-scale in order to reach steady state (e.g. UCL_PDR used 100 Myr).

4.2.2. Benchmark geometry

All model clouds are plane-parallel, semi-infinite clouds of constant total hydrogen density $n = n(\text{H}) + 2n(\text{H}_2)$. Spherical codes approximated this by assuming a very large radius for the cloud.

4.2.3. Physical specifications

As many model parameters as possible were agreed upon at the start of the benchmark calculations, to avoid confusion in comparing model results. To this end we set the most crucial model parameters to the following values: the value for the standard UV field was taken as $\chi = 10$ and 10^5 times the Draine (1978) field. For a semi-infinite plane parallel cloud the CO dissociation rate at the cloud surface for $\chi = 10$ should equal 10^{-9} s^{-1} , using that for optically thin conditions (for which a point is exposed to the full 4π steradians, as opposed to 2π at the cloud surface) the CO dissociation rate is $2 \times 10^{-10} \text{ s}^{-1}$ in a unit Draine field. The cosmic ray H ionization rate is assumed to be $\zeta = 5 \times 10^{-17} \text{ s}^{-1}$ and the visual extinction $A_V = 6.289 \times 10^{-22} N_{\text{H,tot}}$. If the codes do not explicitly calculate the H_2 photo-dissociation rates (by summing over oscillator strengths etc.) we assume that the unattenuated H_2 photo-dissociation rate in a unit Draine field is equal to $5.18 \times 10^{-11} \text{ s}^{-1}$, so that at the surface of a semi-infinite cloud for 10 times the Draine field the H_2 dissociation rate is $2.59 \times 10^{-10} \text{ s}^{-1}$ (numerical values from Sternberg. See Sect. 5.1 for a discussion on H_2 dissociation rates). For the dust attenuation factor in the H_2 dissociation rate we assumed $\exp(-k A_V)$ if not treated explicitly wavelength dependent. The value $k = 3.02$ is representative for the effective opacity in the 912–1120 Å range (for a specific value of $R_V \approx 3$). We use a very simple H_2 formation rate coefficient $R = 3 \times 10^{-18} T^{1/2} = 2.121 \times 10^{-17} \text{ cm}^3 \text{ s}^{-1}$ (Sternberg & Dalgarno 1995) at $T = 50 \text{ K}$, assuming that every atom that hits a grain sticks and reacts to H_2 . A summary of the most important model parameters is given in Table 5.

5. Results

In the following section we give a short overview of the up to date results of the PDR model comparison. The names of the model codes are printed in typewriter font (e.g. COSTAR). We will refer to the two stages of the benchmarking results by pre- and post-benchmark, denoting the model results at the beginning of the comparison and at its end respectively. All pre- and post-benchmark results are posted at <http://www.ph1.uni-koeLn.de/pdr-comparison>. One model from the initial 12 participating model was left out in the post-benchmark plots because the authors could not attend the workshop. In addition, the KOSMA- τ models (Röllig et al. 2006) and the models by Bensch, which participated in the comparison as separate codes, have been merged to a single set (labeled KOSMA- τ) as they are variants on of the same basic model which do not differ for the given benchmarking parameter set, and consequently give identical results. To demonstrate the impact of the benchmark effort on the results of the

Table 5. Overview of the most important model parameter. All abundances are given w.r.t. total H abundance.

Model Parameters		
A_{He}	0.1	Elemental He abundance
A_{O}	3×10^{-4}	Elemental O abundance
A_{C}	1×10^{-4}	Elemental C abundance
ζ_{CR}	$5 \times 10^{-17} \text{ s}^{-1}$	CR ionization rate
A_V	$6.289 \times 10^{-22} N_{\text{H,tot}}$	Visual extinction
τ_{UV}	$3.02A_v$	FUV dust attenuation
v_b	1 km s^{-1}	Doppler width
D_{H_2}	$5 \times 10^{-18} \cdot \frac{\chi}{10} \text{ s}^{-1}$	H_2 dissociation rate
R	$3 \times 10^{-18} T^{1/2} \text{ cm}^3 \text{ s}^{-1}$	H_2 formation rate
$T_{\text{gas,fix}}$	50 K	Gas temperature (for F1–F4)
$T_{\text{dust,fix}}$	20 K	Dust temperature (for F1–F4)
n	$10^3, 10^{5.5} \text{ cm}^{-3}$	Total density
χ	$10, 10^5$	Draine (1978) field (i.e. $\chi = 1.71 G_0$)

participating PDR codes we plot the well known C/C⁺/CO transition for a typical PDR environment before and after the changes identified as necessary during the benchmark in Fig. 7. The photo-dissociation of carbon monoxide is thought to be well understood for almost 20 years (van Dishoeck & Black 1988). Nevertheless we see a significant scatter for the densities of C⁺, C, and CO in the top plot of Fig. 7. The scatter in the pre-benchmark rates is significant. Most deviations could be assigned to either bugs in the pre-benchmark codes, misunderstandings, or to incorrect geometrical factors (e.g. 2π vs. 4π). This emphasizes the importance of this comparative study to establish a uniform understanding about how to calculate even these basic figures. Despite the considerable current interest because of, e.g. SPITZER results, we do not give the post-benchmark predictions for the H_2 mid-IR and near IR lines (or the corresponding Boltzmann diagram). Only a small fraction of the participating codes is able to compute the detailed H_2 population and emission, and the focus of this analysis is the comparison between the benchmark codes.

5.1. Models with constant temperature F1–F4

The benchmark models F1 to F4 were calculated for a fixed gas temperature of 50 K. Thus, neglecting any numerical issues, all differences in the chemical structure of the cloud are due to the different photo-rates, or non-standard chemistry. Some PDR codes used slightly different chemical networks. The code Sternberg uses the standard chemistry with the addition of vibrational excited hydrogen and a smaller H-H₂ formation network. The results by Cloudy were obtained with two different chemical setups: The pre-benchmark chemistry had the chemical network of Tielens & Hollenbach (1985). The post benchmark results use the corrected UMIST database. Cloudy also used a different set of radiative recombination coefficients for the pre-benchmark calculations which were the major source for their different results (Abel et al. 2005). The carbon photoionization and radiative recombination rates are very sensitive to radiative transfer and hence to dust properties. The dust properties in Cloudy are different from what is implicitly assumed in the UMIST fits. Cloudy's post-benchmark results are achieved after switching to the benchmark specifications. After

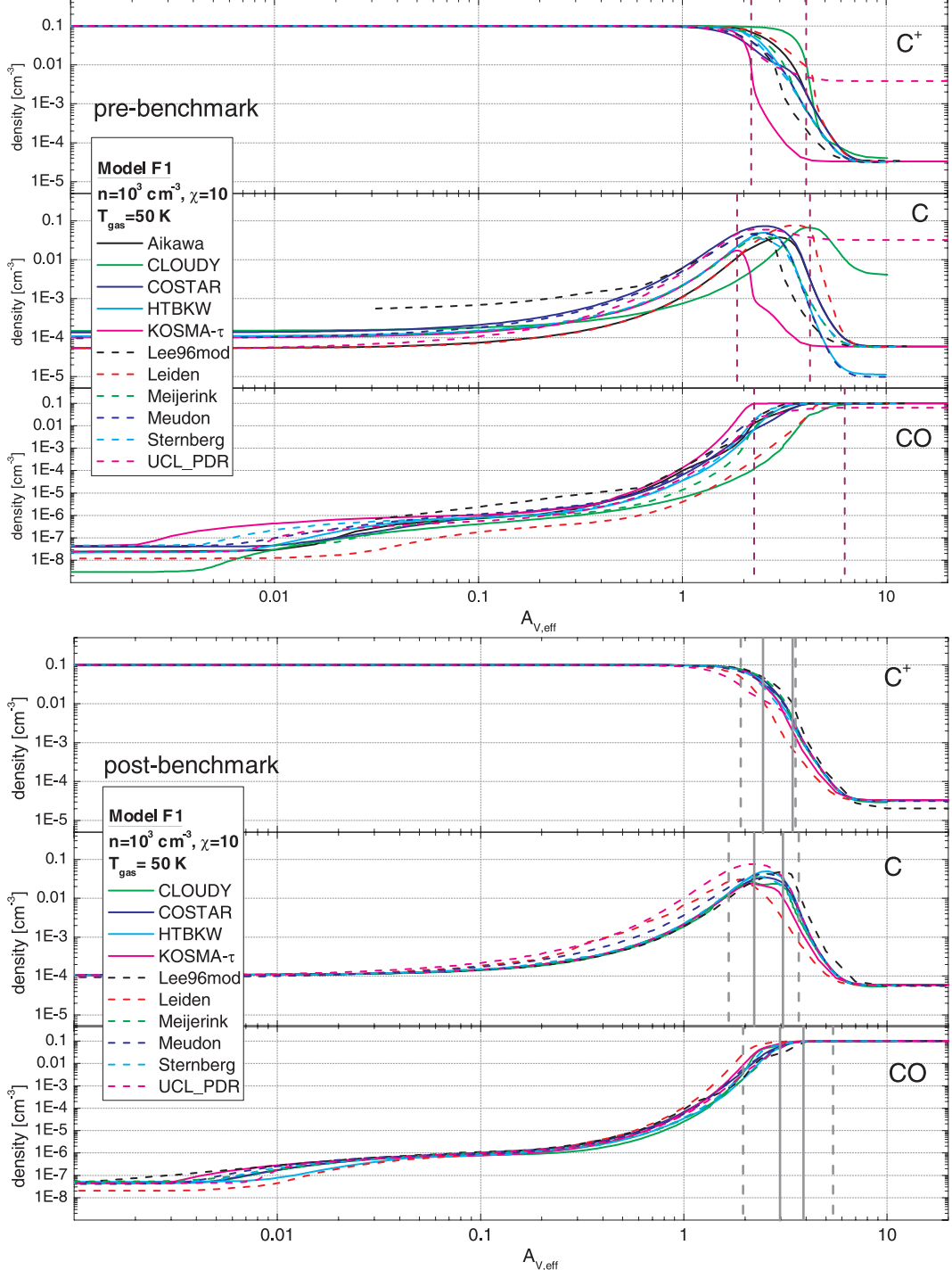


Fig. 7. Model F1 ($n = 10^3 \text{ cm}^{-3}$, $\chi = 10$): comparison between the density profiles of C⁺ (top), C (middle), and CO (bottom) before (top) and after (bottom) the comparison study. The vertical lines indicate the code dependent scatter. For C and CO they indicate the depths at which the maximum density is reached, while for C⁺ they indicate the depths at which the density dropped by a factor of 10. Dashed lines indicate pre-benchmark results, while solid lines are post-benchmark.

the switch they agree very well with the other codes. In Fig. 7 we present the pre- and post-benchmark results for the main carbon bearing species C⁺, C, and CO. To emphasize the pre-to-post changes we added several vertical marker lines to the plots. For C and CO they indicate the depths at which the maximum density is reached, while for C⁺ they indicate the depths at which the density has dropped by a factor of 10. Dashed lines indicate pre-benchmark results, while solid lines are post-benchmark. In the pre-benchmark results the code dependent scatter for these

depths is $\Delta A_{V,\text{eff}} \approx 2\text{--}4$ and drops to $\Delta A_{V,\text{eff}} \approx 1$ in the post-benchmark results.

In the post-benchmark results, the Leiden and UCL_PDR models show a slightly different behavior. The predicted peak depth of C is somewhat smaller than for the other codes. The peak C density of UCL_PDR is roughly 50% higher than in the other codes. A comparison with the photo-ionization of C shown in Fig. 8 confirms that a slightly stronger shielding for the ionization of C is the reason for the different behavior of C and C⁺.

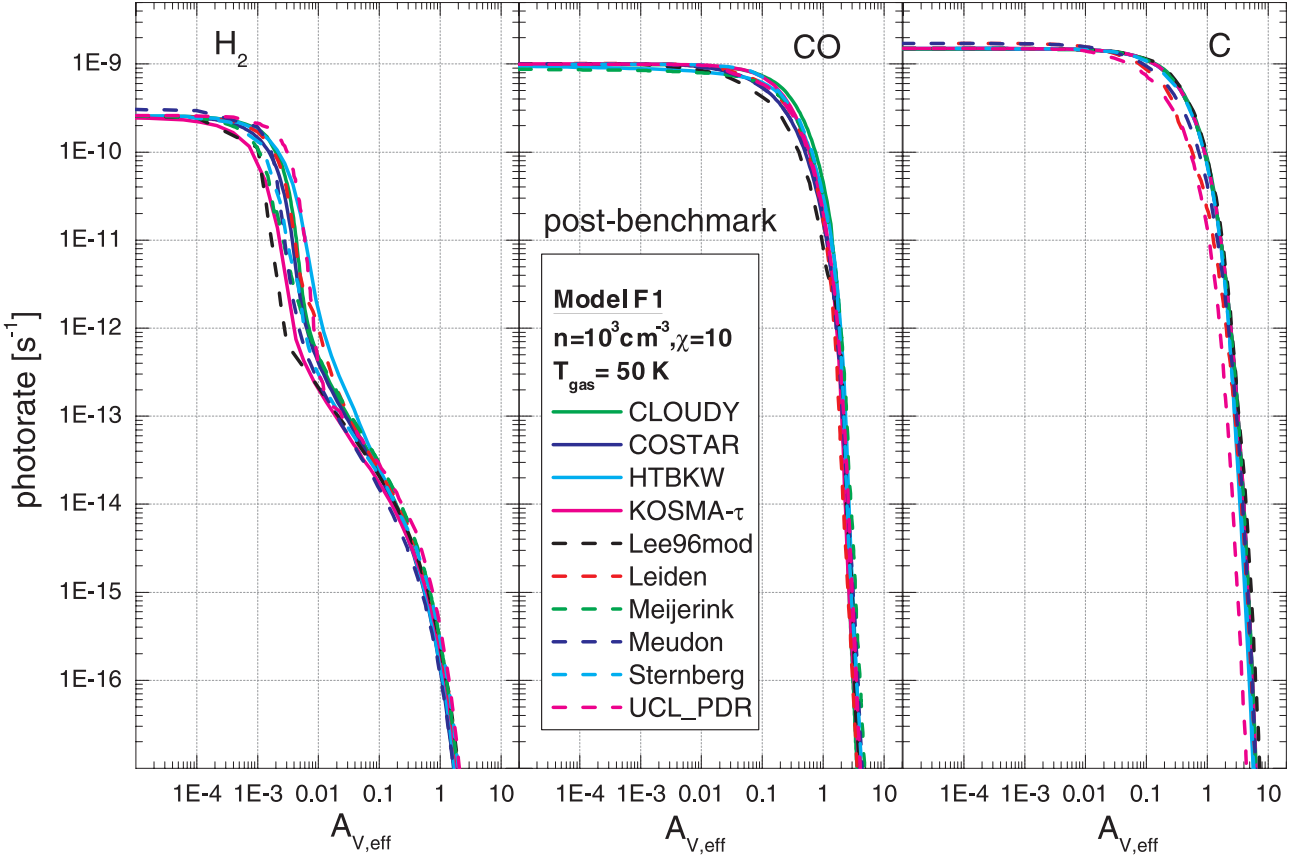


Fig. 8. Model F1 ($n = 10^3 \text{ cm}^{-3}$, $\chi = 10$): the photo-dissociation rates of H_2 (left column), of CO (middle column) and the photo-ionization rate of C (right column) after the comparison study.

The dark cloud densities for C^+ , C, and CO agree very well, except for a somewhat smaller C^+ density in the Lee96mod results.

In Fig. 8 we plot the post-benchmark photo-rates for dissociation of H_2 (left column) and CO (middle column) and for the ionization of C (right column), computed for model F1. Even for this simple model there are some significant differences between the models in the various rates. In the pre-benchmark results, several codes calculated different photo-rates at the edge of the model cloud, i.e. for very low values of $A_{V,\text{eff}}$. Some codes calculated surface photo-dissociation rates between $4\text{--}5 \times 10^{-10} \text{ s}^{-1}$ compared to the expected value of $2.59 \times 10^{-10} \text{ s}^{-1}$. Most of these deviations were due to exposure to the full 4π steradians FUV field instead the correct 2π , but also due to different effects, like the FUV photon back-scattering in the Meudon results. The pre-benchmark rates of KOSMA- τ were shifted toward slightly lower values of A_V because of an incorrect scaling between A_V and $A_{V,\text{eff}}$ and an incorrect calculation of the angular averaged photo-rate (the model features a spherical geometry with isotropic FUV illumination). The post-benchmark results (Fig. 8) show that most deviations have been corrected. The remaining offset for the Meudon result is due to the consideration of backscattered FUV photons, increasing the local mean FUV intensity. The pre- to post-benchmark changes for the photo-rates of CO and C are even more convincing (see online archive). The post-benchmark results are in very good agreement except for some minor difference, e.g. UCL_PDR's photo-ionization rate of C showing some deviation from the main field.

The depth-dependence of the H_2 photo-dissociation rate is reflected in the structure of the H-H₂ transition zone. Figure 9 shows the densities of atomic and molecular hydrogen after

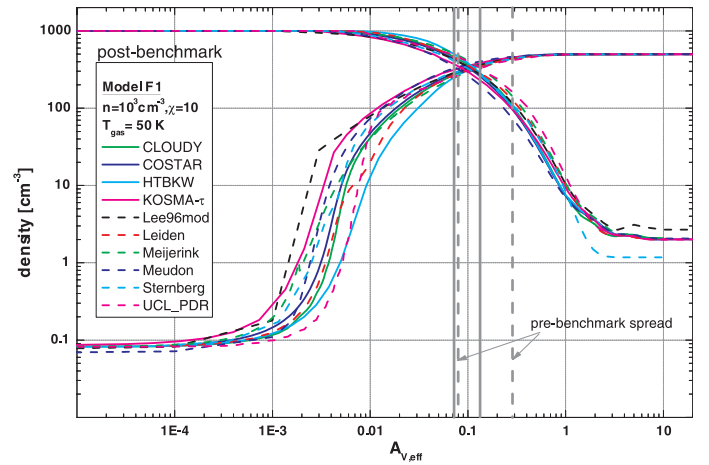


Fig. 9. Model F1 ($n = 10^3 \text{ cm}^{-3}$, $\chi = 10$) The H-H₂ transition zone after the comparison study. Plotted is the number density of atomic and molecular hydrogen as a function of $A_{V,\text{eff}}$. The vertical lines denote the range of the predicted transition depths for pre- and post-benchmark results (dashed and solid lines respectively).

the benchmark. The vertical lines denote the minimum and maximum transition depths before (dashed) and after the benchmark (solid). In the pre-benchmark results the predicted transition depth ranges from $0.08 A_{V,\text{eff}}$ to $0.29 A_{V,\text{eff}}$. In the post-benchmark results this scatter is reduced by more than a factor of 3. Sternberg gives a slightly smaller H density in the dark cloud part. In this code, cosmic ray (CR) destruction and grain surface formation are the only reactions considered in

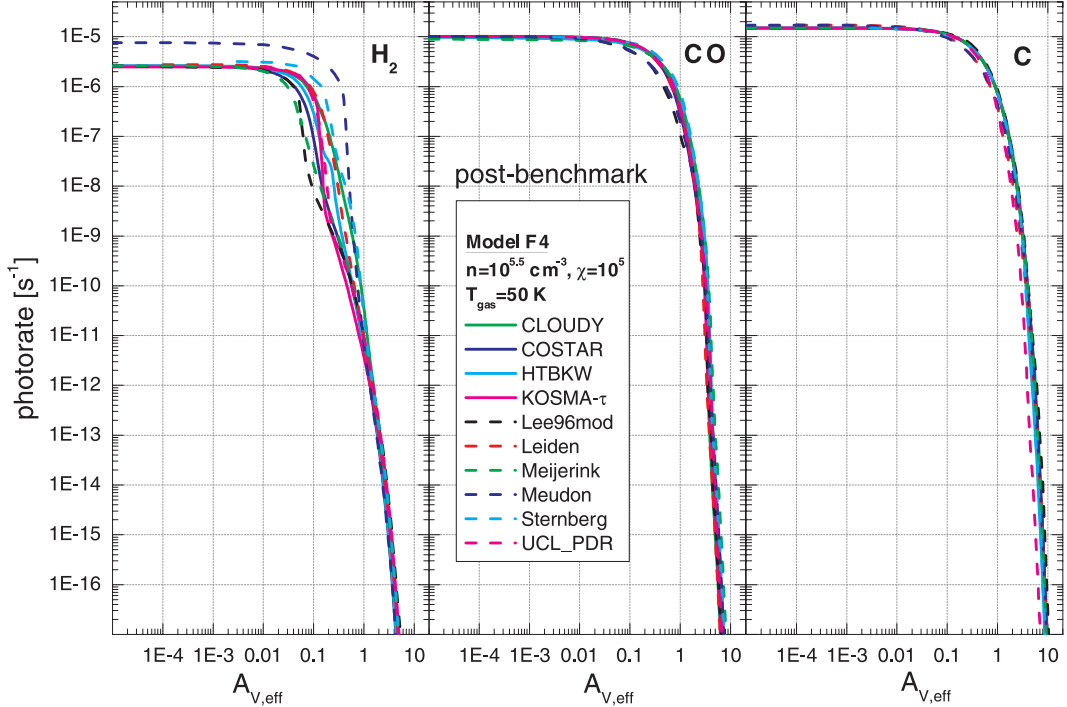
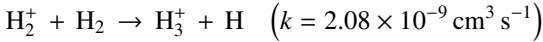


Fig. 10. Model F4 ($n = 10^{5.5} \text{ cm}^{-3}$, $\chi = 10^5$): the post-benchmark photo-dissociation rates of H_2 (left column), of CO (middle column) and the photo-ionization rate of C (right column) (upper plot).

the calculation of the H_2 density. The other codes use additional reactions. The reactions:



contribute to the total H density at high $A_{V,\text{eff}}$. This results in a somewhat higher H density as shown in Fig. 9. The Meudon model gives a slightly smaller H_2 density at the edge of the cloud than the other codes. This is due to the already mentioned higher photo-dissociation rate of molecular hydrogen applied in their calculations.

The model F1 may represent a typical translucent cloud PDR, e.g., the line of sight toward HD 147889 in Ophiuchus (Liseau et al. 1999). The low density and FUV intensity conditions emphasize some effects that would be hard to notice otherwise. This includes purely numerical issues like gridding and interpolation/extrapolation of shielding rates. These differences explain why the various codes still show some post-benchmark scatter. We relate differences in the predicted abundances to the corresponding rates for ionization and dissociation.

Since most of the codes use the same chemical network and apply the same temperature, the major source for remaining deviations should be related to the FUV radiative transfer. To study this we present some results of benchmark model F4 featuring a density $n = 10^{5.5} \text{ cm}^{-3}$ and a FUV intensity $\chi = 10^5$, in order to enhance any RT related differences and discuss them in more detail. Figure 10 shows the post-benchmark photo-rates for the model F4. The higher unshielded H_2 photo-rate in the Meudon results, already visible in model F1 (Fig. 8) is now significantly enhanced due to the increased FUV flux. Meudon, as well as Cloudy, Leiden and Sternberg, treat the hydrogen molecule by calculating the local level population and determining the photo-dissociation rate by integrating each absorption line over the absorption cross section and summing over all absorption

lines. Meudon, Cloudy, and Leiden integrate the line profile over the attenuated spectrum, in order to account for line overlap effects, while Sternberg treats each line separately, neglecting line overlap. Most other codes just assume that the photodissociation scales with the incident radiation field, neglecting any influence from varying H_2 level populations. One reason for the different H_2 photo-rate is a different local mean FUV intensity, caused by backscattered photons. However, this should only account for approximately 10% of the increased dissociation rate. The remaining differences are due to different treatment of H_2 . Either they use different equations, e.g. full ro-vib resolution in Meudon and Sternberg vs. only vib. population in KOSMA- τ , or they apply different molecular data. Sternberg uses data from Sternberg & Dalgarno (1989); Sternberg & Neufeld (1999). Meudon uses collisional data from Flower (1997, 1998); Flower & Roueff (1999) and associated papers, and radiative data from Abgrall et al. (2000), including dissociation efficiencies. These different data sets result in:

1. excited rotational states are much more populated in Meudon's results than in Sternberg;
2. dissociation from an excited rotational level increases much faster with J in Meudon's data.

Both effects lead to dissociation probabilities that differ by 2–3 in case of Model F4. Due to the structure of the code these features could not be turned off in Meudon results.

The photo-rates for CO and C are in very good accord, but we notice a considerable spread in the shielding behavior of the hydrogen photo-rate. This spread is due to the particular implementation of H_2 shielding native to every code, by either using tabulated shielding functions or explicitly calculating the total cross section at each wavelength. The different photo-rates directly cause a different $\text{H}-\text{H}_2$ transition profile, shown in the top panel of Fig. 11. The low molecular hydrogen densities in the Meudon and Cloudy models are again due to the higher H_2

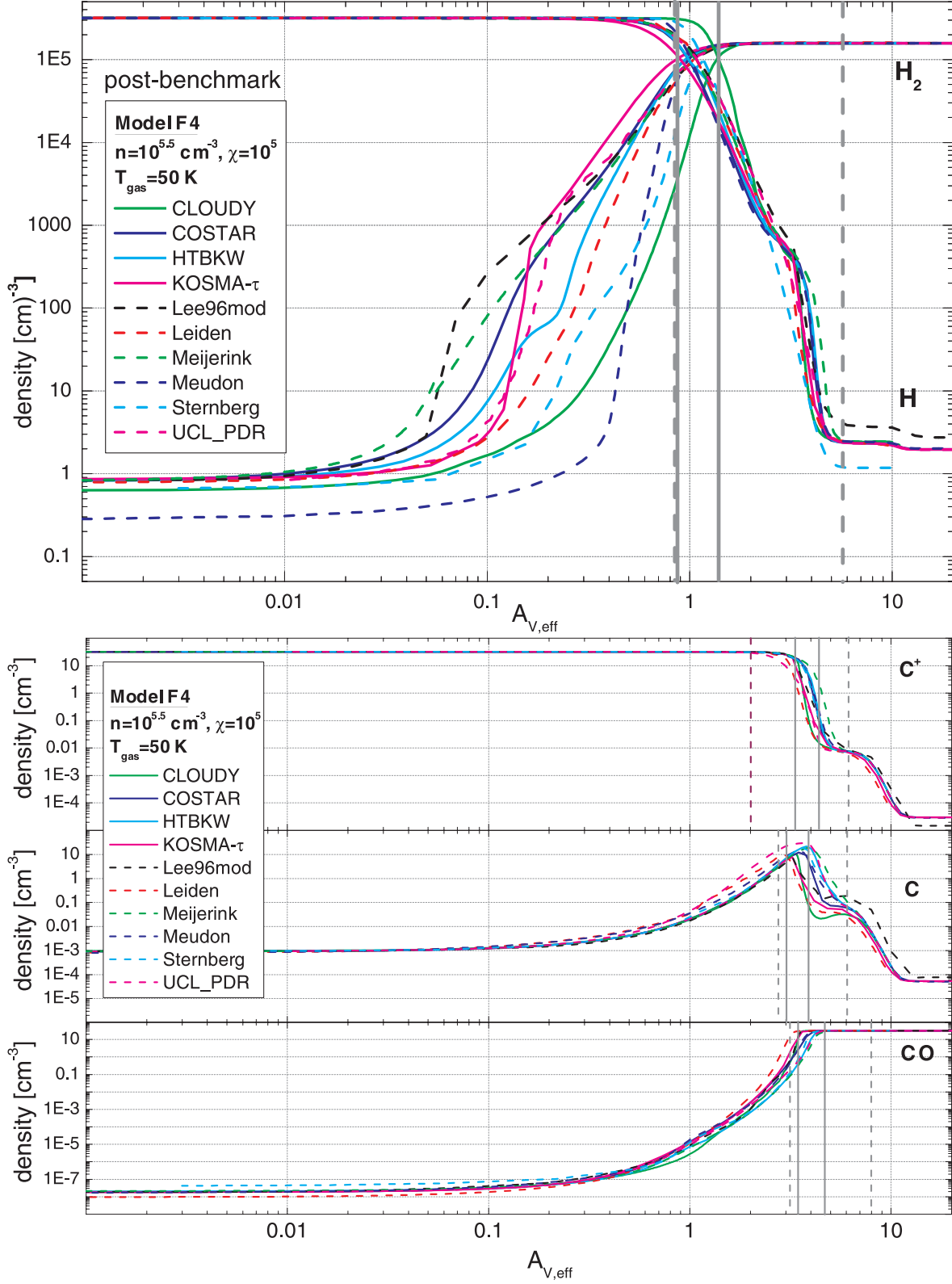


Fig. 11. Model F4 ($n = 10^{5.5} \text{ cm}^{-3}, \chi = 10^5$): The upper panel shows the post-benchmark results for the H and H_2 densities. The lower panel shows the post-benchmark density profiles of C^+ , C , and CO . The vertical gray lines in both panels indicate the pre-to-post changes.

photo-dissociation rate. Sternberg's slightly lower H_2 abundance at the edge of the cloud is consistent with the marginally higher, unshielded H_2 photo-dissociation rate, seen in the top plot in Fig. 10. The Meijerink code shows the earliest drop in the photo-rate, reflected by the corresponding increase in the

H_2 density. The qualitatively different H_2 profile in KOSMA- τ is most likely due to the spherical geometry in the code. Again Sternberg produces slightly smaller H densities for high values of $A_{V,\text{eff}}$. Since Sternberg does not consider additional reactions for the H/H_2 balance its H density profile is the only one

not showing the slight kink at $A_{V,\text{eff}} \approx 2\ldots3$. These deviations do not significantly change the total column density of hydrogen. Hence the impact on any comparison with observational findings is small. Nevertheless one would expect that under the standardized benchmark conditions all codes produce very similar results, yet we note a considerable spread in hydrogen abundances for $A_{V,\text{eff}} > 2$. This again emphasizes how complex and difficult the numerical modeling of PDRs is. The bottom panel in Fig. 11 shows the density profiles of C^+ , C, and CO. Here, the different codes are in good agreement. The largest spread is visible for the C density between $A_{V,\text{eff}} \approx 3\ldots6$. The results for C^+ and CO differ less. Lee96mod's results for C^+ and C show a small offset for $A_{V,\text{eff}} > 6$. They produce slightly higher C abundances and lower C^+ abundances in the dark cloud part. The different codes agree very well in the predicted depth where most carbon is locked up in CO ($A_{V,\text{eff}} \approx 3.5\ldots4.5$). This range improved considerably compared to the pre-benchmark predictions of $A_{V,\text{eff}} \approx 3\ldots8$.

The results from models F1–F4 clearly demonstrate the importance of the PDR code benchmarking effort. The pre-benchmark results show a significant code-dependent scatter. Although many of these deviations have been removed during the benchmark activity, we did not achieve identical results with different codes. Many uncertainties remained even in the isothermal case, raising the need for a deeper follow up study.

5.2. Models with variable temperature V1–V4

In the benchmark models V1–V4 the various codes were required to also solve the energy balance equations in order to derive the temperature structure of the model clouds. This of course introduces an additional source of variation between the codes. The chemical rate equations strongly depend on the local temperature, hence we expect a strong correlation between temperature differences and different chemical profiles of the model codes. As a consequence of a differing density profile of e.g. CO and H_2 we also expect different shielding signatures. We will restrict ourselves to just a few exemplary non-isothermal results because a full analysis of the important non-isothermal models goes beyond the scope of this paper. To demonstrate the influence of a strong FUV irradiation we show results for the benchmark model V2 with $n = 10^3 \text{ cm}^{-3}$, and $\chi = 10^5$ in Figs. 12–16. The detailed treatment of the various heating and cooling processes differs significantly from code to code. The only initial benchmark requirements was to treat the photoelectric (PE) heating according to Bakes & Tielens (1994). On one hand, this turned out to be not strict enough to achieve a sufficient agreement for the gas temperatures, on the other hand it was already too strict to be easily implemented for some codes, like Cloudy, which calculates the PE heating self-consistently from a given dust composition. This demonstrates that there are limits to the degree of standardization. The calculation of the dust temperature was not standardized and varies from code to code. Since Lee96mod only accounts for constant temperatures, their model is not shown in the following plots. We only plot the final, post-benchmark status.

In Fig. 12 we show the gas temperature over $A_{V,\text{eff}}$. The general temperature profile is reproduced by all codes. Even so we note considerable differences between different codes. The derived temperatures at the surface vary between 1600 and 2500 K. For low values of $A_{V,\text{eff}}$ the heating is dominated by PE heating due to the high FUV irradiation, and the main cooling is provided by [OI] and [CII] emission. It is interesting, that the dominant cooling line is the [OI] 63 μm line (cf. Fig. 16, left plot),

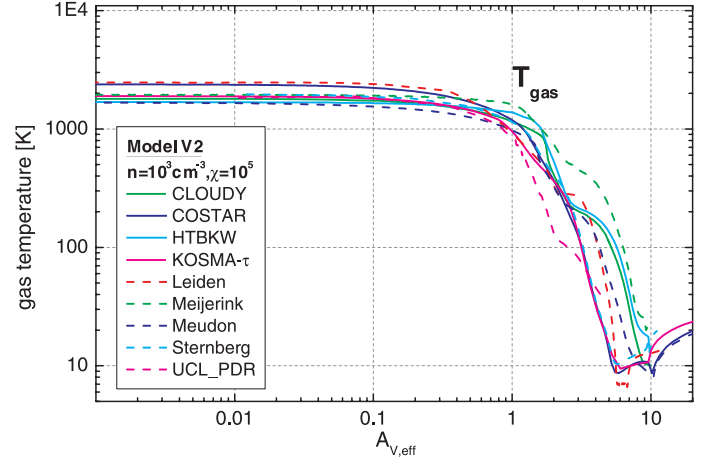


Fig. 12. Model V2 ($n = 10^3 \text{ cm}^{-3}$, $\chi = 10^5$): the plot shows the post-benchmark results for the gas temperature.

although its critical density is two orders of magnitude higher than the local density ($n_{\text{cr}} \approx 5 \times 10^5 \text{ cm}^{-3}$). The highest surface temperature is calculated by Leiden, while Meudon computes the lowest temperature. The bulk of models gives surface temperatures near 1900 K. All models qualitatively reproduce the temperature behavior at higher values of $A_{V,\text{eff}}$ and show a minimum temperature of 10 K between $A_{V,\text{eff}} \approx 5\ldots10$, followed by a subsequent rise in temperature. The only relevant heating contribution at $A_{V,\text{eff}} > 5$ comes from cosmic ray heating, which hardly depends on $A_{V,\text{eff}}$. At $A_{V,\text{eff}} > 4$, the dominant cooling is by [CI] fine structure emission. This is a very efficient cooling process and the temperature reaches its minimum. At $A_{V,\text{eff}} = 10$ the atomic carbon density rapidly drops and CO cooling starts to exceed the fine structure cooling (cf. abundance profiles in Fig. 14). However, cooling by CO line emission is much less efficient, especially at these low total densities, and thus the temperature increases again.

For the bulk of the cloud the heating contribution by H_2 vibrational deexcitation is negligible compared to photoelectric heating. Only Meijerink and Leiden predict comparable contributions from both processes. Unfortunately, the exact treatment of this process was not standardized and depends very much on the detailed implementation (e.g. the two-level approximation from Burton et al. (1990) or Röllig et al. (2006) vs. the solution of the full H_2 problem like in Meudon, Cloudy, and Sternberg). Generally the heating by H_2 vibrational deexcitation depends on the local density and the local mean FUV intensity, and should thus decrease at large values of $A_{V,\text{eff}}$ and dominate the heating for denser clouds.

At $A_{V,\text{eff}} \approx 2\ldots3$ we note a flattening of the temperature curve in many models, followed by a steeper decline somewhat deeper inside the cloud. This is not the case for HTBK, KOSMA- τ , and Sternberg. The reason for this difference is the [OI] 63 μm cooling, showing a steeper decline for the three codes (Fig. 16, left plot). For very large depths, KOSMA- τ produces slightly higher gas temperatures. This is due to the larger dust temperature and the strongest H_2 vibrational deexcitation heating at $A_{V,\text{eff}} > 10$.

In Fig. 13 we plot the photodissociation rate of H_2 (top left), the photoionization rate of C (top right), and the density of H and H_2 over $A_{V,\text{eff}}$ (bottom). Meudon's unshielded dissociation rate is by a factor three larger than the median of $2.6 \times 10^{-6} \text{ s}^{-1}$, and the Sternberg value of $3.8 \times 10^{-6} \text{ s}^{-1}$ is slightly larger for the same reason as discussed in Sect. 5.1. The depth dependent

shielding shows good agreement between all codes, with slight variations. The different model geometry of KOSMA- τ is reflected in the slightly stronger shielding. Leiden has the weakest shielding. Like some of the other codes (see Appendix), they account for the detailed H₂ problem when calculating the photodissociation rate, instead of applying tabulated shielding rates. Yet these differences are small, since we are in a parameter regime ($\chi/n = 100$), where the main shielding is dominated by dust rather than by self shielding (Draine & Bertoldi 1996). The density profiles of H and H₂ are in good agreement. The stronger photodissociation in Meudon is reflected in their smaller H₂ density at the surface. All other H₂ densities correspond well to their dissociation rates except for Cloudy, which has a lower density at the surface without a corresponding photodissociation rate. This is a temperature effect. Cloudy computes relatively low surface temperatures which lead to slightly lower H densities at the surface. The central densities are also in good accord. The different H densities reflect the corresponding temperature profiles from Fig. 12.

The photoionization rate of C is given in the top right plot in Fig. 13. All models are in good agreement at the surface of the cloud. Meudon and UCL_PDR drop slightly earlier than the bulk of the results. This is also reflected in their C density profiles in Fig. 14 (top right) which incline slightly earlier. Deep inside the cloud Sternberg and HTBKW show a steeper decline compared to the other codes. The agreement for the C⁺ profile is also very good. At $A_{V,\text{eff}} = 5$ the densities drop by a factor of 10 and remain constant until they drop at $A_{V,\text{eff}} \approx 10$. This plateau is caused by the increase in C density, compensating the FUV attenuating. Leiden's results show some deviations for $A_{V,\text{eff}} > 10$. Their C density remains higher throughout the center, causing a slightly different carbon and oxygen chemistry at $A_{V,\text{eff}} > 10$. The calculated O and O₂ densities are given in Fig. 14 (bottom, right). The dark cloud densities are in very good agreement among the models, with some deviations in the Leiden values. The O₂ profiles show some variations between $A_{V,\text{eff}} \approx 1$ and 10 but these are minor deviations especially taking the fact that the densities vary over 14 orders of magnitude from the outside to the center of the cloud! The differences in O₂ are also reflected in the CO plot (Fig. 14, bottom left). All codes produce very similar density profiles and dark cloud values. Leiden gives a smaller CO density beyond $A_{V,\text{eff}} = 10$.

In Fig. 15 we plot the total surface brightnesses of the main fine-structure cooling lines for the V2 model: [CII] 158 μm , [OI] 63, and 146 μm , and [CI] 610 and 370 μm . For the spherical PDR models, the surface brightness averaged over the projected area of the clump is shown. The surface brightness of these fine-structure lines is smaller by typically a few 10%, if calculated along a pencil-beam toward the clump center as they are enhanced in the outer cloud layers. Compared with the pre-benchmark results, the spread in T_B has been decreased significantly from almost 3 orders of magnitude to a factor of 3–5 for [CII] and [OI]. To explain the differences in Fig. 15 we plot in Fig. 16 the radial profiles of the local emissivities of [OI] 63 μm and [CI] 310 μm . Leiden gives the highest [OI] brightnesses and also computes higher local [OI] 63 μm emissivities for small values of $A_{V,\text{eff}}$, shown in Fig. 16. COSTAR, with very similar results for the density profile and comparable gas temperatures, gives much smaller emissivities. The reason for these deviations is still unclear. The model dependent spread in surface brightnesses is largest for the [CI] lines. HTBKW computes 10 times higher line intensities for the [CI] 370 μm transition than Sternberg. This can be explained as follows.

Both codes show almost identical column densities and abundance profiles of C⁰, yet the local emissivities are very different between $A_{V,\text{eff}} = 4\dots 9$ (Fig. 16). Sternberg, together with some other codes, compute a local minimum for the cooling at $A_{V,\text{eff}} \approx 6$, while the HTBKW, Cloudy, Meijerink, and Meudon models peak at the same depth. This can be explained as a pure temperature effect, since the codes showing a [CI] peak compute a significantly higher temperature at $A_{V,\text{eff}} = 6$: $T(\text{HTBKW}) = 83 \text{ K}$, $T(\text{Sternberg}) = 10 \text{ K}$. These different temperatures at the C⁰ abundance peak strongly influences the resulting [CI] surface brightnesses. Overall, the model-dependent surface temperatures still vary significantly. This is due to the additional nonlinearity of the radiative transfer problem, which, under certain circumstances, amplifies even small abundance/temperature differences.

5.3. Review of participating codes

It is not our intent to rate the various PDR model codes. Each code was developed with a particular field of application in mind and is capable to fulfill its developers expectations. The restrictions artificially posed by the benchmark standards were additionally limiting the capacity of the participating model codes. Some models encountered for example major numerical difficulties in reaching a stable temperature solution for the benchmark models V4, mainly caused by the requested H₂ formation rate of $R = 3 \times 10^{-18} T^{1/2} \text{ cm}^3 \text{s}^{-1}$. This gives reasonable results for low temperatures, but diverges for very high temperatures, resulting in an unreasonably high H₂ formation heating. Other codes also show similar numerical problems especially for the model V4. This numerical noise vanishes when we apply more physically reasonable conditions. Nevertheless it was very instructive to study the codes under these extreme conditions.

Every participating code has its own strengths. The Meudon code and Cloudy are certainly the most complex codes in the benchmark, accounting for most physical effects by explicit calculations, starting from the detailed micro-physical processes, making the least use of fitting formulae.

Cloudy was originally developed to simulate extreme environments near accreting black holes (Ferland & Rees 1988), although it has been applied to HII regions, planetary nebulae, and the ISM. Ferland et al. (1994) describe an early PDR calculation. Its capabilities have been greatly extended over the past several years (van Hoof et al. 2004; Abel et al. 2005; Shaw et al. 2005). Due to the complexity of the code, it was initially not possible to turn off all implemented physical processes as required for the benchmark, but during this study they were able to adopt all benchmark requirements thus removing all major deviations.

The codes HTBKW, Leiden, Sternberg and KOSMA- τ are based on PDR models that began their development 20 years ago and have been supported and improved since then. One of the main differences between them is the model geometry and illumination. Plane-parallel geometry and uni-directional illumination is assumed in HTBKW, Leiden and Sternberg and spherical geometry with an isotropically impinging FUV field in KOSMA- τ . The chemistry adopted generally in HTBKW is the smallest (46 species) compared with Sternberg (78) and Leiden/KOSMA- τ (variable). Leiden, Sternberg and KOSMA- τ explicitly solve the H₂ problem (full ro-vib level population) and determine the corresponding shielding by integrating all absorption coefficients while HTBKW uses shielding functions and a single-line approximation for H₂. Cloudy is also capable of explicitly calculating a fully (v, J) resolved H₂ model, but this capability was switched off in the final model. Instead

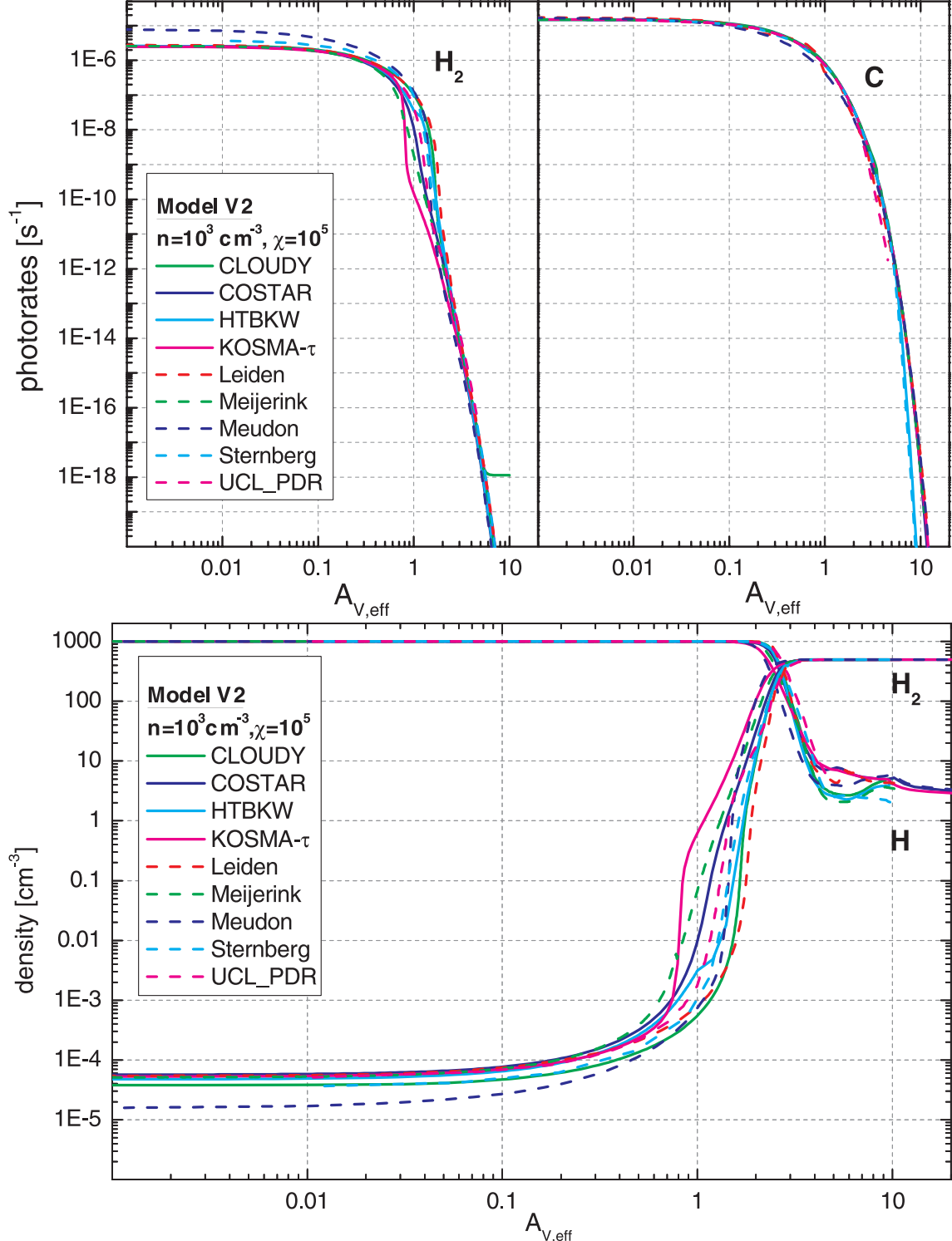


Fig. 13. Model V2 ($n = 10^3 \text{ cm}^{-3}$, $\chi = 10^5$): the post-benchmark photo-dissociation rates of H_2 (left column), and the photo-ionization rate of C (right column) (upper plot). The lower plots shows the H and H_2 densities.

they used a 3-level approximation there. Leiden and Meudon are the only codes in the benchmark explicitly calculating the CO shielding, all other codes use shielding factors. HTBKW is additionally accounting for X ray and PAH heating and computes a large number of observational line intensities, while Leiden focuses on the line emission from the main PDR coolants C^+ , C, O, and CO. However it is possible to couple their PDR output with a more sophisticated radiative transfer code such

as RATRAN (Hogerheijde & van der Tak 2000) to calculate emission lines. This is also done by KOSMA- τ , using ONION (Gierens et al. 1992) or SimLine (Ossenkopf et al. 2001). COSTAR was developed in order to model circumstellar disks, featuring any given disk density profile in radial direction and scale height in vertical direction. It uses uni-directional FUV illumination and can treat a surrounding isotropic interstellar FUV field in addition to the uni-directional stellar field. It computes

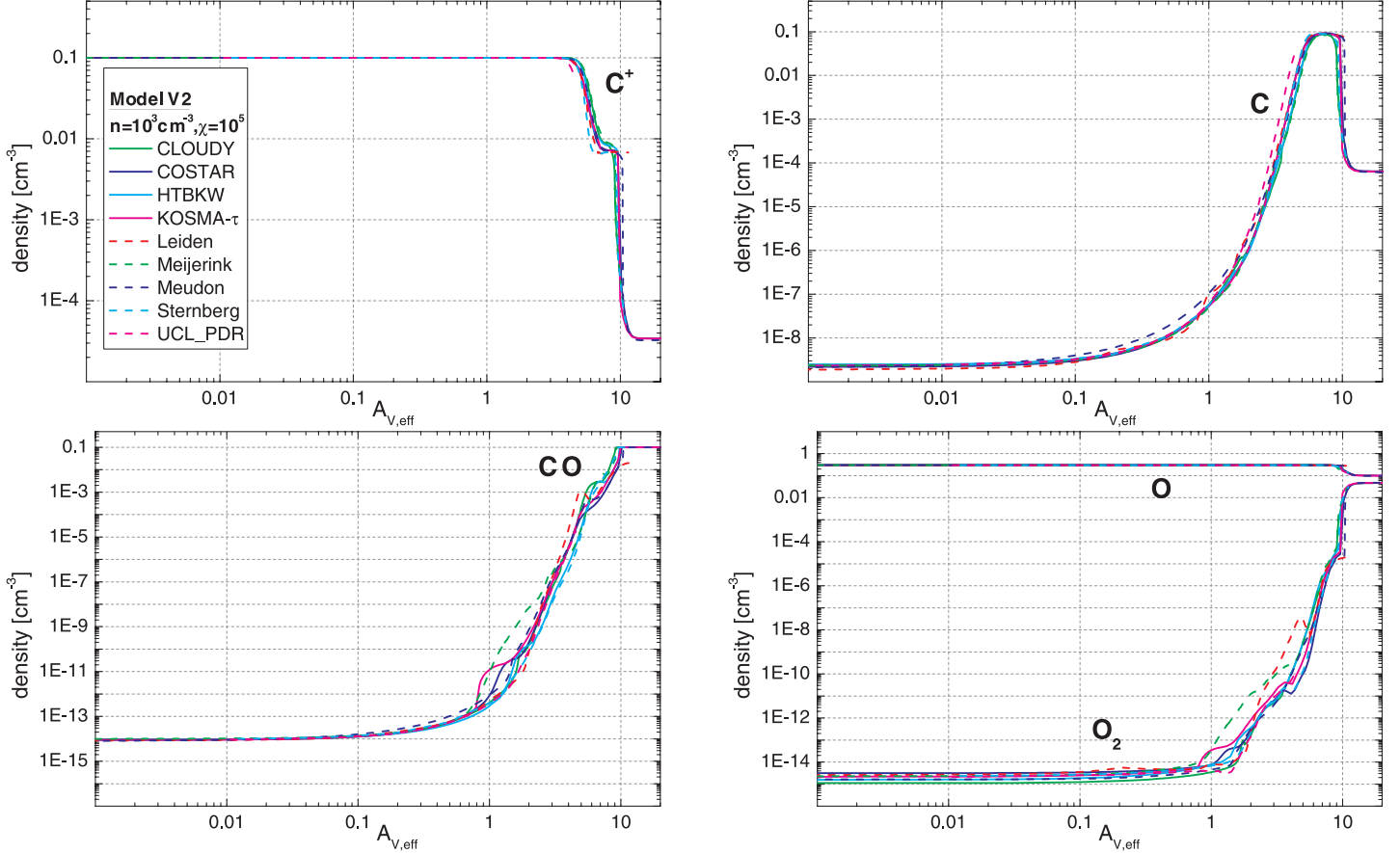


Fig. 14. Model V2 ($n = 10^3 \text{ cm}^{-3}$, $\chi = 10^5$): the post-benchmark results for the densities of C^+ (top left), the densities of C (top right), and the densities of CO (bottom left) and O and O_2 (bottom right).

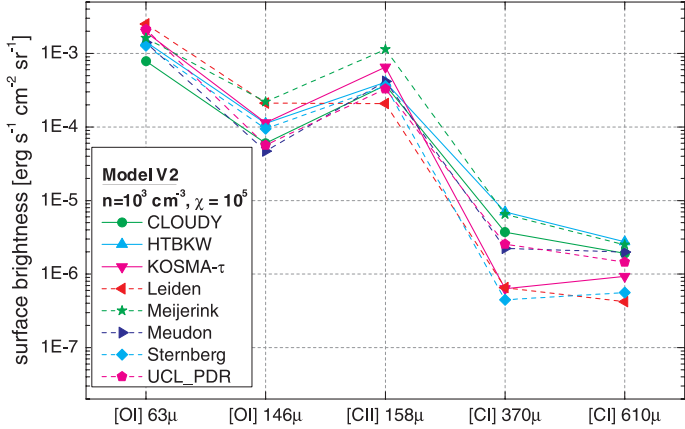


Fig. 15. Model V2 ($n = 10^3 \text{ cm}^{-3}$, $\chi = 10^5$): the plot shows the post-benchmark surface brightnesses of the main fine-structure cooling lines: [CII] 158 μm , [OI] 63, and 146 μm , and [CI] 610 and 370 μm .

a relatively small chemical network (48 species) but also accounts for freeze-out onto grains and desorption effects. It relies on shielding functions for H_2 and CO and does not calculate observational line intensities up to now. Nevertheless most of the COSTAR results are in good agreement with the other code results for most of the benchmark models, demonstrating that it correctly accounts for the important PDR physics and chemistry. UCL_PDR is a plane-parallel model focused on time-dependent chemistries with freeze-out and desorption. Its main features are a fully time-dependent treatment – including time-varying

density and radiation profiles – and its speed, which makes it suitable for parameter search studies where a large number of models need to be run. It can also be coupled with the SMMOL radiative transfer code (Rawlings & Yates 2001) for a detailed treatment of the PDR emission properties. Lee96mod was developed from the time-dependent chemical model by Lee, Herbst, and collaborators. It is strongly geared toward complex chemical calculations and only accounts for constant temperatures, neglecting local cooling and heating. Meijerink is a relatively young model with special emphasis on XDRs (X-ray dominated regions) which quickly evolved in the course of this study and we refer to Meijerink & Spaans (2005) for a detailed review of the current status. In the Appendix we give a tabular overview of all main model characteristics.

6. Concluding remarks

We present the latest result in a community wide comparative study among PDR model codes. PDR models are available for almost 30 years now and are established as a common and trusted tool for the interpretation of observational data. The PDR model experts and code-developers have long recognized that the existing codes may deviate significantly in their results, so that observers must not blindly use the output from one of the codes to interpret line observations. The PDR-benchmarking workshop was a first attempt to solve this problem by separating numerical and conceptional differences in the codes, and removing ordinary bugs so that the PDR codes finally turn into a reliable tool for the interpretation of observational data.

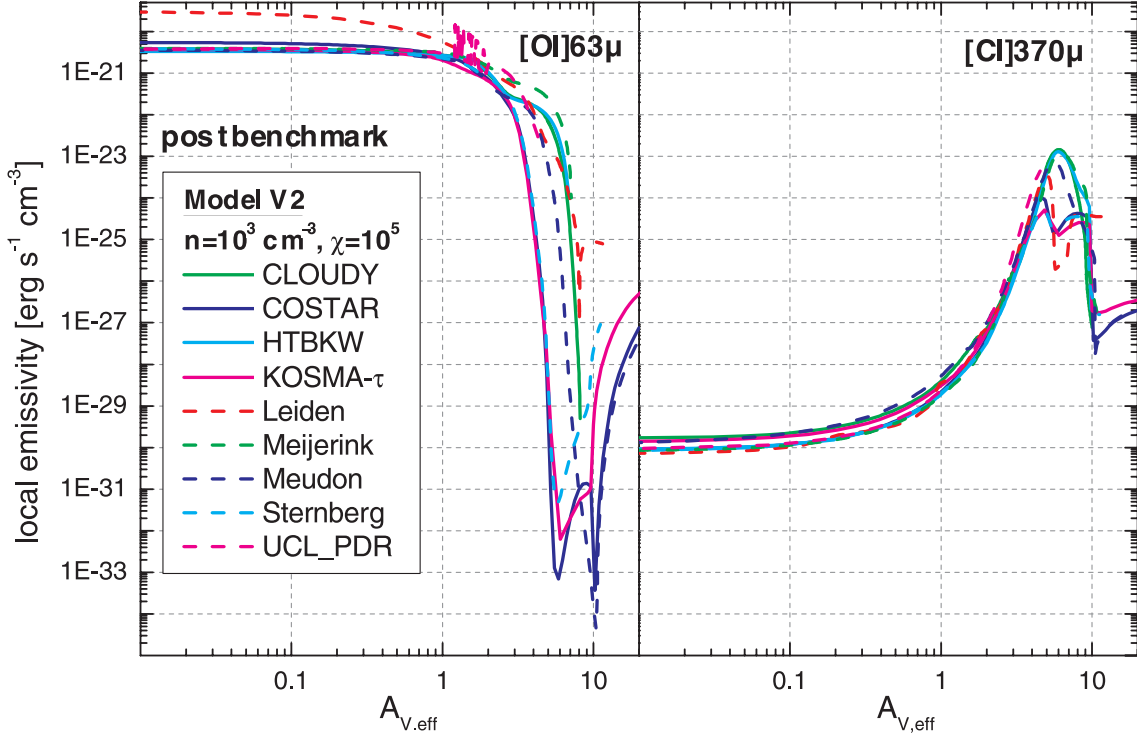


Fig. 16. Model V2 ($n = 10^3 \text{ cm}^{-3}$, $\chi = 10^5$): the post-benchmark local emissivities of [OI] 63μm (left column), and [CI] 310 μm (right column).

Due to their complex nature it is not always straightforward to compare results from different PDR models with each other. Given the large number of input parameters, it is usually possible to derive more than one set of physical parameters by comparing observations with model predictions, especially when one is chiefly interested in mean densities and temperatures. Our goal was to understand the mutual differences in the different model results and to work toward a better understanding of the key processes involved in PDR modeling. The comparison has revealed the importance of an accurate treatment of various processes, which require further studies.

The workshop and the following benchmarking activities were a success regardless of many open issues. The major results of this study are:

- The collected results from all participating models represent an excellent reference for all present PDR codes and for those to be developed in the future. For the first time such a reference is easily available not only in graphical form but also as raw data. (URL: <http://www.ph1.uni-koeln.de/pdr-comparison>)
- We present an overview of the common PDR model codes and summarize their properties and field of application
- As a natural result all participating PDR codes are now better debugged, much better understood, and many differences between the results from different groups are now much clearer resulting in good guidance for further improvements.
- Many critical parameters, model properties and physical processes have been identified or better understood in the course of this study.
- We were able to increase the agreement in model prediction for all benchmark models. Uncertainties still remain, visible e.g. in the deviating temperature profiles of model V2 (Fig. 12) or the large differences for the H₂ photo-rates and density profiles in model V4 (cf. online data archive).

– All PDR models are heavily dependent on the chemistry and micro-physics involved in PDRs. Consequently the results from PDR models are only as reliable as the description of the microphysics (rate coefficients, etc.) they are based on.

One of the lessons from this study is that observers should not take the PDR results too literally to constrain, for example, physical parameters like density and radiation field in the region they observe. The current benchmarking shows that all trends are consistent between codes but that there remain differences in absolute values of observables. Moreover it is not possible to simply infer how detailed differences in density or temperature translate into differences in observables. They are the result of a complex, nonlinear interplay between density, temperature, and radiative transfer. We want to emphasize again, that all participating PDR codes are much “smarter” than required during the benchmark. Many sophisticated model features have been switched off in order to provide comparable results. Our intention was technical not physical. The presented results are not meant to model any real astronomical object and should not be applied as such to any such analysis. The current benchmarking results are not meant as our recommended or best values, but simply as a comparison test. During this study we demonstrated, that an increasing level of standardization results in a significant reduction of the model dependent scatter in PDR model predictions. It is encouraging to note the overall agreement in model results. On the other hand it is important to understand that small changes may make a big difference. We were able to identify a number of these key points, e.g. the influence of excited hydrogen, or the importance of secondary photons induced by cosmic rays.

Future work should focus on the energy balance problem, clearly evident from the sometimes significant scatter in the results for the non-isothermal models V1–V4. The heating by photoelectric emission is closely related to the electron density and to the detailed description of grain charges, grain surface

recombinations and photoelectric yield. The high temperature regime also requires an enlarged set of cooling processes. Another important consideration to be addressed, especially when it comes to comparisons with observations is the model density structure, i.e. clumping or gradients. As a consequence we plan to continue our benchmark effort in the future. This should include a calibration on real observational findings as well.

Acknowledgements. We thank the Lorentz Center, Leiden, for hosting the workshop and for the perfect organization, supplying a very productive environment. The workshop and this work was partly funded by the Deutsche Forschungs Gesellschaft DFG via Grant SFB494 and by a Spinoza grant from the Netherlands Organization for Scientific Research (NWO). We also would like to thank the referee and the editor for making helpful suggestions which helped to improve the manuscript.

References

- Abel, N. P., Ferland, G. J., van Hoof, P. A. M., & G. Shaw 2005, ApJ, in press [arXiv:astro-ph/0506514]
- Abgrall, H., Le Bourlot, J., Pineau Des Forêts, G., et al. 1992, A&A, 253, 525
- Abgrall, H., Roueff, E., Drira, I. 2000, A&AS, 141, 297
- Andriesse, C. D. 1978, A&A, 66, 196
- Arimoto, N., Sofue, Y., & Tsujimoto, T. 1996, PASJ, 48, 275
- Bakes, E. L. O., & Tielens, A. G. G. M. 1994, ApJ, 427, 822
- Bakes, E. L. O., & Tielens, A. G. G. M. 1998, ApJ, 499, 258
- Bell, T. A., Viti, S., Williams, D. A., Crawford, I. A., & Price, R. J. 2005, MNRAS, 357, 961
- Bensch, F., Leuenhagen, U., Stutzki, J., & Shieder, R. 2003, ApJ, 591, 1913
- Bergin, E. A., Melnick, G. J., Stauffer, J. R., et al. 2000, ApJ, 539, L129
- Bertoldi, F., & Draine, B. T. 1996, ApJ, 458, 222
- Black, J. H., & Dalgarno, A. 1977, ApJS, 34, 405
- Black, J. H., & van Dishoeck, E. F. 1987, ApJ, 322, 412
- Boger, G. I., & Sternberg, A. 2005, ApJ, 633, 105
- Boger, G. I., & Sternberg, A. 2006, ApJ, in press (see also [arXiv:astro-ph/0601323])
- Boissé, P. 1990, A&A, 228, 483
- Bolatto, A. D., Jackson, J. M., & Ingalls, J. G. 1999, ApJ, 513, 275
- Bolatto, A. D., Jackson, J. M., Wilson, C. D., & Moriarty-Schieven, G. 2000, ApJ, 532, 909
- Boselli, A., Lequeux, J., & Gavazzi, G. 2002a, A&A, 384, 33
- Boselli, A., Gavazzi, G., Lequeux, J., Pierini, D. 2002b, A&A, 385, 454
- Bresolin, F., Garnett, D. R., & Kennicutt, R. C. 2004, ApJ, 615, 228
- Burke, J. R., Hollenbach, D. J. 1983, ApJ, 265, 223
- Burton, M. G., Hollenbach, D. J., & Tielens, A. G. G. M. 1990, ApJ, 365, 620
- Cazaux, S., & Tielens, A. G. G. M. 2004, ApJ, 604, 222
- de Boisanger, C. B., Chieze, J.-P., & Meltz, B. 1992, ApJ, 401, 182
- de Jong, T., Boland, W., & Dalgarno, A. 1980, A&A, 91, 68
- d'Hendecourt, L., & Léger, A. 1987, A&A, 180, L9
- Dominik, C., Ceccarelli, C., Hollenbach, D., & Kaufman, M. 2005, ApJ, in press
- Draine, B. T. 1978, ApJS, 36, 595
- Draine, B. T. 2003, ARA&A, 41, 241
- Draine, B. T., & Bertoldi, F. 1996, ApJ, 468, 269
- Duley et al. 1992, MNRAS, 255, 463
- Elmegreen, B. G., & Falgarone, E. 1996, ApJ, 471, 816
- Escalante, V., Sternberg, A., & Dalgarno, A. 1991, ApJ, 375, 630
- Ferland, G. J., & Rees, M. J. 1988, ApJ, 332, 141
- Ferland, G. J., Fabian, A. C., & Johnstone, R. M. 1994, MNRAS, 266, 399
- Ferland, G. J., Korista, K. T., Verner, D. A., et al. 1998, PASP, 110, 761
- Flannery, B. P., Robege, W., & Rybicki, G. B. 1980, ApJ, 236, 598
- Flower, D. R. 1997, MNRAS, 288, 627
- Flower, D. R. 1998, MNRAS, 297, 334
- Flower, D. R., & Roueff, E. 1999, MNRAS, 309, 833
- Fuente, A., Martin-Pintado, J., Cernicharo, J., & Bachiller, R. 1993, A&A, 276, 473
- Fuente, A., Martin-Pintado, J., & Gaume, R. 1995, A&A, 442, L33
- Fuente, A., García-Burillo, S., Gerin, M., et al. 2005, ApJ, 619, L155
- Gierens, K. M., Stutzki, J., & Winnewisser, G. 1992, 259, 271
- Glassgold, A. E., & Langer, W. D. 1975, ApJ, 197, 347
- Goldsmith, P. F., Melnick, G. J., Bergin, E. A., et al. 2000, ApJ, 539, L123
- Gorti, U., & Hollenbach, D. 2002, ApJ, 573, 215
- Gredel, R., Lepp, S., & Dalgarno, A. 1987, ApJ, 323, L137
- Habing, H. J. 1968, Bull. Astron. Inst. Netherlands, 19, 421
- Hegmann, M., & Kegel, W. H. 1996, MNRAS, 283, 167
- Hegmann, M., & Kegel, W. H. 2003, MNRAS, 342, 453
- Heithausen, A., Bensch, F., Stutzki, J., Falgarone, E., & Panis, J. F. 1998, A&A, 331, L65
- Henyey, L. G., & Greenstein, J. L. 1941, ApJ, 93, 70
- Hill, J. K., & Hollenbach, D. J. 1978, ApJ, 225, 390
- Hogerheijde, M. R., & van der Tak, F. F. S. 2000, A&A, 362, 697
- Hollenbach, D., & Salpeter, E. E. 1971, ApJ, 163, 155
- Hollenbach, D., & McKee, C. F. 1979, ApJS, 41, 555
- Hollenbach, D., Werner, M. W., & Salpeter, E. E. 1971, ApJ, 163, 165
- Hollenbach, D. J., Takahashi, T., Tielens, A. G. G. M. 1991, ApJ, 377, 192
- Hollenbach, D. J., Tielens, A. G. G. M. 1997, ARA&A, 35, 179
- Hollenbach, D. J., Tielens, A. G. G. M. 1999, Rev. Mod. Phys., 71, 173
- Howe, J. E., Jaffe, D. T., Genzel, R., & Stacey, G. J. 1991, ApJ, 373, 158
- Hunter, D. A., Kaufman, M., Hollenbach, D. J., et al. 2001, ApJ, 553, 121
- Israel, F. P. 1997, A&A, 328, 471
- Israel, F. P., Baas, F., Rudy, R. J., Skillman, E. D., & Woodward, C. E. 2003, A&A, 397, 87I
- Jansen, D. J., van Dishoeck, E. F., Black, J. H., Spaans, M., & Sosin, C. 1995, A&A, 302, 223
- Jura, M., 1974, ApJ, 191, 375
- Kamp, I., & Bertoldi, F. 2000, A&A, 353, 276
- Kamp, I., & van Zadelhoff, G.-J. 2001, A&A, 373, 641
- Kaufman, M. J., Wolfire, M. G., Hollenbach, D. J., & Luhman, M. L. 1999, ApJ, 527, 795
- Köster, B., Störzer, H., Stutzki, J., & Sternberg, A. 1994, A&A, 284, 545
- Kramer, C., Stutzki, J., Rohrig, R., & Cornelissen, U. 1998, A&A, 329, 249
- Le Bourlot, J., Pineau Des Forêts, G., Roueff, E., & Flower, D. R. 1993, A&A, 267, 233
- Le Bourlot, J. 2006, private communication
- Le Petit, F. 2006, A&A, in press
- Le Petit, F., Roueff, E., & Le Bourlot, J. 2002, A&A, 390, 369
- Le Petit, F., Roeuff, E., & Herbst, E. 2004, A&A, 417, 993
- Le Teuff, Y. H., Millar, T. J., & Markwick, A. J. 2000, A&AS, 146, 157
- Lee, H.-H., Herbst, E., Pineau des Forêts, G., Roueff, E., & Le Bourlot, J. 1996, A&A, 311, 690
- Lepp, S., & Dalgarno A. 1988, ApJ, 335, 769
- Lequeux, J., Le Bourlot, J., Des Forêts, G. P., et al. 1994, A&A, 292, 371
- Li, A., & Draine, B. T. 2002, ApJ, 576, 762
- Lintott, C. J., & Rawlings, J. M. C. 2006, A&A, 448, 425
- Liseau, R., White, G. J., Larsson, B., et al. 1999, A&A, 344, 342
- Madden, S. C., Poglitsch, A., Geis, N., Stacey, G. J., & Townes, C. H. 1997, ApJ, 483, 200
- Madden, S. C. 2000, NewAR, 44, 249
- Markwick-Kemper, A. J. 2005, IAU Symp. 231, ed. A. J. Markwick-Kemper
- Meijerink, R., & Spaans, M. 2005, A&A, 436, 397
- McKee, C. F. 1989, ApJ, 345, 782
- Meixner, M., & Tielens, A. G. G. M. 1993, ApJ, 405, 216
- Millar, T. J., Farquhar, P. R. A., & Willacy, K. 1997, A&AS, 121, 139
- Mochizuki, K., Onaka, T., & Nakagawa, T. 1998, ASP Conf. Ser., 132, 386
- Nejad, L. A. M., Wagenblast, R. 1999, A&A, 350, 204
- Ossenkopf, V., Trojan, C., & Stutzki, J. 2001, A&A, 378, 608
- Pagani, L., Olofsson, A. O. H., Bergmann, P., et al. 2003, A&A, 402, L69
- Pak, S., Jaffe, D. T., van Dishoeck, E. F., Johansson, L. E. B., & Booth, R. S. 1998, ApJ, 498, 735
- Papadopoulos, P. P., Thi, W.-F., Viti, S. 2002, ApJ, 579, 270
- Rawlings, J. M. C., Yates, J. A. 2001, MNRAS, 326, 1423
- Röllig, M., Hegmann, M., Kegel, W. H. 2002, A&A, 392, 1081
- Röllig, M., Ossenkopf, V., Jeyakumar, S., Stutzki, J., Sternberg, A. 2006, A&A, 451, 917
- Robege, W. G., Jones, D., Lepp, S., & Dalgarno, A. 1991, ApJS, 77, 287
- Roberts, H., & Herbst, E., A&A, 395, 233
- Rubio, M., Boulanger, F., Rantakyro, F., & Contursi, A. 2004, A&A, 425, L1
- Savage, C., & Ziurys, L. M. 2004, ApJ, 616, 966
- Shaw, G., Ferland, G. J., Abel, N. P., Stancil, P., & van Hoof P. A. M. 2005, ApJ, 624, 794
- Shalabiea, O. M., & Greenberg, J. M. 1995, A&A, 296, 779
- Simon, R., Jackson, J. M., Clemens, D. P., Bania, T. M., & Heyer, M. H. 2001, ApJ, 551, 747
- Spaans, M. 1996, A&A, 307, 271
- Spaans, M., & van Dishoeck, E. F. 1997, A&A, 323, 953
- Spaans, M., & van Dishoeck, E. F. 2001, ApJ, 548, L217
- Stacey, G. J., Geis, N., Genzel, R., et al. 1991, ApJ, 373, 423
- Steiman-Cameron, T. Y., Haas, M. R., Tielens, A. G. G. M., & Burton, M. G. 1997, ApJ, 478, 261
- Sternberg, A. 1988, ApJ, 332, 400
- Sternberg, A. 1989, ApJ, 347, 863
- Sternberg, A. 1990, ApJ, 361, 121
- Sternberg, A., & Dalgarno, A. 1989, ApJ, 338, 197

- Sternberg, A., & Dalgarno, A. 1995, ApJS, 99, 565
- Sternberg, A., & Neufeld, D. A. 1999, ApJ, 516, 371
- Störzer, H., Stutzki, J., & Sternberg, A. 1996, A&A, 310, 592
- Störzer, H., & Hollenbach, D. 1998, ApJ, 495, 853
- Störzer, H., Zielinsky, M., Stutzki, J., & Sternberg, A. 2000, A&A, 358, 682
- Stutzki, J. 1984, Ph. D. Thesis, Universität zu Köln
- Stutzki, J., Stacey, G. J., Genzel, R., et al. 1988, ApJ, 332, 379
- Taylor, S. D., Hartquist, T. W., & Williams, D. A. 1993, MNRAS, 264, 929
- Terzieva, R., & Herbst, E. 1998, ApJ, 501, 207
- Teyssier, D., Fossé, D., Gerin, M., et al. 2004, A&A, 417, 135
- Thuan, T. X., Sauvage, M., & Madden, S. 1999, ApJ, 516, 783
- Tielens, A. G. G. M., Hollenbach, D. 1985, ApJ, 291, 722
- Trumpler, R. J. 1930, PASP, 42, 267
- van Dishoeck, E. F. 1988, in Rate Coefficients in Astrochemistry, ed. T. J. Millar, & D. A. Williams (Dordrecht: Kluwer Academic Publishers), 49
- van Dishoeck, E. F., Black, & John, H. 1988, ApJ, 334, 771
- van Hoof, P. A. M., Weingartner, J. C., Martin, P. G., Volk, K., & Ferland, G. J. 2004, MNRAS, 350, 1330
- van Zadelhoff, G.-J., Dullemond, C. P., van der Tak, F. F. S., et al. 2002, A&A, 395, 373
- Verstrate, L., Léger, A., d'Hendecourt, L., Dutuit, O., & Defourneau, D. 1990, A&A, 237, 436
- Viti, S., Roueff, E., Hartquist, T. W., Pineau des Forets, G., & Williams, D. A. 2001, A&A, 370, 557
- Weingartner, J. C., & Draine, B. T. 2001, ApJ, 563, 842
- Wagenblast, R., & Hartquist, T. W. 1988, MNRAS, 230, 363
- Wakelam, V. 2004, A&A, 413, 609
- Wakelam, V., Selsis, F., Herbst, E., & Caselli, P. 2005a, A&A, submitted
- Wakelam, V., Herbst, E., & Selsis, F. 2005b, IAU Symp. 231, ed. A. J. Markwick-Kemper
- Walmsley, C. M., Pineau des Forets, G., Flower, D. R. 1999, A&A, 342, 542
- Warin, S., Benayoun, J. J., & Viala, Y. P. 1996, A&A, 308, 535
- Wilson, C. D. 1995, ApJ, 448, L97
- Wilson, C. D., Olofsson, A. O. H., Pagani, L., et al. 2005, A&A, 433, L5
- Wolfire, M. G., Hollenbach, D., McKee, C. F., Tielens, A. G. G. M., & Bakes, E. L. O. 1995, ApJ, 443, 152
- Wolfire, M. G., McKee, C. F., Hollenbach, D., & Tielens, A. G. G. M. 2003, ApJ, 587, 278
- Zaritsky, D., Kennicutt, R. C., Jr., & Huchra, J. P. 1994, ApJ, 420, 87
- Zielinsky, M., Stutzki J., & Störzer, H. 2000, A&A, 358

Online Material

Appendix A: Characteristics of participating PDR codes

In Table A.1 we summarize the most important characteristics of the participating PDR codes. This table summarizes the full capabilities of the PDR codes and is not limited to the benchmark standards. It has been extracted from detailed characteristics sheets, available online for all codes: <http://www.ph1.uni-koeln.de/pdr-comparison>.

Table A.1. Full capabilities of the PDR model codes participating in the Leiden comparison study.

	Cloudy	COSTAR	Meudon	UCL_PDR	HTBKW	KOSMA-τ	Aikawa	Leiden	Lee96mod	Sternberg	Meijerink
GEOMETRY											
spherical	X					X					
plane-parallel, finite	X		X		X			X			
plane-parallel, semi-infinite	X		X	X	X		X	X	X	X	X
circumstellar disc	X	X						X			
ensemble of clouds						X					
DENSITY											
homogeneous	X	X	X	X	X	X	X	X	X	X	X
density-law	X	X	X	X		X	X	X	X	X	X
time dependent	X			X							
velocity field	X					X					
$v = const$	X					X					
$v = v(r, \dots)$	X										
RADIATION											
isotropic radiation field			X			X					
uni-directional radiation field	X	X	X	X	X		X	X	X	X	X
combination of isotropic+illuminating star			X								
Habing field	X			X	X			X			X
Draine field	X	X	X		X	X		X		X	
optional star	X		X					X			
detailed SED	X		X								
other	X						X	X	X		
external radiation source	X	X	X	X	X	X	X	X	X	X	X
internal radiation source											
CHEMISTRY											
stationary chemistry	X	X	X		X	X		X		X	X
time-dependent chemistry	X			X			X		X		
advection flow	X										
UMIST95	X		X	X		X		X		X	X
UMIST99	X			X	X	X				X	X
NSM			X				X		X		
other database	X	X	X			X		X		X	
fixed number of species	X	X		X	X		X		X	X	
variable number of species			X			X		X			X
number of species	96	48		128	46		577		419	78	
PAH's included	X		X		X	X		X			X
freeze-out on grains included	X	X	X	X				X			
H ₂ formation on grains	X	X	X	X	X	X	X	X	X	X	X
formation of other molecules on grains			X	X			X				
desorption mechanisms included		X	X				X				
<i>thermal desorption</i>	X	X					X				
<i>photoevaporation</i>			X								
<i>CR spot heating</i>	X		X				X				

Table A.1. continued.

Table A.1. continued.

	Cloudy	COSTAR	Meudon	UCL_PDR	HTBKW	KOSMA-τ	Aikawa	Leiden	Lee96mod	Sternberg	Meijerink
solved self-consistently	x	x	x	x	x	x		x		x	x
simple exponential attenuation	x	x	x	x	x	x	x	x	x	x	x
bi-exponential attenuation		x								x	
full RT in lines			x					x			
DUST											
treatment of rad. transfer	x		x		x	x		x		x	x
grain size distribution	x		x	x		x					
extinction/scattering law	x	x	x	x	x	x	x	x	x	x	
albedo	x		x	x				x			x
scattering law	x		x					x			
H₂ SHIELDING											
shielding factors	x	x			x		x		x	x	x
single line	x			x							x
detailed solution	x		x			x		x			
CO SHIELDING											
shielding factors	x	x		x	x	x	x	x	x	x	x
single line	x							x			x
detailed solution			x					x			
isotope selective photodissociation			x		x		x				x
UV PROFILE FUNCTION											
Gaussian				x	x						
Voigt	x		x					x		x	x
Box											
other											
RADIATIVE TRANSFER IN COOLING LINES											
escape probability	x	x	x	x	x	x	x	x		x	x
other											
IR pumping	x	x			x			x			x
OBSERVATIONAL LINES											
self-consistent treatment with cooling	x			x							
escape probability	x			x		x	x	x		x	x
other			x			x					
H ₂	x		x					x		x	
HD			x					x		x	
¹² CO	x		x	x	x	x	x				x
¹³ CO	x		x			x					x
C ¹⁸ O			x			x					
¹³ C ¹⁸ O			x			x					
[OI]	x		x	x	x	x	x	x		x	x
[CII]	x		x	x	x	x	x	x		x	x
[CI]	x		x	x	x	x	x	x		x	x
Si ⁺	x		x		x						x
CS			x								x
H ₂ O					x						
H ₂ ¹⁸ O											
HCO ⁺			x		x	x					x
OH						x					
[SiI]	x				x	x					
[SI],[SII]	x				x	x					x

Table A.1. continued.

	Cloudy	COSTAR	Mेन्डोन	UCL_PDR	HTBKW	KOSMA-τ	Aikawa	Leiden	Lee9mod	Stenberg	Meijerink
[FeI], [FeII]	x				x	x		x			x
COMPUTED LINE PROPERTIES											
resolved line profile		x			x	x		x			
continuum rad./rad transfer in UV	x		x								
line center intensities	x	x				x		x			
line integrated intensities	x		x	x	x	x		x			x
optical depths	x		x	x	x	x		x			x
Gaussian line profile	x	x			x	x		x			x
box line profile											
turbulence included	x	x				x					x
COLLISIONS											
H-H	x				x					x	
H ₂ -H	x		x	x	x			x		x	x
H ₂ - H+	x	x								x	
H ₂ - e	x		x		x					x	
H ₂ - H ₂	x		x		x			x		x	x
CO-H	x	x	x	x	x			x			x
CO-H ₂	x	x	x	x	x	x		x			x
CO-e	x	x		x		x					x
CO - He			x	x							x
C-H	x	x	x	x	x	x		x		x	x
C-H ₂	x	x	x	x	x	x		x			x
C-e	x		x	x							x
C - He	x		x	x							
C - H ₂ O											
C ⁺ - H	x	x	x	x	x			x			x
C ⁺ - H ₂	x	x	x	x	x	x		x			x
C ⁺ - e	x	x		x	x	x		x			x
O - H	x	x	x	x	x	x		x		x	x
O - H ₂	x	x	x	x	x	x		x		x	x
O - H+	x		x	x				x			
O - e	x	x	x	x	x						
O - He	x		x	x							
OH - H											
OH - He											
OH - H ₂					x	x					
H ⁻ - H	x										
H ₂ O - e											
H ₂ O - H											x
H ₂ O - H ₂					x						x
H ₂ O - O											
dust - H/H ₂	x				x						
dust-any	x										
Si ⁺ - H	x		x			x					
HD - H			x								
HD - H ₂			x								
PAH-any	x				x						
OUTPUT											
abundance profile over (A_V /depth)	x	x	x	x	x	x	x	x	x	x	x
column density over (A_V /depth)	x	x	x	x		x				x	x
temperature profile over (A_V /depth)	x	x	x	x	x	x	x	x		x	x
emitted intensities	x		x	x	x	x	x	x		x	x

Table A.1. continued.

	Cloudy	COSTAR	Meudon	UCL_PDR	HTBKW	KOSMA-τ	Aikawa	Leiden	Lee96mod	Sternberg	Meijerink
opacities at line center		x			x	x		x		x	x
heating and cooling rates over (A_V/depth)	x		x	x		x		x		x	x
chemical rates over (A_V/depth)			x	x		x		x		x	x
excitation diagram of H ₂	x		x					x		x	

HIFI observations of warm gas in DR21: Shock versus radiative heating[★]

V. Ossenkopf^{1,2}, M. Röllig¹, R. Simon¹, N. Schneider³, Y. Okada¹, J. Stutzki¹, M. Gerin⁴, M. Akyilmaz¹, D. Beintema², A. O. Benz⁵, O. Berne⁶, F. Boulanger⁷, B. Bumble⁸, O. Coeur-Joly^{9,10}, C. Dedes⁵, M. C. Diez-Gonzalez¹¹, K. France¹², A. Fuente¹³, J. D. Gallego¹¹, J. R. Goicoechea¹⁴, R. Güsten¹⁵, A. Harris¹⁶, R. Higgins^{17,1}, B. Jackson², C. Jarchow¹⁸, C. Joblin^{9,10}, T. Klein¹⁵, C. Kramer¹⁹, S. Lord²⁰, P. Martin¹², J. Martin-Pintado¹⁴, B. Mookerjea²¹, D. A. Neufeld²², T. Phillips²³, J. R. Rizzo¹⁴, F. F. S. van der Tak^{2,24}, D. Teyssier²⁵, and H. Yorke⁸

(Affiliations are available in the online edition)

Received 30 March 2010 / Accepted 20 April 2010

ABSTRACT

Context. The molecular gas in the DR21 massive star formation region is known to be affected by the strong UV field from the central star cluster and by a fast outflow creating a bright shock. The relative contribution of both heating mechanisms is the matter of a long debate.

Aims. By better sampling the excitation ladder of various tracers we provide a quantitative distinction between the different heating mechanisms.

Methods. HIFI observations of mid- J transitions of CO and HCO⁺ isotopes allow us to bridge the gap in excitation energies between observations from the ground, characterizing the cooler gas, and existing ISO LWS spectra, constraining the properties of the hot gas. Comparing the detailed line profiles allows to identify the physical structure of the different components.

Results. In spite of the known shock-excitation of H₂ and the clearly visible strong outflow, we find that the emission of all lines up to $\gtrsim 2$ THz can be explained by purely radiative heating of the material. However, the new *Herschel*/HIFI observations reveal two types of excitation conditions. We find hot and dense clumps close to the central cluster, probably dynamically affected by the outflow, and a more widespread distribution of cooler, but nevertheless dense, molecular clumps.

Key words. ISM: structure – ISM: kinematics and dynamics – ISM: molecules – HII regions – submillimeter: ISM

1. Introduction

DR21 is a deeply embedded H_{II} region created by the radiation from at least six OB stars (Roelfsema et al. 1989). It sits within a ridge of dense molecular material that obscures the H_{II}-region at optical wavelengths. The embedded cluster drives a violent bipolar outflow in north-east to south-west direction. It is prominent in the 2 μ m emission of vibrationally excited H₂, tracing hot, shocked gas and in the *Spitzer* 4.5 μ m channel (Garden et al. 1986; Davis et al. 2007). As the cluster is located close to the eastern edge of the molecular ridge, the eastern, blue-shifted outflow expands in a blister-like fountain, while the western, red-shifted outflow is highly collimated (Lane et al. 1990).

Spitzer 8 μ m images reveal spots of bright PAH emission with a size below 10'' (Marston et al. 2004). They represent the surfaces of high-density, UV irradiated clumps, forming photon-dominated (or photo-dissociation) regions (PDRs), transition zones from ionized and atomic gas to dense molecular gas where physics and chemistry are dominated by UV radiation from young stars (Hollenbach & Tielens 1999; Ossenkopf et al. 2007). These hot and dense regions give rise to the emission of PDR tracers, such as HCO⁺, high- J CO, atomic and ionized carbon, and atomic oxygen.

An overview on the numerous existing observations in DR21 is given by Schneider et al. (2006) and Jakob et al. (2007). In

spite of the wealth of data, the heating of the molecular gas is still debated. The bright H₂ emission indicates shock heating in the outflow and the wings of the molecular lines prove its dynamical impact, but excitation models of the observed emission of CO, [C], [C], and [O] by Lane et al. (1990) and Jakob et al. (2007) have shown that the emission of those tracers cannot be explained by shocks, but is consistent with a pure UV heating, i.e., PDR physics.

To quantify the heating of the gas, we analyze spectra taken with the *HIFI* instrument (de Graauw et al. 2010) on board the *Herschel* Space Observatory (Pilbratt et al. 2010) during the performance verification campaign. Observations of high- J HCO⁺ transitions trace hot material, ionized by UV radiation or X-rays (Sternberg & Dalgarno 1995). Hot water lines are produced in shocked gas (Snell et al. 2005), and observations of CO isotopes around $J = 10$ close the gap in the excitation ladder between ground-based observations and existing ISO data, allowing to obtain a full picture of the temperature distribution.

In Sect. 2 we present the observational data. Section 3 compares the measured line profiles to distinguish different components based on their velocity distribution. In Sect. 4 we provide a model for the emission, supporting the PDR character of the source, and discuss the results in Sect. 5.

2. Observations

2.1. HIFI observations

All spectra presented here were obtained in performance verification observations for the HIFI instrument. As their main goal

[★] *Herschel* is an ESA space observatory with science instruments provided by European-led Principal Investigator consortia and with important participation from NASA.

Table 1. Summary of the used HIFI observational data.

Transition	ν_{line} [GHz]	HPBW "	Observing mode ¹	$t_{\text{int,source}}$ [s]	rms [K]
HCO ⁺ 6–5	535.062	40	OTF map	16	0.04
HCO ⁺ 12–11	1069.694	21	FSW spectral scan	150	0.1
¹³ CO 10–9	1101.350	21	LC spectral scan	270	0.08
C ¹⁸ O 10–9	1097.163	21	LC spectral scan	270	0.08
[C]	1900.537	12	DBS raster map	14	1
		20	convolved+binned	112	0.2
		40	convolved+binned	420	0.1

Notes. ⁽¹⁾ DBS = dual-beam-switch, OTF = On-The-Fly, FSW = frequency-switch, LC = load-chop, OFF position = 20h37m10s, 42°37'00".

was to demonstrate the functionality and performance of the different observing modes, the spectra were taken with a large variety of observing modes and strategies. Consequently, every spectrum was taken in a slightly different manner. All observational parameters are summarized in Table 1.

Most observations where single-point observations towards the central position of the DR21 H region at RA = 20h39m01.1s, Dec = 42°19'43.0" (J2000). Fully sampled maps were only obtained in the [C] line. Data were taken with the wideband spectrometer (WBS) at a resolution of 1.1 MHz, corresponding to 0.2 km s⁻¹ (at 1900 GHz) – 0.7 km s⁻¹ (at 500 GHz). The [C] data were rebinned to a velocity resolution of 0.45 km s⁻¹ to improve the signal to noise.

2.2. Complementary data

ISO long wavelength spectrometer 43–197 μm grating scans were obtained for the DR21 central position from the ISO Data Archive (TDT 15200786). Integrated line intensities were extracted for [O] at 63 and 145 μm and the CO 14–13 to 17–16 transitions. Mid- J CO lines of the DR21 region were mapped with the KOSMA 3 m submm telescope (Jakob et al. 2007). We use the lines of CO and ¹³CO from J = 3–2 to 7–6, which have been observed at native angular resolutions from 80" to 40". The HCO⁺ 1–0, H¹³CO⁺ 1–0, and HCO⁺ 3–2 observations were taken with the IRAM 30 m telescope (Schneider et al. 2010). Native angular resolutions at the 1–0 and 3–2 transition frequencies are 28" and 9", respectively.

2.3. Beam size effects

For a direct comparison of the different data sets we smoothed the available data to the coarsest common angular resolution of 80", matching that of the CO 3–2 KOSMA beam and the lowest frequency ISO observations. This is impossible for the single-point HIFI observations. Moreover, the *Herschel* beam varies between 40" HPBW for the HCO⁺ line at 535 GHz and 20" for ¹³CO at 1100 GHz. Those data were corrected for the different beam filling by estimating the source size from the HCO⁺ 3–2 line as a PDR tracer (Sternberg & Dalgarno 1995) with quite compact emission (20" to 30" in diameter). Successively convolving from the native angular resolution of 9" to the angular resolution of the *Herschel* data, and further to the final, smoothed spectra at 80", we obtained scaling factors for the HIFI spectra, being 0.5 when going from 40" to 80" and 0.33 when going from 20" to 80". The maps obtained in [C] allow a direct smoothing to a resolution of 40" (see Table 1). Beyond that size, the same scaling factor as above was applied.

3. Line profiles

The molecular ridge including the DR21 H region has an intrinsic LSR velocity of -3 km s⁻¹. The quiescent material is

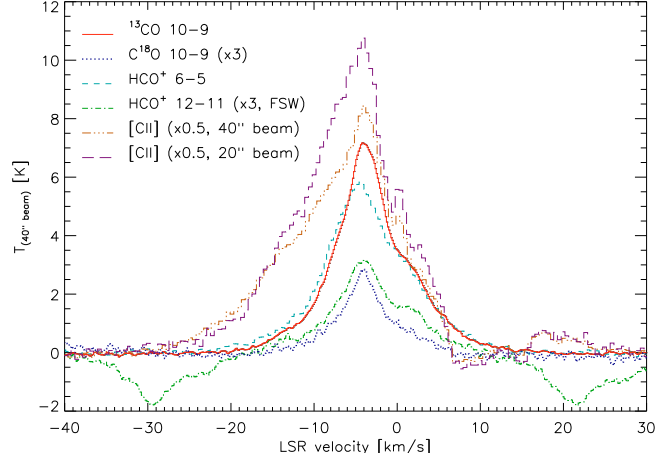


Fig. 1. HIFI spectra of the lines used in the fit of the PDR properties. The [C] data are convolved either to the resolution of the HCO⁺ 6–5 line or to that of the CO 10–9 lines. The negative features in the HCO⁺ 12–11 line are artifacts from the frequency-switch observing mode.

visible in narrow absorption lines of NH₃ (Matsakis et al. 1977) and H₂CO (Bieging et al. 1982). A second velocity component at 8–10 km s⁻¹ is known to be associated with the W75N complex. It appears in emission in CO and [C] (Jakob et al. 2007), as a narrow absorption feature in HCO⁺ 1–0 (Nyman 1983), and has a very broad velocity distribution in the H 21 cm absorption (Thompson et al. 1969; Roberts et al. 1997). The wings of the low- J CO lines trace outflow velocities down to about -20 km s⁻¹ for the eastern, blister outflow and up to ≈10 km s⁻¹ for the western outflow.

Figure 1 shows the profiles of the HIFI spectra of CO isotopes, HCO⁺ and [C]. All lines peak at about -4 km s⁻¹. The CO and HCO⁺ lines have a similar shape, but the [C] line shows an additional broad blue wing extending down to -30 km s⁻¹. This indicates that the warm molecular material is slightly blue-shifted relative to the cold gas and that the [C] emission is not only originating from that warm gas, but also from the ionized wind in the blister outflow.

Figure 2 compares the shapes of the CO and HCO⁺ isotope lines with complementary ground-based measurements towards the same positions. We show only a few selected transitions as, e.g., the data for the CO 7–6 or 4–3 lines provide no additional information. All CO isotopic lines up to 7–6 are roughly symmetric, centered at the ridge velocity of -3 km s⁻¹. The lines of the main isotope are heavily self-absorbed with the absorption dip marking line center. The 10–9 lines, tracing hotter material, are slightly asymmetric and shifted to -4 km s⁻¹. All HCO⁺ lines, except H¹³CO⁺ 1–0, have a profile very similar to the 10–9 lines of the CO isotopes indicating that HCO⁺ is mainly abundant in the heated layer and less in the overall molecular material. The H¹³CO⁺ 1–0 line has a deviating profile centered at -2 km s⁻¹ tracing global infall (Kirby 2009). CO 3–2 and HCO⁺ 1–0 show an additional feature at the W75N complex velocity.

To better understand the exact velocity distribution in the source, we plot some additional HIFI lines towards the same position (see Falgarone et al. 2010; Ossenkopf et al. 2010; van der Tak et al. 2010) in Fig. 3. The 1097 GHz line of hot water matches the rest of the PDR tracers. The foreground at -3 km s⁻¹ is visible in absorption in the ground state transitions of water, but in emission in a nearby OFF position for [C]. At velocities of about +2 km s⁻¹, we find the warm gas facing the redshifted western outflow, apparent as a secondary peak in the ground state

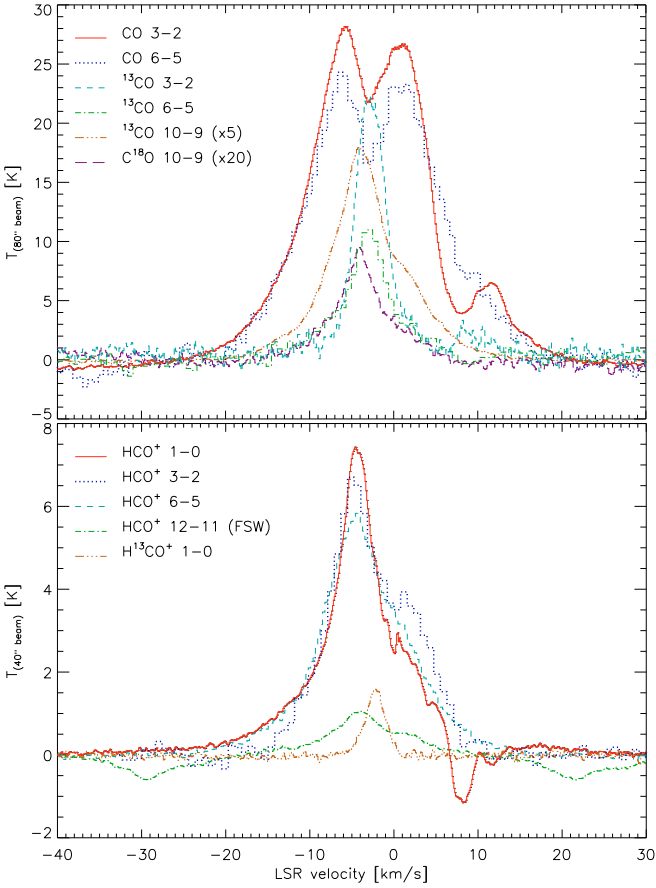


Fig. 2. Selected profiles of CO isotope lines (upper plot) and HCO⁺ isotope lines towards the DR21 central position. All lines are convolved or scaled to the coarsest common resolution (see Sect. 2.3).

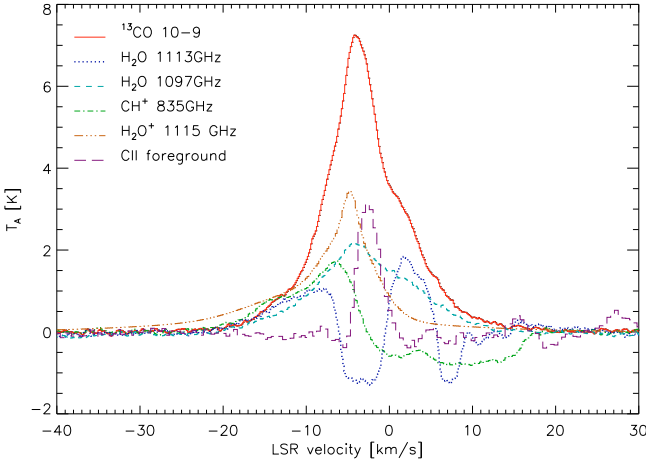


Fig. 3. Auxiliary lines measured by HIFI towards the same position. They can be used to estimate the contribution of the foreground material. The ¹³CO 10–9 profile is also displayed for comparison.

water and CH⁺ lines and as a shoulder in ¹³CO and the hot water line. Finally, we can clearly identify the cold W75N component at ≈ -9 km s⁻¹.

For the warm gas we can distinguish two velocity components – a blue shifted one related to the blister outflow at -4 km s⁻¹ and a second one, at 2 km s⁻¹, related to the western outflow. This is consistent with the clumpy PDR geometry proposed by Lane et al. (1990). In terms of line modelling, it is, however, impossible to separate the two outflow directions as their emission is overlapping to a large degree. We simply add

their intensities. The [C_]] emission requires a special treatment because of the additional emission from the ionized outflow. To take this into account, we have obtained an integrated [C_]] intensity by scaling the ¹³CO 10–9 line profile to match the peak and the red wing of the [C_]] profile and ignoring the remaining blue-wing emission.

4. Modelling

We use the KOSMA- τ PDR code (Röllig et al. 2006) to model the emission of PDR ensembles, representing a distribution of spherical clumps with $dN/dM \propto M^{-1.8}$ (Cubick et al. 2008). For DR21 two ensembles with different properties had to be superimposed, a hot component, close to the inner H₂ region with strong FUV illumination, but only a small fraction of the total mass, and a cooler component that fills a larger solid angle and provides the bulk of the material. Each clumpy PDR ensemble has five free parameters: the average ensemble density, n_{ens} , the ensemble mass, M_{ens} , the UV field strength, χ given in units of the Draine field, and the minimum and maximum mass of the clump ensemble, [M_{\min}, M_{\max}]. In contrast to most other PDR models, we fit absolute line intensities, using the available ground-based observations, complementary ISO data, and the HIFI lines of the CO isotopes, HCO⁺, atomic and ionized carbon, and atomic oxygen. The chemical network that has been applied in these calculations includes ¹³C but not ¹⁸O. The C¹⁸O lines were scaled from the ¹³CO intensities with a conversion of 1:8. Simulated annealing was used to find the optimum parameter combination.

The significance of the model is limited by the fact that the clump superposition ignores mutual line shading between different clumps, i.e., optical depth effects are only considered within individual clumps. This is usually justified by the virialised velocity dispersion between different clumps, but for optically very thick and broad lines some correction is needed. To estimate the effect we have computed the optical depth for the bulk of the individual clumps. This is of the order of unity or below for the majority of the observed transitions, reaches values up to ten for ¹³CO and HCO⁺ transitions up to $J = 4$, but exceeds ten for the CO main isotope lines up to $J = 6$ and the [O_] 63 μ m line. For the CO lines showing clear self-absorption dips, we performed a Gaussian fit to the line wings and used the integrated intensity of that Gaussian to compute the total emission including the blocked radiation from the inner clumps close to the H₂-region. As we have no spectral information for the [O_] line, we have no estimate for the blocked radiation in this case, so that we excluded that data point from the fit.

The best fit result is shown in Fig. 4. The corresponding model parameters are:

$$\begin{aligned} \text{Ensemble 1: } & \chi = 1.0 \times 10^5, n_{\text{ens}} = 1.3 \times 10^6 \text{ cm}^{-3}, \\ & M_{\text{ens}} = 150 M_{\odot}, [M_{\min}, M_{\max}] = [10^{-2}, 8 \times 10^1] M_{\odot} \\ \text{Ensemble 2: } & \chi = 3.2 \times 10^2, n_{\text{ens}} = 1.1 \times 10^6 \text{ cm}^{-3}, \\ & M_{\text{ens}} = 830 M_{\odot}, [M_{\min}, M_{\max}] = [10^{-3}, 10^1] M_{\odot}. \end{aligned}$$

The two-ensemble model provides a reasonable fit to all 22 data points. The model slightly overestimates the emission for the optically thick rotational lines of ¹³CO and HCO⁺ which showed no clear self-absorption dip, so that we have insufficient optical depth corrections. The reduced χ^2 value of the fit amounts to 11.1, where a contribution of 9.5 results from the three optically thick low- J data points of ¹³CO and HCO⁺. For the remaining 19 data points we would obtain an excellent reduced χ^2 value of 1.6. The topology of the χ^2 function shows several side minima, but they are worse by at least a factor two. As expected, the

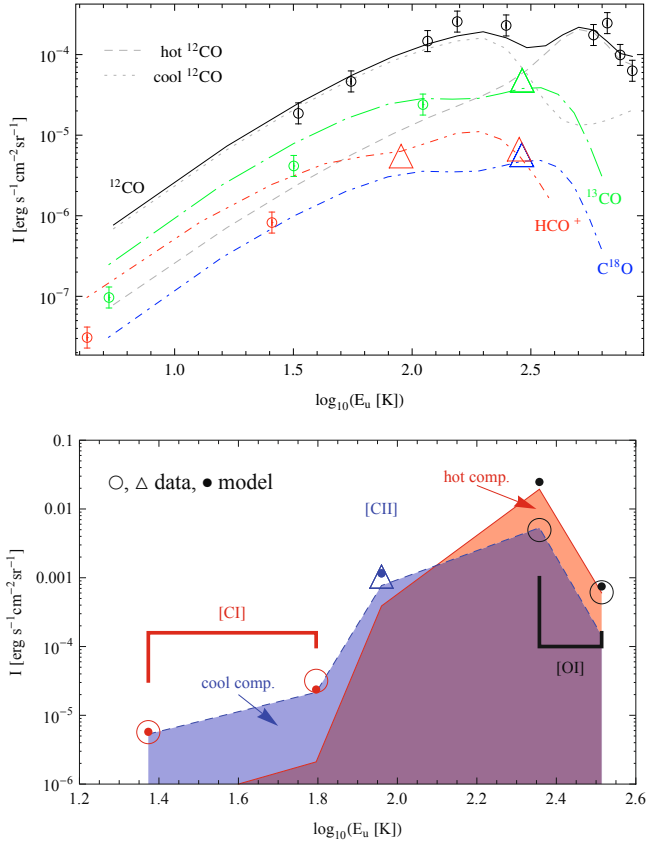


Fig. 4. Two-ensemble PDR model fit to the observed CO, HCO⁺, and fine structure line intensities, shown as function of the upper level energy. HIFI measurements are depicted as open triangles, complementary data points as open circles. The dotted line and the shaded areas indicate the contributions from the two ensembles to the CO and the fine structure lines, respectively.

model predicts a too high [O] intensity, as it ignores that the outer clumps of the cooler ensemble block the contribution from the hot inner component.

5. Discussion

The double-peak structure of the predicted CO intensities across the excitation ladder reflects the two different UV fields leading to different excitation conditions. No single-parameter ensemble can fit all data, but distinct low temperature and high temperature components are needed. The parameters of the model are in agreement with independent estimates. A UV flux of 10^5 Draine fields corresponds to a geometrical distance of 0.06 pc, i.e. 7'', from the central cluster, matching the size of the PAH emission (Marston et al. 2004). Our clump densities match those determined by Jakob et al. (2007) for the extended cool gas, but are slightly higher than their hot-gas density ($4 \times 10^5 \text{ cm}^{-3}$). In contrast, Jones et al. (1994); van der Tak et al. (2010) find still somewhat higher densities for the hot gas, up to 10^7 cm^{-3} . The hot ensemble mass is close to the $170 M_\odot$ derived from early CO 7–6 observations by Jaffe et al. (1989). The total mass of the PDR ensembles falls between the mass limits derived by Jakob et al. (2007) from dust observations and from line radiative transfer fits.

While the existing ground-based observations provide a very good constraint on the properties of the extended cool gas, and the ISO lines show the total amount of hot gas, it is only the set of new HIFI data that puts the hot and cold distributions

well apart from each other in terms of the temperature structure. While Jakob et al. (2007) obtained cooling curves with single peaks, the new data for the 10–9 lines of the CO isotopes and the HCO⁺ transitions force the fit to a bimodal distribution of excitation conditions. When we exclude the *Herschel* data from the model fit, we obtain a parameter set that shows a UV field that is lower by a factor ten for the hot ensemble, i.e., that would imply molecular clumps farther away from the central cluster. For the cold ensemble, the fitted UV field is also somewhat lower, while all other parameters remain similar to those from the full fit. Only with the *Herschel* data, we therefore obtain a parameter set that is consistent with the source geometry.

As the two-ensemble PDR model is able to fit all of the observed lines, we find no evidence for a shock heating of the dense gas. This is in agreement with the analysis of Lane et al. (1990), explicitly excluding a shock origin of the fine-structure lines, but seems to be in contradiction with the analysis of the line profiles in Sect. 3 that shows excited outflow material. We conclude that the material visible in the blue line wing, characterizing the blister outflow, is contained in dense clumps that are accelerated by the outflow, but that are chemically and energetically fully dominated by the UV field and not by the associated shock.

Acknowledgements. HIFI has been designed and built by a consortium of institutes and university departments from across Europe, Canada and the United States under the leadership of SRON Netherlands Institute for Space Research, Groningen, The Netherlands and with major contributions from Germany, France and the US. Consortium members are: Canada: CSA, U.Waterloo; France: CESR, LAB, LERMA, IRAM; Germany: KOSMA, MPIfR, MPS; Ireland: NUI Maynooth; Italy: ASI, IFSI-INAF, Osservatorio Astrofisico di Arcetri- INAF; Netherlands: SRON, TUD; Poland: CAMK, CBK; Spain: Observatorio Astronómico Nacional (IGN), Centro de Astrobiología (CSIC-INTA). Sweden: Chalmers University of Technology – MC2, RSS & GARD; Onsala Space Observatory; Swedish National Space Board, Stockholm University – Stockholm Observatory; Switzerland: ETH Zurich, FHNW; USA: Caltech, JPL, NHSC.

This work was supported by the German *Deutsche Forschungsgemeinschaft*, DFG project number Os 177/1-1. A portion of this research was performed at the Jet Propulsion Laboratory, California Institute of Technology, under contract with the National Aeronautics and Space Administration.

References

- Bieging, J. H., Wilson, T. L., & Downes, D. 1982, A&AS, 49, 607
- Cubick, M., Stutzki, J., Ossenkopf, V., et al. 2008, A&A, 488, 623
- Davis, C. J., Kumar, M. S. N., Sandell, G., et al. 2007, MNRAS, 374, 29
- Falgarone, E., Ossenkopf, V., Gerin, M., et al. 2010, A&A, 518, L118
- Garden, R., Geballe, T. R., Gatley, I., & Nadeau, D. 1986, MNRAS, 220, 203
- de Graauw, Th., et al. 2010, 518, L6
- Jaffe, D. T., Genzel, R., Harris, A. I., et al. 1989, ApJ, 344, 265
- Hollenbach, D. J., & Tielens, A. G. M. 1999, Rev. Mod. Phys., 71, 173
- Jakob, H., Kramer, C., Simon, R., et al. 2007, A&A, 461, 999
- Jones, K. N., Field, D., Gray, M. D., & Walker, R. N. F. 1994, A&A, 288, 581
- Kirby, L. 2009, ApJ, 694, 1056
- Lane, A. P., Haas, M. R., Hollenbach, D. J., & Erickson, E. F. 1990, ApJ, 361, 132
- Marston, A. P., Reach, W. T., Noriega-Crespo, A., et al. 2004, ApJS, 154, 333
- Matsakis, D. N., Brandshaft, D., Chui, M. F., et al. 1977, ApJ, 214, L67
- Ossenkopf, V., Röllig, M., Cubick, M., & Stutzki, J. 2007, in Molecules in Space and Laboratory, ed. J. L. Lemaire, & F. Combes, S. Diana publ., 95
- Ossenkopf, V., Müller, H. S. P., Lis, D., et al. 2010, A&A, 518, L111
- Nyman, L.-Å. 1983, A&A, 120, 307
- Pilbratt, G. L., et al. 2010, 518, L1
- Roberts, D. A., Dickel, H. R., & Goss, W. M. 1997, ApJ, 476, 209
- Roelfsema, P. R., Goss, W. M., & Geballe, T. R. 1989, A&A, 222, 247
- Röllig, M., Ossenkopf, V., Jayakumar, S., et al. 2006, A&A, 451, 917
- Schneider, N., Bontemps, S., Simon, R., et al. 2006, A&A, 458, 855
- Schneider, N., Csengeri, T., & Bontemps, S. 2010, A&A, accepted [arXiv:1003.4198]
- Snell, R. L., Hollenbach, D., Howe, J. E., et al. 2005, ApJ, 620, 758
- Sternberg, A., & Dalgarno, A. 1995, ApJS, 99, 565
- Thompson, A. R., Colvin, R. S., & Hughes, M. P. 1969, ApJ, 158, 939
- van der Tak, F. F. S., Marseille, M. G., Herpin, F., et al. 2010, A&A, 518, L107

-
- ¹ I. Physikalisches Institut der Universität zu Köln, Zülpicher Straße 77, 50937 Köln, Germany
- ² SRON Netherlands Institute for Space Research, PO Box 800, 9700 AV Groningen, The Netherlands
- ³ Laboratoire AIM, CEA/DSM – INSU/CNRS – Université Paris Diderot, IRFU/SAp CEA-Saclay, 91191 Gif-sur-Yvette, France
- ⁴ LERMA & UMR 8112 du CNRS, Observatoire de Paris and École Normale Supérieure, 24 Rue Lhomond, 75231 Paris Cedex 05, France
- ⁵ Institute for Astronomy, ETH Zürich, 8093 Zürich, Switzerland
- ⁶ Leiden Observatory, Universiteit Leiden, PO Box 9513, 2300 RA Leiden, The Netherlands
- ⁷ Institut d’Astrophysique Spatiale, Université Paris-Sud, Bât. 121, 91405 Orsay Cedex, France
- ⁸ Jet Propulsion Laboratory, 4800 Oak Grove Drive, MC 302-231, Pasadena, CA 91109, USA
- ⁹ Université de Toulouse, UPS, CESR, 9 avenue du colonel Roche, 31028 Toulouse Cedex 4, France
- ¹⁰ CNRS, UMR 5187, 31028 Toulouse, France
- ¹¹ Observatorio Astronómico Nacional (IGN), Centro Astronómico de Yebes, Apartado 148, 19080 Guadalajara, Spain
- ¹² Department of Astronomy and Astrophysics, University of Toronto, 60 St. George Street, Toronto, ON M5S 3H8, Canada
- ¹³ Observatorio Astronómico Nacional (OAN), Apdo. 112, 28803 Alcalá de Henares (Madrid), Spain
- ¹⁴ Centro de Astrobiología, CSIC-INTA, 28850 Madrid, Spain
- ¹⁵ Max-Planck-Institut für Radioastronomie, Auf dem Hügel 69, 53121 Bonn, Germany
- ¹⁶ Astronomy Department, University of Maryland, College Park, MD 20742, USA
- ¹⁷ Experimental Physics Dept., National University of Ireland: Maynooth, Co. Kildare, Ireland
- ¹⁸ MPI für Sonnensystemforschung, 37191 Katlenburg-Lindau, Germany
- ¹⁹ Instituto de Radio Astronomía Milimétrica (IRAM), Avenida Divina Pastora 7, Local 20, 18012 Granada, Spain
- ²⁰ IPAC/Caltech, MS 100-22, Pasadena, CA 91125, USA
- ²¹ Tata Institute of Fundamental Research (TIFR), Homi Bhabha Road, Mumbai 400005, India
- ²² Department of Physics and Astronomy, Johns Hopkins University, 3400 North Charles Street, Baltimore, MD 21218, USA
- ²³ California Institute of Technology, 320-47, Pasadena, CA 91125-4700, USA
- ²⁴ Kapteyn Astronomical Institute, University of Groningen, PO Box 800, 9700 AV Groningen, The Netherlands
- ²⁵ European Space Astronomy Centre, Urb. Villafranca del Castillo, PO Box 50727, Madrid 28080, Spain

Refit to numerically problematic UMIST reaction rate coefficients

M. Röllig

I. Physikalisches Institut, Universität zu Köln, Zülpicher Str. 77, 50937 Köln, Germany
e-mail: roellig@ph1.uni-koeln.de

Received 7 April 2010 / Accepted 21 March 2011

ABSTRACT

Aims. Chemical databases such as the UMIST Database for Astrochemistry (UDFA) are indispensable in the numerical modeling of astrochemical networks. Several of the listed reactions in the UDFA have properties that are problematic in numerical computations: some are parametrized in a way that leads to extremely divergent behavior for low kinetic temperatures. Other reactions possess multiple entries that are each valid in a different temperature regime, but have no smooth transition when switching from one to another. Numerically, this introduces many difficulties. We present corrected parametrizations for these sets of reactions in the UDFA06 database.

Methods. From the tabulated parametrization in UDFA, we created artificial data points and used a Levenberg-Marquardt algorithm to find a set of improved fit parameters without divergent behavior for low temperatures. For reactions with multiple entries in the database that each possess a different temperature regime, we present one joint parametrization that is designed to be valid over the whole cumulative temperature range of all individual reactions.

Results. We show that it is possible to parametrize numerically problematic reactions from UDFA in a form that avoids low temperature divergence. Additionally, we demonstrate that it is possible to give a collective parametrization for reaction rate coefficients of reactions with multiple entries in UDFA. We present these new fitted values in tabulated form.

Key words. astrochemistry – astronomical databases: miscellaneous – methods: numerical – ISM: general

1. Introduction

Astrochemistry is a field of increasing scientific attention. Over the last three decades, a lot of effort went into understanding how interstellar chemical species are formed, destroyed, and how interstellar chemistry works in detail. For a review of recent astrochemical progress see for instance Lis et al. (2005); Herbst (2006); Lemaire & Combes (2007); van der Tak (2008). To model interstellar chemistry, reliable laboratory data on the respective reaction rate coefficients are of utmost importance. A few comprehensive databases of astrochemical reactions are available today, such as UDFA¹ (Woodall et al. 2007), the Ohio database OSU² (e.g., Garrod et al. 2008), and NIST Chemistry Webbook³. There are also efforts to pool all available reaction data into a unified database (KIDA: Kinetic Database for Astrochemistry)⁴ (Wakelam 2009). Results from astrochemical laboratory experiments are collected in these databases in an indispensable effort to make these results known to the wider community. They represent the interface between chemistry and astrophysical modeling. In the following we will mainly concentrate on UDFA06, which contains parametrized reaction rate coefficients for more than 4500 reactions, involving 13 different elements and 420 different chemical species – far more than have actually been observed in interstellar space.

UDFA (and most other databases as well) tabulate two-body reactions together with a set of fit parameters α, β, γ in the form $k(T) = \alpha(T/300 \text{ K})^\beta \exp(-\gamma/T)$ and a temperature range at

which the rate coefficients hold. For some reactions, more than one entry with non-overlapping temperature ranges and respective fit parameters is present because of multiple sets of experimental data. In the given fit form, γ is equivalent to the reaction's activation energy, the energy barrier that has to be overcome for the reaction to start. When fitting the measured reaction rates over a particular range of temperatures, a negative γ may sometimes give the best fit. Special care has to be taken when using these rate coefficients outside their given range. Especially at very low temperatures, which are relevant for many astrophysical situations, negative γ may lead to unphysically high reaction rates.

To prevent unreasonable results, Woodall et al. (2007) give a list of reactions whose rate coefficients should be set to zero at 10 K. This may be feasible in chemical models, where the gas temperature is a constant, given parameter. However, in the framework of, e.g., numerical models of photon-dominated regions (PDRs), where the temperature is determined from detailed energy balance and may cover a wide range (~ 5 –5000 K), it is preferable to use reaction rate coefficients, which do not show discontinuities across the applied temperature range (see, e.g., Hollenbach & Tielens 1999; Röllig et al. 2007).

In Fig. 1 we show two example reactions that have a diverging reaction rate coefficient at low temperatures because of $\gamma \ll 0$. Using these extrapolated values in a chemical network calculation may lead to artificial and very unrealistic results!

To illustrate the problem, we compare the results of three PDR model calculations using the KOSMA- τ PDR model (Röllig et al. 2006). We calculated spherical model clouds with mass $M = 1 M_\odot$, surface gas density $n = 10^6 \text{ cm}^{-3}$, and FUV illumination $\chi_{\text{Draine}} = 10^6$. The chemical network consists of

¹ <http://www.udfa.net>

² <http://www.physics.ohio-state.edu/eric/research.html>

³ <http://webbook.nist.gov/chemistry/>

⁴ <http://kida.obs.u-bordeaux1.fr/>

Table 1. All reactions with negative γ coefficients that were refitted.

Educts			Products			α_{old}	β_{old}	γ_{old}	T_{\min}	T_{\max}	α_{new}	β_{new}	γ_{new}	[Error]	
C	+	O ₂	→	CO	+	O	2.48(-12)	1.54	-613	295	8000	9.94(-12)	1.05	-42.48	-0.42, 0.26
N	+	OH	→	NO	+	H	4.06(-11)	0.05	-78	103	2500	5.73(-11)	-0.15	1.34	-0.19, 0.09
NH	+	NH	→	NH ₂	+	N	1.03(-14)	3.07	-1123	300	3000	1.81(-13)	1.80	-70.03	-0.47, 0.36
NH	+	NO ₂	→	N ₂ O	+	OH	1.44(-13)	0	-1140	200	300	1.06(-11)	-5.36	168	-0.07, 0.04
CH ₃	+	NH ₂	→	CH ₂	+	NH ₃	4.76(-17)	5.77	-151	300	2000	4.07(-17)	5.85	-205	-0.03, 0.03
O	+	NH ₂	→	HNO	+	H	4.56(-11)	0	-10	200	3000	4.72(-11)	-0.02	0.38	-0.01, 0.01
O	+	OH	→	O ₂	+	H	1.77(-11)	0	-178	158	5000	3.35(-11)	-0.28	4.30	-0.29, 0.15
O	+	O ₂ H	→	O ₂	+	OH	3.17(-11)	0	-174	200	2500	5.76(-11)	-0.30	7.48	-0.17, 0.09
O	+	HS	→	SO	+	H	8.25(-11)	0.17	-254	298	2000	1.74(-10)	-0.20	5.70	-0.12, 0.06
O	+	NO ₂	→	O ₂	+	NO	6.5(-12)	0	-120	200	2500	9.82(-12)	-0.21	5.16	-0.12, 0.06
NH ₂	+	OH	→	H ₂ O	+	NH	7.78(-13)	1.50	-230	250	3000	1.35(-12)	1.25	-43.45	-0.14, 0.07
OH	+	C ₂ H ₂	→	CO	+	CH ₃	6.51(-18)	4.00	-1006	500	2500	4.75(-17)	3.16	-128	-0.18, 0.10
OH	+	H ₂ CO	→	HCO	+	H ₂ O	2.22(-12)	1.42	-416	200	3000	7.76(-12)	0.82	-30.62	-0.35, 0.21
OH	+	HNO	→	NO	+	H ₂ O	4.44(-12)	1.37	-169	298	4000	6.17(-12)	1.23	-44.29	-0.09, 0.04
OH	+	O ₂ H	→	O ₂	+	H ₂ O	3.66(-11)	-0.13	-244	200	2500	8.58(-11)	-0.56	14.76	-0.23, 0.13
NH ₃	+	CN	→	HCN	+	NH ₂	3.41(-11)	-0.90	-9.90	25	761	3.73(-11)	-1.08	10.00	-0.23, 0.09
C ₂ H	+	C ₂ H ₂	→	H ₂ CCCC	+	H	1.31(-10)	0	-25	143	3400	1.44(-10)	-0.05	0.80	-0.05, 0.02
CN	+	CH ₃ CH ₃	→	C ₂ H ₅	+	HCN	4.8(-12)	2.08	-484	185	1140	2.34(-11)	1.02	-34.95	-0.28, 0.17
CN	+	O ₂	→	NO	+	CO	5.01(-12)	-0.46	-8	13	1565	5.12(-12)	-0.49	-5.16	-0.11, 0.02
CN	+	O ₂	→	OCN	+	O	1.86(-11)	-0.13	-40	13	4526	2.02(-11)	-0.19	-31.91	-0.30, 0.07
CN	+	NO ₂	→	NO	+	OCN	3.93(-11)	0	-199	297	2500	7.02(-11)	-0.27	8.27	-0.11, 0.06
C ₂ H ₃	+	O ₂	→	H ₂ CO	+	HCO	4.62(-12)	0	-171	200	362	8.87(-12)	-0.73	22.67	-0.02, 0.01
C ₂ H ₃	+	O ₂	→	O ₂ H	+	C ₂ H ₂	2.16(-14)	1.61	-193	300	3500	3.15(-14)	1.45	-51.97	-0.09, 0.04
HCO	+	O ₂	→	O ₂ H	+	CO	1.58(-12)	1.24	-353	200	2500	4.64(-12)	0.70	-25.61	-0.29, 0.17
O ₂	+	S	→	SO	+	O	4.74(-13)	1.41	-439	200	3460	1.76(-12)	0.81	-30.75	-0.38, 0.24

Notes. The coefficients on the left are the original UDFA values, the new fits to the coefficients are given on the right side (numbers in parentheses mean: times ten raised to that power). The last column gives the relative error brackets across the given temperature range (given in K) with respect to the original fit.

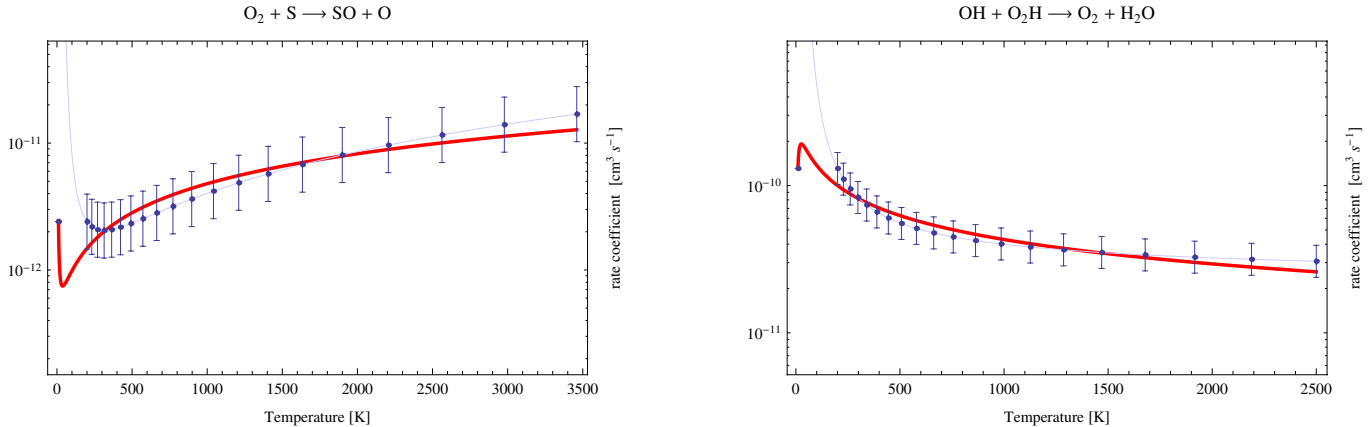


Fig. 1. Two example reactions to demonstrate how extremely reactions might diverge from physically reasonable numbers if $\gamma \ll 0$. The final fit is shown in red, the UDFA rates are shown in light blue. *Left:* the UDFA extrapolation to $k(10 \text{ K}) = 4.5 \times 10^4$ compared to 2.5×10^{-12} in our new fit. *Right:* the UDFA extrapolation to $k(10 \text{ K}) = 2.3$ compared to 1.3×10^{-10} in our new fit.

198 species and 3237 reactions. Except for the surface formation of molecular hydrogen, a pure gas-phase chemistry was calculated. The only difference between the models is the applied set of reaction rate coefficients. In the first model we used the original parametrization of the reaction rate coefficients⁵. In the second model we deactivated these reactions by setting their reaction rates to zero. In a third model we used our new fit to the reaction rate coefficients from Table 1. In Fig. 2 we show the relative sulfur abundance versus A_V for all three cases. For $A_V > 7$

the models start to deviate significantly. The relevant reaction for this comparison is



The original UDFA rates are valid for $T > 200 \text{ K}$ (see Fig. 1, left). The model temperature goes down to 40 K at $A_V = 3.5$. At this temperature, the UDFA reaction rate coefficient is a factor 670 higher than at 200 K, leading to a very efficient destruction of S. At $A_V = 20$ reaction 1 is three orders of magnitudes stronger than the next important destruction reaction. Switching off this reaction allows the atomic sulfur to remain in the gas up to large A_V . Our new rate coefficients give a result between these

⁵ Using the original UDFA rates may lead to non-converging models depending on the given parameters. The model shown in Fig. 2 is one of the few that converged at all within our parameter grid.

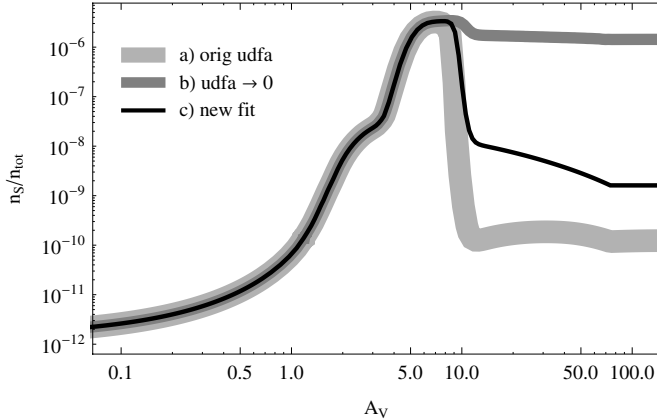


Fig. 2. Relative sulfur abundance as function of A_V for a spherical cloud. The model parameters are mass: $M = 1 M_\odot$, surface density $n = 10^6 \text{ cm}^{-3}$, and FUV intensity $\chi = 10^6$ in units of Draine. Three different chemical networks were applied: **a)** the original UDFA rates; **b)** the original UDFA rates with all reactions possessing $\gamma < 0$ set to zero; and **c)** all reactions with $\gamma < 0$ replaced by the new fits from Table 1.

two extremes. In our comparison, the choice between the scenarios a)–c) strongly affects the whole sulfur chemistry at large A_V .

The UDFA lists the accuracies of the given fits, usually ranging between 25–50%. However, outside their given temperature ranges, negative γ may lead to errors many orders of magnitude larger. For these reactions we calculated new fit parameters to allow for continuous rate coefficients even when T becomes very low. Furthermore, we calculated a single set of fit parameters for those reactions that have multiple entries in the database. These multiple sets may or may not have overlapping temperature ranges. Our final fit is designed to be valid over the total temperature interval with only small deviations.

It is well possible that the results obtained with our new fits have large errors, especially outside the original temperature regime. The peculiar shape of the fit in Fig. 1 below T_{\min} is a direct result of the choice of the parametrization function in UDFA and it is unlikely that the low temperature behavior of this reaction follows that particular shape. However, the divergent low temperature rates of the original UDFA parametrization are unphysical, and the new fit is our best attempt at improving this behavior while minimizing any new uncertainties.

2. Fit procedure

Below we describe the applied fit strategy. Generally, we are willing to sacrifice some of the originally given accuracy to gain continuity down to very low temperatures. To be precise, we did not calculate a new fit to previously attained experimental data. We calculated a new fit to rate coefficients calculated from the original UDFA fits over the given range. The steps are the following:

1. tabulate the reaction rate coefficients over the given temperature range, using the given fit-accuracy as error. These are our artificial data;
2. if $\gamma < 0$, fix $k(T = 10 \text{ K})$;
3. calculate new fit parameters α, β, γ^6 ;

⁶ The fitting was made with Mathematica from Wolfram Research, using a Levenberg-Marquardt algorithm. The fitting procedure is available upon request.

4. calculate the error of the new fit with respect to the original UDFA parametrization.

In the Appendix we show plots of all new fits presented in this paper.

2.1. Discussion of the fit strategy

The details of the fit strategy may have considerable influence on the final fit result. Particularly point 2 prevents the reaction rates from becoming unphysically high. Of course, this procedure introduces new, possibly very large errors to the rate coefficients. But these errors are usually of the same order as those from the UDFA fits. We now consider some major influences on the fit results.

2.1.1. Placement of “data” points

The number and placement of “data” points has a direct influence on the quality of the fit because it implicitly introduces a weighting of the respective temperatures. Using the Levenberg-Marquardt algorithm is in effect applying a sequence of linear least-squares fits to a nonlinear function. Regions with more “data” points contribute more to the total sum of squares and force the fit function closer to these “data” points. For instance, placing temperature points equidistant in log-space will place more grid points at lower temperatures compared to equidistant linear spacing, weighting lower temperatures stronger than higher temperatures. Optimal fit results could be achieved by adaptively changing the number and positions of grid points until the error is minimal, but to keep a consistent error estimate, we used the same temperature gridding for all fits. To fit reactions with $\gamma < 0$, we employed an equidistant temperature grid in log-space with 20 grid points, while we used linear spacing for fitting reactions with multiple entries, using 20 grid points per temperature interval.

2.1.2. Fixing $k(T = 10 \text{ K})$

Choosing a fixed $k(T = 10 \text{ K})$ prevents the reaction rates from becoming unphysically high. However, the exact choice of $k(T = 10 \text{ K})$ is completely arbitrary since no real measurement is available. Moreover, it poses a major constraint to the fit and an unfortunate choice will lead to very large deviations from the true reaction rate coefficient. Woodall et al. (2007) suggest to set $k(10 \text{ K}) = 0$. It is possible that $\lim_{T \rightarrow 10} k(T) = 0$. It is also possible that $k(10 \text{ K}) \gg 0$, we simply do not know. To minimize the deviations from the only available “data”, we chose to set $k(10 \text{ K}) = k(T_{\min})$ if $\gamma < 0$ with T_{\min} the minimal valid temperature from the UDFA parametrization. This also reduces any over/under-swinging behavior of the new fit. To illustrate how the choice of $k(10 \text{ K})$ influences the form of the final fit function we compare in Fig. 3 the fit for $k(10 \text{ K}) = k(T_{\min})$ (red, solid line) and for $k(10 \text{ K}) = 10^{-50}$ (red, dashed line). In this particular case, the latter leads to significantly stronger deviations from the UDFA parametrization than for $k(10 \text{ K}) = k(T_{\min})$.

2.1.3. Calculating new fit parameters

We fitted the fit function $k(T) = \alpha \left(\frac{T}{300}\right)^\beta e^{-\frac{\gamma}{T}}$ to the list of “data” points created in steps 1 and 2. In most cases it is better to perform the fit in log-space, i.e. use $\log(k(T))$ instead of $k(T)$ as fit function. Otherwise, the Levenberg-Marquardt fit would have

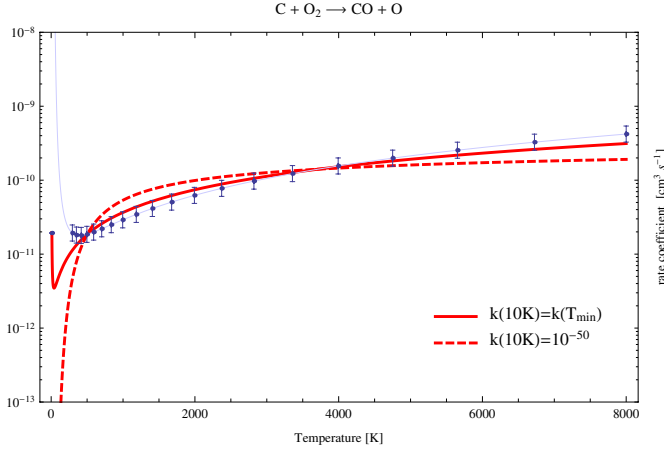


Fig. 3. Comparison of two fit results for different choices of $k(T = 10 \text{ K})$. The UDFA rate coefficient, valid between 295 and 8000 K, is shown in light blue. The best fit for $k(10 \text{ K}) = 10^{-50}$ is shown as red, dashed line ($\alpha = 1.01(-11), \beta = 0.23, \gamma = 913$). The best fit for $k(10 \text{ K}) = k(T_{\min})$ is shown as red, solid line ($\alpha = 9.95(-12), \beta = 1.05, \gamma = -42.5$).

the tendency to fit $k(T)$ to absolutely higher temperatures, while we are interested in the lower temperature regime. In some cases however, a linear fit function is more appropriate. This case is shown in Fig. 4. We try to find a simultaneous fit across the multiple temperature regimes of the reaction $\text{C} + \text{N} \rightarrow \text{CN}$. The linear fit produces a continuously declining result for $T \rightarrow 0$, while a logarithmic fit function produces the opposite behavior, which results in large deviations of the 10 K rate predicted by the UMIST parametrization and our fit result. Again, the true reaction rate behavior at very low temperatures is unknown, hence, our aim is to minimize any deviation from the UDFA fit. The logarithmic fit differs from the 10 K UDFA rate by 8 orders of magnitude, while the linear fit differs only by a factor of 40. For this reaction we chose a linear fit function, for all other fits in this paper a logarithmic fit function was used.

2.1.4. Error calculation

Strictly speaking, the term error is misleading in our context, since it suggest model deviations from real measurements⁷. Instead, whenever we are speaking of fit errors, we actually compare how two different models deviate from each other. Nevertheless, because our aim is to change the original parametrization as little as possible, we will use this deviation to quantify the quality of our fits.

In Tables 1 and 2 we give the relative error brackets of our new fit, i.e. $[\min(e_i), \max(e_i)]$, with $e_i = (k^f(T_i) - k^U(T_i)) / k^U(T_i)$ for all $T_i \in [T_{\min}, T_{\max}]$. Here, k^U is the UDFA parametrization of the reaction, and k^f is our new fit.

2.2. Fitting reactions with negative γ

To obtain a new fit for reactions with $\gamma \ll 0$, we used a log-spaced temperature grid with 20 grid points and a logarithmic fit function. Collider reactions, i.e. reactions of type “CL” in UDFA, were excluded from the fit. Apparently it is possible to find a very good fit for some reactions without any divergence at low

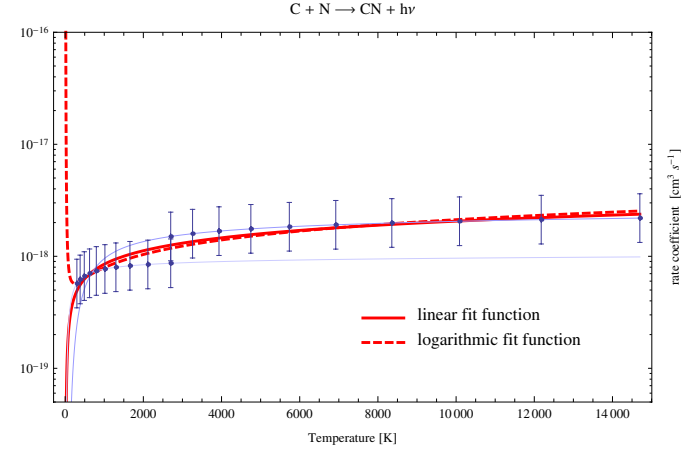


Fig. 4. Comparison of fit results for a linear fit function $k(T)$, shown as solid, red line, and a logarithmic fit function $\log(k(T))$, shown as dashed, red line.

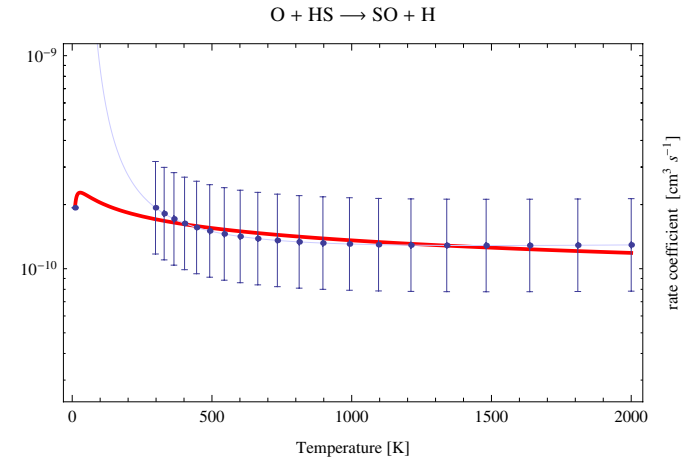


Fig. 5. Example reaction that can be fitted very well (maximum additional error is 11%), but has a less extreme low temperature behavior. The final fit is shown in red, the UDFA rates for each individual temperature regime are shown in light blue. The difference in $k(10 \text{ K})$ is 10 orders of magnitudes between the UDFA rates and our new fitted rates.

temperatures and without introducing any significant additional error. The prime example for this is shown in Fig. 5. Using the UDFA reaction rates gives an unreasonably high reaction rate coefficient at 10 K of 5! The new fitted rate coefficient at 10 K is 2×10^{-10} . Even though we do not know the real reaction strength at 10 K, we consider our new result to be much more reasonable compared to the extrapolated numbers from UDFA.

Some of our new fits even have negative γ , which shows that $\gamma < 0$ not always has to lead to divergent behavior. If $\gamma \gtrsim -100$, the rate inclination for low temperatures is moderate and should not lead to unreasonable results⁸. In Table 1 we present the fit results for reactions that are listed in UDFA with $\gamma < 0$. We give the original and the new fit parameters as well as the relative error brackets of the new fit.

Some of the reactions given in Table 1 also appear in Table 2 because they have counterparts with different temperature regimes. Some of the numerical problems described

⁷ The error bars in some of the figures show the uncertainties of the UDFA reaction rates. These errors are not taken into account by the Levenberg-Marquardt algorithm when fitting a new parametrization.

⁸ UDFA list more reactions with $\gamma < 0$ than given in Table 1. We omitted those reactions because they showed no significant divergence at low temperatures.

Table 2. All reactions with multiple reaction rate coefficients for several temperature ranges.

Educts			Products		T_{\min}	T_{\max}	α_{new}	β_{new}	γ_{new}	[Error]			
H	+	NH ₂	→	NH	+	H ₂	73	3000	4.61(-12)	1.02	2161	-0.05, 0.32	
C	+	O ₂	→	CO	+	O	10	8000	5.56(-11)	0.41	-26.87	-0.50, 2.89	
CH	+	O	→	CO	+	H	10	6000	6.02(-11)	0.10	-4.46	-0.17, 0.13	
N	+	OH	→	NO	+	H	10	2500	6.65(-11)	-0.23	0.24	-0.12, 0.26	
O	+	OH	→	O ₂	+	H	10	5000	5.28(-11)	-0.46	4.14	-0.22, 0.66	
O	+	C ₂	→	CO	+	C	10	8000	1.25(-10)	0.47	-16.13	-0.27, 0.32	
H ₂	+	CH ₄ ⁺	→	CH ₅ ⁺	+	H	15	41000	4.89(-11)	-0.14	-36.14	-0.47, 0.96	
H ₂	+	NH ₃ ⁺	→	NH ₄ ⁺	+	H	10	41000	3.09(-13)	1.08	-50.87	-0.80, 0.83	
He ⁺	+	CO	→	O	+	C ⁺	+ He	10	41000	2.27(-10)	0.28	-29.10	-0.83, 1.51
CH ₃ ⁺	+	HCl	→	H ₂ CCl ⁺	+	H ₂	10	520	5.72(-11)	-2.25	47.50	-0.40, 0.36	
O ⁺	+	N ₂	→	NO ⁺	+	N	23	41000	2.42(-12)	-0.21	-43.99	-0.19, 1.61	
H	+	He ⁺	→	He	+	H ⁺	10	41000	8.41(-16)	0.43	-9.59	-0.36, 0.30	
H ⁺	+	O	→	O ⁺	+	H	10	41000	6.86(-10)	0.26	224	-0.08, 0.05	
NH ₂ ⁺	+	e ⁻	→	N	+	H	+ H	12	12400	1.78(-7)	-0.80	17.14	-0.23, 0.31
NH ₂ ⁺	+	e ⁻	→	NH	+	H	12	12400	9.21(-8)	-0.79	17.11	-0.23, 0.31	
NH ₄ ⁺	+	e ⁻	→	NH ₂	+	H	+ H	12	34670	4.67(-7)	-1.25	41.88	-0.50, 4.02
NH ₄ ⁺	+	e ⁻	→	NH ₂	+	H ₂	12	34670	2.22(-7)	-1.25	41.91	-0.50, 4.02	
NH ₄ ⁺	+	e ⁻	→	NH ₃	+	H	12	34670	1.54(-6)	-1.25	41.92	-0.50, 4.02	
H	+	e ⁻	→	H ⁻	+	hν	10	41000	3.37(-16)	0.64	9.17	-0.20, 0.37	
C ⁺	+	e ⁻	→	C	+	hν	10	41000	2.36(-12)	-0.29	-17.55	-0.58, 0.41	
N ⁺	+	e ⁻	→	N	+	hν	10	41000	3.5(-12)	-0.53	-3.18	-0.34, 0.08	
H ⁺	+	H	→	H ₂ ⁺	+	hν	200	32000	1.15(-18)	1.49	228	-0.18, 0.42	
C	+	N	→	CN	+	hν	300	14700	5.72(-19)	0.37	50.95	-0.16, 0.46	
C	+	O	→	CO	+	hν	10	14700	4.69(-19)	1.52	-50.51	-0.69, 3.10	
C ⁺	+	O	→	CO ⁺	+	hν	10	13900	2.44(-18)	-0.07	2.77	-0.09, 0.06	
O	+	Si ⁺	→	SiO ⁺	+	hν	10	14700	5.92(-18)	-0.67	19.37	-0.45, 4.87	
H	+	HNC	→	HCN	+	H	10	1000	1.14(-13)	4.23	-115	-0.70, 5.10	

Notes. The last column gives the relative error brackets. For the fitting, we limited the upper temperature range to 20 000 K, neglecting higher temperatures. The errors for higher temperatures might be significantly larger. The temperature limits for UDFA are given in Kelvin.

above can be circumvented by choosing an alternative reaction rate coefficient with a more appropriate temperature regime. Nevertheless, we list these reactions for cases where that is not possible.

2.3. Fitting reactions with multiple entries

The fits to reactions with multiple database entries are, in most cases, much less sensitive to the details of the fit strategy, but, overall, the errors of the simultaneous fits are larger compared to the fits to reactions with $\gamma < 0$. Here, the partly very inconsistent entries in UDFA for the different temperature ranges contribute the most to the errors in the final, simultaneous fit. For cases that span a very large temperature range, the choice of T_{\max} when setting up the artificial “data” points poses a major constraint on the fit result. This is demonstrated in Fig. 6.

In Table 2 we present the fit results for reactions with multiple entries in UDFA. The valid temperature ranges of these reaction rates may or may not overlap. Even worse, some of the multiple entries appear to be mutually exclusive. Especially the high temperature rate coefficients for the reaction $\text{He}^+ + \text{CO} \rightarrow \text{O} + \text{C}^+ + \text{He}$ appear to be at odds with both theory and experiment and it may be advisable to only use the low temperature rate coefficients (see Fig. 7). However, this assessment is far beyond the scope of this paper. We apply our fit routine to all reactions in UDFA with multiple entries and leave it to the informed reader to decide whether to use the simultaneous fit or whether to select a reaction with an appropriate temperature regime.

For the fitting, we limited the upper temperature range to 20 000 K where T_{\max} is higher, thus neglecting higher

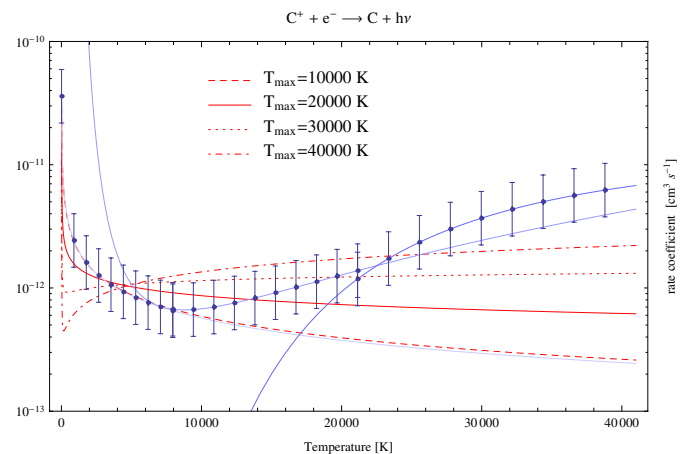


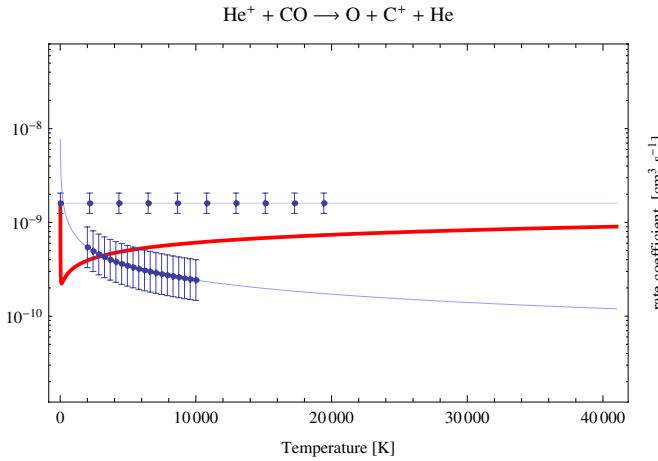
Fig. 6. UDFA lists three C^+ recombination reactions for temperatures from 10 to 41 000 K. The two reaction rates for the higher temperatures show a very different behavior compared to the reaction that is valid from 10 to 8000 K. Applying different values of T_{\max} during the fit leads to significantly different results.

temperatures. The errors are explicitly calculated for this range and may be significantly larger for higher temperatures. Despite the apparently large errors we consider the fits relatively good in most cases. Remember that we fit multiple, sometimes very disparate sets of “data” points, and therefore, large errors are unavoidable. This is demonstrated in Fig. 8 for two cases from Table 2.

The reader should also recall that the reaction rates from UDFA usually have errors on the order of 25–200%. One could

Table 3. Comparison of the recommended 10 K reaction rate coefficients available in KIDA $k^K(10 \text{ K})$ with $k^f(10 \text{ K})$ from our new fits.

Educts	Products	$k^K(10 \text{ K})$ $\text{cm}^3 \text{s}^{-1}$	$k^f(10 \text{ K})$ $\text{cm}^3 \text{s}^{-1}$	References
N + OH	→ NO + H	4.5×10^{-11}	8.44×10^{-11}	Jorfi et al. (2009)
O + OH	→ H + O ₂	4×10^{-11}	5.57×10^{-11}	Lique et al. (2009); Quéméner et al. (2009)
O + NH ₂	→ HNO + H	1×10^{-10}	4.80×10^{-11}	Baulch et al. (2005)

**Fig. 7.** Example reaction with apparently mutually exclusive reaction rates listed in UDFA. The final fit is shown in red, the UDFA rates for each individual temperature regime are shown in light blue. The two temperature ranges overlap and the respective fits to the reaction rates, here shown in light blue, display a very different behavior.

be tempted not to use the UDFA rates to prevent the errors to rise even more because of our simultaneous fitting. However, by doing so one might implicitly accept much larger errors when moving from one temperature regime to the other. This is demonstrated in Fig. 9.

The simultaneously fitted reaction rates in Fig. 9 have a maximum relative error of 32%. This may appear large compared to the individual errors for each temperature regime. But when only using either one of the two reactions we would implicitly accept a very large error when the temperature is around 400–500 K, where both individual rates disagree by one to two orders of magnitude. Our simultaneous fit is a reasonable fit in an attempt to keep the experimental findings for both temperature regimes.

The special case of carbon recombination is shown in Fig. 6. Three different sets of fit parameters are given in UDFA for three distinct temperature ranges up to 41 000 K. Especially the high temperature rates show a very different behavior compared to the low temperature range. A simultaneous fit gives very large errors because of the large deviations from the high temperature rates. However, for most applications, temperatures up to 8000 K are sufficient and we can neglect the errors for high temperatures. In that case, the new fit has much smaller errors. For many practical purposes, one could even completely discard the two higher temperature ranges and only use the low temperature rates. For the sake of completeness, we still list the new fit temperatures up to 20 000 K.

2.4. Discussion

For three reactions in Tables 1 and 2 one finds updated measurements and theoretical values of the reaction rate coefficients in KIDA $k^K(T)$. A detailed comparison of the respective reaction

rate coefficient behavior is beyond the scope of this paper. We will only take a look at the updated recommended 10 K values for these reactions and compare them to our new values $k^f(10 \text{ K})$ in Table 3.

For all three reactions, the 10 K rate coefficients achieved from our new fits are within a factor of two compared to the recommendations from the KIDA Kinetic Database for Astrochemistry. For the reaction O + OH, our value is only 40% higher than the recommended value. Given the overall uncertainties, the agreement between our new fits and the KIDA values is remarkable and an indication that our general fit approach is viable to achieve reasonable results.

3. Summary and conclusions

We presented an approach to overcome some numerical and practical difficulties in present-day databases of chemical reaction rates. One of these difficulties is the existence of fits to reaction rate coefficient that unphysically diverge at very low temperatures. This is especially problematic for numerical codes, which calculate chemical networks down to very low temperatures and thus have to use many of the reaction rate coefficients that are listed in chemical databases beyond their given temperature regime. We demonstrate that it is possible to find a new parametrization of these reactions that ensures a less erroneous behavior and allows calculations to temperatures of 10 K and lower.

A second complication that occurs in chemical databases is that some of the listed reactions have multiple entries because the experimental data were obtained for different temperature ranges. Any user is instructed to use the listed reaction rate coefficients only in their valid temperature regime. Unfortunately, multiple entries in these databases very often display fairly inconsistent properties. This is particularly problematic for numerical codes that continuously change the temperatures when calculating chemical networks because it introduces artificial numerical jumps in the coefficient matrix of the equation system to be solved. One solution could be to restrict oneself to only use the one reaction rate that has a temperature regime closest to the computational regime. However, in many cases this is not possible because the parameter space relevant for application spans multiple temperature regimes. Additionally, this means that one implicitly accepts quite large errors when leaving the valid temperature regime. We suggest to replace these multiple entries with a single, new rate which is fitted simultaneously to the individual ones. This minimizes the error when moving from one temperature regime to the other and additionally overcomes the problem of discontinuous reaction rate jumps.

We consider the new parametrization presented in this paper only a temporary solution until better experimental data for low temperature reaction rates are available.

As a side effect we demonstrate that in some cases one might find an equally good parametrization of the reaction rate coefficients without any artificial numerical side effects just by taking

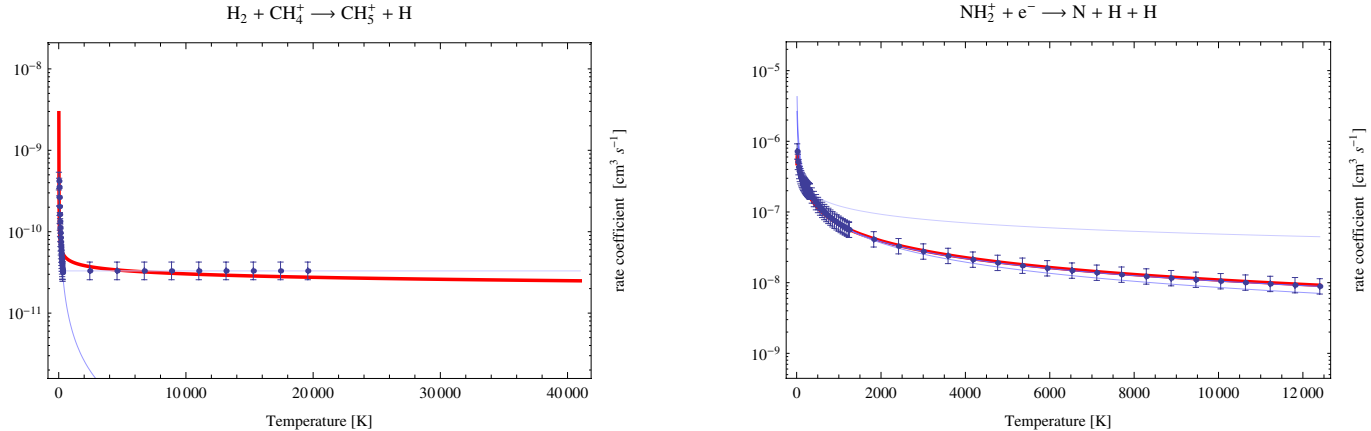


Fig. 8. Two example reactions to demonstrate the wide range of error values. The final fit is shown in red, the UDFA rates for each individual temperature regime are shown in light blue. *Left:* this reaction is listed with two very differently behaving reaction rates. Consequently, the simultaneous fit has relatively large errors especially at the interface between bow temperature regimes. Still, we consider the fit to be very good because of its overall capability to reproduce the general behavior in both regimes. *Right:* this reaction is listed with three distinct temperature regimes. The simultaneous fit is nevertheless a very good approximation to all three UDFA rates in the relevant temperature ranges.

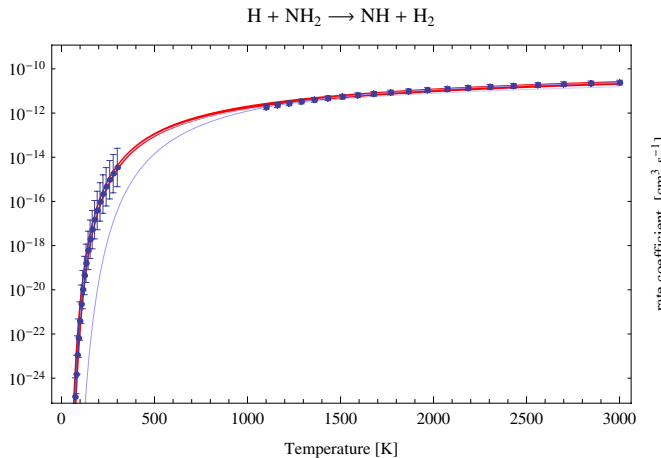


Fig. 9. Simultaneously fitted reaction rates in this figure have a maximum relative error of 33%. The final fit is shown in red, the UDFA rates for each individual temperature regime are shown in light blue.

care not to allow too low negative values of γ . The chemical databases try to express the possibly very complicated physics of the various chemical reactions with only three fitting parameters. Of course, this is an extremely strong constraint on any parameter fit to the complex experimental data. Although, under certain circumstances, chemical reactions listed in chemical databases like UDFA, OSU, and others might reasonably be applied even outside their given scope, it is important to ensure that numerical side effects from parametrization are minimized when possible. For many numerical applications this is much more important than a smaller total error of the reaction rate coefficients in a limited range in temperature.

Any user should always take care not to blindly use reaction rate coefficients from chemical databases outside their

temperature scope. This is also true for the new parametrizations listed in this paper. In each case, one has to balance advantages against disadvantages. If you are sure that you will keep within the given temperature regime, then there is no need to use our rate coefficients because they add an additional error to the computation. Under certain circumstances, this additional error might be negligible compared to the numerical problems that come with the original rate coefficients.

Acknowledgements. This work was supported by the German *Deutsche Forschungsgemeinschaft, DFG* project number Os 177/1-1. We acknowledge the use of UDFA (a.k.a. UMIST) (<http://www.udfa.net/>) chemical reaction databases. Some kinetic data we used were downloaded from the online database KIDA (Kinetic Database for Astrochemistry, <http://kida.obs.u-bordeaux1.fr>). The author thanks R. Simon and V. Ossenkopf for their helpful comments on the text. The author thanks the anonymous referee for his or her comments, which helped the final text a lot.

References

- Baulch, D. L., Bowman, C. T., Cobos, C. J., et al. 2005, *J. Phys. Chem. Ref. Data*, 34, 757
- Garrod, R. T., Weaver, S. L. W., & Herbst, E. 2008, *ApJ*, 682, 283
- Herbst, E. 2006, in *Rev. Mod. Astron.*, ed. S. Roeser, 19, 167
- Hollenbach, D. J., & Tielens, A. G. G. M. 1999, *Rev. Mod. Phys.*, 71, 173
- Jorfi, M., Honvault, P., & Halvick, P. 2009, *Chem. Phys. Lett.*, 471, 65
- Lemaire, J., & Combes, F. 2007, meeting held in Paris, France, May 14–18 (S.Diana)
- Lique, F., Jorfi, M., Honvault, P. H., et al. 2009, *J. Chem. Phys.*, 131, 221104
- Lis, D. C., Blake, G. A., & Herbst, E. 2005, *IAU Symp.*, 231
- Quéméner, G., Balakrishnan, N., & Kendrick, B. 2009, *Phys. Rev. A*, 79, 022703
- Röllig, M., Ossenkopf, V., Jeyakumar, S., Stutzki, J., & Sternberg, A. 2006, *A&A*, 451, 917
- Röllig, M., Abel, N. P., Bell, T., et al. 2007, *A&A*, 467, 187
- van der Tak, F. 2008, in *Massive Star Formation: Observations Confront Theory*, ed. H. Beuther, H. Linz, & T. Henning, *ASP Conf. Ser.*, 387, 101
- Wakelam, V. 2009, *Am. Astron. Soc. Meet. Abstr.*, 214, 402.15
- Woodall, J., Agúndez, M., Markwick-Kemper, A. J., & Millar, T. J. 2007, *A&A*, 466, 1197

Appendix A: Plots of all new fits

Here, we show the plots of all new fits to allow the user an assessment of the fit quality over the entire fitted temperature range. The plots are shown in the same order as in Tables 1 and 2.

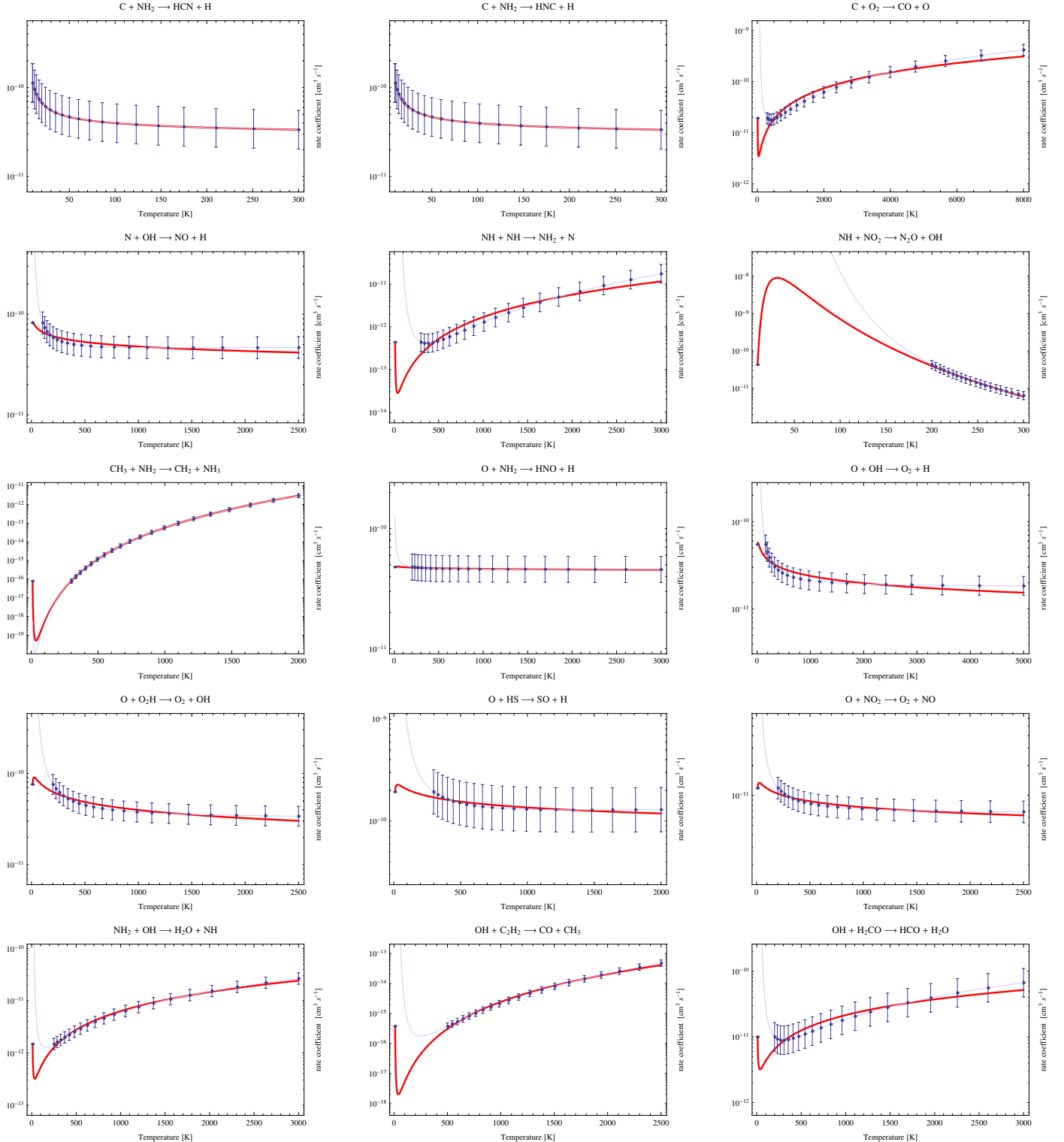


Fig. A.1. Fits to reactions with negative γ .

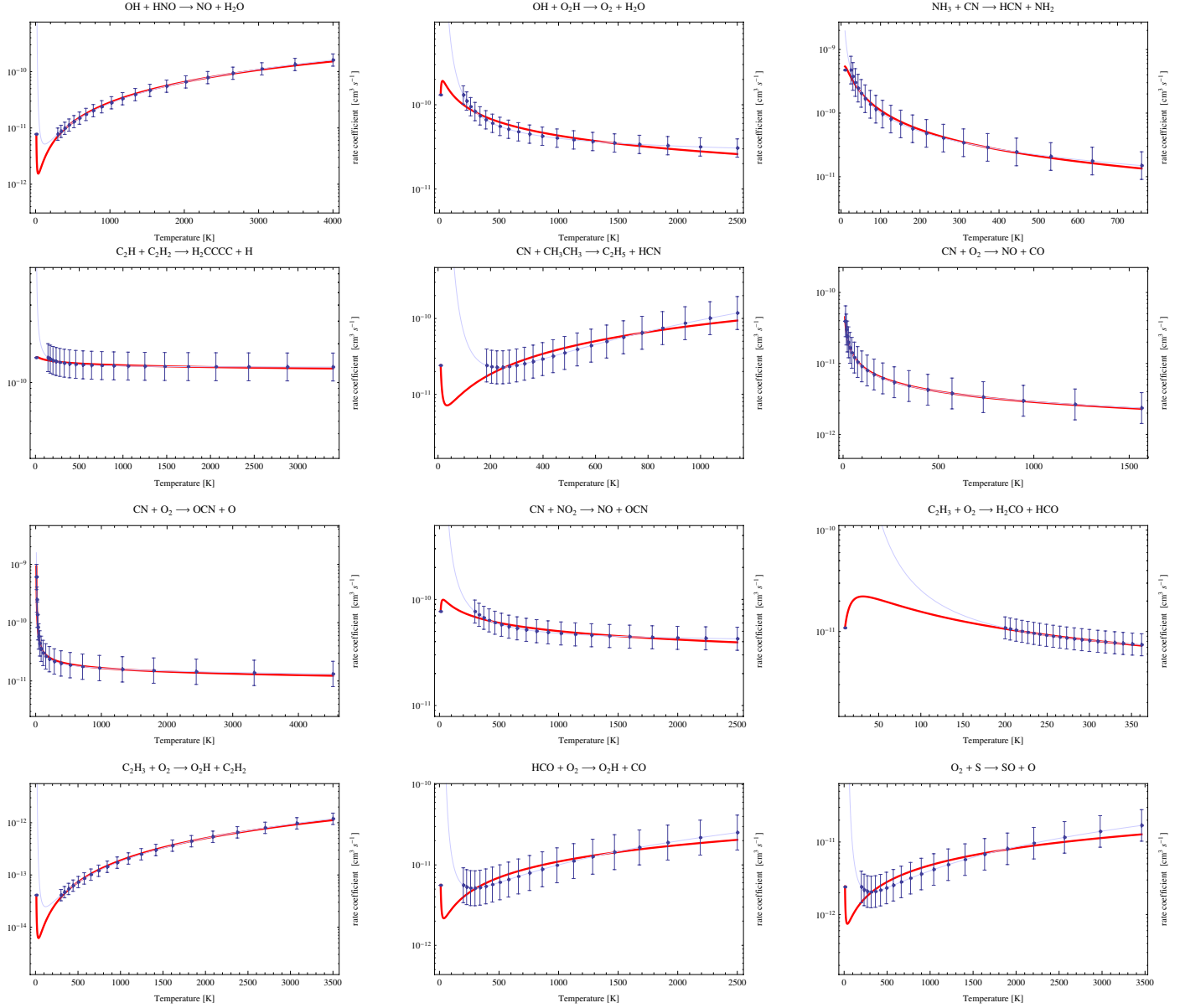
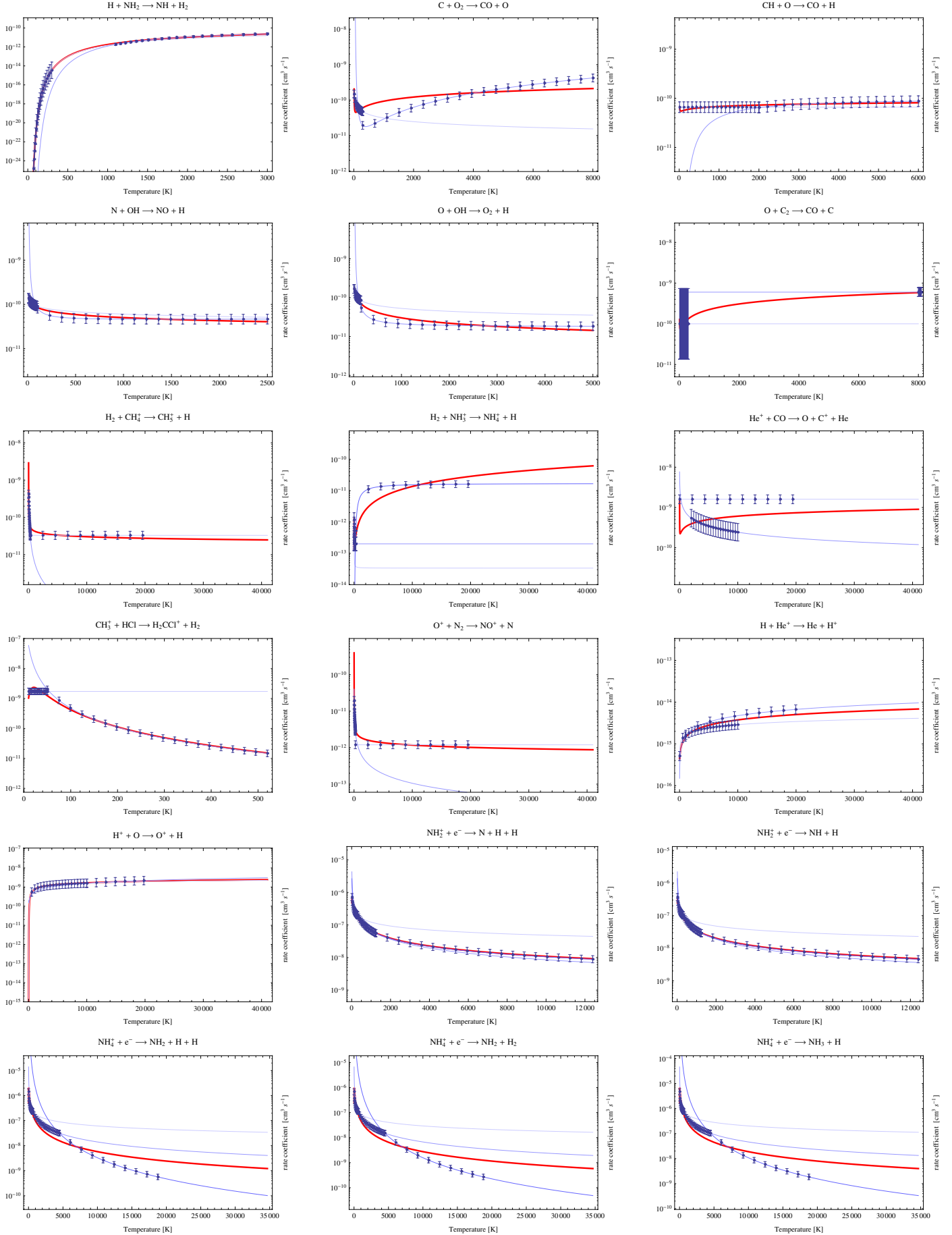


Fig. A.1. continued.

**Fig. A.2.** Fits to reactions with multiple entries.

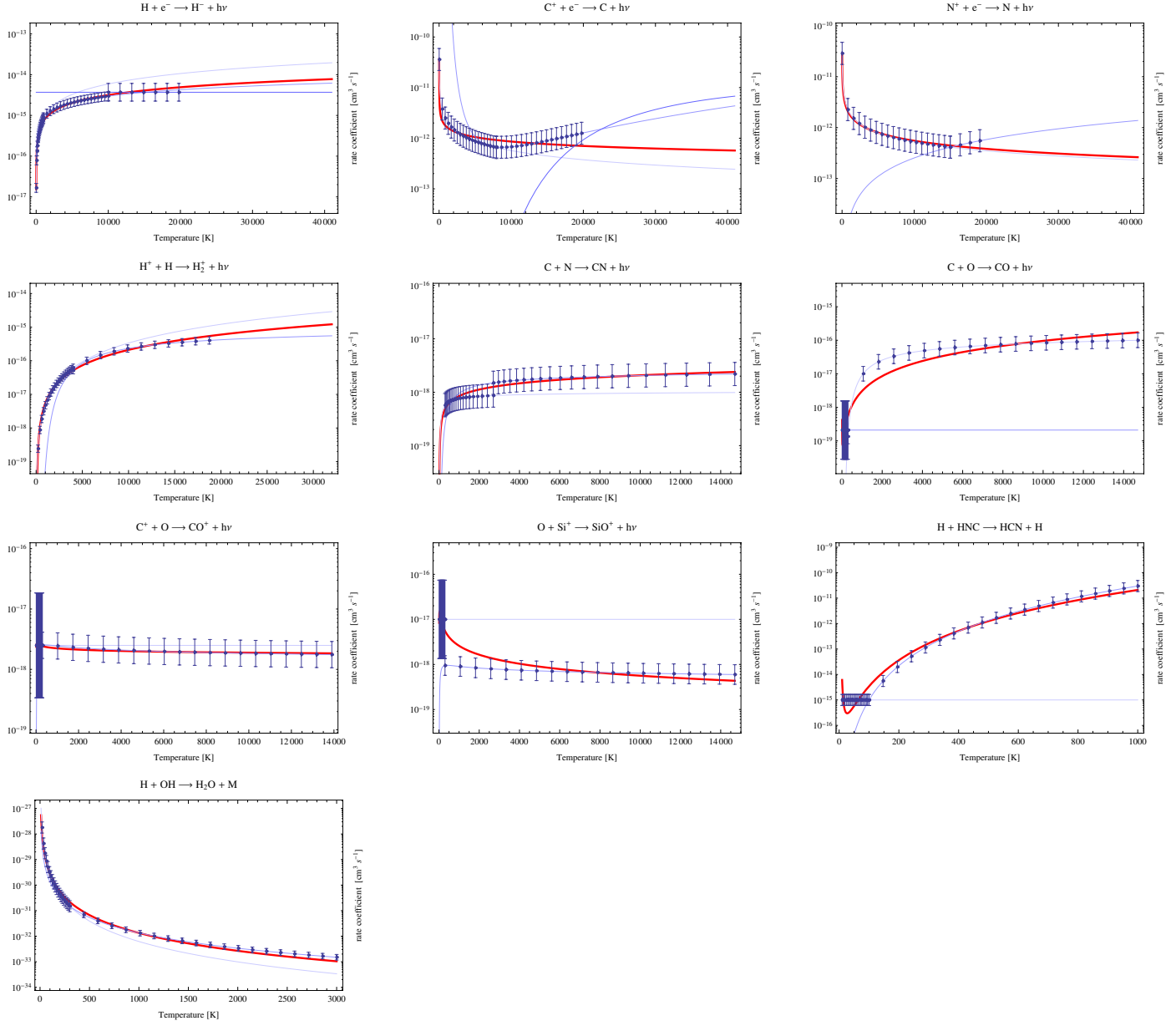


Fig. A.2. continued.

[CII] gas in IC 342

M. Röllig¹, R. Simon¹, R. Güsten², J. Stutzki¹, H. W. Hübers^{3,4}, P. Hartogh⁵, K. Jacobs¹, X. Guan¹, and F. Israel⁶

¹ I. Physikalisches Institut der Universität zu Köln, Zülpicher Straße 77, 50937 Köln, Germany
e-mail: roellig@ph1.uni-koeln.de

² Max-Planck-Institut für Radioastronomie, Auf dem Hügel 69, 53121 Bonn, Germany

³ Deutsches Zentrum für Luft- und Raumfahrt, Institut für Planetenforschung, Rutherfordstraße 2, 12489 Berlin, Germany

⁴ Institut für Optik und Atomare Physik, Technische Universität Berlin, Hardenbergstraße 36, 10623 Berlin, Germany

⁵ Max-Planck-Institut für Sonnensystemforschung, Max-Planck-Straße 2, 37191 Katlenburg-Lindau, Germany

⁶ Leiden Observatory, Leiden University, PO Box 9513, 2300 RA Leiden, The Netherlands

Received 31 January 2012 / Accepted 30 March 2012

ABSTRACT

We used the dual-band receiver GREAT on board the SOFIA airborne telescope to perform observations of the [C II] 158 μm fine-structure line at the positions of two giant molecular clouds (GMC) in the center of IC 342 (GMCs C and E) and compared the spectra with corresponding ground-based data for low- and mid- J CO and [C I]. We performed model calculations assuming a clumpy photo-dissociation region (PDR) environment using the KOSMA- τ PDR model code to derive physical parameters of the local medium. The [C II] 158 μm emission resembles the spectral signature of ground-based atomic and molecular lines, which indicates a common origin. The emission from GMC E can be decomposed into a cool, molecular component with weak far-ultraviolet (FUV) fields and low, mean densities of 10^3 cm^{-3} and a strongly excited starburst/PDR region with higher densities of 10^4 cm^{-3} and FUV intensities of 250–300 Draine fields. The emission from GMC C is consistent with gas densities of 5000 cm^{-3} , FUV intensities of a few Draine fields and total gas masses of $20 \times 10^6 M_\odot$. The high spectral resolution of the GREAT receiver allowed us to decompose the [C II] emission of the GMC E into a strongly excited gas component resembling a PDR/starburst environment and a quieter, less excited gas component and to analyze the different components within a single beam individually.

Key words. galaxies: ISM – galaxies: individual: IC 342 – radio lines: galaxies – radio lines: ISM – ISM: atoms

1. Introduction

IC 342 is a gas-rich spiral galaxy with active star formation in its nucleus. IC 342 is located behind the Galactic plane and is therefore highly obscured; the distance to the nearly face-on galaxy is still debated. Tikhonov & Galazutdinova (2010) give a distance of 3.9 ± 0.1 Mpc derived from stellar photometry. Observations of planetary nebulae (Herrmann et al. 2008) and cepheids (Saha et al. 2002) give distances of 3.4 ± 0.2 Mpc.

Within its central 30'' two molecular arms of a mini-spiral end in a clumpy central ring of dense gas, which surrounds a young star cluster. Downes et al. (1992) showed the presence of five giant molecular clouds, A to E, around the nucleus of IC 342 with masses of $\sim 10^6 M_\odot$. This structure can be seen in Fig. 1, which shows a map of line-integrated $^{12}\text{CO}(1-0)$ emission observed with BIMA (Berkeley Illinois Maryland Association). The central molecular ring surrounds a nuclear star cluster with active star formation and strong far-ultraviolet (FUV) radiation, illuminating the molecular ring and producing photo-dissociation regions (PDRs) on the side facing the central cluster. Energetic FUV photons dissociate and ionize molecules and atoms in the gas and effectively heat the gas and dust via photoelectric heating. Consequently, PDRs strongly emit radiation from species that are abundant and excited under these conditions, like [C II]. Meier & Turner (2005) find that the chemistry in the ring is a mixture of PDR gas and regions of denser, more shielded material. Especially the GMC complex B appears

to show properties of PDRs produced by the surrounding starburst environment (Downes et al. 1992; Israel & Baas 2003). The spatial sizes of the central GMCs and the infrared luminosity of the inner 400 pc of IC 342 are both similar to the center of our Galaxy. Especially the relative contribution of the diffuse material to the overall [C II] emission remains unknown but it appears that the PDRs remain largely confined to the central ring.

Detailed knowledge of the H_2 column densities, excitation temperatures, and densities in IC 342 exists from CO and its isotopomers as a basis for comparison with the [C II] lines (e.g. Ishizuki et al. 1990; Downes et al. 1992; Turner & Hurt 1992; Wright et al. 1993; Turner et al. 1993; Meier et al. 2000; Meier & Turner 2001; Israel & Baas 2003; Meier & Turner 2005). Comparison with this complementary data, particularly with their spectral shape, allows us to distinguish different kinematic components from the [C II] lines and to assess the interaction of the star formation activity on the gas.

In this work we present velocity-resolved spectra of ionized atomic ([C II] 158 μm) gas, with spatial resolutions of $\sim 15''.6$. The observations were performed with the German REceiver for Astronomy at Terahertz frequencies (GREAT¹, Heyminck et al. 2012) on board the Stratospheric Observatory For Infrared Astronomy (SOFIA).

¹ GREAT is a development by the MPI für Radioastronomie and cooperation with the MPI für Sonnensystemforschung and the DLR Institut für Planetenforschung.

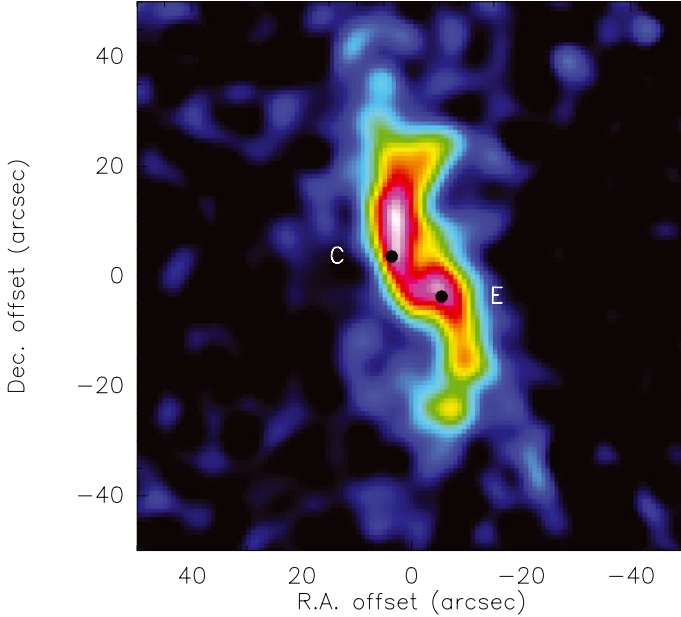


Fig. 1. Line-integrated map of the $^{12}\text{CO}(1-0)$ transition from the BIMA-SONG sample. The black dots denote the positions of our two [C II] detections in IC 342. The positions correspond to giant molecular clouds C and E. The (0, 0) position corresponds to (RA, Dec) (J2000) (03:46:48.5 68:05:47).

In Sect. 2 we describe the observations. The spectra are presented in Sect. 3. The analysis of the data and ambient conditions are discussed in Sect. 4, and conclusions are drawn in Sect. 5.

2. Observations

We used the dual-channel receiver GREAT on SOFIA in September 2011 to perform pointed observations of the [C II] $158\ \mu\text{m}$ fine-structure transition of C^+ at $1900.536900\ \text{GHz}$ and the $^{12}\text{CO}(11-10)$ transition at $1496.922909\ \text{GHz}$ near the center of IC 342. The observations were performed in dual beam-switch mode (chop rate 1 Hz) toward selected positions, see Table 1 for details. The chopper offset was $100''$ with a chopper angle of 110 degrees against north (counter-clockwise). The observations were taken during the transfer flight from the US to Europe. Owing to unknown technical errors on the flight we had to discard one of the observed positions.

The center position is RA, Dec (J2000) 03:46:48.5 68:05:47. We observed 2 GMCs at the following offsets in arcsecond: GMC C (+3.6, +3.6), and GMC E (-5.5, -3.7) using the designation by Downes et al. (1992) (see also Fig. 1). The integration times were 9.3, and 3.7 min, respectively. [C II] emission was detected at both positions. We did not detect any $^{12}\text{CO}(11-10)$ emission. The rms of the baseline for position C and E was 0.10 and $0.21\ \text{K km s}^{-1}$, respectively, with a channel width of $4\ \text{km s}^{-1}$.

We used a fast Fourier transform spectrometer (FFTS), with 8192 channels providing $1.5\ \text{GHz}$ bandwidth and about $212\ \text{kHz}$ of spectral resolution. Calibration was performed with the standard pipeline (Guan et al. 2012). Using the beam efficiency $\eta_c \approx 0.51$ and the forward efficiency (η_f) of 0.95 (Heyminck et al. 2012), we converted all data to line brightness temperature scale, $T_B = \eta_f \times T_A^* / \eta_c$. The reduction of these calibrated data, as well as the maps shown throughout the paper, were made with the GILDAS² package CLASS90. The pointing was established

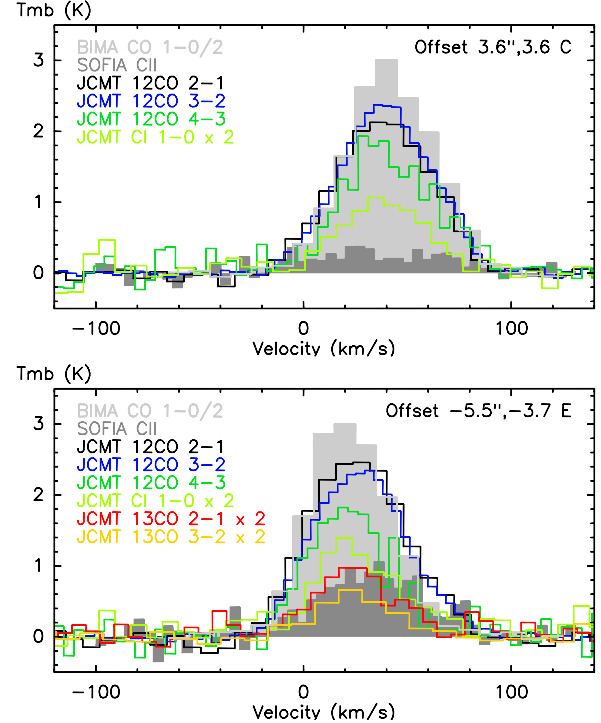


Fig. 2. Averaged [C II] spectra (dark gray, filled) toward the GMC C (top), and GMC E (bottom) positions. The $^{12}\text{CO}(2-1)$ spectra are divided by 2, the [CI] ${}^3\text{P}_1 - {}^3\text{P}_0$ and ^{13}CO spectra are multiplied with 2.

with the optical guide cameras to about $1''$ precision, and was found to have deviated by about $3-5''$ after 20 min.

3. Results

In Fig. 2 we show the [C II] emission observed with GREAT (dark gray, filled) for both positions. On each spectrum we overlay $^{12}\text{CO}(1-0)$ data from BIMA-SONG³ (Helper et al. 2003), as well as $^{12}\text{CO}(2-1)$, $^{12}\text{CO}(3-2)$, $^{12}\text{CO}(4-3)$, $^{13}\text{CO}(2-1)$, $^{13}\text{CO}(3-2)$, and [CI] ${}^3\text{P}_1 - {}^3\text{P}_0$ spectra from Israel & Baas (2003). Because of the different beam sizes, gridding, and map coverage it was not always possible to regrid and convolve all spectra to the positions and beam sizes of the GREAT observations.

Where possible, we smoothed the other data sets to the $15''$ resolution of our [C II] line observations. We kept the $^{12}\text{CO}(2-1)$ and $^{13}\text{CO}(2-1)$ spectra on their native resolution of $22''$ and $23''$. We kept $^{12}\text{CO}(3-2)$ and $^{13}\text{CO}(3-2)$ on their native resolution of $15''$. $^{12}\text{CO}(1-0)$, $^{12}\text{CO}(4-3)$, and [CI] ${}^3\text{P}_1 - {}^3\text{P}_0$ spectra were smoothed to the resolution of our [C II] data and interpolated at the two positions C and E. For the remaining ground-based spectra at the positions C and E we averaged the data points closest to our [C II] observations.

The [C II] emission is strongest at position E. At both positions the different transitions show a good correlation of the central line velocities and line widths. The spectra at position C exhibit a consistent central velocity of $40\ \text{km s}^{-1}$ and similar line widths of about $50\ \text{km s}^{-1}$. Only the [C II] line has a broader line width and is blueshifted by a few km s^{-1} . Position E shows slight variations in the different spectral lines. All lines have a comparable line width of slightly less than $50\ \text{km s}^{-1}$. Most lines

³ <http://ned.ipac.caltech.edu/level5/March02/SONG/SONG.html>

appear to be centered around 24 km s^{-1} , except for $^{12}\text{CO}(2-1)$ and $(3-2)$ with slightly redshifted central velocities.

We performed a Gaussian fit for all lines at the two positions to determine their respective line parameters such as peak- and line-integrated intensity $T_{\text{mb}}^{\text{peak}}$ and $\int T_{\text{mb}} \text{d}v$, line width ΔV , and line center velocity v_0 . For position C we fitted a single-component Gaussian to the data without any additional constraints. The results are given in Table 1. At position E we already noted the slight asymmetry in several of the CO lines, possibly resulting from two different, spatially and kinematically unrelated gas components. We used the optically thinnest lines from our data set, the ^{13}CO lines (Israel & Baas 2003), to specify the line center velocity of 24 km s^{-1} of the main component by fitting a single Gaussian to their profiles. To quantify the contributions of two separate components to the spectra, we fitted two separate Gaussian components to the spectra while keeping the line center velocity of the main component fixed to 24 km s^{-1} . Only for $^{12}\text{CO}(4-3)$ and [C I] it was not possible to find a second line-component, therefore we performed an unconstrained single-component fit that we can attribute to the main component because of the comparable velocities. For $^{12}\text{CO}(1-0)$ we fixed the velocity and width of the high-velocity component to 53 and 47 km s^{-1} , respectively, and derived the line parameters for the low-velocity component. The decomposition into two different components is also supported by the BIMA $^{12}\text{CO}(1-0)$ data at $5.5''$ resolution, which shows a line center velocity $v_0 \approx 50 \text{ km s}^{-1}$ at our center position. Therefore, emission from the PDR-dominated gas close to the central cluster is expected at $v_0 \approx 50 \text{ km s}^{-1}$.

As an independent method to derive the [C II] line parameters, we also calculated the zeroth, first and second moment of the spectra, i.e. the integrated intensity, mean velocity and line width. The derived emission line parameters are summarized in Table 1 (moments are given as italic numbers).

The GMC E and B are both located southwest of the central position of IC 342 with an angular separation of only $3.5''$. Accordingly, the $15''$ [C II] beam will always pick up emission of both GMCs. The [C II] spectrum of position E shows the strongest emission from both positions most likely because of the already known PDR/starburst contribution from GMC B (Meier & Turner 2005). Position C is situated in the molecular ring, closest to the central cluster and will most likely contain contributions from dense molecular gas as well as from PDRs.

Israel & Baas (2003) showed the existence of strong velocity gradients in the central region of IC 342. To quantify what pointing shift could alternatively mimic the observed line shift, we convolved the BIMA ^{12}CO (1-0) data to $15''$. We found that a pointing offset of $7''$, significantly higher than the quoted accumulative pointing accuracy after 20 min, exactly in the direction of the central cluster could explain the [C II] line profile. Therefore, it is unlikely, though it cannot be fully excluded, that a systematic pointing error may have caused the observed velocity shift.

4. Discussion

Table 2 lists line ratios of [C II] and [C I] to $^{12}\text{CO}(1-0)$ and $^{12}\text{CO}(2-1)$ and $^{12}\text{CO}(4-3)/^{12}\text{CO}(1-0)$ (if available, the numbers for position E are given in the order high/low velocity component). Stronger PDR emission will be reflected in a higher ratio of the fine structure lines to the molecular lines. Apparently, GMC E shows the strongest PDR contribution. Stacey et al. (1991) give a [C II]/ $^{12}\text{CO}(1-0)$ ratio of 5000 (corrected for main

Table 1. IC 342 line parameters derived from Gaussian fits.

Transition	$\int T_{\text{mb}} \text{d}v$ [K km s $^{-1}$]	v_0 [km s $^{-1}$]	ΔV [km s $^{-1}$]	$T_{\text{mb}}^{\text{peak}}$ [K]
Position C ($+3.6'', +3.6''$)				
[C II]	24.3 ± 2.7	33.1 ± 4.5	78 ± 9	0.3
[C II] ^a	23.5	31.8	67.5	
$^{12}\text{CO}(1-0)^b$	307 ± 2	41.5 ± 0.2	50 ± 1	5.83
$^{12}\text{CO}(2-1)$	131 ± 3	38.2 ± 0.5	55 ± 1	2.21
$^{12}\text{CO}(3-2)$	134 ± 1	39.4 ± 0.2	53 ± 1	2.37
$^{12}\text{CO}(4-3)$	98 ± 3	39.7 ± 0.9	54 ± 2	1.71
[C I] ^c $^3\text{P}_1 - ^3\text{P}_0$	25.6 ± 2.2	38.3 ± 2.0	47 ± 5	0.51
Position E ($-5.5'', -3.7''$)				
[C II]	37 ± 15	24^c	48 ± 9	0.72
	20.6 ± 9.9	52.7 ± 11.3	47 ± 20	0.42
[C II] ^a	59	34.9	51	
$^{12}\text{CO}(1-0)^b$	280 ± 11	20	43 ± 2	6.29
	21.8 ± 9.4	53^d	47^e	1.45
$^{12}\text{CO}(2-1)$	139 ± 6	24^c	50 ± 2	2.59
	9.5 ± 4.2	59.8 ± 4.5	34 ± 11	0.26
$^{12}\text{CO}(3-2)$	120 ± 5	24^c	49 ± 1	2.27
	16 ± 3	53.3 ± 4.3	46 ± 8	0.32
$^{13}\text{CO}(2-1)$	23.6 ± 2.7	24.0 ± 1.7	48 ± 4	0.46
$^{13}\text{CO}(3-2)$	$-$	$-$	$-$	-
	13.9 ± 2.0	24.4 ± 1.8	41 ± 4	0.32
$^{12}\text{CO}(4-3)$	88 ± 5	21.2 ± 0.9	46 ± 2	1.81
[C I] ^c $^3\text{P}_1 - ^3\text{P}_0$	34 ± 4	24.4 ± 1.7	51 ± 4	0.61

Notes. One Gaussian component was fitted to all spectra at position C. At position E we fitted two Gaussian components to the spectra with a line center velocity of component 1 fixed to 24 km s^{-1} as derived from the single-component fit to the $^{13}\text{CO}(2-1)$ spectrum. The line parameters for [C II] are additionally calculated from their moments between -30 and 100 km s^{-1} (numbers in italics). ^(a) Results from calculating the moments of the line. ^(b) To convert from flux density Jy beam $^{-1}$ km s $^{-1}$ to brightness temperatures we applied a factor of 4.4 assuming an effective beam size of $5.5''$ (Helper et al. 2003). ^(c) The line center velocity was set to 24 km s^{-1} . ^(d) The line center velocity was set to 53 km s^{-1} . ^(e) The line width was set to 47 km s^{-1} .

beam efficiency and assuming unity beam filling). They cite [C II] intensities (beamsize $55''$) of $3 \times 10^{-4} \text{ erg s}^{-1} \text{ cm}^{-2} \text{ sr}^{-1}$, but only 40 K km s^{-1} for the $^{12}\text{CO}(1-0)$ line intensity in a $60''$ beam. The [C II] and $^{12}\text{CO}(1-0)$ data were taken using the Kuiper Airborn Observatory (KAO) and the Owens Valley Radio Observatory (OVRO), respectively. Given the larger beam sizes and unknown filling factors, their values are consistent with our data.

Stacey et al. (1991) showed that starburst galaxies have a high [C II]/ $^{12}\text{CO}(1-0)$ ratio of 4100 while cooler, less active galaxies show much weaker ratios. Decomposition of the $^{12}\text{CO}(1-0)$ data into a low- and high-velocity component at 24 and 53 km s^{-1} , respectively, gives [C II]/ $^{12}\text{CO}(1-0)$ ratios of 600 and 4000, which indicates contributions from quiescent, weakly excited gas plus a strong, starburst-like contribution from the local PDRs.

The [C II] emitting level lies 91 K above the ground state and has a critical density of $\gtrsim 3500 \text{ cm}^{-3}$. Assuming optically thin emission and a level population in the high-temperature, high-density limit, we can calculate a lower limit of the C $^+$ column density from the integrated intensity (Crawford et al. 1985). The results are given in Table 2. The beam-averaged column densities have values between $0.9-1.6 \times 10^{17} \text{ cm}^{-2}$, relatively low numbers for massive PDRs. The source intrinsic column density will be accordingly higher for a compact source, lower than the beam: a beam filling factor of 1/10, not unlikely given the small size of the cores visible in the interferometric $^{12}\text{CO}(1-0)$ map, will give a column density that is a factor of 10 higher. Column

Table 2. Line ratios and estimated column densities of the observed GMCs.

	GMC C	GMC E
[C II]/ ¹² CO(1–0)	482	4236/692
[C II]/ ¹² CO(2–1)	142	1223/150
[C I]/ ¹² CO(1–0)	6.5	–/9.4
[C I]/ ¹² CO(2–1)	1.9	–/2.4
¹² CO(4–3)/ ¹² CO(1–0)	20.7	21.1(–)
$N_{\text{[CII]}}/[10^{17} \text{ cm}^{-2}]^a$	1.4	0.9/1.6
PDR model results		
$\langle n \rangle [10^3 \text{ cm}^{-3}]$	5.0	10/2.0
$M_{\text{tot}} [10^6 M_{\odot}]$	20	2.0/15
χ [Draine]	7	300/5

Notes. For GMC E we give the values for the high/low velocity components. The PDR fit assumes a distance of 3.9 Mpc. The line ratios were calculated from line-integrated intensities in units of $\text{erg s}^{-1} \text{ cm}^{-2} \text{ sr}^{-1}$.

(a) Assuming a high-temperature and high-density limit and optical thin emission.

densities of $1\text{--}2 \times 10^{17} \text{ cm}^{-2}$ and a $[\text{C}^+]/[\text{H}]$ ratio of 10^{-4} gives a total mass in the $15''$ beam of $5\text{--}10 \times 10^6 M_{\odot}$ at a distance of 3.9 Mpc. Israel & Baas (2003) give comparable central masses of IC 342 of $5\text{--}7 \times 10^6 M_{\odot}$, given the uncertainties in the relative abundance of ionized carbon, filling factors, and distance.

To confine the local gas parameters we used the KOSMA-T PDR model code (Störzer et al. 1996; Röllig et al. 2006) to model the emission of an ensemble of clumpy PDRs in a beam of $15''$ (Cubick et al. 2008). We fitted the model to the absolute intensities therefore making the total model gas mass sensitive to the distance of the PDR. As a result from the fit we receive the mean gas density in the beam, the total gas mass, and the FUV intensity that illuminates the PDRs in units of the Draine field (Draine 1978). The derived parameters for all positions are given in Table 2 assuming a distance of 3.9 Mpc. Employing a shorter distance will reduce the total gas mass estimates accordingly.

To perform a consistent fit across both positions we excluded the ¹³CO lines from the fitting. Note that the ¹³CO lines show relative weak emission, which requires lower model densities of $\sim 1000 \text{ cm}^{-3}$ for both positions. Without fitting to the ¹³CO lines the densities are higher by a factor of a few. Furthermore, the [C II] and [C I] line intensities relative to the CO emission can only be explained by densities below 10^4 cm^{-3} and low FUV fields. Note that the model computations assume solar metallicities, while Engelbracht et al. (2008) give somewhat higher values for IC 342. Higher metallicities will lead to lower [C II]/CO ratios.

The fit results from GMC E support the decomposition into two separate gas components. The lower velocity of 24 km s^{-1} would be consistent with assuming that the emission originates in the trailing, spiral arm region, which is connected to the molecular ring. The emission of the high-velocity component resembles the PDR signature of a starburst/PDR environment with mean FUV fields of 250–300 (in units of the Draine field) and densities of 10^4 cm^{-3} . If we assume that the observations at position E were mispointed (see discussion in the previous section), we derive the following PDR model parameters: $\langle n \rangle = 1000 \text{ cm}^{-3}$, $M_{\text{tot}} = 19 \times 10^6 M_{\odot}$ and $\chi = 5$. These gas parameters are in conflict with a scenario where a PDR/starburst dominates at the center of the galaxy.

5. Conclusions

We used the dual-band heterodyne receiver GREAT on board the airborne telescope SOFIA to observe two giant molecular clouds situated around the nucleus of IC 342 in the ¹²CO $J = 11 \rightarrow 10$ transition and the [C II] $158 \mu\text{m}$ fine-structure line. We detected [C II] emission at both positions but could not detect any ¹²CO $J = 11 \rightarrow 10$ emission.

The new SOFIA/GREAT spectra reveal a spectral distribution of the [C II] emission that follows the distribution of the neutral and molecular gas, [C I] and CO. The [C II] spectrum observed at the position of GMC E shows two velocity components, a high-velocity component that we attribute to emission from a PDR/starburst region in the molecular ring close to the central cluster with densities of 10^4 cm^{-3} , FUV field of 250–300 and a total mass of $2 \times 10^6 M_{\odot}$ and a cooler, low-velocity component with densities of $2 \times 10^3 \text{ cm}^{-3}$, FUV fields of a few and a total mass 7–8 times higher than the starburst component. The model for GMC C gives model parameters of densities of $5 \times 10^3 \text{ cm}^{-3}$, FUV field of 7 and a total mass of $2 \times 10^7 M_{\odot}$.

Despite the challenges that one might expect in an early transfer flight of SOFIA to Germany, we were able to deduce important astrophysical results primarily owing to the high spectral resolution available with the GREAT receiver. These data demonstrate the promise of the GREAT/SOFIA facility for future work, such as detailed mapping of the [C II] emission from the central regions of IC 342 and other nearby galaxies.

Acknowledgements. We thank the SOFIA engineering and operations teams, whose tireless support and good-spirit teamwork has been essential for the GREAT accomplishments during Early Science, and say Herzlichen Dank to the DSI telescope engineering team. Based [in part] on observations made with the NASA/DLR Stratospheric Observatory for Infrared Astronomy. SOFIA Science Mission Operations are conducted jointly by the Universities Space Research Association, Inc., under NASA contract NAS2-97001, and the Deutsches SOFIA Institut under DLR contract 50 OK 0901. The research presented here was supported by the *Deutsche Forschungsgemeinschaft*, DFG through project number SFB956C.

References

- Crawford, M. K., Genzel, R., Townes, C. H., & Watson, D. M. 1985, ApJ, 291, 755
- Cubick, M., Stutzki, J., Ossenkopf, V., Kramer, C., & Röllig, M. 2008, A&A, 488, 623
- Downes, D., Radford, S. J. E., Guilloteau, S., et al. 1992, A&A, 262, 424
- Draine, B. T. 1978, ApJS, 36, 595
- Engelbracht, C. W., Rieke, G. H., Gordon, K. D., et al. 2008, ApJ, 678, 804
- Guan, X., Stutzki, J., Graf, U. U., et al. 2012, A&A, 542, L4
- Helfer, T. T., Thornley, M. D., Regan, M. W., et al. 2003, Ap&SS, 145, 259
- Herrmann, K. A., Ciardullo, R., Feldmeier, J. J., & Vinciguerra, M. 2008, ApJ, 683, 630
- Heyminck, S., Graf, U. U., Güsten, R., et al. 2012, A&A, 542, L1
- Ishizuki, S., Kawabe, R., Ishiguro, M., Okumura, S. K., & Morita, K.-I. 1990, Nature, 344, 224
- Israel, F. P., & Baas, F. 2003, A&A, 404, 495
- Meier, D. S., & Turner, J. L. 2001, ApJ, 551, 687
- Meier, D. S., & Turner, J. L. 2005, ApJ, 618, 259
- Meier, D. S., Turner, J. L., & Hurt, R. L. 2000, ApJ, 531, 200
- Röllig, M., Ossenkopf, V., Jeyakumar, S., Stutzki, J., & Sternberg, A. 2006, A&A, 451, 917
- Saha, A., Claver, J., & Hoessel, J. G. 2002, AJ, 124, 839
- Stacey, G. J., Geis, N., Genzel, R., et al. 1991, ApJ, 373, 423
- Störzer, H., Stutzki, J., & Sternberg, A. 1996, A&A, 310, 592
- Tikhonov, N. A., & Galazutdinova, O. A. 2010, Astron. Lett., 36, 167
- Turner, J. L., & Hurt, R. L. 1992, ApJ, 384, 72
- Turner, J. L., Hurt, R. L., & Hudson, D. Y. 1993, ApJ, 413, L19
- Wright, M. C. H., Ishizuki, S., Turner, J. L., Ho, P. T. P., & Lo, K. Y. 1993, ApJ, 406, 470

Submillimeter line emission from LMC 30 Doradus: The impact of a starburst on a low-metallicity environment

J. L. Pineda¹, N. Mizuno², M. Röllig³, J. Stutzki³, C. Kramer⁴, U. Klein⁵, M. Rubio⁶, A. Kawamura², T. Minamidani⁷, A. Benz⁸, M. Burton⁹, Y. Fukui¹⁰, B.-C. Koo¹¹, and T. Onishi¹²

¹ Jet Propulsion Laboratory, California Institute of Technology, 4800 Oak Grove Drive, Pasadena, CA 91109-8099, USA
e-mail: Jorge.Pineda@jpl.nasa.gov

² ALMA-J Project Office, National Astronomical Observatory of Japan, 2-21-1 Osawa, Mitaka, 181-8588 Tokyo, Japan

³ KOSMA, I. Physikalisches Institut, Universität zu Köln, Zülpicher Straße 77, 50937 Köln, Germany

⁴ Instituto Radioastronomía Milimétrica, Av. Divina Pastora 7, Nucleo Central, 18012 Granada, Spain

⁵ Argelander-Institut für Astronomie, Auf dem Hügel 71, 53121 Bonn, Germany

⁶ Departamento de Astronomía, Universidad de Chile, Casilla 36-D, Santiago, Chile

⁷ Department of Physics, Faculty of Science, Hokkaido University, N10W8, Kita-ku, 060-0810 Sapporo, Japan

⁸ Institute of Astronomy, ETH Zürich, 8093 Zürich, Switzerland

⁹ School of Physics, UNSW, Sydney, NSW 2052, Australia

¹⁰ Department of Astrophysics, Nagoya University, Chikusa-ku, 464-8602 Nagoya, Japan

¹¹ Seoul National University, Seoul 151-742, Korea

¹² Department of Astrophysics, Osaka Prefecture University, 1-1 Gakuen-cho, 599-8531 Osaka, Japan

Received 22 October 2011 / Accepted 15 June 2012

ABSTRACT

Context. The 30 Dor region in the Large Magellanic Cloud (LMC) is the most vigorous star-forming region in the Local Group. Star formation in this region is taking place in low-metallicity molecular gas that is exposed to an extreme far-ultraviolet (FUV) radiation field powered by the massive compact star cluster R136. 30 Dor is therefore ideally suited to study the conditions in which stars formed at earlier cosmological times.

Aims. Observations of (sub)mm and far-infrared (FIR) spectral lines of the main carbon-carrying species, CO, [C I] and [C II], which originate in the surface layers of molecular clouds illuminated by the FUV radiation of young stars, can be used to constrain the physical and chemical state of the star-forming ISM.

Methods. We used the NANTEX2 telescope to obtain high-angular resolution observations of the ^{12}CO $J = 4 \rightarrow 3$, $J = 7 \rightarrow 6$, and ^{13}CO $J = 4 \rightarrow 3$ rotational lines and [C I] $^3\text{P}_1 - ^3\text{P}_0$ and $^3\text{P}_2 - ^3\text{P}_1$ fine-structure submillimeter transitions in 30 Dor-10, the brightest CO and FIR-emitting cloud at the center of the 30 Dor region. We derived the physical and chemical properties of the low-metallicity molecular gas using an excitation/radiative transfer code and found a self-consistent solution of the chemistry and thermal balance of the gas in the framework of a clumpy cloud PDR model. We compared the derived properties with those in the N159W region, which is exposed to a more moderate far-ultraviolet radiation field compared with 30 Dor-10, but has similar metallicity. We also combined our CO detections with previously observed low- J CO transitions to derive the CO spectral-line energy distribution in 30 Dor-10 and N159W.

Results. The separate excitation analysis of the submm CO lines and the neutral carbon fine structure lines shows that the mid- J CO and [C I]-emitting gas in the 30 Dor-10 region has a temperature of about 160 K and a H₂ density of about 10^4 cm^{-3} . We find that the molecular gas in 30 Dor-10 is warmer and has a lower beam filling factor compared to that of N159W, which might be a result of the effect of a strong FUV radiation field heating and disrupting the low-metallicity molecular gas. We use a clumpy PDR model (including the [C II] line intensity reported in the literature) to constrain the FUV intensity to about $\chi_0 \approx 3100$ and an average total H density of the clump ensemble of about 10^5 cm^{-3} in 30 Dor-10.

Key words. ISM: general – submillimeter: ISM – galaxies: ISM – ISM: clouds – Magellanic Clouds

1. Introduction

The radiative feedback of star formation on its progenitor molecular gas is of great interest in modern astrophysics because it can be a determining factor in the regulation of star formation in galaxies. In particular, there is special interest in the interaction of stellar far-ultraviolet (FUV) photons with a lower metallicity, lower dust-to-gas ratio gas, because it is thought to be the material from which stars formed at earlier cosmological times.

The region of the interstellar medium where the chemistry and thermal balance is dominated by the influence of stellar FUV

photons is called a photon-dominated region (or photodissociation region, or PDR; Hollenbach & Tielemans 1999, and references therein). Owing to the reduced attenuation of FUV photons by dust in low-metallicity PDRs, the CO molecule is more readily photo-dissociated, increasing the abundance of C⁺ and C relative to that of CO. Therefore, the observational signatures of low-metallicity gas (increased [C II]/CO and [C I]/CO intensity ratios) are a result of the combined effect of a strong FUV radiation field and of reduced metallicity. It is therefore difficult to study separately the influence of these two parameters on the properties of the low-metallicity molecular gas.

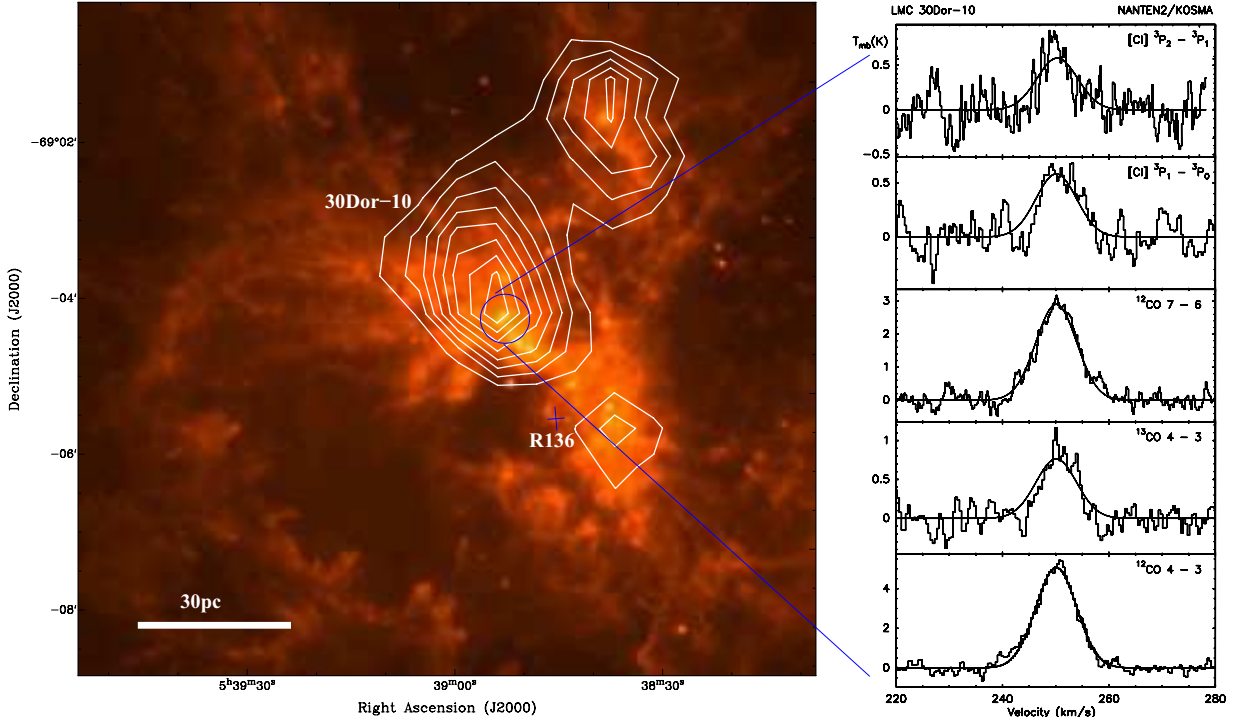


Fig. 1. (Left panel) *Spitzer* 8 μm emission map of the 30 Dor region (Meixner et al. 2006) overlaid by an integrated intensity map of the ^{12}CO $J = 1 \rightarrow 0$ line (Wong et al. 2011). The contour levels correspond to 20% to 80% of the peak intensity (11.3 K km s^{-1}), in steps of 10%. The angular resolution of the *Spitzer* 8 μm and CO maps are 2'' and 45'', respectively. The center of the R136 super star cluster and the NANTEL2 38'' beam are marked by a cross and a circle, respectively. (Right panel) Observed lines and corresponding Gaussian fits.

The Large Magellanic Cloud is an ideal extragalactic laboratory in which to study star formation in low-metallicity environments. Its proximity (50 kpc; Feast 1999) and nearly face-on orientation ($i = 35^\circ$; van der Marel & Cioni 2001) allow us to isolate individual clouds and study them at the highest spatial resolution possible for external galaxies. The LMC also shows strongly varying FUV radiation fields and therefore very different physical conditions in a low-metallicity ($Z_\odot \approx 0.4 Z_\odot$; Westerlund 1997) interstellar medium.

Regions of special interest are the molecular clouds associated with the 30 Doradus H II complex. This complex is powered by one of the most dense and massive star clusters in the local universe, R136. Therefore, the 30 Doradus region exemplifies the special case in which the low-metallicity molecular gas is exposed to a very strong FUV radiation field. Among several CO-clouds located around R136, the 30 Dor-10 cloud (Johansson et al. 1998) is associated with the center of the 30 Dor nebula. The *Spitzer* 8 μm and CO maps shown in Fig. 1 show that this region is the brightest CO cloud at the center of 30 Dor and is located at a projected distance of 20 pc from the center of R136. This proximity to R136 and the presence of associated 8 μm sources, which might indicate embedded star formation, suggest that the gas in 30 Dor-10 is exposed to an extreme FUV environment. The CO peak of 30 Dor-10 also associated with the [C II] (Poglitsch et al. 1995) and FIR (Werner et al. 1978) peaks. Although 30 Dor-10 is the CO peak at the center of the 30 Dor nebula, the sub-mm CO and [C I] line intensities are weaker compared with other active regions in the LMC (e.g. N159W; Pineda et al. 2008). On scales of about 10 pc, several low- J transitions of ^{12}CO and ^{13}CO have been observed in this cloud (Johansson et al. 1998; Minamidani et al. 2008, 2011) as well as the [C II] 158 μm line (Boreiko & Betz 1991; Poglitsch et al. 1995). At larger spatial scales of about 50 pc, the

^{12}CO $J = 7 \rightarrow 6$, ^{12}CO $J = 4 \rightarrow 3$ and [C I] $^3\text{P}_1 \rightarrow ^3\text{P}_0$ lines have been observed with the AST/RO telescope (Stark et al. 1997; Kim 2006).

In this paper we present observations of the ^{12}CO $J = 4 \rightarrow 3$, $J = 7 \rightarrow 6$, and ^{13}CO $J = 4 \rightarrow 3$ rotational and [C I] $^3\text{P}_1 \rightarrow ^3\text{P}_0$ and $^3\text{P}_2 \rightarrow ^3\text{P}_1$ fine-structure transitions in the 30 Dor-10 cloud in the LMC using the NANTEL2 telescope. The angular resolution of these observations allow us for the first time to study submillimeter lines at spatial scales of about 10 pc. We complement this data set with low- J ^{12}CO and ^{13}CO transitions observed with Mopra, and ASTE, with similar angular resolution.

The physical conditions of the molecular gas in 30 Dor-10 are compared with those derived in a region with a similar metallicity but with a more moderate incident FUV radiation field, the LMC N159W region (Pineda et al. 2008). N159W is located in one the edges of the N159 H II region and is actively forming massive stars, as suggested by the presence of several embedded massive young stellar objects (Chen et al. 2010). However, the FUV and H α fluxes in N159 are 10-20 and 7 times lower than in the 30 Dor region, respectively, suggesting that although N159W is an active region it does not have the extreme FUV environment to which 30 Dor-10 is exposed. The comparison between the physical conditions of the gas in 30 Dor-10 and N159W will help us to understand the effects of the strength of the FUV field on the properties of the low-metallicity molecular gas in the LMC.

This paper is organized as follows. We describe the NANTEL2 observations in Sect. 2 and the observational results in Sect. 3. We derive physical properties of the low-metallicity molecular gas using a radiative transfer code independently for the CO and [C I] lines in Sect. 4. We give a self-consistent solution of the chemistry and thermal balance of the gas using a clumpy photon-dominated region (PDR) model in Sect. 5. We

Table 1. Gaussian-fit line parameters derived from the NANTEN2 observations of LMC 30Dor-10 and from the literature.

Line	Amplitude ^a [K]	Center ^b [km s ⁻¹]	FWHM ^b [km s ⁻¹]	Integrated intensity [K km s ⁻¹]
NANTEN2 data				
¹² CO $J = 4 \rightarrow 3$	5.06 (0.19)	250.1 (0.053)	9.02 (0.13)	48.5 (1.9)
¹² CO $J = 7 \rightarrow 6$	2.89 (0.19)			27.7 (1.7)
¹³ CO $J = 4 \rightarrow 3$	0.76 (0.14)			7.3 (1.3)
[C I] $^3\text{P}_1 \rightarrow ^3\text{P}_0$	0.58 (0.14)			5.6 (1.3)
[C I] $^3\text{P}_2 \rightarrow ^3\text{P}_1$	0.58 (0.19)			5.6 (1.8)
Literature data ^c				
¹² CO $J = 1 \rightarrow 0$	1.1 (0.03)	250.3 (0.1)	8.79 (0.23)	11.3 (0.27)
¹² CO $J = 3 \rightarrow 2$	5.2 (0.4)	250.4 (0.1)	8.4 (0.23)	49.6 (0.27)
¹³ CO $J = 1 \rightarrow 0$	0.17 (0.02)	250.7 (0.27)	5.35 (0.64)	0.88 (0.12)
[C II] $^2\text{P}_{3/2} \rightarrow ^2\text{P}_{1/2}$	6.3 (0.6)	247.8 (1.6)	20.5 (1.8)	109.4 (8.5)

Notes. ^(a) The rms noise for lines observed with NANTEN2 are for channel widths of 0.37 km s⁻¹ and 0.21 km s⁻¹ for the 460–490 and 810 GHz channels, respectively. ^(b) Center and width fixed to ¹²CO $J = 4 \rightarrow 3$ best-fit values for NANTEN2 data other than this line. ^(c) References for literature data are presented in Sect. 3.2.

compare our results to those constrained in the LMC-N159W region in Sect. 6.1 and we study the CO spectral line distribution in both regions in Sect. 6.2. We summarize the results in Sect. 7.

2. Observations

We used the new NANTEN2 4-m telescope situated at 4865 m altitude at Pampa la Bola in northern Chile to observe the ¹²CO $J = 4 \rightarrow 3$ (461.0408 GHz), $J = 7 \rightarrow 6$ (806.6517 GHz), and ¹³CO $J = 4 \rightarrow 3$ (440.7654 GHz) rotational and [C I] $^3\text{P}_1 \rightarrow ^3\text{P}_0$ (492.1607 GHz) and $^3\text{P}_2 \rightarrow ^3\text{P}_1$ (809.3446 GHz) fine-structure transitions toward LMC 30 Dor-10. The line parameters derived from the NANTEN2 observations of LMC 30 Dor-10 are listed in Table 1 and the observed spectra are shown in Fig. 1.

The observations were made toward the peak ¹²CO $J = 1 \rightarrow 0$ intensity position in 30 Dor-10 (Johansson et al. 1998), located at $\alpha = 5^{\text{h}}38^{\text{m}}48\overset{\text{s}}{.}56$ and $\delta = -69^{\circ}04'43\overset{\text{s}}{.}2$ (J2000), using the total-power observing mode. We used a reference position at $\alpha = 5^{\text{h}}39^{\text{m}}33\overset{\text{s}}{.}7$ and $\delta = -69^{\circ}04'00\overset{\text{s}}{.}0$ (J2000), which is free of ¹²CO $J = 1 \rightarrow 0$ emission. The duration of each beam switch cycle was varied between 20 and 30 s, depending on the atmospheric stability during the observations. The final spectra result from total on-position integration times of 40 min to about 3 h. The pointing was checked regularly on Jupiter, IRC+10216, and IRc2 in OrionA. The applied corrections were always smaller than 10''. We do not expect significant uncertainties in the line fluxes due to pointing errors because the CO flux distribution in 30 Dor-10 is smooth at scales smaller than 10'' (e.g. Minamidani et al. 2008). The angular resolution of the observations is 38'' for the 460–490 GHz and 26'' for the 810 GHz channel, respectively. The main beam efficiencies are 0.5 and 0.4 for the 460–490 GHz and 810 GHz channels, respectively.

The observations were conducted with a dual-channel 460/810 GHz receiver installed for verifying the submillimeter performance of the telescope. Double-sideband (DSB) receiver temperatures were ~ 250 K in the lower channel and ~ 750 K in the upper channel. The intermediate frequencies (IF) are 4 GHz and 1.5 GHz, respectively. The latter IF allows simultaneous observations of the ¹²CO $J = 7 \rightarrow 6$ line in the lower and of the [C I] $^3\text{P}_2 \rightarrow ^3\text{P}_1$ line in the upper sideband. These two lines were observed simultaneously with one of the lines in the

460 GHz channel. As backends we used two acousto-optical spectrometers (AOS) with a bandwidth of 1 GHz and a channel resolution of 0.37 km s⁻¹ at 460 GHz and 0.21 km s⁻¹ at 806 GHz.

As discussed in Pineda et al. (2008), the main sources of uncertainty in the absolute line calibration are the precision with which the beam efficiencies are determined and the accuracy of the atmospheric calibration. We estimate that both sources of uncertainty contribute to a total absolute calibration uncertainty of 20%. In our analysis we added these errors quadratically with the radiometric noise, assumed to be given by the formal errors of the Gaussian fits. Propagating these absolute calibration uncertainties for line ratios between lines in the 460–490 and 810 GHz channels, we obtain a relative calibration uncertainty of 28%. Line ratios between lines located in the same frequency channel do not suffer from the uncertainty on the determination of the beam efficiencies ($\sim 10\%$) and we propagate the errors only considering the uncertainties on the atmospheric calibration ($\sim 17\%$).

3. Observational results

3.1. NANTEN2 data

The spectra observed toward 30 Dor-10 are shown in Fig. 1, together with Gaussian fits whose results are listed in Table 1. We determined the line center and width from the high signal-to-noise ¹²CO $J = 4 \rightarrow 3$ spectrum and we held them fixed for the Gaussian fit of the line amplitude of the other lines. This method is adequate because their profiles are, within their limited signal-to-noise ratio, consistent with that of the ¹²CO $J = 4 \rightarrow 3$ line.

To calculate intensity ratios between lines in the upper and lower frequency channels we need to account for the different beam sizes (38'' and 26'', respectively). We therefore determined the source extent using lower resolution data. As described in Pineda et al. (2008), assuming a Gaussian source distribution with FWHM Θ_s and a source peak brightness temperature of $T_{s,\text{peak}}$, the beam filling correction gives a main beam brightness temperature in a beam of $FWHM\Theta_b$ of $T_{mb} = \Theta_s^2 / (\Theta_s^2 + \Theta_b^2) T_{s,\text{peak}}$. The ratio of the main beam brightness temperature in two different beams 1 and 2 is given by $R_{1,2} = T_{mb,1} / T_{mb,2} = (\Theta_{b,2}^2 + \Theta_s^2) / (\Theta_{b,1}^2 + \Theta_s^2)$. With this, we can

Table 2. Observed line intensity ratios, corrected for beam coupling to an assumed common FWHM source size of 90''.

Species	Ratio ^a	Fit error	Calibration error	Total error
$^{12}\text{CO } J = 7 \rightarrow 6 / ^{12}\text{CO } J = 4 \rightarrow 3$	0.52	0.04	28%	0.15
$[\text{C I}] ^3\text{P}_2 \rightarrow ^3\text{P}_1 / [\text{C I}] ^3\text{P}_1 \rightarrow ^3\text{P}_0$	0.92	0.37	28%	0.45
$^{13}\text{CO } J = 4 \rightarrow 3 / ^{12}\text{CO } J = 4 \rightarrow 3$	0.15	0.03	17%	0.05
$[\text{C I}] ^3\text{P}_2 \rightarrow ^3\text{P}_1 / \text{CO } J = 7 \rightarrow 6$	0.20	0.07	17	0.09
$^{12}\text{CO } J = 1 \rightarrow 0 / ^{12}\text{CO } J = 4 \rightarrow 3$	0.22	0.05	28%	0.08
$^{13}\text{CO } J = 1 \rightarrow 0 / ^{12}\text{CO } J = 1 \rightarrow 0$	0.08	0.01	28%	0.02
$[\text{C II}] ^2\text{P}_{3/2} \rightarrow ^2\text{P}_{1/2} / ^{12}\text{CO } J = 4 \rightarrow 3$	1.24	0.13	28%	0.37

Notes. ^(a) Ratio of amplitudes from Gaussian fits.

derive the source size from the observed brightness ratio in two beam sizes:

$$\Theta_s^2 = \frac{R_{1,2}\Theta_{b,1}^2 - \Theta_{b,2}^2}{1 - R_{1,2}}. \quad (1)$$

With the source size we can correct the observed intensity ratios for the beam coupling of the different beam sizes at two observing bands x and y to the source intrinsic intensity ratio R_s via

$$R_s = \frac{T_{\text{mb},x}}{T_{\text{mb},y}} \frac{\Theta_s^2 + \Theta_{b,x}^2}{\Theta_s^2 + \Theta_{b,y}^2}. \quad (2)$$

We used observations of the $[\text{C I}] ^3\text{P}_1 \rightarrow ^3\text{P}_0$ line made with the SWAS satellite (Frank Bensch, priv. comm.) with an angular resolution of 258''. The integrated line intensity of this line observed by SWAS is 0.44 K km s⁻¹. With NANTEN2 we obtained an integrated line intensity of 5.58 K km s⁻¹ in a 38'' beam. Thus, from Eq. (1) we obtain a source size of $\Theta_s = 64''$, which according to Eq. (2), corresponds to a 18% correction to the line ratios between the upper and lower channels. We also determined the source size by considering the $^{12}\text{CO } J = 1 \rightarrow 0$ integrated line intensity observed by the NANTEN telescope (e.g. Fukui et al. 2008) of 4.1 K km s⁻¹ in a 158'' beam and by the Mopra telescope (Jürgen Ott, priv. comm.) of 11.3 K km s⁻¹ in a 33'' beam. Equation (1) results in a source size of $\Theta_s = 110''$, corresponding to a 8% correction. We assumed an intermediate value for the source size of $\Theta_s = 90''$ corresponding to a correction of 10%. A source size of 90'' is consistent with the angular size of 30 Dor-10's CO-emitting region shown in Fig. 1. We note that assuming a source size introduces an uncertainty of about 5% to the line ratios between the upper and lower channels. The correction also assumes that the source structure is the same at the spatial scales observed with the 460 and 810 GHz channels. The validity of this assumption likely dominates the uncertainties in the line ratios. However, as we will see in Sects. 4 and 5, the good fit obtained for the physical parameters supports this assumption. Table 2 shows the line ratios thus corrected, which we used for the excitation analysis discussed below.

Kim et al. (2005) presented maps of the $^{12}\text{CO } J = 4 \rightarrow 3$ line in the 30 Dor region with a 109'' beam using the AST/RO telescope. In addition to the $^{12}\text{CO } J = 4 \rightarrow 3$ component at ~ 250 km s⁻¹ they detected another component at ~ 302 km s⁻¹, a factor of ~ 3 weaker. We did not find this additional component in our $^{12}\text{CO } J = 4 \rightarrow 3$ spectrum. Considering their derived FWHM line-width for this component of 5.1 km s⁻¹, we derive an 3σ upper limit of 0.52 K km s⁻¹, which is a factor of ~ 10 weaker than the main component of $^{12}\text{CO } J = 4 \rightarrow 3$ in 30 Dor-10.

3.2. Additional lines from the literature

To better constrain the physical parameters of the emitting gas in 30 Dor-10, we combined the lines observed with NANTEN2 with additional observations of the $^{12}\text{CO } J = 1 \rightarrow 0, J = 3 \rightarrow 2$, $^{13}\text{CO } J = 1 \rightarrow 0$ and $[\text{C II}] 158 \mu\text{m}$ lines. The ^{12}CO and $^{13}\text{CO } J = 1 \rightarrow 0$ lines were observed with the ATNF Mopra 22 m telescope (Jürgen Ott, priv. comm.) at the position of the NANTEN2 observations. The data have an angular resolution of 33'' and a channel width of 0.7 km s⁻¹. The $^{12}\text{CO } J = 3 \rightarrow 2$ observations were observed with the ASTE telescope and were presented by Minamidani et al. (2008). The angular resolution for both lines is about 22'' and the channel width is 0.45 km s⁻¹. The Kuiper Airborne Observatory (KAO) observed velocity-resolved $[\text{C II}] 158 \mu\text{m}$ emission toward 30 Dor-10 with an angular resolution of 43'' (Boreiko & Betz 1991). The pointing of the KAO observations is about 20'' farther southwest than the NANTEN2 position. We adopted their values without further corrections. Indeed, the integrated intensity of the $[\text{C II}]$ line from the KAO observations of 7.7×10^{-4} erg cm⁻² s⁻¹ sr⁻¹ is consistent to within 30% with the integrated intensity at the position of the NANTEN2 observations in the $[\text{C II}]$ map published by Poglitsch et al. (1995), observed with low-velocity resolution ($\Delta v = 75$ km s⁻¹) using the FIFI spectral imaging instrument on the KAO. In Table 3 we present a summary of rest frequencies, energies above the ground level, and critical densities of the spectral lines used in our analysis.

We assumed that the uncertainty of the absolute calibration of all independently observed lines is about 20%, and propagated these errors to obtain a line ratio calibration accuracy of 28%. Table 2 quotes the derived total errors, obtained by quadratically summing the formal fit error and the calibration uncertainty.

4. Excitation analysis

We first constrained the properties of the emitting gas by comparing line intensity ratios and absolute intensities with the results of a radiative transfer code. We analyzed $[\text{C I}]$ and CO separately, but assume that they originate from the same regions with identical beam filling factors. This assumption is justified considering that the CO and $[\text{C I}]$ emission arise from the FUV illuminated surfaces of clouds that are unresolved at the scale of our observations.

We used the RADEX non-LTE radiative transfer code by van der Tak et al. (2007), using the uniform sphere approximation, to calculate line intensities as a function of the kinetic temperature, H₂ volume density, and the column density per velocity interval $N/\Delta v$ of the species of interest. The collision cross sections were taken from the Leiden Atomic and Molecular Database (LAMDA; Schöier et al. 2005). The code provides the average line intensity of a spherical cloud. We therefore scaled

the data by a filling factor to compare them with the observed absolute intensities. As mentioned above, considering a medium consisting of clumps that are much smaller than the scale of our observations, the C I and CO species can be considered as occupying the same volume, hence the line ratios are independent of beam dilution. For optically thin clumps (or for clumps with moderate opacity), the observed-to-model integrated intensity ratio gives the ratio of the beam-averaged column density to the clump intrinsic column density, assuming that the total integrated intensity is proportional to the number of clumps, i.e. no velocity crowding is present. We therefore determined the beam filling by comparing the observed absolute intensity of a line with a constrained model.

4.1. [C I]-emission

In Table 2 we see that the ratio between the two [C I] lines is 0.92. We compare this ratio with predictions from the radiative transfer calculations in Fig. 2. We present model line ratios for three different kinetic temperatures 80, 120, and 160 K, as a function of the [C I] column density per velocity interval, $N_{[C\text{I}]}/\Delta v$, and H₂ volume density, $n(\text{H}_2)$. The coverage in $N_{[C\text{I}]}/\Delta v$ is $10^{15}\text{--}10^{19}\text{ cm}^{-2}$ and in $n(\text{H}_2)$ is $10^2\text{--}10^6\text{ cm}^{-3}$. The observed ratio can only be reproduced by kinetic temperatures above 60 K and H₂ densities of about $1\text{--}3 \times 10^3\text{ cm}^{-3}$. This H₂ density is similar to, or somewhat higher than, the critical density of the [C I] ${}^3\text{P}_1 \rightarrow {}^3\text{P}_0$ line ($\sim 1 \times 10^3\text{ cm}^{-3}$), and therefore its emission is close to being thermalized. From the analysis of the CO emission (see below) we found that the beam-filling factor in 30 Dor-10 is about 1/16, so that the observed [C I] ${}^3\text{P}_1 \rightarrow {}^3\text{P}_0$ brightness of 0.58 K should be scaled up to 9.3 K. This brightness temperature corresponds to a [C I] column density per velocity interval of about $1 \times 10^{17}\text{ cm}^{-2}/\text{km s}^{-1}$. The multiplication by a filling factor is appropriate because, in the range of kinetic temperatures and H₂ densities inferred above, the [C I] ${}^3\text{P}_1 \rightarrow {}^3\text{P}_0$ line is likely optically thin.

4.2. CO-emission

We compare the observed ${}^{12}\text{CO } J = 7 \rightarrow 6 / {}^{12}\text{CO } J = 4 \rightarrow 3$ and ${}^{13}\text{CO } J = 4 \rightarrow 3 / {}^{12}\text{CO } J = 4 \rightarrow 3$ ratios with predictions of the radiative transfer code in Fig. 3. We assumed the ${}^{12}\text{CO}/{}^{13}\text{CO}$ abundance ratio of 35 derived in 30 Dor-10 by Heikkilä et al. (1999). We required that the volume density of the CO-emitting region is equal to, or somewhat higher than, that constrained for the [C I] emission, because we expect that both [C I] and mid-J CO lines are emitted from adjacent layers in a PDR-like structure¹, where the neutral carbon is located in an equal or lower-density region compared to the one at which CO is located, and that the cloud's volume density profile is smooth. In Fig. 3, this condition is only valid for kinetic temperatures higher than 120 K for a volume density range between $3 \times 10^3\text{--}10^4\text{ cm}^{-3}$. The intersection of the two CO line ratios constrains the CO column density per velocity interval to about $3 \times 10^{17}\text{ cm}^{-2}/\text{km s}^{-1}$ at $T_{\text{kin}} \approx 160\text{ K}$. The derived kinetic temperature and H₂ density are consistent with previously published excitation analyzes based on CO observations (Johansson et al. 1998; Kim 2006; Minamidani et al. 2008, 2011).

Figure 4 shows that the model-predicted clump-averaged absolute line intensity of the ${}^{13}\text{CO } J = 4 \rightarrow 3$ line, at the column

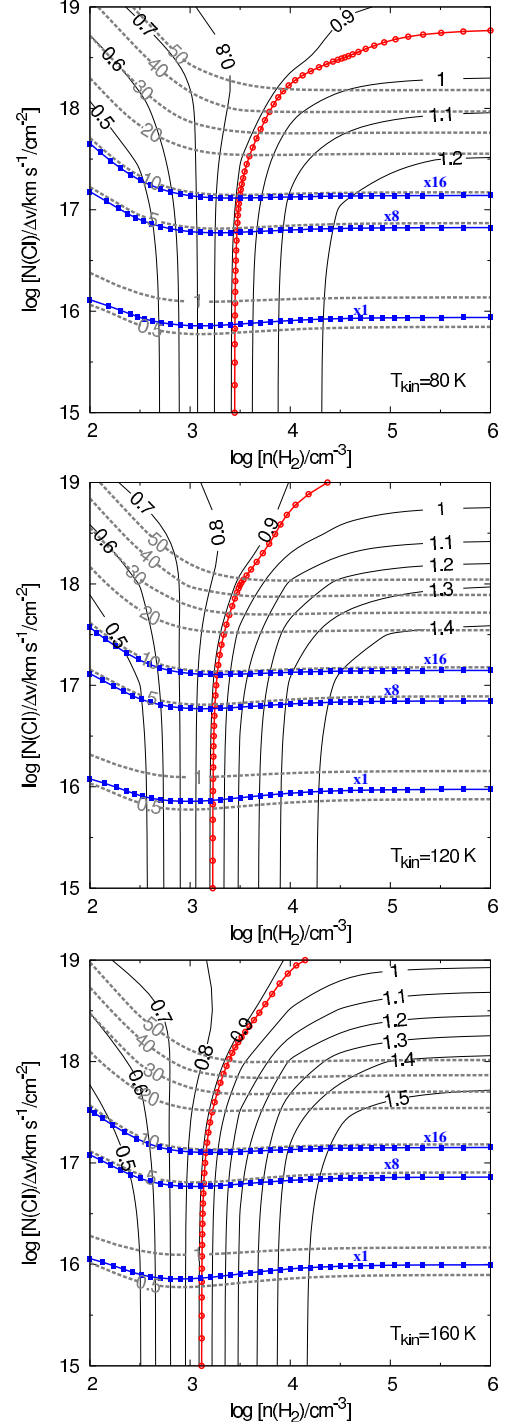


Fig. 2. Comparison between the observations and the predictions from the radiative transfer model for the [C I] ${}^3\text{P}_2 \rightarrow {}^3\text{P}_1$ /[C I] ${}^3\text{P}_1 \rightarrow {}^3\text{P}_0$ line ratio (black-solid lines) and the [C I] ${}^3\text{P}_1 \rightarrow {}^3\text{P}_0$ absolute intensity (gray-dashed lines) for kinetic temperatures of 80, 120, and 160 K. The observed [C I] ${}^3\text{P}_2 \rightarrow {}^3\text{P}_1$ /[C I] ${}^3\text{P}_1 \rightarrow {}^3\text{P}_0$ line ratio of 0.92 is shown as a red line with circles. The observed [C I] ${}^3\text{P}_1 \rightarrow {}^3\text{P}_0$ line intensity of 0.58 K and its value scaled by a beam filling factor of 1/8 and 1/16 are shown as blue lines with boxes.

and volume density regime constrained by the observed line ratios, is about 16 times higher than that observed at $T_{\text{kin}} = 160\text{ K}$. This implies a beam filling factor for CO of about 1/16, which corresponds to a typical clump size of $10''$. Recent ATCA observations of HCO⁺ revealed several compact clumps in 30 Dor-10 (Anderson et al., in prep.). The clumps have a typical angular

¹ For an example of a typical temperature distribution and abundance structure of the main carbon species in PDRs, see e.g. Figs. 7 and 9 in Tielens & Hollenbach (1985).

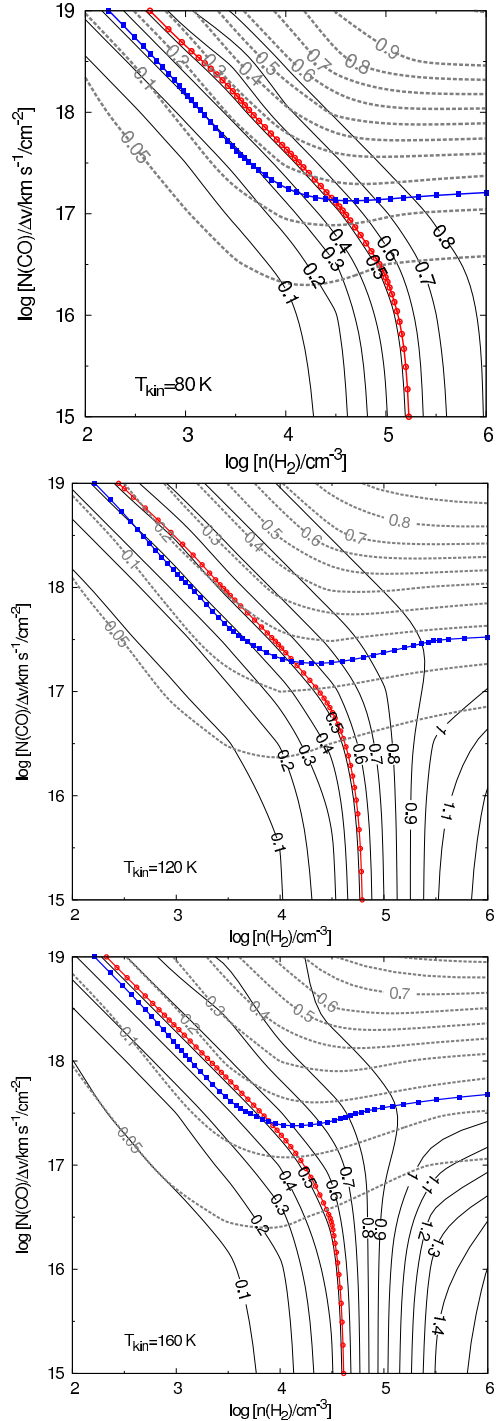


Fig. 3. Comparison between the observations and the predictions from the radiative transfer model for the $^{12}\text{CO } J = 7 \rightarrow 6$ to $J = 4 \rightarrow 3$ (black-solid contours) and ^{13}CO to $^{12}\text{CO } J = 4 \rightarrow 3$ (gray-dashed contours) line ratios for kinetic temperatures of 80, 120, and 160 K. The plots assume a fractional abundance of $^{12}\text{CO}/^{13}\text{CO}$ of 35. The observed $^{12}\text{CO } J = 7 \rightarrow 6$ to $J = 4 \rightarrow 3$ ratio of 0.52 is shown as a blue line with boxes while the ^{13}CO to $^{12}\text{CO } J = 4 \rightarrow 3$ ratio of 0.15 is shown as a red line with circles.

size of $10''$, and are marginally resolved at the resolution of their observations, $6''$. More observations with higher angular resolution are required to confirm the observed clump sizes in 30 Dor-1.

In Fig. 5 we consider line ratios involving the ^{12}CO and $^{13}\text{CO } J = 1 \rightarrow 0$ transitions for $T_{\text{kin}} = 160$ K. The $^{12}\text{CO } J = 1 \rightarrow 0$

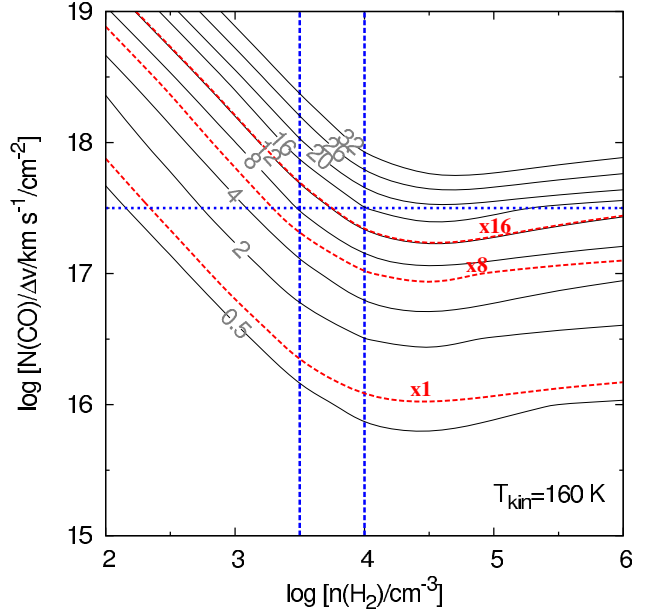


Fig. 4. Radiative transfer predictions and the observed absolute intensity of $^{13}\text{CO } J = 4 \rightarrow 3$ for $T_{\text{kin}} = 160$ K. The three red-dashed contours show the observed intensity and its value scaled up by factors of 8 and 16, respectively. The blue-dashed lines show the range of column and volume densities constrained by the analysis of the CO line ratios. The absolute intensity of $^{13}\text{CO } J = 4 \rightarrow 3$ needs to be scaled up by a factor of about 16 to reproduce the constrained column and volume densities.

to $J = 4 \rightarrow 3$ ratio of 0.21, however, suggests lower column and higher volume densities than those constrained above. The low $^{12}\text{CO } J = 1 \rightarrow 0$ to $J = 4 \rightarrow 3$ ratio is due to the observed $^{12}\text{CO } J = 1 \rightarrow 0$ line that is too weak for the physical conditions we derived. The observed $^{13}\text{CO}/^{12}\text{CO}$ ratio is therefore also affected by this weaker $^{12}\text{CO } J = 1 \rightarrow 0$ emission. This may indicate an additional colder gas component. We were only able to reproduce absolute intensities of the ^{12}CO and $^{13}\text{CO } J = 1 \rightarrow 0$ lines using a model with the conditions obtained for the column and volume density derived for [C_I] (Sect. 4.1) and kinetic temperatures of $T_{\text{kin}} = 10$ –30 K. This is consistent with observations of higher density tracers, suggesting a colder (~ 50 K) and denser ($\sim 10^5 \text{ cm}^{-3}$) gas component in 30 Dor-1 (Heikkilä et al. 1999).

4.3. [C_I] and CO column densities

Combining our estimate of the CO and C_I column density per velocity interval, the observed line width of 9 km s^{-1} , and the beam filling factor of 1/16, we derive a beam-averaged column density of $1.7 \times 10^{17} \text{ cm}^{-2}$ and $5.6 \times 10^{16} \text{ cm}^{-2}$ for CO and C_I, respectively. Thus, the ratio of the column density of [C_I] to that of CO is ~ 3 . Since the ^{12}CO and $^{13}\text{CO } J = 1 \rightarrow 0$ lines indicate an additional, cooler component, this ratio is an upper limit. Assuming that all gas-phase carbon is in the form of C_I and CO in their respective line-emitting regions, we used a carbon abundance relative to H₂ in the LMC of 1.6×10^{-4} (derived from [C]/[H] = 8×10^{-5} ; Dufour et al. 1982) to obtain an H₂ mass of $1625 M_{\odot}$ associated with CO and of $531 M_{\odot}$ associated with C_I. Thus, the total mass within the beam of our observations is $2156 M_{\odot}$. Note that our beam size of $38'' \text{ FWHM}$ corresponds to 9.5 pc at the distance of the LMC and hence covers 1/2 of the 30 Dor-10 cloud's extent of about 20 pc. If the H₂ column

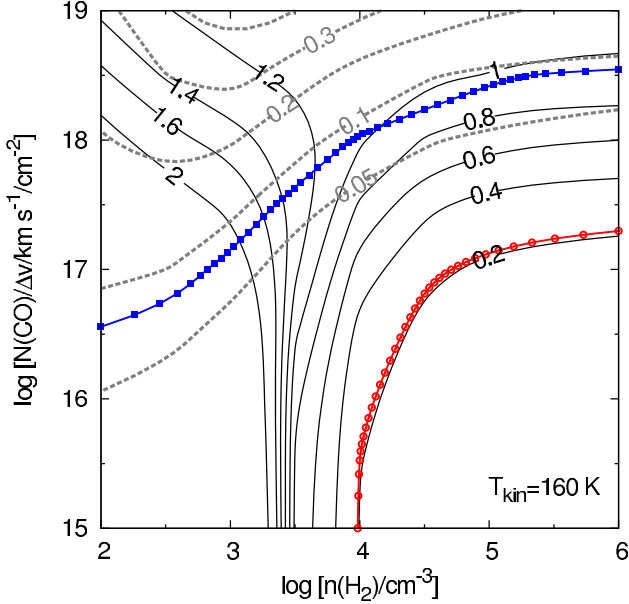


Fig. 5. Comparison between the observations and the predictions from the radiative transfer model for the $^{12}\text{CO } J = 1 \rightarrow 0$ and $J = 4 \rightarrow 3$ line ratios (black-solid contour) and the ^{13}CO to $^{12}\text{CO } J = 1 \rightarrow 0$ line ratio (gray-dashed contour) for $T_{\text{kin}} = 160$ K. The observed ^{13}CO to $^{12}\text{CO } J = 1 \rightarrow 0$ ratio of 0.08 is shown as a blue line with boxes while the $^{12}\text{CO } J = 1 \rightarrow 0$ to $J = 4 \rightarrow 3$ ratio of 0.22 is shown as a red line with circles.

density is uniform over 30 Dor-10, the total mass of the cloud should be a factor of 4 larger than the mass derived within the beam of our observations, reflecting the difference in area. Thus, the total H_2 mass in 30 Dor-10 should be about $8.6 \times 10^4 M_\odot$. This derived mass agrees well with the CO-luminosity mass of $8.5 \times 10^4 M_\odot$ derived by Johansson et al. (1998) assuming a CO-to- H_2 conversion factor of $4 \times 10^{20} \text{ cm}^{-2} (\text{K km s}^{-1})^{-1}$ (e.g. Israel 1997; Hughes et al. 2010; Pineda et al. 2009). Note that some H_2 might be not traced by CO or $[\text{C I}]$ but by $[\text{C II}]$ (the “hidden H_2 gas”). This can account for about 30–50% of the H_2 in the Galaxy (e.g. Grenier et al. 2005; Langer et al. 2010; Velusamy et al. 2010; Planck Collaboration 2011), and is expected to have an even larger mass in low-metallicity environments (Madden et al. 1997; Wolfire et al. 2010). Therefore, the mass estimate derived here should be considered a lower limit to the total H_2 mass.

5. PDR-model analysis

In the following we investigate whether our observations toward 30 Dor-10 can be explained in terms of an ensemble of PDRs distributed in a clumpy interstellar medium. We used the KOSMA- τ PDR model (Störzer et al. 1996; Röllig et al. 2006) to model an ensemble of spherical clumps with a power-law mass spectrum $dN/dM \propto M^{-1.8}$ and a mass-size relation $M \propto r^{2.3}$ (Cubick et al. 2008). The model provides a self-consistent solution of the chemistry and thermal balance. The free parameters of the clumpy PDR ensemble are (1) average ensemble total H volume density ($n_{\text{H}} + 2n_{\text{H}_2}$), n_{ens} , (2) ensemble mass, M_{ens} , (3) strength of the FUV radiation field in units of the Draine (1978) field, χ_0 , and (4) the minimum and maximum mass of the clump ensemble, $[M_{\text{min}}, M_{\text{max}}]$. We fix the metallicity in the model to $Z_\odot = 0.4$. We attempted to fit the observed lines with a model with $Z_\odot = 1$, but this solar metallicity model could not reproduce the mid- J CO observations with a χ^2 about factor of

Table 3. Parameters for different relevant molecular and atomic transitions.

Line	Frequency/GHz	$E_{\text{upper}}/\text{K}$	$n_{\text{cr}}/\text{cm}^{-3}$
$^{12}\text{CO } J = 1 \rightarrow 0$	115.2712	5.5	2×10^3
$^{12}\text{CO } J = 3 \rightarrow 2$	345.7959	33.2	4×10^4
$^{12}\text{CO } J = 4 \rightarrow 3$	461.0408	55.3	9×10^4
$^{12}\text{CO } J = 7 \rightarrow 6$	806.6517	154.9	4×10^5
$^{12}\text{CO } J = 9 \rightarrow 8$	1036.912	248.9	1×10^6
$^{13}\text{CO } J = 1 \rightarrow 0$	110.2013	5.3	2×10^3
$^{13}\text{CO } J = 4 \rightarrow 3$	440.7654	52.9	8×10^4
$[\text{C II}] ^3\text{P}_1 \rightarrow ^3\text{P}_0$	492.1607	23.6	1×10^3
$[\text{C II}] ^3\text{P}_2 \rightarrow ^3\text{P}_1$	809.3446	62.5	1×10^3
$[\text{O I}] ^3\text{P}_1 \rightarrow ^3\text{P}_2$	4744.777	227.7	6×10^5
$[\text{O I}] ^3\text{P}_0 \rightarrow ^3\text{P}_1$	2060.069	326.6	7×10^4
$[\text{C II}] ^2\text{P}_{3/2} \rightarrow ^2\text{P}_{1/2}$	1900.5377	91.2	5×10^3

Notes. The listed critical densities were calculated for collisions with $p\text{-H}_2$ and a kinetic temperature of 100 K. The critical densities were calculated using the Einstein A – and collisional rate coefficients taken from the Leiden Atomic and Molecular Database (LAMDA; Schöier et al. 2005).

10 larger than for the low-metallicity model. Note that we assumed that the clumps do not spatially overlap, therefore we considered optical depth effects only within individual clumps. We also assumed that the FUV field is uniform within the beam of the observations.

We constrained the model with the absolute intensities of all five lines observed with NANTEN2 together with the $^{12}\text{CO } J = 3 \rightarrow 2$ and $[\text{C II}] 158 \mu\text{m}$ lines taken from the literature (Sect. 3.2). Fitting absolute line intensities instead of line ratios allowed us to study the internal structure of the cloud (clumpiness) via the area and volume filling factors, and it adds the cloud mass and size as model parameters. The source size was fixed to be $90''$ (Sect. 3.1). We did not include the ^{12}CO and $^{13}\text{CO } J = 1 \rightarrow 0$ transitions in the model fit because these transitions are likely affected by optical depth effects between clumps that are not accounted for by the model. We still compared the intensities of the ^{12}CO and $^{13}\text{CO } J = 1 \rightarrow 0$ transitions with the predictions of the PDR model and discuss below the possible reason of the discrepancy between model and observations. We used simulated annealing to find the optimum model parameter combination that predicts absolute line intensities that match those observed.

The best-fit model results suggest an average ensemble total H volume density $n_{\text{ens}} = 3.3 \times 10^5 \text{ cm}^{-3}$, an ensemble mass $M_{\text{ens}} = 1.2 \times 10^5 M_\odot$. The minimum and maximum masses of the clump ensemble are $M_{\text{min}} = 1 \times 10^{-3} M_\odot$ and $M_{\text{max}} = 0.1 M_\odot$. Note that n_{ens} corresponds to the average total H volume density (i.e. $n_{\text{H}} + 2n_{\text{H}_2}$). Ignoring the contribution from atomic H, the average ensemble H_2 volume density is about $6 \times 10^4 \text{ cm}^{-3}$, consistent with that derived with the excitation analysis in Sect. 4. The ensemble mass is also consistent with that derived for the whole extent of the 30 Dor-10 cloud in Sect. 4.3. A comparison between the observations, the predictions from the PDR model, and the results of the excitation analysis (Sect. 4) is listed in Table 4.

The area filling factor of the clump ensemble is defined as the sum of all clump projected areas over the cloud solid angle (assumed to be $90''$). Similarly, the volume filling factor is defined as the sum of all clump volumes over the volume of a sphere with $90''$ projected diameter. The model fit gives an area filling factor of 2.94 and, assuming a distance of 50 kpc, a volume filling factor of 0.001. These area and volume filling factors imply that

Table 4. Comparison between observed line integrated intensities and the predictions from the KOSMA- τ PDR model and the RADEX radiative transfer code.

Line	Observed	KOSMA ^a	RADEX ^b
$^{12}\text{CO } J = 1 \rightarrow 0$	$2.8 \times 10^{-7}(0.2)$	8.7×10^{-7}	8.1×10^{-7}
$^{12}\text{CO } J = 3 \rightarrow 2$	$3.0 \times 10^{-5}(0.3)$	3.4×10^{-5}	3.2×10^{-5}
$^{12}\text{CO } J = 4 \rightarrow 3$	$7.8 \times 10^{-5}(1.6)$	7.8×10^{-5}	6.8×10^{-5}
$^{12}\text{CO } J = 7 \rightarrow 6$	$2.2 \times 10^{-4}(0.4)$	1.9×10^{-4}	2.1×10^{-4}
$^{12}\text{CO } J = 9 \rightarrow 8$	$< 3.3 \times 10^{-4}$	9.4×10^{-5}	1.9×10^{-4}
$^{13}\text{CO } J = 1 \rightarrow 0$	$1.9 \times 10^{-8}(0.3)$	6.8×10^{-8}	3.1×10^{-8}
$^{13}\text{CO } J = 4 \rightarrow 3$	$1.0 \times 10^{-5}(0.3)$	1.1×10^{-5}	1.0×10^{-5}
$[\text{C I}]^3\text{P}_1 \rightarrow ^3\text{P}_0$	$1.1 \times 10^{-5}(0.3)$	1.0×10^{-5}	5.5×10^{-6}
$[\text{C I}]^3\text{P}_2 \rightarrow ^3\text{P}_1$	$4.1 \times 10^{-5}(1.7)$	4.4×10^{-5}	3.5×10^{-5}
$[\text{C II}]^2\text{P}_{3/2} \rightarrow ^2\text{P}_{1/2}$	$1.2 \times 10^{-2}(0.01)$	2.4×10^{-2}	4.5×10^{-3}

Notes. All intensities are in units of $\text{erg cm}^{-2} \text{s}^{-1} \text{sr}^{-1}$. The observed and RADEX intensities are corrected for beam dilution. The PDR model absolute intensities are calculated assuming a common FWHM source size of $90''$. ^(a) Best-fit model: $n_{\text{ens}} = 3.3 \times 10^5 \text{ cm}^{-3}$, $M_{\text{ens}} = 1.2 \times 10^5 M_{\odot}$, $\chi_0 = 3160$. ^(b) Best-fit model: $n_{\text{H}_2} = 10^4 \text{ cm}^{-3}$, $T_{\text{kin}} = 160 \text{ K}$, beam filling 1/16, $N_{\text{CO}} = 1.7 \times 10^{17} \text{ cm}^{-2}$, $N_{\text{C}^0} = 5.6 \times 10^{16} \text{ cm}^{-2}$.

the model requires many low-mass clumps to reproduce the observed line intensities. As discussed by e.g. Kramer et al. (2008), these low-mass clumps would require very high external thermal pressures to be confined and might be considered as transient features of the turbulent gas and should evaporate on short timescales. Note that the area filling factor defined here is not comparable with the beam filling factor derived in Sect. 4.2, because the PDR model does not predict whether these small clumps are clustered or dispersed within the cloud.

In Fig. 6 we show the dependence of the different observed transitions on different H_2 volume densities and FUV radiation fields. Solutions in the range $n_{\text{ens}} = 1 \times 10^5 - 1 \times 10^{5.6} \text{ cm}^{-3}$ and $\chi_0 = 400 - 6300$ are within three times the minimum $\chi^2_{\text{min}} = 59$. Note that this high value of χ^2 is dominated by the inability of the PDR model to reproduce the $[\text{C II}]$ emission. If we exclude the $[\text{C II}]$ line in the calculation of χ^2 , we obtain a much lower χ^2_{min} of 0.01, without significant changes in the constrained physical conditions.

To illustrate the importance of the observed line intensities in determining the value of χ_0 and n_{ens} , we show in Fig. 7 the predicted model line intensities as a function of n_{ens} for a fixed value of $\chi_0 = 3980$, and as a function of χ_0 for a fixed value of $n_{\text{ens}} = 3.9 \times 10^5 \text{ cm}^{-3}$. The fixed values of χ_0 and n_{ens} were selected to be the closest point in the model grid to the solution found using the simulated annealing technique. The intensity of the mid- J ^{12}CO and ^{13}CO are very sensitive to n_{ens} and drive the value of this parameter. The $[\text{C I}]$ and mid- J CO lines are sensitive to the FUV radiation field but to lesser extent than to n_{ens} . Consequently, as also seen in Fig. 6, the fit to the average ensemble volume density is better than that for the FUV radiation field. The decreasing value of the $[\text{C I}]$ and mid- J CO lines and the increase of value of the $[\text{C II}]$ intensity with χ_0 is related to the shift of the $\text{C}^+/\text{C}^0/\text{CO}$ transition deeper into the cloud as χ_0 increases, reducing the column density of CO and increasing column density of $[\text{C II}]$. As shown by Cubick et al. (2008), the emission from CO transitions with $J > 5$ is mostly arising from low-mass clumps, while lower- J CO and $[\text{C I}]$ transitions arise from clumps with larger masses. Therefore, the observed $^{12}\text{CO } J = 7 \rightarrow 6$ transition is very sensitive to the lower mass limit and drives the value of this model parameter. For the upper mass limit, the dependence on the observed lines is weaker, and

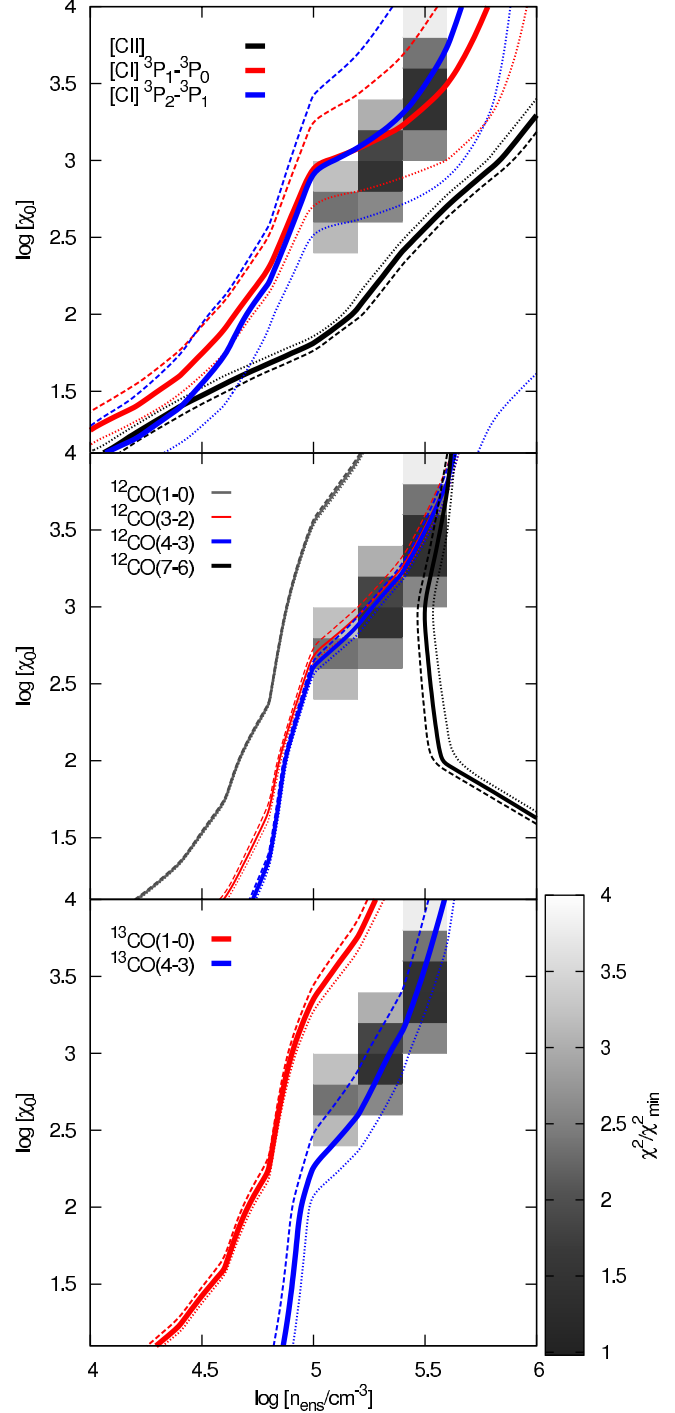


Fig. 6. Comparison between the different observed lines with the predictions from the clumpy-PDR model for a given H_2 volume density and FUV radiation field. In all panels, the solid lines represent the observed values while the dashed and dotted lines represent their lower and upper error bars, respectively. The gray-scale represents the value of χ^2 relative to its minimum value, χ^2_{min} .

varying the upper mass limit to higher values does not have a significant effect on the model fit.

In Fig. 6 and Table 4 (see also Fig. 8), we can see that the best-fit model agrees well with observations of mid- J CO and $[\text{C I}]$ but it overestimates the $[\text{C II}]$, $^{12}\text{CO } J = 1 \rightarrow 0$, and $^{13}\text{CO } J = 1 \rightarrow 0$ line intensities. To reproduce the lines observed by NANTEN2, the model requires clumps with volume densities that are much higher than the critical density of

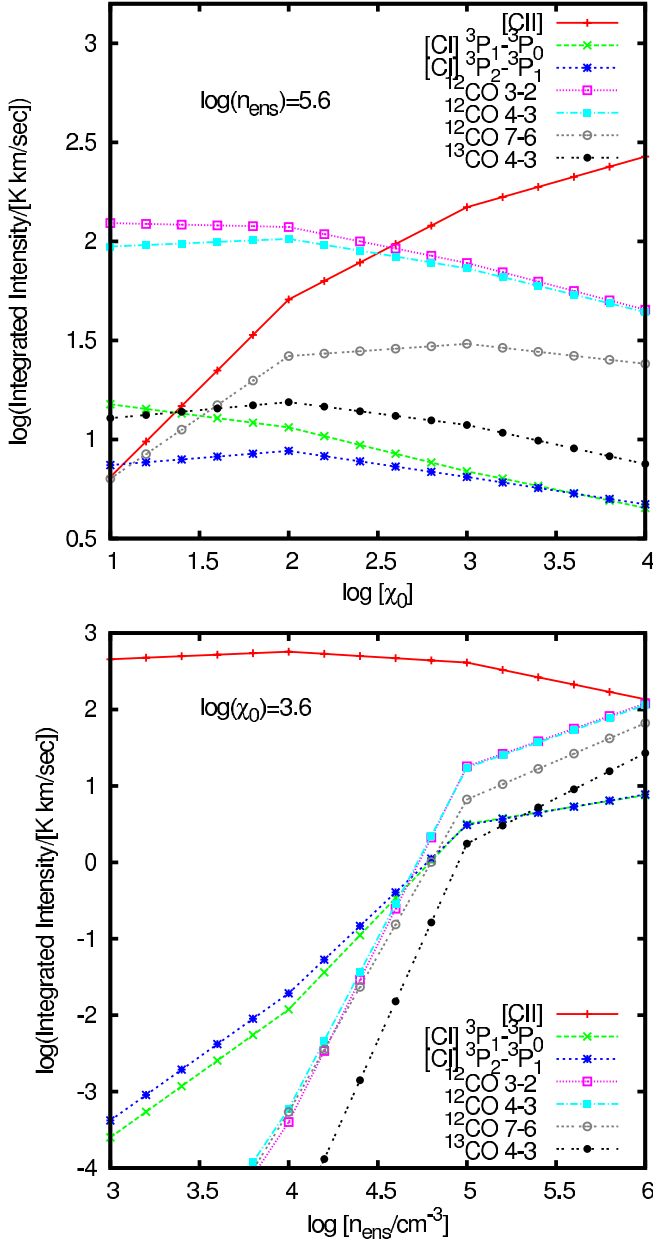


Fig. 7. Model-predicted integrated intensities the spectral lines used to constrain the PDR model as a function of χ_0 for a fixed value of n_{ens} (upper panel) and of n_{ens} for a fixed value of χ_0 (lower panel).

the [C II] line ($5 \times 10^3 \text{ cm}^{-3}$; see Table 3), resulting in a predicted [C II] intensity that is higher than observed. A model with a lower volume density might reproduce the [C II] line better, but it would underestimate the mid- J and [C I] transitions. Another complication is that, as shown in Fig. 1, we can expect that the FUV field is not uniform within 30 Dor-10, because parts of the cloud are closer to R136 than others, while the model assumes a uniform field. Note that we are only considering a single-component model in this analysis. It might be possible to find a better fit to the lines if more gas components were added, but more data (e.g. [O I] lines) would be needed to obtain a good constraint to the model. Note that, as mentioned above, the PDR model neglects any mutual absorption/shielding between clumps. Since the ^{12}CO $J = 1 \rightarrow 0$ is optically thick and ^{13}CO $J = 1 \rightarrow 0$ is likely affected by optical depth effects, radiation from background clumps should be (partly) shielded

by foreground clumps. Because the model ignores this effect, it overestimates the intensity of these transitions. This effect might also partly be the reason for the overestimation of the [C II] line, because this line might be also affected by optical depth effects between clumps.

Our determination of the strength of the FUV field agrees excellently with the independent estimation presented by [Poglitsch et al. \(1995\)](#) of $\chi_0 = 3100\text{--}3600$. The constraints on the H₂ volume density and FUV radiation field for 30 Dor are also consistent with previous determinations based on PDR modeling ([Pak et al. 1998; Kaufman et al. 1999; Bolatto et al. 1999; Röllig et al. 2006](#)). A crucial test to the suggested clumpy structure of the LMC's ISM will be high angular resolution imaging of low- and mid- J CO and [C I] transitions with ALMA.

6. Discussion

6.1. Comparison with LMC-N159W

The 30 Dor-10 region is located at a distance of ~ 20 pc from the center of the R136 star cluster, hence this region is exposed to an extreme FUV radiation field. It is of interest to compare its physical properties with other regions in the LMC that have more moderate ambient radiation fields. Since there are no significant spatial variations of the metallicity in the LMC ([Dufour 1984](#)), this comparison will help us to understand the effect of the FUV radiation field on low-metallicity environments.

In [Pineda et al. \(2008\)](#) we made a similar analysis of the same set of spectral lines as analyzed here in the LMC-N159W region. We constrained the H₂ volume density to be $\sim 10^4 \text{ cm}^{-3}$, a kinetic temperature of ~ 80 K and equal CO and C I column densities of $\sim 1.6 \times 10^{17} \text{ cm}^{-2}$. The beam filling in N159W is about 1/6. Modeling of the photon-dominated region suggests that the strength of the FUV field in N159W is about $\chi_0 = 220$, while we find $\chi_0 = 3160$ in 30 Dor-10 (Sect. 5).

The 30 Dor-10 region is warmer than N159W, with a kinetic temperature of about 160 K and 80 K, respectively. This higher temperature is indicated by the higher ^{12}CO $J = 7 \rightarrow 6$ to $J = 4 \rightarrow 3$ ratio in 30 Dor-10. This warming can be understood because the gas heating is likely dominated by photoelectric heating, which depends on the strength of the FUV field ([Bakes & Tielens 1998](#)). The higher temperatures in 30 Dor-10 do not result in higher brightness temperatures compared with N159W because of the reduced beam filling (1/16). The column/volume densities, however, are similar or somewhat higher in 30 Dor-10 compared with N159W, suggesting that CO clumps in the former region are smaller. These smaller clumps can be interpreted as the effect of the enhanced CO photo-destruction due to the strong FUV radiation field. This enhanced photo-destruction does not result in a higher abundance of C I relative to CO, because the $N(\text{CO})/N(\text{C I})$ column density ratio is even higher in 30 Dor-10, implying that the FUV field moves the C⁺/C/CO transition layer to locations deeper into the clumps, but does not increase the thickness of this layer. Accordingly, most of the carbon in 30 Dor-10 should be in the form of C⁺. This effect has been predicted by PDR models (e.g. [Röllig et al. 2006](#)). Note that we cannot eliminate other mechanisms that might destroy the molecular cloud, such as stellar winds from massive stars. However, the N159W should also be influenced by these effects.

We determined the column density of C⁺ using the integrated intensity observed by [Boreiko & Betz \(1991\)](#) of $7.7 \times 10^{-4} \text{ erg cm}^{-2} \text{ s}^{-1} \text{ sr}^{-1}$. This quantity is related to the C⁺ column density, assuming a kinetic temperature larger than

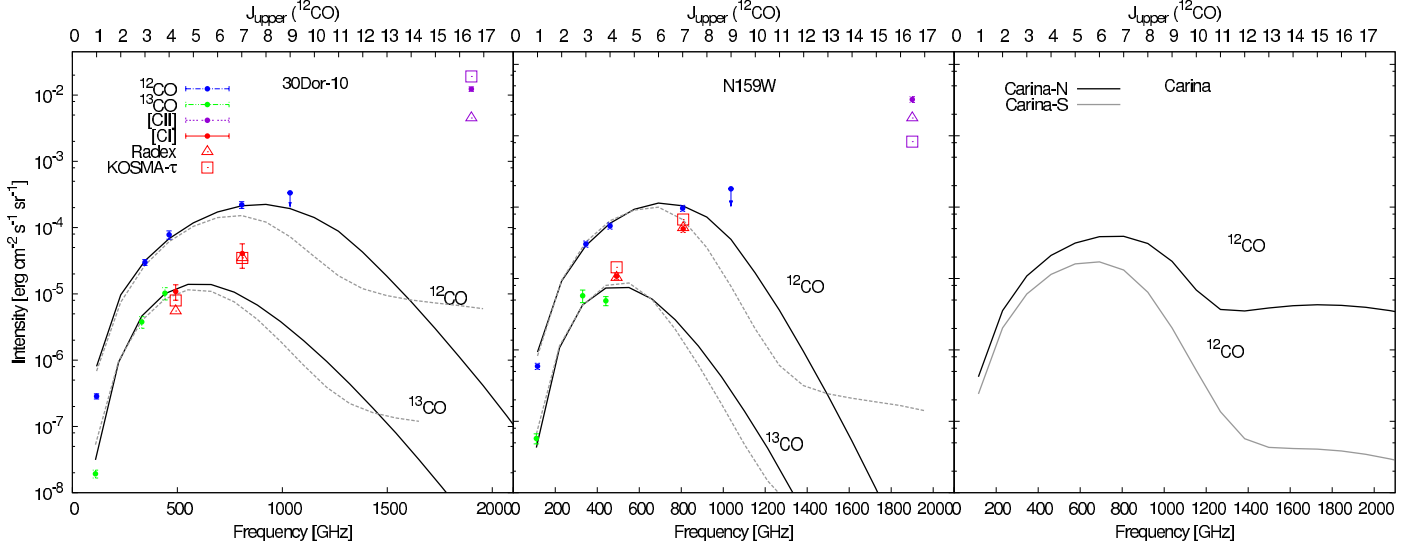


Fig. 8. Spectral-line energy distribution (SLED) for several millimeter and submillimeter lines toward 30 Dor-10 (left), N159W (center), and Carina-N and -S (right). In the left and central panel, the solid lines represent the predictions for the ¹²CO and ¹³CO SLED from the excitation analysis presented in Sect. 4 for 30 Dor-10 and in Pineda et al. (2008) for N159W. The gray-dashed lines represent the ¹²CO and ¹³CO SLED predicted by the clumpy PDR model fits. The excitation analysis and PDR model predictions for the [C I] and [C II] lines are represented by triangles and boxes, respectively. In the right panel we show the ¹²CO SLED for the Carina-N and Carina-S regions presented by Kramer et al. (2008) using the same clumpy PDR model as used in this paper. The physical conditions derived from the PDR model are similar for 30 Dor-10 and Carina-N as well as for N159W and Carina-S, but they have different metallicity (Carina $Z = Z_{\odot}$; LMC $Z = 0.4Z_{\odot}$).

91 K and a volume density higher than $n_{\text{cr}} = 5 \times 10^3 \text{ cm}^{-3}$, by $N(\text{C}^+) = 6.4 \times 10^{20} I([\text{C II}]) \text{ cm}^{-2} (\text{erg cm}^{-2} \text{s}^{-1} \text{sr}^{-1})^{-1}$ (Crawford et al. 1985). With that we obtain a column density of C⁺ of $4.96 \times 10^{17} \text{ cm}^{-2}$ and therefore the total carbon abundance in 30 Dor-10 is distributed as $N_{\text{C}^+}:N_{\text{C}}:N_{\text{CO}} = 69\%:8\%:23\%$. For comparison, the distribution of carbon in the N159W region is 46%:27%:27% while in the Galactic PDR DR21(OH) it is 3%:10%:87% (Jakob et al. 2007). As in N159W, the 30 Dor-10 region has an increased fraction of the gas-phase carbon in the form of C⁺ compared with DR21(OH).

6.2. CO spectral-line energy distribution

We combined our observed mid- J ¹²CO observations with previously observed transitions to derive the CO spectral-line energy distribution (SLED) in 30 Dor-10 and N159W. We present the CO SLEDs in Fig. 8, together with the predictions from our excitation analyses and PDR modeling in both regions. We include observations of ¹²CO $J = 3 \rightarrow 2$ from Minamidani et al. (2008) and upper limits to the intensity of the $J = 9 \rightarrow 8$ line from Boreiko & Betz (1991). We corrected these line intensities, together with that of the $J = 7 \rightarrow 6$ transition, to match the intensity corresponding to a 38'' beam (see Sect. 3). Single-component models agree well with the observed CO transitions. But the model for 30 Dor-10 still predicts a line intensity of the $J = 1 \rightarrow 0$ line that is about a factor of 3 higher than observed. The ¹²CO SLED peaks at $J = 8 \rightarrow 7$ for 30 Dor-10 and $J = 6 \rightarrow 5$ for N159W. The different CO excitation in both regions reflects the difference in their kinetic temperature, which in turn is due to the difference in the FUV radiation field between both regions.

The CO SLED predicted by the clumpy PDR model for 30 Dor-10 is similar to that predicted by the excitation analysis for low- J transitions, but differs significantly for high- J transitions, with the PDR model predicting much higher intensities for $J > 6$. For $J > 14$, however, the PDR model predicts almost constant intensities, while the intensity predicted

by the excitation model drops. The clumpy PDR model predicts a peak of the CO SLED at a lower ¹²CO transition ($J = 6 \rightarrow 5$) compared with the prediction from the excitation analysis ($J = 8 \rightarrow 7$). For N159W the clumpy PDR model CO SLED also predicts lower intensities for high- J transitions but the difference is smaller than for 30 Dor-10. The peak of the CO SLED still coincides with that predicted by the excitation analysis (¹²CO $J = 6 \rightarrow 5$). More observations of high- J CO transitions with e.g. *Herschel* or SOFIA in 30 Dor-10 and N159W are required to test the predictions of the PDR modeling and excitation analysis for high- J CO transitions.

In Fig. 8 we also show the CO SLED for two positions in the Carina region, Carina-N and Carina-S, whose physical conditions have been constrained with the KOSMA- τ PDR model by Kramer et al. (2008) using the same set of line as presented here. The constrained values of (χ_0, n_{ens}) are $(3100, 2 \times 10^5 \text{ cm}^{-3})$ for Carina-N and $(310, 2 \times 10^5 \text{ cm}^{-3})$ for Carina-S. Therefore, both Carina-N and Carina-S have similar physical conditions compared with 30 Dor-10 and N159W, respectively, but solar metallicity. The metallicity, however, seems not to affect the shape of the CO SLED because for both pairs of sources the CO spectral energy distribution is consistent within the small differences in the physical conditions and uncertainties of the models.

The total CO luminosity (L_{CO}) predicted by the radiative transfer code in an area defined by the 38'' beam of our NANTEN2 observations (corresponding to 9.5 pc at a distance of 50 kpc) is $1.1 \times 10^{36} \text{ erg s}^{-1}$ for 30 Dor-10 and $4.3 \times 10^{35} \text{ erg s}^{-1}$ for N159W. The clumpy PDR model predicts a somewhat lower L_{CO} of $8.2 \times 10^{35} \text{ erg s}^{-1}$ for 30 Dor-10 and $2.5 \times 10^{35} \text{ erg s}^{-1}$ for N159W. From the observations, we also estimated the total [C II] and [C I] luminosity (ignoring the much weaker [C I] ${}^3\text{P}_2 \rightarrow {}^3\text{P}_0$ transition) of 9.9×10^{36} and $4.2 \times 10^{34} \text{ erg s}^{-1}$, respectively for 30 Dor-10 and 2.6×10^{36} and $4.9 \times 10^{34} \text{ erg s}^{-1}$, respectively, for N159W. The relative fraction of the luminosity of these species is $L_{[\text{C II}]}:L_{[\text{C I}]}:L_{\text{CO}} = 90\%:0.4\%:9.6\%$ for 30 Dor-10 and $84.4\%:1.6\%:14$ for N159W, when using L_{CO} predicted by the radiative transfer code, and

92%:0.4%:7.6% for 30 Dor-10 and 90%:1.7%:8.3% for N159W, when using L_{CO} predicted by the clumpy PDR model. We also estimates a total [O I] luminosity of 7.4×10^{36} erg s $^{-1}$ from observations of the [O I] 63 μm and 146 μm lines by Poglitsch et al. (1995) in 30 Dor. These estimated luminosities suggest that [C II] and [O I] contribute equally to the gas cooling in 30Dor-10. This significant contribution of [O I] to the line cooling confirms the warm and dense gas conditions derived with the excitation analysis and PDR modeling. Note that we cannot rule out the possibility of an additional component powering even higher CO transitions ($J > 10$) in 30 Dor-10 and N159W. Therefore, our estimate of the total CO luminosity might be a lower limit. As mentioned above more observations will allow us to determine the contribution of high- J CO transitions to the total CO luminosity.

7. Summary and conclusions

We derived the physical conditions of the line-emitting gas in the 30 Dor-10 region in the LMC. We compared an excitation/radiative transfer code and a PDR model with NANTEL2 observations of the ^{12}CO $J = 4 \rightarrow 3$, $J = 7 \rightarrow 6$, and ^{13}CO $J = 4 \rightarrow 3$ rotational and [C I] $^3\text{P}_1 - ^3\text{P}_0$ and $^3\text{P}_2 - ^3\text{P}_1$ fine-structure transitions. Our results can be summarized as follows:

- The analysis of the excitation conditions for both the CO submm-lines and the [C I] fine structure lines shows temperatures of about $T = 160$ K and densities of about $n_{\text{H}_2} = 10^4$ cm $^{-3}$ for the emitting gas.
- We found that 30 Dor-10 is warmer and has a lower beam filling factor compared to N159W. This difference might be the result of the FUV radiation field heating the gas and photodissociating CO molecules. This, however, does not result in an enhanced C abundance relative to CO: we obtained a $N(\text{CO})/N(\text{C I})$ ratio of 3 in 30 Dor-10, which is higher than that found in N159W of $N(\text{CO})/N(\text{C I})$ equal to unity.
- We derived the CO spectral-line energy distribution of 30 Dor-10 and N159W. Considering the excitation conditions constrained using line ratios, we found that this distribution peaks at ^{12}CO $J = 8 \rightarrow 7$ for 30 Dor-10 and at $J = 6 \rightarrow 5$ in N159W. The clumpy PDR model, however, predicts the peak of the CO spectral-line energy distribution at $J = 6 \rightarrow 5$ for both 30 Dor-10 and N159W.
- We compared our observations with the results of a clumpy PDR model. The model that best reproduces the observed absolute integrated intensities has an average ensemble H density of $n_{\text{ens}} \sim 10^5$ cm $^{-3}$, a total mass of the ensemble, $M_{\text{ens}} \sim 10^5 M_{\odot}$, and a strength of the FUV field of $\chi_0 \sim 3100$. The constraints on the H $_2$ volume density and the strength FUV radiation field agree well with independent determinations and previous PDR modeling results.

The 30Dorarus region is the closest example of vigorous star-formation taking place in a low-metallicity environment, which is thought to be common in the early universe. Our results suggest that the star-forming ISM in 30 Dor-10, and perhaps in starburst galaxies in the early universe, is dense, and warm, and clumpy. The clumpy structure of the 30Dor-10 gas is a result of the extreme FUV environment to which the low-metallicity gas is exposed. Our results also highlight the importance of ionized carbon in tracing the total gas mass and, together with atomic oxygen, in regulating the thermal balance of the gas. Future observations of fine-structure transitions of [C II], [O I],

[N II], and [C I] and rotational transitions of CO in the local Universe are essential for our understanding of star-formation in low-metallicity environments and are an important tool for the interpretation of observations of high-redshift galaxies with ALMA.

Acknowledgements. This research was conducted at the Jet Propulsion Laboratory, California Institute of Technology under contract with the National Aeronautics and Space Administration. We would like to thank William Langer and Paul Goldsmith for careful reading of the manuscript and enlightening discussions. The NANTEL2 project (southern submillimeter observatory consisting of a 4-m telescope) is based on a mutual agreement between Nagoya University and The University of Chile and includes member universities from six countries, Australia, Republic of Chile, Federal Republic of Germany, Japan, Republic of Korea, and Swiss Confederation. M.R. wishes to acknowledge support from FONDECYT(CHILE) grant 1080335.

References

- Bakes, E. L. O., & Tielens, A. G. G. M. 1998, ApJ, 499, 258
 Bolatto, A. D., Jackson, J. M., & Ingalls, J. G. 1999, ApJ, 513, 275
 Boreiko, R. T., & Betz, A. L. 1991, ApJ, 380, L27
 Chen, C.-H. R., Indebetouw, R., Chu, Y.-H., et al. 2010, ApJ, 721, 1206
 Crawford, M. K., Genzel, R., Townes, C. H., & Watson, D. M. 1985, ApJ, 291, 755
 Cubick, M., Stutzki, J., Ossenkopf, V., Kramer, C., & Röllig, M. 2008, A&A, 488, 623
 Draine, B. T. 1978, ApJS, 36, 595
 Dufour, R. J. 1984, in Structure and Evolution of the Magellanic Clouds, eds. S. van den Bergh, & K. S. D. Boer, IAU Symp., 108, 353
 Dufour, R. J., Shields, G. A., & Talbot, Jr., R. J. 1982, ApJ, 252, 461
 Feast, M. 1999, PASP, 111, 775
 Fukui, Y., Kawamura, A., Minamidani, T., et al. 2008, ApJS, 178, 56
 Grenier, I. A., Casandjian, J.-M., & Terrier, R. 2005, Science, 307, 1292
 Heikkilä, A., Johansson, L. E. B., & Olofsson, H. 1999, A&A, 344, 817
 Hollenbach, D. J., & Tielens, A. G. G. M. 1999, Rev. Mod. Phys., 71, 173
 Hughes, A., Wong, T., Ott, J., et al. 2010, MNRAS, 406, 2065
 Israel, F. P. 1997, A&A, 328, 471
 Jakob, H., Kramer, C., Simon, R., et al. 2007, A&A, 461, 999
 Johansson, L. E. B., Greve, A., Booth, R. S., et al. 1998, A&A, 331, 857
 Kaufman, M. J., Wolfire, M. G., Hollenbach, D. J., & Luhman, M. L. 1999, ApJ, 527, 795
 Kim, S. 2006, PASP, 118, 94
 Kim, S., Walsh, W., Xiao, K., & Lane, A. P. 2005, AJ, 130, 1635
 Kramer, C., Cubick, M., Röllig, M., et al. 2008, A&A, 477, 547
 Langer, W. D., Velusamy, T., Pineda, J. L., et al. 2010, A&A, 521, L17
 Madden, S. C., Poglitsch, A., Geis, N., Stacey, G. J., & Townes, C. H. 1997, ApJ, 483, 200
 Meixner, M., Gordon, K. D., Indebetouw, R., et al. 2006, AJ, 132, 2268
 Minamidani, T., Mizuno, N., Mizuno, Y., et al. 2008, ApJS, 175, 485
 Minamidani, T., Tanaka, T., Mizuno, Y., et al. 2011, AJ, 141, 73
 Pak, S., Jaffe, D. T., van Dishoeck, E. F., Johansson, L. E. B., & Booth, R. S. 1998, ApJ, 498, 735
 Pineda, J. L., Mizuno, N., Stutzki, J., et al. 2008, A&A, 482, 197
 Pineda, J. L., Ott, J., Klein, U., et al. 2009, ApJ, 703, 736
 Planck Collaboration 2011, A&A, 536, A19
 Poglitsch, A., Krabbe, A., Madden, S. C., et al. 1995, ApJ, 454, 293
 Röllig, M., Ossenkopf, V., Jeyakumar, S., Stutzki, J., & Sternberg, A. 2006, A&A, 451, 917
 Schöier, F. L., van der Tak, F. F. S., van Dishoeck, E. F., & Black, J. H. 2005, A&A, 432, 369
 Stark, A. A., Bolatto, A. D., Chamberlin, R. A., et al. 1997, ApJ, 480, L59
 Störzer, H., Stutzki, J., & Sternberg, A. 1996, A&A, 310, 592
 Tielens, A. G. G. M., & Hollenbach, D. 1985, ApJ, 291, 722
 van der Marel, R. P., & Cioni, M.-R. L. 2001, AJ, 122, 1807
 van der Tak, F. F. S., Black, J. H., Schöier, F. L., Jansen, D. J., & van Dishoeck, E. F. 2007, A&A, 468, 627
 Velusamy, T., Langer, W. D., Pineda, J. L., et al. 2010, A&A, 521, L18
 Werner, M. W., Becklin, E. E., Gatley, I., et al. 1978, MNRAS, 184, 365
 Westerlund, B. E. 1997, The Magellanic Clouds (New York: Cambridge Univ. Press)
 Wolfire, M. G., Hollenbach, D., & McKee, C. F. 2010, ApJ, 716, 1191
 Wong, T., Hughes, A., Ott, J., et al. 2011, ApJS, 197, 16

Full SED fitting with the KOSMA- τ PDR code - I. Dust modelling

M. Röllig¹, R.Szczerba², V. Ossenkopf¹, C.Glück¹

¹ I. Physikalisches Institut, Universität zu Köln, Zülpicher Str. 77, D-50937 Köln, Germany

² N. Copernicus Astronomical Center, Rabianska 8, 87-100 Toruń, Poland

Preprint online version: November 6, 2012

ABSTRACT

Aims. We revised the treatment of interstellar dust in the KOSMA- τ PDR (photo-dissociation region) model code to achieve a consistent description of the dust-related physics in the code. The detailed knowledge of the dust properties is then used to compute the dust continuum emission together with the line emission of chemical species.

Methods. We coupled the KOSMA- τ PDR code with the MCDRT (multi component dust radiative transfer) code to solve the frequency-dependent radiative transfer equations and the thermal balance equation in a dusty clump under the assumption of spherical symmetry, assuming thermal equilibrium in calculating the dust temperatures, neglecting non-equilibrium effects. We updated the calculation of the photoelectric heating and extended the parametrization range for the photoelectric heating toward high densities and UV fields. We revised the computation of the H₂ formation on grain surfaces to include the Eley-Rideal effect, thus allowing for high-temperature H₂ formation.

Results. We demonstrate how the different optical properties, temperatures, and heating and cooling capabilities of the grains influence the physical and chemical structure of a model cloud. The most influential modification is the treatment of H₂ formation on grain surfaces that allows for chemisorption. This increases the total H₂ formation significantly and the connected H₂ formation heating provides a profound heating contribution in the outer layers of the model clumps. The contribution of polycyclic aromatic hydrocarbons (PAH) surfaces to the photoelectric heating and H₂ formation provides a boost to the temperature of outer cloud layers, which is clearly traced by high- J CO lines. Increasing the fraction of small grains in the dust size distribution results in hotter gas in the outer cloud layers caused by more efficient heating and cooler cloud centers, which is in turn caused by the more efficient FUV extinction.

1. Introduction

Photo-dissociation regions (PDRs) are interstellar neighbors of HII regions that are already shielded from extreme ultraviolet (EUV) photons with an energy sufficient to ionize atomic hydrogen, but where the physical and chemical conditions of the atomic and molecular interstellar medium (ISM) are still governed by the remaining far-ultraviolet (FUV) radiation of nearby massive stars (Hollenbach & Tielens 1999). Here, the transition from the atomic to the molecular ISM takes place, giving rise to a rich astrochemical environment. The combination of a chemically rich pool of species that includes a large reservoir of free electrons and strong energetic excitation conditions produces a wealth of spectroscopic emissions, carrying information on the internal chemical and physical structure of the PDR.

Comparing the results of theoretical and numerical calculations to the observed spectral line emission of PDRs is a frequently used method to infer their local physical conditions. Numerical models to describe the physical and chemical processes in molecular clouds have been successfully used for many years. They involve simultaneously solving the problem of a) radiative transfer for a cloud of gas and dust; b) the chemical structure by balancing formation and destruction processes for all included species; c) determining the thermal structure of the cloud by balancing all important heating and cooling processes.

Properly taking into account all relevant chemical and physical processes is extremely time-consuming in terms of computational power and usually leads to a large number of simplifying

assumptions in the treatment of the physics and the chemistry. The exact choice of these simplifications depends on the field of application, on the expertise of the modeller, and on the available physical and chemical knowledge. Many processes are still not fully understood if not largely unknown. A prominent example is the description of interstellar dust (see Draine 2003a, for a review on interstellar dust). Many important physical and chemical processes require a good knowledge of the properties of interstellar dust grains (Abel et al. 2008). Chemical reactions on the surface of dust grains appear to be the only efficient formation route for a number of important astrochemical species (Garrod et al. 2008; Hall & Millar 2010). The specifics of their reaction kinematics depend to a large degree on the material properties and the structure of the dust grains. Porous, spongy grains provide a large surface for chemical reactions but might hinder the release of the newly formed species into the gas phase (Leger et al. 1985; Roberts et al. 2007; Taquet et al. 2012). Not only the material and shape, but also the size of the grains might be important. Very small grains and very large molecules, such as polycyclic aromatic hydrocarbons (PAHs), efficiently contribute to the gas heating by means of the photoelectric (PE) effect (Bakes & Tielens 1994; Weingartner & Draine 2001a) while larger grains are dominating the scattering and absorption of FUV photons. For a review on PAHs see Tielens (2008).

The rapid development in observational techniques over the last two decades left us with a vast amount of spectroscopic data that defies reproduction with simple numerical PDR models. We are far away from being able to really understand the conditions in any observed PDR (Röllig et al. 2007). In this paper we describe a number of steps that have been taken to increase the

Send offprint requests to: M. Röllig,
e-mail: roellig@ph1.uni-koeln.de

modeling power of the KOSMA- τ PDR model code. We tried to evolve the code toward a consistent treatment of dust physics and chemistry. By calculating the optical and energetic properties of a model cloud with a given dust composition we are now able to describe the full spectral emission characteristic of a model cloud including dust continuum and line emission¹.

2. Code description

2.1. The KOSMA- τ PDR model code

The KOSMA- τ code (Röllig et al. 2006), a welltested and mature PDR model code (Röllig et al. 2007), applies spherical geometry to the problem of simultaneously solving the chemical and energy balance in an interstellar molecular cloud. KOSMA- τ is equipped with a modular chemical network, i.e., chemical species can easily be added or removed from the network and the network will rebuild dynamically, including isotopic chemistry of ^{13}C and ^{18}O . After obtaining the physical and chemical structure of the model cloud, a radiative transfer code is applied to calculate the resulting emissivities for the spectral line emission. Because of the spherical geometry of the model clump, radiation can reach a point inside the clump from any direction.

2.2. Multi-component dust radiative transfer model

The multi-component dust radiative transfer (MCDRT) code allows one to solve the frequency-dependent radiative transfer equations and the thermal balance equation in a dusty clump under the assumption of spherical symmetry (Yorke 1980). A detailed description of the code's main features is given in Szczerba et al. (1997). The code includes isotropic scattering, which is important at high optical depths. Further modifications to that version of the code have been made. First, we have added the possibility to solve the radiative transfer simultaneously for a number of dust sorts (NDS) i that may or may not be co-spatial, and obey any dust size distribution. The grain size distribution is given by the general relation valid for grains with radius $a_{i,-} \leq a \leq a_{i,+}$:

$$dn_i(a) = n f_i(a) da, \quad (1)$$

where: $n_i(a)$ is the number density of grains with size $\leq a$ and n is the number density of H nuclei (in both atoms and molecules: $n = n_{\text{H}} + 2n_{\text{H}_2}$). The function $f_i(a)$ has a modular structure and can be changed easily to a different form. Second, because we adapted the code to the conditions typical for PDRs it was necessary to introduce an option for switching off the central source. In addition, because intense sources of an interstellar radiation field are ubiquitous in PDRs, we changed the spatial distribution of impact parameters (originally logarithmically spaced beginning from the inner shell of the clump) along which the ray equations are integrated. The end result of this code is the infrared radiation flux emitted by the clump, which can be compared to the radiation observed from real PDRs. However, as a byproduct, the code provides the mean intensity of the radiation field, $J_\lambda(r)$ and the dust temperature, $T_{\text{d},i}(r, a)$, which for now is computed from the assumed thermal equilibrium for each dust species and dust grain size at each radius r of the clump. These two quantities (mean radiation field and dust temperature) are now used in the KOSMA- τ PDR model code to obtain a self-consistent gas-dust model.

¹ Other PDR model codes are also able to perform wavelength-dependent UV radiative transfer. Compare for example Le Petit et al. (2006); Abel et al. (2005).

2.3. Dust models

For the purpose of this paper we selected three dust models of interstellar dust from Weingartner & Draine (2001b) (hereafter WD01), and the MRN dust model (Mathis et al. 1977) for comparison. The MRN interstellar dust model was constructed by fitting a dust model to the Galactic mean extinction curve. It consists of two separate dust populations, one for "astronomical silicates" (sil) and one for graphite (gra). In the MRN model the grain size distribution is identical for both dust components and is given by

$$dn_i(a) = n A_i a^{-3.5} da, 0.005 \leq a \leq 0.25 \mu\text{m}, \quad (2)$$

where i stands for sil and gra, $A_{\text{sil}} = 10^{-25.10}$, and $A_{\text{gra}} = 10^{-25.13}$ (WD01).

Recently gathered observational constraints led WD01 to construct new models for interstellar dust. The authors proposed that interstellar dust is composed of four main components: astronomical silicates, graphite, and populations of very small grains that consist of neutral (PAH^0) and ionized (PAH^+) particles. The grain size distributions for these dust components follow the general definition given by Eq. (1) and their functional forms ($f_i(a)$ in Eq. (1)) are given by Eqs. (2–6) of WD01. The authors employ a power-law form for the large grains and a log-normal distribution for the very small grain population. Free parameters of the $f_i(a)$ functions were determined by the best fit to the average extinction with $R_V = A_V/E(B - V)$ of 3.1, 4 and 5.5 (see WD01 for details). A_V is the absolute visual extinction at $V = 5500 \text{ \AA}$ and $E(B - V) = A_B - A_V$. The three dust models from WD01 correspond to lines 7, 21, and 25 from Table 1 in Weingartner & Draine (2001b) and are denoted WD01-7 ($R_V = 3.1$), WD01-21 ($R_V = 4.0$), and WD01-25 ($R_V = 5.5$).

To compute the extinction efficiency Q_{ext} and albedo ω for each dust component, we assumed that grains are spherical and used the Mie theory (Bohren & Huffman 1983). For silicates and graphite we used the dielectric constants from Draine (2003b), while for very small grains we followed the approach given by Li & Draine (2001). The minimal and maximal grain size for the size distribution of each dust component are given in Tab. 4. For very small grains we used 17 grain sizes, while for bigger grains we divided each dex of grain sizes into ten sizes, keeping equal distance in $\log(a)$. The wavelength coverage used in the MCDRT code extends from 10 \AA to $3000 \mu\text{m}$ and is split into 333 wavelengths.

3. Impact on the PDR model

In the following we describe how the new, full radiative transfer (RT) computation compares to the old approximation used in the KOSMA- τ model. For this purpose we evaluated a reference model clump with varying FUV radiative transfer and different dust models. We kept the following model parameters constant for all models: the total clump mass $M = 10 \text{ M}_\odot$, the total surface gas density $n = 10^5 \text{ cm}^{-3}$, and the total FUV field $\chi = 1000$ in units of the Draine field (Draine 1978). We applied a power law density gradient with power index 1.5 with a constant central gas density for radii smaller than $R_{\text{tot}}/5$. This implies $R_{\text{tot}} = 2.46 \times 10^{17} \text{ cm} = 0.08 \text{ pc}$. We assumed a total cosmic ray ionization rate of molecular hydrogen $\zeta_{\text{H}_2} = 5 \times 10^{-17} \text{ s}^{-1}$. The chemistry is based on the UMIST 2006 database for astrochemistry UDFa² (Woodall et al. 2007), using 47 chemical species and 490 reactions in total.

² www.udfa.net

3.1. UV continuum radiative transfer

3.1.1. Dust extinction

For any given line of sight, the optical depth at FUV wavelengths $\tau_{\text{FUV}} = \sigma_{\text{d,FUV}} N_{\text{H}}$ (Sternberg & Dalgarno 1989), with $\sigma_{\text{d,FUV}}$ being the effective dust grain extinction cross section in the FUV, and the total hydrogen column density N_{H} . In the previous version of the KOSMA- τ code, the local radiation field was calculated by computing the optical depth as a function of angle and then performing an angular averaging of the resulting intensity over the full solid angle. A detailed description of the FUV transfer in the spherical model has been given by Störzer et al. (1996).

For a constant dust-to-H ratio the *total* extinction cross section per H nucleus can be derived from

$$\sigma_{\text{ext}}(\lambda) = \frac{\tau_{\text{ext}}(\lambda)}{N_{\text{H}}} = \sum_{i=1}^{\text{NDS}} \int_{a_{i,-}}^{a_{i,+}} f_i(a) C_{\text{ext}}^i(\lambda, a) da, \quad (3)$$

where $C_{\text{ext}}^i(\lambda, a)$ is the extinction cross section of a single dust particle with size a at wavelength λ . Often the absolute extinction in magnitudes is used

$$A(\lambda) = 2.5 \log(e) \tau_{\text{ext}}(\lambda) \approx 1.086 \tau_{\text{ext}}(\lambda). \quad (4)$$

By introducing the average mass extinction coefficient for each dust component, i.e., the mean extinction cross section per dust mass,

$$\langle K_{\text{ext}}^i(\lambda) \rangle_a = \frac{\int_{a_{i,-}}^{a_{i,+}} n_i(a) C_{\text{ext}}^i(\lambda) da}{\int_{a_{i,-}}^{a_{i,+}} n_i(a) 4/3 \pi a^3 \rho_{\text{b},i} da} = \frac{\int_{a_{i,-}}^{a_{i,+}} n_i(a) C_{\text{ext}}^i(\lambda) da}{\rho_{\text{dust},i}}, \quad (5)$$

where $\rho_{\text{b},i}$ is the bulk dust grain density (i.e., the density of material of which dust of given sort is composed) and $\rho_{\text{dust},i}$ is volume density of the i -th dust sort, the optical depth at any given point of the model clump can be written as

$$\tau_{\text{ext}}(\lambda) = \int dr \sum_{i=1}^{\text{NDS}} \langle K_{\text{ext}}^i(\lambda) \rangle_a \rho_{\text{dust},i}. \quad (6)$$

Relating this to the gas density provides

$$\tau_{\text{ext}}(\lambda) = m_{\text{H}} \int dr n \frac{\rho_{\text{dust}}}{n m_{\text{H}}} \sum_{i=1}^{\text{NDS}} \langle K_{\text{ext}}^i(\lambda) \rangle_a \frac{\rho_{\text{dust},i}}{\rho_{\text{dust}}}, \quad (7)$$

where $n m_{\text{H}} = \rho_{\text{gas}}$, and m_{H} is mass of a single H atom. Using $\Psi = \rho_{\text{dust}}/(n m_{\text{H}})$ as the total dust-to-H mass ratio, and $\Psi = \sum_{i=1}^{\text{NDS}} \Psi_i = \sum_{i=1}^{\text{NDS}} \rho_{\text{dust},i}/(n m_{\text{H}})$ we can write

$$\tau_{\text{ext}}(\lambda) = m_{\text{H}} \int dr n \Psi \langle K_{\text{ext}}(\lambda) \rangle, \quad (8)$$

with

$$\langle K_{\text{ext}}(\lambda) \rangle = \frac{1}{\Psi} \sum_{i=1}^{\text{NDS}} \langle K_{\text{ext}}^i(\lambda) \rangle_a \Psi_i. \quad (9)$$

For a constant dust-to-H mass ratio the integration over r in Eq. (8) can be performed giving an H column density N_{H} using

$$\tau_{\text{ext}}(\lambda) = N_{\text{H}} m_{\text{H}} \Psi \langle K_{\text{ext}}(\lambda) \rangle, \quad (10)$$

i.e., $\sigma_{\text{ext}}(\lambda) = \langle K_{\text{ext}}(\lambda) \rangle m_{\text{H}} \Psi$.

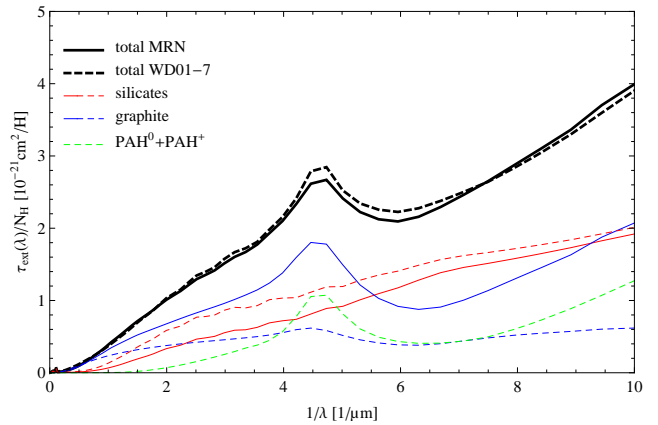


Fig. 1. Extinction cross section per H nucleus for the WD01-7 dust model (dashed lines) and for the MRN model (solid lines). The total cross sections are represented by thick lines. The contribution from each dust component is shown by red lines for silicates, blue lines for graphite, and green lines for very small grains.

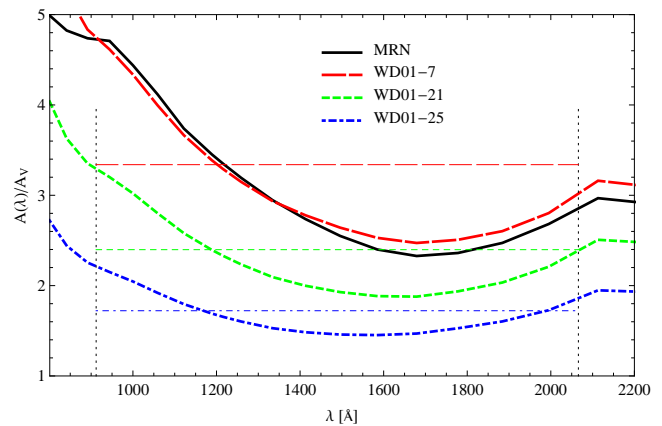


Fig. 2. Relative extinction for the dust models of MRN (solid), WD01-7 (long-dashed; red in electronic version); WD01-21 (short-dashed; green in the electronic version) and WD01-25 (dot-dot-dashed; blue in the electronic version) of interstellar dust. The vertical dotted lines at wavelengths of 912 and 2066 Å, corresponding to 13.6 and 6 eV, show the range of averaging. The horizontal lines show k_{FUV} for the considered models.

3.1.2. Influence of the dust composition

Figure 1 shows the total extinction cross section per H nucleus computed for the WD01-7 (thick dashed line) and the MRN model (thick solid line) of interstellar dust. The other lines show contributions from each dust component incorporated into the WD01-7 model (silicates – dashed, red in the electronic version; graphite – dashed, blue in the electronic version; and PAH⁰+PAH⁺ — dashed green line in the electronic version), and the solid lines present contribution from silicates (red) and graphite (blue) in the MRN model. One can see that in the WD01 model populations of very small grains (PAH⁰ and PAH⁺) are responsible for a large part of the total extinction, especially for the 2200 Å band, while large grains dominate the total mean Galactic extinction in the MRN model.

Fig. 2 shows A_{λ}/A_V for the dust models tested in this paper: MRN (solid), WD01-7 (long-dashed; red in the electronic version), WD01-21 (short-dashed; green in the electronic version), and WD01-25 (dot-dot-dashed; blue in the electronic version). The FUV range relevant for photoelectric heating

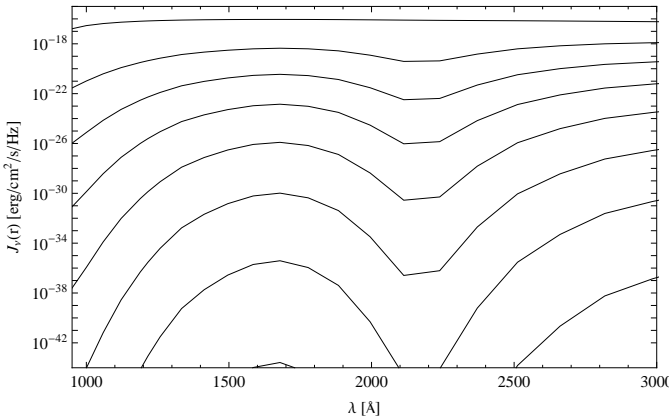


Fig. 3. Mean intensity $J_\lambda(r)$ for a model clump of $M = 10 M_\odot$, $n = 10^5 \text{ cm}^{-3}$, and $\chi = 1000$. The lines show $J_\lambda(r)$ for radii in steps of 10% of R_{tot} .

and photo-dissociation reactions extends between 13.6 and 6 eV³. Consequently, we define an FUV-to-V color as $k_{\text{FUV}} = \langle A(\lambda)/A(V) \rangle_\lambda \equiv \langle A_\lambda/A_V \rangle_\lambda$ where the averaging is performed over an energy from 6 to 13.6 eV and A_V is the visual extinction. The vertical dotted lines in Fig. 2 indicate this range of averaging and the horizontal lines show k_{FUV} for the considered models. Note that the MRN and WD01-7 dust models have the same value of $k_{\text{FUV}} = 3.339$. All values of the average relative dust extinction are collected in Tab. 4. From Fig. 2 it can be seen that k_{FUV} is significantly decreased in the WD01-21 and WD01-25 dust models. This is consistent with the higher values of R_V , i.e., a shallower gradient of $A(\lambda)/A_V$ toward shorter wavelengths causing a lower UV extinction for the same A_V (see Fig. 2). This is the main source for the different UV attenuation properties of different dust types.

3.1.3. Influence of radiative transfer and scattering

As a result of the new radiative transfer computations we obtain the full, wavelength-dependent FUV radiation field $J_\lambda(r) = \frac{1}{4\pi} \int I_\lambda d\Omega$ at all clump radii, where I_λ is the specific intensity at wavelength λ . In Fig. 3 we plot $J_\lambda(r)$ for radii in steps of $R_{\text{tot}}/10$ for the WD01-7 model. The effect of the prominent 2200 Å “bump” is plainly visible in the enhanced reduction of J_λ with decreasing radius.

The FUV optical depth

$$\tau_{\text{FUV}} = k_{\text{FUV}} \tau_V = N_H \sigma_{\text{D,FUV}} \quad (11)$$

can be described by the effective dust extinction cross section

$$\sigma_{\text{D,FUV}} = k_{\text{FUV}} m_H \Psi \langle K_{\text{ext}}(V) \rangle. \quad (12)$$

For adopted dust models, the obtained values of $\sigma_{\text{D,FUV}}$ are collected in Tab. 4.

The original KOSMA- τ code did not include any angular dependence of the dust scattering but implicitly assumed pure forward scattering (Sternberg & Dalgarno 1989) in terms of an extinction coefficient $\sigma_{\text{D,FUV}}$. As long as the models use the same value of $\sigma_{\text{D,FUV}}$, the radiative transfer should always give the same scaling of the UV intensity with $\exp(-N_H \sigma_{\text{D,FUV}})$ at high optical depths because the radiation from scattering at other angles is quickly damped because of the longer optical path, but

³ H₂ only absorbs FUV photons via Lyman and Werner electronic transitions in the 912–1100 Å range.

the scattering will increase the intensity close to the surface (Flannery et al. 1980).

To study the influence of FUV scattering we performed a set of model calculations with different scattering properties but the same effective value of $\sigma_{\text{D,FUV}} = 1.76 \times 10^{-21} \text{ cm}^2$:

1. The old KOSMA- τ FUV calculations using pure forward scattering.
2. The MCDRT result for a MRN dust distribution providing the same $\sigma_{\text{D,FUV}}$, but where the albedo ω is artificially set to zero.
3. The MCDRT result for the MRN distribution with a full treatment of scattering and absorption.

In Appendix A we discuss how the assumption of isotropic scattering compares to more realistic scattering properties and demonstrate that it poses a clear improvement compared to the pure forward scattering case used in our previous model.

Figure 4 shows a comparison of the depth-dependant mean FUV intensity scaled by the unattenuated mean FUV intensity $J(r)/\chi_0$ for these three models. $J(r)$ is the total mean intensity, i.e., averaged over the full solid angle and integrated over the full wavelength range: $J(r) = \int_{912\text{\AA}}^{2066\text{\AA}} J_\lambda(r) d\lambda$. χ_0 is the corresponding total mean intensity of the FUV field in the absence of the molecular cloud, i.e., the full unattenuated photon flux coming from 4π solid angle. For $r = R_{\text{tot}}$, models 1) and 2) are slightly larger than 0.5, which would be the theoretical value for a fully opaque and very large clump. Higher values indicate the contribution from angles slightly larger than 90°. By contrast model 3 shows a value of 0.58, indicating significant contributions to $J(r)$ by scattered photons. Consequently, the mean intensity is higher for model 3) throughout the whole clump because of a large amount of scattered photons. The small differences between models 1) and 2) result from the full wavelength treatment compared to the attenuation by an average τ_{FUV} only. For high optical depths models 2) and 3) converge to the same intensities as all sideways scattered photons turn insignificant there because of the longer optical path (Flannery et al. 1980).

Eq. (12) turns out to be a very good approximation when only forward-scattering occurs, which is clearly reproduced by the detailed radiative transfer computations with the albedo set to zero. However, only the full radiative transfer treatment can produce the full spatial and spectral knowledge of the radiation field and the proper accounting for scattered photons.

The influence of dust composition on the resulting depth-dependent FUV intensity in the clump can be seen in Fig. 5. For the FUV intensity in the WD01 models, the following is true throughout the whole clump: WD01-7 < WD01-21 < WD01-25.

3.1.4. Influence on photo-reactions

The local UV intensity acts on the chemistry of the clump by heating the gas and dust and by inducing ionization and dissociation reactions. This photo-process j with a wavelength-dependent cross section $\sigma_j(\lambda)$ proceeds at a rate (Roberge et al. 1991)

$$\Gamma_j(r) = 4\pi \int_{\lambda_H}^{\lambda_j} J_\lambda(r) \sigma_j(\lambda) d\lambda. \quad (13)$$

$J_\lambda(r)$ is the mean intensity of radiation at radius r in photons $\text{cm}^{-2}\text{s}^{-1}\text{nm}^{-1}$. The integral runs from $\lambda_H = 912 \text{ \AA}$ to the threshold wavelength λ_j for the process j ⁴. Astrochemical databases

⁴ A database of photo-ionization and photo-dissociation cross sections for common astrophysical species can be found at

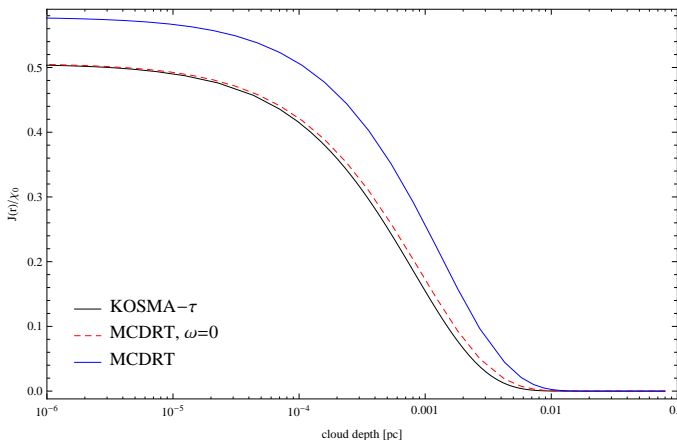


Fig. 4. Mean intensity of the UV radiation vs. cloud depth. The black line corresponds to the old KOSMA- τ result for pure absorption. The blue line corresponds to the MCDRT result for an MRN distribution with full treatment of scattering and absorption. The dashed line is the result for an MRN distribution with the albedo artificially set to zero.

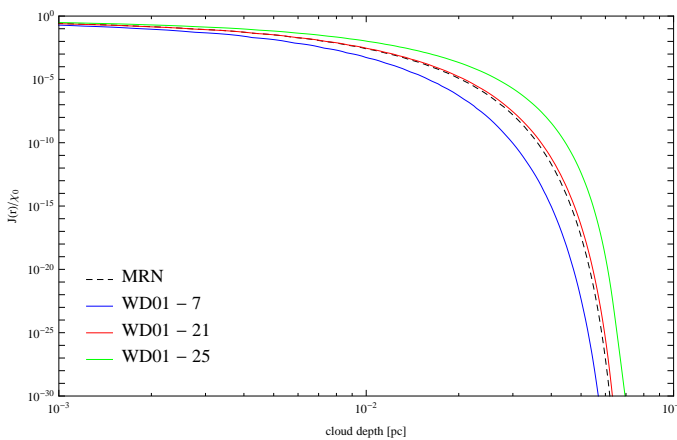


Fig. 5. Mean intensity of the UV radiation $J(r)$ scaled to the unshielded (empty space) Draine field χ_0 vs. cloud depth. Different lines denote different dust compositions.

often provide parametrized reaction rate coefficients to allow the calculation of these photo-reaction rates. For instance, UDFa gives the rate coefficients in the form

$$\Gamma_j(A_V) = \chi_0 \alpha_j \exp(-\gamma_j A_V) \quad (14)$$

assuming an attenuation of the radiation provided by a standard MRN dust model in a plane-parallel configuration using the radiation transfer results from Flannery et al. (1980) parametrized in terms of the perpendicular visual extinction A_V . χ_0 is the FUV field strength at the edge of the cloud and the unshielded, free-space rate coefficient α_j assumes a mean FUV intensity of unity (in units of the Draine field) and FUV photons coming from all directions. At the edge of an optically thick molecular cloud the rate coefficient is about half of this value, depending on the dust scattering properties.

The unshielded rate coefficient α_j does not depend on the dust properties and we concentrated on the attenuation properties, parametrized in form of the γ_j^D . Changing either the dust properties, i.e., the wavelength-dependant FUV attenuation, or

<http://home.strw.leidenuniv.nl/~ewine/photo/>. For more details see van Dishoeck et al. (2006) and van Hemert & van Dishoeck (2008)

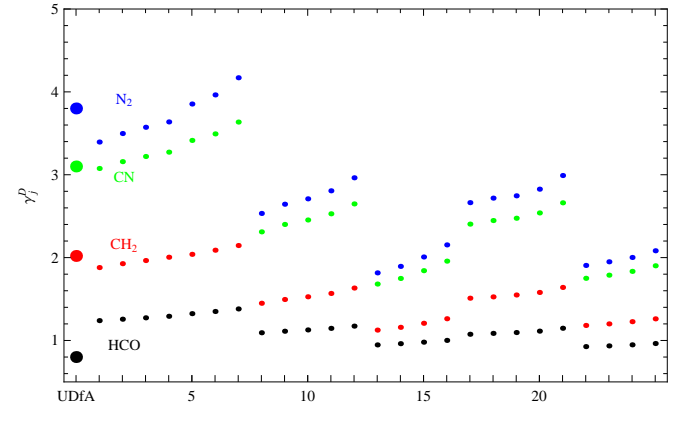


Fig. 6. Fit results for $\gamma_{j,fit}^D$ for HCO (black), CH_2 (red), CN (green), and N_2 (blue) for all dust models from Weingartner & Draine (2001b, their Tab. 1). The abscissa gives the number of the dust model. The large points show the original values of γ_j for the respective molecules.

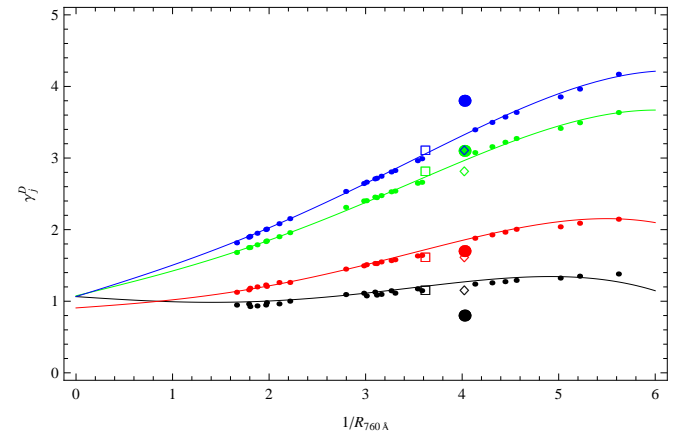


Fig. 7. Comparison of explicitly fitted γ_j^D for HCO (black), CH_2 (red), CN (green), and N_2 (blue) for all dust models from Weingartner & Draine (2001b, their Tab. 1) with scaling relationship Eq. 16. The large points show the original values of γ_j from UDFa, the open diamonds show the values calculated using an MRN dust model, and the open squares denote the explicitly calculated values assuming $1/R_{760\text{\AA}}^{\text{MRN}} = 3.62$.

the spectral distribution of the FUV field leads to a different result for Γ_j and consequently to a different fit parameter γ_j . However, performing the wavelength-dependent integration of Eq. 13 for every reaction and every radial point is often beyond the scope of PDR models, e.g., because it is too time-consuming or because neither dust properties nor ionization cross sections $\sigma_j(\lambda)$ are known accurately enough to justify the computational effort of a full integration of the wavelength-dependent radiative transfer. Furthermore, knowledge of the wavelength-dependent σ_j is not available for all astrophysically relevant species and models have to apply Eq. 14 even if they can perform the full integration in principle.

Here we derive a scaling relation between the γ_j values provided by a data base like UDFa and corresponding fit values for a particular dust model $\gamma_j \rightarrow \gamma_j^D$ to calculate the rate coefficient $\Gamma_j^D(A_V)$ for species j and dust sort D . For a direct comparison with UDFa values we started from a model cloud with a mass of $10^3 M_\odot$ and a radius of 1.71 pc, large enough to neglect the ef-

fects of the spherical symmetry close to the surface, isotropically illuminated and calculated the photo-dissociation and photo-ionization rates of 72 species provided by van Dishoeck et al. (2006); van Hemert & van Dishoeck (2008) for all 25 dust models D from Weingartner & Draine (2001b) according to Eq. 13.

To this end, we performed least-squares fits to $\Gamma_j(A_V)/\Gamma_j(0) = \exp(-\gamma_{j,fit}^D A_V)$ up to an $A_V = 10$ to determine new $\gamma_{j,fit}^D$ coefficients for all D and j . Figure 6 shows the new $\gamma_{j,fit}^D$ for four example molecules, HCO, CH₂, CN, and N₂ for all 25 dust models.

The big dots on the left show the original value γ_j from UDfA⁵. The figure shows that the new $\gamma_{j,fit}^D$ show the same behavior along the abscissa for all four example species. There are also three branches of $\gamma_{j,fit}^D$, visible as prominent quantitative steps in Fig. 6 that correspond to the respective R_V values.

The next step is to identify what dust model property is best correlated with $\gamma_{j,fit}^D$. An extensive analysis of the dust properties reveals that we can find a wavelength $\lambda = 760\text{\AA}$ for which

$$1/R_\lambda = \left(\frac{A(V)}{A(\lambda) - A(V)} \right)^{-1} \quad (15)$$

shows a monotonic ordering for the $\gamma_{j,fit}^D$ of the 25 dust models. Consequently, we chose $1/R_{760\text{\AA}}^D$ as the parameter describing the dust. Table 1 gives $1/R_{760\text{\AA}}^D$ for all 25 WD01 dust models. Using this parameter, we can approximate the dependence of γ_j^D on γ_j and the dust model by

$$\begin{aligned} \gamma_j^D = & w_1 + w_2 \left(\frac{1}{R_{760\text{\AA}}^D} \right) + w_3 \left(\frac{1}{R_{760\text{\AA}}^D} \right)^3 + w_4 \left(\frac{1}{R_{760\text{\AA}}^D} \right)^4 \\ & + w_5 \gamma_j + w_6 \gamma_j^3 + w_7 \gamma_j^4 + w_8 \frac{\gamma_j}{R_{760\text{\AA}}^D} + w_9 \frac{\gamma_j^2}{R_{760\text{\AA}}^D}. \end{aligned} \quad (16)$$

Equation 16 reproduces the explicitly calculated attenuation of the rate coefficients within an accuracy of $\sigma = 0.05$, and a maximum absolute residual of 0.22. This is comparable to the uncertainties of $\gamma_{j,fit}^D$ due to fitting $\Gamma_j(A_V)/\Gamma_j(0)$ up to a different maximum A_V . Note that for the fitting we removed seven species (photo-dissociation of CH⁺, SH⁺, OH⁺, HCO⁺, CO, O₂⁺, and SiO) from the data set because their γ_j^D represent strong outliers with respect to the remainder of the data set. We discuss possible reasons for these deviations in Appendix B. To apply Eq. 16 to them, we had to use corrected coefficients $\hat{\gamma}_j$ instead of the UDfA values when computing γ_j^D . The $\hat{\gamma}_j$ values are given in Tab. 3.

It turns out that the original MRN distribution with $1/R_{760\text{\AA}}^{\text{MRN}} = 4.03$ does not exactly follow the parametrization of Eq. 16, based on the WD01 dust models, but that it can be easily used in the same function when adjusting the parameter $1/R_{760\text{\AA}}^{\text{MRN}} = 3.62$. Figure 7 compares $\gamma_{j,fit}^D$ for HCO, CH₂, CN, and N₂ with the results of Eq. 16. In addition we show the MRN results in the plot: the original γ_j , the explicitly calculated γ_j^{MRN} , and the γ_j^{MRN} assuming $1/R_{760\text{\AA}}^{\text{MRN}} = 3.62$ using large points, open diamonds, and open squares, respectively (the arrows in the figure demonstrate the shifting of the rescaled γ_j^D closer to Eq. 16).

⁵ van Dishoeck et al. (2006) and van Hemert & van Dishoeck (2008) provide their own fitted values of $\gamma_{j,EVD}$ (up to a maximum $A_V = 3$) for all species for which they also give tables of $\sigma_j(\lambda)$.

Table 1. Dust model parametrization of all WD01 dust models. See Weingartner & Draine (2001b) for more details.

D^a	R_V^b	$10^5 b_c^c$	Case ^d	$1/R_{760\text{\AA}}^D$ ^e	order ^f
1	3.1	0.0	A	4.13	19
2	3.1	1.0	A	4.31	20
3	3.1	2.0	A	4.44	21
4	3.1	3.0	A	4.56	22
5	3.1	4.0	A	5.02	23
6	3.1	5.0	A	5.22	24
7	3.1	6.0	A	5.62	25
8	4.0	0.0	A	2.79	9
9	4.0	1.0	A	2.98	10
10	4.0	2.0	A	3.10	12
11	4.0	3.0	A	3.26	15
12	4.0	4.0	A	3.54	17
13	5.5	0.0	A	1.66	1
14	5.5	1.0	A	1.79	2
15	5.5	2.0	A	1.97	6
16	5.5	3.0	A	2.21	8
17	4.0	0.0	B	3.01	11
18	4.0	1.0	B	3.11	13
19	4.0	2.0	B	3.16	14
20	4.0	3.0	B	3.30	16
21	4.0	4.0	B	3.58	18
22	5.5	0.0	B	1.80	3
23	5.5	1.0	B	1.88	4
24	5.5	2.0	B	1.96	5
25	5.5	3.0	B	2.10	7

Notes.

(a) Dust model D , see Tab. 1 in WD01

(b) $R_V = A(V)/E_{B-V}$, ratio of visual extinction to reddening.

(c) C abundance in double log-normal very small grain population.

(d) Case A: variable grain volumes. Case B: grain volumes fixed at approximately the values found for $R_V = 3.1$.

(e) $1/R_\lambda = (A(V)/(A(\lambda) - A(V)))^{-1}$

(f) Ordering of the various dust models from lowest to highest value of $1/R_{760\text{\AA}}$.

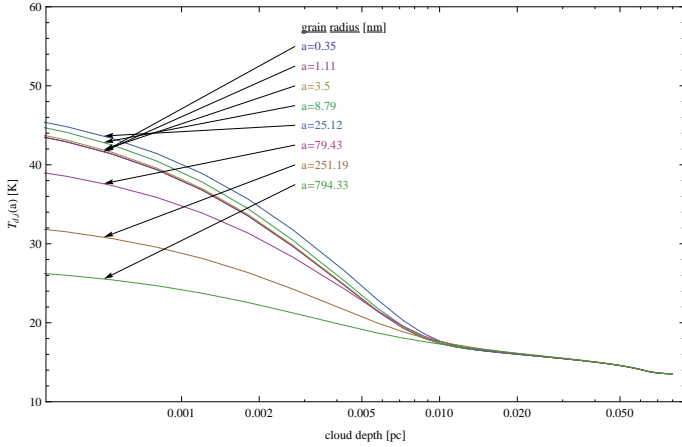
Table 2. Fit parameters in Eq. 16.

fit parameter	
w_1	1.39460
w_2	-0.27655
w_3	0.02053
w_4	-0.00295
w_5	-0.45990
w_6	0.08725
w_7	-0.01616
w_8	0.24747
w_9	-0.01677

It is unclear why the γ_j from UDfA, i.e., the MRN values, do not follow the parametrization of Eq. 16. There is a number of possible reasons for the deviation. Woodall et al. (2007) did not use a Draine FUV radiation field but assumed a 10000 K black-body radiation field. The different spectral shape usually accounts for approximately 10% difference but can in a few special cases result in a significant difference. Secondly, different $A_{V,\text{max}}$ up to which the γ_j is fitted give different values of γ_j (see Appendix B for a more detailed discussion). The details of the radiation scattering is another possible reason for different results. Assuming different anisotropy factors g and dust albedo ω will change the radiation field and accordingly affect the γ_j (see

Table 3. Corrected $\hat{\gamma}_j$ for the outlying species.

species	γ_j	$\hat{\gamma}_j$
CH^+	2.5	2.11
SH^+	1.8	1.39
OH^+	1.8	2.76
HCO^+	2.	3.036
CO	2.5	3.03
O_2^+	2.	1.61
SiO	2.3	1.87

**Fig. 8.** Dust temperatures of silicate grains for a model clump of $M = 10 \text{ M}_\odot$, $n = 10^5 \text{ cm}^{-3}$, and $\chi = 1000$ using the WD01-7 dust model. The different lines denote different grain sizes.

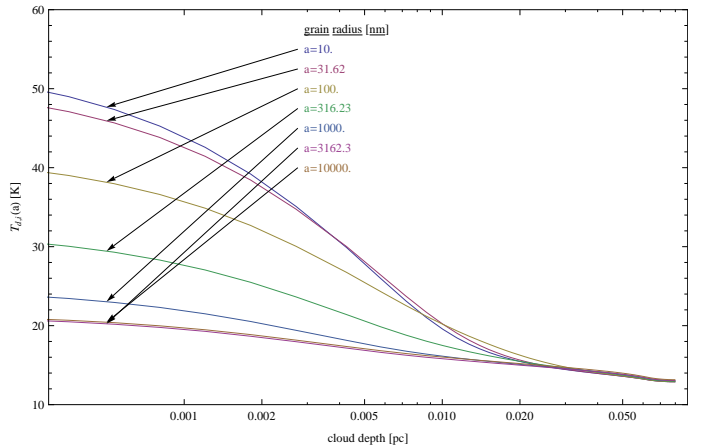
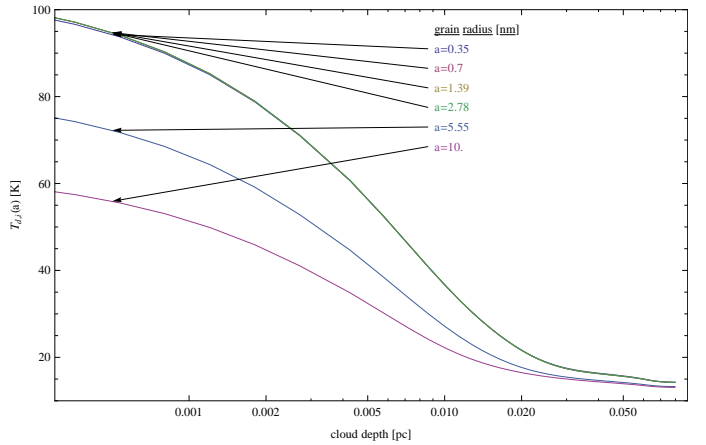
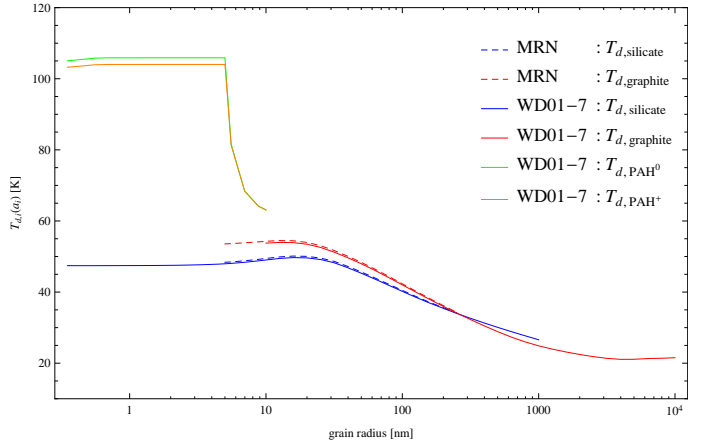
Appendix A for a discussion on the effect of different values of g .

We conclude that the scaling relation Eq. 16 is able to rescale the tabulated γ_j from UDFa to the dust-specific $\gamma_{j,fit}^D$ (fitted to the fully calculated $\Gamma_j(A_V)/\Gamma_j(0)$) with an accuracy of about 10%.

3.2. Dust temperatures

Dust temperatures are calculated independently for each dust component and size. Figures 8, 9, and 10 show depth-dependent grain temperatures for a number of differently sized grains for three of the four components. The plot for the ionized PAHs is omitted because their temperature behaves like that of neutral PAHs. The general behavior is that smaller grains exhibit higher grain temperatures.

Figure 11 compares grain temperatures of the components of the MRN and WD01-07 dust model at the surface of a model clump as a function of grain radius a_i . Graphites tend to have a higher temperature than silicate grains except for very large grain sizes. Small grains tend to be hotter than bigger grains. The PAHs are heated much more efficiently than the larger grains and have significantly higher grain temperatures. For simplicity, we deliberately neglected the non-equilibrium heating of very small grains and PAHs here and assumed equilibrium heating in this paper. In a subsequent paper, we will include the comparison with real observations accounting for the stochastic heating of the very small particles. The dependence on a_i vanishes for sufficiently high extinctions i.e., once most of the remaining photons have wavelengths longer than the grains. The resulting equilibrium grain temperature then only depends on the absorption coefficient of the material.

**Fig. 9.** Dust temperatures of carbonaceous grains for a model clump of $M = 10 \text{ M}_\odot$, $n = 10^5 \text{ cm}^{-3}$, and $\chi = 1000$ using the WD01-7 dust model. The different lines denote different grain sizes.**Fig. 10.** Dust temperatures of neutral PAHs for a model clump of $M = 10 \text{ M}_\odot$, $n = 10^5 \text{ cm}^{-3}$, and $\chi = 1000$ using the WD01-7 dust model. The different lines denote different PAH sizes.**Fig. 11.** Grain temperature for the components of the MRN and WD01-07 dust models as a function of the radius a_i in nm. The grain temperatures are calculated at the surface of a model clump of $M = 10 \text{ M}_\odot$, $n = 10^5 \text{ cm}^{-3}$, and $\chi = 1000$. The different lines denote different dust components. Dashed lines show the MRN components and solid lines show the WD01-07 components.

The detailed knowledge of the dust temperature as a function of radius, grain size, and grain type enables us to treat all dust-related processes separately for all grain sizes and types. However, since most relevant processes are grain surface reactions, e.g., formation of the H₂ or photoelectric heating, it is usually sufficient to calculate surface-averaged quantities. For the i -th dust component we can define the relevant mean dust temperature as

$$\langle T_{d,i} \rangle_a = \frac{\int_{a_{i,-}}^{a_{i,+}} T_{d,i}(a) n_i(a) a^2 da}{\int_{a_{i,-}}^{a_{i,+}} n_i(a) a^2 da}. \quad (17)$$

Averaging over all dust sorts is done according to

$$\langle T_d \rangle_{NDS} = \sum_{i=1}^{NDS} \langle T_{d,i} \rangle_a \frac{\sigma_{d,i}}{\sigma_d} \quad (18)$$

with the geometrical cross section of the i -th sort $\sigma_{d,i}$ and the total dust cross section σ_d . We will use the short-hand notation $T_d = \langle T_d \rangle_{NDS}$ and $T_{d,i} = \langle T_{d,i} \rangle_a$ from here on.

Figure 12 shows the mean dust temperature $T_{d,i}$ for the WD-7 dust model as a function of cloud depth for all four dust components. As at the surface (Fig. 11), silicates, indicated by the solid blue line, are cooler than graphite grains (solid, red line). Graphite and silicate grain temperatures are very close, but the mean silicate temperature drops slightly faster for increased cloud depths than the graphites. The PAHs have a much higher $T_{d,i}$. Neutral PAHs tend to be marginally hotter than the ionized PAHs. The black line denotes the average dust temperature T_d for the WD01-7 dust.

The influence of the different dust models can be seen from Fig. 13. The black line shows the old dust temperature calculation in KOSMA- τ following Hollenbach et al. (1991), which gives a central dust temperatures $T_d \approx 22$ K. Accounting for the full wavelength dependence and the detailed grain size distribution gives a significantly lower $T_d \approx 13$ K at the center of the model clump. On the other hand, it also leads to warmer dust at the surface of the cloud compared to Hollenbach et al. (1991).

The dust temperature for the WD01 models follow their corresponding FUV intensities (see Fig. 5). The MRN model has a much lower T_d . Figure 11 shows that the $T_{d,i}$ for MRN and WD01-7 are very similar for equal grain sizes. However, the temperature of the PAHs in the WD01-7 model contributes significantly to the average dust temperatures in Eq. (18) and leads to higher T_d in models with PAH content.

The lower central dust temperatures of models with WD01 dust types also influences the gas temperatures. Models with WD01 dust show significantly lower central gas temperatures because gas-grain collisions are becoming the dominant cooling process.

3.3. H₂ formation

Molecular hydrogen is the most abundant molecule in the universe. The formation of H₂ most effectively takes place on the surface of dust grains. The proper treatment of the H₂ formation is crucial in any numerical PDR model (see e.g. Le Bourlot et al. 2012, for a recent update of the Meudon PDR code.). We updated the KOSMA- τ calculation of the H₂ formation efficiency R_{H_2} from the method described by SD89 to account for physisorption and chemisorption binding energies on silicate and graphite surfaces (Cazaux & Tielens 2002, 2004, 2010, (hereafter CT)).

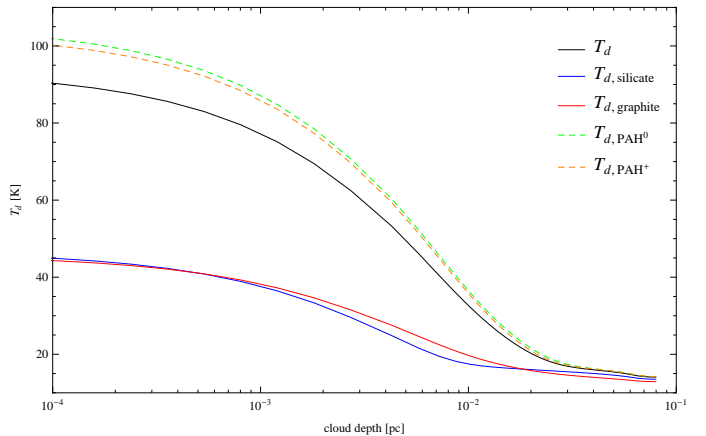


Fig. 12. Mean dust temperature for the WD01-7 dust model for a model clump of $M = 10 M_\odot$, $n = 10^5 \text{ cm}^{-3}$, and $\chi = 1000$. The different lines denote the average temperature of the individual dust components. The black line shows the overall mean dust temperature.

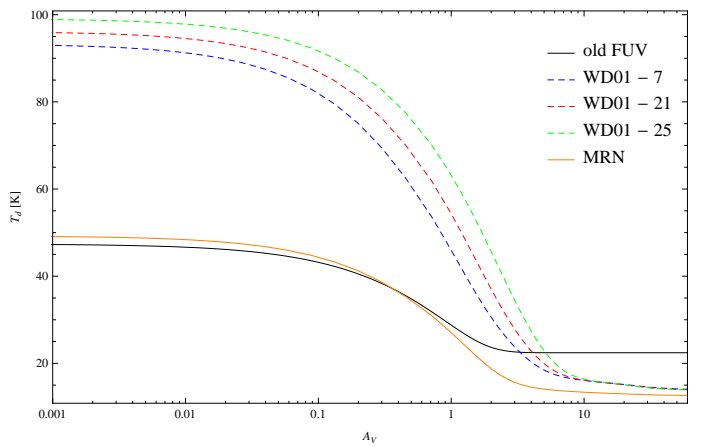


Fig. 13. Mean dust temperature as a function of A_V for a model clump of $M = 10 M_\odot$, $n = 10^5 \text{ cm}^{-3}$, and $\chi = 1000$. The different lines denote different dust compositions.

This model is based on two main points: (1) H atoms can stick to the grain surface in two different binding sites, a physisorption site and a chemisorption site. Physisorption is a weak atom-surface binding resulting from a Van der Waals force (dipole-dipole interaction). Chemisorption is a strong atom-surface binding interaction involving the valence electrons, known as covalent bond. These interactions determine whether atoms move on the surface, and thus, how quickly they can meet a recombination partner. (2) The mobility of a surface H atom results from the combination of two physical processes: tunneling and thermal diffusion; tunneling dominates at the lowest temperatures while thermal diffusion is most important at the highest temperatures. The calculation of the transmission coefficients, to go from site to site, are given in Cazaux & Tielens (2004, 2010).

At low temperature ($T \leq 100$ K), H₂ formation involves the migration of physisorbed H atoms. At higher temperatures ($T \geq 100$ K), H₂ formation results from chemisorbed H recombination. The presence of these two types of binding sites allows H₂ formation to proceed relatively efficiently at low and elevated temperatures.

Table 4. Parameter of the WD01 and MRN dust models

model	parameter	silicates	graphite	PAH ⁰	PAH ⁺	total
MRN	a_- [Å]	50	50			
	a_+ [μm]	0.25	0.25			
	k_{FUV}					3.339
	$\sigma_{\text{D,FUV}} [\text{cm}^2]$	5.43×10^{-22}	1.22×10^{-21}			1.76×10^{-21}
	$\sigma_d [\text{cm}^2]$	6.05×10^{-22}	5.65×10^{-22}			1.17×10^{-21}
	$\Psi [\%]$	0.598	0.357			0.955
WD01-07	a_- [Å]	3.5	100	3.5	3.5	
	a_+ [μm]	1.	10.	0.01	0.01	
	k_{FUV}					3.339
	$\sigma_{\text{D,FUV}} [\text{cm}^2]$	9.59×10^{-22}	6.94×10^{-22}	4.73×10^{-23}	4.58×10^{-23}	1.75×10^{-21}
	$\sigma_d [\text{cm}^2]$	1.14×10^{-21}	1.34×10^{-22}	2.71×10^{-21}	2.71×10^{-22}	6.69×10^{-21}
	$\Psi [\%]$	0.828	0.0228	0.038	0.038	1.130
WD01-21	a_- [Å]	3.5	100	3.5	3.5	
	a_+ [μm]	1.	10.	0.01	0.01	
	k_{FUV}					2.398
	$\sigma_{\text{D,FUV}} [\text{cm}^2]$	8.56×10^{-22}	3.06×10^{-22}	2.44×10^{-23}	2.37×10^{-23}	1.21×10^{-21}
	$\sigma_d [\text{cm}^2]$	4.93×10^{-22}	9.99×10^{-23}	1.85×10^{-21}	1.85×10^{-21}	4.29×10^{-21}
	$\Psi [\%]$	0.815	0.0252	0.027	0.027	1.120
WD01-25	a_- [Å]	3.5	100	3.5	3.5	
	a_+ [μm]	1.	10.	0.01	0.01	
	k_{FUV}					1.722
	$\sigma_{\text{D,FUV}} [\text{cm}^2]$	6.78×10^{-22}	1.40×10^{-22}	1.22×10^{-23}	1.18×10^{-23}	8.41×10^{-22}
	$\sigma_d [\text{cm}^2]$	2.12×10^{-22}	5.08×10^{-23}	1.36×10^{-21}	1.36×10^{-21}	2.98×10^{-21}
	$\Psi [\%]$	0.812	0.0268	0.019	0.019	1.118

For the dust component i , the formation rate can be written as

$$R_{\text{H}_2,i} = \frac{1}{2} n_{\text{H}} v_{\text{H}} n_{d,i} \sigma_{d,i} \epsilon_{\text{H}_2,i} S_{\text{H}}, \quad (19)$$

where n_{H} and v_{H} are the number density and thermal velocity of H atoms in the gas phase, $n_{d,i} \sigma_{d,i}$ is the total cross section of the grain component i , $\epsilon_{\text{H}_2,i}$ is the formation efficiency (Cazaux & Tielens 2004) on surfaces of the i -th component, and S_{H} is the sticking coefficient of the H atoms

$$S_{\text{H}} = \left(1 + 0.04 \left(\frac{T_g + T_d}{100} \right)^{1/2} + 0.2 \frac{T_g}{100} + 0.08 \left(\frac{T_g}{100} \right)^2 \right)^{-1}, \quad (20)$$

which depends on the gas and dust temperature, T_g and T_d (Hollenbach & McKee 1979). The thermal velocity is $1.45 \times 10^5 (T_g/100)^{1/2} \text{ cm s}^{-1}$. The i -th dust cross section per H nucleus is given by

$$\sigma_{d,i} = \int_{a_{i,-}}^{a_{i,+}} n_i(a) \pi a^2 da. \quad (21)$$

Table 4 lists $\sigma_{d,i}$ for the different dust models. Cazaux & Tielens (2002) expressed the general expression for the i -th H_2 formation efficiency:

$$\epsilon_{\text{H}_2,i} = \frac{\xi_i}{\mathcal{A} + 1 + \mathcal{B}}. \quad (22)$$

$\epsilon_{\text{H}_2,i}$ is limited by three terms: the first term \mathcal{A} prohibits the evaporation of the newly formed molecules at low temperatures. The second term, equal to unity, dominates at higher grain temperatures; all incoming H atoms leave the surface as H_2 . The third term \mathcal{B} governs the high-temperature regime, where evaporation of physisorbed atoms removes H from the surface before it can recombine to H_2 . It competes with the hopping of atoms into chemisorbed binding sites where the atoms can remain on the surface to form H_2 at significantly higher temperatures. The

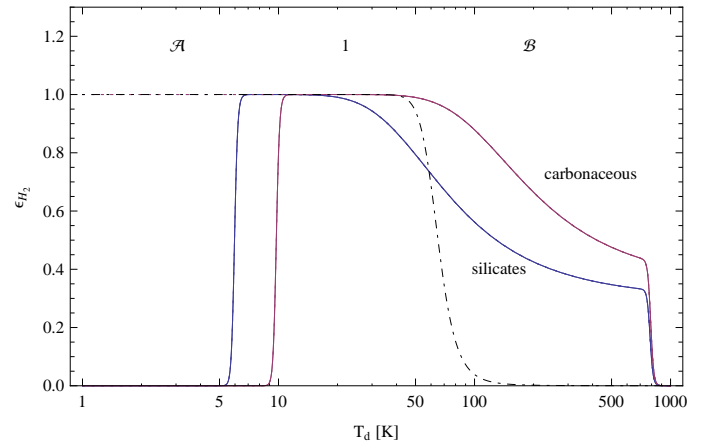


Fig. 14. H_2 formation efficiency for carbon and silicate surfaces. \mathcal{A} and \mathcal{B} denote the temperature regimes of the corresponding terms in Eq. (22). The dash-dotted line denotes the standard formation efficiency given by Hollenbach & McKee (1979).

numerator ξ_i , describing the chemisorption, terminates the H_2 formation at much higher temperatures, above several hundred Kelvin, when even chemisorbed atoms start to evaporate.

Figure 14 shows ϵ_{H_2} as a function of T_d for silicate (blue line) and graphite (red line) surfaces. The old formation efficiency from Hollenbach & McKee (1979) is shown as a dash-dotted line for comparison. When applying this formation in the framework of the PDR model, see Fig. 14, the term \mathcal{A} turned out to be problematic because it shuts down the H_2 release into the gas phase once $T < 10\text{K}$, accumulating all molecules on the grain surfaces. We question this term because Eq. (22) does not account for the H_2 binding energy of 4.48 eV that upon formation is available to allow release into the gas phase even at very low temperatures. As a remedy we set $\mathcal{A} = 0$ to ensure efficient

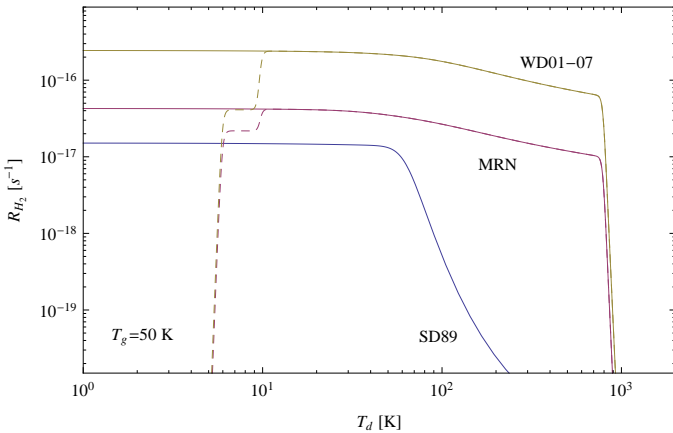


Fig. 15. H_2 formation rate R_{H_2} as a function of dust temperature T_d for different formation models and dust compositions. The gas temperature T_g is set to 50 K. The dashed lines indicate the low temperature formation in the original CT formation rates with $\mathcal{A} \neq 0$. SD89 is the formation rate from Sternberg & Dalgarno (1989).

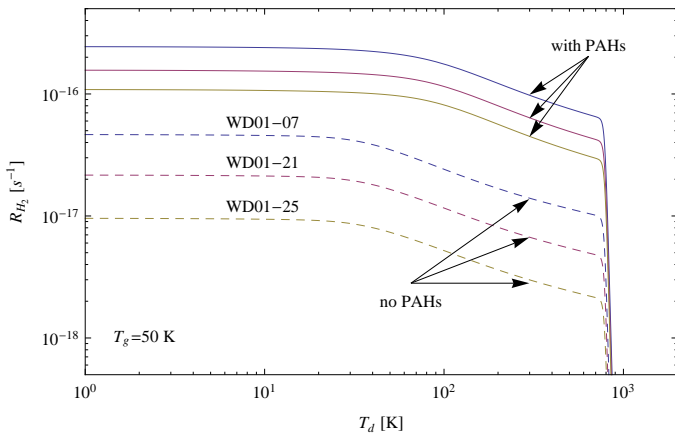


Fig. 16. H_2 formation rate R_{H_2} as a function of dust temperature T_d for different dust compositions. The gas temperature T_g is set to 50 K. The dashed lines show the formation rate with suppressed H_2 formation on PAHs. The solid lines show the formation rate allowing for H_2 formation on PAH surfaces.

H_2 formation even on cold dust surfaces (Cazaux (2011), priv. comm.)⁶. More details on how to calculate the H_2 formation efficiency are given in Appendix C. The total H_2 formation rate can then be written as

$$R_{H_2} = \sum_{i=1}^{NDS} R_{H_2,i} = \frac{1}{2} n_{H\nu_H} \sum_{i=1}^{NDS} S_{H,i} n_{d,i} \sigma_{d,i} \epsilon_{H_2,i}, \quad (23)$$

Fig. 15 compares the new and old H_2 formation rates. The formation efficiency given by SD89 follows the treatment of Hollenbach & McKee (1979), which adopted a critical dust temperature of $T_{cr} \approx 65$ K above which the H_2 formation efficiency drops below 0.5. H_2 formation becomes inefficient above ≈ 100 K. The H_2 formation in the CT dust model remains efficient up to 1000 K. The model by Cazaux & Tielens allows a much more efficient H_2 formation at higher temperatures. Additionally, the significantly larger dust surface in the MRN

⁶ All model results accounting for CT H_2 formation shown in this paper assume $\mathcal{A} = 0$.

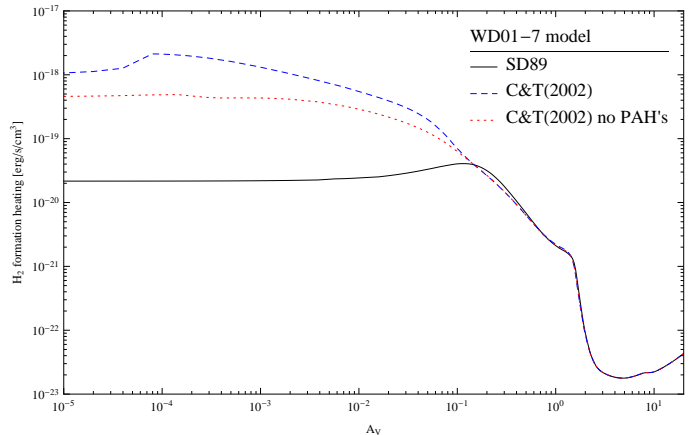


Fig. 17. H_2 formation heating rate for a model clump of $M = 10 M_\odot$, $n = 10^5 \text{ cm}^{-3}$, and $\chi = 1000$. The different lines show the effect of different H_2 formation treatment. All models have been computed using the WD01-7 dust properties regarding the radiative transfer and the PE heating.

and WD01-7 model lead to a much higher H_2 formation rate than SD89.

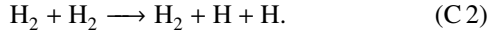
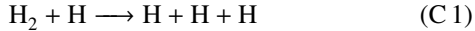
While accounting for chemisorbed H atoms significantly increases the H_2 formation efficiency at higher surface temperatures, it is the total available grain cross section that distinguishes between different dust models. Table 4 also compares the total dust cross section per H nucleus for the different dust compositions. The PAH cross sections contribute the majority to the final H_2 formation rate. The resulting H_2 formation rate for one $H \text{ atom cm}^{-3}$ is shown in Fig. 16. Solid lines show the formation rate as a function of T_d for a constant $T_g = 50$ K for the WD01-7, WD01-21, and WD01-25 models allowing for H_2 formation on the surface of PAHs. The dashed lines show the formation rates if the PAH surfaces are excluded from the H_2 formation calculation. Consequently, the dust model with the largest effective cross section, WD01-7 shows the highest formation rate in both cases.

The strong increase in the total H_2 formation rate has an important effect in addition to the easier H_2 production. Each formed H_2 molecule releases its binding energy of 4.48 eV. A common assumption (e.g., Habart et al. 2004) is that this energy is equally used to a) release the molecule into the gas phase, b) increase the kinetic energy of the molecule, and for c) internal rotational-vibrational excitation. If we assume a uniform distribution, 1.5 eV are available to heat the gas. Here we can measure the H_2 formation rate across the cloud by equivalently looking at the H_2 formation heating.

By including H_2 formation according to Eq. (23) we also increase the formation rate significantly at low values of A_V . This is shown in Fig. 17. All models in the plot were computed using the WD01-7 dust properties regarding the radiative transfer and the PE heating. The solid line shows the results for the formation rate from Sternberg & Dalgarno (1989). The result for the full H_2 formation treatment from CT (with $\mathcal{A} = 0$), suppressing and allowing H_2 formation on PAH surfaces, are shown by the dotted and dashed line. The much larger surface area of the WD01-7 dust model leads to a significant increase of the formation rate. Particularly the large PAH surface in that dust model contributes dominantly to the total grain surface and consequently to the total H_2 formation heating.

It is important to note that the H_2 formation heating is extensive at cloud depths where most of the hydrogen is in the form

of H. This leads to the curious situation of a strong H₂ formation heating in the absence of H₂ molecules. The gas temperatures at these depths can reach more than thousand Kelvin. Under these conditions two more H₂ destruction reaction become important:



Each destruction process requires 4.48 eV to break the binding, in contrast to the release of 4.48 eV during the formation. The much more efficient formation of molecular hydrogen by Cazaux & Tielens makes it necessary to adopt an additional cooling term in the chemical network, accounting for the 4.48 eV energy consumption during the kinetic dissociation (Lepp & Shull 1983). The cooling rate can be written as

$$\Lambda_{kd} = 7.2 \times 10^{-12} n_{\text{H}_2} (k_{(\text{C } 1)} n_{\text{H}} + k_{(\text{C } 2)} n_{\text{H}_2}) \text{ erg s}^{-1} \text{ cm}^{-3}, \quad (24)$$

where $k_{(\text{C } 1)}$ and $k_{(\text{C } 2)}$ are the temperature-dependent rate coefficients for reactions (C 1) and (C 2).

The role of interstellar dust in ISM physics and chemistry remains one of the key problems in modern astrophysics. In this section we demonstrate the strong effect of H₂ formation on PAH surfaces on the chemistry and the thermal conditions in PDRs. However, it remains unknown whether PAHs really contribute to the formation of molecular hydrogen. Naturally, this is connected to the uncertainty about the detailed form and distribution of interstellar PAHs.

By assuming that H₂ formation can take place on PAH surfaces the formation rate from Cazaux & Tielens predicts rates of a few times 10^{-16} s^{-1} when applied to the dust distributions presented by WD01. This is about a factor 10 higher than what has commonly been found for the diffuse medium (Jura 1974; Browning et al. 2003; Gry et al. 2002; Welty et al. 2003; Wolfire et al. 2008). However, the usual values of $R \sim 2 - 4 \times 10^{-17} \text{ cm}^3 \text{ s}^{-1}$ are mean values along the line of sight while our results are local values and a direct comparison is difficult. Recently, Le Bourlot et al. (2012) presented an update to the H₂ formation formalism in the Meudon PDR code and also found a strong increase of the local H₂ formation rates. If we prevent H₂ formation on PAH surfaces, the total grain surface available to form molecular hydrogen is significantly reduced and we predict formation rates of the same order as found in the diffuse ISM. However, PDR models assuming diffuse gas formation rates are not able to reproduce the observed extent of H₂ line excitation (Habart et al. 2011). H₂ formation on PAHs has also been proposed by Habart et al. (2003) to explain the H₂ emission in ρ Oph, and recently Mennella et al. (2012) concluded from experimental studies that hydrogenated neutral polycyclic aromatic hydrocarbon molecules act as catalysts for the formation of molecular hydrogen.

3.4. Photoelectric heating

Weingartner & Draine (2001a) presented the photoelectric heating rate for the WD01 grain size distributions in a parametrized form as a function of $\psi = (G \sqrt{T})/n_e$, where T is the gas temperature in Kelvin and ψ is in units of $\text{K}^{1/2} \text{ cm}^3$. To convert the FUV field from Habing G to Draine χ units use $G = 1.71\chi$. These parametrizations are fairly accurate when $10^3 \text{ K} \leq T \leq 10^4 \text{ K}$ and $10^2 \text{ K}^{1/2} \text{ cm}^3 \leq \psi \leq 10^6 \text{ K}^{1/2} \text{ cm}^3$. However, the parameter range in PDR models allows ψ to reach values as high as $10^9 \text{ K}^{1/2} \text{ cm}^3$ and as low as $10^{-2} \text{ K}^{1/2} \text{ cm}^3$. Weingartner (2009) provided updated calculations of Γ_{pc} and Λ_{gr} for the dust distributions

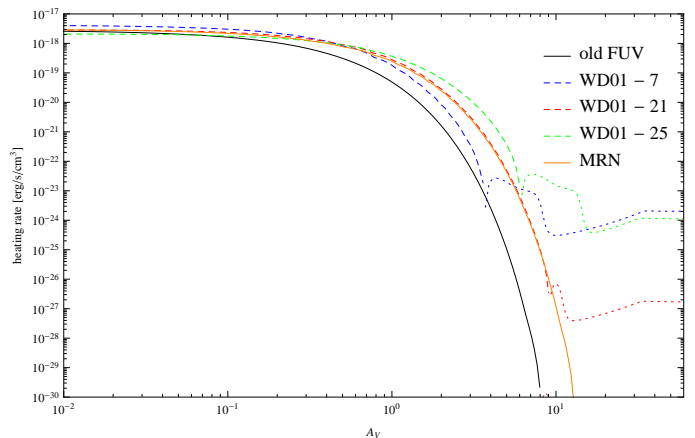


Fig. 18. Photoelectric heating rate for a model clump of $M = 10 \text{ M}_{\odot}$, $n = 10^5 \text{ cm}^{-3}$, and $\chi = 1000$. The different lines denote different dust compositions. Models with an MRN dust composition apply the PE heating efficiency as given by Bakes & Tielens (1994). Dotted lines indicate a shift from heating to cooling because of $\Lambda_{\text{gr}} > \Gamma_{\text{pc}}$.

WD01-7, WD01-21, and WD01-25 up to $\psi = 10^9 \text{ K}^{1/2} \text{ cm}^3$. These rates are fairly well reproduced by the new analytic fits:

$$\Gamma_{\text{pc}} = G n_{\text{H}} \left(\frac{C_0 + C_1 T^{C_4}}{1 + C_2 \psi^{C_5} [1 + C_3 \psi^{C_6}]} + C_7 \right) 10^{-26} \text{ erg s}^{-1} \text{ cm}^{-3} \quad (25)$$

and

$$\begin{aligned} \Lambda_{\text{gr}} = & n_e n_{\text{H}} \left(D_1 (D_2 T^{D_3} + D_4) T^{D_0} \right. \\ & \left(D_5 e^{D_6(x-10.3)(-T^{D_7})} + 1 \right)^{-D_5} \\ & + T^{D_8} + D_9 T^{D_{10}} + D_{11} \right) \\ & 10^{-28} \text{ erg s}^{-1} \text{ cm}^{-3}. \end{aligned} \quad (26)$$

Numerical values for C_i and D_i are tabulated in the appendix in Table D.1 and D.2.

Figure 18 shows the PE heating rates for a model clump of $M = 10 \text{ M}_{\odot}$, $n = 10^5 \text{ cm}^{-3}$, and $\chi = 1000$. The solid lines show the photoelectric heating (PEH) rates using the method described by Bakes & Tielens (1994). The PEH rate obtained for an MRN dust composition when solving the full FUV radiative transfer problem is enhanced compared to the old KOSMA- τ values because of the stronger FUV intensities due to the scattering. The dashed lines in Fig. 18 show the heating rates using the updated parametrizations from Eqs. (25) and (26) for the different dust models. Dotted lines indicate negative values, i.e., a transition from heating to cooling because $\Lambda_{\text{gr}} > \Gamma_{\text{pc}}$. For $A_V > 1$ the PEH rate of the WD01 dust models follow the FUV intensity of the respective models, i.e., the model with the highest mean FUV intensity, WD01-25, shows the strongest PEH rate while the model WD01-07 drops quickest. However, it is interesting to note that for $A_V < 0.1$ the PEH rate for the WD01-07 dust produces the strongest PEH rate, leading to the highest gas temperature of all models (see Fig. 19).

4. Application of the single clump model

4.1. Impact on gas temperature

The changes in computing the PE heating and the H₂ formation, which depend on the applied dust model, have a profound effect on the thermal structure of the model clump. Figure

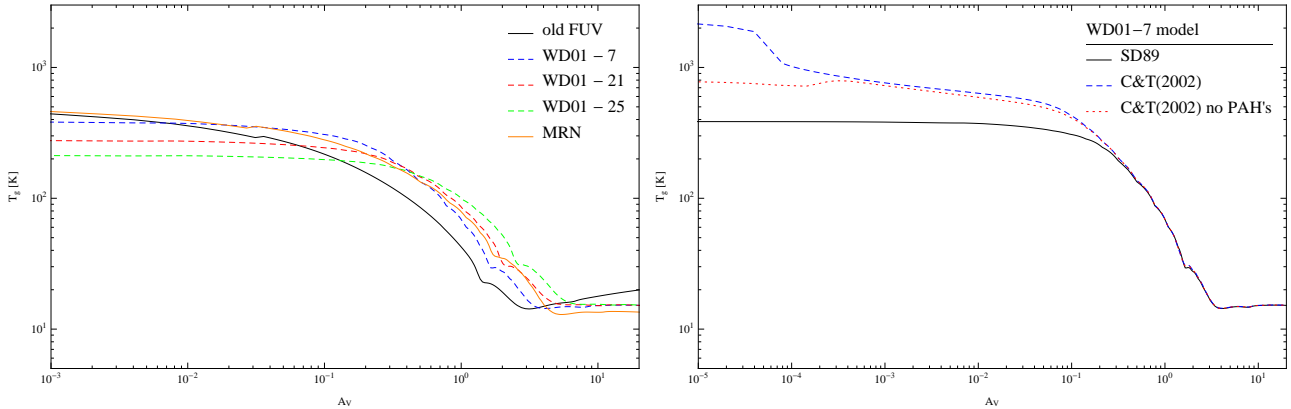


Fig. 19. Gas temperature T_g for a model clump of $M = 10 M_\odot$, $n = 10^5 \text{ cm}^{-3}$, and $\chi = 1000$. **Left panel:** The different lines denote different dust models that affect the FUV radiative transfer and the PE heating. All models in the left panel were recalculated using the SD89 H_2 formation. **Right panel:** The different lines show the effect of different H_2 formation treatment. All models in the right panel were computed using the WD01-7 dust properties regarding the radiative transfer and the PE heating.

19 shows the separate effects of the changed FUV and resulting PE heating (left panel) and different H_2 formation treatment (right panel). Among the different dust models presented by Weingartner & Draine (2001b) the WD01-7 dust models shows the highest total PE heating rate because it contains the largest population of very small grains (Weingartner & Draine 2001a). Depending on ψ , the PE heating rate from Bakes & Tielens (1994) can become higher than in the WD01 models despite its smaller population of very small grains. This is because they assume a higher electron sticking coefficient. In the chemically very active zone of $0.1 < A_V < 2$, the new FUV treatment leads to systematically warmer gas temperatures. The net effect of the dust model on the PE heating strongly depends on the applied dust model, with the PE heating efficiency proportional to the size of the very small grain population. A second effect comes from the H_2 formation heating. The right panel in Fig. 19 shows how the increase in the total available grain surface raises the gas temperature. However, this mostly affects the outer layers of a model clump where the high grain temperatures require accounting for chemisorbed H atoms to allow the formation of molecular hydrogen.

Overall, we can distinguish two regions: For optical depths $A_V \gtrsim 0.5$, the different attenuation of the FUV field by different dust distributions dominates the gas temperature. The model with the lowest reddening, i.e., the highest FUV intensity at those depths, shows the highest gas temperature. At lower optical depths, the FUV intensity is in all cases high enough that the total dust surface available for PE heating and H_2 formation determines the gas temperature. Here, the models with PAHs and many small grains, which also produce a higher reddening, show the highest gas temperature.

4.2. Impact on gas chemistry

The described changes to the model have a significant effect on the chemical structure of the cloud. The influence of the assumed dust composition and dust size distribution affects the FUV radiative transfer and the improved treatment of dust scattering increases the FUV intensity throughout the clump compared to the original approximation. Chemical species that are dominantly formed or destroyed via photo-ionization or photo-dissociation processes are affected. Secondly, the stronger H_2 formation efficiency leads to an increased H_2 formation heating contribution,

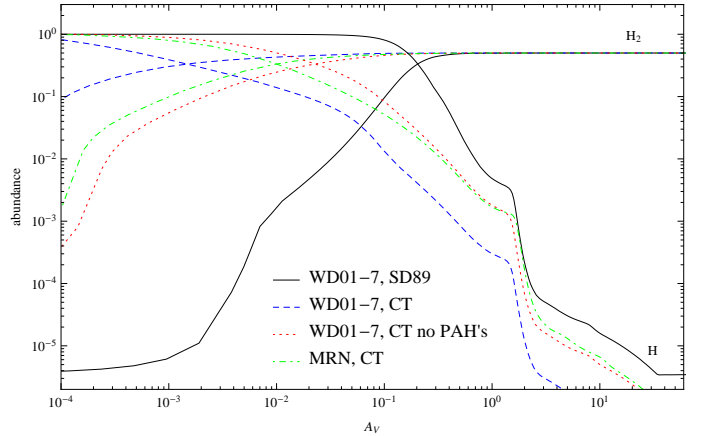


Fig. 20. H and H_2 abundances for a model clump of $M = 10 M_\odot$, $n = 10^5 \text{ cm}^{-3}$, and $\chi = 1000$. The different lines denote different treatments of the H_2 formation. The solid line shows a model using the standard H_2 formation rate as given by Sternberg & Dalgarno (1989). The dashed and dotted lines show model results for H_2 formation according to CT where the formation on PAH surfaces is switched on and off, respectively. All three models assume a WD01-7 dust distribution. The green dash-dotted line assumes an MRN dust model and uses the CT H_2 formation.

which in turn produces an increase in gas temperature at low A_V . Consequently, the abundance of the species that are dominantly formed in the outer regions of the molecular clump is changed because the higher gas temperature accelerates their respective formation and destruction reactions in the gas phase.

Both effects can go in opposite directions, but usually one effect dominates. In Fig. (20) we show the dependence of the H - H_2 transition zone on the applied H_2 formation rate. We compare three models assuming a WD01-7 dust model with full radiative transfer and photoelectric heating treatment. The only difference between the model calculations is the treatment of H_2 formation. We apply (1) the standard H_2 formation rate as given by Sternberg & Dalgarno (1989) (black, solid line), (2) the H_2 formation given by CT with H_2 formation taking place on the PAH surface (blue, dashed line), (3) and the H_2 formation given by CT with H_2 formation on PAHs suppressed (red, dotted line). H_2 chemistry is unique in the sense that it only weakly depends on the gas temperature (see Eqs. (19, 20)). Figure 20 shows how the

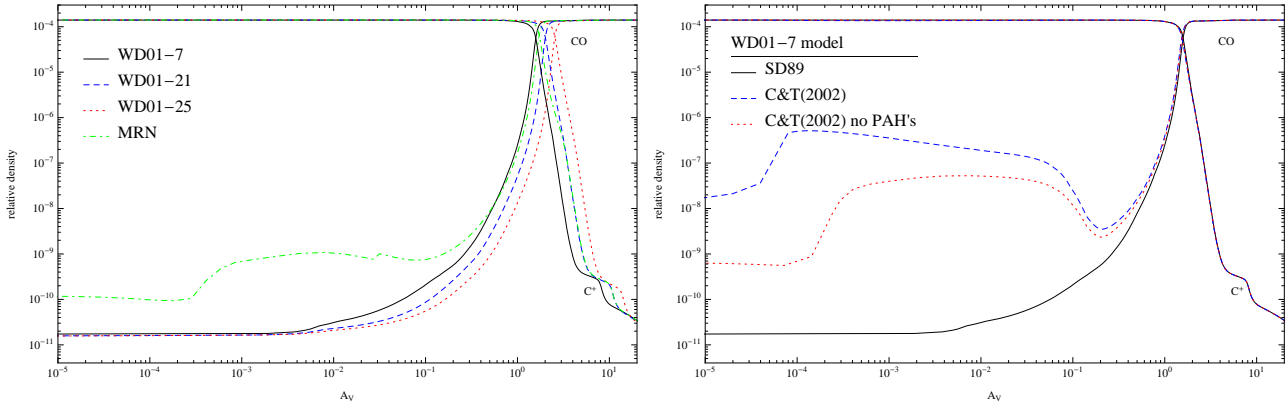


Fig. 21. CO and C⁺ abundances for a model clump of $M = 10 M_{\odot}$, $n = 10^5 \text{ cm}^{-3}$, and $\chi = 1000$. **Left panel:** The different lines denote different dust models that affect the FUV radiative transfer and the PE heating. All models in the left panel have been calculated using the SD89 H₂ formation. **Right panel:** The different lines show the effect of different H₂ formation treatment. All models in the right panel have been computed using the WD01-7 dust properties regarding the radiative transfer and the PE heating.

different treatment of the H₂ formation influences the details of the H-H₂ transition. In that particular model clump, the dust temperature is about 50 K and almost identical in all models, leading to a H₂ formation efficiency of unity across the dust models shown. The only significant difference is the total dust surface of the various models. The SD89 approximation, case (1), has the smallest available surface ($\sigma_d = 4.14 \times 10^{-22} \text{ cm}^2$) followed by CT without PAHs and CT including PAHs (see Table 4). This agrees with the H-H₂ transition moving outwards with growing dust surface in Fig. 20. To emphasize this behavior, we added a fourth dust model to the plot, showing the results for the MRN model. The total surface in the MRN model is only slightly smaller than the WD01-7 model without PAHs and consequently, both models show a very similar behavior. Please note that the contribution of graphite and silicate to the total dust surface is still very different in the different dust models. The MRN model possesses about equal surfaces in both kinds, while the majority of the big grain surfaces in the WD01-7 model comes from silicates.

In contrast to H₂, all other chemical species in the gas phase are affected by variations of the local FUV intensity and the local gas temperature. This is apparent, for example, in the C⁺ to CO transition. Figure 21 shows the density profile of C⁺ and CO for different model calculations. In the left panel we show the influence of the different dust models in terms of radiative transfer and PE heating, while the right panel demonstrates how the different H₂ formation treatment influences the chemistry. All models in the left panel were calculated using the SD89 H₂ formation. The transition from C⁺ to CO occurs at different A_V for all models. Consistent with the FUV intensities shown in Figs. 4 and 5, the models with the lowest FUV intensities show a C⁺ to CO transition at lowest A_V , while models with a weak dust attenuation, e.g. WD01-25, exhibit the same transition deeper in the cloud. Additionally, we note an enhanced CO density at low A_V in the WD01-7 model. This is a result of the higher gas temperature due to the stronger PE heating efficiencies of that dust model.

The right panel in Fig. 21 shows the isolated effect of the different H₂ formation treatment. All models in the right panel were computed using the WD01-7 dust properties regarding the radiative transfer and the PE heating. The C⁺-CO transition is similar across all shown models, since the FUV intensity, which controls the photo-dissociation of CO, is the same across all models. However, the CO abundance at lower A_V shows very large

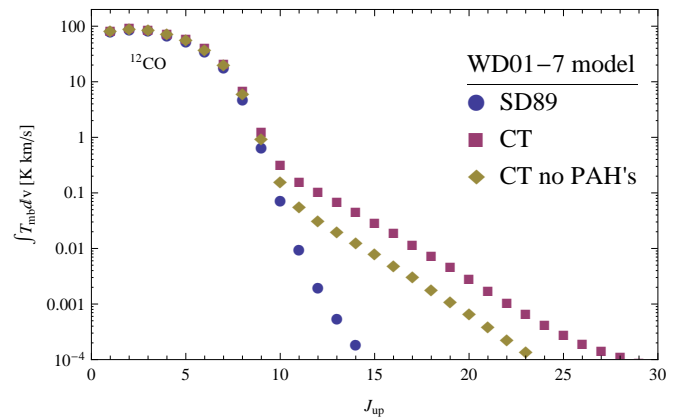


Fig. 22. Total line integrated clump-averaged intensities of ^{12}CO transitions for a model clump of $M = 10 M_{\odot}$, $n = 10^5 \text{ cm}^{-3}$, and $\chi = 1000$. The different lines show the effect of different H₂ formation treatment. All models were computed using the WD01-7 dust properties regarding the radiative transfer and the PE heating.

differences. The models using the CT dust formation scheme produce more CO at the cloud edge compared to the SD89 H₂ formation. The CT models provide a stronger H₂ formation heating contribution. The additional heating term produces a significant population of hot CO in the outer layers of the model clump.

The production of hot, i.e., strongly excited, CO is visible in the spectral line emission of the model clumps. In Fig. 22 we show the corresponding total CO line emission of the model clumps shown in the right panel in Fig. 21. For transitions higher than $J=8-7$, the line-integrated intensities start to show significant differences for the three models. In this particular case, the strength of the high- J CO transitions is proportional to the total H₂-forming grain surface. The outer layers of the model clumps contribute significantly to the total CO line emission of this model. As a consequence, any modeling with a large surface of the clouds, e.g., assuming a clumpy structure, will show much stronger high- J CO emission lines compared to non-clumpy model attempts.

As an additional example of chemical species that predominantly form in the outer regions of molecular clouds and thus are affected by the H₂ formation treatment we show in Fig. 23 the

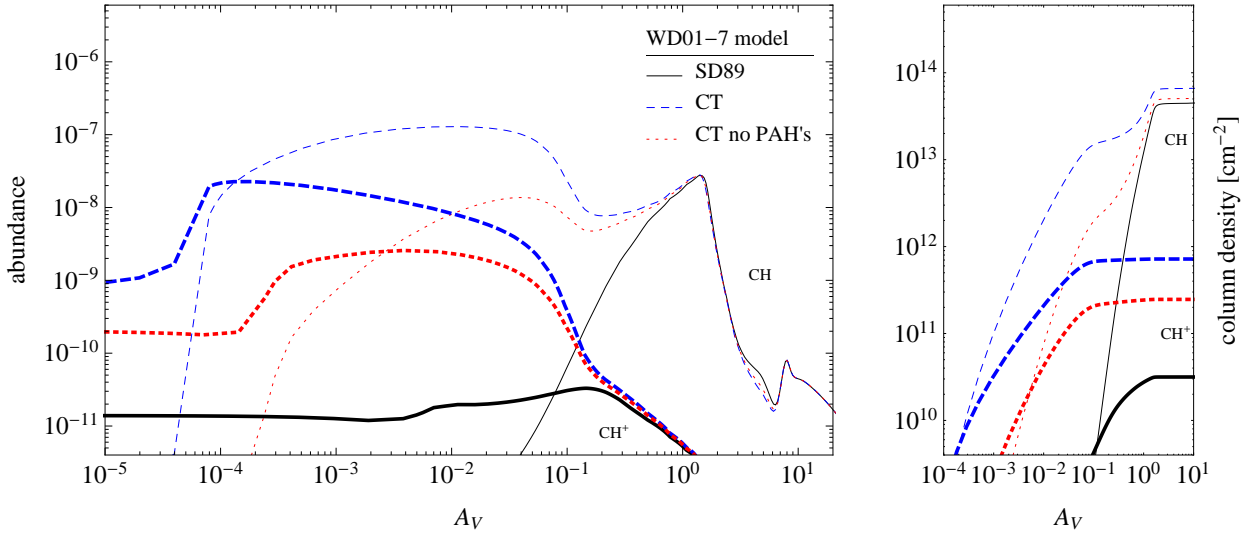


Fig. 23. CH and CH⁺ abundances (left) and column densities (right) for a model clump of $M = 10 \text{ M}_\odot$, $n = 10^5 \text{ cm}^{-3}$, and $\chi = 1000$. The different lines show the effect of different H₂ formation treatment. All models were computed using the WD01-7 dust properties regarding the radiative transfer and the PE heating.

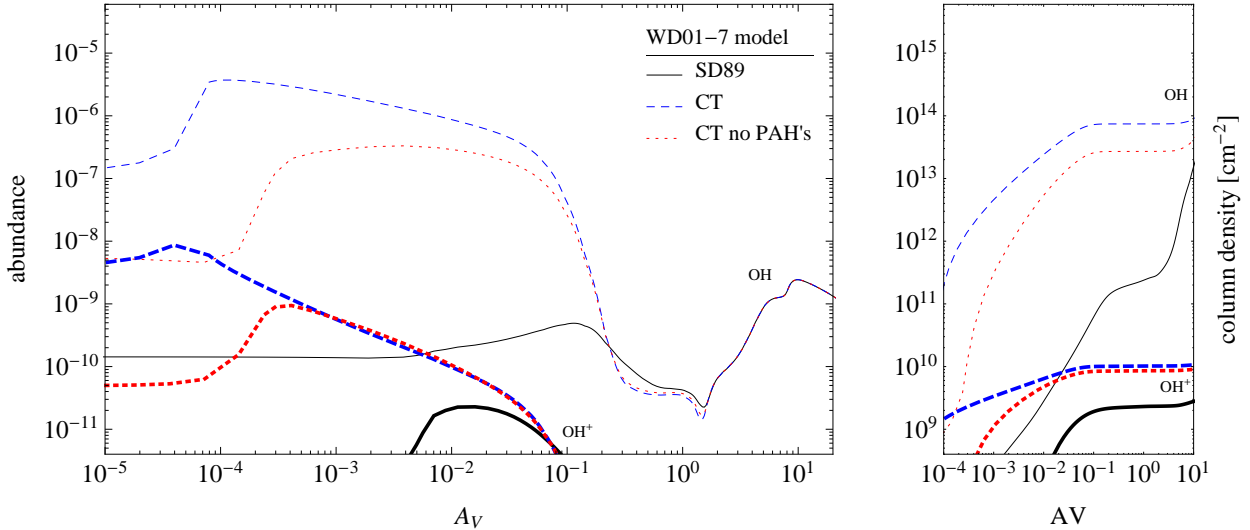


Fig. 24. OH and OH⁺ abundances (left) and column densities (right) for a model clump of $M = 10 \text{ M}_\odot$, $n = 10^5 \text{ cm}^{-3}$, and $\chi = 1000$. The different lines show the effect of different H₂ formation treatment. All models were computed using the WD01-7 dust properties regarding the radiative transfer and the PE heating.

CH and CH⁺ abundances and column densities and in Fig. 24 the OH and OH⁺ abundances and column densities. All these species are significantly affected by the strong H₂ formation heating effect in the outer parts of the model clump. The column density effect is weakest for the CH because of the abundance peak at $A_V \approx 1$. The other three species show a stronger effect on the column density because of the weak formation in deeper clump regions. Recent Herschel observations show high column densities of these surface tracers (e.g. Qin et al. 2010; Falgarone et al. 2010), which were difficult to reproduce in existing PDR models. A more efficient H₂ formation modeling with the accompanying formation heating effect may help to resolve the discrepancy between models and observations.

4.2.1. Full model SED

In Fig. 25 we show the full continuum and spectral line flux (in units of Jy) emitted by a model clump of $M = 10 \text{ M}_\odot$, $n = 10^5 \text{ cm}^{-3}$, and $\chi = 1000$. The two panels show the results for different dust models. The top panel shows the result for the dust model with the largest effective surface contributing to the gas heating, the WD01-7 model, equivalent to a $R_V = 3.1$. The strong gas heating is visible in the large population of intense high- J CO emission lines with $J > 10$ stemming from the outer layers of the cloud (see Table 5). ⁷ In the bottom panel we show the result for a MRN dust model, visible through the lack of PAH emission features in the NIR.

⁷ The level population of the CO energy levels was computed up to $J=50$.

Table 5. Line emission $\int I dv$ for the three models shown in Fig. 25.

line	λ [μm]	WD01-7 w/o PAHs [erg/s/cm 2 /sr]	WD01-7 with PAHS [erg/s/cm 2 /sr]	WD01-25 w/o PAHS [erg/s/cm 2 /sr]	WD01-25 with PAHS [erg/s/cm 2 /sr]	MRN [erg/s/cm 2 /sr]
I_{TIR}		0.290	0.290	0.286	0.280	0.278
[C II]	$^2P_{3/2} - ^2P_{1/2}$	158	7.5×10^{-4}	7.5×10^{-4}	9.2×10^{-4}	9.3×10^{-4}
[O I]	$^3P_1 - ^3P_2$	63	6.8×10^{-3}	6.6×10^{-3}	5.7×10^{-3}	6.0×10^{-3}
[O I]	$^3P_0 - ^3P_1$	146	5.0×10^{-4}	5.1×10^{-4}	4.2×10^{-4}	4.9×10^{-4}
[C I]	$^3P_1 - ^3P_0$	609	1.2×10^{-6}	1.2×10^{-6}	1.4×10^{-6}	1.3×10^{-6}
[C I]	$^3P_2 - ^3P_1$	370	3.9×10^{-6}	3.9×10^{-6}	4.6×10^{-6}	4.2×10^{-6}
CO	(1–0)	2601	1.3×10^{-7}	1.3×10^{-7}	1.2×10^{-7}	1.3×10^{-7}
CO	(4–3)	650	7.3×10^{-6}	7.4×10^{-6}	7.0×10^{-6}	7.5×10^{-6}
CO	(7–6)	372	1.1×10^{-5}	1.1×10^{-5}	1.3×10^{-5}	1.5×10^{-5}
CO	(10–9)	260	2.7×10^{-7}	5.0×10^{-7}	2.8×10^{-7}	4.5×10^{-7}
CO	(15–14)	174	5.6×10^{-8}	1.6×10^{-7}	2.4×10^{-10}	2.5×10^{-8}
CO	(20–19)	130	1.2×10^{-8}	3.7×10^{-8}	8.7×10^{-12}	7.3×10^{-9}

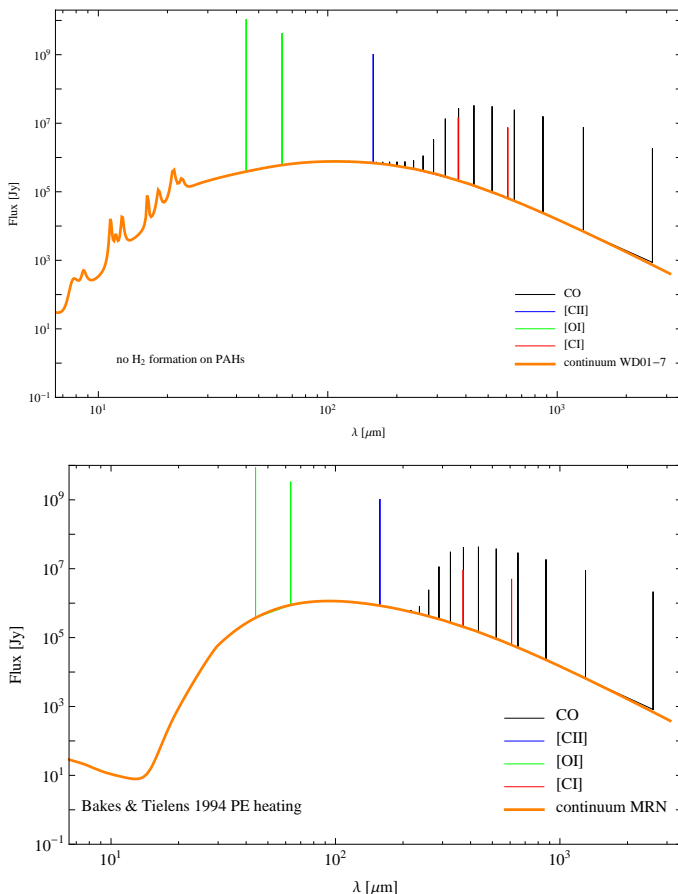


Fig. 25. Full continuum and spectral line flux emitted by a model clump of $M = 10 M_\odot$, $n = 10^5 \text{ cm}^{-3}$, and $\chi = 1000$. The two panels show the results for different dust models. **Top:** WD01-7 dust model, equivalent to a $R_V = 3.1$. This is the dust model with the largest grain surface contributing to the heating. **Bottom:** MRN dust mode. This is a dust model with a slightly smaller grain surface compared to WD01-7. The PE heating was calculated according to Bakes & Tielens (1994).

In Table 5 we summarize the line emission of the WD01-7 and WD01-25 (with and without H_2 formation on PAHs), as well as the MRN models quantitatively. The differences between the WD01-7 and WD01-25 models are limited to the line emission, the continuum emission is only marginally different. The

WD01-25 models show weaker high- J CO emission because of the smaller grain surface and correspondingly a weaker H_2 formation heating. The high- J CO emission of the MRN model falls between the WD01-7 and the WD01-25 dust models without H_2 formation on PAHs. Allowing for H_2 formation on PAHs will add a strong heating contribution from the formation processes on the large PAH surface, exciting the high- J CO transitions by a large factor.

5. Summary

We revised the treatment of the dust in the KOSMA- τ PDR model code to achieve a consistent description of the dust related physics in the code. The computation of dust properties in numerical models of photo-dissociation regions afflicts the chemical and physical structure of a model cloud via multiple effects. The major areas where dust properties play an important role are

1. the optical dust properties, i.e., their influence on the radiative transfer
2. the dust temperature (neglecting non-equilibrium heating for the very small grains), which influences surface chemistry, most importantly the formation of molecular hydrogen
3. the heating and cooling capabilities of dust grains via photo-electric heating and gas-grain collisional cooling.

The effect of changes in these areas on the physical and chemical structure of a model can be profound and we described their respective influence in detail.

We notice two opposite effects: Increasing the fraction of small grains steepens the slope of the extinction curve so that the FUV intensity drops faster when going into the cloud, which leads to a temperature decrease at high optical depths. However, it also provides more surface for PE heating and H_2 formation, thus increasing the heating efficiency. As a consequence, the gas becomes hotter in the outer layers, but colder inside the cloud when the fraction of small grains and PAHs is increased. Only tracers of the outer layers are able to reliably measure the gas heating efficiency. In contrast to common wisdom, this is not even true for ionized carbon [CII], which traces both regimes.

The most influential modification of the code is the treatment of H_2 formation on the surface of dust grains. Allowing for chemisorption, i.e., including the Eley-Rideal effect into the formulation of the H_2 formation efficiency, significantly increases

the overall formation rate of molecular hydrogen. If a significant fraction of the dust consists of very small grains and PAHs, their very large contribution to the total grain surface leads to an additional enhancement of the total H₂ formation. If the molecule formation is enhanced, the formation heating is enhanced as well, providing a profound heating contribution in the outer layers of the model clumps, which significantly affects the local chemistry.

Acknowledgements. This work was supported by the German *Deutsche Forschungsgemeinschaft*, DFG project number Os 177/1–1. R.S. acknowledges support partly from the Polish NCN grant 2011/01/B/ST9/02229. We acknowledge the use of the Udfa (a.k.a. UMIST) (<http://www.udfa.net/>) chemical reaction databases. Some kinetic data we used were downloaded from the online database KIDA (KInetic Database for Astrochemistry, <http://kida.obs.u-bordeaux1.fr>). We thank the anonymous referee for many remarks that significantly improved this paper. We would like to thank J. Weingartner for the calculation of the photoelectric heating rates and collisional cooling rates for the extended parameter range and for the helpful remarks on the calculation of the total heating rate.

References

- Abel, N. P., Ferland, G. J., Shaw, G., & van Hoof, P. A. M. 2005, ApJS, 161, 65
 Abel, N. P., Hoof, P. A. M. v., Shaw, G., Ferland, G. J., & Elwert, T. 2008, ApJ, 686, 1125
 Bakes, E. L. O. & Tielens, A. G. G. M. 1994, ApJ, 427, 822
 Bohren, C. F. & Huffman, D. R. 1983, Absorption and scattering of light by small particles, ed. Bohren, C. F. & Huffman, D. R.
 Browning, M. K., Tumlinson, J., & Shull, J. M. 2003, ApJ, 582, 810
 Cazaux, S. & Tielens, A. G. G. M. 2002, ApJ, 575, L29
 Cazaux, S. & Tielens, A. G. G. M. 2004, ApJ, 604, 222
 Cazaux, S. & Tielens, A. G. G. M. 2010, ApJ, 715, 698
 Draine, B. T. 1978, ApJS, 36, 595
 Draine, B. T. 2003a, ARA&A, 41, 241
 Draine, B. T. 2003b, ApJ, 598, 1017
 Falgarone, E., Ossenkopf, V., Gerin, M., et al. 2010, A&A, 518, L118+
 Flannery, B. P., Roberge, W., & Rybicki, G. B. 1980, ApJ, 236, 598
 Garrod, R. T., Weaver, S. L. W., & Herbst, E. 2008, ApJ, 682, 283
 Goicoechea, J. R. & Le Bourlot, J. 2007, A&A, 467, 1
 Gry, C., Boulanger, F., Nehmé, C., et al. 2002, A&A, 391, 675
 Habart, E., Abergel, A., Boulanger, F., et al. 2011, A&A, 527, A122
 Habart, E., Boulanger, F., Verstraete, L., et al. 2003, A&A, 397, 623
 Habart, E., Boulanger, F., Verstraete, L., Walmsley, C. M., & Pineau des Forêts, G. 2004, A&A, 414, 531
 Hall, P. & Millar, T. J. 2010, A&A, 517, A1
 Hollenbach, D. & McKee, C. F. 1979, ApJS, 41, 555
 Hollenbach, D. J., Takahashi, T., & Tielens, A. G. G. M. 1991, ApJ, 377, 192
 Hollenbach, D. J. & Tielens, A. G. G. M. 1999, Reviews of Modern Physics, 71, 173
 Jura, M. 1974, ApJ, 191, 375
 Kirby, K., Roberge, W. G., Saxon, R. P., & Liu, B. 1980, ApJ, 239, 855
 Le Bourlot, J., Le Petit, F., Pinto, C., Roueff, E., & Roy, F. 2012, A&A, 541, A76
 Le Petit, F., Nehmé, C., Le Bourlot, J., & Roueff, E. 2006, ApJS, 164, 506
 Leger, A., Jura, M., & Omont, A. 1985, A&A, 144, 147
 Lepp, S. & Shull, J. M. 1983, ApJ, 270, 578
 Li, A. & Draine, B. T. 2001, ApJ, 554, 778
 Mathis, J. S., Rumpl, W., & Nordsieck, K. H. 1977, ApJ, 217, 425
 Mennella, V., Hornekær, L., Thrower, J., & Accolla, M. 2012, ApJ, 745, L2
 Qin, S.-L., Schilke, P., Comito, C., et al. 2010, A&A, 521, L14+
 Roberge, W. G. 1983, ApJ, 275, 292
 Roberge, W. G., Jones, D., Lepp, S., & Dalgarno, A. 1991, ApJS, 77, 287
 Roberts, J. F., Rawlings, J. M. C., Viti, S., & Williams, D. A. 2007, MNRAS, 382, 733
 Röllig, M., Abel, N. P., Bell, T., et al. 2007, A&A, 467, 187
 Röllig, M., Ossenkopf, V., Jeyakumar, S., Stutzki, J., & Sternberg, A. 2006, A&A, 451, 917
 Saxon, R. P. & Liu, B. 1986, J. Chem. Phys., 85, 2099
 Sternberg, A. & Dalgarno, A. 1989, ApJ, 338, 197
 Störzer, H., Stutzki, J., & Sternberg, A. 1996, A&A, 310, 592
 Szczepański, R., Omont, A., Volk, K., Cox, P., & Kwok, S. 1997, A&A, 317, 859
 Taquet, V., Ceccarelli, C., & Kahane, C. 2012, A&A, 538, A42
 Tielens, A. G. G. M. 2008, ARA&A, 46, 289
 van Dishoeck, E. F. & Black, J. H. 1982, ApJ, 258, 533
 van Dishoeck, E. F. & Black, J. H. 1988, ApJ, 334, 771
 van Dishoeck, E. F., Jonkheid, B., & van Hemert, M. C. 2006, Faraday Discussions, 133, 231
 van Hemert, M. C. & van Dishoeck, E. F. 2008, Chemical Physics, 343, 292
 Weingartner, J. & Draine, B. 2001a, ApJS, 134, 263
 Weingartner, J. C. 2009, priv. communication
 Weingartner, J. C. & Draine, B. T. 2001b, ApJ, 548, 296
 Welty, D. E., Hobbs, L. M., & Morton, D. C. 2003, ApJS, 147, 61
 Wolfire, M. G., Tielens, A. G. G. M., Hollenbach, D., & Kaufman, M. J. 2008, ApJ, 680, 384
 Woodall, J., Agúndez, M., Markwick-Kemper, A. J., & Millar, T. J. 2007, A&A, 466, 1197
 Yorke, H. W. 1980, A&A, 86, 286

Appendix A: Isotropic vs. non-isotropic scattering

The MCDRT code assumes isotropic scattering, i.e., a mean scattering angle $g = \langle \cos \Theta \rangle = 0$ when calculating the frequency-dependent FUV radiative transfer. However, taking into account the detailed material properties and size distribution of interstellar dust results in different values of g . Reasonable values for interstellar dust in the FUV range fall around $g \approx 0.7$ and $\omega \approx 0.4$ (Li & Draine 2001). In the following we show that even in this case of strong forward-scattering the isotropic scattering treatment poses a clear improvement compared to the pure forward-scattering cased used in our previous model.

To quantify the error we used the *spherical harmonics* method, presented by Flannery et al. (1980) to calculate the penetration of UV radiation of a spherical cloud. Applying their method, we calculated the attenuation of the mean intensity as a function of optical depth for a given asymmetry factor g and albedo ω . For more details on the method see also Roberge (1983); Le Petit et al. (2006); Goicoechea & Le Bourlot (2007).

In Fig. A.1, left panel, we plot the solution of the mean intensity for $\omega = 0.4$, $g = 0.7$ normalized to the incident radiation field for a homogeneous spherical cloud with an optical depth to the center $\tau_c = 20$ (black curve). The dashed blue curve shows the solution for the same albedo, but for isotropic scattering. This represents the solution of the MCDRT code. The dotted red curve gives the result for pure forward-scattering, i.e., the case $\exp(-(1-\omega)\tau)$. This is equivalent to the previous approximation in KOSMA- τ . The right panel shows the corresponding error when assuming isotropic or pure forward-scattering. It is apparent that the assumption of isotropic scattering is an improvement over our previous approach up to optical depths of about 16, only for very high τ the forward-scattering is the solution closer to the $g = 0.7$ case. However, the FUV influence at $\tau > 10$ is negligible. Presently, we therefore sacrifice the dark cloud accuracy in favor of a more accurate description of the cloud surface, but in a future work we plan to update the MCDRT code to properly account for non-isotropic scattering.

Appendix B: Rescaling of photo-rates to account for different dust properties

In the following we discuss the uncertainties of the proposed rescaling $\gamma_j \rightarrow \gamma_j^D$ for different dust models D .

One important factor is the spectral shape of the assumed FUV radiation field. In Fig. B.1 we plot the photo-dissociation cross sections σ of two different molecules (CH₂ in the left panel, SiH⁺ in the right panel) together with the FUV radiation field (thick black line: unshielded Draine field, colored lines: FUV field inside the clump at 95% of the total radius for the dust models WD01-7, 21, and 25). The total photo-dissociation cross section is calculated using Eq. 13. The different wavelength behavior of σ in the two panels demonstrates why the

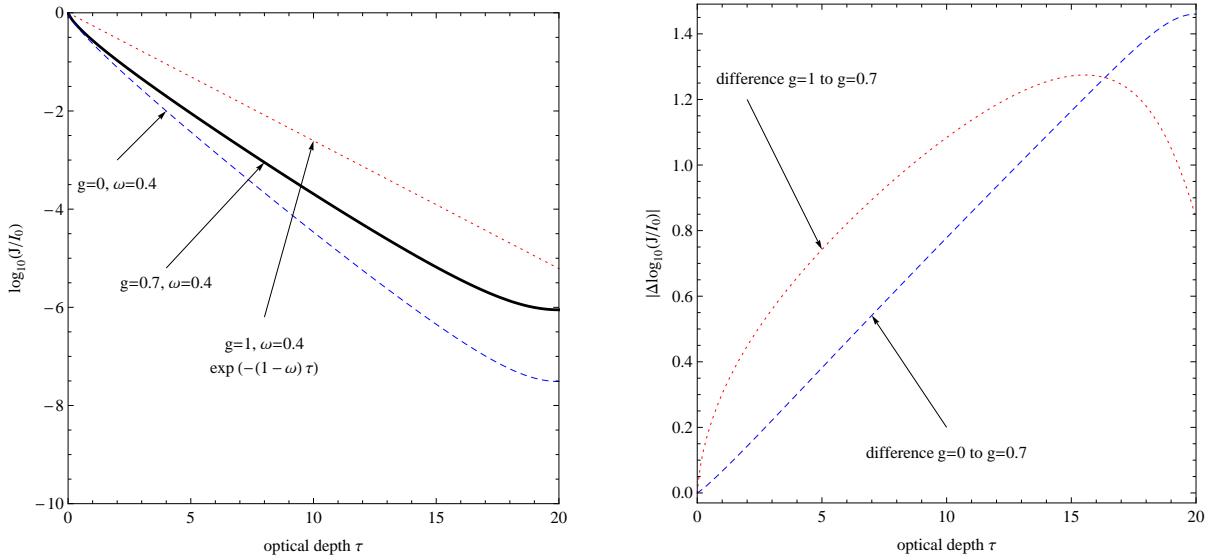


Fig. A.1. Left panel: Mean intensity versus optical depth τ normalized to the incident specific intensity I_0 . The solid black curve shows the depth dependence of the mean intensity assuming dust parameters $\omega = 0.4$, $g = 0.7$, approximately describing the WD01-7 dust sort. The dashed and dotted curves denote mean intensities using the same albedo ω , but assuming isotropic and pure forward-scattering, respectively. **Right panel:** Absolute error $|\log(J_i/I_0) - \log(J_k/I_0)|$ of assuming isotropic $g = 0$ and pure forward-scattering $g = 1$ with respect to more realistic values $\omega = 0.4$, $g = 0.7$ (dashed and dotted lines, respectively).

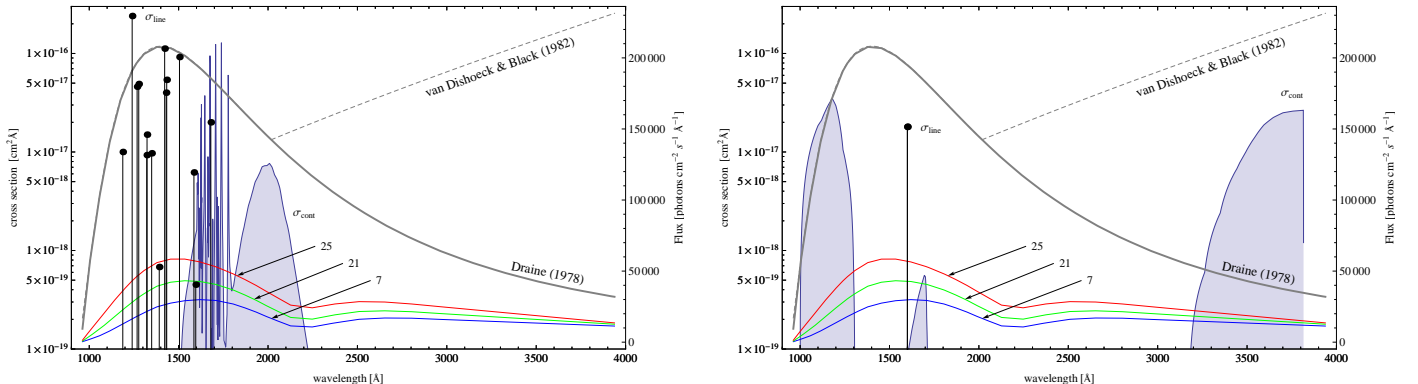


Fig. B.1. Wavelength dependence of the assumed UV illumination and the photo-dissociation cross sections. The thick black line shows the unshielded empty-space Draine FUV field, the dashed line shows an extension of the Draine field longward of 2000 Å suggested by van Dishoeck & Black (1982). The blue, green and red lines show the FUV radiation field inside the reference cloud at 95% R_{tot} for the WD01-7, WD01-21, and WD01-25 dust models, respectively. **Left panel:** The blue filled curve shows the continuum absorption cross section σ_{cont} of CH₂ that leads to dissociation, the black dots with drop lines show the corresponding line absorption cross section σ_{line} . **Right panel:** Same as left panel but for the SiH⁺ photo-dissociation cross sections.

photo-dissociation rates of different species are attenuated differently when going deeper into the cloud. The right panel also emphasizes that the choice of the spectral shape of the illuminating FUV radiation field may influence the photo-dissociation rate of some species significantly; the choice between the two FUV fields results in an unshielded photo-dissociation rate difference of a factor two. However, differences in the attenuation behavior between different dust models will still be dominated by wavelengths shorter than 2000 Å because $A(\lambda)/A(V)$ varies only weakly for $\lambda > 3000$ Å.

Another uncertainty results from the choice of $A_{V,\text{max}}$ up to which the $\gamma_{j,\text{fit}}$ from Eq. 14 is fitted to the values $\Gamma_j(A_V)/\Gamma_j(0)$. In Fig. B.2 we show the $\Gamma_{\text{CH}_2}(A_V)/\Gamma_{\text{CH}_2}(0)$ for three dust models: WD01-7, WD01-21, and WD01-25. The lines show the corresponding $\exp(-\gamma_{j,\text{fit}}^D A_V)$ fits for different $A_{V,\text{max}}$. The range

of $\gamma_{j,\text{fit}}^D$ is 1.92-2.24, 1.48-1.71, and 1.14-1.3 for the three dust models, equivalent to a 10-15% uncertainty. We calculated fits to $\gamma_{j,\text{fit}}^D$ for all available species and for all dust models to $A_{V,\text{max}} = 10$.

The third source of uncertainties is the functional dependence used in the fit through Eq. 16. We performed least-squares fits to polynomials $\gamma_j^D = p(\gamma_j, 1/R_{760\text{\AA}}^D)$ up to order 4 to derive a suitable scaling relation between the input parameters γ_j , describing the wavelength-dependent attenuation of the photo-dissociation rate of species j with A_V , $1/R_{760\text{\AA}}^D$, describing the wavelength-dependent attenuation of the FUV radiation field depending on the dust model D , and the output parameter γ_j^D . Figure B.3 visualizes Eq. 16 (black grid) and the explicitly calculated fits $\gamma_{j,\text{fit}}^D$ (colored dots) for the 25 WD01 dust models

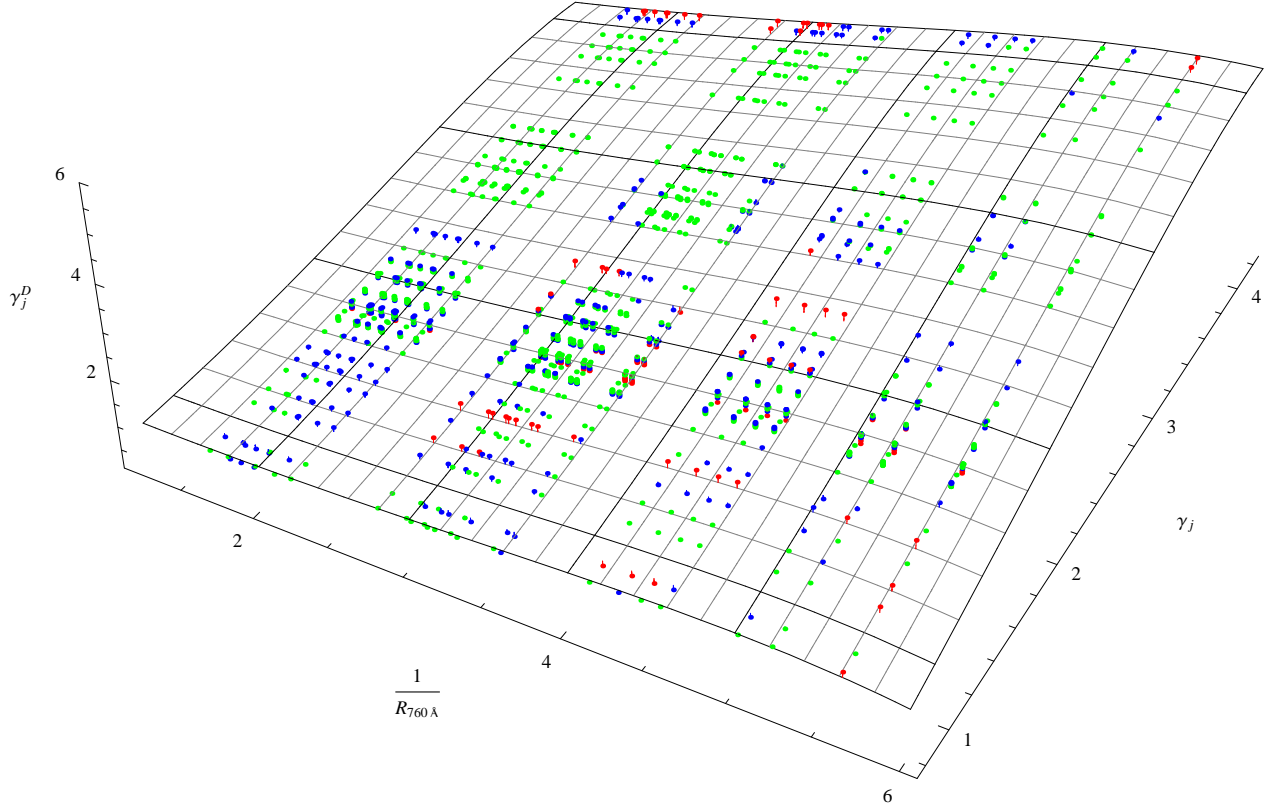


Fig. B.3. Visualization of Eq. 16 (black grid) and the explicitly calculated fits $\gamma_{j,fit}^D$ (colored dots) for the 25 WD01 dust models for all species with available cross sections. The data points are colored according to their deviation from Eq. 16. Green and blue denotes deviations of less than 0.05 and 0.1. Red points signal deviations exceeding 0.1. All deviations are smaller than 0.22.

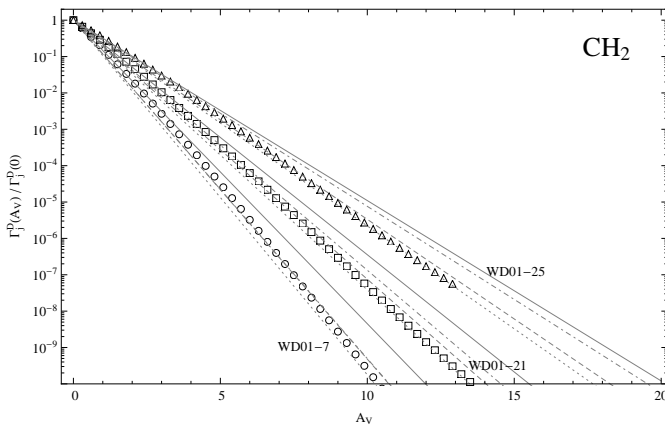


Fig. B.2. Comparison of the explicitly integrated photo-dissociation rates of CH_2 for the WD01-7, WD01-21, and WD01-25 dust models (circles, squares, triangles, respectively) and the corresponding fits to the rates according to Eq. 14. The different line styles denote fits up to different maximum visual extinctions (solid: $A_{V,\max} = 3$, dashed: $A_{V,\max} = 10$, dotted: $A_{V,\max} = 15$, and dot-dashed: $A_{V,\max} = 20$).

for all species with available cross sections. The data points are colored according to their deviation from Eq. 16.

Seven species, CH^+ , SH^+ , OH^+ , HCO^+ , CO , O_2^+ , and SiO , deviate significantly from our Eq. 16 with residual >0.4 . By shifting their γ_j to a corrected $\hat{\gamma}_j$ we are able to compensate for these deviations. Figure B.4 shows the fitted $\gamma_{j,fit}^D$ of the three strongest outliers and the corresponding γ_j^D from Eq. 16 using the original γ_j (dashed lines) and the corrected $\hat{\gamma}_j$ (solid lines).

The deviations $|\gamma_{j,fit} - \gamma_j^D|$ of the seven outlying species are large compared to the rest of the 63 species that we calculated (compare Fig. B.3). In the following we will discuss the strongest outliers individually⁸.

HCO⁺

HCO^+ showed the strongest maximum deviation of 1.12 from the plane defined by Eq. 16. UDfA gives $\gamma = 2.0$ referring to van Dishoeck et al. (2006) who give a value of $\gamma = 3.32$ in their Tab. 2. Unfortunately, all photo-dissociation rate coefficients from UDfA that refer to van Dishoeck et al. (2006) are inconsistent with their published numbers and should be replaced with more recent numbers. Their paper was still in preparation

⁸ We ignore deviations for CO because photo-dissociation of CO is treated separately in any PDR code (van Dishoeck & Black 1988)

when Woodall et al. (2007) was published, so the mismatch is possibly due to pre-publication updates of the final values.

OH^+

OH^+ showed the second-strongest deviations of up to 0.8 from Eq. 16. It possesses a strong absorption continuum only for wavelengths shorter than 1100 Å so that extensions to the Draine FUV field at longer wavelengths should not affect the final photo-dissociation rate. However, computing the unshielded photo-dissociation rate coefficient α for a Draine field yields $1.27 \times 10^{-11} \text{ s}^{-1}$, comparable to $1.1 \times 10^{-11} \text{ s}^{-1}$ from van Dishoeck et al. (2006), while UDfA lists $1 \times 10^{-12} \text{ s}^{-1}$. The reason for the mismatch is unclear, all sources refer to the same photo-dissociation cross section by Saxon & Liu (1986). We also find inconsistent values of γ published, between 1.8 and 3.5. We find a best fit to Eq. 16 with $\hat{\gamma}_j^D = 2.76$.

CH^+

For CH^+ deviations from Eq. 16 of up to 0.6 were found. Woodall et al. (2007) give $\alpha = 2.5 \times 10^{-10} \text{ s}^{-1}$ and $\gamma = 2.5$ referring to Robege et al. (1991), van Dishoeck et al. (2006) give $\alpha = 3.3 \times 10^{-10} \text{ s}^{-1}$ and $\gamma = 2.94$ using cross sections from Kirby et al. (1980). We find $\gamma_{j,fit}^D = 1.5 - 2.4$ and $\hat{\gamma}_j^D = 2.11$. At A_V these lower values of γ lead to photo-dissociation rates 3–6 orders of magnitude stronger compared to rates calculated with the higher γ from above. The reason for the γ offsets is unclear.

SH^+

SH^+ has comparable values of α , and γ in UDfA and in van Dishoeck et al. (2006). Small differences in α can be attributed to a strong absorption line at 3100 Å, which leads to a stronger unshielded photo-dissociation rate when applying a 10000 K black-body radiation field as used by Woodall et al. (2007). We find $\gamma_{j,fit}^D = 1.2 - 1.8$ and $\hat{\gamma}_j^D = 1.39$. Differences of γ from the literature and our calculations most likely result from different assumed dust properties and fits to lower maximum $A_{V,\max}$.

SiO and O_2^+

Both molecules show maximum deviations of 0.4 from Eq. 16. The unshielded SiO rate coefficients from UDfA and van Dishoeck et al. (2006) differ by a factor 16 (see comment on HCO^+) while their γ_j are the same.

In Fig. B.5 we show a histogram of the residuals $\gamma_{j,fit}^D - \hat{\gamma}_j^D$ after removing the outlying species. The standard deviation is $\sigma = 0.05$, the maximum absolute residual is 0.22. Photo-dissociation cross sections are available for a number of species that are not yet included in UDfA (van Hemert & van Dishoeck 2008). In Tab. B.1 we give α and γ from <http://home.strw.leidenuniv.nl/~ewine/photo> as well as our $\hat{\gamma}_j$.

Appendix C: H_2 formation rate

We followed the model of H_2 formation on interstellar dust grains via physisorption and chemisorption from Cazaux & Tielens (Cazaux & Tielens 2002, 2004, 2010).

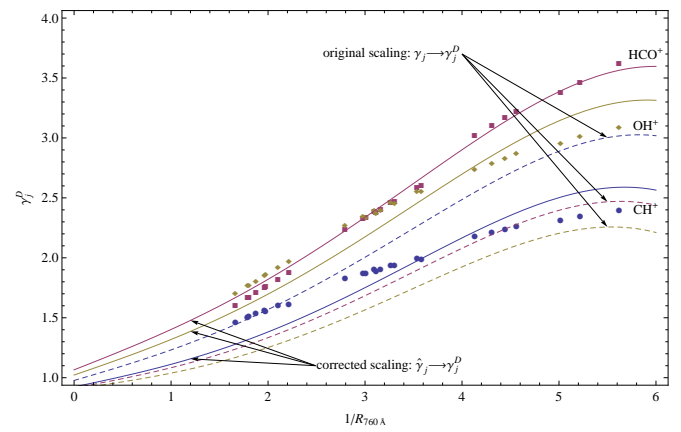


Fig. B.4. Comparison of the $\gamma_{j,fit}^D$ for the three strongest outliers CH^+ , OH^+ , and HCO^+ and the corresponding scaling behavior of Eq. 16 using the original γ_j (dashed line) and the corrected $\hat{\gamma}_j$,

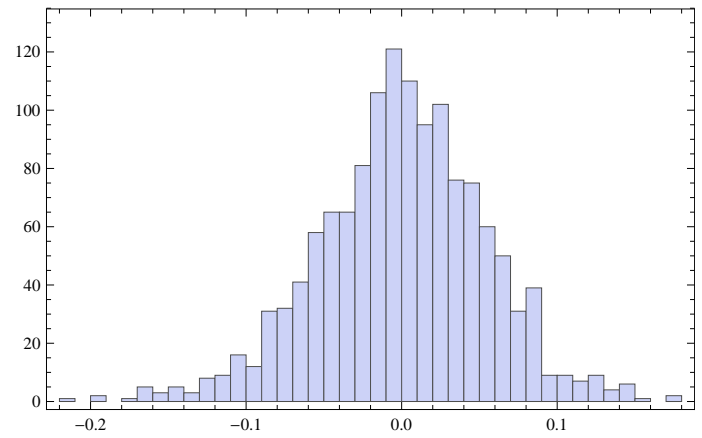


Fig. B.5. Histogram of the residuals $\gamma_{j,fit}^D - \hat{\gamma}_j^D$ after removing outliers.

Table B.1. Rate coefficients and corrected $\hat{\gamma}_j$ for species not included in UDfA. PI and PD denotes photo-ionization and photo-dissociation.

process	species	$\alpha (\text{s}^{-1})$	γ_j	$\hat{\gamma}_j$
PI	CH_4	6.8×10^{-12}	3.94	4.13
PD	CS_2	6.1×10^{-9}	2.06	1.75
PI	CS_2	1.7×10^{-9}	3.16	2.68
PD	HO_2	6.7×10^{-10}	2.12	1.81
PD	N_2O	1.9×10^{-9}	2.44	2.02
PI	N_2O	1.7×10^{-10}	3.93	4.06
PD	NH^+	5.4×10^{-11}	1.64	1.32
PI	NO_2	1.5×10^{-10}	3.33	2.86
PD	O_3	1.9×10^{-9}	1.85	1.48

For a given dust type, the total H_2 formation rate is given by equation 19 (omitting the subscript index i in the following)

$$R_{\text{H}_2} = \frac{1}{2} n_{\text{H}} v_{\text{H}} n_d \sigma_d \epsilon_{\text{H}_2} S_{\text{H}},$$

where the formation efficiency is given by equation 22:

$$\begin{aligned} \epsilon_{\text{H}_2} &= (\mathcal{A} + 1 + \mathcal{B})^{-1} \xi \\ \epsilon_{\text{H}_2} &= \left(\frac{\mu F}{2\beta_{\text{H}_2}} + 1 + \frac{\beta_{\text{H}_p}}{\alpha_{\text{P}_C}} \right)^{-1} \xi. \end{aligned} \quad (\text{C.1})$$

We set $(\mu F)/(2\beta_{\text{H}_2})$ to zero to make sure that newly formed H_2 molecules are able to leave very cold dust surfaces, equivalent to

Table C.1. Model parameter for silicate and graphite surfaces. For more details about the determination and calculation of these parameters, see Cazaux & Tielens (2002)

Parameter	silicate	graphite
E_{H_2} [K] ^a	320	520
μ^b	0.3	0.4
E_S [K] ^c	110	260
E_{H_P} [K] ^d	450	800
E_{H_C} [K] ^e	30000	30000
$a \sqrt{\frac{2m(E_{\text{H}_P} - E_S)}{\hbar^2}}$ ^f	14.4	14.0
ν_{H_2} [s ⁻¹] ^g	3×10^{12}	3×10^{12}
ν_{H_C} [s ⁻¹] ^h	1.3×10^{13}	1.3×10^{13}
F [mLy s ⁻¹] ⁱ		10^{-10}

Notes. ^(a) Desorption energy of H₂. ^(b) Fraction of newly formed H₂ that stays on the surface. ^(c) Energy of the saddle point between a chemisorbed and a physisorbed site. ^(d) Desorption energy of physisorbed H. ^(e) Desorption energy of chemisorbed H. ^(f) Product of the width and height of the energy barrier between a physisorbed and a chemisorbed site. For more details see Cazaux & Tielens (2004) ^(g) vibrational frequency of H₂ in surface sites. ^(h) vibrational frequency of H in surface sites. ⁽ⁱ⁾ Flux of H atoms in monolayers per second.

equation (13) in Cazaux & Tielens (2002). We can approximate ξ and $\beta_{\text{H}_P}/\alpha_{PC}$ by

$$\xi = 1 + \left[\nu_{\text{H}_C} \exp\left(\frac{1.5E_{\text{H}_C}}{T_d}\right) \left(1 + \sqrt{\frac{E_{\text{H}_C} - E_S}{E_{\text{H}_P} - E_S}}\right)^2 \right] / (2F)^{-1}. \quad (\text{C.2})$$

$$\frac{\beta_{\text{H}_P}}{\alpha_{PC}} = \left(4 \exp\left(\frac{E_S}{T_d}\right) \sqrt{\frac{E_{\text{H}_P} - E_S}{E_{\text{H}_C} - E_S}} + \frac{8 \sqrt{\pi T_d} \exp\left(-2a \sqrt{\frac{2m(E_{\text{H}_P} - E_S)}{\hbar^2}}\right) \exp\left(\frac{E_{\text{H}_P}}{T_d}\right) \sqrt{E_{\text{H}_C} - E_{\text{H}_P}}}{E_{\text{H}_C} - E_S} \right)^{-1}. \quad (\text{C.3})$$

Equation C.3 takes into account the corrections from Cazaux & Tielens (2010). Table (C.1) gives the applied model parameters for silicate and graphite surfaces.

Appendix D: Photoelectric heating rates

Weingartner & Draine (2001a) showed that the photoelectric heating rate for the WD01 grain size distributions is fairly well reproduced by the parametrization

$$\Gamma_{\text{pc}} = G n_{\text{H}} \frac{C_0 + C_1 T^{C_4}}{1 + C_2 \psi^{C_5} [1 + C_3 \psi^{C_6}]} 10^{-26} \text{ erg s}^{-1} \text{ cm}^{-3}, \quad (\text{D.1})$$

with $\psi = (G \sqrt{T})/n_e$, where T is the gas temperature in Kelvins and ψ is in units of K^{1/2}cm³, and $G = 1.71\chi$. Numerical values for the parameters C_i in Eq. (D.1) are given in Table 2 in Weingartner & Draine (2001a) for each dust distribution. The rate of cooling due to charged particle collisions can be approximated by

$$\Lambda_{\text{gr}} = n_e n_{\text{H}} T^{D_0 + D_1/x} \exp D_2 + D_3 x - D_4 x^2 \times 10^{-28} \text{ erg s}^{-1} \text{ cm}^{-3}, \quad (\text{D.2})$$

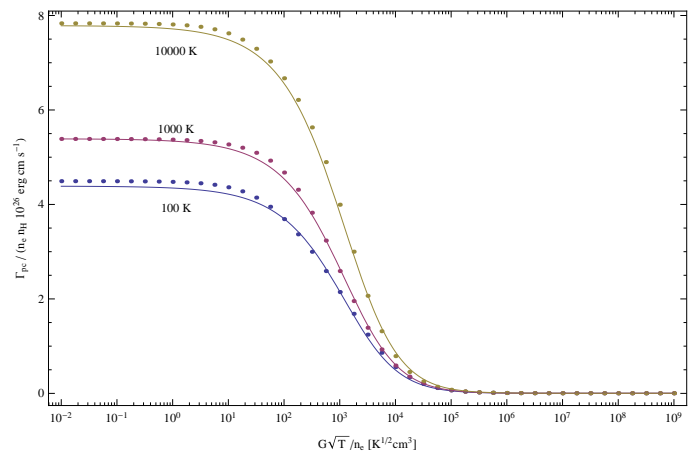


Fig. D.1. Fit results to the photoelectric heating rate, calculated for an extended range of $G \sqrt{T}/n_e$. The different lines show results for gas temperatures 100 K, 1000 K, and 10000 K. Γ_{pc} is given in units of 10^{-26} ergs⁻¹.

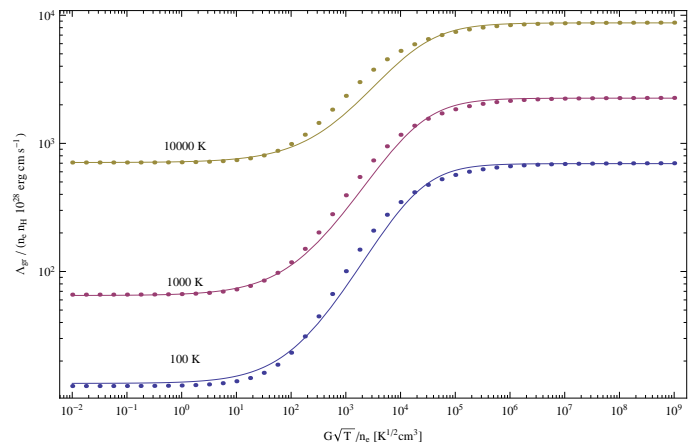


Fig. D.2. Fit result to the net cooling rate due to collisions with charged particles, calculated for an extended range of $G \sqrt{T}/n_e$. The different lines show results for gas temperatures 100 K, 1000 K, and 10000 K. Γ_{pc} is given in units of 10^{-26} ergs⁻¹.

where $x = \ln(G \sqrt{T}/n_e)$. Values for the D_i for all WD01 grain distributions are given in Table 3 in Weingartner & Draine (2001a).

Equations (D.1) and (D.2) are fairly accurate when $10^3 \text{ K} \leq T \leq 10^4 \text{ K}$ and $10^2 \text{ K}^{1/2} \text{ cm}^3 \leq \psi \leq 10^6 \text{ K}^{1/2} \text{ cm}^3$. However, the parameter range in PDR models allows ψ to reach values as high as $10^9 \text{ K}^{1/2} \text{ cm}^3$ and as low as $10^{-2} \text{ K}^{1/2} \text{ cm}^3$. Weingartner (2009) provided updated calculations of Γ_{pc} and Λ_{gr} for the dust distributions WD01-7, WD01-21, and WD01-25 up to $\psi = 10^9 \text{ K}^{1/2} \text{ cm}^3$.

We performed numerical fits to the updated photoelectric heating rates and to the cooling rate due to collisions with charged particles according to the parametrizations 25 and 26. The heating and cooling rates have been calculated by Weingartner (2009) with an extended parameter range of $10^{-2} \text{ K}^{1/2} \text{ cm}^3 \leq \psi \leq 10^9 \text{ K}^{1/2} \text{ cm}^3$. The details of the computation are described in Weingartner & Draine (2001a). To achieve a good fit over the full extended parameter range it was necessary to modify the algebraic form of the parametrizations relative to its original form in Weingartner & Draine (2001a). The final form is given in equations 25 and 26. In Figs. D.1 and D.2 we

Table D.1. Photoelectric heating parameters (equation 25). See Weingartner & Draine (2001a) for detailed descriptions of the dust size distributions and applied physical parameters.

R_V	b_C	Distr.	Rad. Field	C_0	C_1	C_2	C_3	C_4	C_5	C_6	C_7
3.1	6.0	A	B0	8.36780	0.20755	0.00969	0.01354	0.41047	0.62072	0.53099	0.00589
4.0	4.0	B	B0	5.67140	0.13563	0.00994	0.01568	0.41122	0.60659	0.53265	0.00382
5.5	3.0	B	B0	5.67140	0.13563	0.00994	0.01568	0.41122	0.60659	0.53265	0.00382

Table D.2. Collisional cooling parameters (equation 26). See Weingartner & Draine (2001a) for detailed descriptions of the dust size distributions and applied physical parameters.

R_V	b_C	Distr.	Rad. Field	D_0	D_1	D_2	D_3	D_4	D_5	D_6	D_7	D_8	D_9	D_{10}	D_{11}
3.1	6.0	A	B0	0.493	0.556	0.031	0.842	287	0.360	3.640	-0.098	0.642	3.25×10^{-6}	2.080	-1.500
4.0	4.0	B	B0	0.493	0.362	0.038	0.803	287	0.360	2.460	-0.035	0.	2.35×10^{-5}	1.870	-1
5.5	3.0	B	B0	0.484	0.720	0.118	0.597	100	0.710	1.240	-0.030	0.603	1.11×10^{-6}	2.150	-2.720

show the fits to calculations of Γ_{pc} and Λ_{gr} for gas temperatures of 100 K, 1000 K and 10000 K to demonstrate the quality of the parametrization. The C_i and D_i parameters are given in Table D.1 and D.2 and will provide a fairly accurate reproduction of the total photoelectric heating rate Γ_{tot} between $10 K \leq T \leq 10000 K$ and $10^{-2} K^{1/2} cm^3 \leq \psi \leq 10^9 K^{1/2} cm^3$.

Carbon Fractionation in PDRs

M. Röllig and V. Ossenkopf

I. Physikalisches Institut, Universität zu Köln, Zülpicher Str. 77, D-50937 Köln, Germany

Preprint online version: November 15, 2012

ABSTRACT

We upgraded the chemical network from the UMIST Database for Astrochemistry 2006 to include isotopes such as ^{13}C and ^{18}O . This includes all corresponding isotopologues, their chemical reactions and the properly scaled reaction rate coefficients. We study the fractionation behavior of astrochemically relevant species over a wide range of model parameters, relevant for modelling of photo-dissociation regions (PDRs). We separately analyze the fractionation of the local abundances, fractionation of the total column densities, and fractionation visible in the emission line ratios. We find that strong C^+ fractionation is possible in cool C^+ gas. Optical thickness as well as excitation effects produce intensity ratios between 40 and 400. The fractionation of CO in PDRs is significantly different from the diffuse interstellar medium. PDR model results never show a fractionation ratio of the CO column density larger than the elemental ratio. Isotope-selective photo-dissociation is always dominated by the isotope-selective chemistry in dense PDR gas. The fractionation of C, CH, CH^+ and HCO^+ is studied in detail, showing that the fractionation of C, CH and CH^+ is dominated by the fractionation of their parental species. The light hydrides chemically derive from C^+ , and, consequently, their fractionation state is coupled to that of C^+ . The fractionation of C is a mixed case depending on whether formation from CO or HCO^+ dominates. Ratios of the emission lines of [C II], [C I], ^{13}CO , and H^{13}CO^+ provide individual diagnostics to the fractionation status of C^+ , C, and CO.

Key words. Astrochemistry – ISM: abundances – ISM: structure – photon-dominated region (PDR) – ISM: clouds

1. Introduction

Astronomical observations of molecules and their respective isotopologues reveal, that abundance ratios of the main species to their respective isotopologues may differ significantly from e.g. solar system isotope ratios. While isotopic fractionation in the interstellar medium is widely discussed in the framework of deuterium chemistry, its relevance for the $^{12}\text{C}/^{13}\text{C}$ ratio in various species usually gains much less attention. In this paper we investigate chemical fractionation in the context of models of photo-dissociation regions (PDR) with the focus on effects that result from introducing ^{13}C into the applied chemical network.

The most important fractionation reaction is



(see Woods & Willacy 2009, and references therein). At high temperature back and forth reaction are equally probable and no apparent deviation from the elemental isotope ratio takes place. The lower the temperature gets, the less probable the back reaction becomes, resulting in a one-way channel shifting ^{13}C into ^{13}CO and decreasing the abundance ratio of $^{12}\text{CO}/^{13}\text{CO}$. At the same time the abundance ratio of $^{12}\text{C}^+/^{13}\text{C}^+$ is shifted oppositely. Langer et al. (1984) performed numerical calculations of a time-dependant chemical network for a variety of physical parameter and given kinetic temperatures concluding that chemical fractionation of carbon bearing species is of increasing significance the lower the temperate is, confirming the relevance of zero-point energy differences of a few ten K at low temperatures. In dark cloud models, where radiation is usually neglected, the kinetic temperature is the major parameter in opening and closing reaction channels. For a given density, the chemical network

only depends on the temperature and the cosmic ray ionization rate ζ_{CR} (, and history in case of time-dependant calculations).

Carbon fractionation in molecular and diffuse clouds has been discussed systematically by Keene et al. (1998) and Liszt (2007). Following Wakelam & Herbst (2008) we assume a standard elemental abundance of $^{13}\text{C}/^{12}\text{C}$ of 67 in the solar neighbourhood. Observing ^{13}C and $^{13}\text{C}^{18}\text{O}$ in the Orion Bar Keene et al. (1998) found little evidence for chemical fractionation. Their observations showed a slight enhancement of $^{13}\text{C}^{18}\text{O}/^{13}\text{C}^{18}\text{O}=75$ and no enhancement of $[^{13}\text{CI}]/[\text{CI}]$ relative to the standard elemental abundance while the chemical models predicted the opposite. The systematic study of the $^{13}\text{C}^{18}\text{O}/^{13}\text{C}^{18}\text{O}$ by Langer & Penzias (1990, 1993) showed a systematic gradient with Galactocentric radius, i.e. significantly higher ^{13}C abundances in the inner Milky Way, but also variations between 57 and 78 at the solar circle. Wouterloot & Brand (1996) showed that the trend continues to the outer Galaxy with ratios above 100 in WB89-437. Optical spectroscopy of $^{13}\text{CH}^+$ in diffuse clouds has shown that the $^{13}\text{CH}^+/\text{CH}^+$ ratio matches the elemental abundance ratio in the solar vicinity very closely (see e.g. Centurion et al. 1995). Liszt (2007) showed that the fractionation reaction (C1) is even the dominating CO destruction process for high and moderate densities. They also report fractionation ratios of the CO column density between 15 and 170 with a tendency for the ratio to drop with increasing column density. Their analysis is based on observation of diffuse clouds and covers a CO column density range up to $N(^{12}\text{CO}) \approx 2 \times 10^{16} \text{ cm}^{-2}$ and densities $\lesssim 100 \text{ cm}^{-3}$. Here we complement this study by concentrating on PDRs with higher densities ($n \geq 10^3 \text{ cm}^{-3}$).

This paper is organized as follows: in Sect. 2 we will briefly overview the KOSMA- τ PDR model which has been used to perform the model computations. The updated isotope chemistry is described in detail in Sect. 2.2. In Sect. 3 we will present results

Send offprint requests to: M. Röllig,
 e-mail: roeellig@ph1.uni-koeln.de

from our model calculations. In a second paper (Ossenkopf et al. 2012, Paper II) we present observations of the $[C\,II]/[^{13}C\,II]$ ratio in various PDRs and investigate the fractionation ratio of C^+ in more detail.

2. The KOSMA- τ PDR model

A large number of numerical PDR codes is presently in use and an overview of many established PDR models is presented in Röllig et al. (2007)¹. We use the KOSMA- τ PDR code (Störzer et al. 1996; Röllig et al. 2006)² to numerically solve the coupled equations of energy balance (heating and cooling), chemical equilibrium, and radiative transfer. The main features of the KOSMA- τ PDR model are: a) spherical model symmetry, i.e. finite model clouds, b) modular chemistry, which means, that chemical species can easily be added or removed from the network and the network will rebuild dynamically, c) isotope chemistry including ^{13}C and ^{18}O , and d) optimization toward large model grids in parameter space, allowing for example to build up any composition of individual clouds in order to simulate clumpy material (for details see Cubick et al. 2008). The KOSMA- τ results can be accessed on-line at: <http://www.astro.uni-koeln.de/~pdr>.

2.1. Model physics

Individual PDR-clumps are characterized by the total gas density n at the cloud surface, the clump mass M in units of the solar mass, the incident, isotropic far ultraviolet (FUV: $6\text{ eV} \leq E \leq 13.6\text{ eV}$) intensity χ , given in units of the mean interstellar radiation field of Draine (1978), and the metallicity Z . We assume a density power-law profile $n(r) = n_0(r/R_{\text{tot}})^{-\alpha}$ for $R_{\text{core}} \leq r \leq R_{\text{tot}}$, and $n(r) = \text{const.}$ for $0 \leq r \leq R_{\text{core}}$. The standard parameters are: $\alpha = 1.5$, $R_{\text{core}} = 0.2 R_{\text{tot}}$, roughly approximating the structure of Bonnor-Ebert spheres. Figure 1 shows the applied density structure. In Appendix D we describe how to compute mean column densities for spherical model results.

Excitation of the H_2 molecule is computed by collapsing all rotational levels with the same vibrational quantum number into a corresponding, virtual v level. We then solve the detailed population problem accounting for 15 ground-state levels ($v = 0 - 14$) and 24 levels from the Lyman band as well as 10 Werner band levels. We assume that chemical reactions with the population of vibrationally excited H_2 have no activation energy barrier to overcome. This is especially important for species such as CH (Röllig et al. 2007) and CH^+ (Agúndez et al. 2010). The heating by collisional de-excitation of vibrationally excited H_2 is calculated from the detailed level population. Photo-electric heating is calculated according to Bakes & Tielens (1994). Overall, we account for 20 heating and cooling processes. For a detailed description see Röllig et al. (2006) and Röllig et al. (2007). All model results in this paper are for single-clump models without contribution from interclump gas and without clump superposition.

¹ The comparison results and code descriptions are available at <http://www.astro.uni-koeln.de/pdr-comparison>

² We recently updated KOSMA- τ to self-consistently account for various dust compositions and dust size distributions including wavelength-dependent continuum radiative transfer, dust temperature computation and photo-electric heating. For details see Röllig et al. (2012). However, the update was not fully available when we started this study, so we do not fully use the updated code capabilities here.

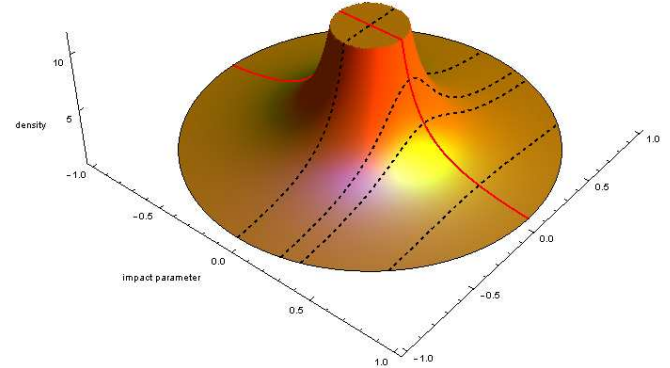


Fig. 1. Radial density profile of a model clump. The dashed lines show the density profile along various lines of sight (for different impact parameters p).

2.2. Model chemistry

In KOSMA- τ we solve pure gas-phase steady-state chemistry with the exception of H_2 forming on grains (Sternberg & Dalgarno 1995). It relies on the availability of comprehensive databases of chemical reaction rate coefficients. Today a few databases are publicly available, such as UDfA³ (Woodall et al. 2007), the Ohio database OSU⁴, and the NIST Chemistry Webbook⁵. There are also efforts to pool all available reaction data into a unified database (KIDA: KInetic Database for Astrochemistry)⁶.

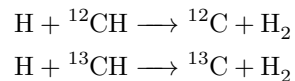
In the following we use UDfA06. Retrieved at the 09/29/2009 the database consists of 4556 reaction rates, involving 421 chemical species (420 species + electrons). 34 of these reactions are present with 2 or 3 entries, valid in different temperature ranges (Röllig 2011). All species in UDfA06 are composed of the main isotopes only.

2.2.1. Isotopization

In order to calculate chemical reactions involving different isotopologues, i.e. molecules that differ only by their isotopic composition, it is necessary to extend the chemical reaction set. For example, reaction 1 in UDfA06:



becomes



We developed a software routine to automatically implement isotopic reactions into a given reaction set⁷. A similar automatic procedure was used by Le Bourlot et al. (1993); Le Petit et al.

³ <http://www.udfa.net>

⁴ <http://www.physics.ohio-state.edu/~eric/research.html>

⁵ <http://webbook.nist.gov/chemistry/>

⁶ <http://kida.obs.u-bordeaux1.fr/>

⁷ We realized the isotopization routine in Mathematica©by Wolfram Research.

(2006). We applied our routine to the UDfA06 reaction set, but it can be applied to any given set of chemical reactions. The routine features are:

- inclusion of a single ^{13}C and a single ^{18}O isotope (multiple isotopizations are neglected in this study)
- UDfA often does not give structural information, for instance C_2H_3 does not distinguish between linear and circular configurations ($\text{l}-\text{C}_2\text{H}_3$ and $\text{c}-\text{C}_2\text{H}_3$). In such cases we consider all carbon atoms (denoted by C_n) as indistinguishable. However, if structure information is provided we account for each possible isotopologue individually:
- molecular symmetries are preserved, i.e. $\text{NC}^{13}\text{CN} = \text{N}^{13}\text{CCN}$, but $\text{HC}^{18}\text{OOH} \neq \text{HCO}^{18}\text{OH}$
- functional groups like CH_n are preserved (see also Woods & Willacy 2009)
- when the above assumptions are in conflict to each other we assume *minimal scrambling*, i.e. we choose reactions such, that the fewest possible number of particles switch partners.
- we favor proton/H transfer over transfer of heavier atoms
- we favor destruction of weaker bonds

In Appendix A we describe in detail how isotopologues were introduced into the chemical network. The rescaling of the newly introduced reaction rates is described in Appendix B.⁸

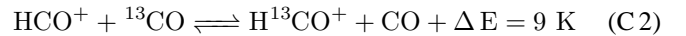
2.2.2. Choice of the chemical data set

Some data sets, e.g. OSU, are more relevant for the cold ISM while others, for instance by including reactions with higher activation energy barriers, are better suited to describe the warm ISM. Consequently, the results of chemical model calculations may differ significantly depending on the applied chemical data set. Reactions that can be found in different chemical sets can have significantly different rate coefficients among the various sets. Even very prominent reactions, such as the photo-dissociation of CO (from now on we will omit the isotopic superscript when denoting the main isotope) are listed with very different rate coefficients: UDfA06 gives an unshielded rate coefficient of $2 \times 10^{-10} \text{ s}^{-1}$, OSU and KIDA give $3.1 \times 10^{-11} \text{ s}^{-1}$. This is a huge difference and will lead to a significantly different chemical structure of a model PDR. It is not the purpose of this paper to perform a detailed analysis of how the choice of a chemical data set affects PDR model results. However, we show in Appendix C how the (isotope-free) chemistry of the main species discussed later in this paper changes for three different chemical sets. For a similar discussion see also Wakelam et al. (2012).

2.2.3. Isotope exchange reactions

In this frame reaction (C1) turns into two reactions, one for the forward, one for the back reaction, where both have the value of α (the rate coefficient for reaction (C1) is $k_{(C1 \rightarrow)} = 4.42 \times 10^{-10} (T/300K)^{-0.29}$), but where the back reaction is suppressed by the factor $\exp(-\gamma/T)$ with $\gamma = 35 \text{ K}$. Watson et al. (1976) proposed that carbon isotope transfer between interstellar species can occur as a result of reaction (C1). At low temperatures, reaction (C1) transfers ^{13}C isotopes from $^{13}\text{C}^+ \rightarrow ^{13}\text{CO}$, enhancing the abundances of ^{13}CO and $^{12}\text{C}^+$. This reaction needs three main ingredients: sufficient amounts

of $^{13}\text{C}^+$ and CO and temperatures well below 100 K. In the PDR context, reaction (C1) is especially interesting, because in the outer transition regions, where CO is still strongly dissociated, the $^{13}\text{C}^+$ abundance is very large while ^{13}CO is very rare. Even small numbers of ^{13}CO products from reaction (C1) will have a significant influence on the total ^{13}CO abundance and thus on the $[\text{CO}]/[^{13}\text{CO}]$ ratio. Vice versa, $^{13}\text{C}^+$ will be depleted strongly, increasing $[\text{C}^+]/[^{13}\text{C}^+]$. Smith & Adams (1980) measured another isotope-exchange reaction:



with less effect on the hotter parts of the PDR, due to the low differences in back and forward reaction rates at higher temperatures. Langer et al. (1984) tabulated reaction rates and reaction enthalpies for the various isotopic variants of reactions (C1) and (C2) and we use their values in our calculations. Slightly different reaction rate coefficients are also given by Liszt (2007) and Woods & Willacy (2009) but the differences are small.

3. Application

3.1. Model parameter grid

We test the outcome of the isotopic network under various conditions by computing a large grid of models spanning the possible parameter space. Our chemical network consists of 198 species, involved in a total of 3250 reactions. We did not include ^{18}O into the chemistry here.

We separate the model parameters into two sets: fixed and variable. The fixed parameters determine the fundamental physical and chemical conditions for the model clouds, e.g. gas density profile parameters α and $R_{\text{core}}/R_{\text{tot}}$, cosmic ray ionization rate ζ_{CR} of molecular hydrogen elemental abundances X_i , metallicity, and dust composition. The variable parameters compose the final model parameter grid. A common set of variable parameters is: total surface gas density $n_0 = n(R_{\text{tot}}) = n_{\text{H}} + 2n_{\text{H}_2}$, cloud mass M , and ambient FUV field strength χ in units of the Draine field (Draine 1978). For a given density law, α and $f_c = R_{\text{core}}/R_{\text{tot}}$, the total cloud radius $R_{\text{tot}} = 5.3 \times 10^{18} \sqrt[3]{M/n} \text{ cm}$ and the maximum (radial) column density $N_{\text{max}} = 4.7nR \text{ cm}^{-2}$ (see also App. D).

For the present study we varied the clump parameters n_0 , M , χ and kept all other parameters constant. Table 1 gives an overview over the used parameters. We assume a dust composition according to Weingartner & Draine (2001) (entry 7 in their Tab. 1, which is equivalent to $R_V = A_V/E_{B-V} = 3.1$). From the extinction cross section of each dust component we compute an average, effective FUV dust cross section per H σ_D . For a given total gas column density N_{tot} , then follows: $\tau_{\text{FUV}} = N_{\text{tot}}\sigma_D$, and $A_V = \sigma_D N_{\text{tot}} 1.086/3.08$. The term in the denominator corrects from visual to FUV extinction. Note, that the elemental abundances of carbon show an elemental ratio (ER) of 67, close to the average ratio in the local ISM (Sheffer et al. 2007). We computed 168 models. The computation times per model range from 36 to 930 minutes with a median of 100 minutes.¹⁰

3.2. Structure of the $\text{C}^+/\text{C}/\text{CO}$ transition

The chemical stratification of $\text{C}^+ - \text{C} - \text{CO}$, the carbon transition (CT), is a well known signature of PDR chemistry (e.g.

⁸ The isotopized chemical data set as well as the isotopization routine are available online: <http://www.astro.uni-koeln.de/~kosma-tau>.

¹⁰ On an Intel Xeon, 2.5 GHz CPU

Table 1. Overview of the most important model parameter. All abundances are given with respect to the total H abundance. The numbers in parentheses indicate powers of ten.

Model Parameters		
He/H	0.0851	Asplund et al. (2005)
O/H	2.56(−4)	Wakelam & Herbst (2008)
C/H	1.2(−4)	Wakelam & Herbst (2008)
$^{13}\text{C}/\text{H}$	1.8(−6)	
N/H	6.03(−5)	Asplund et al. (2005)
S/H	3.5(−6)	Goicoechea et al. (2006)
Z	1	solar metallicity
ζ_{CR}	5(−17) s ^{−1}	CR ionization rate
R_V	3.1	Weingartner & Draine (2001)
σ_D	1.75(−21) cm ²	UV dust cross section per H
$< A(\lambda)/A_V >$	3.339	mean FUV extinction
τ_{UV}	3.074 A_V	FUV dust attenuation
v_b	1 km s ^{−1}	Doppler width
n_0	$10^{3,...,6} \text{ cm}^{-3}$	total surface gas density
M	$10^{-2,...,3} M_\odot$	cloud mass
χ	$10^{0,...,6}$	FUV intensity w.r.t. Draine (1978) field ⁹
α	1.5	density power law index
R_{core}	$0.2R_{\text{tot}}$	size of const. density core
N_{tot}/A_V	1.62(21) cm ^{−2}	

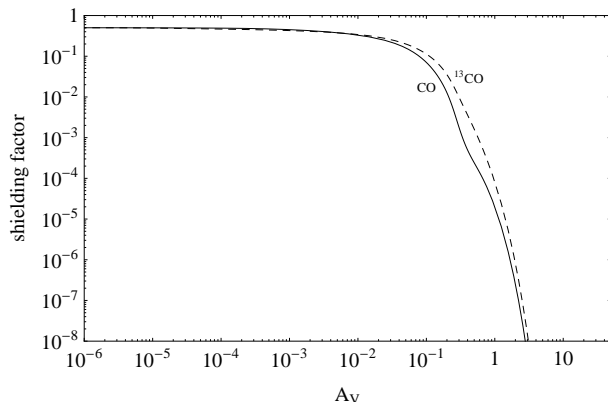


Fig. 2. CO shielding factors¹² of a model clump with the following model parameters: $n_0 = 10^5 \text{ cm}^{-3}$, $M = 100 M_\odot$, $\chi = 10$ (CO: solid line, ^{13}CO : dashed line).

Hollenbach & Tielens 1999). The stratification is the result of a number of competing formation and destruction processes like photo-dissociation, dissociative recombination, and others. Photo-dissociation of CO by FUV photons is a line absorption process, and as such subject to shielding effects (van Dishoeck & Black 1988). Numerically, this can be described by shielding factors that depend on the column densities of dust and of all species that absorb at the frequency of the line. The shielding factor multiplicatively enters the photo-dissociation rate, i.e. describes the reduction of the photo-dissociation through the line absorption. In the case of carbon monoxide the shielding depends on the columns of H_2 and CO (e.g. van Dishoeck & Black

¹² Because of the isotropic illumination one has to compute the average shielding over 4π at each A_V . Optical thickness and scattering then leads to a mean shielding factor at the cloud surface of approximately 0.5.

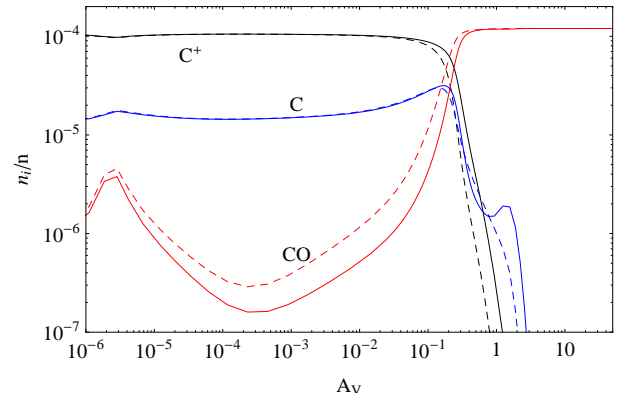


Fig. 3. Chemical structure of a model clump with the following model parameters: $n_0 = 10^5 \text{ cm}^{-3}$, $M = 100 M_\odot$, $\chi = 10$. (main isotopologue: solid line, ^{13}C isotopologue multiplied by $ER=67$: dashed line).

1988; Lee et al. 1996; Warin et al. 1996; Visser et al. 2009)¹³. The self-shielding of the CO leads to stronger photo-dissociation of the rarer isotopologues at a given A_V ¹⁴. This is also shown in Fig. 2. Because of the lower column density of ^{13}CO , with respect to the main isotopologue, it takes a larger cloud depth for ^{13}CO to become optically thick than it takes for CO. From Fig. 2 it can be seen that photo-dissociation of ^{13}CO is still strong at $A_V \approx 0.3$ where CO is already optically thick.

The physical conditions, such as density structure and FUV illumination, determine where the CT is situated. For the purpose of this paper we define CT as the position in a cloud where $n(\text{C}^+) = n(\text{CO})$. The details of the $\text{C}^+ - \text{C} - \text{CO}$ structure are changed by various effects. C^+ remains the least affected species. At the outside of the cloud photo-ionization turns basically all carbon into C^+ . The strength of the FUV field and the attenuation by dust determine the depth where recombination dominates over ionization and the C^+ abundances decreases. Carbon now becomes distributed between numerous species, but once shielding of CO becomes effective, usually at $A_V \gtrsim 1$, the large majority of all carbon atoms is bound into carbon monoxide. Both species, C^+ and CO, are quite insensitive to changes in the chemistry or the temperature structure, at least in cloud regions where they dominate the carbon population. However, in regions where they represent only a minor fraction of all carbon species, their chemical structure may depend sensitively on details of the cloud chemistry and physics. For example, increasing the H_2 formation efficiency on hot dust grains, i.e. at low A_V , increases the corresponding H_2 formation heating efficiency, leading to higher gas temperatures in these cloud parts. This can produce an increase of the CO population in the hot gas and consequently produce strong emission of high- J emission (Le Bourlot et al. 2012; Röllig et al. 2012). The same effect can also positively affect the abundance of light hydrates, such as CH^+ and CH, which are primarily formed in these regions.

Atomic carbon is the species that is probably most affected by changes in the chemistry and physics, because it is involved in the chemistry of C^+ as well as CO and chemically constitu-

¹³ The most recent set of shielding rates is predicted by Visser et al. (2009). In this work we still used the rates from van Dishoeck & Black (1988). Under most parameter conditions the model results differ only marginally ($\sim 10\%$) when switching to the new shielding rates.

¹⁴ ^{12}CO could also shield its less abundant relatives, if their absorption lines are sufficiently close together. However, only very few of the efficiently dissociating lines overlap, too few for mutual shielding to be important (Warin et al. 1996).

tutes a transitional species. It is the major carbon species, that is least understood. Observations and model predictions of the spatial distribution of C show big differences. The classical C^+ -C-CO stratification, with C being sandwiched between its two big brothers is hardly observed at all. Instead, atomic carbon shows a widespread distribution that remains to be understood (e.g. Kramer et al. 2004; Mookerjea et al. 2006; Kramer et al. 2008; Röllig et al. 2011; Mookerjea et al. 2012).

3.3. Cloud fractionation structure

Unfortunately it is impossible to discuss the fractionation for all species from our chemical dataset so that we focus on a few molecules of particular astronomical interest. A complete coverage of the fractionation ratio (FR) for the selected species in our model grid is presented in Appendix E.

3.3.1. C^+ and CO

Figure 3 shows the chemical structure of the main carbon species in the model clump. Solid lines show the main isotopologues, dashed lines the ^{13}C variants. In the outer parts of the clump, most of the carbon is in the form of C^+ . The CT for the model shown in Fig. 3 is at $A_V \approx 0.2$ where the CO photo-dissociation rate has dropped sufficiently in order to build large quantities of CO, which leads to a steep decline in $n(C^+)$ and $n(C)$. In Fig. 4 we show the corresponding FR of the species from Fig. 3. We

sufficiently large for the reaction to work equally well in both directions. Once the temperature drops below 50 K the back reaction becomes less probable and the FR increases rapidly and can be kept at large values as long as enough $^{13}C^+$ ions are available to feed the reaction. Deep inside the clump, the FR is a result of the balance between $^{13}C^+$ formation via $He^+ + ^{13}CO$ and destruction via the fractionation reaction. Dominance of reaction (C 1) automatically leads to fractionation, in this case to C^+ enrichment relative to $^{13}C^+$. The absolute magnitude of the FR is controlled by the He^+ abundance which is a direct result of the cosmic ray ionization rate. In Fig. 4 this can be seen by the roughly constant FR of C^+ deep inside the cloud. The same qualitative behavior is visible for all other model parameters in our model grid. Only the particular position, width and height of the FR peak of C^+ varies with density and FUV field strength. Woods & Willacy (2009) find the same fractionation behavior in their protoplanetary disk model calculations. At the surface C^+ is not fractionated while at large depths they find $FR > ER$.

The fractionation of CO is different because a second isotope-selective process is at work, the shielding of CO and ^{13}CO from FUV photons. We would expect that if photo-dissociation was the dominant process, i.e. if ^{13}CO photo-dissociation was relatively stronger than the photo-dissociation of the main isotopologue, then this would result in $FR(CO) > ER$. This is not the case for any model clump in our calculations. It happens in thinner clouds with $n < 10^2 \text{ cm}^{-3}$ as discussed by Liszt (2007). All models show a $FR(CO) < ER$ indicating that the FR is dominated by the chemistry, i.e. by reaction (C 1) which can only produce $FR < ER$. Exceptions to this behavior are discussed in Sect. 3.3.2.

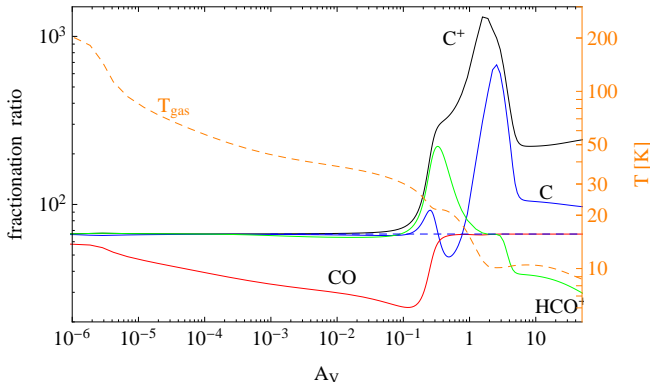


Fig. 4. Fractionation structure of the same model clump as shown in Fig. 3 (solid lines: fractionation ratios $n(X)/n(^{13}X)$, dashed line: kinetic gas temperature (right axis).

note a number of features:

1. the FR of C^+ is always larger than or equal to the ER , i.e. $^{13}C^+$ is always under-abundant with respect to C^+
2. the FR of C^+ equals the ER at low A_V
3. the FR of C^+ increases significantly at large A_V
4. the FR of CO is always smaller or equal to the ER except for conditions described in Sect. 3.3.2.
5. the FR of CO deviates the strongest from the ER at low A_V and equals the ER at large A_V
6. the FR of C and HCO^+ show mixed behavior

Points 1-3 are a direct consequence of reaction (C 1). Any fractionation of C^+ has to be a direct result of this reaction. C^+ stands at the beginning of the chemical chains and there is no other direct mechanism acting in the opposite direction, such as isotope-selective photo-destruction. At low A_V temperatures are

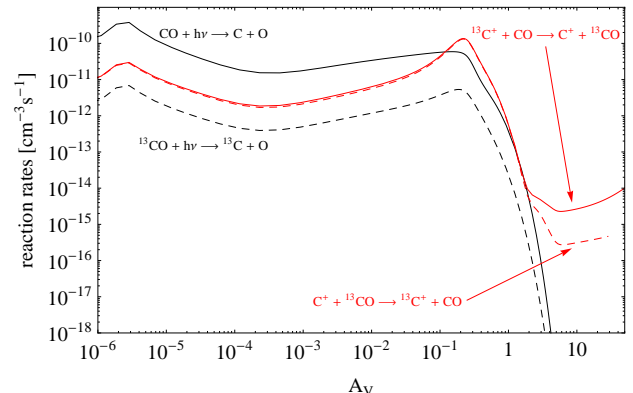


Fig. 5. Reaction rates for the same model clump as shown in Figure 3 (photo-dissociation of CO: black, solid; ^{13}CO : black, dashed; back and forth reaction rates in reaction (C 1): red).

This is also visible from Fig. 5, where the destruction of CO (black, solid line) and ^{13}CO (black, dashed line) via photo-dissociation is compared to the respective formation via reaction (C 1) (red lines). For CO photo-dissociation is the major destruction process until $A_V > 0.1$. Then chemical destruction by the fractionation reaction takes over. Formation via the fractionation reaction is not the dominant formation channel of CO for most of the clump. Only for the small A_V range of $0.1 \leq A_V \leq 0.6$ CO formation is dominated by the fractionation reaction. This is different for ^{13}CO where destruction via photo-dissociation is weaker than formation by reaction (C 1) throughout the clump. Both, formation and destruction of ^{13}CO is governed by reaction (C 1) (both red lines in Fig. 5). At $A_V > 2$ electron recombination with $H^{13}CO^+$ becomes the main forma-

tion channel. Hence, for the whole low A_V part of the clump, the ^{13}CO abundance is controlled by the chemical fractionation reaction and accordingly, ^{13}CO is significantly enriched relative to CO.

Figure 6 compares the FR of C^+ (left panel) and CO (right panel) for $n = 10^3 \text{ cm}^{-3}$ and $M = 1 M_\odot$. Each sector in the figure corresponds to a different FUV intensity χ . The FR , as function of the relative clump radius r/R_{tot} , is color coded, ratios within $\pm 10\%$ of the ER are shown in green. Figure 6 gives a visual summary of the analysis above. The pie chart representation visualizes the relative contribution of the abundance profile at different radii of our spherical clumps to the integrated clump ratio. At $n = 10^3 \text{ cm}^{-3}$, fractionation of C^+ only occurs deep inside the clump, while CO shows most fractionation further out. However, we also note, that for higher values of χ , the cloud is so hot that no fractionation occurs any more. The stronger the FUV intensity the deeper the dominance of the photo-dissociation of CO. No shielding or selective photo-dissociation can yet take place and the FR equals the ER . However, in case of $n = 10^3 \text{ cm}^{-3}$ and $\chi \geq 10^2$, CO can not be shielded efficiently and most of the carbon is locked in its ionized form. This is different for higher densities.

The situation at higher gas density is presented in Fig. 7. The fractionation of C^+ is much more prominent and dominates a much larger clump volume compared to lower densities. As explained above, cold ($T < 100 \text{ K}$) C^+ is always fractionated with $FR \gg ER$. This is true for the entire parameter grid. CO on the other hand, requires CO and sufficient $^{13}\text{C}^+$ to become fractionated. These conditions are only met in a limited radius range, that is pushed to larger depths if χ increases. Deeper inside and further outside, the FR of CO equals the ER .

The effect of different clump masses is easier to understand. Adding mass is effectively equivalent to adding shielded, cold material to the clump, since it approximately requires a constant column of gas to attenuate the FUV radiation. Once this column is reached any additional material will be shielded and therefore located in the center of the clump. The appendix gives sector plots such as Figs. 6 and 7 for the full parameter grid.

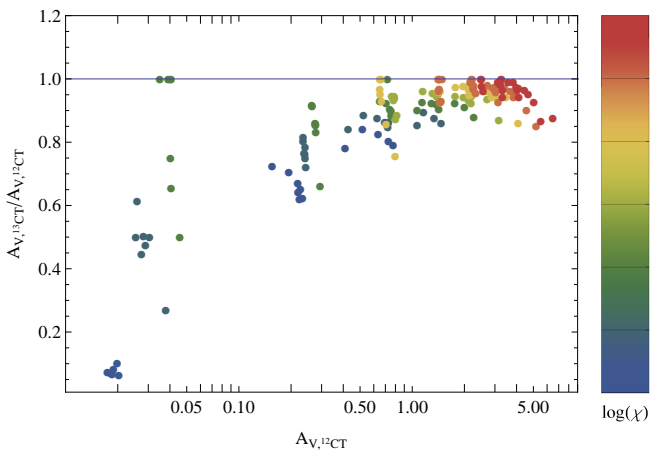


Fig. 8. Comparison of the $A_{V,12\text{CT}}$ and $A_{V,13\text{CT}}$, i.e. the A_V , where $n(\text{C}^+) = n(\text{CO})$ and $n(^{13}\text{C}^+) = n(^{13}\text{CO})$ for all models in our parameter grid. Each data point is colored according to the ambient FUV field χ . The solid line corresponds to $A_{V,12\text{CT}} = A_{V,13\text{CT}}$.

As an additional effect, the ^{13}CO recombination occurs at lower values of A_V than the recombination of the main isotopologues, despite the lower shielding capabilities of ^{13}CO com-

pared to CO. This is true for all models in our parameter grid. Across our parameter grid, the CT of the main isotopologue occurs at a $\log(N_{\text{CO}}) = 15.8 \pm 0.4$, while for the ^{13}C variant (^{13}CT) $\log(N_{\text{CO}}) = 15.4 \pm 0.4$. The difference between both is smallest for models where photo-dissociation is more important, i.e. for larger values of χ . The comparison of the CO column density at the CTs of CO and ^{13}CO for all models in our parameter grid is shown in Fig. 8. The colors of the data points represent the FUV field strength χ of the respective model.

The resulting impact on the column densities is shown in Fig. 9. Each symbol represents the column density $\langle N(\text{CO}) \rangle / \langle N(^{13}\text{CO}) \rangle$ of a model clump with given density n , mass M , and FUV irradiation χ (clump column densities are defined in Appendix D). Clumps with low CO column densities deviate most from the ER . Measurements of the column density ratio $N(\text{CO}) / N(^{13}\text{CO})$ are usually performed on diffuse or translucent clouds and thus naturally confined to a low $N(\text{CO})$ regime.

The low column density region of Fig. 9 is roughly consistent with UV absorption-line observations by Sonnentrucker et al. (2007). For translucent clouds they found an anti-correlation of $\langle N(\text{CO}) \rangle / \langle N(^{13}\text{CO}) \rangle$ with $\langle N(\text{CO}) \rangle$ in the range of $10^{14} \text{ cm}^{-2} \leq \langle N(\text{CO}) \rangle \leq 10^{16.5} \text{ cm}^{-2}$. Liszt (2007) found $15 < N(\text{CO}) / N(^{13}\text{CO}) < 170$ with a tendency for the ratio to decline for higher column densities and a total CO column densities of a few 10^{16} cm^{-2} from Galactic CO absorption and emission at 1.3 and 2.1 mm wavelengths for clouds with a total CO column density $N(\text{CO}) \leq 10^{16} \text{ cm}^{-2}$. Sheffer et al. (2007) showed, that UV data toward diffuse/translucent lines of sight can give $0.5 \leq FR(\text{CO}) / ER \leq 2$.

Clumps with stronger FUV fields show almost no fractionation, either because the molecular inner parts are so small that the gas temperatures throughout the clump are too high or because fractionation only affects the CO at the outer clump regions but not the bulk of the CO gas. For sufficiently large CO column densities, the column density ratio of CO/ ^{13}CO turns out to be a relatively good tracer of the elemental abundance ratio of a given cloud.

The fractionation of the column density ratio of C^+ is shown in Fig. 10. The lower FUV models show the largest FR while the models with very large FUV fields have a $FR = ER$. Models with low density show a much weaker fractionation (see also Fig. E.1) because the molecular part of the low density clouds contributes less to the total C^+ column density. Increasing the model density (larger symbols in the figure) for given model mass and FUV illumination moves the models in Fig. 10 to the top left because larger densities lead to a stronger shielding of the gas from the FUV and therefore a CT closer to the clump surface. Consequently, the total C^+ column density is decreased. On the other hand, the larger amount of cold CO gas acts in favor of the stronger C^+ fractionation. However, these strongly fractionated model clumps show the lowest C^+ column density making observations difficult. Observability will be further discussed in Sect. 3.4.

As an additional consequence, when keeping density and FUV constant, the FR of C^+ is proportional to the clump mass. Increasing the clump mass leads to an increased FR , moving model points, visible as different symbols in Fig. 10, to the top right.

3.3.2. High density conditions with $FR(\text{CO}) > ER$

For typical molecular cloud conditions isotope-selective photo-dissociation is never strong enough to keep ^{13}CO photo-

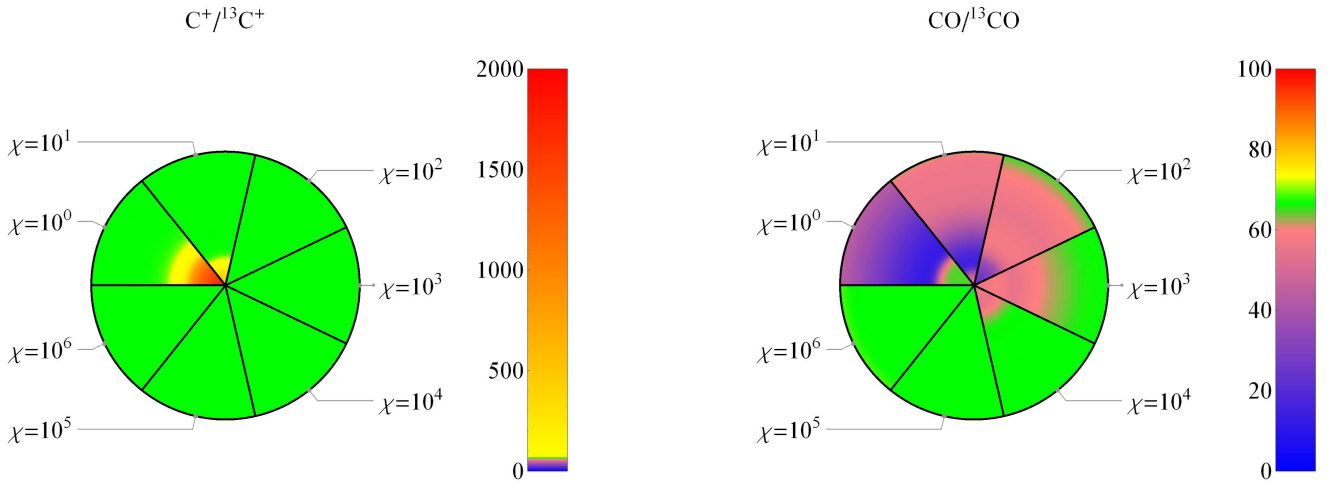


Fig. 6. Fractionation structure as function of relative clump radius r/R_{tot} for $n = 10^3 \text{ cm}^{-3}$ and $M = 1 \text{ M}_\odot$. Each sector corresponds to a different χ value. The FR is color coded, ratios within $\pm 10\%$ of the ER are shown in green. Left panel: FR of C^+ , the color scale goes from 0 to 2000. Right panel: FR of CO, the color scale goes from 0 to 100.

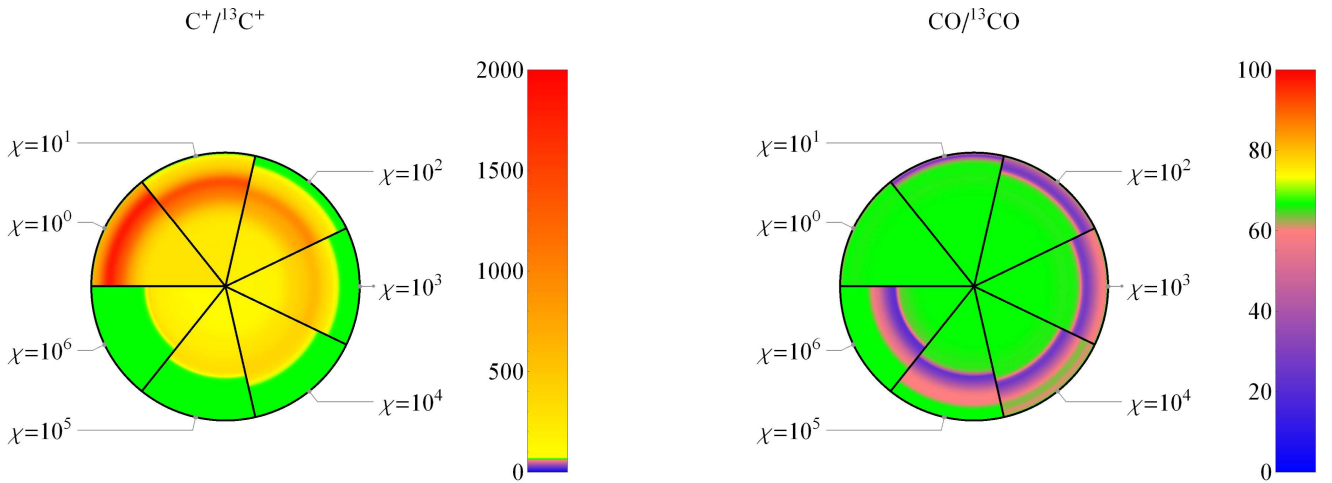


Fig. 7. Same as Fig. 6 for $n = 10^5 \text{ cm}^{-3}$ and $M = 1 \text{ M}_\odot$.

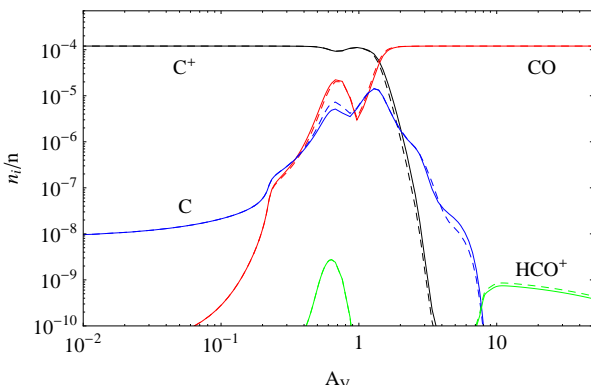


Fig. 11. Fractionation structure of the very dense model clump. The model parameters are $n = 10^7 \text{ cm}^{-3}$, $M = 0.01 M_\odot$, $\chi = 10^5$. (main isotopologue: solid lines, ^{13}C isotopologue multiplied by $ER=67$: dashed lines)

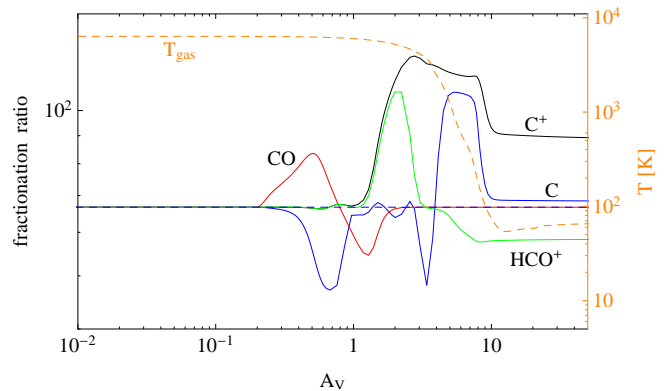


Fig. 12. Fractionation structure of the same model clump as shown in Figure 11.

dissociated while CO is already recombined. If isotope-selective photo-dissociation was dominating the CO chemistry one would

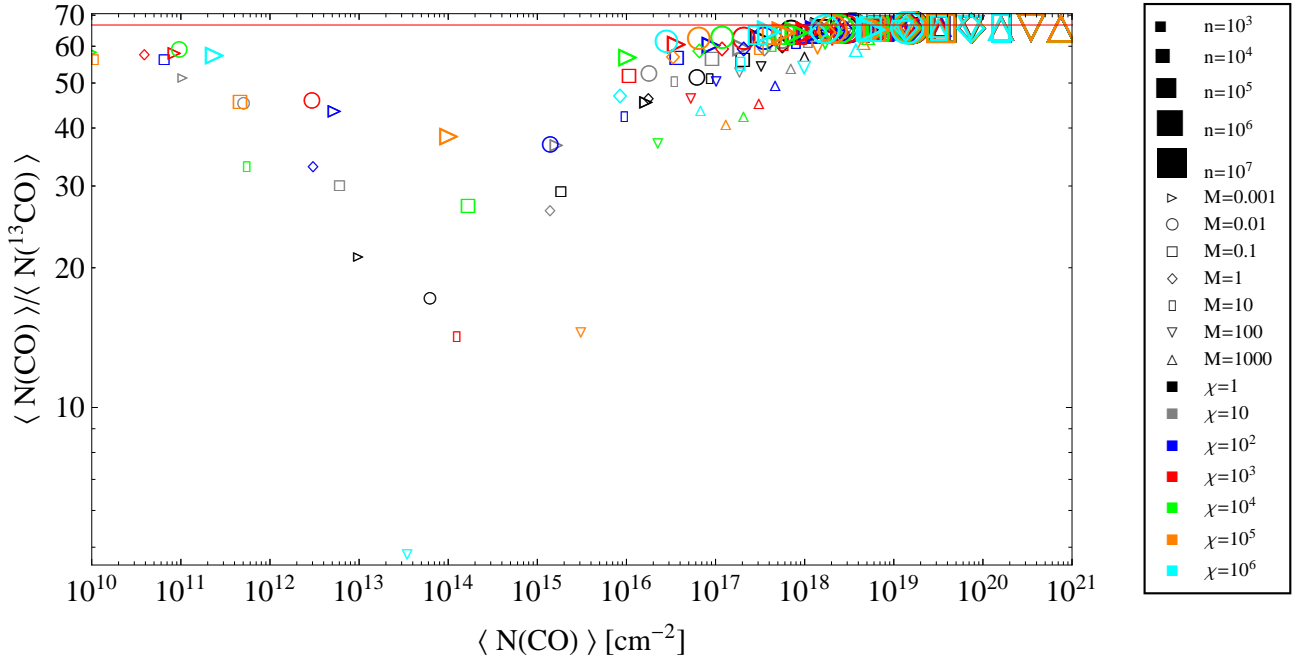


Fig. 9. Scatter plot of the mean column density fractionation ratio vs. the mean column density of the main isotopologue of CO/ ^{13}CO of the whole parameter space. The model parameters n , M , and χ , are coded as size, shape, and color of the respective symbols. The red line denotes the model elemental abundance $[^{12}\text{C}]/[^{13}\text{C}] = 67$.

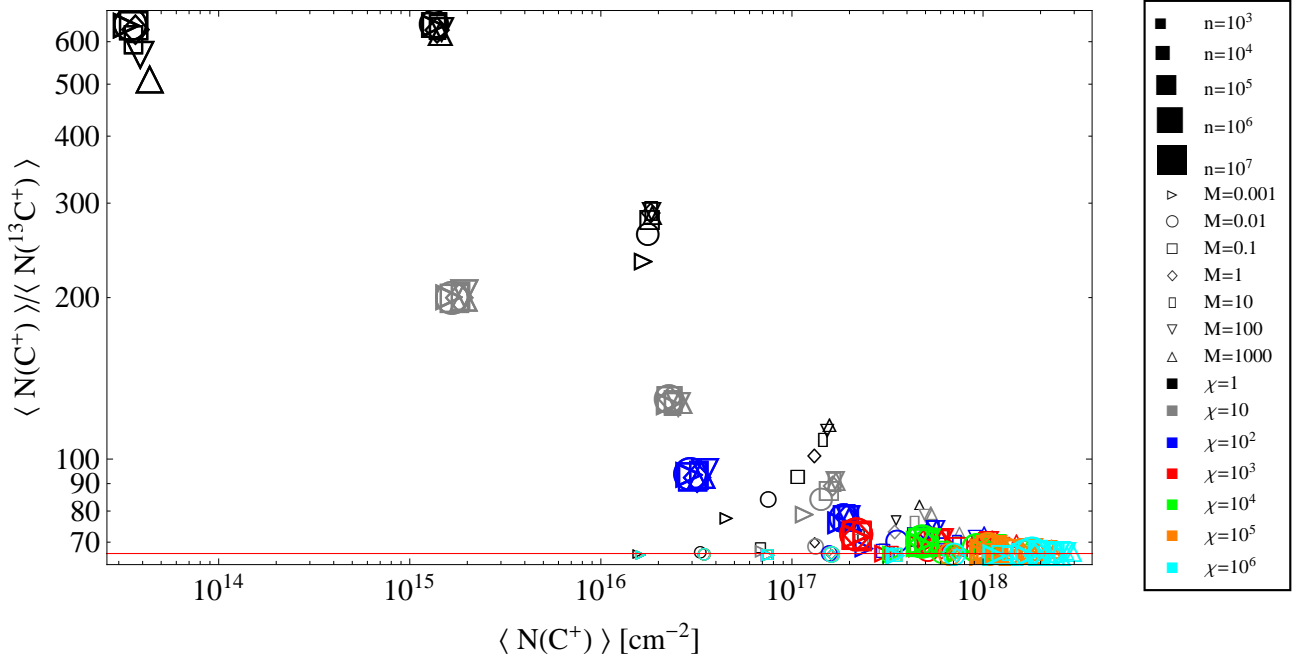


Fig. 10. Same as Fig. 9 for C^+ .

obtain $FR > ER$, like it is found e.g. in diffuse clouds Liszt (2007). For special conditions, particularly for densities of $n \geq 10^6$ and sufficient FUV illumination, $FR > ER$ is still possible across a limited A_V range. Figures 11 and 12 show the density and fractionation structure of such a clump. CO shows a first, relatively strong abundance peak at $A_V = 0.6$, before the CT. The gas temperature at this A_V is around 600 K. At this part of the clump, the FR of CO is higher than the ER . Closer examination

of the parameter reveals that similar behavior can be found for models with $n \geq 10^6$ and $\chi \geq 10^4$ (compare Fig. E.3).

Detailed chemical analysis of these models shows that $FR > ER$ occurs at significantly lower cloud depth than the CT (see Fig. 11). The already mentioned CO abundance peak results from dissociative recombination of HCO^+ , which is effective in hot gas (Sternberg & Dalgarno 1989) and gives rise to the CO peak before the CT. At these cloud depths HCO^+ it-

self is primarily formed by collisions of HOC^+ and CO^+ with H_2 (CO^+ forms through $\text{C}^+ + \text{OH} \rightarrow \text{CO}^+ + \text{H}$ and HOC^+ has two main formation reactions: $\text{C}^+ + \text{H}_2\text{O} \rightarrow \text{HOC}^+ + \text{H}$ and $\text{CO}^+ + \text{H}_2 \rightarrow \text{HOC}^+ + \text{H}$).

The maximum CO abundance in this peak strongly increases with the total gas density. Even so, we have not yet reached the CT, the total CO column density from the cloud's edge to that peak position can already reach values $\gtrsim 10^{15} \text{ cm}^{-2}$, which is sufficient for self-shielding (van Dishoeck & Black 1988). Any CO self-shielding will be stronger for the main isotopologue than for ^{13}CO and if photo-dissociation is the main destruction process for both isotopologues than the stronger shielding of CO can give rise to $FR > ER$. If the destruction of ^{13}CO is controlled by reaction (C 1) than $FR \leq ER$.

To understand which conditions can lead to $FR > ER$ we balance the main formation and destruction processes of ^{13}CO . We already noted that formation via dissociative recombination of HCO^+ is a general requirement, otherwise CO self-shielding will not be effective. A second possible formation route is by the isotope exchange reaction (C 1). Destruction can be either via the back reaction (C 1) or by photo-dissociation. The gas temperatures are high enough to neglect the energy barrier of the back reaction and assume $k_{(\text{C} 1 \rightarrow)} \approx k_{(\text{C} 1 \leftarrow)}$. The rate coefficient for dissociative recombination of HCO^+ is $k_{(\text{DR})} = 2.4 \times 10^{-7} (T/300K)^{-0.29} \text{ s}^{-1} \text{ cm}^3$, and ζ_{13} is the photo-dissociation rate of ^{13}CO . Hence

$$\begin{aligned} k_{(\text{C} 1 \rightarrow)} n(\text{C}^+) n(^{13}\text{CO}) + n(^{13}\text{CO}) \zeta_{13} = \\ k_{(\text{C} 1 \leftarrow)} n(^{13}\text{C}^+) n(\text{CO}) + n(\text{H}^{13}\text{CO}^+) n(e^-) k_{(\text{DR})}. \end{aligned} \quad (1)$$

With $n(\text{CO}) = FR \times n(^{13}\text{CO})$, $n(e^-) \approx n(\text{C}^+) \approx 1.2 \times 10^{-4} n_{\text{tot}}$, and $n(\text{C}^+) = ER \times n(^{13}\text{C}^+)$ follows

$$FR \approx ER \left(1 - \frac{5317}{T^{0.4}} \frac{n(\text{H}^{13}\text{CO}^+)}{n(^{13}\text{CO})} + 3.6 \times 10^{12} T^{0.29} \frac{\zeta_{13}}{n_{\text{tot}}} \right) \quad (2)$$

The last two terms in parentheses compete in changing the FR relative to ER . In the relevant cloud regime, each term lies between $\approx 0.1 - 10$, depending on the detailed conditions, and $FR(\text{CO})$ can increase to $\approx 80 - 100$.

We emphasize, that this behavior is not just a simple competition between chemistry and photo-dissociation as Liszt (2007) described for diffuse clouds. A $FR > ER$ in PDRs is the result of a local, chemically induced, dominance of the photo-dissociation of ^{13}CO over its chemical destruction. Only for $10^6 \leq n \leq 10^7 \text{ cm}^{-3}$ and $10^4 \leq n\chi \leq 10^6$ are the conditions such that in a narrow A_V range isotope-selective photo-dissociation leads to $FR > ER$.

3.3.3. C

From Figs. 4 and 13 we see that the FR of C has a small regime at low A_V and low FUV intensities where $FR < ER$, while under all other conditions the $FR \geq ER$. The $FR(\text{C})$ starts to peak at the rise of $FR(\text{C}^+)$ followed by a dip where CO turns to the ER and by a second peak at the declining flank of $FR(\text{C}^+)$. Until $A_V < 5 - 10$ atomic carbon is dominantly formed through one of the following reactions:

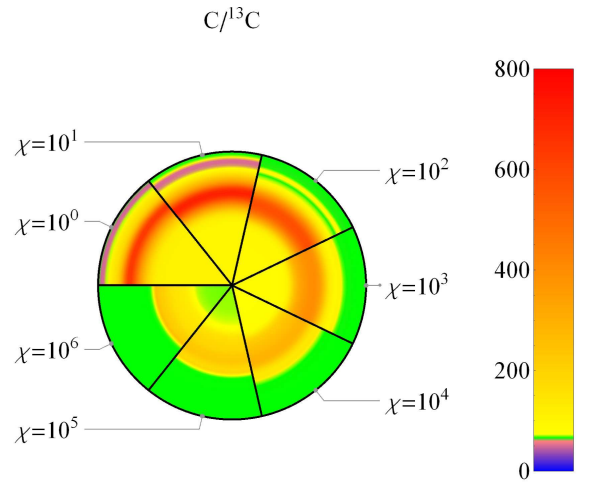
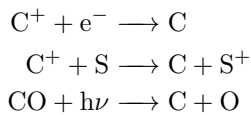


Fig. 13. Same as Fig. 6 for C for $n = 10^5 \text{ cm}^{-3}$ and $M = 1 \text{ M}_\odot$.

while destruction occurs mainly via photo-ionization. As discussed, the FR of CO and C^+ behave oppositely in distinct cloud depths; $FR(\text{CO}) \leq ER$, mainly in outer layers, while $FR(\text{C}^+) \geq ER$, somewhat deeper in.

At low A_V both isotopic variants of atomic carbon will be dominantly formed from the recombination of their ionized forms and C will share the FR of C^+ . This is visible as first peak in $FR(\text{C})$. The weaker shielding of ^{13}CO and the strong fractionation of C^+ makes photo-dissociation of ^{13}CO the major formation reaction for ^{13}C for $A_V > 0.2$. The isotope-selective shielding drives the FR of C toward lower values and gives rise to the dip in the curve in Fig. 13. The magnitude of this diminishment depends on the differences in the shielding of ^{12}CO and ^{13}CO and the cloud depth where the shielding is still weak. If this difference is still significant when $FR(\text{C})$ reaches its first peak it can push the FR to values smaller than the ER .

For $A_V > 0.2$, until FUV shielding becomes strong, $^{13}\text{CO} + h\nu$ will be one order of magnitude faster than any of the other formation reactions while photo-dissociation of ^{12}CO will never be the dominant formation reaction. At $A_V > 1$, $FR(\text{CO}) = ER$ and the $FR(\text{C})$ will increase again. Charge transfer between C^+ and S becomes the major formation reaction and consequently, C will share the FR of C^+ . At very large cloud depths cosmic-ray-induced photo-dissociation of CO becomes a main formation reaction together with charge transfer between C^+ and SO for C and charge transfer between N^+ and ^{13}CO for ^{13}C . As a result, the $FR(\text{C})$ will slowly decrease with increasing A_V .

3.3.4. CH^+ and CH

Figure 14 summarizes the dominant formation and destruction channels of the discussed hydrocarbons. The arrows denote the primary reaction channels for CH^+ , CH_2^+ , and CH_3^+ (left panel) and for CH (right panel) across the model clumps. Figure 15 shows the FR of C^+ , CH^+ , CH_2^+ , CH_3^+ , and CH and Fig. 18 shows the abundance profile of hydrocarbons and their respective isotopologues.

The reaction $\text{C}^+ + \text{H}_2 + \Delta E \rightarrow \text{CH}^+ + \text{H}$ requires an activation energy of $\Delta E = 4600 \text{ K}$, but collisions with vibrationally excited H_2^* allow to overcome the barrier (Röllig et al. 2007; Agúndez et al. 2010). At the edge of the cloud, CH^+ is primarily produced from C^+ colliding with excited, molec-

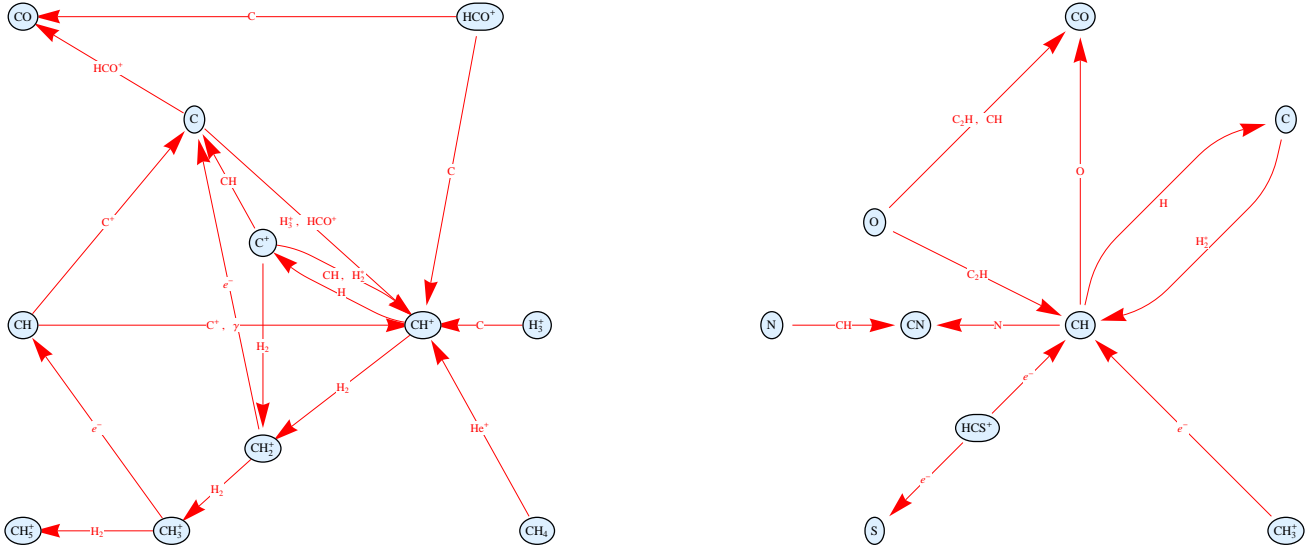
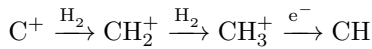


Fig. 14. Chemical network of the dominant formation and destruction channels for: **left panel:** CH^+ , CH_2^+ , and CH_3^+ ; **right panel:** CH

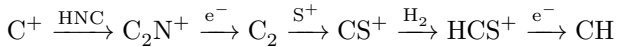
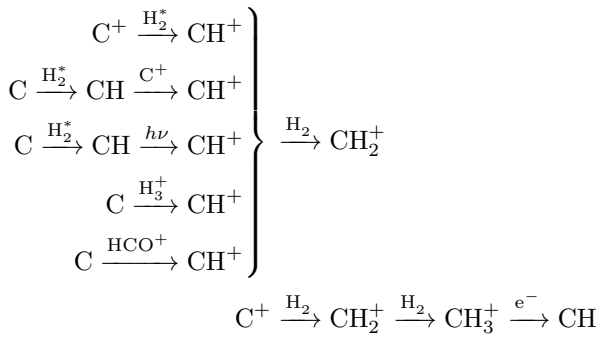
ular hydrogen. At $A_V \sim 10^{-3}$, the proton exchange reaction $\text{C}^+ + \text{CH} \rightarrow \text{CH}^+ + \text{C}$ together with ionization of CH become the main formation reactions. In those two regimes, the *FR* is controlled by C^+ (see also Fig. 15). At $A_V \sim 1$ the main formation occurs via collisions of C with HCO^+ or H_3^+ .

Under very high density and very low χ conditions, C^+ will be less abundant than C throughout the clump. As a result the dip between the two peaks visible in the *FR*(CH^+) in Fig. 15 becomes much more prominent and can reach values below *ER*. This is visible in Fig. E.6.

The formation of CH originates at C^+ . Successive collisions with H_2 form the chain:



At the end of the reaction chain dissociative recombination leads to CH and CH_2 . At low A_V , CH can also be formed from C , at high A_V it forms via dissociative recombination of HCS^+ . The reaction paths to CH (in order of cloud depths where they dominate) then are:



From Fig. 15 and from the above chain of reactions it is obvious, that the fractionation ratio of C^+ will be handed down through

the chain, unless other carbon species become involved. This is the case for CH . At very low A_V where the formation via $\text{C} + \text{H}_2^*$ is most important, and the *FR* is closely related to C which mostly equals the *ER* under these conditions. Once the *FR* of C^+ starts increase, it will affect the fractionation of all the related CH_n^+ and consequently that of CH .

Deeper in the cloud the same happens along a different chemical track. Recombination of CH_3^+ and of HCS^+ (once $A_V > 3$) are the main formation reactions for CH . The chemical chain $\text{C}^+, \text{C}_2\text{N}^+, \text{C}_2, \text{CS}^+, \text{HCS}^+, \text{CH}$ shares a common behavior of the *FR* (see also Fig. 15). As a side remark we would like to emphasize this chain as a good example of how the chemical networks of different elements, sulphur and nitrogen in this case, are mixed. Consequently it is important to include both networks to correctly compute the carbon chemistry.

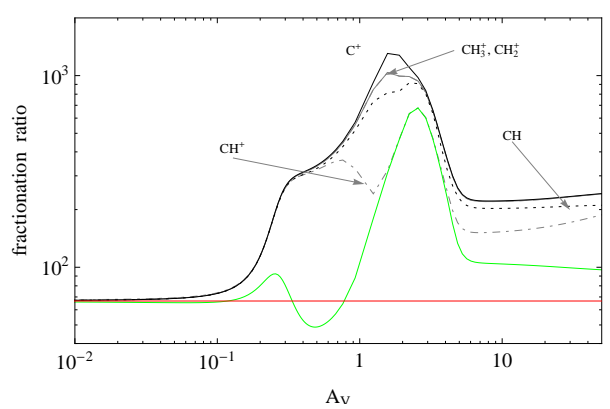


Fig. 15. Fractionation structure of light hydrocarbons for $n_0 = 10^5 \text{ cm}^{-3}$, $M = 100 M_\odot$, $\chi = 10$ (green: *FR*(C^+), red *ER*).

In Figs. 16 and 17 we show the *FR* of CH^+ and CH respectively. The *FR*(C^+) deviates from the *ER* only at larger values of A_V and column densities of species whose *FR* depends on *FR*(C^+) will only be affected if these deeper cloud regions contribute significantly to their total column density. For CH^+ this is

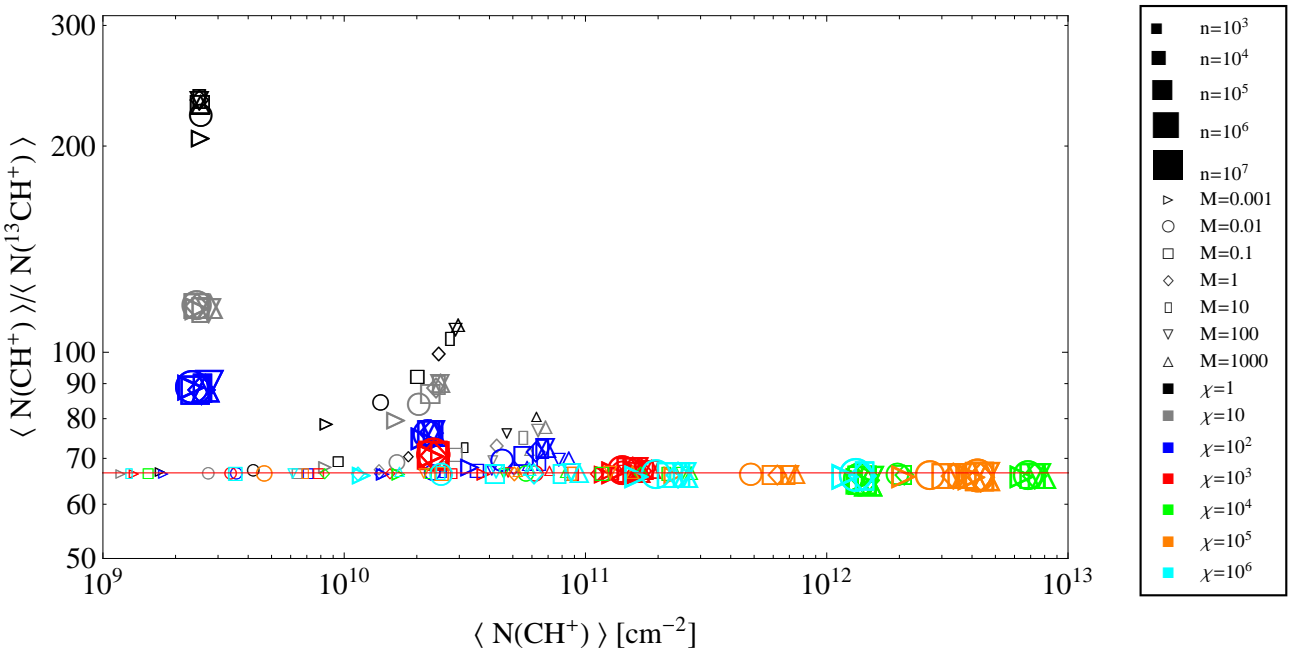


Fig. 16. Same as Fig. 9 for CH^+ .

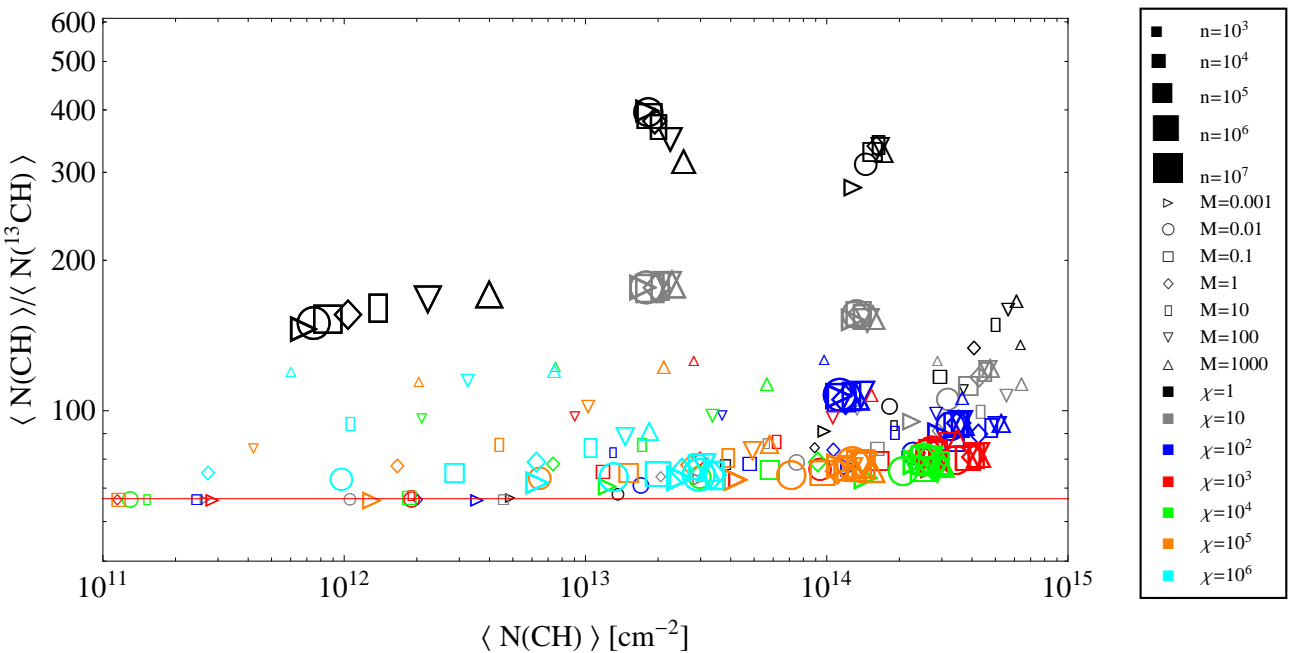


Fig. 17. Same as Fig. 9 for CH .

the case for the same parameters where also C^+ is fractionated and Fig. 16 shows their close chemical relationship. Deviations from the ER occur only for the low χ models with sufficient total column densities, similar to C^+ (see Fig. 10).

The weak deviations of the $FR(CH^+)$ from the ER is consistent with observations. Centurion et al. (1995) found a mean value of the $CH^+/^{13}CH^+$ column density ratio of 67 ± 3 for five lines of sight, very close to the interstellar ER . Casassus et al. (2005) report an average ratio of 78 ± 2 from measurements along 9 lines of sight. Recent absorption-line observations by

Ritchey et al. (2011) along 13 lines of sight through diffuse molecular clouds confirm a $FR(CH^+)$ close to the ambient ER . They report total column densities of CH^+ of a few $10^{13} cm^{-2}$.

CH remains abundant approximately until A_V approaches unity. As a consequence, a larger fraction of its total column density will be affected by the fractionation. This is visible in Fig. 17. Above a mean column density of $10^{13} cm^{-2}$, all models show an enhanced FR . Because of the strong coupling to $FR(C^+)$, weaker FUV models tend to have the strongest fractionation. Therefore, CH promises to be a good observational

fractionation tracer as it combines enhanced *FR* with high column densities.

3.3.5. HCO^+

The fractionation of HCO^+ is special because it is affected by two processes acting in opposite directions. At very low A_V HCO^+ is formed by H_2 collision with HOC^+ and CO^+ . Both precursors are not fractionated, thus $\text{FR}(\text{HCO}^+) \approx \text{ER}$ (see Sect. 3.3.2). A little deeper into the clump, the main formation reaction changes to $\text{CH} + \text{O} \rightarrow \text{HCO}^+ + \text{e}^-$, thus its fractionation indirectly depends on reaction (C1). CH is strongly fractionated with $\text{FR} > \text{ER}$ and passes down the fractionation to HCO^+ . This fractionation peak is seen in Figs. 4 and 19. With growing χ the peak is pushed to larger cloud depths. Once CO is sufficiently abundant, the reaction $\text{H}_3^+ + \text{CO} \rightarrow \text{HCO}^+ + \text{H}_2$ takes over as dominant formation reaction and the *FR* approaches that of CO (compare with Fig. 7, right panel). At even higher values of A_V the gas temperature becomes very low ($T \leq 10$ K) and reaction (C2) starts to dominate formation and destruction of HCO^+ and pushes the *FR* significantly below the *ER*. In the appendix we show the *FR* of HCO^+ over a significant portion of our model grid. The central cloud regime with $\text{FR} < \text{ER}$ is visible in all clumps that are sufficiently shielded from the external FUV radiation.

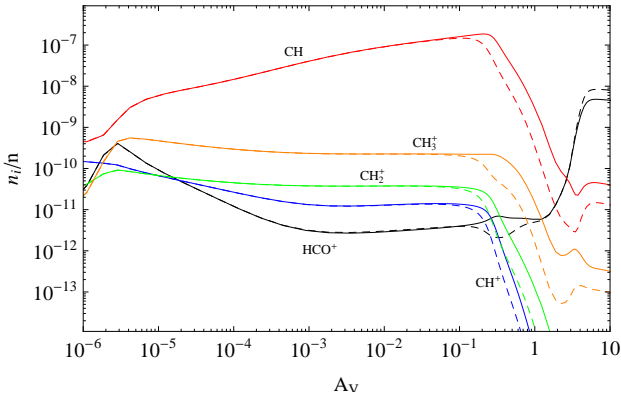


Fig. 18. Same as Figure 3 for species HCO^+ , CH , CH^+ , CH_2^+ , and CH_3^+ .

In Fig. 20 we show the column density fractionation ratio of HCO^+ . Fractionation of HCO^+ is strongest for clumps with large columns of cold gas, where reaction (C2) can contribute strongly to the total H^{13}CO^+ abundance. Low mass and low density models have a *FR* equal to the *ER* or slightly higher. For a given density, the *FR* is largely independent of the model mass, which is consistent with the HCO^+ and H^{13}CO^+ density profiles shown in Fig. 18 which show an increase for large A_V and a roughly constant *FR* (see also Fig. 4). Hence, the *FR* of HCO^+ is only marginally affected if the clump mass is increased. The model results show a strong correlation of the column density ratio with χ .

3.4. Emission line ratios

Even though column densities are no direct observables, they have to be derived from measured line strengths resulting from the full radiative transfer, including effects of a variable temperature of exciting collision partners and optical depths. However, the derivation of intensities requires numerous additional as-

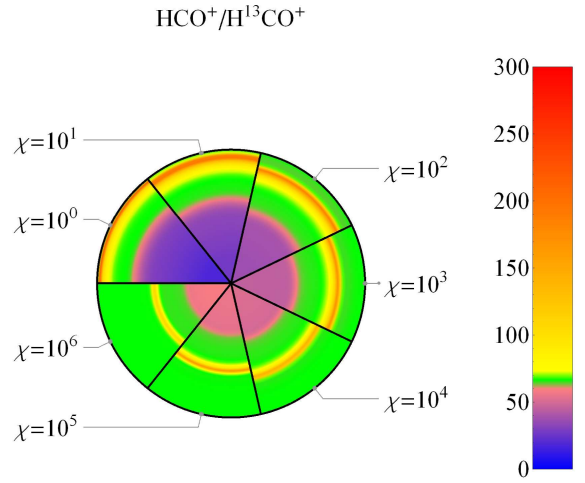


Fig. 19. Same as Fig. 6 for HCO^+ for $n = 10^5 \text{ cm}^{-3}$ and $M = 1 \text{ M}_\odot$.

sumptions, such as collision rates, details of the geometry, assumptions on chemical and radiative pumping, and so on. Consequently, from a modellers perspective intensities have larger uncertainties than column densities. Therefore we only compute intensities for a selected subset of commonly observed species and transitions. Here, we directly compare the isotopic ratio of clump averaged line intensities (for definition see Röllig et al. 2006) which can be compared directly to observations. We always assume unity beam filling factor. The large number of possible line combinations prohibits a complete presentation. We give just a few examples to demonstrate that line ratios between various isotopologues can differ from the corresponding column density ratios.

Fig. 21 shows the ratio of $T_{\text{mb}}([\text{CII}]) / T_{\text{mb}}([{}^{13}\text{CII}])$ with $T_{\text{mb}} = \int T_{\text{mb}} dv$ (For ${}^{13}\text{C}^+$ we summed over all hyperfine components.). While the column density ratio is larger than the *ER* for all model clumps the same is not true for the intensity ratio (*IR*). All models with $\chi > 100$ show a $\text{IR} < \text{ER}$ down to values of 38. Only models with very low χ and large densities have a $\text{IR} > \text{ER}$. For a given density and mass, the *IR* decreases with increasing χ , because of the larger optical thickness of C^+ relative to ${}^{13}\text{C}^+$. $[{}^{13}\text{CII}]$ observations of the Orion nebula by Stacey et al. (1991) show a very similar behavior and are consistent with our model predictions. They report line ratios between 36 and 122 with the highest optical depths $\tau = 3.3_{-0.8}^{+1.1}$ belonging to the lowest line ratio of 36 ± 9 and low optical depths where ratios are high. Boreiko & Betz (1996) derive an intensity ratio of 46 in M42, consistent with an intrinsic *ER* of 58_{-5}^{+6} and an optical depth of $[\text{CII}]$ of 1.3. For a given χ , the *IR* drops with decreasing density and increasing mass. Increasing the mass for a given χ and n will add cool, molecular mass. Provided that C^+ is fractionated this will increase the *FR* as long as the $[{}^{12}\text{CII}]$ line remains optically thin and decrease the *FR* once it becomes optically thick (compare Fig. 21).

In the previous section we showed, that the column density ratio of $\text{CO}/{}^{13}\text{CO}$ is close to the *ER* of the clump for most of the parameter space. CO emission lines suffer much more from optical thickness effects than most other species. This is also shown in Fig. 22 where we plot the ratio of the integrated intensities of $\text{CO}_{(1-0)}/{}^{13}\text{CO}_{(1-0)}$. For most of the models, this ratio is between 1 and 10, much smaller than the *ER*. Quite a few models

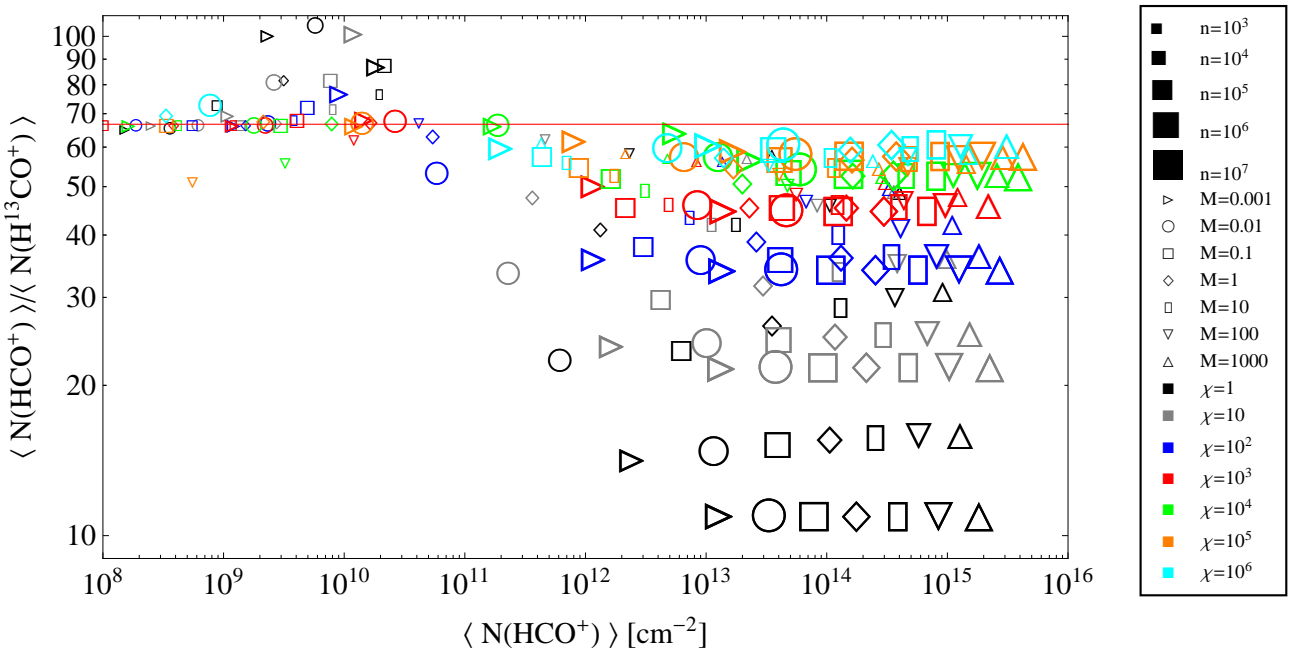


Fig. 20. Same as Fig. 9 for HCO^+ .

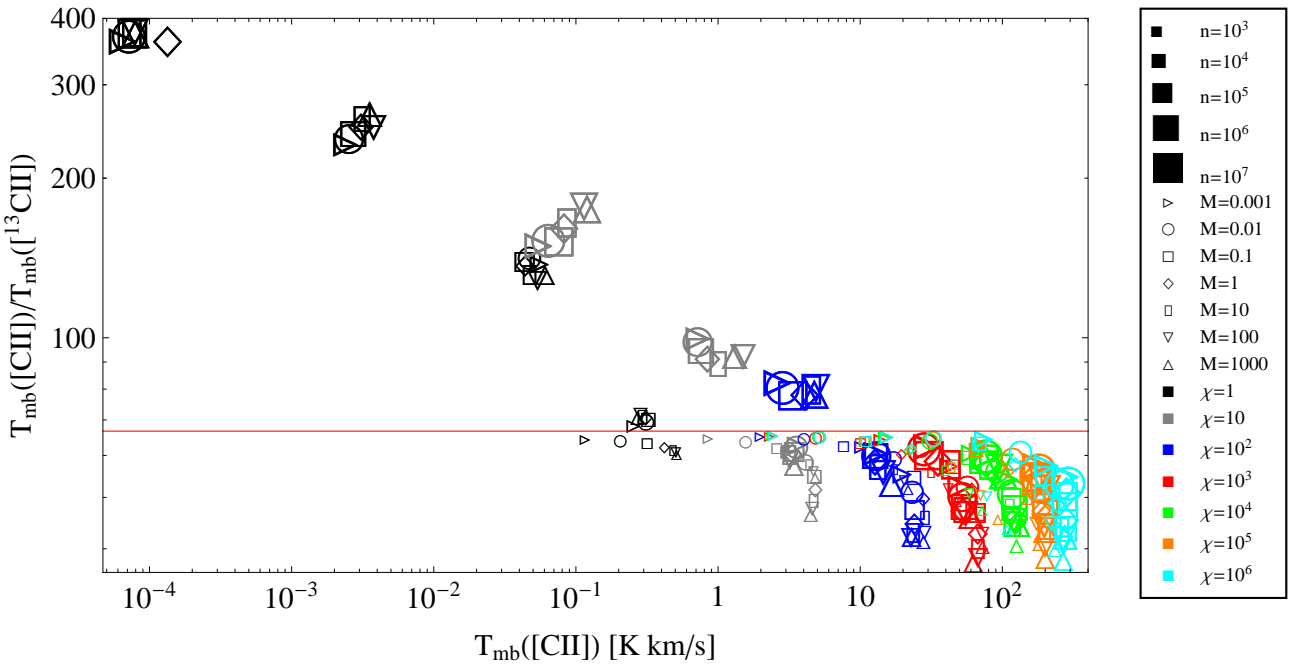


Fig. 21. Same as Fig. 9 for the intensity ratio $T_{mb}([CII]) / T_{mb}([^{13}CII])$ vs. $T_{mb}([CII])$.

have intensities of the rarer isotopologue comparable to those of the main species.

The low mass, high density models show an increasing IR with χ , opposite to the high mass, low density models. This is a result of the CO abundance structure of these model (see Fig. 11). The lowest IR is shown at the highest model mass model ($IR \leq 2$) while the highest IR belongs to models with the lowest mass. Both can be explained as optical depth effect. Models with $n \geq 10^7 \text{ cm}^{-3}$ have an increasing $T_{mb}(\text{CO}_{(1-0)})$ with χ and the IR increases for the lower mass models and de-

creases for the higher mass models. The latter results from high optical thicknesses while the former results from the emission of very hot, strongly excited CO gas in the primarily ionized fraction of the clump.

In Fig. 23 we plot the intensity ratio of CO lines $T_{mb}(\text{CO}(J \rightarrow J-1)) / T_{mb}({^{13}\text{CO}}(J \rightarrow J-1))$ as a function of J for models with $M = 10_\odot$ and line intensities $> 0.01 \text{ K km s}^{-1}$. For the lowest transition, the ratio lies between 1 and 10 and approaches ER for high values of J , when both lines become optically thin. The J where the ratio reaches the ER in-

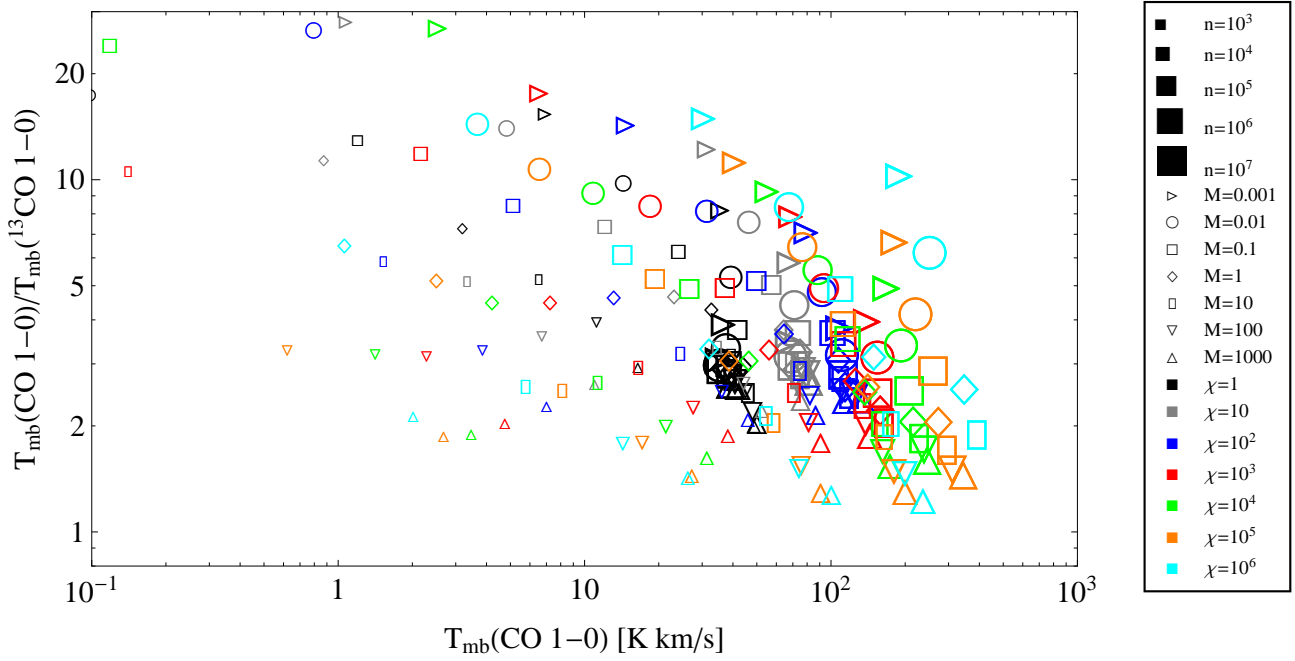


Fig. 22. Same as Fig. 21 for $T_{\text{mb}}(\text{CO}(1-0))/T_{\text{mb}}(^{13}\text{CO}(1-0))$ vs. $T_{\text{mb}}(\text{CO}(1-0))$.

creases with n and χ . For instance, models with $n = 10^7 \text{ cm}^{-3}$ and $\chi = 10^6$ have a ratio of close to unity, until $J > 10$ and reaches ER at $J \gtrsim 25$, while models with the same density and $\chi = 10^3$ reach ER already at $J = 15$. We find that either the CO lines are optically thick so that the IR is lowered below the ER or the ^{13}CO is too weak to be detectable. Only in dense clouds the ER is observable. The CO IR is therefore not a good diagnostics of carbon fractionation.

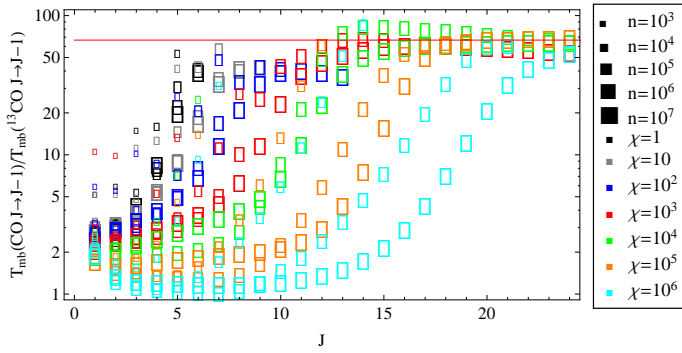


Fig. 23. Emission line ratio $T_{\text{mb}}(\text{CO}(J \rightarrow J-1))/T_{\text{mb}}(^{13}\text{CO}(J \rightarrow J-1))$ vs. J for all models with $M = 10 M_{\odot}$. Models with line intensities $< 0.01 \text{ K km s}^{-1}$ have been omitted.

3.5. Diagnostics

Finally, we studied several line ratios with respect to their diagnostic value for the local FR of CO and C^+ as well as to the local ER . We already concluded that CH and HCO^+ appear to be sensitive tracers of the FR . Lacking collision rate coefficients for CH we only calculated HCO^+ (and H^{13}CO^+) intensities for our model clouds.

We selected transitions that are observable from the ground or through SOFIA (Stratospheric Observatory For Infrared Astronomy) and show at most moderate optical depths of a few. Figure 24 demonstrates how the emission line ratio $T_{\text{mb}}([\text{CII}])/T_{\text{mb}}(\text{H}^{13}\text{CO}^+(1-0))$ traces the column density FR of C^+ , C and CO. The figure reproduces the general trend of the FR as discussed in the previous sections. We find a clear dependence of the emission line ratios on the column density FR of C and C^+ , but not of CO. However, it is only partially applicable to observational data. All ratios above ~ 30000 are practically not observable as they correspond to H^{13}CO^+ intensities below 10 mK km/s . If we exclude models with line intensities $< 0.01 \text{ K km s}^{-1}$ the column density ratios of CO and C^+ show much weaker variations so that the emission line ratio only traces the fractionation of atomic carbon in the observable intensity range. We have repeated this exercise for many other line ratios that are available through ground based and satellite observatories, and that are strong enough to be observable¹⁵. All three panels in Fig. 24 show a transition around an emission ratio of $10^2 - 10^3$. This ratio corresponds to models with the highest $T_{\text{mb}}(\text{H}^{13}\text{CO}^+(1-0)) \approx 1 - 2 \text{ K km s}^{-1}$ and $FR(\text{C})$ slightly below the ER . It requires $\chi = 10^4 - 10^5$ and densities of $n = 10^7$ to reach these high values. Towards lower intensities, the models split into two branches: very high density models with $n = 10^7 \text{ cm}^{-3}$ and decreasing $FR(\text{C})$, and models with $n = 10^6 \text{ cm}^{-3}$, $\chi \geq 100$ and increasing $FR(\text{C})$. This parameter regime corresponds to model clumps with the highest $[\text{CII}]$ emission, increasing with n and χ . Accordingly, the $[\text{CII}]/\text{H}^{13}\text{CO}^+$ intensity ratio can increase to very high values if the density and the FUV field are high enough, albeit with the visible transition.

¹⁵ Even though the PDR model takes optical thickness effects into account we tried, whenever possible, to find optically thin tracers in order to be as independent as possible from the local structure of the emitting source.

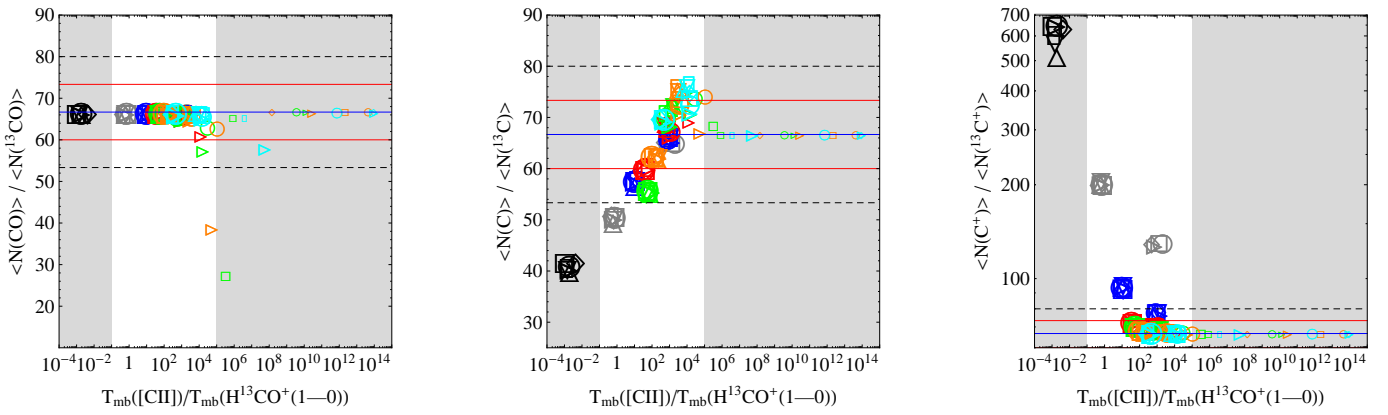


Fig. 24. Column density fractionation ratios plotted against the emission line ratio $T_{\text{mb}}([\text{CII}])/T_{\text{mb}}(\text{H}^{13}\text{CO}^+(1-0))$ for all models from our parameter space (blue: ER , red: $ER \pm 10\%$, dashed: $ER \pm 20\%$). The symbols follow the coding from Fig. 9. The gray areas denote the regime below a sensitivity limit of $T_{\text{mb}} < 0.01 \text{ K km s}^{-1}$. **Left panel:** $N(\text{CO})/N(^{13}\text{CO})$, **middle panel:** $N(\text{C})/N(^{13}\text{C})$, **right panel:** $N(\text{C}^+)/N(^{13}\text{C}^+)$.

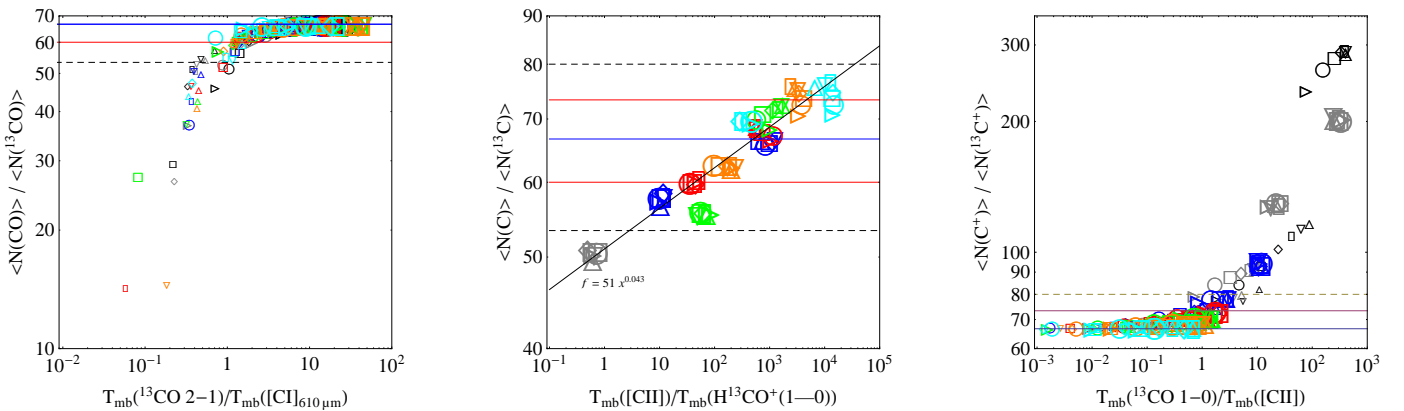


Fig. 25. Column density fractionation ratios plotted against emission line ratios for all models from our parameter space. (blue: ER , red: $ER \pm 10\%$, dashed: $ER \pm 20\%$). Models with line intensities $< 0.01 \text{ K km s}^{-1}$ have been omitted. The symbols follow the coding from Fig. 9. **Left panel:** $N(\text{CO})/N(^{13}\text{CO})$ vs. $T_{\text{mb}}(^{13}\text{CO}(2-1))/T_{\text{mb}}([\text{CI}]_{610\mu\text{m}})$, **middle panel:** $N(\text{C})/N(^{13}\text{C})$ vs. $T_{\text{mb}}([\text{CII}])/T_{\text{mb}}(\text{H}^{13}\text{CO}^+(1-0))$, **right panel:** $N(\text{C}^+)/N(^{13}\text{C}^+)$ vs. $T_{\text{mb}}(^{13}\text{CO}(1-0))/T_{\text{mb}}([\text{CII}])$.

Fig. 25 shows the result for the three ratios that seem to be suitable to trace the column density *FR* of C^+ , C , and CO individually. The left panel shows $T_{\text{mb}}(^{13}\text{CO}(2-1))/T_{\text{mb}}([\text{CI}]_{610\mu\text{m}})$ on the x-axis and the CO column density ratio on the y-axis. The level energy of ^{13}CO (2-1) is 16 K, while the [CI] line requires 24 K for excitation. Looking at the plot, we note, that any line ratio < 1 signals significantly fractionated CO column densities. Any emission line ratio higher than a few reflects a normal *FR* in the CO gas. All models with an emission line ratio smaller than ≈ 1 have $n \leq 10^4 \text{ cm}^{-3}$ and will consequently host a small ^{13}CO population but significant amounts of atomic carbon.

The middle panel plots the column density fractionation ratio of atomic carbon versus $T_{\text{mb}}([\text{CII}])/T_{\text{mb}}(\text{H}^{13}\text{CO}^+(1-0))$ (same as in Fig. 24, but excluding all model lines too weak to be detectable). The model results show a strong correlation between the *FR* and the emission line ratio. The black line in the plot corresponds to a least-squares-fit $f = 51x^{0.043}$ with the emission line ratio x . The [CII] emission is strongest for low to intermediate densities while HCO^+ is a typical density tracer. Both lines are typical PDR tracers, sensitive to significant FUV illumination. Consequently, a line ratio higher than 10^3 signals $\text{FR} > ER$. The corresponding points in the plot belong to models with $n \approx 10^6 \text{ cm}^{-3}$ and $\chi \geq 10^4$. The points with a $\text{FR} < ER$ correspond to models with even higher densities and somewhat lower χ .

The panel on the right side shows the C^+ column density ratio plotted against $T_{\text{mb}}(^{13}\text{CO}(1-0))/T_{\text{mb}}([\text{CII}])$. All models with a line ratio higher than 2 contain fractionated C^+ . We saw in Fig. 10 that the *FR*(C^+) is strongest for low UV models with high densities. These models have weak C^+ emission, usually smaller than a few K km s^{-1} , while these conditions favor ^{13}CO emission resulting in large line ratios.

4. Summary

We present an update of the isotope chemistry used in our PDR model code KOSMA- τ . An automated routine was created to allow for the inclusion of isotope reactions into the chemical database files that are used in numerical PDR computations. This is combined with a proper rescaling of the new isotope reactions. We computed a large parameter grid of spherical PDR model clumps and investigated the effect of the isotope chemistry, particularly that of the isotope exchange reaction (C 1), on the chemical structure of the model clumps as well as on their emission characteristics.

In the transition from ionized carbon to carbon monoxide the fractionation ratio of C^+ is always larger than the elemental ratio in the gas. Strong C^+ fractionation is possible in cool C^+ gas. However, this is only partly visible in the corresponding intensity ratios of the model clumps. Optical thickness and excitation

effects produce intensity ratios between 40 and 400, strongly dependent on the model parameters.

In the dense ($n \geq 10^3 \text{ cm}^{-3}$) gas, CO behaves differently and is never found with a fractionation ratio larger than the element ratio with the exception of a very limited A_V range under very special parameter conditions. In the diffuse gas Liszt (2007) found qualitatively different behavior for $n < 10^2 \text{ cm}^{-3}$ and $M > 10^3 \text{ M}_\odot$. It turns out that isotope-selective photo-dissociation, the major process able to produce a $FR > ER$, is always dominated by the chemistry in the denser PDR gas. This also affects the depth at which the transition from C^+ to CO occurs. The formation and destruction of ^{13}CO is much stronger controlled by reaction (C 1). A direct consequence is that in all models in our grid ^{13}CO is formed at smaller A_V than CO despite the weaker shielding capabilities of the rarer isotopologue.

The fractionation of other species can be understood in terms of their formation history. If their major formation channel originates from C^+ their FR is related to $FR(\text{C}^+)$. This is the case for many light hydrides, especially CH , CH_2^+ , and CH_3^+ . If the FR of the parental species is controlled by other reactions than (C 1) the behavior might change. Atomic carbon is a mixed case with a regime at lower A_V where formation occurs mainly via recombination of C^+ and a regime where it is chemically derived from CO and HCO^+ . Consequently, the $FR(\text{C})$ exhibits a mixture of both cases. At particular depths, CH^+ might be formed from C. If that is the case the relation of its FR to $FR(\text{C}^+)$ breaks down until formation via a C^+ route takes over again.

Our computations have shown that CH and HCO^+ may be very sensitive tracers for chemical fractionation in PDRs. CH amplifies the FR of C^+ and HCO^+ amplifies the FR from CO in the CT. Both are abundant in the region where chemical fractionation plays a big role and suffer less from optical depth effects than their chemical progenitors.

We demonstrated that fractionation of the local densities not necessarily transforms into a fractionated column density. C^+ is a prominent example. Fractionation of ionized carbon only takes part in cool C^+ gas which in most clouds only makes up a small fraction of the total gas column. Only low FUV models are able to produce larger columns of cool C^+ and will have a fractionated column density. CO behaves oppositely in that it requires warm CO in order to become fractionated. Again, this affects the column density only under certain conditions.

Finally, we provide diagnostics for the fractionation status of C^+ , C and CO through suitable emission line ratios. We showed that a line ratio of $T_{\text{mb}}(^{13}\text{CO}(2-1))/T_{\text{mb}}([\text{CI}]_{610\mu\text{m}}) < 1$ signals a significant fractionation of the CO column density. The line ratio of $T_{\text{mb}}([\text{CI}]_{610\mu\text{m}})/T_{\text{mb}}(\text{H}^{13}\text{CO}^+(1-0))$ has a power law dependence on the fractionation ratio of the column density of atomic carbon. The column density fractionation of ionized carbon is reflected in $T_{\text{mb}}(^{13}\text{CO}(1-0))/T_{\text{mb}}([\text{CII}]) > 2$.

Acknowledgements. We acknowledge the use of OSU (<http://www.physics.ohio-state.edu/~eric/research.html>), KIDA (Kinetic Database for Astrochemistry (<http://kida.obs.u-bordeaux1.fr>)), and UDFA (<http://www.udfa.net/>) chemical reaction data bases. This work was supported by the German *Deutsche Forschungsgemeinschaft*, DFG project number Os 177/1-1 as well as within the Collaborative Research Council 956, sub-project C1, funded by the DFG.

- Stellar Evolution and Nucleosynthesis, ed. T. G. Barnes, III & F. N. Bash, 25+
- Bakes, E. L. O. & Tielens, A. G. G. M. 1994, ApJ, 427, 822
- Boreiko, R. T. & Betz, A. L. 1996, ApJ, 467, L113+
- Casassus, S., Stahl, O., & Wilson, T. L. 2005, A&A, 441, 181
- Centurion, M., Cassola, C., & Vladilo, G. 1995, A&A, 302, 243
- Cubick, M., Stutzki, J., Ossenkopf, V., Kramer, C., & Röllig, M. 2008, A&A, 488, 623
- Draine, B. T. 1978, ApJS, 36, 595
- Gerin, M., de Luca, M., Goicoechea, J. R., et al. 2010, A&A, 521, L16
- Goicoechea, J. R., Pety, J., Gerin, M., et al. 2006, A&A, 456, 565
- Hollenbach, D. J. & Tielens, A. G. G. M. 1999, Reviews of Modern Physics, 71, 173
- Keene, J., Schilke, P., Kooi, J., et al. 1998, ApJ, 494, L107+
- Kramer, C., Cubick, M., Röllig, M., et al. 2008, A&A, 477, 547
- Kramer, C., Jakob, H., Mookerjea, B., et al. 2004, A&A, 424, 887
- Langer, W. D., Graedel, T. E., Frerking, M. A., & Armentrout, P. B. 1984, ApJ, 277, 581
- Langer, W. D. & Penzias, A. A. 1990, ApJ, 357, 477
- Langer, W. D. & Penzias, A. A. 1993, ApJ, 408, 539
- Le Bourlot, J., Le Petit, F., Pinto, C., Roueff, E., & Roy, F. 2012, A&A, 541, A76
- Le Bourlot, J., Pineau Des Forets, G., Roueff, E., & Flower, D. R. 1993, A&A, 267, 233
- Le Petit, F., Nehmé, C., Le Bourlot, J., & Roueff, E. 2006, ApJS, 164, 506
- Lee, H.-H., Herbst, E., Pineau des Forets, G., Roueff, E., & Le Bourlot, J. 1996, A&A, 311, 690
- Liszt, H. S. 2007, A&A, 476, 291
- Magnani, L., Lugo, S., & Dame, T. M. 2005, AJ, 130, 2725
- Magnani, L., Zelenik, S., Dame, T. M., & Engebreth, B. 2006, ApJ, 636, 267
- Mattila, K. 1986, A&A, 160, 157
- Mookerjea, B., Kramer, C., Röllig, M., & Masur, M. 2006, A&A, 456, 235
- Mookerjea, B., Ossenkopf, V., Ricken, O., et al. 2012, A&A, 542, L17
- Ossenkopf, V., Röllig, M., Neufeld, D., et al. 2012, A&A, this issue, Paper II
- Qin, S.-L., Schilke, P., Comito, C., et al. 2010, A&A, 521, L14
- Rachford, B. L., Snow, T. P., Tumlinson, J., et al. 2002, ApJ, 577, 221
- Ritchey, A. M., Federman, S. R., & Lambert, D. L. 2011, ApJ, 728, 36
- Röllig, M. 2011, A&A, 530, A9+
- Röllig, M., Abel, N. P., Bell, T., et al. 2007, A&A, 467, 187
- Röllig, M., Kramer, C., Rajbahak, C., et al. 2011, A&A, 525, A8+
- Röllig, M., Ossenkopf, V., Jeyakumar, S., Stutzki, J., & Sternberg, A. 2006, A&A, 451, 917
- Röllig, M., Szczepańska, R., Ossenkopf, V., & Glück, C. 2012, A&A, submitted
- Sheffer, Y., Rogers, M., Federman, S. R., et al. 2008, ApJ, 687, 1075
- Sheffer, Y., Rogers, M., Federman, S. R., Lambert, D. L., & Gredel, R. 2007, ApJ, 667, 1002
- Smith, D. & Adams, N. G. 1980, ApJ, 242, 424
- Sonnentrucker, P., Welty, D. E., Thorburn, J. A., & York, D. G. 2007, ApJS, 168, 58
- Stacey, G. J., Townes, C. H., Geis, N., et al. 1991, ApJ, 382, L37
- Sternberg, A. & Dalgarno, A. 1989, ApJ, 338, 197
- Sternberg, A. & Dalgarno, A. 1995, ApJS, 99, 565
- Störzer, H., Stutzki, J., & Sternberg, A. 1996, A&A, 310, 592
- Suutarinen, A., Geppert, W. D., Harju, J., et al. 2011, A&A, 531, A121
- van Dishoeck, E. F. & Black, J. H. 1988, ApJ, 334, 771
- van Dishoeck, E. F., Jonkheid, B., & van Hemert, M. C. 2006, Faraday Discussions, 133, 231
- van Hemert, M. C. & van Dishoeck, E. F. 2008, Chemical Physics, 343, 292
- Visser, R., van Dishoeck, E. F., & Black, J. H. 2009, A&A, 503, 323
- Wakelam, V. & Herbst, E. 2008, ApJ, 680, 371
- Wakelam, V., Herbst, E., Loison, J.-C., et al. 2012, ApJS, 199, 21
- Warin, S., Benayoun, J. J., & Viala, Y. P. 1996, A&A, 308, 535
- Watson, W. D., Anicich, V. G., & Huntress, Jr., W. T. 1976, ApJ, 205, L165
- Weingartner, J. C. & Draine, B. T. 2001, ApJ, 548, 296
- Woodall, J., Agúndez, M., Markwick-Kemper, A. J., & Millar, T. J. 2007, A&A, 466, 1197
- Woods, P. M. & Willacy, K. 2009, ApJ, 693, 1360
- Woon, D. E. & Herbst, E. 2009, ApJS, 185, 273
- Wouterloot, J. G. A. & Brand, J. 1996, A&AS, 119, 439

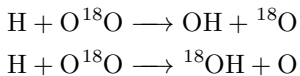
References

- Agúndez, M., Goicoechea, J. R., Cernicharo, J., Faure, A., & Roueff, E. 2010, ApJ, 713, 662
- Asplund, M., Grevesse, N., & Sauval, A. J. 2005, in Astronomical Society of the Pacific Conference Series, Vol. 336, Cosmic Abundances as Records of

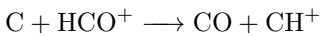
Appendix A: Isotopization rules

Usually, only the main isotopes are considered in astrochemical databases, despite the fact that many isotopologues have been detected in astronomical observations so far. We will describe here our efforts to include ^{13}C and ^{18}O isotopes into the chemical database. However, in this paper we will only discuss the scientific implications of carbon fractionation not going into the details of the ^{18}O chemistry.

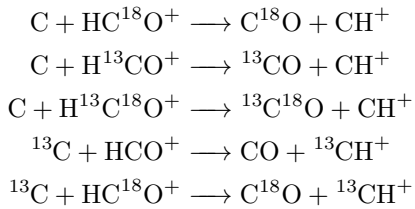
Usually, in a reaction formula like $\text{H} + \text{O}_2 \rightarrow \text{OH} + \text{O}$ it is not possible to identify which oxygen atom binds with hydrogen. Both atoms in O_2 are indistinguishable. This changes by including an isotope into a molecule. Now both atoms in O^{18}O are distinguishable and we get:



Unfortunately, this becomes more complicated if the isotope can be placed in more than one spot. The main isotope reaction

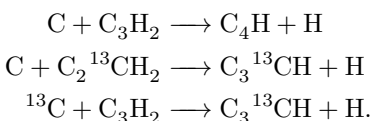


splits into 5 isotopic reactions



taking into account that the $\text{C}=\text{O}$ binding is preserved (again we omit the isotopic superscript when denoting the main isotope). For more complex species the above scheme becomes much more complicated. Furthermore, the number of additional reactions is so large that it becomes difficult to perform the isotopization by hand, especially if one plans to update the chemical network regularly and manual isotopization is quite error-prone. We developed a software routine to automatically implement isotopic reactions into a given reaction set¹⁶. The routine features are:

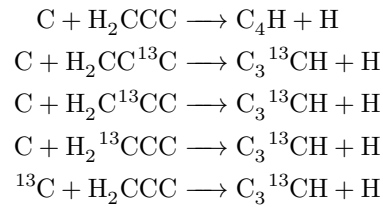
- inclusion of a single ^{13}C and a single ^{18}O isotope (multiple isotopizations are neglected in this study)
- UDfA often does not give structural information, for instance C_2H_3 does not distinguish between linear and circular configurations (l— C_2H_3 and c— C_2H_3). In such cases we consider all carbon atoms (denoted by C_n) as indistinguishable¹⁷, i.e.



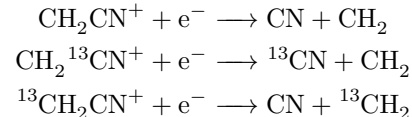
¹⁶ We realized the isotopization routine in Mathematica® by Wolfram Research.

¹⁷ Notation remark: isotopization of C_n leads to $\text{C}_{n-1} {}^{13}\text{C}$, e.g. $\text{C}_2 \rightarrow \text{C} {}^{13}\text{C}$. We always quote the full set of new reaction in the isotopic network derived from one UDfA reaction

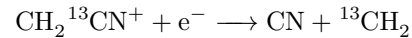
However, if structure information is provided we account for each possible isotopologue individually:



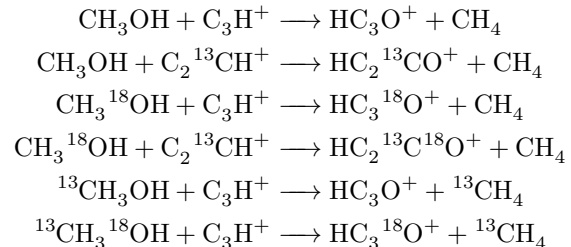
- molecular symmetries are preserved, i.e. $\text{NC} {}^{13}\text{CN} = \text{N} {}^{13}\text{CCN}$, but $\text{HC} {}^{18}\text{OOH} \neq \text{HCO} {}^{18}\text{OH}$
- functional groups like CH_n are preserved (see also Woods & Willacy 2009), e.g.:



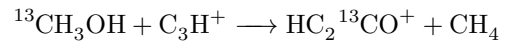
but not:



- when the above assumptions are in conflict to each other we assume *minimal scrambling*, i.e. we choose reactions such, that the fewest possible number of particles switch partners. For example:

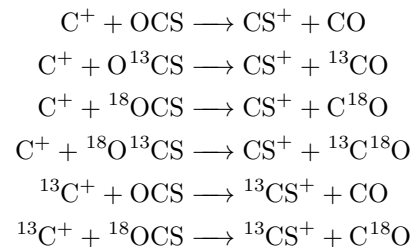


but not

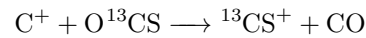


which would preserve the ${}^{13}\text{C}=\text{O}$ bond but would require 5 particles to switch partners.

- we favor proton/H transfer over transfer of heavier atoms
- we favor destruction of weaker bonds, e.g.:



but not:



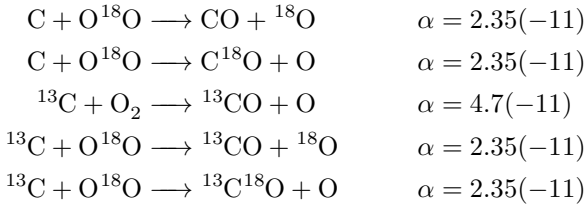
In the above example the binding enthalpies in $\text{O}=\text{C}=\text{S}$ are 745 kJ/mol for $\text{O}=\text{C}$ and 536 kJ/mol $\text{C}=\text{S}$. We only allow reactions, that break the weaker bond. In other words, we preserve $\text{O}=\text{C}$ bonds above others, since it is the strongest double bound. Please note that this is a strong assumption that can be sacrificed if more detailed knowledge on the reaction kinetics is at hand.

Appendix B: Rescaling of reaction rates

By introducing isotopologues into the chemistry we introduce many new reaction channels and we need to make sure that reaction rates are properly scaled. Unfortunately, not only the reaction rates for isotopologue reactions are unknown, we neither have information on branching ratios for reactions with several possible product channels. Thus, we assume equal probabilities for all branches, i.e. all isotopologue reactions possessing the same reactants but different products have their rate coefficient divided by the number of different product branches. For example:



with α being the fit coefficient from UDfA06 at $T = 300$ K and the number in parentheses indicates the decimal power. Introducing ^{13}C and ^{18}O into this reactions opens up additional channels:



Assuming equal probabilities for different reaction branches is a strong assumption and the reader should keep in mind, that many of the introduced reactions might have different reaction rate coefficients with potentially strong impact on the solution of the chemical network. The isotope exchange reactions discussed in the following are a notable exception from this.

Appendix C: Influence of chemical data sets

To illustrate how the choice of the chemical data set affects the outcome of our astrochemical calculations we calculate our reference model for three different chemical sets: UDfA06 (Woodall et al. 2007), OSU (version osu_01_2009), and KIDA (version kida.uva.2011, Wakelam et al. 2012). To allow a consistent computation it was necessary to slightly alter the original data sets:

- The formation of H_2 on grain surfaces is calculated separately in KOSMA- τ and we removed the reaction $\text{H} + \text{H} \longrightarrow \text{H}_2$ from OSU.
- The same holds for the photo-dissociation of H_2 , we removed the reaction $\text{H}_2 + h\nu \longrightarrow \text{H} + \text{H}$. KOSMA- τ explicitly calculates the H_2 formation rate from the population of the (vibrational) v -levels (all rotational levels of one vibrational state summed, ground state $v = 0 - 14$, Lyman band 24 level + Werner band 10 level)
- The unshielded CO photo-dissociation rate coefficient differs significantly among the three sets. We recomputed the unshielded photo-dissociation rate for a standard Draine FUV field using absorption cross sections available from <http://home.strw.leidenuniv.nl/~ewine/photo/> and can confirm the value of $2 \times 10^{-10} \text{ s}^{-1}$ (van Dishoeck et al. 2006) from UDfA06. We replaced the corresponding α values in OSU and KIDA. For a discussion on differing photo-reaction rates see e.g. van Hemert & van Dishoeck (2008) and Röllig et al. (2012).
- We replaced reactions with very large negative rate coefficients γ with a refitted expressions according to Röllig (2011).

- KIDA uses the Su-Chesnavich capture approach to compute rate coefficients for unmeasured reactions between ions and neutral species with a dipole moment (Woon & Herbst 2009). Their formalism is incompatible with KOSMA- τ and we replace the corresponding 1877 reaction rate coefficients with a new set of rate coefficients α , β , and γ , suitable for the Arrhenius-Kooij formula $\alpha(T/300\text{K})^\beta \exp(-\gamma T)$, which are fitted such that they approximate the original rates between 10 and 1000 K.
- For species where KOSMA- τ does not distinguish between linear and cyclic isomeric forms we consider all species only in terms of their molecular formula, e.g. C_3H instead of $l - \text{C}_3\text{H}$ and $c - \text{C}_3\text{H}$.

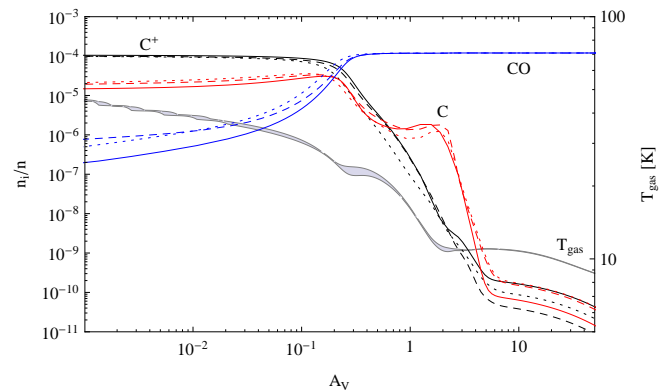


Fig. C.1. Chemical structure of a model clump with the following model parameters: $n_0 = 10^5 \text{ cm}^{-3}$, $M = 100 M_\odot$, $\chi = 10$. (UDfA06 (solid), OSU (dashed), KIDA (dotted)). The gray shaded area shows the gas temperature spanned by the three models calculations.

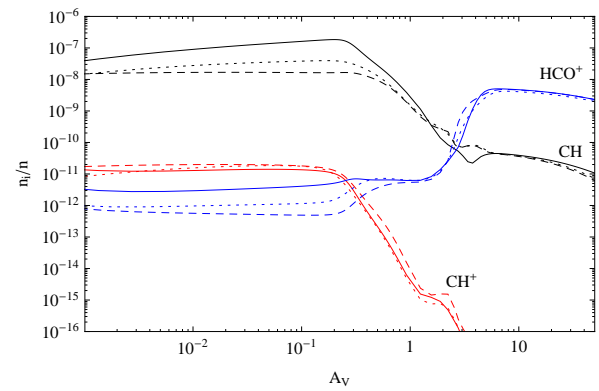


Fig. C.2. Same as Fig. C.1 for HCO^+ , CH , and CH^+ .

In Fig. C.1 we show the relative abundances of C^+ , C , and CO for model calculations with $n = 10^5 \text{ cm}^{-3}$, $M = 1000 M_\odot$, and $\chi = 10$ using different chemical data sets: UDfA06 (solid lines), OSU (dashed lines), KIDA (dotted lines) and the resulting range of gas temperatures. All three sets give the same chemical structure but with slight variations in the abundance profiles. The biggest difference is a higher CO abundance of OSU and KIDA at very low values of Av (factor 2-3 at $Av = 0.01$). This also leads to a carbon transition from C^+ to CO at slightly lower values of Av compared to UDfA. Overall, the chemical structure of the main carbon species is comparable, particularly the effect

on the total column density is small. The similar chemical structure and the almost identical gas temperatures around the carbon transition will result in a consistent fractionation behavior of the three species across all three chemical sets.

Fig. C.2 shows how the different chemical sets influence the chemistry of HCO^+ , CH , and CH^+ . The differences are larger than those in Fig. C.1. UDFa06 produces a significantly higher CH abundance in the outer layer of the cloud, at some positions by a factor of 10 higher than OSU. However, we discussed earlier that fractionation of CH is the result of C^+ fractionation. We do not expect any significant deviations in the fractionation ratio (FR) of C^+ for the three chemical sets, hence the effect on the $FR(\text{CH})$ should be weak. The same should be the case for CH^+ which shows even smaller differences for the three chemical sets. HCO^+ shows the same abundance in the cloud center, but some significant differences for $A_V < 1$. This could lead to different fractionation behavior at these parts of the cloud when using different chemical sets. It is unlikely that this leads to observable effects because of the 100 times lower HCO^+ abundance with respect to the center of the cloud and the respective weak influence on the total column density.

Appendix D: Spherical model context

D.1. Cloud radius

The model primarily computes radius dependent quantities. For a given density law, i.e., values α and $f_c = R_{\text{core}}/R_{\text{tot}}$, the total cloud radius R_{tot} (in cm) can be calculated from n_0 (in cm^{-3}) and M (in M_\odot) using

$$R_{\text{tot}} = 6.57 \times 10^{18} \sqrt[3]{-\frac{(\alpha - 3)M f_c^\alpha}{n_0 (3f_c^\alpha - \alpha f_c^3)}} \text{ cm} \quad (\text{D.1})$$

For $\alpha = 3/2$ and $f_c = 0.2$ this reduces to $R_{\text{tot}} = 5.3 \times 10^{18} \sqrt[3]{M/n} \text{ cm}$.

D.2. Column density

The general expression for the maximum (radial) column density¹⁸ is

$$N_{\text{max}} = \frac{n R_{\text{tot}} (\alpha f_c^{1-\alpha} - 1)}{\alpha - 1} \text{ cm}^{-2} \quad (\text{D.2})$$

that is $N_{\text{max}} = 4.7 n R \text{ cm}^{-2}$ for $\alpha = 3/2$ and $f_c = 0.2$.

However, they are not observables. Observations always yield an projected, beam-convolved figure. We describe them in terms of measurable column densities.

In the framework of spherical model clouds, column densities differ depending on where we look at. To get a position-independent measure for the column density of a given species i , we calculate the average column density for the whole clump

$$\langle N_i \rangle = \frac{4\pi}{\pi R^2} \int_0^R n_i(r) r^2 dr \quad (\text{D.3})$$

When referring to model column densities we always mean a clump averaged column density according to Eq. D.3. This definition assumes that observations always cover whole clumps. This is equivalent to the traditional description of beam-filling factors for the observation of spatially unresolved clumps, i.e. we

¹⁸ N_{max} is the total gas column density from the cloud surface to the center along the cloud radius.

assume that we have (typically many) unresolved clumps within the telescope beam. In that sense, the fractionation of the column density is always the result of a convolution of the fractionation structure with the absolute abundance profile.

D.3. CH column densities

Modelling the formation of the light hydrides, such as CH^+ and CH , still poses a challenge to chemical models. In Fig. C.3 we plot the mean CH column density versus the total mean column density of the respective clump. The coloured dots are observations from absorption and emission line measurements. The red and black lines are simple parametrized models to describe the column density (Mattila 1986; Qin et al. 2010). We note, that the column density splits into two distinct regimes with significantly different behavior. Diffuse clouds with total column densities below 10^{21} cm^{-2} show a steeper slope than denser clouds, where the CH column density appears to approach a limit of about 10^{15} cm^{-2} . This behavior is approximately reproduced by the model calculations. The column densities in our model are consistent with values for TMC-1 given by Suutarinen et al. (2011) as well as with diffuse cloud observations presented by Gerin et al. (2010) which give $N(\text{CH}) \approx 1 - 26 \times 10^{13} \text{ cm}^{-2}$ for total H_2 columns between $10^{21} - 10^{22} \text{ cm}^{-2}$.

Sheffer et al. (2008) present column densities along 42 diffuse molecular Galactic sight lines. They find total columns between 10^{12} and 10^{14} cm^{-2} and a very strong correlation between column densities of CH and H_2 . Mattila (1986) confirms this trend for dark clouds. Magnani et al. (2005) derived CH column densities from 3335 MHz observations in the Galactic plane and used the linear relation given by Mattila (1986) to derive corresponding H_2 column densities. They find $10^{13} \leq N(\text{CH}) < 10^{15} \text{ cm}^{-2}$.

Magnani et al. (2006) observed the $\text{CH}^2 \Pi_{1/2}, J = 1/2, F = 1 - 1$ transition toward the Galactic center. They find $N(\text{CH}) \approx 3 - 7 \times 10^{15} \text{ cm}^{-2}$. In addition to determining $N(\text{H}_2)$ from its linear correlation to $N(\text{CH})$ they also used a factor 1.8×10^{20} to derive $N(\text{H}_2)$ from integrated CO(1-0) line emission.

Qin et al. (2010) presented recent *Herschel/HIFI* observations against Sgr B2(M) which revealed that the linear relationship between CH and H_2 flattens at higher visual extinctions. They give a log-log slope of 0.38 ± 0.07 for $N(\text{H}_2) \geq 10^{21} \text{ cm}^{-2}$. In Fig. C.3 we show our model results for $N(\text{CH})$ versus $N(\text{H}_2)$ together with the observational data (Rachford et al. 2002; Magnani et al. 2005, 2006; Sheffer et al. 2008; Qin et al. 2010; Gerin et al. 2010; Suutarinen et al. 2011).

We cannot reproduce the large column densities derived by Magnani et al. (2006). Their data is derived from emission line measurements, while all other studies used absorption lines, and consequently suffers from higher uncertainties due to its dependence on the assumed excitation temperature. To our knowledge ^{13}CH has not yet been detected. The lack of ^{13}CH observations makes it difficult to assess the model results. The total CH column densities that we find in our model results stay below 10^{15} cm^{-2} . Nevertheless, the general behavior is well reproduced.

Appendix E: Fractionation plots of selected species

Here we show fractionation plots of selected species over a large portion of our model parameter space. We left out models with $M = 10^3 \text{ M}_\odot$ because they show very simi-

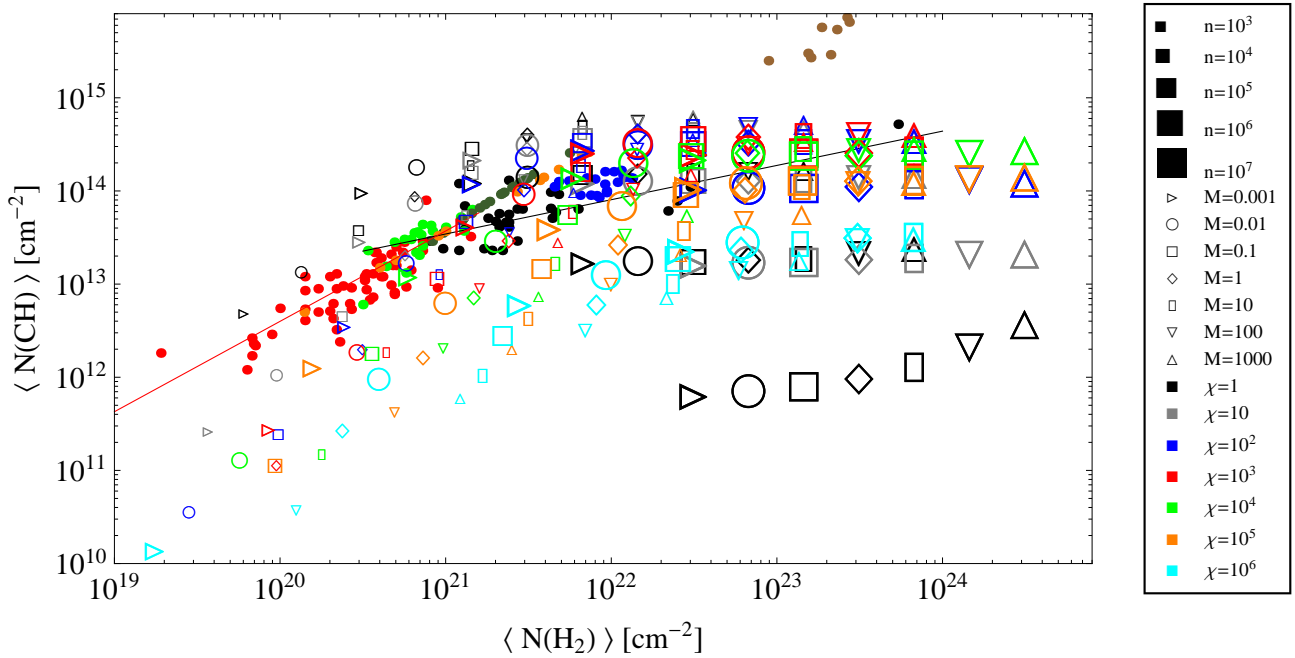


Fig. C.3. Mean CH column density versus H₂ column density (color/shape coding same as Fig. 9). Observational results are plotted as colored points (red: Sheffer et al. (2008); green: Rachford et al. (2002); olive: Magnani et al. (2005); black: Qin et al. (2010); brown: Magnani et al. (2006); orange Gerin et al. (2010); blue Suutarinen et al. (2011)). The two lines are the CH-H₂ relations from Mattila (1986) (red) and Qin et al. (2010) (black).

lar results as models with $M = 10^2 M_\odot$. The fractionation plots are also available for download: <http://www.astro.uni-koeln.de/kosma-tau>.

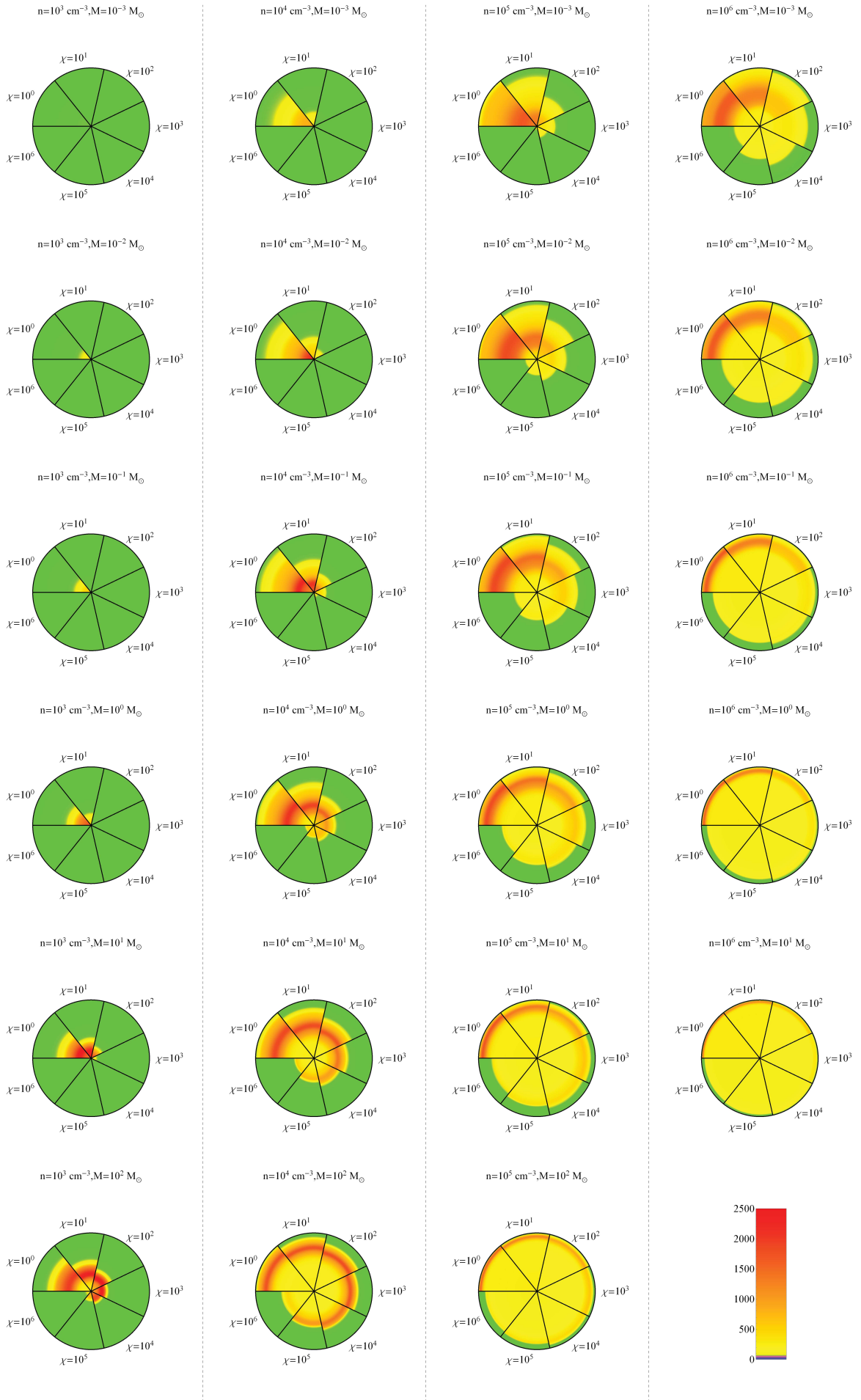


Fig.E.1. C^+ fractionation structure as function of relative clump radius r/R_{tot} for different values of n and M . Each sector corresponds to a different χ value. The FR is color coded, ratios within $\pm 10\%$ of the ER are shown in green. Blue and violet denotes $FR < ER$, yellow and red denotes $FR > ER$.

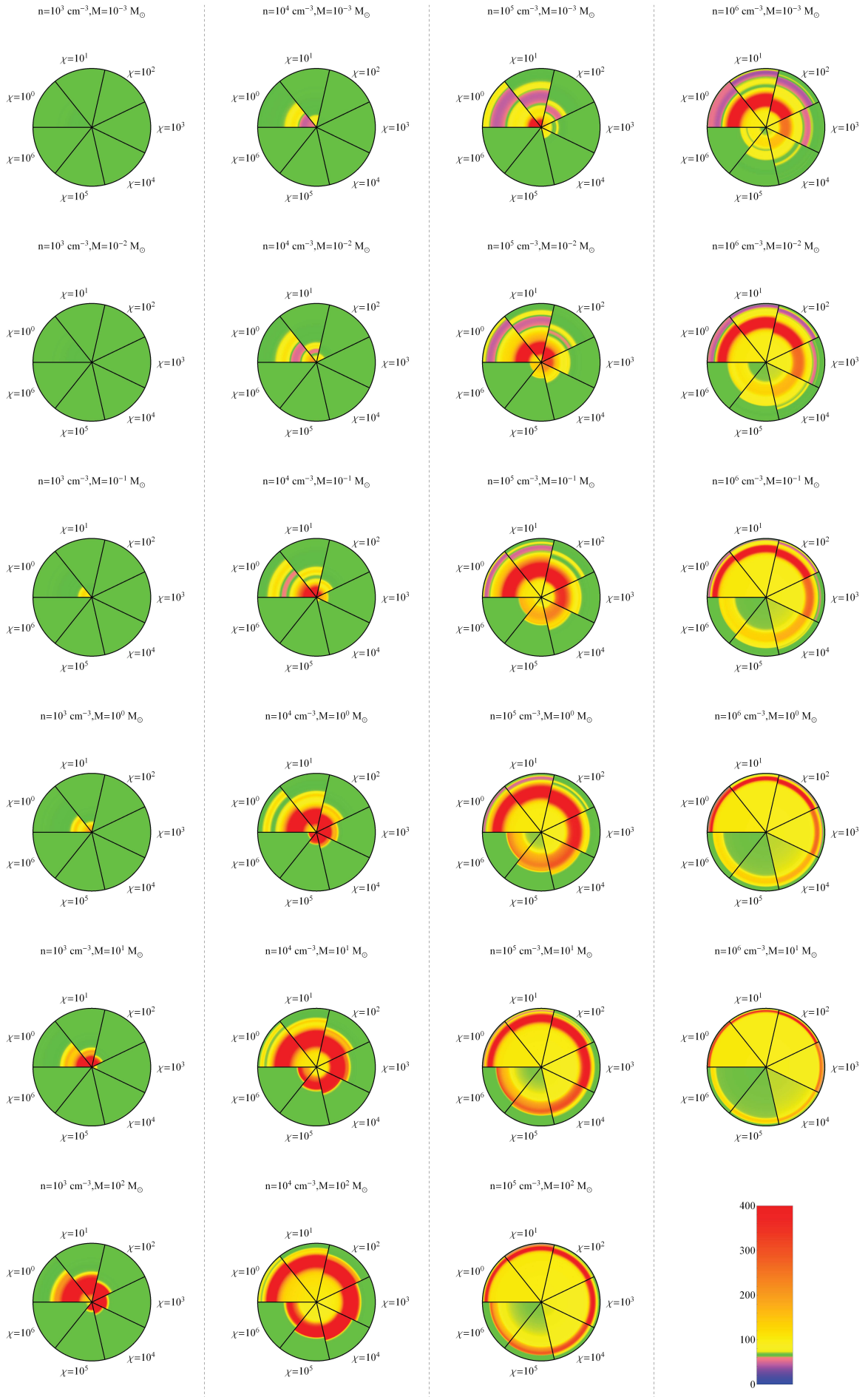


Fig.E.2. Same as Fig.E.1 for C.

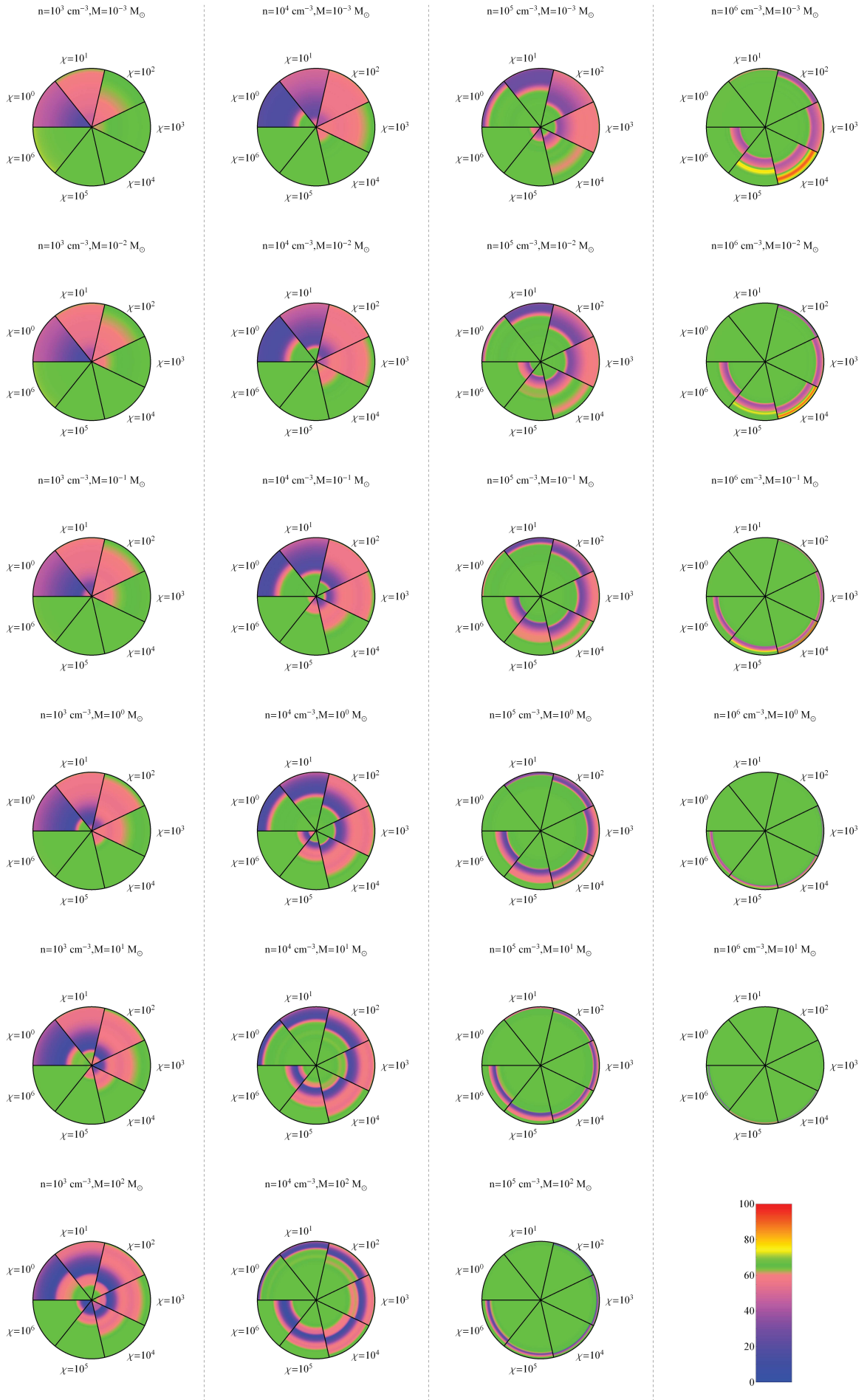


Fig.E.3. Same as Fig.E.1 for CO.

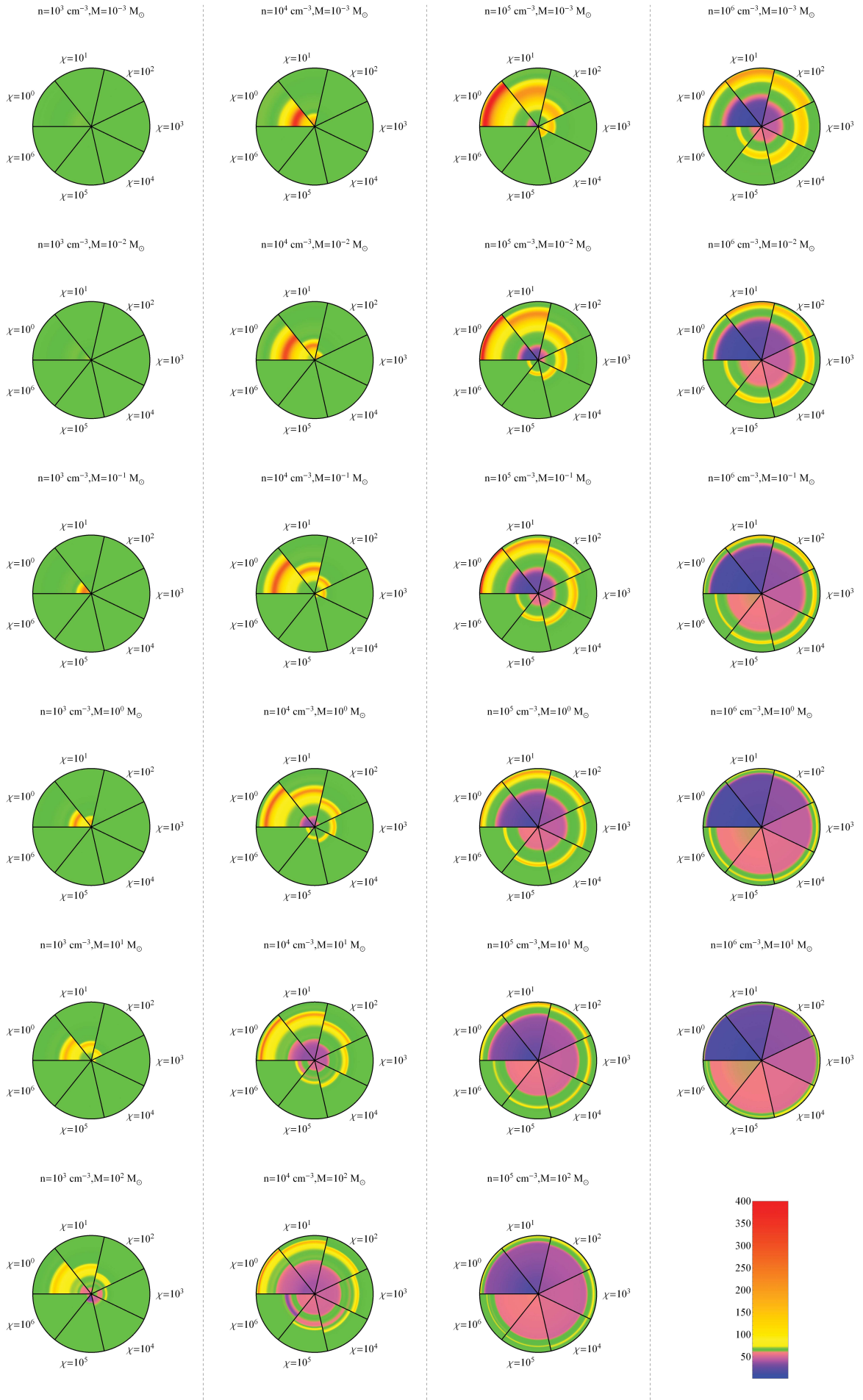


Fig.E.4. Same as Fig.E.1 for HCO^+ .

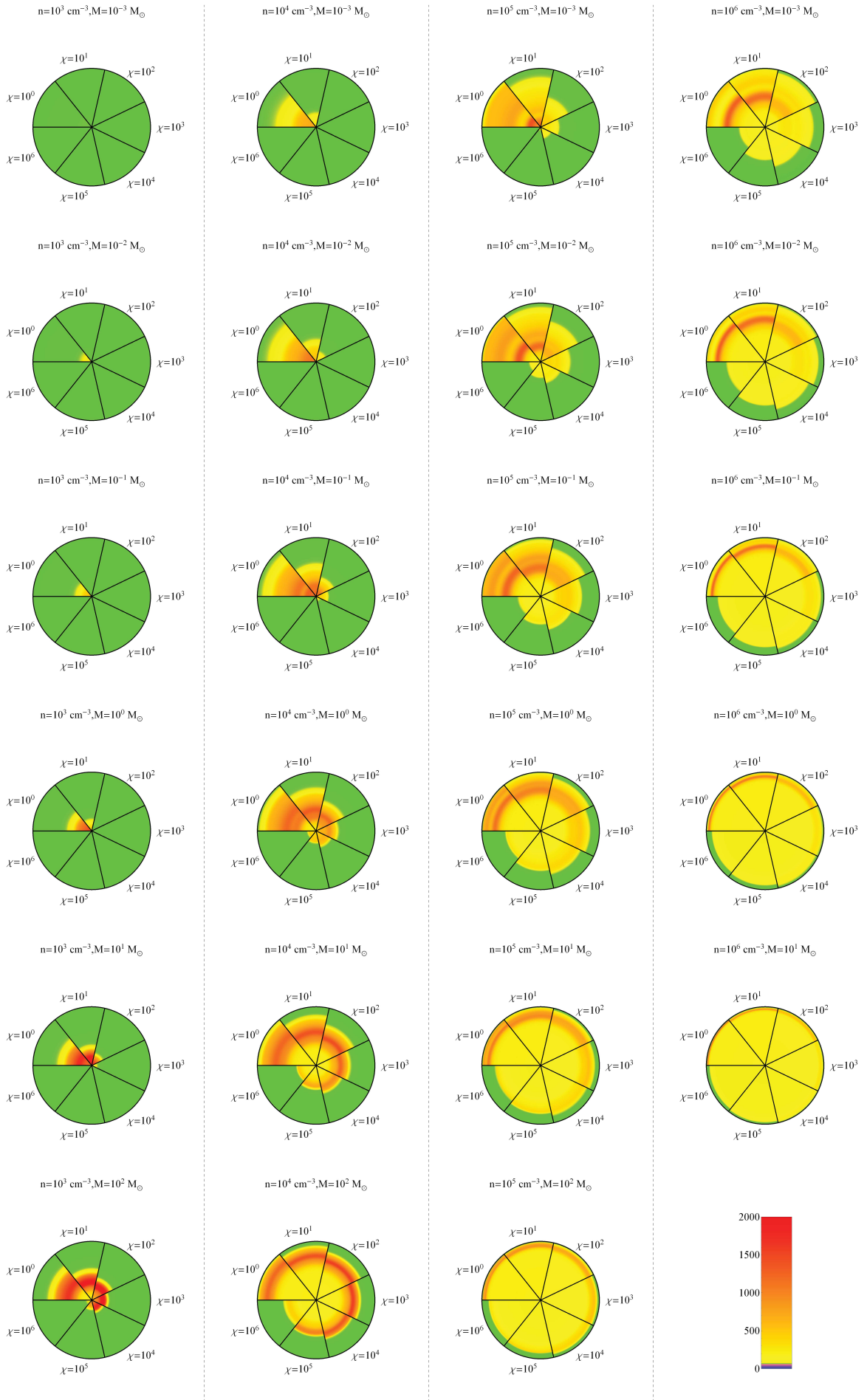


Fig.E.5. Same as Fig.E.1 for CH.

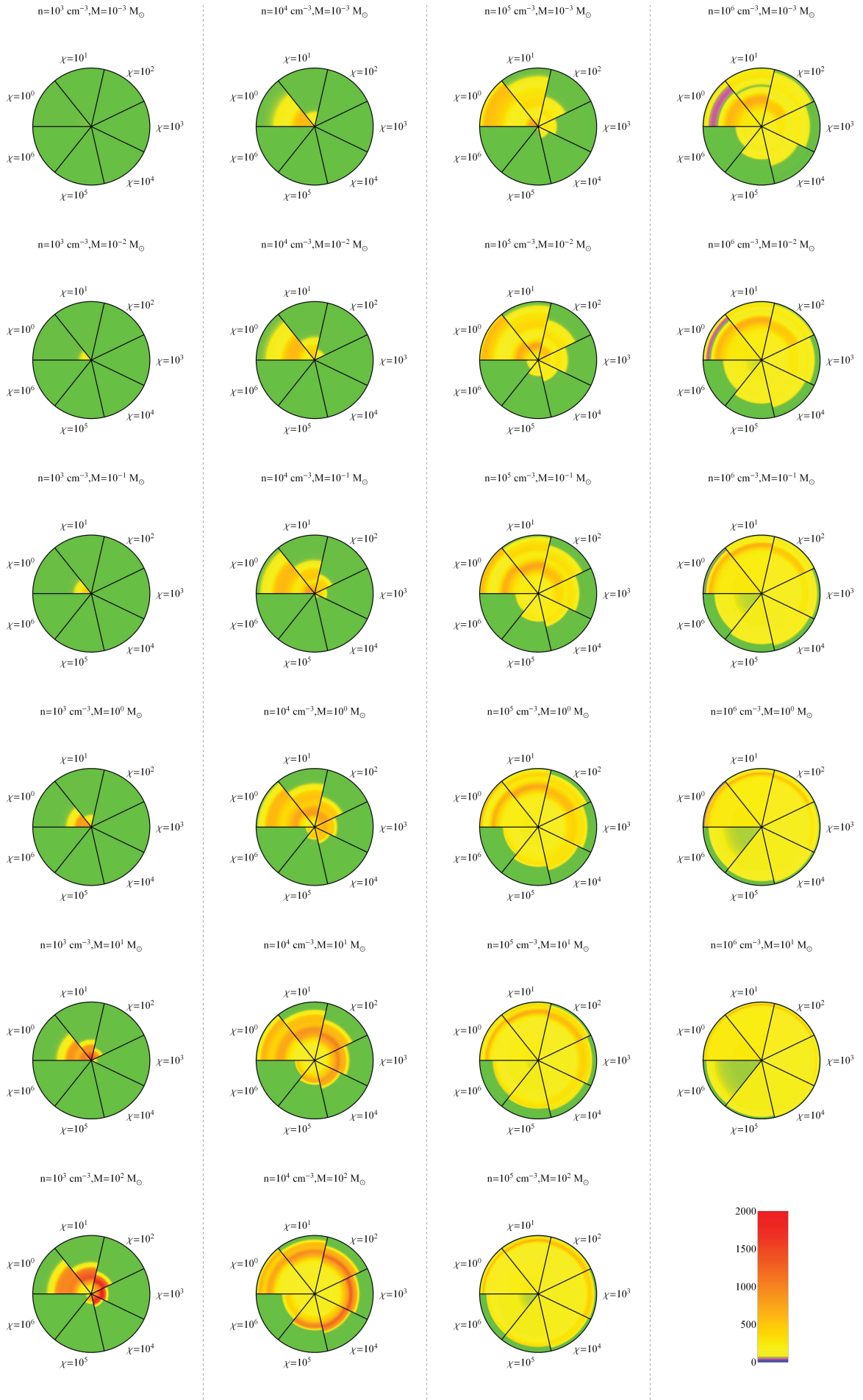


Fig.E.6. Same as Fig.E.1 for CH^+ .

Herschel/HIFI observations of [C II] and [^{13}C II] in PDRs*

V. Ossenkopf¹, M. Röllig¹, D.A. Neufeld², P. Pilleri^{3,4}, D.C. Lis⁵, A. Fuente³, F.F.S. van der Tak^{6,7}, E. Bergin⁸

¹ I. Physikalisches Institut, Universität zu Köln, Zülpicher Str. 77, D-50937 Köln, Germany
 e-mail: ossk@ph1.uni-koeln.de

² Department of Physics and Astronomy, Johns Hopkins University, 3400 North Charles Street, Baltimore, MD 21218, USA

³ Observatorio Astronómico Nacional, Apdo. 112, E-28803 Alcalá de Henares (Madrid), Spain

⁴ Centro de Astrobiología (INTA-CSIC), Ctra. M-108, km. 4, E-28850 Torrejón de Ardoz, Spain

⁵ California Institute of Technology, Cahill Center for Astronomy and Astrophysics 301-17, Pasadena, CA 91125 USA

⁶ SRON Netherlands Institute for Space Research, Landleven 12, 9747 AD Groningen, The Netherlands

⁷ Kapteyn Astronomical Institute, University of Groningen, PO box 800, 9700 AV Groningen, The Netherlands

⁸ University of Michigan, Ann Arbor, MI 48197 USA

Preprint online version: November 14, 2012

ABSTRACT

Context. Chemical fractionation in the interstellar medium can create isotopologue abundance ratios that differ by many orders of magnitude from the normal isotopic abundance ratios. By understanding how these differences are reflected in astronomical observations under various conditions, we try to obtain a new tool to sensitively probe these conditions.

Aims. Recently, we introduced detailed isotopic chemistry into the KOSMA- τ model for photon-dominated regions (PDRs) to give theoretical predictions for the abundance of the carbon isotopologues as a function of PDR parameters. Combined with radiative transfer computations for specific geometries, we estimated the possible intensity ratio of the [C II]/[^{13}C II] lines. Here, we compare these predictions with new Herschel observations.

Methods. We performed Herschel/HIFI observations of the [C II] 158 μm line in a number of PDRs. In all sources we observed at least two hyperfine components of the [^{13}C II] transition allowing to determine the [C II]/[^{13}C II] intensity ratio, after some revision of the intrinsic hyperfine ratios. Comparing the intensity ratios with the results from the updated KOSMA- τ model, we identify cases dominated by chemical fractionation and cases dominated by the optical depth of the main isotopic line.

Results. An observable enhancement of the [C II]/[^{13}C II] intensity ratio due to chemical fractionation depends mostly on geometry and velocity structure, and less on the gas density and radiation field. It is expected to be at maximum for PDR layers that are somewhat shielded from UV radiation, but not hidden by surface layers of optically thick [C II]. In our observations the [C II]/[^{13}C II] ratio for the integrated line intensity was always dominated by the optical depth of the main isotopic line. However, an enhanced intensity ratio is found for particular velocity components in a few sources: the red-shifted material in the ultracompact H II region Mon R2, the wings of the turbulent profile in the Orion Bar, and possibly a blue wing in NGC 7023. The mapping of the [^{13}C II] lines in the Orion Bar allows to derive a C $^+$ column density map confirming the temperature stratification of the C $^+$ layer, in agreement with the chemical stratification of the Bar.

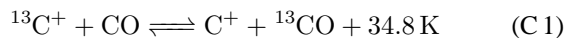
Conclusions. Carbon fractionation can be significant, even in relatively warm PDRs, but a resulting enhanced [C II]/[^{13}C II] intensity ratio is only observable for special configurations. In most cases, a reduced [C II]/[^{13}C II] intensity ratio can be used instead to derive the [C II] optical depth to achieve reliable column density estimates that can be compared with PDR models. The C $^+$ column densities for all sources show that at the position of the [C II] peak emission, a dominant fraction of the gas-phase carbon is in the form of C $^+$.

Key words. ISM: abundances – ISM: structure – ISM: clouds

1. Introduction

The isotopic abundance ratios of elements such as C, N and O in the interstellar medium reflect the star formation history of the environment, and observations of molecular isotopic line ratios at (sub)mm wavelengths are a common way to measure this effect (e.g. Wilson 1999).

Isotopic fractionation of carbon in the interstellar medium, i.e. the $^{12}\text{C}/^{13}\text{C}$ ratio in various species, is driven mainly through the fractionation reaction



providing a significant energy excess for binding the ^{13}C to the oxygen (Langer et al. 1984). Thus chemical fractionation of car-

bon is important even for relatively warm gas, as long as there is a significant fraction of ionized carbon available¹. The reaction (C1) favors formation of ^{13}CO and depletion of $^{13}\text{C}^+$ at low temperatures, shifting the fractional abundances of the two species relative to the normal solar isotopic ratio, but competes with isotope-selective dissociation governed by a different shielding through dust, H $_2$ and other CO isotopologues (Visser et al. 2009).

A systematic discussion of the observational results on carbon fractionation was provided by Keene et al. (1998) for dense molecular clouds and Liszt (2007) with emphasis on more diffuse clouds. Through observations of [^{13}C I] and $^{13}\text{C}^{18}\text{O}$ in the Orion Bar Keene et al. (1998) found little evidence for chemical fractionation, but noticed a contradiction between the chemical

* Herschel is an ESA space observatory with science instruments provided by European-led Principal Investigator consortia and with important participation from NASA.

¹ All other fractionation reactions for ^{13}C have lower excess energies, therefore being relevant only in cold gas.

models predicting a slight relative enhancement of ^{13}C , but a reduction of $^{13}\text{C}^{18}\text{O}$ while the observations showed the opposite behavior. In contrast to the CO results, Sakai et al. (2010) found clear evidence for fractionation in C_2H under the dark cloud conditions of TMC 1. In line with previous results (Sonnenrecker et al. 2007; Sheffer et al. 2007; Burgh et al. 2007) Liszt (2007) summarized the clear indications for fractionation of CO in translucent and diffuse clouds. They confirmed that the fractionation reaction (C 1) dominates the carbon chemistry for densities $n_{\text{H}_2} \geq 100 \text{ cm}^{-3}$ and provided new reaction rates for low temperatures, but also showed the importance of the CO destruction in reactions with He^+ for lower densities.

In paper I (Röllig & Ossenkopf 2012), we present results from the update of the KOSMA- τ model for photon-dominated regions (PDRs) to the full isotopic chemistry, providing isotopologue ratios for various species. Comparing the fractionation ratio of the $^{12}\text{C}^+/\text{C}^+$ abundances with the elemental isotopic ratio, we note that

- the fractionation ratio is always higher than or equal to the elemental ratio, i.e. $^{13}\text{C}^+$ is always underabundant with respect to C^+ .
- the fractionation ratio equals the elemental ratio at low A_V , but increases significantly towards larger A_V .

These are direct consequences of reaction (C 1). No other important reaction or isotope-selective photodestruction acts in the opposite direction. At low A_V , temperatures are usually high enough so that the excess energy plays no role, but once the temperature drops below 50 K the back reaction becomes less probable and the fractionation ratio increases rapidly. It stays at high values as long as enough $^{13}\text{C}^+$ ions are available to feed the reaction. Deep into the cloud interiors, these ions are formed through the dissociative reaction $\text{He}^+ + ^{13}\text{CO}$. The fractionation ratio is then controlled by cosmic ray ionization providing a roughly constant $^{12}\text{C}^+/\text{C}^+$ enhancement.

However, two competing processes change the $[\text{C II}]/[^{13}\text{C II}]$ ratio in PDRs: chemical fractionation raises the $[\text{C II}]/[^{13}\text{C II}]$ intensity ratio relative to the elemental abundance ratio, while the optical depth of the main isotopic line lowers its intensity relative to the $[^{13}\text{C II}]$ transitions.

$[^{13}\text{C II}]$ was first resolved by early heterodyne observations at the Kuiper Airborne Observatory (KAO, e.g. Boreiko et al. 1988; Boreiko & Betz 1996) showing no increase of the corresponding $[\text{C II}]/[^{13}\text{C II}]$ intensity ratio, but a reduction relative to the isotopic elemental ratio corresponding to a significant optical depth of the main isotopic line reducing the intensity ratio. With the low spatial and velocity resolution of these observations, it was, however, impossible to determine whether this average reduction represents all density or velocity components in the beam or whether individual components are dominated by either of the two competing processes. Only from additional observations with high velocity resolution preferentially covering varying conditions it is therefore possible to separate the impact of the two processes in PDRs.

The HIFI instrument (de Graauw et al. 2010) on-board the Herschel satellite (Pilbratt et al. 2010) allowed for the first time to systematically observe $[^{13}\text{C II}]$ with a good sensitivity and high spatial resolution in a number of objects. This allows to study the $^{12}\text{C}/^{13}\text{C}$ ratio in different environments by comparing the observations with the theoretical predictions. We detected $[^{13}\text{C II}]$ in four bright PDRs, allowing to look for the signature of chemical carbon fractionation in the warm PDR gas or to determine the optical depth and column density of C^+ .

In Sect. 2 we elaborate on the detailed theoretical predictions for $^{12}\text{C}^+/^{13}\text{C}^+$ and the resulting intensity ratio $[\text{C II}]/[^{13}\text{C II}]$ under varying physical conditions in the frame of the KOSMA- τ PDR model. In Sect. 3 we present the HIFI observations of $[\text{C II}]$ and $[^{13}\text{C II}]$. Section 4 discusses the observational results for the Orion Bar, Mon R2, NGC 3603, Carina, and NGC 7023 and Sect. 5 concludes with a summary of the matches and discrepancies.

2. Model predictions for the $[\text{C II}]/[^{13}\text{C II}]$ ratio

The development of theoretical models for PDRs is an active field of research because of the complex interplay of geometrical constraints, properties of the UV field, and chemical and physical processes in the gas (Röllig et al. 2007). Because of this complexity, all models with an elaborated description of the PDR chemistry are currently restricted to one-dimensional geometries, therefore describing PDRs either as plane-parallel slabs or as (ensemble of) spheres. However, real sources like the prototypical PDR of the Orion Bar, show more complex geometries, containing elements of both descriptions, e.g. a large-scale plane-parallel configuration superimposed on a clumpy small-scale structure, better described by an ensemble of spherical cores (see e.g. Hogerheijde et al. 1995).

We consider both limiting cases in the frame of the KOSMA- τ PDR model, a code designed to simulate spherical clumps, where we can approximate a plane-parallel PDR by considering very massive clumps ($M \geq 100M_\odot$) that form an almost plane-parallel structure in their outer layers. This approach allows us to use the new implementation of the fractionation network in the KOSMA- τ PDR model code and to easily compare the results with other PDR models (see Röllig et al. 2007) that lack isotope networks so far.

2.1. Model setup

The KOSMA- τ PDR model assumes a spherical cloud geometry exposed to isotropic UV illumination, measured in units of the interstellar radiation field, χ_0 (Draine 1978). Model parameters are the hydrogen density at the surface, n_{surf} , UV field, χ , and cloud mass, M . The density structure assumes a power law increase, $n_H(r) = n_{\text{surf}}(r/R_0)^{-1.5}$, from the surface to 1/5 of the outer radius, R_0 , and a constant density further in. For the results presented here, we keep the metallicity at solar values and assume a standard elemental isotopic ratio of $^{12}\text{C}/^{13}\text{C}$ of 67 (Wakelam & Herbst 2008). The actual elemental isotopic ratio is subject to systematic variations with galactocentric radius (Wilson 1999) but all the sources discussed in Sect. 3.2 have approximately solar galactocentric radii. However, even within the solar neighborhood there exist noticeable variations with values between 57 and 78 where the value of 67 matches the ratio observed in Orion (Langer & Penzias 1990, 1993). We therefore assume an error bar of up to 15 % for the elemental abundance ratio.

The PDR model iteratively computes the steady-state chemistry, the local cooling and heating processes, and the radiative transfer to predict the density of the different species and the intensity of the line and continuum radiation emitted by them.

The restriction of the code to an isotropic illumination is not a fundamental limitation when comparing different geometries. The penetration of an isotropic radiation field can be computed from the penetration of a uni-directional radiation field by rescaling the optical depth according to the formalism from Flannery

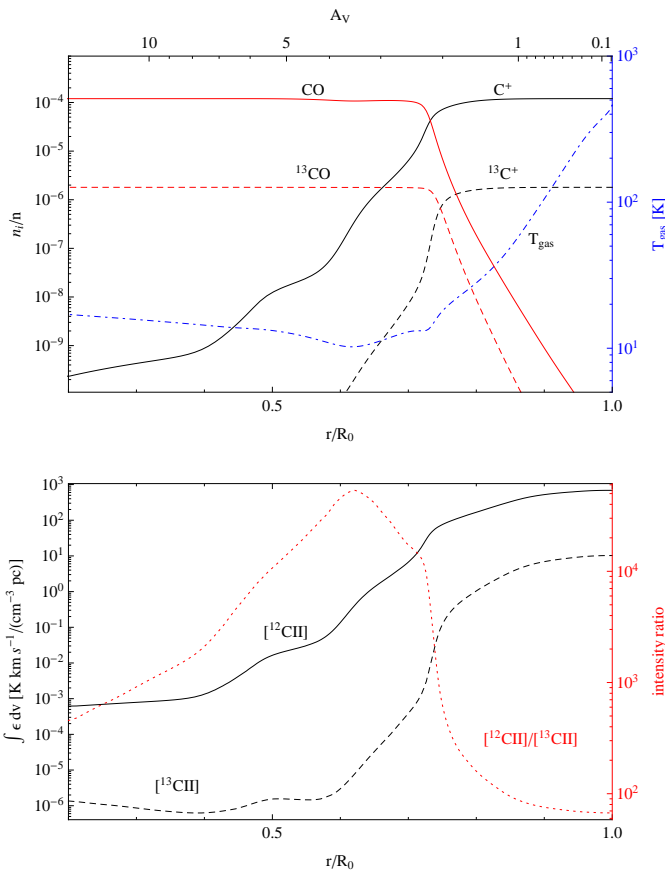


Fig. 1. **Top:** Abundance distribution of C^+ and CO and the corresponding ^{13}C isotopologues for a model with $n_{\text{surf}} = 10^4 \text{ cm}^{-3}$, $1000 \chi_0$ and $1000 M_\odot$. The blue curve shows the corresponding gas temperature structure determining the emissivity. **Bottom:** Resulting integrated optically thin line emissivity $f \epsilon dv$ in $\text{K km s}^{-1}/(\text{cm}^{-3} \text{ pc})$ for the [C II] and [^{13}C II] lines (black curves) as a function of the clump radius. The red line shows the intensity ratio provided by the two curves.

et al. (1980) and vice versa. Röllig et al. (2007) showed a very good match of the different PDR models when the rescaling was applied. When re-interpreting the KOSMA- τ results for a unidirectional illumination, one thus has to stretch the width of the outer layers relative to the given scale.

2.2. The effect of chemical fractionation on the [C II]/[^{13}C II] ratio

Paper I already provides some predictions for clump-integrated intensities for ^{13}C -bearing species for the special configuration of a spherical PDRs. To understand in detail how the chemical fractionation structure can translate into an observable [C II]/[^{13}C II] intensity ratio, we investigate here how the depth-dependent carbon fractionation translates into a varying local [^{13}C II] and [C II] emissivity, using the simplified picture of a plane-parallel configuration described by two parameters only: the density and the impinging UV field. In the resulting one-dimensional PDR, different layers reflect a decreasing UV penetration. This allows us to disentangle the relative contributions of these layers to the observable [C II]/[^{13}C II] intensity ratio. The approach ignores all effects resulting from the uncertain details of the cloud geometries and of the optical depth of the line along the line of sight to the observer in a particular geometry.

Fig. 1 shows the temperature and abundance structure of the dominating carbon bearing species and the resulting [C II] and [^{13}C II] line emissivity as a function of the relative radius – or depth from the surface into the cloud, respectively – for an example model with a density at cloud surface of 10^4 cm^{-3} and a radiation field of $1000 \chi_0$. The local [C II] line emissivity can be computed in terms of a two-level system

$$\int \epsilon dv = \frac{hc^3 A}{8\pi k\nu^2} \times N_{\text{C}^+} \frac{g_u \exp(-\Delta E/kT_{\text{ex}})}{g_l + g_u \exp(-\Delta E/kT_{\text{ex}})} \quad (1)$$

with $\Delta E = h\nu = k \times 91.2 \text{ K}$, the statistical weights $g_u = 4$ and $g_l = 2$, and the Einstein- A coefficient of $A = 2.3 \times 10^{-6} \text{ s}^{-1}$ (Wiese & Fuhr 2007), providing

$$\int \epsilon dv \approx 1011 \frac{\text{K km s}^{-1}}{\text{cm}^{-3} \text{ pc}} \times N_{\text{C}^+} \frac{2 \exp(-91.2 \text{ K}/T_{\text{ex}})}{1 + 2 \exp(-91.2 \text{ K}/T_{\text{ex}})} \quad (2)$$

and we obtain the excitation temperature T_{ex} from the detailed balance including collisional excitation through H_2 (Flower & Launay 1977), atomic hydrogen (Launay & Roueff 1977), and electrons (Wilson & Bell 2002) and radiative de-excitation and trapping². For [^{13}C II], this approach sums over all hyperfine components. The emissivity represents the integrated line intensity per hydrogen column density without optical depth correction.

In this example model, most of the [C II] emission stems from the cloud surface where all carbon is in ionized form and at high temperatures the $\text{C}^+/^{13}\text{C}^+$ fractionation ratio is equal to the elemental isotopic abundance ratio so that the [C II]/[^{13}C II] intensity ratio also matches the elemental ratio. Deep inside the cloud, where most of carbon is in the form of CO and $^{13}\text{C}^+$ is only produced by cosmic ray ionized He^+ , the intensity ratio is enhanced by about a factor of ten relative to the elemental isotopic ratio, but the C^+ abundance is reduced by six orders of magnitude so that the enhanced ratio is hidden by the surface emission. The region where chemical fractionation may be detectable is the transition zone from C^+ to CO where the $\text{C}^+/^{13}\text{C}^+$ fractionation ratio amounts to a few hundred and the intensity is only a factor ten weaker than at the surface (around $r/R_0 = 0.73$ in Fig. 1). The actual emissivity ratio can be boosted to values above the fractionation ratio by radiative excitation of C^+ in the cool and darker inner regions. As C^+ “feels” the strong line emission from the clump surface, it gains excitation temperatures above the kinetic temperature while the [^{13}C II] excitation temperature closely follows the kinetic temperature. Due to the exponential term in Eq. 2 this can provide up to a factor ten enhancement of the [C II]/[^{13}C II] intensity ratio for cold gas at moderate densities deeper in the cloud.

To better evaluate for which conditions we might observationally detect chemical fractionation, we compute the difference between the [C II] emissivity and the [^{13}C II] emissivity scaled by the elemental abundance ratio. This quantity does not directly reflect the intensity ratio, as shown in Fig. 1, but enhancements in this difference indicate conditions under which an increased $\text{C}^+/^{13}\text{C}^+$ fractionation ratio eventually turns into an observable increased [C II]/[^{13}C II] intensity ratio. Figure 2 shows the emissivity difference as a function of the distance from the outer radius for varying PDR parameters. In the upper panel, we vary the gas density for a constant radiation field of $1000 \chi_0$ while the lower panel shows the impact of different radiation fields for a constant gas density of $n_{\text{surf}} =$

² $1011 \text{ K km s}^{-1} = 7.11 \times 10^{-3} \text{ ergs}^{-1} \text{ cm}^{-2} \text{ sr}$ at the frequency of the [C II] transition

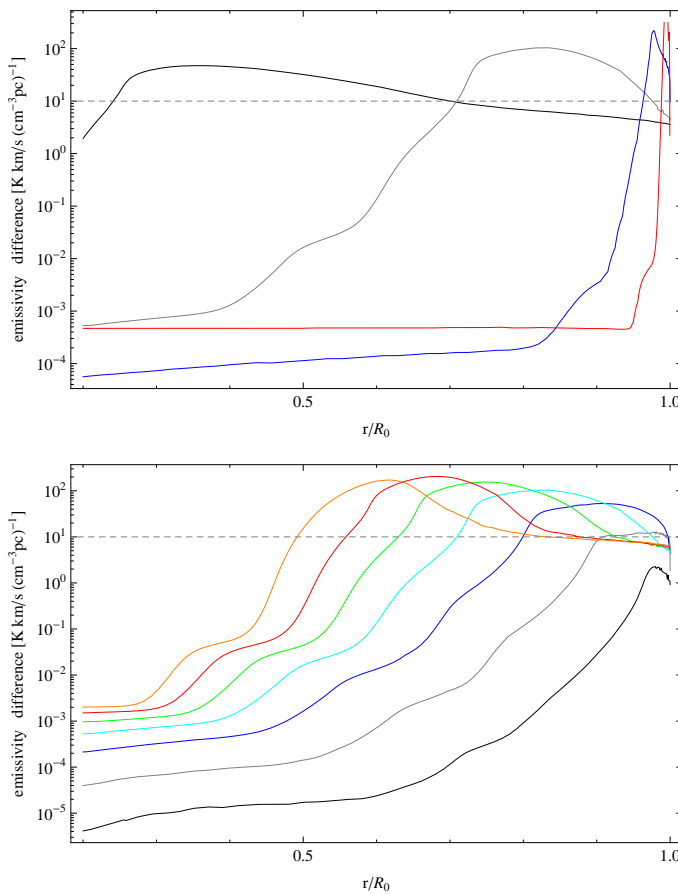


Fig. 2. Differences between [C II] emissivity and [^{13}C II] emissivity multiplied by the standard elemental isotopic ratio of 67 showing conditions where a increased $\text{C}^+/\text{^{13}C}^+$ fractionation ratio turns into an observable increased [C II]/[^{13}C II] intensity ratio. The upper plot uses a radiation field of $1000\chi_0$ and varies the surface gas density: 10^3 cm^{-3} (black), 10^4 cm^{-3} (grey), 10^5 cm^{-3} (blue), 10^6 cm^{-3} (red). The lower plot uses a gas density of $n_{\text{surf}} = 10^4 \text{ cm}^{-3}$ and varies the radiation field: $1\chi_0$ (black), $10\chi_0$ (grey), $100\chi_0$ (blue), $10^3\chi_0$ (cyan), $10^4\chi_0$ (green), $10^5\chi_0$ (red), $10^6\chi_0$ (orange). The dashed line at $10 \text{ K km s}^{-1} (\text{cm}^{-3} \text{ pc})^{-1}$ gives a rough indication what differences might be observable with current technology in a deep integration.

10^4 cm^{-3} . Whenever the difference is lower than about $1 \text{ K km s}^{-1} (\text{cm}^{-3} \text{ pc})^{-1}$ no [C II] enhancement is practically observable, either because the [^{13}C II] emission is too weak or because there is no enhanced $\text{C}^+/\text{^{13}C}^+$ fractionation ratio. Three factors determine the detectability of an enhanced fractionation ratio in the optically thin picture. The radiation field has to be strong enough to produce a significant column of ionized carbon, the corresponding layer has to be cool enough so that the reaction (C 1) is effective, and the layer of enhanced $\text{C}^+/\text{^{13}C}^+$ needs to be thick enough to provide a significant beam filling in a finite telescope beam. Paper I has shown that these conditions can be met for a wide variety of conditions, provided that there is a sufficient mass of dense gas. With at least $1 M_\odot$ at densities of 10^4 cm^{-3} a significant fractionation layer occurs even at high UV fields. In the upper panel of Figure 2 we see, however, that at densities of 10^5 cm^{-3} or above, the C^+ -CO transition region, producing an enhanced [C II]/[^{13}C II] intensity ratio associated with strong emission, is very thin. The lower panel shows that we find only small [C II] intensities from clumps exposed to radiation fields of $10\chi_0$ or below, making every [C II] observation

difficult. At all higher radiation fields, fractionation should be detectable. When considering the full parameter range, we find some degeneracy in the sense that for higher densities fractionation may also be observable at low UV fields. The ideal environment for an increased $\text{C}^+/\text{^{13}C}^+$ fractionation ratio is thus the mildly shielded gas in classical PDRs with $\chi \gtrsim 100\chi_0$ and densities in the order of $10^4 - 10^5 \text{ cm}^{-3}$.

2.3. Radiative transfer effects on the [C II]/[^{13}C II] ratio

The [C II] optical depth can be computed in the same way as the emissivity (Eq. 2) through

$$\int \tau dv = 7.15 \times 10^{-18} \frac{\text{kms}^{-1}}{\text{cm}^{-2}} \times N_{\text{C}^+} \frac{1 - \exp(-91.2K/T_{\text{ex}})}{1 + 2 \exp(-91.2K/T_{\text{ex}})} \\ \approx 7.15 \times 10^{-18} \frac{\text{kms}^{-1}}{\text{cm}^{-2}} \times N_{\text{C}^+} \frac{32.9K}{T_{\text{ex}}} . \quad (3)$$

For a Gaussian velocity distribution this is equal to

$$\int \tau dv = \frac{1}{2} \sqrt{\frac{\pi}{\ln 2}} \Delta v \times \hat{\tau} \quad (4)$$

where $\hat{\tau}$ denotes the peak optical depth and Δv the FWHM of the velocity distribution.

Vice versa, we can determine the optical depth from a measured [C II]/[^{13}C II] intensity ratio (IR), at any given frequency in the line when knowing the $\text{C}^+/\text{^{13}C}^+$ fractionation ratio (FR), assuming optically thin [^{13}C II] lines, and assuming equal excitation temperatures of [C II] and [^{13}C II]:

$$\frac{IR_\nu}{FR} = \frac{1 - \exp(-\tau_{[\text{CII}]})}{\tau_{[\text{CII}]}} \quad (5)$$

For the line integrated intensity ratio, one has to take the broadening of the [C II] line due to the optical depth into account. For a Gaussian velocity distribution and a line-center optical depth $\hat{\tau} < 10$, the increase of the line width can be linearly approximated by the simple factor $1 + 0.115\hat{\tau}$, and the average optical depth measured through the integrated line intensity is³

$$\langle \tau \rangle \approx 0.64\hat{\tau} . \quad (6)$$

To quantify the impact of the line-of-sight optical depth on the [C II]/[^{13}C II] intensity ratio we have to switch from the semi-infinite plane-parallel description to a finite geometry, containing a description for the C^+ column density, not only in the direction towards the illuminating source, but also in the line of sight towards the observer. This is naturally taken into account when using the clumpy picture that forms the base of the KOSMA- τ model, i.e. considering the case of spherical PDRs. It introduces the clump mass, i.e. the absolute radius of the clump, as a third independent parameter⁴. By integrating over the full volume of each clump and averaging the intensity over the projected area of the spherical model clumps, we mimic the situation of a fractal cloud, consisting of an ensemble of many clumps, where individual structures cannot be resolved (Stutzki et al. 1998).

In Fig. 3 we compare the ratio of clump averaged integrated line intensities, $\int I([\text{C II}])dv / \int I([\text{^{13}C II}])dv$ for a wide range

³ The general, more complex expression, also covering the large optical depth limit, is given e.g. by Phillips et al. (1979).

⁴ We do not include a separate interclump medium, but rather represent interclump material by the equivalent mass of an ensemble of small, transient, low-density clumps.

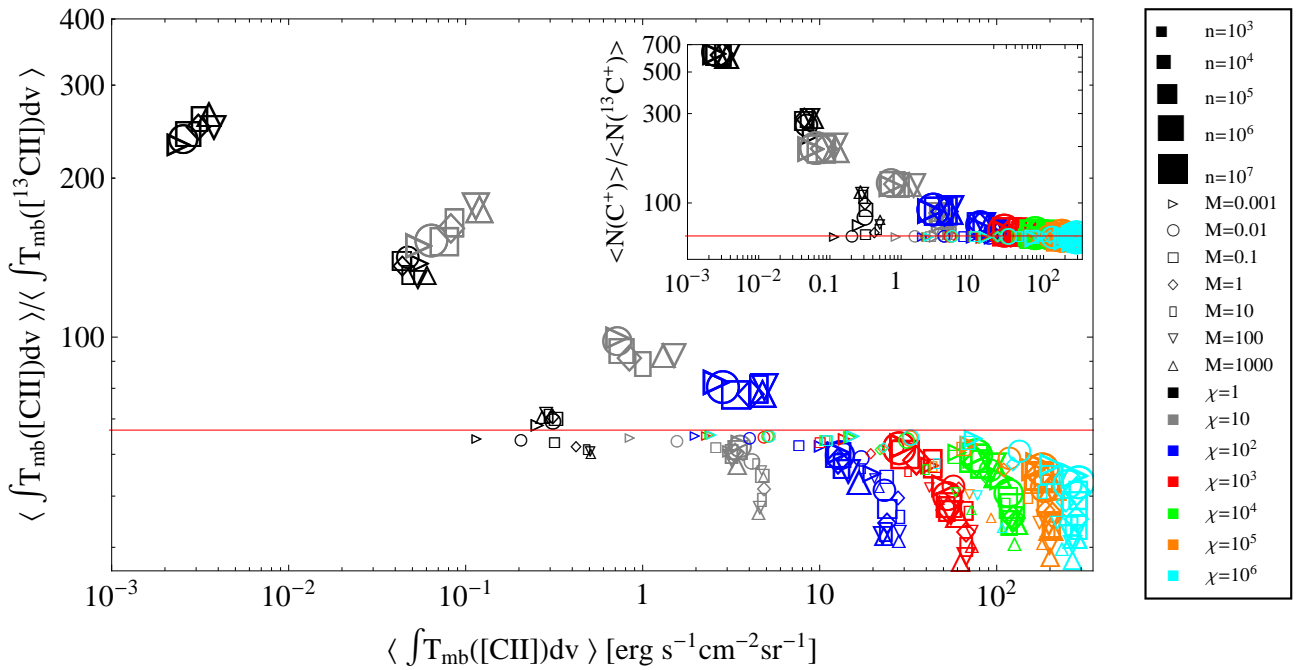


Fig. 3. Clump integrated intensity ratio $\int I([\text{CII}])dv / \int I([^{13}\text{CII}])dv$ vs. [C II] intensity from the KOSMA- τ model for different parameters. The model parameters n, M , and χ , are coded as size, shape, and color of the respective symbols. The red horizontal line denotes the assumed elemental abundance ratio $[^{12}\text{C}]/[^{13}\text{C}]$ of 67. The insert demonstrates the underlying column density ratio for the different clumps. For $[^{13}\text{CII}]$, we sum over all hyperfine components.

of densities, clump masses and impinging radiation fields. The insert shows the underlying mean column density ratio for the clumps producing the observed intensity ratio (see paper I).

While the column density ratio falls above the elemental isotopic ratio for all model clumps, this does not hold for the [C II]/[^{13}CII] intensity ratio. Models with low densities and all models with $\chi > 100$ show an intensity ratio below the elemental ratio, down to a value of 38. In these models, the fractionation ratio in the column densities is close to the elemental ratio so that the reduced intensity ratio is a direct measure of the average optical depth of the main isotopic line through Eq. 5. The reduction of the line integrated intensity ratio by a factor two corresponds to a moderate [C II] optical depth, $\langle \tau \rangle \approx 1.6$ or $\hat{\tau} \approx 2.5$, respectively, for the individual clumps. That means that in all models exposed to high UV fields an ionized carbon layer of about the same column density is formed, independent of the other clump parameters. This is naturally explained by the transition from C^+ to CO at about $A_V \approx 0.2$. Different PDR parameters only change the physical depth and temperature of this transition point. Higher [C II] optical depths only occur if multiple clumps add up their optical depth on the line of sight at the same velocity without mutual shielding of the impinging UV field, i.e. in special geometries.

In the clump-integrated picture, only models with low UV field χ and high densities trace the chemical fractionation, showing an intensity ratio that is enhanced relative to the elemental abundance ratio. A detailed comparison shows that even for those clumps some line saturation occurs, so that the intensity ratio does not measure the true $\text{C}^+/^{13}\text{C}^+$ fractionation ratio, but falls somewhat below it. This result is in contrast to the pure emissivity considerations in Sect. 2.2 that indicated that medium-density clumps produce an enhanced intensity ratio.

Optical depth effects are always significant in the considered geometry with similar column densities of C^+ towards

the illuminating sources and towards the observer. C^+ is abundant down to a shielding gas and dust column of $A_V \approx 1$ (see Fig. 1). If all carbon is ionized in this column, it provides $N_{\text{C}^+} \approx 2.5 \times 10^{17} \text{ cm}^{-2}$, corresponding to a [C II] optical depth of 0.8 for a slightly subthermal excitation temperature of $T_{\text{ex}} = 50 \text{ K}$ and the line width of 1.5 km s^{-1} used in the model. That means that in isotropic configurations with narrow lines, as in the clumpy PDR model, [C II] always turns slightly optically thick when the condition for an efficient fractionation is met. Hence, we find a relatively constant [C II] optical depth of 0.8–1.6 for all clumps that are big enough to contain the critical column for $A_V = 1$ and that are exposed to a radiation field strong enough to ionize the carbon. As a consequence, we expect a behavior as in Fig. 3 for isotropic PDRs with narrow velocity distributions. Most of the fractionation effect in the $\text{C}^+/^{13}\text{C}^+$ abundance ratio that was seen in the local [C II]/[^{13}CII] emissivity ratio in Sect. 2.2, is therefore hidden from the observer by an optical depth close to unity in this case.

A recovery of the true fractionation ratio, i.e. the $\text{C}^+/^{13}\text{C}^+$ column densities, through the observable [C II]/[^{13}CII] intensity ratio requires optically thin [C II] emission, either through a much wider velocity dispersion, reducing the [C II] optical depth in a broader line (see Eq. 4), or an anisotropic geometry that provides a higher column of gas for the UV shielding than in the line-of-sight towards the observer. Only in these configurations we can expect to detect chemical fractionation through the [C II]/[^{13}CII] ratio matching the predictions from Sect. 2.2. In contrast we may also find edge-on configurations with a larger column on the line of sight towards the observer than towards the illuminating sources (see the Orion Bar in Sect. 4.1) where the [C II] optical depth may grow beyond 2 providing an intensity ratio much below the local $\text{C}^+/^{13}\text{C}^+$ fractionation ratio.

Altogether, we must conclude that in most typical PDRs with bright [C II] emission, no significant fractionation is expected to

appear in the C^+ column densities, i.e. the fractionation ratio will match the elemental abundance ratio while the intensity ratio is dominated by the optical depth of the [C II] line pushing it below the elemental ratio. In those cases we can only use the intensity ratio to compute the C^+ column density through Eqs. (5) and (3). This is an essential parameter to compare with models for deriving e.g. the ionization degree or the photoelectric heating efficiency. Some carbon fractionation may be detectable through an increased [C II]/[^{13}C II] intensity ratio compared to the elemental abundance ratio for sources with high densities and moderate UV fields in case of a favorable geometry or relatively broad velocity distributions. However, even in these cases it may be impossible to deduce the exact $\text{C}^+/\text{C}^{13}\text{C}^+$ fractionation ratio due to the superimposed optical depth effects.

3. Observations

3.1. [^{13}C II] spectroscopy

C^+ has a single fine structure transition, [C II] $^2P_{3/2} - ^2P_{1/2}$, at 1900.537 GHz, which for $^{13}\text{C}^+$ is split into three hyperfine components due to the unbalanced additional neutron spin. The frequencies of these transitions have been determined by Cooksy et al. (1986) based on the combination of laser magnetic resonance measurements with ab-initio computations of Schaefer & Klemm (1970). Our observations from Sect. 4.1.2 confirm these frequencies with an accuracy of about 3 MHz, as the relatively narrow [C II] and [^{13}C II] lines in the Orion Bar match each other and numerous other molecular transitions to within 0.5 km s^{-1} in velocity space when using these rest frequencies.

We have computed the relative line strengths expected for the three hyperfine transitions in local thermodynamic equilibrium (LTE), which – for a magnetic dipole transition – are given by

$$S_{\text{hfs}} = \frac{(2F' + 1)(2F + 1)}{2I + 1} \left\{ \begin{array}{ccc} J & F & I \\ F' & J' & 1 \end{array} \right\} \quad (7)$$

(Eq. 8 in Garstang (1995), normalized to unity). Here, $J' = 3/2$ and $J = 1/2$ are the total electronic angular momenta for the upper and lower states, $I = 1/2$ is the nuclear spin of the ^{13}C nucleus, F' and F are the total angular momenta (including nuclear spin) for the upper and lower states, and the curly brackets denote a Wigner $6j$ -symbol. This expression – which rests on the standard assumptions that magnetic dipole (M1) radiation dominates over electric quadrupole (E2) radiation, and that the Hamiltonian commutes with all relevant angular momentum operators – yields a ratio of 0.625 : 0.25 : 0.125 for the $F' - F = 2 - 1 : 1 - 0 : 1 - 1$ transitions⁵. All spectroscopic parameters are summarized in Table 1.

⁵ Our line ratios differ from those (0.444 : 0.356 : 0.20) given by Cooksy et al. (1986) and used in previous astronomical studies. This discrepancy may account for the anomaly reported recently by Graf et al. (2012), who observed a $F = 2 - 1 : F = 1 - 0$ ratio in NGC 2024 that was considerably larger than that predicted by Cooksy et al. (1986). It also requires a minor revision to the elemental isotopic ratio inferred by Boreiko & Betz (1996) from observations of the $F = 2 - 1$ and $1 - 0$ transitions observed toward M42. That study applied a correction factor to account for the $F = 1 - 1$ transition, which was not covered by the available instrumental bandwidth. With our revised line strengths, the correction factor decreases from 5/4 to 8/7, resulting in a 9.4% increase in the inferred elemental ratio, from the range of 52 – 61 given by Boreiko & Betz (1996) to a range of 57 – 67. This then resolves a small discrepancy, noted by Boreiko & Betz (1996), between the ratio obtained from observations of [^{13}C II] and the value of 67 ± 3 inferred from observations of ^{13}CO .

Table 1. Spectroscopic parameters of the [^{13}C II] $^2P_{3/2} - ^2P_{1/2}$ transition

line	ν [GHz]	g_u	g_l	relative intensity
$F = 2 - 1$	1900.466	5	3	0.625
$F = 1 - 0$	1900.950	3	1	0.250
$F = 1 - 1$	1900.136	3	3	0.125

3.2. HIFI measurements

We performed [^{13}C II] observations with the HIFI instrument (de Graauw et al. 2010) on-board the Herschel satellite (Pilbratt et al. 2010) towards four bright PDRs in the framework of the key projects HEXOS (Bergin & Herschel Hexos Team 2011) and WADI (Ossenkopf et al. 2011). The first region is the Orion Bar (map center: $5^{\text{h}}35^{\text{m}}20.81^{\text{s}}$, $-5^{\circ}25'17.1''$), an edge-on, almost linear PDR at a distance of 415 pc (Menten et al. 2007), formed by material of the Orion Molecular Cloud 1 (OMC-1) exposed to the radiation from the Trapezium cluster providing an FUV flux of $4 - 5 \times 10^4 \chi_0$ in terms of the Draine (1978) field. Previous, spectrally unresolved observations of [C II] in the Orion Bar have been carried out by Stacey et al. (1993) and Herrmann et al. (1997) using the Kuiper Airborne Observatory (KAO). In terms of a pure edge-on configuration, the Orion Bar PDR is an improbable candidate for the detection of $^{13}\text{C}^+$ fractionation because of the large column density of C^+ on the line of sight. However, fractionation effects may be observable if the [C II] emission is dominated by the clumpy structure as seen by Hogerheijde et al. (1995) and Lis & Schilke (2003). They found clumps with a density well above 10^6 cm^{-3} embedded in a more widely distributed “interclump” gas with a density of $10^4 - 2 \times 10^5 \text{ cm}^{-3}$ (Simon et al. 1997). Moreover, the gas in front and behind the main Orion Bar should have a more favorable geometry. By mapping [^{13}C II], we were able to distinguish the three regions.

The second PDR is formed by the molecular interface around the ultracompact H II region Mon R2 at a distance of 830 pc ($6^{\text{h}}07^{\text{m}}46.2^{\text{s}}$, $-6^{\circ}23'08.0''$). Due to the larger distance, the PDR is weaker in [C II] than the Orion Bar, in spite of the larger FUV intensity from the central source of about $3 \times 10^5 \chi_0$ (Fuente et al. 2010). The almost spherical PDR geometry around the H II region provides a situation close to the plane-parallel model from Sect. 2.2 when observing the source center, with two PDR layers at high velocities behind and in front of the H II region along one line of sight. The velocity dispersion of up to 10 km s^{-1} (e.g. Ginard et al. 2012) promises a low optical depth at high integrated line intensities making Mon R2 one of the best candidates to detect an enhanced [C II]/[^{13}C II] intensity ratio (Pilleri et al. 2012a). The situation is, however, complicated by the unknown local role of outflows that have been observed on a somewhat larger scale (Xu et al. 2006).

As a third PDR we observed the clump MM2 close to NGC 3603 at a distance of about 6 kpc (Stolte et al. 2006) ($11^{\text{h}}15^{\text{m}}10.89^{\text{s}}$, $-61^{\circ}16'15.2''$), illuminated by a FUV intensity of about $10^4 \chi_0$ from the OB stars in NGC 3603 (Röllig et al. 2011). The fourth source is the Carina Nebula at a distance of about 2.3 kpc (Smith 2006), illuminated by the OB stars in the massive clusters Trumpler 14 and 16 with a FUV flux of about $4 \times 10^3 \chi_0$ (Okada et al. 2012). Here, we observed two interfaces, the Carina North PDR ($10^{\text{h}}43^{\text{m}}35.14^{\text{s}}$, $-59^{\circ}34'04.3''$) close to Trumpler 14, and the Carina South PDR ($10^{\text{h}}45^{\text{m}}11.54^{\text{s}}$, $-59^{\circ}47'34.3''$) south of η Car, including the core IRAS-10430-5931. In NGC3603 and Carina, the PDRs are known to occur at the surface of clumps, partially visible as pillars in the near

infrared. Therefore, we expect a behavior matching the clumpy model from Sect. 2.3 that predicted no observable enhancement of the [C II]/[^{13}C II] intensity ratio for UV fields above $10^2 \chi_0$.

The last PDR is the northern filament in NGC 7023 ($21^{\text{h}}01^{\text{m}}32.4^{\text{s}}$, $68^{\circ}10'25.0''$) at a distance of 430 pc (van den Ancker et al. 1997) illuminated by the pre-main-sequence B3Ve star HD200775 providing a FUV flux of $1100\chi_0$ at the position of our observation (Joblin et al. 2010; Pilleri et al. 2012b). Here, previous observations (e.g Gerin et al. 1998) show a smooth density increase towards the filament and a stratified PDR structure so that we may find the situation modelled in Sect. 2.2. The [C II] mapping results have been presented already by Joblin et al. (2010).

All five PDRs were mapped in [C II] using the on-the-fly (OTF) observing mode, however, only the Orion Bar was bright enough to detect [^{13}C II] in the map. Therefore, separate deeper dual-beam switch (DBS) measurements were performed towards the given coordinates in the other four PDRs. Unfortunately, the Orion Bar observations used an LO setting that placed the $F = 1 - 1$ transition out of the covered IF range, so that only the $F = 2 - 1$ and $F = 1 - 0$ components were observed there.

The data were calibrated with the standard HIFI pipeline in the Herschel Common Software System (HCSS Ott 2010) in version 9.0 (2226). All data presented here are given on the scale of the antenna temperature corrected for the forward efficiency, T_A^* . The preference for this temperature scale is motivated by the fact that all maps show very extended emission. The T_A^* scale provides correct brightness temperatures if the error beam of the telescope is uniformly filled by emission of the same magnitude as the main beam. The HIFI error beam at 1900 GHz is mainly provided by the side lobes of the illumination pattern appearing at radii of less than two arcminutes (Jellema et al. in prep). Scaling to main-beam temperatures, in contrast, would assume a negligible contribution of the error beam pickup to the measured intensity, increasing the resulting temperatures by a factor 1.39 (Roelfsema et al. 2012). The two scales will bracket the true brightness temperature. As the actual emission decreases with growing distance from the sources, the T_A^* scale will slightly overestimate the error beam contribution and underestimate the brightness temperature, but due to the very extended emission it should be considerably better than the main beam temperature scale. We estimate therefore that the antenna temperature underestimates the brightness temperature by 10-20 %.

The resulting spectra suffer from baseline ripples due to instrumental drifts. They were subtracted using the `HifiFitFringe` task of the HCSS including the baseline option with a minimum period of 200 MHz covering all ripples visible in the spectra. This method attributes structures wider than 200 MHz to instrumental artifacts and all narrower structures to sky signal. In this way we only get reliable intensity information for lines narrower than 30 km s^{-1} , a condition that is met for all our PDRs. In the DBS observations, the resulting spectra also suffered from self-chopping because the chopper throw of $3'$ often ends at OFF positions that are still contaminated by some emission. This affected the detection of the $F = 2 - 1$ hyperfine component in NGC 3603 and Carina falling into the range of self-chopping features of the main isotopic line. We tried to circumvent this problem by looking into the individual single-beam switch spectra, that only use one OFF position left or right of the source, not combining them. Although they show different degrees of contamination from the two OFF positions, some contamination always appeared in both spectra, so that we obtained no qualitative improvement with respect to a clear detection of the hyperfine component. Therefore, we show in the

following only the dual beam switch spectra providing the better signal-to-noise ratio.

With the high signal to noise ratio of the [C II] line in the Orion Bar map we noticed a small zig-zag structure in reported positions and the resulting Orion Bar map, originating from the alternating direction in the observation of subsequent OTF lines. An ad-hoc correction of the pointing information by $1.4''$, mutually shifting the OTF lines relative to each other, resulted in a straight Orion Bar structure. This correction will be implemented in future versions of the HIFI pipeline, but for this paper the correction just gives an estimate for the pointing accuracy. The original Orion Bar map also suffered from relatively strong emission at the OFF position ($5^{\text{h}}35^{\text{m}}44.92^{\text{s}}$, $-5^{\circ}25'17.1''$) visible as absorption feature in numerous points of the map. A separate observation of the OFF position was performed using the internal HIFI cold load as primary reference and a secondary OFF position more than $12'$ away from the Bar ($5^{\text{h}}35^{\text{m}}55.0^{\text{s}}$, $-5^{\circ}13'18.1''$) as secondary reference. Fortunately, it turned out that the baseline from the subtraction of the cold load spectrum was good enough so that the secondary OFF position did not have to be used because we detected even from this very remote position [C II] emission as bright as 10 K (see Fig. 5) in agreement with the large-scale map of Mookerjea et al. (2003). This has to be considered as a very widely distributed emission floor in the Orion region.

4. Observational results

Table 2 lists the integrated intensities of the [C II] line and the [^{13}C II] components for all sources. The relative intensities of the [^{13}C II] hyperfine components are roughly consistent with the intensity ratios from Table 1. However, in the observations with the best signal-to-noise ratio, the Orion Bar peak and NGC 7023, we find a somewhat lower $F = 2 - 1/F = 1 - 0$ ratio of 2 – 2.4 instead of 2.5. The uncertainty of the integrated intensities consist of three contributions: radiometric noise, the definition of the appropriate velocity integration range, and the uncertainty in the baseline subtraction. When measuring the noise in the spectra, we found that its contribution to the total uncertainty is actually negligible compared to the two other sources of uncertainty for all our observations.

The definition of the best integration range asks for a compromise because broad wings in the [C II] profile, in particular in Mon R2, favor very broad integration ranges to trace the whole [C II] emission while the small separation between the [C II] line and the [^{13}C II] $F = 2 - 1$ transition and wavy baseline structures ask for narrow integration ranges. As the wings are not detectable in the [^{13}C II] components and their intensity ratio forms the main focus of this study, we used common relatively narrow integration ranges here (column 2 of Tab. 2). In this way, we ignore the wing emission that is detectable in the main isotopic line, but compare the same velocity ranges for the isotopic ratios. In the extreme case of Mon R2, the integrated [C II] intensity is higher by 15 K km s^{-1} , i.e. 4 %, compared to the value in Tab. 2 when using a very broad integration range including all the wings and in the Orion Bar the value would be increased by 7 K km s^{-1} , i.e. 1 %, in this way. For the other sources no wing components can be detected due to self-chopping signatures in the spectra (see Fig. 12).

The uncertainty that actually determines the error bars given in Tab. 2 stems from the baseline subtraction in the spectra. Only to a small degree they are given by radiometric noise, but they are dominated by correlated residuals in the baselines that are not easily described by statistic measures. We performed numerical

Table 2. Summary of integrated line intensities from the observations and derived parameters.

source	integration range [km s $^{-1}$]	[C II] [K km s $^{-1}$]	[^{13}C II] [K km s $^{-1}$]	$F = 2 - 1$	$F = 1 - 0$	$F = 1 - 1$	IR a	$\langle \tau_{[\text{CII}]} \rangle$ [10 18 cm $^{-2}$]	$N_{\text{C}^+}^b$
Orion Bar, peak	7 – 13	857 \pm 5		17.2 \pm 1.0	7.8 \pm 0.5	—	30 \pm 2	1.9 \pm 0.2	10.1
Orion Bar, ridge c	7 – 13	772 \pm 5		12.6 \pm 1.0	5.1 \pm 0.5	—	38 \pm 3	1.3 \pm 0.2	7.2
Orion Bar, front d	7 – 13	506 \pm 7		4.3 \pm 0.7	2.1 \pm 0.6	—	69 \pm 12	0.0 \pm 0.4	2.3
Orion Bar, back e	7 – 13	529 \pm 6		6.3 \pm 0.6	2.9 \pm 0.6	—	50 \pm 6	0.7 \pm 0.3	3.9
Mon R2, total	5 – 25	362 \pm 5		—	2.9 \pm 0.7	0.7 \pm 0.5	38 \pm 10	1.3 \pm 0.6	5.7
Mon R2, blue	5 – 12.5	173 \pm 3		—	2.4 \pm 0.7	0.8 \pm 0.3	20 \pm 5	3.2 \pm 0.8	4.8
Mon R2, red	12.5 – 25	188 \pm 4		—	0.7 \pm 0.5	-0.3 \pm 0.4	170 \pm 120	0.0 \pm 0.5	0.9
NGC 3603	10 – 19	130 \pm 2		—	1.4 \pm 0.2	0.55 \pm 0.15	25 \pm 5	2.4 \pm 0.4	3.6
Carina N	-20 – -5	143 \pm 4		—	1.3 \pm 0.3	0.7 \pm 0.3	27 \pm 7	2.2 \pm 0.6	5.0
Carina S	-38 – -25	38 \pm 2		2.7 \pm 0.3 f	-0.1 \pm 0.3	0.0 \pm 0.3	> 22	< 2.9	0.2 g
NGC 7023	-1 – 7	91 \pm 2		1.07 \pm 0.05	0.53 \pm 0.07	0.19 \pm 0.04	51 \pm 6	0.6 \pm 0.3	1.0

Notes. $(^a)$ [C II]/[^{13}C II] intensity ratio. From the sum over all [^{13}C II] hyperfine components assuming the ratios from Table 1 to correct for non-detected components. $(^b)$ Assuming a uniform Gaussian velocity profile for C $^+$ and ^{13}C C $^+$. $(^c)$ Average over the ≈ 1000 square-arcsec with $I([\text{CII}]) \geq 700$ K km s $^{-1}$ representing the main Bar emission (see contours in Fig. 4). $(^d)$ Average over the ≈ 750 square-arcsec with 450 K km s $^{-1} \leq I([\text{CII}]) \leq 650$ K km s $^{-1}$ north-west of the Bar. $(^e)$ Average over the ≈ 900 square-arcsec with 450 K km s $^{-1} \leq I([\text{CII}]) \leq 650$ K km s $^{-1}$ south-east of the Bar. $(^f)$ The identification of this emission as [^{13}C II] $F = 2 - 1$ is questionable because of the small separation from the [C II] line. It may rather represent a different velocity component. $(^g)$ Assuming $\tau = 0.0$ to compute the column density.

experiments by varying the number of sinusoidal components in the `HifiFitFringe` task between 1 and 4 and changing the size of the window that is masked, i.e. excluded from the baseline fit, from the pure integration range to a range that is about three times wider in five steps. We inspected all baseline fits manually excluding those where self-chopping signatures or line wings affected the fit. The uncertainties in Tab. 2 describe the variation in the remaining sample in terms of the total covered range, i.e. they do not quantify 1σ errors but the extremes of that sample. It is obvious that the relative errors are small for the Orion Bar with narrow lines while they increase with the line width and the resulting larger baseline uncertainty. For the figures shown in the next section we used the subjective “best baseline fit” from the sample.

4.1. Orion Bar

4.1.1. [C II]

[C II] was mapped along a strip perpendicular to the direction of the Bar. Figure 4 shows the overlay of the integrated intensity on the corresponding IRAC 8 μm image. [C II] shows a very smooth structure without any indication for clumpiness as seen e.g. in the different isotopologues of CO, HCN, HCO $^+$, CS and H₂CO by Hogerheijde et al. (1995) and Lis & Schilke (2003) and to a lower degree also in the C91 α carbon radio recombination line by Wyrowski et al. (1997). This indicates that [C II] traces mainly the widely distributed, relatively uniform interclump medium. Position, structure, and overall extent of the [C II] Orion Bar emission are similar to the C91 α radio recombination line map. That map shows, however, a larger contrast and some clumpy substructure within the emission peak. To some degree that may be due to insufficient short-spacing of the interferometer data, but it probably also reflects real differences in the excitation of the C $^+$. As the C91 α emission depends much more sensitively on the gas density and temperature than [C II] (see e.g. Natta et al. 1994), the ratio of the two lines may provide a way to better characterize the transition between the widely distributed gas and the embedded clumps. The [C II] emission peaks approximately 10'' deeper in the cloud compared to the PAH emission traced by the IRAC 8 μm map. This coincides ap-

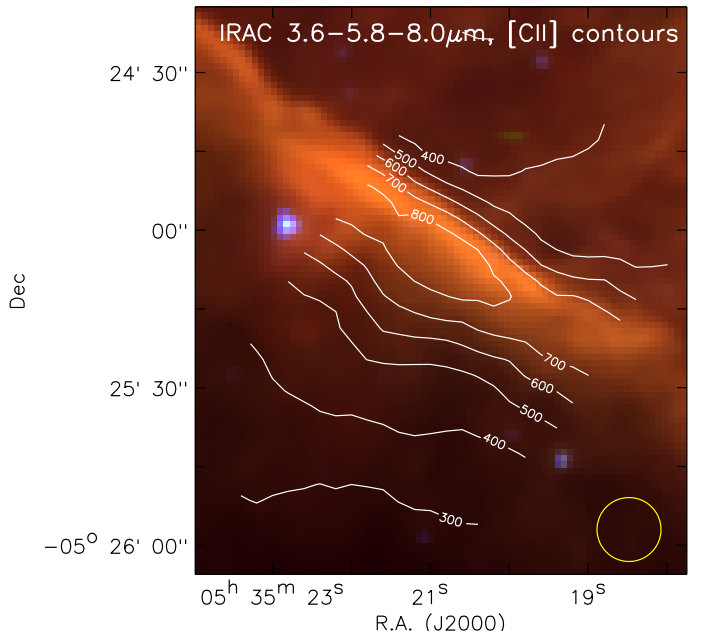


Fig. 4. Integrated [C II] contours over-laid on the false-color IRAC map of the Orion Bar (red: 8.0 μm : 0–3000 MJy/sr, green: 5.8 μm : 0–7000 MJy/sr, blue: 3.6 μm : 0–10000 MJy/sr). [C II] is mapped in a strip perpendicular to the Orion Bar. Intensities are labelled in units of K km s $^{-1}$. The colors in the IRAC map are provided by the signal in the 3.6, 5.8, and 8 μm channels. The yellow circle indicates the HIFI beam size.

proximately with the peak of the H₂ 1-0 S(1) line measured by Walmsley et al. (2000) and correlates very well with the C₂H emission observed by van der Wiel et al. (2009). The detailed comparison of the stratification in the different lines will be the topic of a forthcoming paper (Makai et al. in prep).

We can compare our data with previous KAO observations of [C II] in Orion. Boreiko et al. (1988) and Boreiko & Betz (1996) obtained frequency-resolved spectra towards $\Theta^1\text{C}$, but not towards the Orion Bar. The spectrally unresolved maps by Stacey et al. (1993) and Herrmann et al. (1997) showed approximately the same integrated intensity at the peak of the Orion

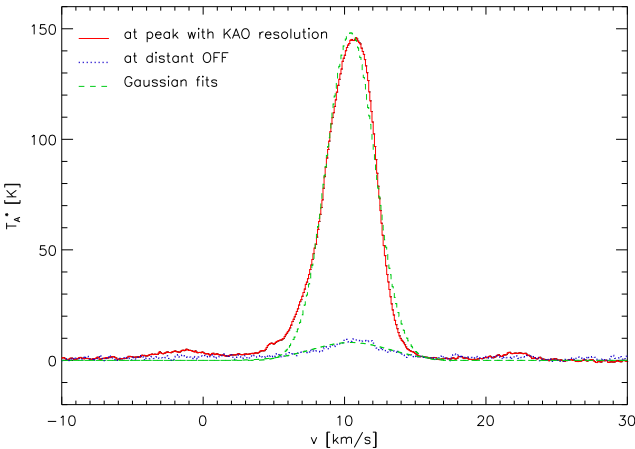


Fig. 5. [C II] profile towards the peak of the Orion Bar emission ($5^{\text{h}}35^{\text{m}}20.6^{\text{s}}$, $-5^{\circ}25'5''$) averaged over a $43''$ (FWHM) Gaussian beam representing the resolution of the previous KAO observations (solid line). The dotted spectrum represents the widely distributed emission as measured on our secondary OFF position $12.3'$ away from the Orion Bar in a region without molecular emission. The dashed lines show Gaussian fits to the two profiles.

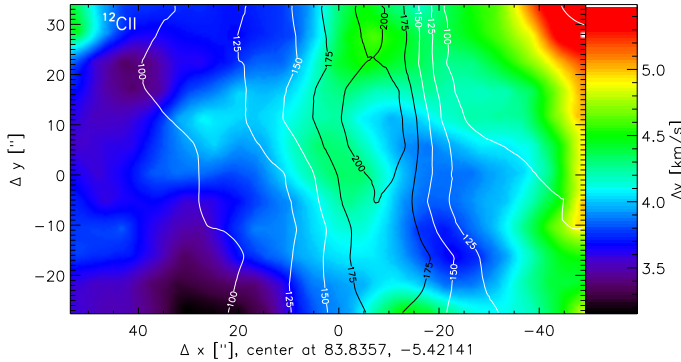


Fig. 6. Contours of the [C II] line peak intensity overlaid on the line width (FWHM) obtained from a Gaussian fit to the [C II] lines at all points in the Orion Bar map.

Bar and towards $\Theta^1\text{C}$. The $\Theta^1\text{C}$ value from Boreiko & Betz (1996) of 3.8×10^{-3} erg cm $^{-2}$ s $^{-1}$ sr $^{-1}$ is, however, 16% lower than the 4.5×10^{-3} erg cm $^{-2}$ s $^{-1}$ sr $^{-1}$ derived for the integrated [C II] intensity at the Orion Bar by Herrmann et al. (1997) scaling all intensities to match the previous value from Stacey et al. (1993) towards Orion KL. Figure 5 shows our [C II] HIFI profile towards the peak in the Orion Bar after convolution to the $43''$ resolution of the KAO. The integrated intensity of 585 K km s $^{-1}$ = 4.1×10^{-3} erg cm $^{-2}$ s $^{-1}$ sr $^{-1}$ falls between the two quoted KAO values. The discrepancy with the lower value from Boreiko & Betz (1996) can be partially explained by self-chopping of the KAO observations in the very extended emission. Our observation of the secondary OFF position (also shown in Fig. 5) gives an estimate for this extended emission providing a 6% correction of the KAO values. The 9% discrepancy with the Herrmann et al. (1997) value could be due to the uncertainty in the error beam pickup discussed above or the scaling method used in their paper.

As we find almost perfect Gaussian profiles for the lines in the Orion Bar (see Fig. 5) we performed Gaussian fits to all [C II] spectra. In Fig. 6 we show the resulting map of amplitudes and widths. As the observations by Boreiko & Betz (1996) indicated

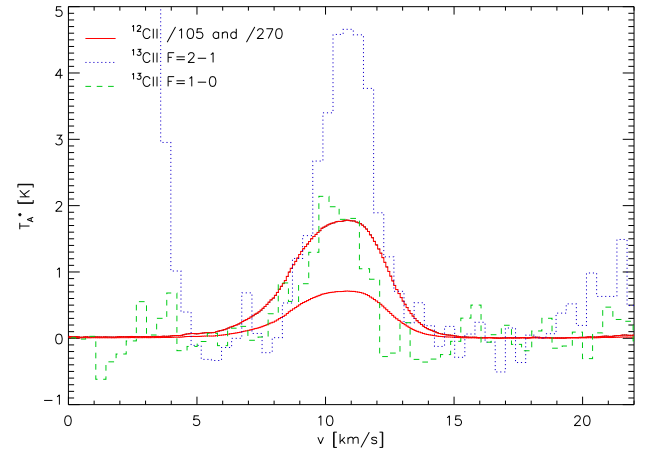


Fig. 7. Average profile of the two strongest [^{13}C II] hyper-fine components in the Orion Bar compared to the [C II] profile scaled by factors of $0.625/67$ and $0.25/67$. The profiles were averaged over all pixels with a [C II] integrated intensity above 700K km/s .

partially optically thick lines, we expect that the lines become broader towards the peak of the emission due to optical depth broadening. The map, however, does not show any significant change of the line width across the Orion Bar. The FWHM of the line falls between 4.0 and 4.5 km s $^{-1}$ only turning broader for the more diffuse emission in the north. Consequently, the amplitude map gives a perfect match to the integrated line map in Fig. 4. As we confirm the significant optical depth in the following section, this indicates that the [C II] line must be composed of many velocity components which are individually optically thick, instead of a continuous microturbulent medium that only turns optically thick at the largest column density sum. The corresponding map of line velocities only shows a small gradient along the Bar with velocities of about 11 km s $^{-1}$ in the north-east and 10.5 km s $^{-1}$ in the south-west.

4.1.2. [^{13}C II]

Due to the narrow line width in the Orion Bar, we are able to detect the $F = 2 - 1$ and $F = 1 - 0$ lines of [^{13}C II] without noticeable blending with the [C II] line. Figure 7 shows the line profiles of the two [^{13}C II] components when averaged over the region with the brightest emission, i.e. with [C II] intensities of more than 700 K km s $^{-1}$. For a comparison we have added the corresponding [C II] spectra, scaled by factor of $0.625/67$ and $0.25/67$. This scaling corresponds approximately to the line intensity of the two [^{13}C II] transitions that would be expected when we assume the canonical abundance ratio and optically thin lines.

When considering the line amplitudes, we find that both hyperfine transitions are approximately 2.5 times brighter than expected from optically thin [C II] emission and the normal isotopic ratio. Assuming the canonical abundance ratio, this corresponds to a line-center optical depth, $\hat{\tau}$ of 2.2. The good signal to noise ratio of the data allows us to perform Gaussian fits to the hyperfine lines over the full map providing a full map of intensity ratios. Using Eq. 5 and assuming no chemical fractionation, we can translate this into a map of optical depths. Figure 8 shows the resulting line center optical depth, $\hat{\tau}$, overlaid on the integrated [C II] intensities. Here, we have added both hyperfine transitions to increase the signal to noise. No reliable values can be derived

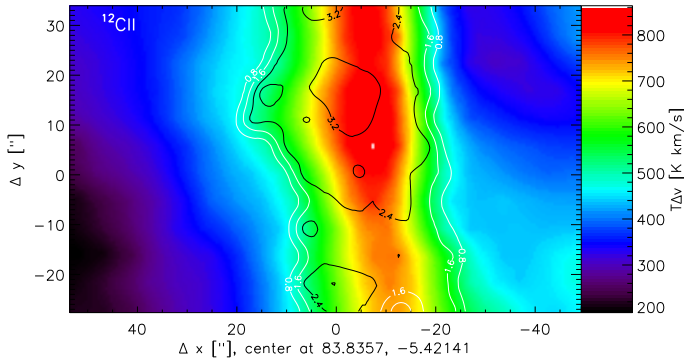


Fig. 8. Contours of the [C II] line center optical depth, derived from the [C II]/[^{13}C II] ratio, overlaid on the integrated [C II] intensities observed towards the Orion Bar.

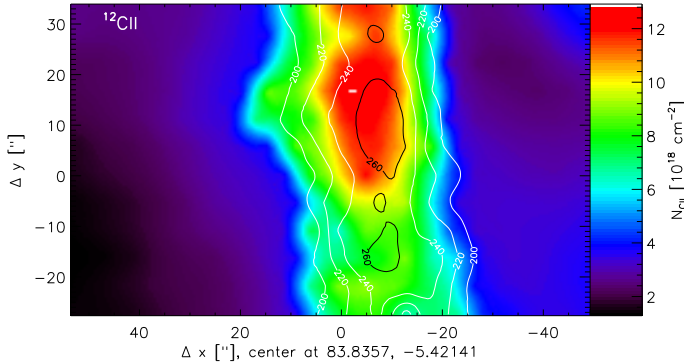


Fig. 9. Contours of the [C II] excitation temperature overlaid on the derived column densities towards the Orion Bar.

for $\tau \lesssim 0.8$ as Eq. 5 turns very flat for low optical depths. Hence, all points with lower optical depth have been masked-out. We find a good correlation of the optical depth structure with the intensity map. The map confirms that the area of bright [C II] emission has optical depths above two and the peak optical depth of 3.4 occurs close to the intensity peak, but we also see a small general shift of the optical depth structure relative to the intensity structure away from the exciting Trapezium cluster. This is consistent with the picture of hotter gas at the PDR front and somewhat cooler gas, but a higher column density deeper into the cloud.

To better quantify this, we use Eq. 3 to compute the excitation temperatures, and Eq. 2 together with the optical depth correction in Eq. 5 to compute the total C⁺ column density. The resulting distribution is shown in Fig. 9.⁶ In the range of significant optical depths, the excitation temperatures fall between 190 and 265 K. For $\tau \leq 0.8$ we assumed a constant excitation temperature of 190 K and directly used the optically thin approximation of Eq. 2 to compute the C⁺ column density.

Our excitation temperatures are in agreement with the average value of 220 K and 215 K derived by Herrmann et al. (1997) and Sorochenko & Tsivilev (2000), respectively, for the Orion Bar. Interclump gas at this temperature with a density around 10^5 cm^{-3} also explains the C91 α observations by Wyrowski et al. (1997). However, Natta et al. (1994) and Walmsley et al. (2000) obtain much higher temperatures from the radio recombination lines. This could indicate nonthermal emission, dielec-

⁶ When scaling the measured intensities to the main beam efficiency, i.e. assuming less extended emission, the optical depth does not change, but the excitation temperature and C⁺ column densities increase by 30 % relative to the values given here.

tronic recombination, or simply different gas components contributing to the [C II] and C91 α emission (Natta et al. 1994; Sorochenko & Tsivilev 2000).

At the scale of the KAO resolution, our approach provides a column density of $7 - 8 \times 10^{18} \text{ cm}^{-2}$ being more than two times higher than the value of Herrmann et al. (1997), consistent with our [C II] optical depth exceeding the value derived by Boreiko & Betz (1996) by about the same factor. The discrepancy can be explained to a large degree by their use of the line-averaged optical depth, underestimating the peak depth by a factor 0.64 for a Gaussian velocity distribution (see Sect. 2.3), and their use of different spectroscopic parameters, as discussed in Sect. 3.1. Our peak C⁺ column density of $13 \times 10^{18} \text{ cm}^{-2}$ implies a configuration where most of the line-of-sight column density of the Orion Bar of $N_{\text{H}} \approx 13 \times 10^{22} \text{ cm}^{-2}$ (e.g. Hogerheijde et al. 1995) forms a PDR with complete ionization of the gas phase carbon – abundance $X(\text{C}) = n(\text{C})/(n(\text{H}) + 2n(\text{H}_2)) = 1.2 \times 10^{-4}$ for dense clouds (Wakelam & Herbst 2008). A surprising result is, however, the relatively large C⁺ column density in front and behind the Bar. Molecular line observations (e.g. Hogerheijde et al. 1995; van der Werf et al. 1996) deduced column densities that are a factor ten lower than in the Bar. Consequently, at least half of the [C II] emission in the veil must stem from atomic, more diffuse material.

Fig. 9 also shows the relative shift between the column density and the excitation temperature distributions by 5–8" with the higher temperatures towards the illuminating source. The new observations thus resolve a temperature gradient in C⁺ consistent with the overall stratified structure of the Orion Bar PDR. The resulting intensity profile then represents a convolution of density and temperature structures.

4.1.3. Line averages

To verify the dependence of the results on the assumption of the Gaussian velocity distribution, we repeated the analysis for selected subregions when considering the line-averaged [C II]/[^{13}C II] intensity ratio, i.e. $\langle \tau \rangle$ instead of $\hat{\tau}$. This is also the only possible analysis for the other sources where the signal-to-noise ratio is lower and the line profiles are highly structured so that the assumption of a Gaussian velocity distribution is clearly violated. The use of the line averaged optical depths, $\langle \tau \rangle$, corresponds to the assumption of a macro-turbulent situation, where [C II] turns independently optically thick in all velocity channels, while the $\hat{\tau}$ method assumes a microturbulent Gaussian velocity distribution for all tracers, where [C II] turns optically thick only in the line center. A preference for one of the methods is only possible based on detailed knowledge of the source structure. The $\langle \tau \rangle$ results for all sources are included in the last two columns in Table 2.

For the Orion Bar, the $\langle \tau \rangle$ results always fall below the column densities from the line-center optical depth by 30–35 % in spite of the almost Gaussian line profiles. A possible cause is the systematic difference in the line width between the [^{13}C II] and the [C II] lines going beyond the expected optical-depth broadening. As seen in the average spectrum shown in Fig. 7, but also in the map of [^{13}C II] line widths corresponding to Fig. 6, the [^{13}C II] line is always 1.0–1.5 km s^{-1} narrower than the [C II] line. As a consequence, the intensity ratio is even larger than the standard elemental isotopic ratio in the line wings (well visible in the blue wing in Fig. 7). Together with the constant [C II] line width discussed in the previous section, the enhanced intensity ratio in the wings indicates different velocity distributions for C⁺ and ^{13}C so that neither the $\hat{\tau}$ method nor the $\langle \tau \rangle$ method

can provide accurate results. The 30–35 % of the emission remaining in the wings of the [C II] line when fitting it with the profile of the [^{13}C II] lines provide an estimate for the accuracy of the method.

The $\langle \tau \rangle$ values from the average spectra in Table 2 also confirm the spatial gradient of the column densities discussed for Fig. 9. When analyzing the bright gas in front and behind the Orion Bar by selecting all pixels with a [C II] intensity between 450 and 650 K km s^{-1} north-west, i.e. in the direction of the illuminating Trapezium stars, and south-east of the Bar, we find significantly higher optical depths behind the Bar while the gas in front of the Bar is typically hotter by about 20 K, but thinner by a factor 1.7.

None of the average spectra show an indication for an enhanced $\text{C}^+/\text{C}^{13}\text{C}^+$ fractionation ratio. This also applies to the spectra from the veil in front and behind the Bar where we were not able to detect a significant deviation from the elemental abundance ratio due to the relatively larger baseline uncertainties at lower intensities of the [^{13}C II] lines. Our [^{13}C II] observations are consistent with negligible carbon fractionation and an enhanced optical depth of the main isotopic line for high column densities. This is in agreement with a previous detection of the [^{13}C I] $F = 5/2 - 3/2$ transition by Keene et al. (1998) in a selected clump where the observed $^{13}\text{C}/\text{C}$ ratio showed no fractionation effect in contrast to the complementary observations for $^{13}\text{C}^{18}\text{O}$ and C^{18}O .

An indication for an enhanced fractionation ratio is, however, seen in the velocity structure when considering the wings of the bright line profiles. The broader [C II] lines showing enhanced [C II]/[^{13}C II] intensity ratio in the wings (e.g. in Fig. 7) indicate that an additional gas component, with broader velocity dispersion and enhanced fractionation ratio, thus invisible in [^{13}C II], contributes to the [C II] profiles. The constancy of the [C II] line width then could be explained by the mutual compensation of the relatively larger contribution from the low-velocity dispersion Orion Bar material with the optical depth broadening there. To sustain the enhanced intensity ratio, the broad velocity gas component should have moderate gas densities of $10^3 - 10^4 \text{ cm}^{-3}$ and face moderate UV fields ($\chi \approx 10^3$, see Sect. 2).

4.2. Mon R2

4.2.1. [C II]

The [C II] OTF map of Mon R2 consists of a single strip across the ultracompact H II region from north-east to south-west (see Fuente et al. 2010). In Fig. 10 we show the position-velocity diagram for that cut. This is important for understanding the origin of the components of the spectral profile in the comparison with the [^{13}C II] lines. We find a ring-like structure in position-velocity space, with two well separated components towards the center of the H II region. A better understanding of the position velocity structure can be obtained by combining this information with equivalent maps in several other tracers (Pilleri et al. 2012a). In particular the comparison with water lines, that show up in absorption in the blue component but in emission in the red component, suggests that the diagram traces a PDR around the H II region that is accelerated by the radiative pressure from the central source, so that the back side is red-shifted and the front blue shifted relative to the systemic velocity of the medium. However, the observations show the existence of some asymmetry between the expanding and receding layer and part of the central dip could also stem from self-absorption in the optically thick line.

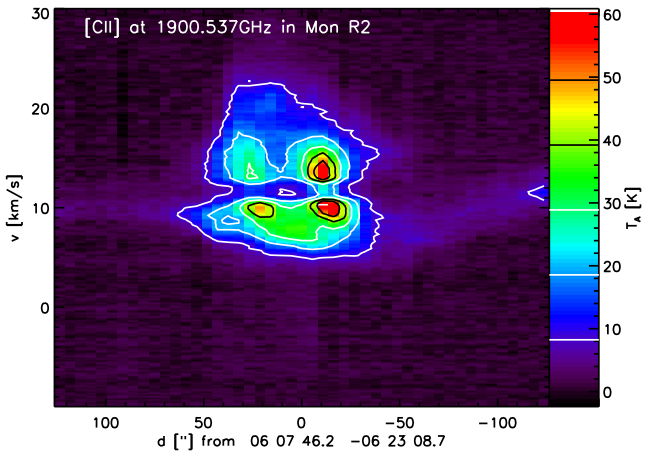


Fig. 10. Position-velocity diagram of the [C II] line for the measured cut through the Mon R2 PDR.

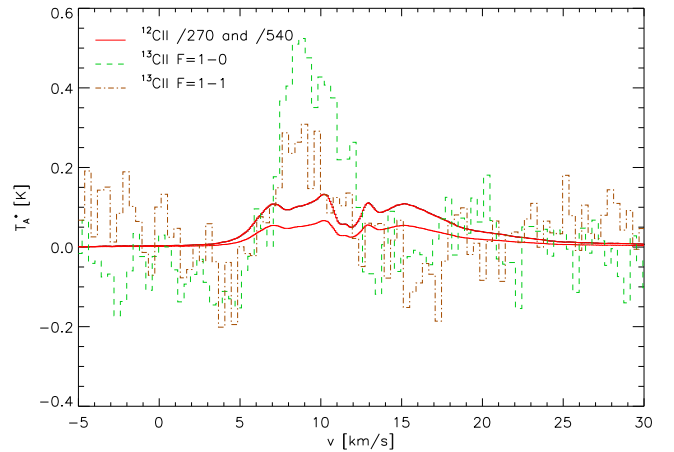


Fig. 11. Comparison of the profiles of the [^{13}C II] hyperfine lines in Mon R2 with the [C II] profile in the same spectrum scaled by the factors 0.25/67 and 0.125/67. The [^{13}C II] $F=2-1$ component is blended with the main isotopic line so that is not shown here.

4.2.2. [^{13}C II]

The dual-beam-switch observations of the [^{13}C II] lines were performed at the center position of the OTF strip (position 0 in Fig. 10), i.e. not at the peak of the [C II] emission. Future follow-up observations at the peak position will provide a better accuracy.

Figure 11 shows the line profiles of the [^{13}C II] components compared to the corresponding [C II] spectrum, scaled by the factor 0.25/67 and 0.125/67 indicating the expected strength of the $F = 1 - 0$ and $F = 1 - 1$ hyperfine components in case of optically thin emission and a canonical abundance ratio (see Sect. 3.1). Due to the large width of the [C II] line, the $F = 2 - 1$ component falls in the wing of the [C II] emission, so that we cannot estimate its strength. The striking result for the other two transitions is the large difference in the spectral shape compared to the main isotopic line. The two hyperfine components are consistent with each other in terms of the spectral shape, peaking at about 9 km s^{-1} and in terms of the intensity ratio of about a factor two. The peak agrees with a flat-top emission part of the [C II] line that would be characteristic for optically thick emission and is about three times brighter than the scaled blue [C II]

component. This is not reflected in the average optical depth $\langle \tau \rangle$ derived from the integrated line in Table 2 due to the strong mutual difference in the line shapes. To get an estimate for the two main velocity components, we have split the integration interval at 12.5 km s^{-1} and include the corresponding results in Table 2. This increases the relative uncertainties, but allows to derive independent quantitative results for the components that show a very different behavior. For the blue-shifted foreground component, we find the highest [C II] optical depth in our sample.

The big surprise is the complete absence of redshifted emission from the back of the H II region in [^{13}C II]. The red-shifted [C II] line has approximately the same brightness as the blue component, but any possible [^{13}C II] emission must be weaker than expected from optically thin emission and normal abundance ratios. For both hyperfine components an emission at the 0.1 K level can be excluded in spite of the baseline uncertainties. This indicates the direct observation of fractionation in a PDR driving an enhanced $^{12}\text{C}^+ / ^{13}\text{C}^+$ ratio. However, when considering the extreme uncertainties in Table 2, stemming from all possible baseline subtractions and the possibility that the redshifted [C II] line might be optically thin while the blueshifted line has an optical depth > 3 , the error bars for the $^{12}\text{C}^+ / ^{13}\text{C}^+$ fractionation ratio still cover the standard elemental isotopic ratio so that even this case is not unambiguous.

4.3. NGC 3603, Carina, and NGC 7023

Figure 12 shows the spectra for NGC 3603, Carina North, and NGC 7023, obtained in the same way as Fig. 11 for Mon R2. As discussed in Sect. 3.2, in NGC 3603 and Carina the $F = 2 - 1$ component falls into a [C II] spectral feature resulting from self-chopping in the observation, so that it cannot be resolved. The two weaker components are resolved. There is no indication for a spectral difference with respect to the [C II] line and the mutual line ratio reflects the expected value from Sect. 3.1. In both sources, the [^{13}C II] lines are about 2.5 times stronger than expected from optically thin [C II] emission and the normal abundance ratio. The increase indicates an optical depth in the main isotopic line of $2.2 - 2.4$.

The equivalent observation of the Carina South PDR, provided no detections of [^{13}C II]. At the frequency of the $F = 2 - 1$ transition we find a weak emission component, but we rather attribute this to a separate [C II] velocity component in the complex velocity profile. As the [C II] line brightness was more than three times weaker than in the other sources, the non-detection is consistent with the expected line strength in the optically thin case or cases with a moderate [^{13}C II] line enhancement as in the other sources.

The narrow [C II] line in NGC 7023 is well separated from the [^{13}C II] $F = 2 - 1$ component, so that this is the only observation in which we resolve all three hyperfine components. Moreover the narrow lines provide a very small uncertainty for the line intensity from the baseline subtraction so that we get quite accurate relative intensities. The average optical depth enhancement of the [^{13}C II] lines is moderate, but we also find a significantly different behavior of different velocity components resolved in the [C II] line. The [^{13}C II] lines mainly trace the component at 2.8 km s^{-1} corresponding to the molecular material in the PDR (see e.g. Gerin et al. 1998). Here, we find a significant optical depth of the [C II] line in terms of a decreased [C II]/[^{13}C II] intensity ratio. The component at 4 km s^{-1} was identified as separate filament by Fuente et al. (1996) and associated with ionized material in the cavity by Joblin et al. (2010). It is also seen in [^{13}C II] and shows an intensity ratio correspond-

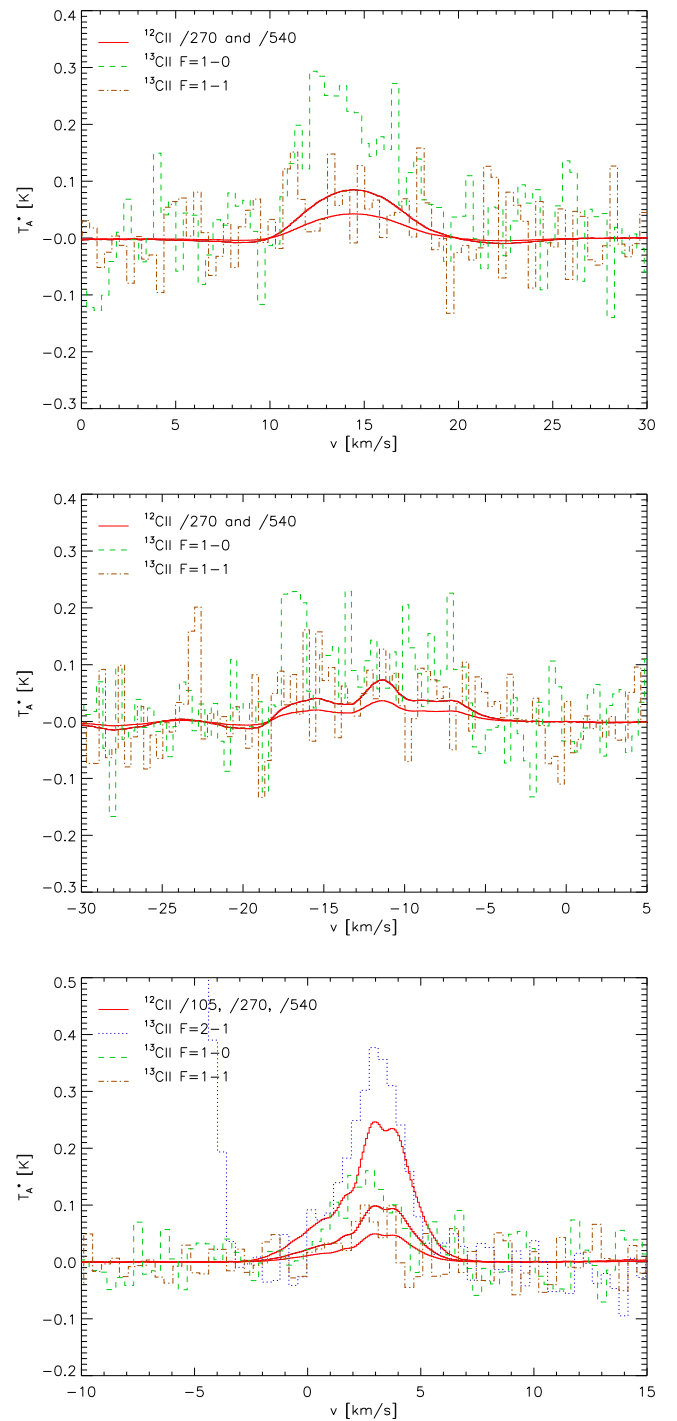


Fig. 12. Comparison of the profiles of the [^{13}C II] hyperfine lines in NGC 3603 MM2 (upper panel), the Carina North PDR (central panel), and NGC 7023 North (lower panel) with the [C II] profiles from the same positions scaled by the factors corresponding to optically thin emission and the standard abundance ratio for the resolved hyperfine components. For NGC 3603 MM2 and Carina North, the [^{13}C II] $F=2-1$ component falls into a self-chopping feature of the main isotopic line so that is not shown here.

ing to the elemental isotopic ratio. Finally there is a high velocity wing with velocities around 0 km s^{-1} . This component may show an increased $^{12}\text{C}^+ / ^{13}\text{C}^+$ fractionation ratio through [^{13}C II] intensities below the scaled [C II] intensity for all three hyperfine components. However, our signal-to-noise ratio is not

good enough to derive a definite statement on the [C II]/[^{13}C II] intensity ratio in that wing. Due to the almost Gaussian velocity components, the estimate of the C $^+$ column density from the integrated line parameters should be a reasonable average by slightly underestimating the optical depth from the PDR and slightly overestimating the contribution from the ionized gas in the cavity. For a total column density $N_{\text{H}} \approx 1.3 \times 10^{22} \text{ cm}^{-2}$ at the position of our observation (Joblin et al. 2010) this indicates that more than half of the carbon in the gas phase is in the form of C $^+$.

5. Discussion

The detection of carbon fractionation under dense cloud conditions remains difficult. For the two species involved in the most important carbon fractionation reaction, C $^+$ and CO, the lines of the main isotopologue are often optically thick with a considerable uncertainty in the optical depth. Consequently, it is hard to determine the absolute column density and the CO/ ^{13}CO or C $^+/\text{^{13}C}^+$ ratio. Our observations and simulations have confirmed this general knowledge for the C $^+/\text{^{13}C}^+$ ratio. Observations of $^{13}\text{C}^{18}\text{O}$ are a possible way out, but challenging due to the low line intensities, biased towards high column densities, and they cannot trace the impact of isotope-selective photodissociation provided by the self-shielding of the main isotopologue.

Our model predictions for PDRs indicate that the observed fractionation ratio in all tracers is dominated by the chemical fractionation reaction (C1) while isotopic-selective photodissociation plays a minor role. The chemical fractionation increases the C $^+/\text{^{13}C}^+$ ratio relative to the elemental isotopic ratio in the gas. In terms of the observable [C II]/[^{13}C II] ratio, this could lead to an increase by a factor of a few under favorable conditions. They can be provided by inner layers of moderate density, moderate UV PDRs or by dense gas that is exposed to low UV fields like clumps in an inhomogeneous PDR, embedded in and partially shielded by a thinner interclump medium. The main condition for an observable increase of the [C II]/[^{13}C II] ratio is, however, that geometry and velocity distribution prevent a large [C II] optical depth. In most geometries, the conditions providing an increased isotopic ratio are paired with high optical depths of the [C II] line that rather reduces the [C II]/[^{13}C II] intensity ratio below the canonical value.

Our observations show that most of the [C II] emission must stem from a widely distributed, low-density component in PDRs, being more smoothly distributed than many high-density tracers. Only in Mon R2, where the H II region is still expanding into the surrounding high-density core, a probably relatively homogeneous high-density PDR is formed. The observational results on the [C II]/[^{13}C II] intensity ratio roughly follow the predictions from the models in Sect.2 without providing enough statistics for a qualitative confirmation yet. For most of the PDRs, the average [C II]/[^{13}C II] intensity ratio is reduced compared to the isotopic ratio due to the optical thickness of the [C II] line. Details strongly depend on the exact geometry. Assuming the standard elemental ratio for the C $^+/\text{^{13}C}^+$ abundance ratio, we can measure the optical depth and consequently the C $^+$ column density through the intensity ratio. The optical depth of the main isotopic line varies considerably across the line profile and between the different PDRs, showing peak values above three for the Orion Bar and Mon R2.

Indications for an increased [C II]/[^{13}C II] intensity ratio are found when studying details of the line profiles allowing to distinguish different velocity components in the same source. In

three cases, we find components showing C $^+$ fractionation in a PDR. Unfortunately, none of them allows to unambiguously quantify the degree of fractionation due to the large error bars from the noise and baseline uncertainties (see Table 2). The clearest case is the non-detection of [^{13}C II] in the red-shifted component in Mon R2. If we interpret the red component as the receding inner backside of the expanding H II region, it represents a dense, face-on PDR layer which should be at least partially optically thick in [C II]. As the front side shows the same integrated [C II] intensity, but no fractionation and a very high [C II] optical depth instead, the actual configuration must be asymmetric. The situation is even more puzzling as our models predict negligible fractionation for this high-UV field PDR. Further high-resolution observations are required to understand why the red-shifted material differs from the front material. The second case is provided by the wings of the line profiles in the Orion Bar, probably created by diffuse gas with a broader velocity distribution. It may represent extended, possibly diffuse H II gas in the Orion veil. To confirm this origin, deeper integrations in positions apart from the Orion Bar are needed. A final case may be given by the blue wing material seen in NGC 7023. However, in all three cases the step from a pure detection of fractionation to a full quantitative assessment requires observations with a somewhat better signal-to-noise ratio than obtained here.

Acknowledgements. This work was supported by the *Deutsche Forschungsgemeinschaft*, DFG project number Os 177/1-1 and SFB 956 C1. Additional support for this paper was provided by NASA through an award issued by JPL/Caltech and by Spanish program CONSOLIDAR INGENIO 2010, under grant CSD2009-00038 Molecular Astrophysics: The Herschel and ALMA Era (ASTROMOL). We thank Paul Goldsmith and an anonymous referee for many helpful comments.

HIFI has been designed and built by a consortium of institutes and university departments from across Europe, Canada and the US under the leadership of SRON Netherlands Institute for Space Research, Groningen, The Netherlands with major contributions from Germany, France and the US. Consortium members are: Canada: CSA, U.Waterloo; France: CESR, LAB, LERMA, IRAM; Germany: KOSMA, MPIfR, MPS; Ireland, NUI Maynooth; Italy: ASI, IFSI-INAF, Arcetri-INAF; Netherlands: SRON, TUD; Poland: CAMK, CBK; Spain: Observatorio Astronómico Nacional (IGN), Centro de Astrobiología (CSIC-INTA); Sweden: Chalmers University of Technology - MC2, RSS & GARD, Onsala Space Observatory, Swedish National Space Board, Stockholm University - Stockholm Observatory; Switzerland: ETH Zürich, FHNW; USA: Caltech, JPL, NHSC.

References

- Bergin, E. A. & Herschel Hexos Team. 2011, in IAU Symposium, Vol. 280, IAU Symposium, 93P
- Boreiko, R. T. & Betz, A. L. 1996, ApJ, 467, L113+
- Boreiko, R. T., Betz, A. L., & Zmuidzinas, J. 1988, ApJ, 325, L47
- Burgh, E. B., France, K., & McCandliss, S. R. 2007, ApJ, 658, 446
- Cooksey, A. L., Blake, G. A., & Saykally, R. J. 1986, ApJ, 305, L89
- de Graauw, T., Helmich, F. P., Phillips, T. G., et al. 2010, A&A, 518, L6+
- Draine, B. T. 1978, ApJS, 36, 595
- Flannery, B. P., Robege, W., & Rybicki, G. B. 1980, ApJ, 236, 598
- Flower, D. R. & Launay, J. M. 1977, Journal of Physics B Atomic Molecular Physics, 10, 3673
- Fuente, A., Berné, O., Cernicharo, J., et al. 2010, A&A, 521, L23+
- Fuente, A., Martin-Pintado, J., Neri, R., Rogers, C., & Moriarty-Schieven, G. 1996, A&A, 310, 286
- Garstang, R. H. 1995, ApJ, 447, 962
- Gerin, M., Phillips, T. G., Keene, J., Betz, A. L., & Boreiko, R. T. 1998, ApJ, 500, 329
- Ginard, D., González-García, M., Fuente, A., et al. 2012, A&A, 543, A27
- Graf, U. U., Simon, R., Stutzki, J., et al. 2012, A&A, in press
- Herrmann, F., Madden, S. C., Nikola, T., et al. 1997, ApJ, 481, 343
- Hogerheijde, M. R., Jansen, D. J., & van Dishoeck, E. F. 1995, A&A, 294, 792
- Joblin, C., Pilleri, P., Montillaud, J., et al. 2010, A&A, 521, L25
- Keene, J., Schilke, P., Kooi, J., et al. 1998, ApJ, 494, L107+
- Langer, W. D., Graedel, T. E., Frerking, M. A., & Armentrout, P. B. 1984, ApJ, 277, 581

- Langer, W. D. & Penzias, A. A. 1990, ApJ, 357, 477
 Langer, W. D. & Penzias, A. A. 1993, ApJ, 408, 539
 Launay, J.-M. & Roueff, E. 1977, Journal of Physics B Atomic Molecular Physics, 10, 879
 Lis, D. C. & Schilke, P. 2003, ApJ, 597, L145
 Liszt, H. S. 2007, A&A, 476, 291
 Menten, K. M., Reid, M. J., Forbrich, J., & Brunthaler, A. 2007, A&A, 474, 515
 Mookerjea, B., Ghosh, S. K., Kaneda, H., et al. 2003, A&A, 404, 569
 Natta, A., Walmsley, C. M., & Tielens, A. G. G. M. 1994, ApJ, 428, 209
 Okada, Y., Pilleri, P., Berné, O., et al. 2012, A&A, submitted.
 Ossenkopf, V., Röllig, M., Kramer, C., et al. 2011, in EAS Publications Series, Vol. 52, EAS Publications Series, ed. M. Röllig, R. Simon, V. Ossenkopf, & J. Stutzki, 181–186
 Ott, S. 2010, in Astronomical Society of the Pacific Conference Series, Vol. 434, Astronomical Data Analysis Software and Systems XIX, ed. Y. Mizumoto, K.-I. Morita, & M. Ohishi, 139–
 Phillips, T. G., Huggins, P. J., Wannier, P. G., & Scoville, N. Z. 1979, ApJ, 231, 720
 Pilbratt, G. L., Riedinger, J. R., Passvogel, T., et al. 2010, A&A, 518, L1+
 Pilleri, P., Fuente, A., Cernicharo, J., et al. 2012a, A&A, 544, A110
 Pilleri, P., Montillaud, J., Berné, O., & Joblin, C. 2012b, A&A, 542, A69
 Roelfsema, P. R., Helmich, F. P., Teyssier, D., et al. 2012, A&A, 537, A17
 Röllig, M., Abel, N. P., Bell, T., et al. 2007, A&A, 467, 187
 Röllig, M., Kramer, C., Rajbahak, C., et al. 2011, A&A, 525, A8+
 Röllig, M. & Ossenkopf, V. 2012, A&A, submitted, paper I.
 Sakai, N., Saruwatari, O., Sakai, T., Takano, S., & Yamamoto, S. 2010, A&A, 512, A31
 Schaefer, H. F. & Klemm, R. A. 1970, Phys. Rev. A, 1, 1063
 Sheffer, Y., Rogers, M., Federman, S. R., Lambert, D. L., & Gredel, R. 2007, ApJ, 667, 1002
 Simon, R., Stutzki, J., Sternberg, A., & Winnewisser, G. 1997, A&A, 327, L9
 Smith, N. 2006, MNRAS, 367, 763
 Sonnentrucker, P., Welty, D. E., Thorburn, J. A., & York, D. G. 2007, ApJS, 168, 58
 Sorochenko, R. L. & Tsivilev, A. P. 2000, Astronomy Reports, 44, 426
 Stacey, G. J., Jaffe, D. T., Geis, N., et al. 1993, ApJ, 404, 219
 Stolte, A., Brandner, W., Brandl, B., & Zinnecker, H. 2006, AJ, 132, 253
 Stutzki, J., Bensch, F., Heithausen, A., Ossenkopf, V., & Zielinsky, M. 1998, A&A, 336, 697
 van den Ancker, M. E., The, P. S., Tjin A Djie, H. R. E., et al. 1997, A&A, 324, L33
 van der Werf, P. P., Stutzki, J., Sternberg, A., & Krabbe, A. 1996, A&A, 313, 633
 van der Wiel, M. H. D., van der Tak, F. F. S., Ossenkopf, V., et al. 2009, A&A, 498, 161
 Visser, R., van Dishoeck, E. F., & Black, J. H. 2009, A&A, 503, 323
 Wakelam, V. & Herbst, E. 2008, ApJ, 680, 371
 Walmsley, C. M., Natta, A., Oliva, E., & Testi, L. 2000, A&A, 364, 301
 Wiese, W. & Fuhr, J. 2007, J. Phys. Chem. Ref. Data, 36, 1287
 Wilson, N. J. & Bell, K. L. 2002, MNRAS, 337, 1027
 Wilson, T. L. 1999, Reports on Progress in Physics, 62, 143
 Wyrowski, F., Schilke, P., Hofner, P., & Walmsley, C. M. 1997, ApJ, 487, L171
 Xu, Y., Shen, Z.-Q., Yang, J., et al. 2006, AJ, 132, 20

Lebenslauf

Name: Markus Röllig
Geburtsdatum: 22.11.1969, Offenbach a.M.

Schulbildung:

1976-1982: Grundschule & Förderstufe Eichendorffschule, Obertshausen
1982-1986: Gymnasium, Hermann-Hesse Schule Obertshausen
1986-1989: Gymnasiale Oberstufe,
Technisch-Gewerbliche Schulen Offenbach a.M.
19.05.1989: Abitur

Zivildienst:

1989-1990: Rettungsdienst, Deutsches Rotes Kreuz, Offenbach a.M.

Studium:

1990-1992: Studium der Physik an der T.H. Darmstadt
30.09.1992 Vordiplom-Physik an der T.H. Darmstadt
1992-1997: Studium der Physik und der Wirtschaftswissenschaften an
der J.W.Goethe-Universität Frankfurt a.M.
13.05.1994: Vordiplom in Betriebswirtschaftslehre
10.07.1997: Physik-Diplom
Diplomarbeit am Inst. für Theoretische Physik bei
Prof.Dr. W.H. Kegel,
Thema: *A-Typ Methanol Maser in interstellaren Molekülwolken unter Berücksichtigung von IR/HII Quellen und Linienüberlapp*
07/1997-01/2002 Promotion am Inst. für Theoretische Physik bei
Prof.Dr. W.H. Kegel
Thema: *Der Einfluss von turbulenten Strömungen auf die Photodissoziation von CO in interstellaren Wolken*

Berufserfahrung:

1997-1998	Stipendiat der FAZIT Stiftung/PhD Student, Frankfurt am Main
1998-2001	wissenschaftlicher Angestellter (Teilzeit)/PhD Student am Institut für Theoretische Physik der J.W. Goethe Universität in Frankfurt am Main
1999-12/2001	IT-Berater (Teilzeitstelle), USD GmbH, Langen
01/2002-12/2002	Forschungsassistent am Institut für Theoretische Physik der J.W. Goethe Universität in Frankfurt am Main
01/2003-06/2006	wissenschaftlicher Angestellter/Post-Doc am I. Physikalisches Institut der Universität zu Köln
06/2006-12/2007	wissenschaftlicher Angestellter/Post-Doc am Argelander-Institut für Astronomie der Universität Bonn
seit 2008	wissenschaftlicher Angestellter/Post-Doc am I. Physikalisches Institut der Universität zu Köln

Berufliche Weiterbildung:

• **Astronomische Beobachtungen**

15m Heinrich-Hertz-Teleskop (HHT), Mount Graham, Arizona, USA (2001),
4m NANTEN2, Pampa La Bola, Chile (2006,2008,2009,2010).

• **Arbeitsbesuche und Forschungsaufenthalte**

Tel Aviv University, Israel, Planung und Vorbereitung des PDR Benchmarks (2004), Nikolaus Kopernicus Institut, Torun, Polen, Integration der Staubphysik in KOSMA- τ (2006,2008), CEA Saclay, Frankreich, PDR Modellierung von Objekten mit niedriger Metallizität (2006), Lorentz Center, Leiden, Niederlande, Workshops zu *PDR Comparison Workshop* und *Exciting CO in the local and high-redshift universe* (2004 und 2012)

Publikationsliste

Bücher/Konferenzproceedings

1. M. Röllig, R. Simon, V. Ossenkopf u. a., Hrsg. (Nov. 2011). *Conditions and Impact of Star Formation*. Bd. 52. EAS Publications Series

Referierte Veröffentlichungen

45. V. Ossenkopf, M. Röllig, D. A. Neufeld u. a. (Nov. 2012). „Herschel/HIFI observations of [CII] and [^{13}CII] in PDRs“. In: *ArXiv e-prints, accepted for publication in A&A*
44. M. Röllig und V. Ossenkopf (Nov. 2012). „Carbon fractionation in PDRs“. In: *ArXiv e-prints, accepted for publication in A&A*
43. M. Röllig, R. Szczerba u. a. (Nov. 2012). „Full SED fitting with the KOSMA- τ PDR code - I. Dust modelling“. In: *ArXiv e-prints, accepted for publication in A&A*
42. T. Möller u. a. (Okt. 2012). „Modeling and Analysis Generic Interface for eXternal numerical codes (MAGIX)“. In: *ArXiv e-prints*
41. J. L. Pineda, N. Mizuno, M. Röllig u. a. (Aug. 2012). „Submillimeter line emission from LMC 30 Doradus: The impact of a starburst on a low-metallicity environment“. In: *A&A* 544, A84, A84
40. M. Röllig, R. Simon, R. Güsten u. a. (Juni 2012). „[CII] gas in IC 342“. In: *A&A* 542, L22, S. L22
39. N. Schneider u. a. (Juni 2012). „Globules and pillars seen in the [CII] 158 μm line with SOFIA“. In: *A&A* 542, L18, S. L18
38. Y. Okada, R. Güsten u. a. (Juni 2012). „Dynamics and photodissociation region properties in IC 1396A“. In: *A&A* 542, L10, S. L10

37. P. Gratier u. a. (Juni 2012b). „Giant molecular clouds in the Local Group galaxy M 33★“. In: *A&A* 542, A108, A108
36. F. Combes u. a. (März 2012). „Dust and gas power spectrum in M 33 (HERM33ES)“. In: *A&A* 539, A67, A67
35. F. F. S. van der Tak u. a. (Jan. 2012). „Detection of HF emission from the Orion Bar“. In: *A&A* 537, L10, S. L10
34. B. Mookerjea u. a. (Jan. 2012). „The Herschel M 33 extended survey (HerM33es): PACS spectroscopy of the star forming region BCLMP 302 (Corrigendum)“. In: *A&A* 537, C3, S. C3
33. B. Mookerjea u. a. (Aug. 2011). „The Herschel M 33 extended survey (HerM33es): PACS spectroscopy of the star-forming region BCLMP 302“. In: *A&A* 532, A152, A152
32. J. R. Goicoechea u. a. (Juni 2011). „OH emission from warm and dense gas in the Orion Bar PDR“. In: *A&A* 530, L16, S. L16
31. M. Röllig (Juni 2011). „Refit to numerically problematic UMIST reaction rate coefficients“. In: *A&A* 530, A9, A9
30. M. Röllig, C. Kramer u. a. (Jan. 2011). „Photon dominated regions in NGC 3603. [CI] and mid-J CO line emission“. In: *A&A* 525, A8, A8
29. P. Gratier, J. Braine, N. J. Rodriguez-Fernandez, K. F. Schuster, C. Kramer, E. M. Xilouris, F. S. Tabatabaei, C. Henkel, E. Corbelli, F. Israel, P. P. van der Werf, D. Calzetti, S. Garcia-Burillo, A. Sievers, F. Combes, T. Wiklind, N. Brouillet, F. Herpin, S. Bontemps, S. Aalto, B. Koribalski, F. van der Tak, M. C. Wiedner, M. Röllig u. a. (Nov. 2010). „Molecular and atomic gas in the Local Group galaxy M 33“. In: *A&A* 522, A3, A3
28. C. Joblin u. a. (Okt. 2010). „Gas morphology and energetics at the surface of PDRs: New insights with Herschel observations of NGC 7023“. In: *A&A* 521, L25, S. L25
27. C. Dedes u. a. (Okt. 2010). „The origin of the [C II] emission in the S140 photon-dominated regions. New insights from HIFI“. In: *A&A* 521, L24, S. L24
26. A. Fuente u. a. (Okt. 2010). „Herschel observations in the ultracompact HII region Mon R2. Water in dense photon-dominated regions (PDRs)“. In: *A&A* 521, L23, S. L23

25. A. F. Loenen u. a. (Okt. 2010). „Excitation of the molecular gas in the nuclear region of M 82“. In: *A&A* 521, L2, S. L2
24. A. Weiß u. a. (Okt. 2010). „HIFI spectroscopy of low-level water transitions in M 82“. In: *A&A* 521, L1, S. L1
23. E. Falgarone u. a. (Juli 2010). „Strong CH⁺ J = 1-0 emission and absorption in DR21“. In: *A&A* 518, L118, S. L118
22. V. Ossenkopf, H. S. P. Müller u. a. (Juli 2010). „Detection of interstellar oxidaniumyl: Abundant H₂O⁺ towards the star-forming regions DR21, Sgr B2, and NGC6334“. In: *A&A* 518, L111, S. L111
21. V. Ossenkopf u. a. (Juli 2010b). „HIFI observations of warm gas in DR21: Shock versus radiative heating“. In: *A&A* 518, L79, S. L79
20. M. Boquien u. a. (Juli 2010). „100 μm and 160 μm emission as resolved star-formation rate estimators in M 33 (HERM33ES)“. In: *A&A* 518, L70, S. L70
19. J. Braine u. a. (Juli 2010). „Cool gas and dust in M 33: Results from the HERschel M 33 Extended Survey (HERM33ES)“. In: *A&A* 518, L69, S. L69
18. C. Kramer, C. Buchbender u. a. (Juli 2010). „PACS and SPIRE photometer maps of M 33: First results of the HERschel M 33 Extended Survey (HERM33ES)“. In: *A&A* 518, L67, S. L67
17. K. Sun, V. Ossenkopf u. a. (Okt. 2008). „The photon dominated region in the IC 348 molecular cloud“. In: *A&A* 489, S. 207–216
16. M. Cubick, J. Stutzki u. a. (Sep. 2008). „A clumpy-cloud photon-dominated regions model of the global far-infrared line emission of the Milky Way“. In: *A&A* 488, S. 623–634
15. J. L. Pineda, N. Mizuno, J. Stutzki u. a. (Apr. 2008). „Submillimeter line emission from LMC N159W: a dense, clumpy PDR in a low metallicity environment“. In: *A&A* 482, S. 197–208
14. M. Hitschfeld u. a. (Feb. 2008). „¹²CO 4-3 and [CI] 1-0 at the centers of NGC 4945 and Circinus“. In: *A&A* 479, S. 75–82
13. C. Kramer, M. Cubick u. a. (Jan. 2008). „Clumpy photon-dominated regions in Carina. I. [C I] and mid-J CO lines in two 4'×4' fields“. In: *A&A* 477, S. 547–555

12. M. Cubick u. a. (Sep. 2007). „PDR Modelling of the Galactic FIR line emission“. In: *Astronomische Nachrichten* 328, S. 643
11. M. Röllig, N. P. Abel u. a. (Mai 2007). „A photon dominated region code comparison study“. In: *A&A* 467, S. 187–206
10. A. Schulz u. a. (Mai 2007). „The interstellar medium of the Antennae galaxies“. In: *A&A* 466, S. 467–479
9. R. Plume u. a. (Jan. 2007). „The James Clerk Maxwell Telescope Spectral Legacy Survey“. In: *PASP* 119, S. 102–111
8. B. Mookerjea, C. Kramer, M. Röllig u. a. (Sep. 2006). „Study of photon dominated regions in Cepheus B“. In: *A&A* 456, S. 235–244
7. M. Röllig, V. Ossenkopf, S. Jeyakumar u. a. (Juni 2006). „[CII] 158 μm emission and metallicity in photon dominated regions“. In: *A&A* 451, S. 917–924
6. M. Hegmann u. a. (Jan. 2006). „The formation of interstellar molecular lines in a turbulent velocity field with finite correlation length. IV. Physical parameters of Bok Gobules“. In: *A&A* 445, S. 591–600
5. B. Mookerjea, K. Sun u. a. (Aug. 2005). „CI/CO Mapping of IC 348 and Cepheus B using SMART on KOSMA.“ In: *Astronomische Nachrichten* 326, S. 581–582
4. M. Röllig (Aug. 2005). „[CII]/CO(1-0) line ratio at low metallicities.“ In: *Astronomische Nachrichten* 326, S. 529–530
3. M. Cubick u. a. (Aug. 2005). „PDR modeling of the COBE far-infrared data of the milky way.“ In: *Astronomische Nachrichten* 326, S. 524–525
2. M. Röllig, M. Hegmann und W. H. Kegel (Sep. 2002b). „Photodissociation of CO in turbulent molecular clouds“. In: *A&A* 392, S. 1081–1088
1. M. Röllig, W. H. Kegel u. a. (März 1999). „A search for methanol masers at 9.978 GHz and 10.058 GHz“. In: *A&A* 343, S. 939–942

Unreferierte Veröffentlichungen

24. P. Gratier u. a. (März 2012a). „Giant molecular clouds in M33 (Gratier+, 2012)“. In: *VizieR Online Data Catalog* 354, S. 29108

23. M. Röllig, C. Dedes u. a. (Nov. 2011). „Before and After Herschel - Modeling Photo-Induced Chemistry and PDR Line Emission in the Warm and Dense ISM (WADI)“. In: *EAS Publications Series*. Hrsg. von M. Röllig u. a. Bd. 52. EAS Publications Series, S. 301–302
22. Y. Okada, O. Berné u. a. (Nov. 2011). „PDR properties and spatial structures probed by Herschel and Spitzer spectroscopy“. In: *EAS Publications Series*. Hrsg. von M. Röllig u. a. Bd. 52. EAS Publications Series, S. 293–294
21. V. Ossenkopf, M. Röllig, C. Kramer u. a. (Nov. 2011). „The WADI key project: New insights to photon-dominated regions from Herschel observations“. In: *EAS Publications Series*. Hrsg. von M. Röllig u. a. Bd. 52. EAS Publications Series, S. 181–186
20. I. Bernst u. a. (Juli 2011). „MAGIX: A Generic Tool for Fitting Models to Astrophysical Data“. In: *Astronomical Data Analysis Software and Systems XX*. Hrsg. von I. N. Evans u. a. Bd. 442. Astronomical Society of the Pacific Conference Series, S. 505
19. V. Ossenkopf, M. Rollig, A. Fuente u. a. (Mai 2011). „Carbon fractionation in photon-dominated regions“. In: *IAU Symposium*. Bd. 280. IAU Symposium, 280P
18. R. Simon, V. Ossenkopf und M. Röllig (Nov. 2010). „JD14 - Examining the PDR-molecular cloud interface at mm and IR wavelengths“. In: *Highlights of Astronomy* 15, S. 399–400
17. P. Gratier, J. Braine, N. J. Rodriguez-Fernandez, K. F. Schuster, C. Kramer, E. M. Xilouris, F. S. Tabatabaei, C. Henkel, E. Corbelli, F. Israel, P. P. van der Werf, D. Calzetti, S. Garcia-Burillo, A. Sievers, F. Combes, T. Wiklind, N. Brouillet, F. Herpin, S. Bontemps, S. Aalto, B. Koribalski, F. van der Tak, M. C. Wiedner, M. Rollig u. a. (Okt. 2010). „M33 CO(2-1) and HI integrated intensity maps (Gratier+, 2010)“. In: *VizieR Online Data Catalog* 352, S. 29003
16. V. Ossenkopf, M. Gerin, G. Rolf u. a. (2010). „The chemistry of the warm and dense ISM seen by Herschel“. In: *38th COSPAR Scientific Assembly*. Bd. 38. COSPAR Meeting, S. 2478
15. K. Sun, C. Kramer, H. Ungerechts u. a. (2008). „A Multiline Study of the Cepheus B Cloud“. In: *EAS Publications Series*. Hrsg. von C. Kramer, S. Aalto und R. Simon. Bd. 31. EAS Publications Series, S. 209–210

14. R. Simon, N. Schneider u. a. (2008). „The PDR structure of the Monoceros Ridge in the Rosette Molecular Cloud“. In: *EAS Publications Series*. Hrsg. von C. Kramer, S. Aalto und R. Simon. Bd. 31. EAS Publications Series, S. 205–207
13. V. Ossenkopf, M. Gerin, R. Güsten u. a. (2008). „Prospectives of Herschel PDR observations“. In: *EAS Publications Series*. Hrsg. von C. Kramer, S. Aalto und R. Simon. Bd. 31. EAS Publications Series, S. 193–194
12. M. Röllig (2008). „Metallicity Effects in PDRs“. In: *EAS Publications Series*. Hrsg. von C. Kramer, S. Aalto und R. Simon. Bd. 31. EAS Publications Series, S. 129–135
11. M. Cubick u. a. (2008). „Modelling of clumpy photon dominated regions“. In: *EAS Publications Series*. Hrsg. von C. Kramer, S. Aalto und R. Simon. Bd. 31. EAS Publications Series, S. 19–22
10. V. Ossenkopf, M. Rollig, M. Cubick u. a. (Dez. 2007). „What are molecular clouds? - PDRs everywhere“. In: *Molecules in Space and Laboratory*
9. K. Sun, C. Kramer, B. Mookerjea u. a. (2007). „Study of photon dominated regions in IC 348“. In: *IAU Symposium*. Hrsg. von B. G. Elmegreen und J. Palous. Bd. 237. IAU Symposium, S. 477–477
8. B. Mookerjea, C. Kramer und M. Roellig (Dez. 2005). „Emission from the Photon Dominated Regions in Cepheus B“. In: *American Astronomical Society Meeting Abstracts*. Bd. 37. Bulletin of the American Astronomical Society, S. 1303
7. M. Röllig, V. Ossenkopf und J. Stutzki (Aug. 2004). „The Surface Temperature of PDFs under Varying Metallicity Conditions“. In: *Astronomische Nachrichten Supplement* 325, S. 97
6. M. Röllig, S. Jeyakumar und J. Stutzki (Juli 2003). „The CII-Layer of Low Metallicity PDR's“. In: *Astronomische Nachrichten Supplement* 324, S. 131
5. M. Hegmann u. a. (Juli 2003). „Physical Parameters of Bok Globules“. In: *Astronomische Nachrichten Supplement* 324, S. 130
4. M. Röllig, M. Hegmann und W. H. Kegel (2001). „Photodissociation of CO in Turbulent Media“. In: *Astronomische Gesellschaft Meeting Abstracts*. Hrsg. von E. R. Schielicke. Bd. 18. Astronomische Gesellschaft Meeting Abstracts, S. 82

3. M. Röllig, M. Hegmann, C. Hengel u. a. (2000). „Formation of CO in turbulent PDR's“. In: *Young European Radio Astronomers' Conference* (YERAC)
2. C. Hengel u. a. (2000). „Determination of the physical parameters of Bok-globules by means of a stochastical radiative transfer method“. In: *Young European Radio Astronomers' Conference* (YERAC)
1. M. Hegmann u. a. (2000). „Fitting a Turbulent Cloud Model to CO Observations of Starless Bok Globules“. In: *Astronomische Gesellschaft Meeting Abstracts*. Hrsg. von R. E. Schielicke. Bd. 17. Astronomische Gesellschaft Meeting Abstracts, S. 10